THE PHYSICAL REVIEW

VOLUME 96 SECOND SERIES NUMBER 4

NOVEMBER 15, 1954

Published for the

AMERICAN PHYSICAL SOCIETY

by the

AMERICAN INSTITUTE OF PHYSICS

Lancaster, Pa., and New York, N. Y.

THE
PHYSICAL REVIEW

A journal of experimental and theoretical physics established by E. L. Nichols in 1893

SECOND SERIES, VOL. 96, No. 4 NOVEMBER, 15, 1954

Reflection of Waves by an Inhomogeneous Medium*

V. A. BAILEY
Ionosphere Research Laboratory, The Pennsylvania State University, State College, Pennsylvania
(Received March 15, 1954)

A new approximate solution is given for the general linear second-order differential equation which is especially appropriate in treating the reflection of waves by an inhomogeneous medium. The well-known approximations to a fundamental pair of solutions made by Liouville, Rayleigh, and Jeffreys, which suffer from singularities at the zeros of a particular function, are replaced by another pair of simple approximations u_1, u_2, which in general agree well with the first pair but remain finite at the zeros. Then a corresponding approximation ρ_1 is obtained for ρ, the coefficient of reflection of plane waves by a specified inhomogeneous medium. Also iterative processes are given which from ρ_1 (or any other approximation) derive a sequence of approximations ρ_2, ρ_3, $\cdots$, which rapidly converge on ρ. Lastly it is shown that the approximation u_1 for a particular equation leads to a good, simple approximation to the Hankel function $H_n^{(2)}(nz)$ which agrees well with the approximations of Hankel, Debye, and Carlini but has a wider range of validity.

1

THE determination of the reflection of plane waves by a medium with a refractive index μ which is an assigned function $\mu(x)$ of but one coordinate x is a problem of great practical and theoretical importance in physics and engineering. The theoretical problem is essentially linked with that of finding a solution to the general linear differential equation of the second order which satisfies two conditions at a given point. The same mathematical problem is fundamental in quantum mechanics.

2

Its solution can always be reduced to that of the normal form

$$d^2u/dx^2+p^2u=0, \tag{1}$$

where $p\equiv p(x)$ is a given function of x (which may be complex). The quantity $p(x)$ may be equal to $2\pi fc^{-1}\mu(x)$ where $\mu(x)$ is the complex refractive index for a radio wave of frequency f which has reached the height x in the ionosphere[1]; or $p^2(x)$ may be proportional to the kinetic energy of a particle in quantum mechanics.

In many important problems, $p^2(x)$ is such that solutions in terms of well-known functions cannot be found. In such problems it is necessary to use approximate solutions such as those discovered by Liouville,[2] Rayleigh,[3] Jeffreys,[4] Langer,[5] and others.[5]

Langer's approximations remain finite near only one zero of $p^2(x)$ and are not easy to use when $p^2(x)$ is complex. Liouville's and Rayleigh's approximations are

$$u_{LR}\sim p^{-\frac{1}{2}}\exp\left(\pm i\int^x p\,dx\right), \tag{2}$$

and are special cases of Jeffreys' approximations,

$$u_J\sim p_0^{-\frac{1}{2}}\exp\left[\pm i\int^x\left(hp_0+\frac{p_1}{2p_0}\right)dx\right], \tag{3}$$

which relate to $p^2(x)$ in the form

$$p^2(x)=h^2p_0^2(x)+hp_1(x),$$

where h is a parameter.

Both u_{LR} and u_J have singularities, at the zeros of $p^2(x)$ and $p_0^2(x)$, respectively, which make it necessary

* The research reported in this note has been sponsored by the Geophysics Research Division of the Air Force Cambridge Research Center, Air Research and Development Command.

[1] For oblique propagation, with the initial angle of incidence θ, we have $p(x)=2\pi fc^{-1}[\mu(x)^2-\sin^2\theta]^{\frac{1}{2}}$.

[2] J. Liouville, J. de Math. **2**, 16 and 418 (1837).

[3] Lord Rayleigh, Proc. Roy. Soc. (London) **A86**, 207 (1912).

[4] H. Jeffreys and B. Jeffreys, *Methods of Mathematical Physics*, Sec. 17.122 (1950).

[5] See E. C. Kemble, *Fundamental Principles of Quantum Mechanics* (1937). It is not clear why so many writers still refer to the approximations of Liouville, Rayleigh, and Jeffreys as the "B.W.K." or "W.B.K." approximations.

to "connect" or "match" them with approximate solutions in terms of Airy integrals or Bessel functions. This procedure has had successes in quantum theory but has not been found very convenient for the study of the reflection of very long waves by the ionosphere.

A pair of simple approximations which are free from these difficulties are the following:

$$u_1=\exp\left(\int^x q\,dx\right), \tag{4}$$

$$u_2=u_1\int^x u_1^{-2}dx, \tag{5}$$

where

$$q=-\frac{p'}{2p}\left[1-\left\{1-\frac{4p^4}{p'^2}\right\}^{\frac{1}{2}}\right], \tag{6}$$

and $p'\equiv dp/dx$.

For u_1 and u_2 are continuous at any zero of p^2, they agree with Jeffreys' approximations u_J, within quantities of order $(1/h)$, at points distant from any zero, and lastly, when $(p^2=-x^m)$, u_1 and u_2 approximate to the known solutions of (1) in terms of cylinder functions of order $n=1/(m+2)$ both when x is very small and when x is very large. [This is shown for u_1 by (31) and (32) below.]

The approximation given by (4) and (6) is suggested by the following discussion. If we set

$$u=\exp\left(\int y\,dx\right), \tag{7}$$

we obtain the Riccati equation,

$$y'+y^2+p^2(x)=0. \tag{8}$$

The substitutions

$$y=pv, \qquad z=\int p\,dx, \tag{9}$$

transform (8) into

$$dv/dz+v^2+2rv+1=0, \tag{10}$$

where

$$r=\frac{1}{2p}\frac{dp}{dz}=\frac{1}{2p^2}\frac{dp}{dx}. \tag{11}$$

When r is constant, solutions of (10) are

$$v_1,v_2=-r\pm(r^2-1)^{\frac{1}{2}}, \tag{12}$$

and the corresponding solutions of (8) are

$$y_1,y_2=-\frac{p'}{2p}\left[1\mp\left\{1-\frac{4p^4}{p'^2}\right\}^{\frac{1}{2}}\right]. \tag{13}$$

When also $|r^2|\ll 1$, we obtain the approximations

$$y_1^{LR},\ y_2^{LR}=-\frac{p'}{2p}\pm ip, \tag{14}$$

which lead to the well-known approximations due to Liouville, Rayleigh, etc., which are given in (2).

Clearly (13) must in general lead to a better approximation than (14). Moreover, by choosing the negative sign before the radical in (13), the corresponding wave function u_1 *is finite at all zeros* and simple poles. This choice of sign is that used in the formula (6).

3

The physical problem is to determine the coefficient of reflection ρ of any kind of plane wave (of wavelength $2\pi k$ in free space) which starts in a uniform medium A of refractive index kp_A, enters at $x=a$ the nonuniform medium B of index $kp(x)$, and emerges at $x=c$ into the uniform medium C of index kp_C.

To satisfy the physical conditions we must take the function

$$y(x)=u'/u \tag{15}$$

as continuous everywhere, and in C take

$$u=u_C=e^{ip_Cx}. \tag{16}$$

From (1), (15), and (16) we see that y is that solution of (8) for which

$$y(c)=ip_C. \tag{17}$$

Since in A we have

$$u_A=A_1e^{ip_A(x-a)}+\rho A_1e^{-ip_A(x-a)},$$

therefore

$$y(a)=y_A(a)=ip_A\left(\frac{1-\rho}{1+\rho}\right),$$

and so

$$\rho=\frac{ip_A-y(a)}{ip_A+y(a)}, \tag{18}$$

where $y(x)$ satisfies (8) and (17).

If now

$$y_0=u_0'/u_0$$

is a *particular* solution of (8) ,then the general solution of (1) is

$$u=u_0+Ku_0\int^x u_0^{-2}dx,$$

where K is any constant, and so by (15) the general solution of (8) is

$$y(x)=y_0+u_0^{-2}\Big/\int_\alpha^x u_0^{-2}dx, \tag{19}$$

where α is an arbitrary constant.

From (19) and (17) we obtain

$$ip_C=y_0(c)+u_0(c)^{-2}\Big/\int_\alpha^c u_0^{-2}dx. \tag{20}$$

On eliminating α between (19) and (20), setting $x=a$ in the resulting expression for $y(x)$, and substituting for

$y(a)$ in (18), we obtain

$$\rho=\frac{\{ip_A-y_0(a)\}f-1}{\{ip_A+y_0(a)\}f+1}, \tag{21}$$

where

$$f=\int_c^a \exp\left(-2\int_a^x y_0dx\right)dx + \frac{\exp\left(-2\int_a^c y_0dx\right)}{ip_C-y_0(c)}. \tag{22}$$

If now we adopt for y_0 the approximation q defined in (6), we obtain the following approximation to ρ:

$$\rho_1=\frac{\{ip_A-q(a)\}f_1-1}{\{ip_A+q(a)\}f_1+1}, \tag{23}$$

where

$$f_1=\int_c^a \exp\left(-2\int_a^x qdx\right)dx+\frac{\exp\left(-2\int_a^c qdx\right)}{ip_C-q(c)}. \tag{24}$$

In a particular case we obtain:

$$\rho_1=[ip_A-q(a)]/[ip_A+q(a)], \tag{25}$$

when p and p' are continuous at $x=c$.

It follows that when p and p' are continuous at both the points $x=c$ and $x=a$, then $\rho_1=0$. This may mean nothing more than that under these conditions $|\rho|$ is small. It is easy to show by means of (18) that $\rho=0$ when p^2 has the complex form

$$p^2=-(x-a)(x-c)i\varphi(x) + \left[\int_a^x (x-a)(x-c)\varphi(x)dx\right]^2, \tag{26}$$

where $\varphi(x)$ is real and finite in the interval $a\leqslant x\leqslant c$, and

$$p_A=\int_a^a (x-a)(x-c)\varphi(x)dx,$$

$$p_C=\int_a^c (x-a)(x-c)\varphi(x)dx.$$

In this example only p is continuous at $x=a$ and c. In order to make also p' continuous we may here set $\varphi(x)=(x-a)(x-c)\psi(x)$, where $\psi(x)$ is finite in the same interval. Then both ρ and ρ_1 are zero.

4

When it is required to obtain a more accurate value of ρ than ρ_1 (or any other approximation), we may use the following iterative process when $p(x)$ is continuous at $x=a$ and $x=c$:

$$\rho_{n+1}(a)=\int_c^a \frac{p'(x)}{2p(x)}\{1+\rho_n(x)^2\} \cdot\exp\left[\int_a^x\left(2ip(s)+\frac{p'(s)}{p(s)}\rho_n(s)\right)ds\right]dx, \tag{27}$$

where $\rho_1(a)$ is given by (23). For it can be shown, first that when $p(x)$ is continuous at $x=a$ and $x=c$ the exact reflection coefficient $\rho(a)$, given by (18), is that solution of the equation[6]

$$\rho'(a)+2ip(a)\rho(a)+\frac{p'(a)}{2p(a)}\{\rho^2(a)-1\}=0, \tag{28}$$

for which $\rho(c)=0$, and then that the sequence of numbers $\rho_n(a)$ given by (27), with a good first approximation $\rho_1(a)$, will converge on this solution with convergence of the second order, i.e., with

$$|\rho-\rho_{n+1}|=O|\rho-\rho_n|^2.$$

When $p(x)$ is discontinuous at $x=a$, (27) and (28) can still be used if we take $p'(x)$ to be very large over a very small range of x and then proceed to the limit at which $p'\to\infty$ and the range$\to 0$.

The relations (27) or (28) may be used also to test the accuracy of any given approximation.

It is interesting to note that when in (27) we set $\rho_1(a)=0$, then we obtain for $\rho_2(a)$ the approximation made by Rayleigh[3] and by Schelkunoff[7] for weak reflection.

Similarly a second-order iteration can be constructed which yields successive approximations $u_2, u_3, \cdots$, to a solution of Eq. (1) starting with any approximation u_1 such as those given in (4) and (5) or those given by Langer[5] and by Miller and Good.[8]

5

If we apply the foregoing results to Rayleigh's example in which

$$p^2=n^2x^{-2},$$

$$a=n/p_A, \quad c=\infty,$$

we obtain from (6) the expression $q=\beta p$, where

$$\beta=\frac{1}{2n}-\left(\frac{1}{4n^2}-1\right)^{\frac{1}{2}},$$

and so, by (23) or (25),

$$\rho=\frac{i-\beta}{i+\beta}=\frac{i}{2n+(4n^2-1)^{\frac{1}{2}}},$$

[6] A similar equation for ρ has been published by L. R. Walker and N. Wax in J. Appl. Phys. **17**, 1043 (1946).

[7] S. Schelkunoff, Report No. EM-37, New York University, November, 1951, (unpublished), p. 117, Eq. (34).

[8] S. C. Miller, Jr., and R. H. Good, Jr., Phys. Rev. **91**, 174 (1953).

which is Rayleigh's exact result (if we note that he used $-i$ where we use i). This expression for ρ is also found to satisfy (28) exactly.

As another application of the approximation u_1, given in (4), we shall use it to determine a particular approximation to the second Hankel function which appears to have a wider range of validity than any one of the well-known approximations. On taking

$$p^2=-x^m, \tag{29}$$

we obtain

$$q=-\frac{m}{4x}[1-(1+16m^{-2}x^{m+2})^{\frac{1}{2}}], \tag{30}$$

and on setting

$$m=n^{-1}-2, \quad x^{m+2}=-\tfrac{1}{4}z^2,$$

and choosing a suitable constant of integration, we obtain, for $m\neq -2$,

$$u_1=2^{\frac{1}{2}}[(1-\alpha^2z^2)^{\frac{1}{2}}+1]^{n-\frac{1}{2}}\exp\{(\tfrac{1}{2}-n)[(1-\alpha^2z^2)^{\frac{1}{2}}-1]\},$$
$$z=2ix^{1/2n}, \quad \alpha=2n/(2n-1). \tag{31}$$

On studying the form of u_1 when $\alpha^2z^2\ll 1$ or $\gg 1$, we arrive at the following results for n not an integer:

$$H_n^{(2)}(nz)\doteqdot i\pi^{-1}\Gamma(n)n^{-n}z^{-n}u_1, \tag{32}$$

when

(1) $\alpha^2z^2\ll 1$ and n positive but not in the range 17/18 to 15/14;
(2) $\alpha^2z^2\gg 1$ and n large;
(3) $n=\frac{1}{2}$, and then (32) is exact for all z.

Also, when x is not large or small but is outside the range 17/18 to 15/14, the approximation (32) is still good if, when $\alpha^2z^2\gg 1$, the right-hand side is multiplied by a certain function of n alone.

Equation (32) agrees with the asymptotic approximations of Hankel, Debye, and Carlini. Moreover, (32) remains finite when $z^2=1$ whereas the last two mentioned approximations then become infinite.

In general we may expect by means of (4) and (5) to be able to obtain similar kinds of approximations to certain functions which arise from a second-order, linear differential equation.

In conclusion I wish to acknowledge the valuable help received from discussions of the general problem with Professors J. Gibbons and N. Davids.

Additional Note. In a paper read by the author on May 5th, at a meeting of the American Committee of the International Union for Scientific Radio, the following second-order iteration was also presented:

$$v_{n+1}(a)=\int_c^a\{p_C^2-p^2(x)+v_n^2(x)\}$$
$$\times\exp\left\{2ip_C(x-a)+\int_a^x 2v_n(s)ds\right\}\cdot dx, \tag{33}$$

combined with

$$\rho_n(a)=\frac{p_A-p_C+iv_n(a)}{p_A+p_C-iv_n(a)}. \tag{34}$$

This is not subject to the restriction that $p(x)$ is continuous at $x=a$ and $x=c$. Also it is particularly convenient for computation when $p^2(x)$ is given by curves representing its real and imaginary parts as in the current work on radio-wave reflection by the D region of the ionosphere. These iterations are at present being used for such work by Mr. J. Wolfe and the results will be reported in due course.

A more detailed account of these approximations and iterations is given by the author in Scientific Report No. 67 of the Ionosphere Research Laboratory.

Note on the Quantum Theory of Irreversible Processes

U. FANO
National Bureau of Standards, Washington, D. C.
(Received July 29, 1954)

Perturbation treatments of irreversible processes are shown to rest on the assumption that the rate of dissipation of disturbances in a system exceeds their rate of input from an external source. This hypothesis is implicit in the concept of a dissipative system and is formulated mathematically in terms of the relaxation time of quantum-mechanical correlation functions or in terms of equivalent properties of the matrices that represent interaction operators in the energy scheme.

1. INTRODUCTION

EFFORTS have been directed recently by various authors towards establishing the theory of irreversible processes on a microscopic, quantum-mechanical basis. With this goal in mind, it is proposed here to develop the implications of perturbation procedures utilized by Callen and co-workers[1] and by Wangsness and Bloch.[2]

Callen and co-workers considered the reaction of a "large" system to an external disturbance represented by a term of the Hamiltonian having the form $\sum_k V_k{}^0 Q_k \exp(i\omega t)$, where the $V_k{}^0$'s are macroscopic constants and the Q_k's are quantum-mechanical operators of the system. Specifically, they calculated the effect of the perturbation on the "mean velocities" $\langle \dot{Q}_j \rangle$. The coefficients Y_{jk} of $\langle \dot{Q}_j \rangle = -\sum_k Y_{jk} V_k{}^0 \exp(i\omega t)$ represent a generalized "admittance" of the system. This calculation was performed by a first-order time-dependent perturbation method, but the validity of this approximation for an indefinite period after the onset of the perturbation was not discussed.

Wangsness and Bloch developed a microscopic theory of the relaxation of spin orientation in nuclear induction experiments. They treated the coupling of the nuclear spins with the surrounding medium by time-dependent perturbation method carried to the second-order approximation (the first order gives no significant contribution in their problem). This approximation procedure was adopted as reasonable for a sufficiently short time interval τ. It was then applied to successive time intervals τ with the understanding that the state of the surrounding medium may be regarded at all times as a state of thermal equilibrium, undisturbed by the interaction. This assumption was supported by qualitative arguments involving the macroscopic size of the medium and its thermal conductivity.

Indeed, the irreversibility of these phenomena does not hinge only on the *size* of the system considered but also on *transport properties* that are implied in the concept of a "dissipative system." In each of the examples considered, the perturbing action is understood to be applied at one point of a large system—more properly, to a few among the numerous degrees of freedom of the large system. The disturbance thus applied during a short time interval is not likely to remain confined to its point of application, but is understood to propagate away quickly to other parts of the large system. Accordingly, the effects of the disturbance should not keep building up at the point of application in the course of time. A sort of steady state is presumably attained within a short time after the onset of the disturbance. This local steady state is all that matters with regard to the *localized reaction* to the disturbance, e.g., for the purpose of calculating the reaction of the medium to nuclear induction. Furthermore it is plausible to assume that the steady state differs but little from the unperturbed state because the disturbance gets dissipated through the large system rapidly as compared to the rate of the external action. (The very concept of an "external action" implies, for example, that the effects of nuclear induction are passed on from the nuclei to the adjacent particles no faster than they can be dissipated, i.e., passed on and on to other particles farther away. Otherwise the nuclei could not be regarded as "external" to the medium.)

Thus, the perturbation procedures of Callen and coworkers, and of Wangsness-Bloch appear to be justified by considerations of *comparative rates of transport* which were not introduced explicitly in the mathematical formalism. In fact, the role of rate-of-transport considerations becomes readily apparent when the analytical treatment is formulated in the manner of Feynman.[3] This will be shown through the analysis of a Callen-type problem; the analogous treatment of a Wangsness-Bloch problem will be outlined at the end of the paper.

2. THE CALLEN PROBLEM

As a Callen-type problem, we shall describe the reaction of a system to a time-variable disturbance V by calculating the effect of the disturbance upon the mean value of an operator of the system, F. The Hamiltonian of the unperturbed system will be indicated by H_0 and the complete Hamiltonian by $H=H_0+V$. All energies are divided by h in this paper, i.e., are expressed in radians/sec. For simplicity we shall assume a sinusoidal

[1] H. B. Callen and T. A. Welton, Phys. Rev. **83**, 34 (1951); Callen, Barasch, and Jackson, Phys. Rev. **88**, 1382 (1952); M. L. Barasch and T. A. Kaplan, University of Pennsylvania, Report Nonr 69800, No. 7, 1954 (unpublished).

[2] R. K. Wangsness and F. Bloch, Phys. Rev. **89**, 728 (1953).

[3] R. P. Feynman, Phys. Rev. **84**, 108 (1951).

dependence of V on time, much as in reference 1, namely

$$V=Qe^{i\omega t}, \tag{1}$$

where Q is a time-independent operator. The unperturbed state of the system will be assumed to be constant in time, i.e., to be a state represented by a density matrix diagonal in the energy scheme, for which time-independent operators have constant mean values.

The calculation will be carried out in a Heisenberg representation, where the operators are variable in time, i.e., are automatically transformed back from the time t to the time $t=0$, which marks the onset of the disturbance and at which the state was still unperturbed. The operators indicated above by F, H_0, V, Q pertain to the ordinary (Schroedinger) representation. The operator of the Heisenberg representation which corresponds to F will be indicated by

$$\mathfrak{F}(t)=e^{iHt}Fe^{-iHt}=e^{i(H_0+V)t}Fe^{-i(H_0+V)t}. \tag{2}$$

The specific purpose of the calculation is to express the mean value of $\mathfrak{F}(t)$ in terms of the mean values of F, V, and their combinations, all averages being taken over the unperturbed state. Utilizing the Feynman procedure[3] of disentangling operators by a sequence of infinitesimal unitary transformations, we write

$$\exp[i(H_0+V)t] = \exp(iH_0t)\exp\left[ie^{i\omega t}\int_0^t dt'V(t-t')\right], \tag{3}$$

where

$$V(t-t')=e^{-i\omega(t-t')}e^{-iH_0(t-t')}Qe^{iH_0(t-t')}, \tag{4}$$

and a similar formula for $\exp[-i(H_0+V)t]$. Because H_0 commutes with the density matrix of the constant unperturbed state, the factors $\exp(\pm iH_0t)$ do not contribute to the mean of $\mathfrak{F}$, which can be written as

$$\langle\mathfrak{F}(t)\rangle=\left\langle\exp\left[ie^{i\omega t}\int_0^t dt'V(t-t')\right]F \times\exp\left[-ie^{i\omega t}\int_0^t dt'V(t-t')\right]\right\rangle. \tag{5}$$

Expand now the exponentials in (5) into power series, which still involves no approximation. The terms of the same order in V operating part to the left and part to the right of F can be grouped into a single multiple integral, and the averaging can be performed before the integration, so that (5) becomes

$$\langle\mathfrak{F}(t)\rangle=\langle F\rangle+ie^{i\omega t}\int_0^t dt'\langle[V(t-t'),F]\rangle -e^{2i\omega t}\int_0^t dt'\int_0^{t'}dt''\langle[V(t-t''),[V(t-t'),F]]\rangle-\cdots, \tag{6}$$

where the square bracket indicates, as usual, "commutator of."

The integrands in this equation are the mean values of products of operators "shifted in time" with respect to one another by intervals $t-t'$, $t'-t''$, etc. They represent correlation functions analogous to those used in the analysis of fluctuations according to classical physics.[4] As pointed out earlier in this paper, a dissipative system is *intuitively* characterized by the fact that a disturbance applied at one point quickly travels away. Accordingly one would expect that the value of $\mathfrak{F}$ at the time t would be unaffected by a disturbance V applied at a time t' much earlier than t, and, therefore, that $V(t-t')$ and F would be uncorrelated, if $t-t'$ is too long. Lack of correlation means that $\langle V(t-t')F\rangle=\langle V(t-t')\rangle\langle F\rangle$ and, hence, that $\langle[V(t-t'),F]\rangle=0$. (It is implied here that F operates approximately at the same point as V; otherwise the correlation would be highest for a value of $t-t'$ which allows for the disturbance to propagate from one point to the other.) According to this argumentation, we suggest that a dissipative system is characterized *mathematically* by the property that the correlation functions of (6) vanish rapidly whenever the time intervals $t-t'$ etc., exceed some suitably defined relaxation time τ.[5]

Under this assumption, the entire contribution to the integrals arises from intervals of the order of τ. Therefore, as we surmised in the initial qualitative discussion the effect of the disturbance does not keep building up in time. Moreover, each successive term of the expansion (6) differs dimensionally from the preceding one by an additional factor V (expressed in frequency units) and by an added integration extended over an interval of the order of τ. Equation (6) is thus seen to be an expansion in powers of the rate of action of the disturbance—the commutator of V—integrated over the relaxation time τ. A first order perturbation treatment, which disregards all terms on the right of (6) after the second, is thereby justified when the commutator of $V\tau$ is much smaller than one. (As mentioned before, the opposite assumption would imply that the source of the disturbance V is so intimately coupled with the system under study as to be virtually a part of it.)

The vanishing of a correlation function for large values of the time interval may be regarded as the result of destructive interference between harmonic components of the function that oscillate with different frequencies. When the operator (4) is represented by a matrix in the energy scheme, with rows and columns labeled by values (φ',φ'') of the energy and by other

[4] See, e.g., N. Wiener, *Extrapolation, Interpolation, and Smoothing of Stationary Time Series* (John Wiley and Sons, Inc., New York, 1949). Quantum-mechanical averages are taken over the set of eigenvalues of the operator product concerned, whereas in classical physics each function is regarded as having a definite, albeit unknown, value at each instant and one resorts to dealing with averages over the values corresponding to extended intervals of time.

[5] This time interval τ corresponds to the reciprocal of the "characteristic frequency" ω^* of reference 2.

quantum numbers (α',α''), if any, each matrix element is a sinusoidal function of the time interval,

$$(\alpha'\varphi'|V(t-t')|\alpha''\varphi'') = e^{-i(\omega+\varphi'-\varphi'')(t-t')}(\alpha'\varphi'|Q|\alpha''\varphi''). \quad (7)$$

All matrix elements having the same value of $\varphi'-\varphi''=\varphi$ oscillate in phase. They constitute together the matrix of an operator that may be regarded as a harmonic component of V. Therefore we write

$$V(t-t') = \int_{-\infty}^{\infty} d\varphi\, Q_\varphi\, e^{-i(\omega+\varphi)(t-t')}, \quad (8)$$

where Q_φ is the operator with the matrix $(\alpha'\varphi'|Q_\varphi|\alpha''\varphi'') = (\alpha'\varphi'|Q|\alpha''\varphi'')\delta(\varphi'-\varphi''-\varphi)$. Substituting (8) in the correlation functions of (6), we have

$$\langle[V(t-t'),F]\rangle = \int_{-\infty}^{\infty} d\varphi \langle[Q_\varphi,F]\rangle e^{-i(\omega+\varphi)(t-t')}, \quad (9)$$

$$\langle[V(t-t''),[V(t-t'),F]]\rangle = \int_{-\infty}^{\infty} d\chi \int_{-\infty}^{\infty} d\varphi \langle[Q_\chi,[Q_\varphi,F]]\rangle \times e^{-i[(\omega+\chi)(t-t'')+(\omega+\varphi)(t-t')]}.$$

These Fourier integrals show that the correlation functions vanish for time intervals exceeding τ when, and only when, the mean values $\langle[Q_\varphi,F]\rangle$, $\langle[Q_\chi,[Q_\varphi,F]]\rangle$ etc., are constant as functions of $\varphi, \chi\cdots$ over ranges of these variables of the order of τ^{-1}. Therefore the mathematical characterization of a dissipative system in terms of the early vanishing of correlation functions is equivalent to a characterization in terms of properties of the operators Q and F. Thus a system has dissipative properties whenever the matrix elements of the pertinent operators Q and F have values independent of the row and column indices (φ',φ'') over a sufficient range of these variables.* This requirement does not look unreasonable for operators acting on a few degrees of freedom of a large, tightly knit, system, because energy eigenfunctions of the system corresponding to rather different eigenvalues may well be effectively equal over the pertinent portion of the system.[6]

Substitution of (9) into (6) renders the integrations over time elementary. We have, for example,

$$\int_0^t dt'\langle[V(t-t'),F]\rangle = \int_{-\infty}^{\infty} d\varphi\langle[Q_\varphi,F]\rangle(1-e^{-i(\omega+\varphi)t})/i(\omega+\varphi). \quad (10)$$

The remaining integral over φ is familiar from perturbation theory. For large values of t the exponentials oscillate very rapidly as functions of the frequency and yield destructive interference, except within a narrow band of width $\sim 1/t$ about the resonance $\varphi=-\omega$. The integral of the term with the exponential equals $\pi\langle[Q_{-\omega},F]\rangle$, provided $\langle[Q_\varphi,F]\rangle$ is constant over a range larger than $1/t$ about $\varphi=-\omega$. This result, independent of t, confirms that the effects of the disturbance do not keep building up locally. The term in the integral that contains the factor $1/i(\omega+\varphi)$, without an exponential, represents the off-resonance effect of the disturbance, which may be negligible as compared to the resonance effect but has been included in the more recent papers by Callen *et al.* We shall not consider the off-resonance effects explicitly, but merely remind the reader of their possible effects by adding a prime to the symbols that represent the resonance effects. With this convention, all the successive terms of the expansion (6) take a very simple form and (6) becomes

$$\langle\mathfrak{F}(t)\rangle = \langle F\rangle + e^{i\omega t}i\pi\langle[Q_{-\omega}',F]\rangle + e^{2i\omega t}(i\pi)^2\langle[Q_{-\omega}',[Q_{-\omega}',F]]\rangle + \cdots. \quad (11)$$

The parameter of the expansion of $\langle\mathfrak{F}(t)\rangle$, which we had identified loosely as the commutator of $V\tau$, becomes now defined somewhat more precisely as the commutator of $\pi Q_{-\omega}'$. Notice from (8) that, since V has the dimension of a frequency, Q_φ has the dimensions of a pure number. Notice further from (9) that, for a given value of the rate of disturbance

$$\langle[V(0),F]\rangle = \int_{-\infty}^{\infty} d\varphi\langle[Q_\varphi,F]\rangle,$$

the larger is the range over which $\langle[Q_\varphi,F]\rangle$ is constant, the smaller must be the values of $\langle[Q_\varphi,F]\rangle$ in this range.[7] Thus the commutator of $Q_{-\omega}'$ appears to constitute a suitable comparative index of the rate of transport of mechanical action from the outside to a point of the system *vs* the rate of transport from this point away to the rest of the system. When this index is much smaller than one, the expansion (11) may be broken off after its term of first order in Q and the Callen perturbation treatment is justified.

Some additional points may be noted. The evaluation of (10) assumes that $\langle[Q_\varphi,F]\rangle$ is constant over a fre-

* *Footnote added in proof.*—Dr. M. S. Green kindly points out that the criterion indicated here for the matrices of Z and F is unnecessarily restrictive and indeed unrealistic. The properties of Q and F, which characterize the system as dissipative and which should probably be the object of further study, are properties of the averages $\langle[Q\varphi,F]\rangle$, $\langle[Q\chi,[Q\varphi,F]]\rangle\ldots$ rather than of the matrices $Q\varphi$ and F *per se*.

[6] This discussion is admittedly sketchy and one ought to examine more closely the correspondence between the presumable mechanical properties of dissipative system and the mathematical properties of operators Q_φ. In this connection it might be relevant that matter has usually a rather homogeneous structure on a semi-macroscopic scale, i.e., it is invariant, in a limited fashion, with respect to translations in space. Because of this invariance, rows and columns of matrices might be labeled simultaneously with energy and momentum quantum numbers. The operators could then be resolved into components $Q_{\varphi\mathbf{q}}$ that change the energy of the system by φ and its momentum by $\mathbf{q}$.

[7] Similarly, for a given value of $\mathrm{Tr}(Q^2)$, the larger is the area of the matrix $(\varphi'|Q|\varphi'')$ over which the elements are constant, the smaller must be the matrix elements themselves.

quency band width $\sim 1/t$. This condition implies, in turn, that t is much longer than the relaxation time τ, which is the reciprocal of the band width over which $\langle[Q_\varphi,F]\rangle$ is constant; for $t \lesssim \tau$ no steady state is attained. The band of constant $\langle[Q_\varphi,F]\rangle$ extends presumably, barring unusual circumstances, from $\varphi=0$ upwards. Accordingly, it should be understood in the derivation of (11) that the driving frequency ω lies within this band, that is, that the disturbance varies but little within the relaxation time of the system. This requirement appears plausible for reasonably slow irreversible processes and has been explicitly postulated by Wangsness and Bloch[2,5] though not by Callen *et al.*

To verify that the main result of Callen, Barasch, and Jackson is contained in (11), one should set $Q=\sum_k V_k^0 Q_k$ and $F=\dot{Q}_j$. The first-order term takes the form $\exp(i\omega t)\sum_k V_k^0 i\pi\langle[Q_{k-\omega}',\dot{Q}_j]\rangle$, and the expression of $i\pi\langle[Q_{k-\omega}',\dot{Q}_j]\rangle$ for an unperturbed state of thermal equilibrium actually coincides with the admittance matrix $Y_{jk}(\omega)$ of reference 1.

3. THE WANGSNESS-BLOCH PROBLEM

The problem of nuclear spin relaxation is closely similar in essence to the Callen problem but sufficiently different in formal structure to deserve a brief treatment. Further details and a discussion from a different point of view will be given in another paper.

The spin relaxation process involves two systems: system No. 1, with unperturbed Hamiltonian H_1, consists of the nuclear spins, and system No. 2, with unperturbed Hamiltonian H_2, consists of the surrounding medium and is regarded as large and dissipative. The coupling of the two systems is indicated in the Schroedinger representation by a time-independent operator V, which operates on both systems. The complete Hamiltonian is $H=H_1+H_2+V$.

We are interested here in the effect of the coupling upon the dynamics of the nuclear spins. This effect is described by the influence of V upon operators F that operate on the nuclear spins (system No. 1), the effect being *averaged over* the unperturbed state of *system No. 2*, the surrounding medium. This unperturbed state is assumed to have been constant in time prior to the onset of the disturbance, as in the Callen problem. Therefore the quantity to be calculated is

$$\langle\mathfrak{F}(t)\rangle_2=\langle e^{i(H_1+H_2+V)t}Fe^{-i(H_1+H_2+V)t}\rangle_2. \tag{12}$$

The operators in the exponents are conveniently disentangled here by

$$e^{i(H_1+H_2+V)t}=\exp\left\{i\int_0^t V(t')dt'\right\}e^{i(H_1+H_2)t}, \tag{13}$$

and an analogous formula, where

$$V(t)=e^{i(H_1+H_2)t}Ve^{-i(H_1+H_2)t}. \tag{14}$$

The operator $\exp(iH_2t)$ commutes with H_1 and F and therefore cancels with $\exp(-iH_2t)$ in (12), after disentanglement, so that (12) reduces to

$$\langle\mathfrak{F}(t)\rangle_2=\left\langle\exp\left[i\int_0^t V(t')dt'\right]e^{iH_1t}Fe^{-iH_1t}\times\exp\left[-i\int_0^t V(t')dt'\right]\right\rangle_2. \tag{15}$$

The factor $\exp(iH_1t)F\exp(-iH_1t)$ does not operate on the system No. 2 and can be removed from the averaging procedure provided one keeps track of the ordering of operators. To this end we introduce a dummy symbol I which serves as an ordering parameter such that operators formally on the left of I act on the left of F and operators on the right of I act on the right of F. Accordingly (15) can be written in the form

$$\langle\mathfrak{F}(t)\rangle_2=Fe^{i[H_1,I]t}\left\langle\exp\left\{i\int_0^t[V(t'),I]dt'\right\}\right\rangle_2. \tag{16}$$

The mean value of an operator of the form $\exp A$, such as we have on the right of (16), can be expressed in terms of the "cumulants," C_n, of A according to the theorem of probability,[8]

$$\langle\exp A\rangle=\exp[\textstyle\sum_n C_n/n!]. \tag{17}$$

The first cumulant, C_1, is simply the mean value $\langle A\rangle$; the cumulants C_2 and C_3 are the mean square and cube deviations of A from its mean; the higher cumulants C_n are simple functions of mean deviations $\langle(A-\langle A\rangle)^r\rangle$ with $r\leq n$. The theorem can be proved by expanding $\exp A$ into powers of A, taking the mean of each power, and manipulating the series thus obtained. The first cumulant of the exponent of (16) is

$$C_1=i\int_0^t dt'\langle[V(t'),I]\rangle_2=i\int_0^t dt'[e^{iH_1t'}\langle V\rangle_2 e^{-iH_1t'},I]. \tag{18}$$

In the expression on the right, $V(t')$ has been replaced with its expression (14), the factors with H_1 have been removed from the averaging and the factors with H_2 have cancelled because they commute with the unperturbed density matrix of system No. 2. Because $\langle V\rangle_2$ is constant in time, it represents a constant interaction energy due to the average electric and magnetic forces exerted by the medium on the nuclear spins.

The second cumulant and the higher ones are functions of the deviation of V from its mean $\langle V\rangle_2$. Therefore

[8] See, e.g., H. Cramér, *Mathematical Methods of Statistics* (Princeton University Press, Princeton, 1946), p. 186. The mean of an operator behaves in this respect like the mean of an ordinary random variable because it can be calculated in the scheme where the operator is diagonal and reduces to its set of eigenvalues.

it simplifies the formulas to introduce the operator $\bar{V}=V-\langle V\rangle_2$ whose mean vanishes and whose second and third cumulants are simply $\langle\bar{V}^2\rangle$ and $\langle\bar{V}^3\rangle$. The second and third cumulants of the exponent of (16) are given by

$$C_2/2!=-\int_0^t dt'\int_0^t dt''\langle[\bar{V}(t''),[\bar{V}(t'),I]]\rangle_2, \tag{19}$$

$$C_3/3!=-i\int_0^t dt'\int_0^{t'} dt''\times\int_0^{t''} dt'''\langle[\bar{V}(t'''),[\bar{V}(t''),[\bar{V}(t'),I]]]\rangle_2.$$

Multiple correlations in the successive cumulants represent the effects of fluctuating electric and magnetic fields on the spins. Owing to their presence, the series of cumulants of the exponent of (16) must converge rapidly if system No. 2 exhibits the properties of a dissipative medium indicated in Sec. 2. Accordingly we shall break off the series after the term $C_2/2!$, an approximation equivalent to that of Wangsness-Bloch, and write

$$\langle\mathfrak{F}(t)\rangle_2=Fe^{i[H_1,I]t}e^{C_2+\frac{1}{2}C_2}. \tag{20}$$

The integration over t'' in (19) can be handled as the integration over t' in (10), but $\bar{V}(t'')$ must be first changed into $\bar{V}(t''-t')$ by a regrouping of the exponentials in (14) which brings the correlation function to the form

$$e^{iH_1t'}\langle[\bar{V}(t''-t'),[V,I]]\rangle_2e^{-iH_1t'}. \tag{21}$$

The integration then yields

$$\tfrac{1}{2}C_2=-\int_0^t dt'e^{iH_1t}\pi\langle[\bar{V}_0',[\bar{V},I]]\rangle_2e^{-iH_1t'}, \tag{22}$$

where, as in Sec. 2, the subscript characterizes a harmonic component of the operator $\bar{V}$, which in this case oscillates with zero frequency, i.e., conserves energy, and the prime reminds one of the possible additional contribution of off-resonance transitions.

The integrands of C_1 and C_2 contain now explicitly the transformation $\exp(iH_1t)$. Therefore, C_1 and C_2 can be conveniently brought back in the same exponential as H_1 by a transformation inverse to that of (14), which yields

$$\langle\mathfrak{F}(t)\rangle=F\exp\{i([H_1,I]+[\langle\bar{V}\rangle_2,I]+i\pi\langle[\bar{V}_0',[\bar{V},I]]\rangle_2)t\}. \tag{23}$$

Equation (23) shows that the mean interaction $\langle V\rangle_2$ may simply be added to the unperturbed Hamiltonian H_1. The next cumulant, however, takes the form of an imaginary contribution to H_1, which is in line with the dissipative character of the effect it represents.

Wangsness and Bloch have represented their result in the form of a Boltzmann equation which is, in essence, the differential counterpart of (23) and may be regarded as a generalization of the Schroedinger equation for the operator F, extended to include the effect of the dissipative interaction with system No. 2. Differentiation of (23) with respect to t yields

$$d\langle\mathfrak{F}_2(t)\rangle/dt=i([H_1+\langle V\rangle_2,F]+i\pi\langle[\bar{V}_0',[\bar{V},F]]\rangle_2)\exp\{\cdots\}, \tag{24}$$

where the exponent is the same as in (23). As emphasized in reference 2, the integration performed over t'' when deriving (23) assumes that the duration of the disturbance from $t=0$ to t greatly exceeds the relaxation time τ of system No. 2. Therefore the differential law (24), and also (23), cannot be extrapolated back to $t=0$, in principle, but holds only for the steady state, which becomes established after the interaction has been in effect for a time longer than τ.

In practice, however, extrapolation back to $t=0$ involves a negligible error because the effect of interaction during τ is assumed to be small.

Properties of Germanium Doped with Iron. I. Electrical Conductivity

W. W. Tyler and H. H. Woodbury
General Electric Research Laboratory, Schnectady, New York
(Received August 11, 1954)

Measurements of the temperature dependence of electrical resistivity in p- and n-type iron-doped germanium crystals indicate that Fe introduces impurity levels in Ge at 0.34 ± 0.02 ev from the valence band and 0.27 ± 0.02 ev from the conduction band. Such samples show very high resistivity at 77°K. At this temperature, n-type samples also show high photosensitivity and slow photoresponse, presumably because of hole traps.

I. INTRODUCTION

CHEMICAL impurities in the Ge lattice may introduce localized energy levels in the energy gap between the valence and conduction bands. Impurity elements which have been studied most extensively are those of columns III and V of the periodic table.[1] For these elements, the hole or electron is considered to be loosely bound in a large hydrogen-like orbit. Ionization energies, calculated on the basis of this model, agree fairly well with the measured values of approximately 0.01 ev. Group III and V elements are assumed to be substitutional in the Ge lattice. Their solubilities are relatively high.

More recent work has yielded information concerning localized energy levels introduced into the Ge band structure by Zn,[2] Cu,[3,4] Ni,[4] Li,[5] Au,[6] and Pt.[7] Except for Li, the levels introduced by these impurities are characterized by ionization energies which are appreciably larger than for the elements of columns III and V. The hydrogen-like model is not applicable, presumably because of the greater localization of wave functions. Also, the maximum impurity concentration attainable in single crystals of Ge is considerably less for these elements than for those of columns III and V.

In order to extend present information concerning the properties of Ge crystals containing impurity elements, we have studied the properties of Fe-doped Ge crystals.[8] The present paper contains information concerning the method of preparation and some electrical properties of these crystals. The following paper reports studies of their optical properties.

II. PREPARATION OF SAMPLES

The Ge crystals used were pulled from a melt in the usual manner using pulling rates of about 2 in. per hour and rotating rates of about 100 rpm. The direction of growth was (100). Zone-melted polycrystalline Ge of resistivity >40 ohm-cm at 300°K was used as raw material. During growth, Fe was introduced into the melt at a concentration between 0.04 and 0.1 atomic percent. Due to the rejection of Fe by the growing Ge crystal, the total amount of Fe in the melt remained substantially constant until its concentration reached about 0.3 atomic percent. At this concentration, under the conditions of growth described, pronounced lineage markings appeared abruptly on the surface of the growing crystal, although the crystals remained grossly single down to the sprout, i.e., the crystal faces persisted after lineage appeared. It was demonstrated, using radioactive Fe, that the onset of lineage in the crystals is accompanied by the incorporation of relatively large amounts of Fe in pockets in the growing crystal. The specific activity of the radioactive Fe used and the amount of Fe incorporated in the crystal before the onset of lineage were so low that no estimate of the Fe concentration in crystal regions containing no observable lineage could be made by this technique. All of the experimental data to be reported pertain to samples cut from those parts of the crystal above the observable lineage.

The two sources of Fe used for doping were "Puron" electrolytic Fe obtained from Westinghouse Manufacturing Company and Fe of carbonyl origin obtained from the National Research Corporation and labeled "NRC-64." Although both of these sources were considered relatively pure, Ge crystals doped with Fe from these sources consistently showed different results. Resistivity data to be described below indicates that the concentration of Fe in the crystals used for experimental work is always less then about 2×10^{13} atoms/cc. This represents an effective distribution coefficient of less than 10^{-6} at the doping levels used. Impurities in the Fe which have high distribution coefficients, such as boron ($k_0\cong10$)[9] and phosphorus ($k_0=0.12$)[10] are important at concentrations as low as one part in ten million for B,[11] and 10 parts per million for P. Chemical analyses of the two types of Fe indicated that the P

[1] E. M. Conwell, Proc. Inst. Radio Engrs. **40**, 1327 (1952); P. P. Debye and E. M. Conwell, Phys. Rev. **93**, 693 (1954).
[2] W. C. Dunlap, Jr., Phys. Rev. **85**, 945 (1952).
[3] F. J. Morin and J. P. Maita, Phys. Rev. **90**, 337 (1953).
[4] Burton, Hull, Morin, and Severiens, J. Phys. Chem. **57**, 853 (1953).
[5] C. S. Fuller and J. A. Ditzenberger, Phys. Rev. **91**, 193 (1953).
[6] W. C. Dunlap, Jr., Phys. Rev. **91**, 1282 (1953).
[7] W. C. Dunlap, Jr., Phys. Rev. **94**, 1419 (1954).
[8] Tyler, Woodbury, and Newman, Phys. Rev. **94**, 1419 (1954).
[9] R. N. Hall, J. Phys. Chem. **57**, 836 (1953).
[10] Burton, Kolb, Slichter, and Struthers, J. Chem. Phys. **21**, 1991 (1953). This paper contains a fairly complete listing of known distribution coefficients for Ge.
[11] Under certain conditions it should be possible to make very sensitive analyses of the relative B content of a series of Fe samples by studying the properties of Ge crystals doped with these samples.

content of each might be as high as 20 ppm (parts per million). To measure the B content, the two sources of Fe were compared spectrographically with a calibrated sample (National Bureau of Standards steel No. 151) containing 27 ppm of B. These tests indicated that the NRC Fe contains about 15±5 ppm of B, whereas the Puron Fe contains less than 5 ppm of B.[12] Spectroscopic analyses of the two types of Fe indicated no significant differences between the two in content of In, Sb, As, or Bi. Ga was detected in the NRC Fe, but was probably at a level of several ppm or less. It was not detected in the Puron. It is believed that the differences in behavior of the NRC and Puron-doped Ge crystals to be described below are due to an effective excess of B over P in the NRC Fe and P over B in the Puron Fe.

The samples studied were about 2 mm×3 mm×10 mm and were cut from the ingots with the long dimension perpendicular to the direction of growth in order to minimize effects of inhomogeneity. After heavy etching (80 percent nitric acid, 20 percent hydrofluoric acid), contacts were fused on in a hydrogen atmosphere after which the samples were again etched. For *n*-type samples contacts were of fused Sn; for *p*-type samples contacts were of fused In. Contacts were considered satisfactory if the current between any two was reversible within 20 percent with maximum applied voltage of one volt and if the saturation photovoltage between any pair was <0.01 volt. Except where mentioned, four contacts were used for resistivity measurements with two additional contacts for Hall measurements. Heavy etching after fusing on contacts was found to be particularly important in *p*-type samples.

III. EXPERIMENTAL DETAILS

A conventional cryostat is used for measurements of resistivity and Hall coefficient as a function of temperature. Figure 1 shows a diagram of the sample holder. A single crystal sapphire plate 0.025 in. thick is used to provide good thermal contact[13] and electrical insulation between the Ge sample and the Cu block to which the thermocouple is attached. In order to seal the sapphire to the Cu, it is first coated on one side with a slurry of titanium hydride and lead which is then fused at high temperature.[14] This surface is then soldered directly to the Cu using a layer of In solder which gives good thermal contact and allows relative motion of sapphire and Cu to accomodate differences in thermal expansion. The sample is then fastened to the sapphire with "calorimeter adhesive."[15] Although the metal cryostat is light tight, the radiation shield, which assumes the same temperature as the sample, is necessary to prevent 300°K radiation from the outer

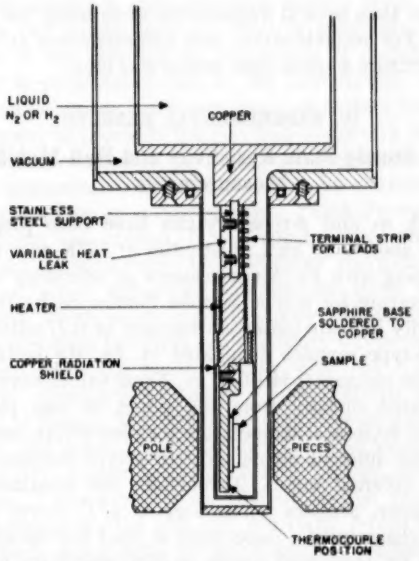

FIG. 1. Cryostat sample holder used for resistivity, Hall coefficient, and photoconductivity decay experiments. For the latter, a small neon light was included next to the sample.

wall of the cryostat from falling on the sample. This shield can be removed in order to observe the effect of room temperature radiation on the properties studied.

All potential measurements for resistivity or Hall coefficient data were taken by using an Applied Physics Corporation vibrating reed electrometer. The high input resistance of this instrument insured that the current drawn through the potential contacts was negligible compared with the current flowing through the sample. The sample current was provided by a calibrated current source which had a series resistance at least 100 times the sample resistance throughout the temperature range investigated. Potential differences across the samples were always less than one volt, minimizing injection and other high field effects.

In order to study steady state and transient photoconductivity effects, the sample holder shown in Fig. 1 was slightly modified. A smaller sapphire plate was used allowing room for a small neon light (G. E. bulb N. E.-2) to be mounted next to the sample, inside the radiation shield. For the measurement of the transient photoconductivity effects, both two and four probe methods were used. No significant differences were noted between these methods as long as the contacts were "ohmic" and gave no evidence of photovoltage. The recovery was studied at short times (<10 seconds) using a Tektronix dc oscilloscope and a DuMont Land-type camera and at long times (up to 20 miuntes) using the electrometer and a stop watch. Although the decay characteristic of the neon lamp is not known in detail, experiments indicated it to be less than one millisecond. No attempt was made to measure times

[12] We are indebted to L. B. Bronk of the Analytical Chemistry Unit for all spectroscopic studies of these samples.
[13] R. Berman, Proc. Roy. Soc. (London) **208**, 90 (1951).
[14] R. J. Bondley, Ceram. Age **58**, 15 (1951).
[15] General Electric compound No. 7031 diluted with alcohol and toluene.

shorter than several milliseconds when using the neon bulb. For recombination rate measurements at room temperature a spark light source was used.

IV. EXPERIMENTAL RESULTS

A. Steady State Resistivity and Hall Mobility Measurements

Both *n*- and *p*-type crystals have been prepared which show very high resistivities at 77°K as a result of doping with Fe. Measurements of resistivity *versus* temperature for *n*-type samples dominated by the Fe impurity indicate ionization energies of 0.27±0.02 ev. For *p*-type samples dominated by Fe, the ionization energies measure 0.34±0.02 ev. These values have been calculated directly from the slopes of logρ plotted against reciprocal temperature for nine *n*-type samples from six different ingots and four *p*-type samples from three different ingots. Throughout the remainder of the paper, samples whose logρ *vs* $1/T$ curves show these characteristic slopes over at least five decades in ρ will be designated simply as high-resistivity *n*-type or high-resistivity *p*-type samples. Samples not dominated by the Fe content but showing a maximum in the equilibrium value of resistivity between 300°K and 100°K will be designated as low resistivity samples. Actually the resistivity for all of the samples to be discussed, except two, is intrinsic at 300°K.

For all ingots in which high resistivity *n*- or *p*-type samples were obtained as a result of Fe doping, the resistivity of samples taken from the ingot before the Fe was added to the melt show a maximum between 200 and 400 ohm-cm when cooled below room temperature. These samples were always *p*-type, indicating that the purity of the melt is limited by an acceptor impurity or that an acceptor impurity, such as Cu, diffuses into the ingot during growth. In any event the concentration of carriers from uncontrolled, uncompensated impurities was about 5×10^{12} per cc or less.

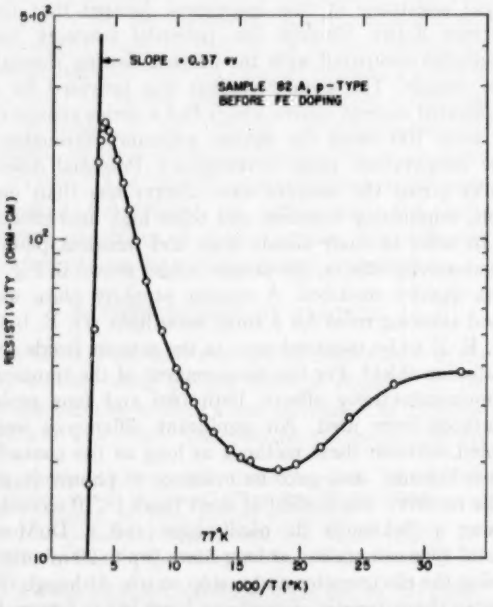

FIG. 2. Resistivity *vs* reciprocal temperature for sample *A* from crystal 82, before Fe doping. This curve is typical of undoped regions of several crystals studied.

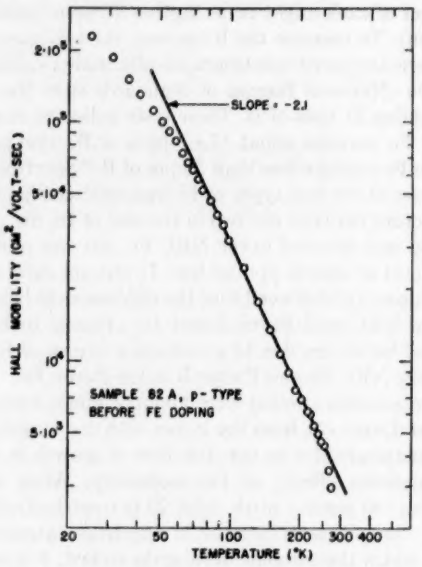

FIG. 3. Hall mobility *vs* temperature for sample 82*A*.

Figure 2 indicates the dependence of ρ on T for a typical sample before Fe doping. The rise in resistivity at 50°K may be due to Cu which is reported to introduce a state with ionization energy of 0.04 ev.[3] Figure 3 shows the dependence of mobility on temperature for the same sample. In agreement with the early work of Dunlap[16] on *p*-type samples, the variation of mobility with temperature is more rapid than the $T^{-\frac{1}{2}}$ law which has been predicted by theory.[17] Mobility values were calculated in the conventional manner[1,3] by taking the ratio of Hall coefficient divided by resistivity. For all of the data on mobility presented in this paper, the value of the magnetic field used was about 4000 gauss. For sample 82*A* careful studies of the dependence of mobility on magnetic field strength have been carried out and agree well with data reported recently by Harman *et al.*[18] It is evident that the observed temperature dependence of the mobility will depend to some extent on the magnetic field strength. However, for the magnetic field strength used, the field dependence appears to have saturated. The departure of mobility data at low temperature from

[16] W. C. Dunlap, Jr., Phys. Rev. **79**, 286 (1950).
[17] F. Seitz, Phys. Rev. **73**, 549 (1948); J. Bardeen and W. Shockley, Phys. Rev. **80**, 72 (1950).
[18] Harman, Willardson, and Beer, Phys. Rev. **94**, 1065 (1954).

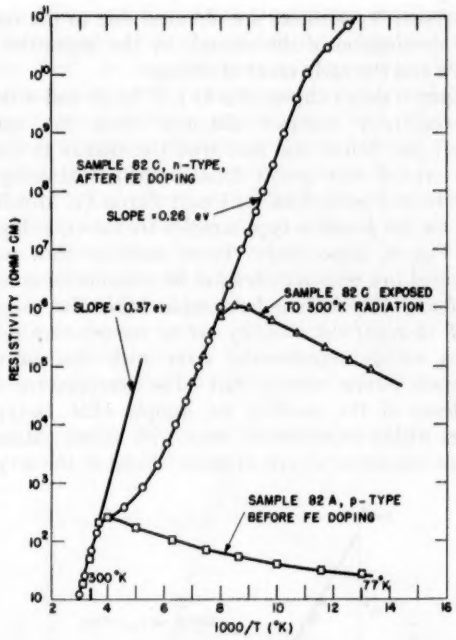

FIG. 4. Resistivity *vs* reciprocal temperature for a high-resistivity *n*-type Fe-doped sample from crystal 82, compared with data for sample 82*A* (Fig. 2) before Fe doping. Also shown is the effect of 300°K radiation from the outer wall of the cryostat on the resistivity of the Fe-doped sample.

the approximate power relationship is probably the result of scattering from imperfections or impurities.[1] The general form of the temperature dependence of the mobility observed for this sample and for high-resistivity samples after Fe doping is cited as evidence that the samples are homogeneous and typical of high-purity Ge, justifying the calculation of ionization energies from resistivity data.

Figure 4 shows the dependence of resistivity on temperature for a high-resistivity Fe-doped *n*-type sample which was cut from crystal 82 after Fe doping. For convenience it is compared with the data of Fig. 2. Two contacts were used in taking these data for sample 82*C*. Later measurements using four contacts were in agreement with the two contact data. With proper shielding of the sample from light and from thermal radiation, the relationship between $\log\rho$ and $1/T$ is linear over seven decades. Removal of the radiation shield (shown in Fig. 1) exposes the sample to 300°K radiation and causes the resistivity to reach a maximum at about 115°K and then decrease to a value at 77°K which is about 7 decades below the extrapolated equilibrium value. With the best radiation shielding attained the data deviate somewhat from the linear relationship at about 10^{10} ohm-cm, presumably because of leakage currents. During initial experiments on this sample, it was observed that a bright etched surface was essential. Grinding or lightly sand blasting the sample creates a low resistance surface layer which shorts the sample with an effective resistance of the order of one megohm as the sample is cooled. This effect is presumably due to the introduction of low ionization energy levels as a result of surface fracture.

Crystal 82 provided the first high-resistivity samples obtained as a result of Fe doping and demonstrated the high photosensitivity later found to be characteristic of high resistivity *n*-type samples. Puron Fe was used in doping this crystal. It was subsequently observed that doping with Puron Fe, if the melt was sufficiently free of other impurities, consistently gives *n*-type material which shows high-resistivity behavior at the point of doping but gives low-resistivity *n*-type material further down the ingot. Doping with the NRC Fe always gives low-resistivity *p*-type material at the point of doping. The resistivity then rises progressively down the ingot, which eventually may yield high-resistivity *p*-type material before lineage develops. Figure 5 shows resistivity plotted against reciprocal temperature for the first high-resistivity *p*-type sample obtained, using NRC Fe for doping. No appreciable change in the curve was observed when the sample was exposed to 300°K radiation.

The properties of a series of crystals doped with either Puron or NRC Fe are consistent with the assumptions that the concentration of Fe included in the growing crystal is relatively independent of the concentration in the melt at the concentrations used (~0.08 percent) and that the Puron Fe contains an excess of P as impurity and the NRC Fe an excess of

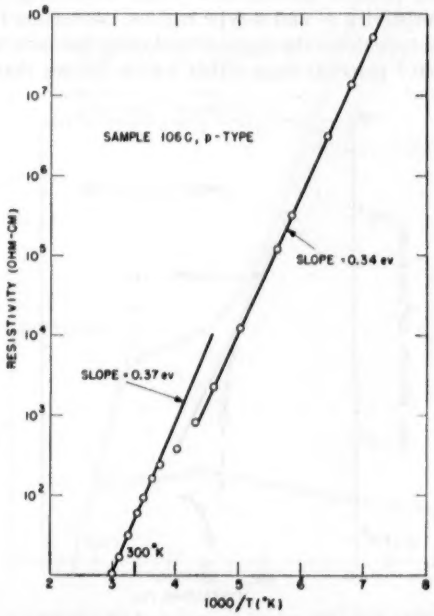

FIG. 5. Resistivity *vs* reciprocal temperature for a high-resistivity *p*-type Fe-doped sample.

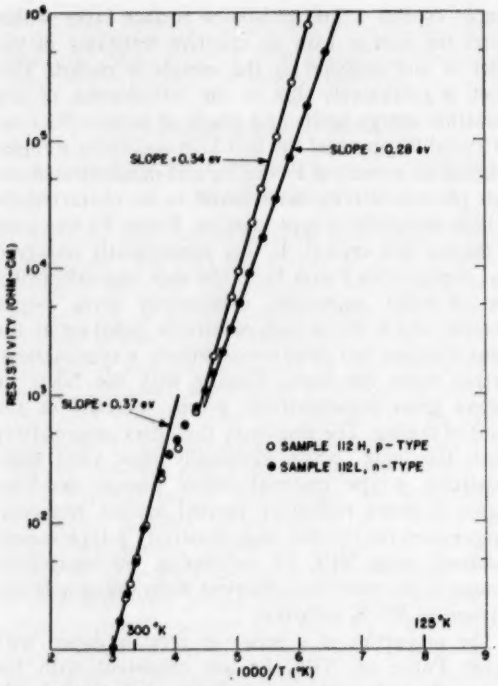

FIG. 6. Resistivity curves for high-resistivity n- and p-type Fe-doped samples cut from crystal 112 just before and after conversion from p- to n-type.

B. Mixing the two sources of Fe in the proper proportions, and thus compensating the impurities in the two sources, permits growth of crystals containing both high-resistivity p- and n-type regions, converting from p- to n-type down the ingot. Overdoping the melt with Fe (>0.1 percent) from either source insures that no high-resistivity samples are obtained due to the complete domination of the crystals by the impurities in the Fe and the early onset of lineage.

Figure 6 shows curves of ρ *vs* $1/T$ for p- and n-type high-resistivity samples obtained from the same crystal just before and just after the change in type. This crystal was grown from a melt containing a mixture of 2 parts NRC to 1 part Puron Fe. Mobility data for the p- and n-type samples are shown in Fig. 7 and Fig. 8, respectively. These mobility data were measured to a resistivity level of 10^9 ohm-cm for sample 112*H* and 10^8 ohm-cm for sample 112*L*. For sample 112*H* (p-type) the mobility *versus* temperature slope agrees within experimental error with that of the undoped p-type sample 82*A*. The temperature dependence of the mobility for sample 112*L* (n-type) agrees within experimental error with values obtained on low-resistance n-type samples.[1] None of the n-type samples studied show any appreciable magnetic field dependence up to 4000 gauss.

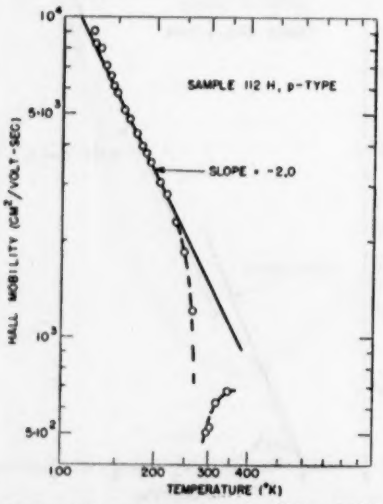

FIG. 7. Hall mobility *vs* temperature for high-resistivity p-type Fe-doped sample 112*H*. The change in sign of the Hall coefficient occurs at about 275°K.

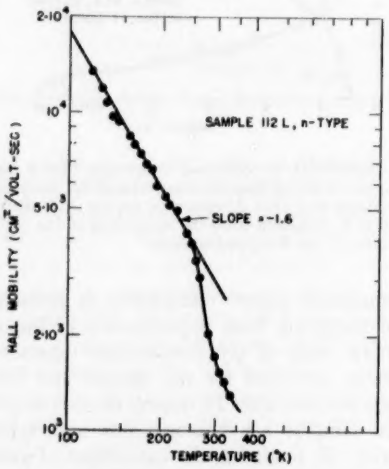

FIG. 8. Hall mobility *vs* temperature for high-resistivity n-type Fe-doped sample 112*L*.

The sensitivity of n-type high-resistivity samples to 300°K radiation permitted the measurement of mobility in such samples down to liquid hydrogen temperatures by simply removing the light shield. Figure 9 compares the dependence of resistivity on temperature for n-type sample 95*G* (Puron-doped) with and without the radiation shield. With the shield, the resistivity continued to rise on the linear curve to a resistivity of at least 10^9 ohm-cm. Without the shield, the resistivity reaches a maximum at 120°K and then decreased as shown to a value of about 8×10^3 ohm-cm at 30°K. Figure 10 shows the corresponding mobility data. Between 250°K and 90°K a slope of -1.6 represents the data fairly well. There is no difference greater than experimental error for mobility data with and without the radiation shield in the region of overlap. The effec-

tive mobility in the presence of radiation continues to be characteristic of electron mobility in slope and magnitude down to low temperatures, even though the number of steady-state carriers induced by the radiation becomes many orders of magnitude greater than the equilibrium number. Similar measurements were made for the *n*-type sample 112*L* with similar results.*

As mentioned above, crystals grown from melts doped with Puron Fe will always give low-resistivity *n*-type samples before lineage develops, due presumably to the accumulation of some donor impurity such as P in the melt. If the failure to show high-resistivity behavior is due to an excess number of electrons, it should be possible to heat treat such samples to compensate for the excess electrons, and thus obtain high

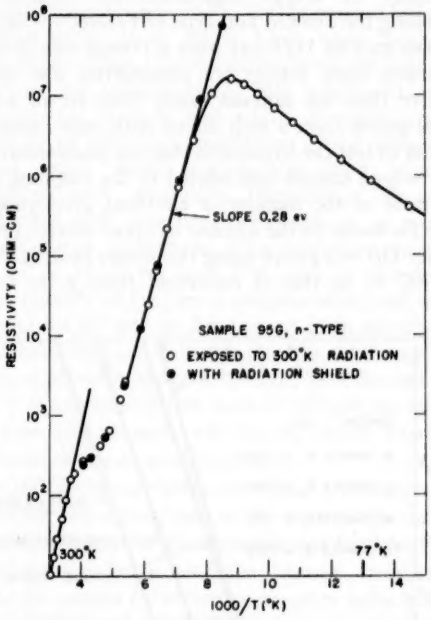

FIG. 9. Resistivity *vs* reciprocal temperature for high-resistivity *n*-type Fe-doped sample 95*G* showing the effect of 300°K radiation.

resistivity material dominated by the Fe states. Figure 11 shows the results of such an experiment. Before heat treatment, the resistivity shows a plateau of approximately 45 ohm-cm, a slight increase at about 200°K due to the presence of the Fe, and then a decrease due to mobility changes. The sample was

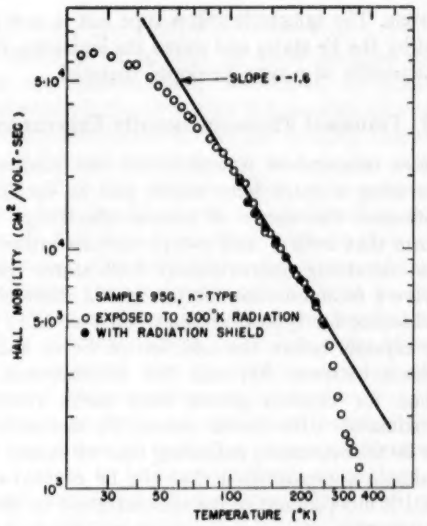

FIG. 10. Hall mobility *vs* temperature for sample 95*G*. Exposure to 300°K radiation permits measurement of mobility down to 25°K. At 107°K, mobility values with and without radiation agree within experimental error although resistivity values differ by a factor of 10^2.

heat treated by rinsing under tap water, drying, and then heating to 650°C for several minutes. This treatment effectively compensates about 5×10^{13} excess

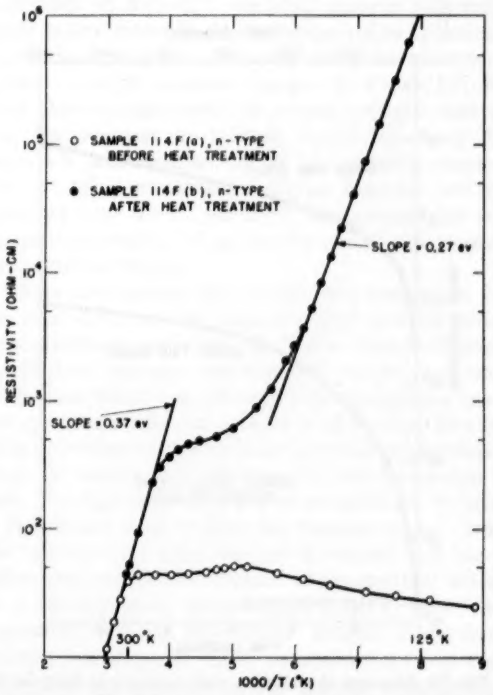

FIG. 11. Resistivity *vs* reciprocal temperature for an initially low-resistivity *n*-type Fe-doped sample before and after heat treatment.

* *Note added in proof.*—The sensitivity of *n*-type Fe-doped samples to 300°K radiation is primarily due to absorption of photons in the energy region from 0.3 ev to 0.7 ev, rather than to intrinsic absorption (see following paper). This was determined by comparing the dependence of resistivity on temperature for sample 82*C* with direct exposure to 300°K radiation and with filtered 300°K radiation. The filter used was a Ge crystal which was thick compared with the test sample and held at the temperature of the test sample. The difference in conductivity with and without the filter could be explained by reflection losses at the surfaces of the filter. Essentially none of the radiation giving rise to carriers was absorbed in the filter.

electrons. The sample is still n-type but is now dominated by the Fe states and shows the ionization energy characteristic of n-type Fe-doped material.

B. Transient Photoconductivity Experiments

Room temperature recombination rate studies were made using a spark light source and an oscilloscope to measure the decay of photoconductivity. These indicate that both n- and p-type crystals grown from melts containing approximately 0.08 atomic percent Fe have a recombination lifetime of <5 microseconds. The lifetime for typical samples (such as 82A) taken from crystals before the addition of Fe to the melt measures between 300 and 500 microseconds. The lifetime for crystals grown from melts containing approximately 0.04 atomic percent Fe measures from 15 to 20 microseconds, indicating that we cannot make the simple approximation that the Fe content of the crystal is independent of the concentration in the melt at this level.

On cooling, it is found that n-type samples show high photosensitivity and also a slow decay of photoconductivity after exposure to light whereas the p-type samples remain relatively fast. Figure 12 shows the relative resistance values for sample 82C measured as a function of time after exposure to unfiltered light from the neon lamp. For p-type high-resistivity samples at the same temperature with the same light source and relative geometry, the steady-state value of the resistivity with light is at least a factor of 100 greater than for 82C. After turning off the neon lamp, the resistivity of all p-type samples increases 100 fold in less than several milliseconds.

The data shown in Fig. 12 combine oscilloscope and electrometer data. They are characteristic of high-resistivity n-type samples showing the highest photosensitivity. Exponential recovery is never observed, and it does not seem possible to explain the results on the basis of a simple model involving only the evaporation of trapped holes from discrete levels. Nor have we as yet been able to deduce from our experiments an approximate number for the density of traps. However, we are able to exert some control over the relative sensitivity of n-type high-resistivity samples by controlling the amount and type of Fe used for doping. Samples such as 112L cut from a crystal shortly after conversion from p-type are consistently less photosensitive than are samples taken from an all n-type crystal grown from a melt doped with only Puron Fe. In order to test the hypothesis that the photosensitivity of an n-type sample was related to the trapping ratio (the ratio of the number of electrons occupying the upper Fe levels, to the number of upper levels), crystal number 110 was grown using the proper ratio of Puron to NRC Fe so that it converted from p- to n-type

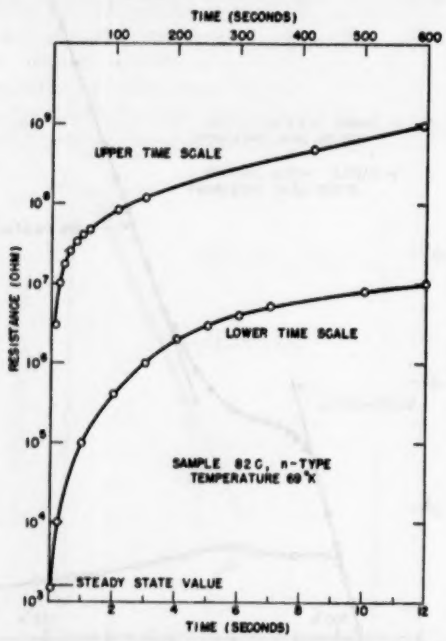

FIG. 12. Recovery of resistance after exposure to light for the high-resistivity n-type Fe-doped sample 82C. The equilibrium value of resistance at the temperature of measurement (69°K) is $\sim 10^{11}$ ohms. These data are characteristic of the most photosensitive samples. The recovery is never exponential.

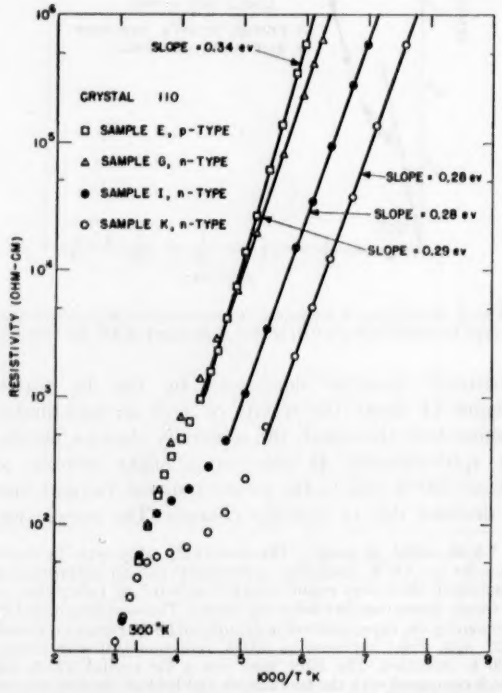

FIG. 13. Resistivity curves for a series of high-resistivity samples from the same Fe-doped crystal. The series of n-type samples G, I, and K show increasing photosensitivities and increasing recovery times.

shortly below the point of doping. This crystal gave a series of high-resistivity n-type samples characterized by increasing amounts of Fe, but, what is considered more important, larger trapping ratios due to the increasing concentration of donor impurities in the melt. Figure 13 shows resistivity data for the four samples. As expected, the three n-type samples show increasing photosensitivity and increasing recovery times progressing from G to K. Comparison of the photosensitivity of these samples and arbitrarily defined recovery times is given in detail in the next paper.

V. SUMMARY

Two energy levels in germanium crystals have been identified with the presence of Fe in the melt from which the crystals are grown. On the basis of resistivity measurements, these levels have been located at 0.27 ± 0.02 ev from the conduction band and 0.34 ± 0.02 ev from the valence band. Hall coefficient studies indicate that both n- and p-type Fe-doped crystals, which go to very high resistivities as the samples are cooled below room temperature, show increasing mobilities with decreasing temperature in general agreement with previous measurements of mobility in high-purity germanium. The maximum concentration of Fe which we have been able to introduce in single crystals of Ge free of obvious structural defects is about 2×10^{13} per cc. Because we have not obtained Fe sufficiently pure to insure that the total number of donor or acceptor atoms introduced into the melt with the Fe is appreciably less than 2×10^{13} per cc, we have not been able to show whether the states introduced by Fe are donor or acceptor states.

At 300°K the only obvious indication of the presence of 2×10^{13} Fe atoms/cm^3 in Ge crystals in the pronounced reduction in the recombination lifetime. Rough calculations indicate that the capture cross section of the Fe centers for either electrons or holes is of the order of 10^{-15} cm^2 at 300°K.

Transient and steady-state photoconductivity measurements below room temperature and in samples dominated by the Fe content indicate that p-type samples are relatively insensitive and fast in response, whereas n-type are more photosensitive and slower in response to changes in light levels. The high photosensitivity in n-type samples is reproducible and controllable in the sense that the photosensitivity of the samples can be varied over a factor of at least 100 by the choice of the amount and type of Fe used for doping. The slow response of the n-type samples suggests the presence of hole traps. This is confirmed by optical measurements to be reported in the following paper. However, studies of photoconductivity decay in n-type samples cannot be interpreted quantitatively in terms of simple trapping model nor is the effective number of hole traps known.

VI. DISCUSSION

It would be of interest to know whether the Fe atoms are substitutional, interstitial, or lodged at imperfections in the Ge lattice. It is possible for instance to accomodate 3×10^{13} atoms per cc along dislocation edges if dislocations are present at a density of about 10^6 per cm^2 in the crystals. There is no evidence to indicate how the Fe atoms are dissolved in the Ge lattice. In fact there is no direct evidence that any Fe is taken into the solid above the region of lineage. Conceivably, the observable results could be due to imperfections in the crystals which develop because of the high concentration of Fe in the melt. However, this is considered very improbable because of the consistency and uniqueness of the results.

Although we have not established whether the Fe levels are donor or acceptor, we tentatively assume both of them to be acceptor levels in analogy with Dunlap's results on gold doping.[6] This assumption leads to a possible explanation for the observation of hole traps in n-type material. Assume N Fe atoms per cc, each contributing two acceptor states. If the crystal contains an excess of holes due to uncontrolled impurities of low ionization energy in the Ge and in the Fe, we shall not observe high-resistivity material as a result of Fe doping. We shall therefore assume that the crystal contains n excess electrons per cubic centimeter due to uncompensated low ionization energy impurities. If $0<n<N$, we shall observe high-resistivity p-type material. At low temperatures in thermal equilibrium, each Fe atom will either be neutral or possess a single negative charge. If $N<n<2N$, we shall observe high-resistivity n-type material, and at low temperatures in thermal equilibrium each Fe atom will possess either one or two negative charges. For $n>2N$, low-resistivity n-type material will be observed with $n-2N$ electrons characterized by low ionization energies. All of the Fe centers will possess two negative charges.

These assumptions give a tentative hypothesis for the observation of hole traps in n-type material under nonequilibrium conditions. An Fe site which in thermal equilibrium possesses two negative charges may trap a hole after which it is still negatively charged and has a low cross section for the capture of an electron because of an activation energy produced by Coulomb repulsion. Thus the return to equilibrium via this mechanism is slow. For high-resistivity p-type material the Fe sites in equilibrium have at most one negative charge. After the capture of a hole, the site is neutral and has a finite cross section for capture of an electron, acting as a recombination center rather than a trap. This hypothesis explains why n-type samples taken from crystals immediately after conversion from p-type show low photosensitivity but become progressively more photosensitive down the ingot. If n varies more rapidly than N, the trapping ratio increases and the effective concentration of hole traps increases, ap-

proaching the value N just before n becomes greater than $2N$.

ACKNOWLEDGMENTS

The authors would like to express their indebtedness to the members of the Semiconductor Studies Section for their continued interest and aid in this work.

In particular, they would like to thank L. Apker for many valuable suggestions concerning mechanisms of photoconductivity and trapping processes, W. C. Dunlap, Jr., for advice on experimental techniques and the interpretation of results, and E. M. Pell for making lifetime measurements in the initial stages of this work.

PHYSICAL REVIEW VOLUME 96, NUMBER 4 NOVEMBER 15, 1954

Properties of Germanium Doped with Iron. II. Photoconductivity

R. NEWMAN AND W. W. TYLER
General Electric Research Laboratory, Schenectady, New York

(Received August 11, 1954)

Photoconductivity in n- and p-type Fe-doped Ge was measured at 77°K. The impurity photoconduction in both types has approximately the same spectral dependence, indicating ionization energies of about 0.3 ev. The intrinsic photoconductive response measured at 0.83 ev was found to be a function of sample composition, the photosensitivity increasing as the samples became more n-type. Intrinsic photosensitivity and the time of response seem linearly related. For n-type samples of highest sensitivity the minimum detectable radiation level at 0.83 ev was estimated to be 2×10^{-13} watt. In such samples quenching effects were found in the spectral region from 0.3 ev to 0.7 ev. Experimental results are discussed in terms of a model in which the impurity center is capable of accepting two excess electrons.

INTRODUCTION

IN the preceding paper[1] it was shown that iron introduces energy levels near the middle of the forbidden region of germanium. The temperature-resistivity measurements located levels 0.27 ev from the conduction band and 0.34 ev from the valence band. It was also shown that the presence of iron in n-type germanium produces effects which can be described in terms of a trapping of photoinjected carriers.

This paper will describe the results of some measurements on the spectral dependence of impurity photoconduction in iron-doped germanium which yield values of the impurity ionization energies. It will also describe some measurements of the intrinsic photoconduction and of quenching phenomena which it is believed bear on the aforementioned trapping effects.[2]

EXPERIMENTAL

Samples were obtained in the form of small bars whose dimensions averaged about $3\times5\times10$ mm. These were cut from the original ingots in such a way as to maximize sample homogeneity. Fused Sn contacts were used for n-type samples. Fused Sn or In contacts were used for p-type samples. The data quoted here were obtained from samples for which temperature-resistivity data were also available. Seven n-type samples (from four ingots) and five p-type samples (from four ingots) were studied. Samples were mounted in a cryostat which was located at the exit port of a Perkin-Elmer spectrometer equipped with a CaF_2 prism. Unless otherwise stated all data were obtained at 77°K.

For the samples which possessed a high intrinsic sensitivity, the problem of distinguishing the true from the stray light response was severe. For example, at photon energies less than ~0.35 ev, even when a Ge filter was used and when the stray light was supposedly monitored by use of a thick glass block, false signals often obtained. Where this occurred the residual response occurring at a monochromator setting of ~0.15 ev was subtracted from the response observed at the higher energies. The correction was only important in the lowest decade of response.

Unless otherwise specified, the data quoted refer to measurements using unmodulated light. A sample was maintained at constant voltage (in most cases 6 volts) in a series circuit consisting of the sample, a battery, and a load. For photocurrents in the range 10^{-12}–10^{-6} amp, the load was a resistor. The current was detected using a "vibrating-reed electrometer" as a voltmeter across the load resistance. For larger photocurrents, the load was simply a sensitive ammeter. At low voltages (<20 volts), the photocurrent was usually linear in voltage. Nonlinearity appeared to be a function of the contacts and with care it could be minimized.

IMPURITY PHOTOCONDUCTION

Figures 1 and 2 show the spectral response of the photoconductivity of n- and p-type Fe-doped germanium at 77°K. The curves shown are typical of those found for all samples studied. The resolution of these curves into two spectral regions is obvious. Above

[1] W. W. Tyler and H. H. Woodbury, Phys. Rev. **96**, 874 (1954).
[2] R. Newman and W. W. Tyler, Phys. Rev. **94**, 1419 (1954). Describes a preliminary report of this work.

~0.7 ev intrinsic photoconduction dominates. Between 0.8 ev and 0.7 ev the photoresponse decreases about 4 decades. Below 0.7 ev the impurity photoconduction is dominant.

The assignment of a point of relative response to define the optical ionization energy for the impurity photoconduction is at best arbitrary. For the present data, the gradual way in which the response changes from a slowly to a rapidly varying function of photon energy makes any definition even more ambiguous. Perhaps the most that should be said is that the ionization energies found from the resistivity data lie in the spectral region where one would define the photoconductive edge. That is, the optical threshold is in the vicinity of 0.3 ev for both *n*- and *p*-types.

It is perhaps surprising that the spectral response curves of *n*- and *p*-type samples are so closely similar. From the resistivity data, a difference in the optical data might have been expected. The anticipated difference of ~0.07 ev for corresponding points on the response curves should have easily been detected.

INTRINSIC PHOTOCONDUCTION

As pointed out in the previous paper, at low-temperatures, Fe in *n*-type germanium produces traps which cause long times of response in the photoconductivity and, by the related time integration effect, high photosensitivity. The effects are similar to those observed in CdS at room temperature, for example.[3]

The previous paper describes a method of growing a single Fe-doped crystal which contains *p*- and *n*-type regions which show high resistance at low temperature. It was of interest to take a series of samples from such a crystal and compare their intrinsic photoresponse. It was observed that their sensitivity increased as they became more *n*-type. Figure 3 shows the photocurrent *vs* incident light intensity at 0.83 ev at a fixed applied voltage for four samples cut from the same crystal. One sample was *p*, the others *n*-type. Curves of resistivity *vs* reciprocal temperature for these samples are shown in Fig. 13 of the previous paper.[1] The samples show a linear photocurrent-intensity curve over a large range of response. It is noteworthy that a region of nonlinearity could be reached with the most light sensitive sample. The break in the curve for this sample occurs for a carrier concentration of the order of 10^{10}–10^{11}/cm^3. If the break corresponds to a transition to a range in which trapping effects saturate and additional photocurrent is limited by a simpler and faster recombination process, then the number quoted is perhaps an estimate of the density of traps which are present in the sample.

It was of interest also to test the so-called reciprocity law which predicts that the speed of response and the sensitivity of the photoconductor are inversely related. Figure 4 shows the photocurrent/unit intensity *vs* time constant for the same series of samples shown in Fig. 3 and one additional sample of high sensitivity from another ingot. The ordinate is the dc photocurrent obtained at an incident light intensity of 10^{-8} watt

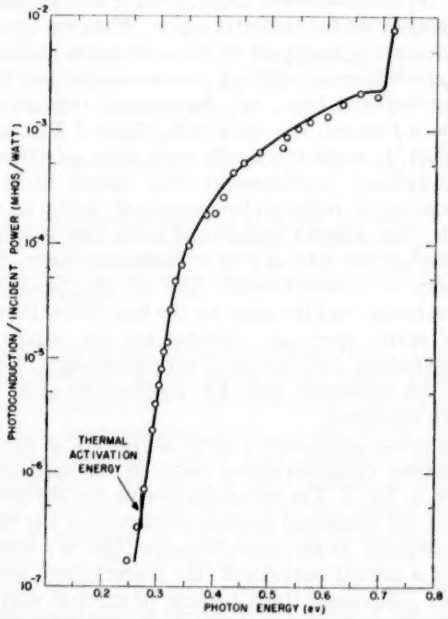

FIG. 1. Photoconductive spectrum of *n*-type Fe-doped Ge (sample 112*L*).

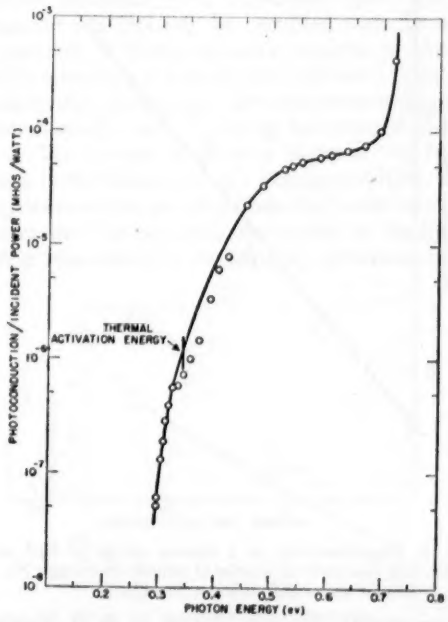

FIG. 2. Photoconductive spectrum of *p*-type Fe-doped Ge (sample 112*H*).

[3] A. Rose, RCA Rev. **12**, 362 (1951).

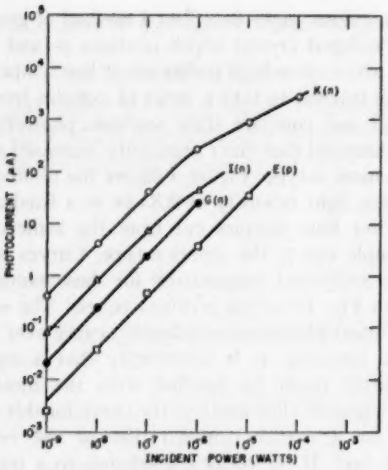

FIG. 3. Intrinsic photocurrent *vs* incident power (photon energy = 0.83 ev) for a series of samples from ingot No. 110. Sample *E* is *p*-type; samples *G*, *I*, and *K* are increasingly *n*-type in that order. The applied voltage was 6 volts.

divided by 10^{-8} watt. The abscissa is arbitrarily defined as the time required for the sample to recover in the dark from a "light on" resistance of about 10^4 ohms to a resistance of 10^7 ohms.[4] Using this definition, however, one does find a reasonably linear relationship between photosensitivity and a time constant describing the major part of the photoeffect. It should be pointed out that the recovery of resistance after exposure to light never approximates a simple exponential relationship and that no such linear relationship holds for recovery times characteristic of the long tails of the response (see preceding paper).

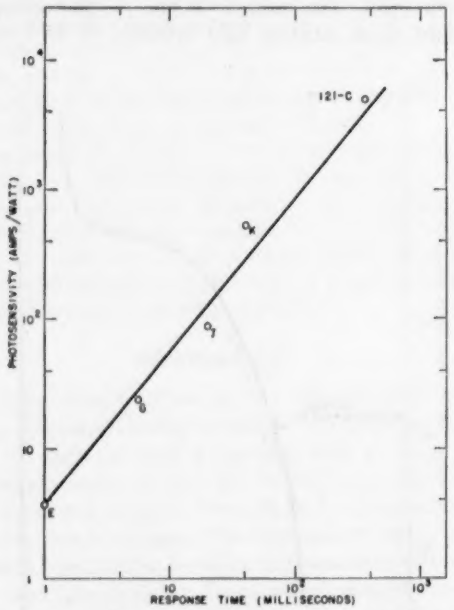

FIG. 4. Photosensitivity at a photon energy of 0.83 ev *vs* response time (see text) for a series of samples from ingot No. 110 (*E*, *G*, *I*, *K*) and a sample from ingot No. 121.

[4] These recovery times were obtained by H. H. Woodbury from photographs of oscilloscope tracings. The definition was one governed by experimental convenience.

The high photosensitivity of *n*-type Fe-doped germanium at low temperatures suggested its use as a detector of thermal radiation. We have made preliminary tests of its characteristics in this connection. With several of the more sensitive samples at 77°K, using the Perkin-Elmer 13 cps phase-sensitive system with an over-all effective band width of approximately 1 cycle, it was possible to detect 10^{-11} watt of 1.5-μ radiation with a signal-to-noise ratio of $\sim$50. This puts the minimum detectable radiation level at about 2×10^{-13} watt. In some rather crude tests, we found that our most sensitive samples were comparable to a commercial PbS cell cooled to 77°K in their ability to detect the thermal radiation from a low-power thermal source. The slow response and the limited spectral region of high sensitivity probably circumscribe the use of *n*-type Fe-doped germanium as a thermal detector.

QUENCHING

In samples of highest intrinsic photosensitivity and of slowest response, the phenomenon of quenching was encountered. Quenching in germanium had previously been found in certain *n*-type Au-doped crystals.[5] The phenomenon can be described as follows: A crystal is made to photoconduct by illuminating it with radiation occurring in the fundamental region. When the crystal is subsequently irradiated by monochromatic radiation in a certain spectral region of photon energies less than the fundamental limit, the photocurrent through the sample is reduced, i.e., quenched. Figure 5 illustrates the effect. It shows the steady state effect on different dc background photocurrents (the dashed lines) of monochromatic radiation simultaneously falling on the sample. The different background levels were obtained by varying the intensity of a fluorescent light. The intensity of monochromatic light at any particular photon energy was the same for the four curves shown. These curves were not corrected for the change in monochromatic light intensity with wavelength. However, this correction does not significantly alter the quench spectrum.

The lowest photocurrent curve of Fig. 5 is, of course, the normal photoconductive curve of the type illustrated in Fig. 1. The remaining curves are characteristic of the quenching process. Assume that the total photoresponse to the monochromatic light is a simple sum of a normal component (the lowest curve) and a quench component. Then because of the low relative magnitude of the normal component its contribution to the upper three curves is negligible. Thus the curves

[5] R. Newman, Phys. Rev. **94**, 278 (1954).

shown probably give a good representation of the spectral efficiency of the quench process. If this is so, then, in contrast to the case of gold where the quenching appeared as sharp bands, the quench spectrum here has more the appearance of a continuum with a low energy threshold in the vicinity of 0.3 ev. This is more clearly brought out if one plots the difference between the quenched photocurrent and the background photocurrent against photon energy.

The transient effects in the quenching will be mentioned only briefly. In the quenching condition, when quench light is turned on the photocurrent rises rapidly to a maximum (peak transient) and then decays slowly to a lower value which is usually less than the photocurrent set by the background light. When the quench light is turned off, the photocurrent rapidly drops and then recovers slowly to the value set by the background. In the Au-doped germanium, it was found that the "quench-light-on" decay time depended upon the intensities of the different light sources. Whereas the time constant for recovery with the quench light off was independent of them and also substantially independent of temperature in the 77°K to 20°K interval. A similar situation occurs here. The "quench-light-off" time constant for recovery was about 1 sec at both 77°K and 20°K. In passing, it should also be mentioned that the magnitude of the quenching increased at lower temperatures. For example, under conditions where a background photocurrent was 40 percent quenched at 77°K, a photocurrent of the same amount was 90 percent quenched at 20°K.

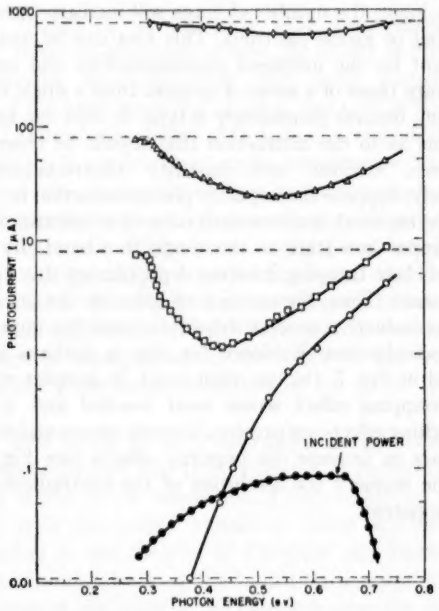

FIG. 5. Quench spectrum of an *n*-type Fe-doped Ge sample (82*C*) at different levels of background photocurrent (dashed lines). Ge filter on monochromator. Six volts applied. The bottom curve (solid circles) shows the power spectrum of the monochromatic beam.

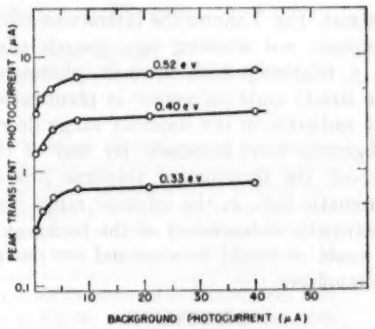

FIG. 6. Peak transient photocurrent at several photon energies *vs* background photocurrent for a sample showing quenching (82*C*). Six volts applied.

There appears to be an interaction between the impurity photoconduction and intrinsic photoconduction. That such an interaction should exist is not surprising. Altering the number of carriers in the conduction and valence bands must alter the population of carriers located at centers in the forbidden region, from which the impurity photoconduction is thought to arise. Figures 6 and 7 illustrate the effects observed. Figure 6 shows the effect for a sample which exhibits quenching. Here the peak transient photocurrent (defined in the foregoing) observed oscilloscopically when monochromatic light in the impurity range is turned on is plotted against the background photocurrent produced by a fluorescent light. The peak transient can probably be identified with the normal component of photoconductive response in situations where quenching is present. It is of interest to note that the impurity photoconduction, as so measured, increases asymptotically with increasing background photocurrent. The increase is about a factor of two from its value in the absence of any background light. This is suggestive of the sort of process that *could* occur if the Fermi level (in the dark) was located at the impurity center responsible for the impurity photoconduction.

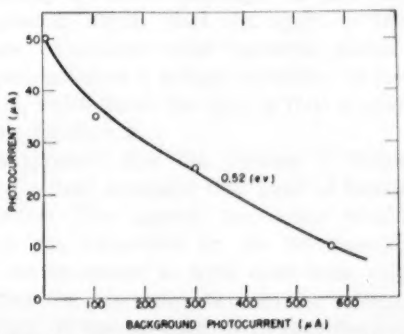

FIG. 7. Steady state photoresponse at 0.52 ev *vs* background photocurrent for an *n*-type sample (110*K*). Six volts applied.

In contrast, Fig. 7 shows the interaction effect in an n-type sample not showing any quench effect, but showing a relatively high intrinsic photosensitivity. Here the steady state increment in photocurrent produced by radiation in the impurity range decreases as the background level increases. By way of check on the method, the incremental response produced by monochromatic light in the intrinsic range was found to be essentially independent of the background level in both cases as would be expected for the range of currents involved.

DISCUSSION

As pointed out above, the spectral dependence of the impurity response for both n- and p-type samples was substantially the same. However, the photoconductive yield measured at some representative point, say 0.5 ev, differed markedly for the two types. The photoconductance/incident power expressed in arbitrary units was in the range 1–10 units for p-type samples and in the range 10^2–10^4 for n-type samples. The time constants for n-type samples were from 10 to 100 times that of p-type samples. It is thus possible to account for about a factor of 10^2 in the yield by the time constant effect. The remaining factor of 10^2 may reflect differences in the population numbers of the active centers and in their appropriate transition probabilities.

The arguments concerning the connection between trapping effects and quenching effects in germanium are discussed elsewhere.[5] In brief, they postulate that the background light produces hole electron pairs. The holes become trapped and by so doing inhibit normal recombination. The function of the quenching light is to empty the hole traps and allow the holes to recombine via recombination centers, thus reducing the electron population in the conduction band and consequently the over-all photoconductivity.

The impurity conditions of a sample in which quenching is found are unknown. There is some indication that it occurs only in ingots with a relatively light doping of iron. In any event, the samples which show the effect are the ones which show the highest photosensitivity and the longest times of response. This is offered as some evidence for the trapping hypothesis.

In the preceding paper a mechanism for trapping was suggested. It involved the trapping of a hole by a doubly negative charged iron center. By this mechanism, if the concentration of iron is relatively constant in an ingot, the number of traps will increase with the number of excess electrons. This idea can be used to account for the increased photosensitivity and longer recovery times of a series of samples from a single ingot as they become increasingly n-type. It also has implications as to the interaction that should be observed between intrinsic and impurity photoconduction. Namely, suppose the impurity photoconduction in, say, n-type material, involves excitation of an electron from the upper iron state to the conduction band. By the model, hole trapping involves depopulating this upper iron state. Thus, the creation of holes by the intrinsic photoconductive process should decrease the impurity photoconduction. Evidence for this is perhaps illustrated in Fig. 7. On the other hand, in samples where the trapping effect seems most marked and where quenching effects are present, intrinsic photoconduction appears to *increase* the impurity effects (see Fig. 6). At the moment the resolution of the contradiction is not apparent.

New Criterion for Superconductivity in Metals

GERHART GROETZINGER, DAVID KAHN, AND PHILIP SCHWED
National Advisory Committee for Aeronautics, Lewis Flight Propulsion Laboratory, Cleveland, Ohio
(Received July 22, 1954)

A criterion for the occurrence of superconductivity based on the (average) freedom number f of the free electrons in the metal is proposed and applied to the nine superconductors and twelve nonsuperconductors for which the freedom number can be calculated on the basis of the available information. For all the superconductors the freedom number lies between $+0.15$ and -0.16 and, while it is equal to 0.14 for one nonsuperconductor, it lies outside these limits for all the other nonsuperconductors. The quantity $\gamma=(n/n_f)f$, where n_f/n is the number of free electrons per atom, can be calculated for a larger number of elements (14 superconductors and 27 nonsuperconductors) than f. A criterion based on this quantity is still fairly successful for elements with normal Hall effect and somewhat less successful for elements with anomalous Hall effect. A comparison of the proposed criteria with criteria due to Kikoin and Lasarew, Fröhlich, and Bardeen shows that the criteria based on f and γ are more successful.

A NUMBER of attempts have been made to relate on an empirical basis the ability of a metal to become superconducting with other properties. One of the most successful of these was that of Kikoin and Lasarew[1] who found that both the magnitude of R, the Hall coefficient at room temperature and its product with the conductivity σ at room temperature, are in general smaller for superconductors. Figure 1(a)[2] shows on a pair of logarithmic scales the value of the quantity $|R|\sigma$ (which provided the better correlation) in the case of elements with normal ($R<0$) and anomalous Hall coefficients ($R>0$). Here, and in the rest of the figure, superconductors are listed to the left of the scale while nonsuperconductors are listed to the right.

In view of the recently discovered isotope effect,[3,4] it is now accepted that the occurrence of superconductivity is due to the interaction of the conduction electrons with the lattice vibrations. More specifically, according to the theories of Fröhlich[5] and Bardeen,[6] this interaction leads at the transition temperature to a change of the state of the electrons near the Fermi surface. Each of these investigators has given a criterion for determining whether this interaction is strong enough to lead to superconductivity in any given element. For this purpose, Fröhlich introduced the quantity α,

$$\alpha=0.5\frac{(n_f/n)^{5/3}\rho n}{\rho_{Ag}n_{Ag}}, \tag{1}$$

where ρ is the resistivity, n and n_f are the number of atoms and of free electrons, respectively, per unit volume of the element in question, and ρ_{Ag} and n_{Ag} are the values of ρ and n for silver. His criterion, which is not supposed to apply for transition metals or metals of the Bi group, is that α be greater than one for superconductors and smaller than one for other metals. Figure 1(b) shows the quantity α on a logarithmic scale for the elements for which the criterion is applicable. Fröhlich consistently took the factor (n_f/n) as being equal to one in computing α and we have done likewise in preparing Fig. 1(b). It should be mentioned that the correlation is not improved if the usually quoted values of n_f/n are employed. Bardeen's criterion, which is not supposed to apply to transition elements, is simply that β, which is defined by

$$\beta=\nu\rho n,$$

where ν is the chemical valence taken as being equal to the group of the element in the periodic table, is larger than 10^6 for superconductors and smaller than 10^6 for nonsuperconductors if ρ and n are expressed in electrostatic cgs units. Although, as just remarked, this criterion strictly does not apply to transition elements, he included those transition metals which are superconductors in testing its validity. In preparing Fig. 1(c), which shows the value of β on a logarithmic scale, we did likewise.

It is apparent that the criterion of Kikoin and Lasarew is more successful than those of Bardeen and of Fröhlich. The question thus arises whether the quantity $R\sigma$, considered by the first investigators, might not be related to some more basic parameter measuring the interaction between the electrons and the lattice. It has occurred to us that the (average) freedom number f is such a parameter. We have

[1] I. Kikoin and B. Lasarew, Nature **129**, 57 (1932).
[2] The following remarks apply to all the parts of Fig. 1. Unless it is stated otherwise, all the metals for which the required information is available in the literature were included. In each case, the most recently published values of the quantities required were used. The value of the resistivity of yttrium was kindly supplied prior to publication by Dr. F. H. Spedding, Ames Laboratory of the U. S. Atomic Energy Commission. The values used for Sn are those characteristic of the tetragonal form. Since mercury is not solid at room temperature the Hall coefficient used was that measured at -60°C and the "room temperature" value of the conductivity was derived from the values below the melting point using the relation $\sigma\sim1/T$.
[3] Reynolds, Serin, Wright, and Nesbitt, Phys. Rev. **78**, 487 (1950).
[4] E. Maxwell, Phys. Rev. **78**, 477 (1950); **79**, 173 (1950).
[5] H. Fröhlich, Phys. Rev. **79**, 845 (1950).
[6] J. Bardeen, Phys. Rev. **80**, 567 (1950).

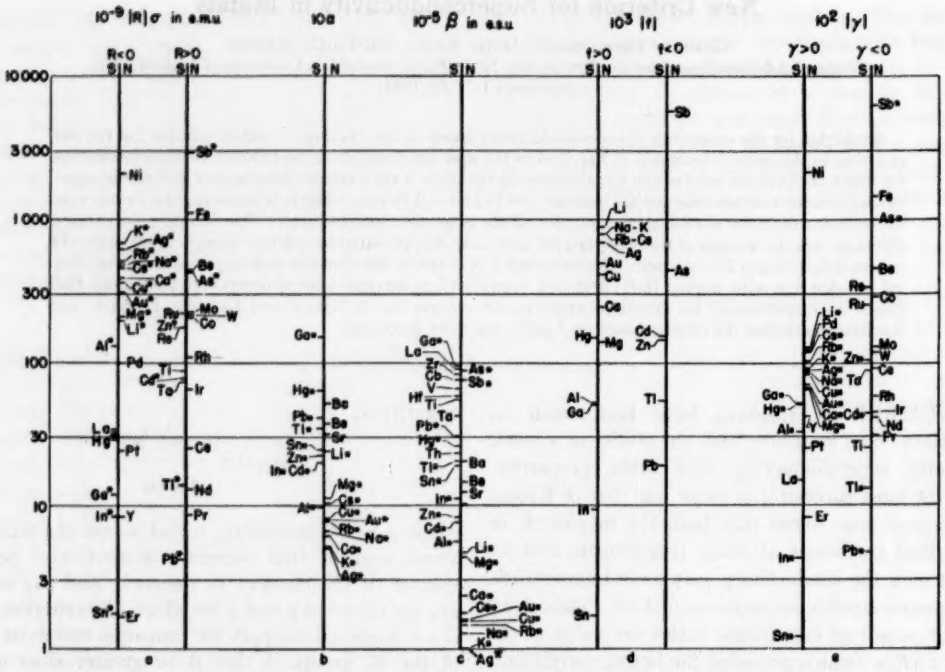

FIG. 1. Rrepresentation of various proposed criteria for the occurrence of superconductivity (a) Kikoin and Lasarew, (b) Fröhlich, (c) Bardeen, (d) and (e) present communication. The elements appearing in (d) are starred in the other parts of the figure. Elements with normal Hall effect are listed on the left-hand scale in (a), (d), and (e).

calculated f from the relation[7]

$$f=n_f eR/c, \tag{3}$$

where R is the (room temperature) Hall constant,[8] e is the (negative) electron charge, and c is the velocity of light. The values of n_f used here for the alkali metals and for Cu, Au, and Ag were obtained from the results of measurements of the refractive index and optical absorption coefficient.[7] With the exception of Be and the transition elements for which the following rule is not valid, the quantity n_f was obtanied for the other metals from the semiempirical relation[7]

$$n_f=nZT/(1650\rho A\Theta^2), \tag{4}$$

where Θ is the Debye temperature, ρ is the resistivity at the absolute temperature $T(\gg\Theta)$, and the other symbols have the conventional meanings. Figure 1(d) shows, on a pair of logarithmic scales, the absolute values of the freedom number thus obtained for metals with positive and negative freedom numbers. It can be seen that for the elements shown the freedom numbers of the superconductors lie between $+0.15$ and -0.16; while with the exception of Mg (for which $f=0.14$)[9] the nonsuperconductors have freedom numbers larger in magnitude than those for any of the superconductors. To expedite comparison between the present criterion and the others shown, the elements contained in Fig. 1(d) are starred in the rest of the figure. The result that $|f|$ is small for superconductors simply means that there is for these elements a strong interaction between certain of the electrons near the Fermi surface and the lattice. Thus, a small value of f ordinarily results if the Fermi surface intersects a Brillouin zone boundary so that electrons on either side of the crossing make opposite contributions to f. The existence of such an intersection, in turn, implies the strong interaction mentioned.

It was found that the value of n_f/n as estimated in the way described does not change too fast from element to element for those metals which have a freedom number in the vicinity of the critical values, i.e., near $f=\pm 0.15$. It seemed reasonable, therefore, to use instead of f the quantity $\gamma=(n/n_f)f$ which can be calculated for a considerably greater number of elements. Figure 1(e) shows on a pair of logarithmic scales the value of this quantity for metals for which it is

[7] See, e.g., H. Fröhlich, *Electronentheorie der Metalle* (Verlag Julius Springer, Berlin, 1936), Chaps. II and III.

[8] The room temperature value was used because in the absence of extraneous effects R is temperature independent and because many Hall coefficients are available only for this temperature. (See, however, reference 2 with regard to Hg.)

[9] The occurrence of this exception may be a consequence of the uncertainties in the values of f as obtained here.

positive and negative. It can be seen that considering the larger number of metals included, the degree of separation achieved between the two classes of metals is still fairly good. The value of γ lies between $+0.5$ and -3.4 for superconductors. The only nonsuperconductors for which γ lies in this range are transition elements which are excluded from all the other criteria except the one by Kikoin and Lasarew which is based on the value of $R\sigma$. A comparison of Fig. 1(a) with Fig. 1(e) shows that the degree of overlapping for γ is, however, smaller than that in $R\sigma$. In conclusion it can be said that the criterion suggested here [Fig. 1(d) and 1(e)] is more successful then any of the others shown in Fig. 1.

PHYSICAL REVIEW VOLUME 96, NUMBER 4 NOVEMBER 15, 1954

Reversible Susceptibility of Ferromagnetics*

D. M. GRIMES AND D. W. MARTIN
Engineering Research Institute and Department of Electrical Engineering, University of Michigan, Ann Arbor, Michigan
(Received July 6, 1954)

An expression is given relating the magnetization dependence of the reversible susceptibility normal to the field direction to that of the parallel reversible susceptibility. Modification of these susceptibility dependences due to the trapping of domain walls in metastable positions by potential holes is considered. The macroscopic magnetization is expressed in terms of a distribution of potential holes by an argument analogous to that of a "mean free path." The desirability of further examination of this approach is discussed. The reversible susceptibilities of three ferrite specimens were measured and found to compare favorably with the theory.

I. INTRODUCTION

IF one defines a susceptibility by the expression

$$\chi_r = \lim_{\Delta H \to 0} \frac{\Delta M}{\Delta H}, \tag{1}$$

when ΔH has a sense opposite to that of the change in H which brought the specimen to the point (M,H), the parallel reversible susceptibility χ_{rp} is defined in the usual manner. When ΔH is perpendicular to the direction of H, the transverse reversible susceptibility χ_{rt} is defined. If ΔH is in the same sense as the last change in total H, the differential susceptibility χ_d is defined. χ_d contains an irreversible component, χ_{rt} and χ_{rp} do not. The initial susceptibility χ_0 is defined as:

$$\chi_0 = \lim_{M \to 0} \chi_{rp}. \tag{2}$$

The parallel reversible susceptibility in ferromagnetic materials has been the subject of several authors since it was discussed by Gans[1] in 1911. A recent paper by Tebble and Corner[2] includes a general review. An expression for the transverse reversible susceptibility, given by Grimes, Orr, and Winsnes,[3] is developed in this paper. Experimental data are given for both reversible susceptibilities.

To develop expressions for these susceptibilities in terms of the magnetic parameters of a specified system, it is necessary to use different models, depending upon the particular calculation being considered. The models are altered as necessary in the following discussion. The justification for this procedure[4] is that the susceptibilities depend upon the statistical distribution of potential holes and the relative energy magnitudes involved. It presumably matters little what the specific assumed model is so long as the proper energy relations are maintained.

II. THEORETICAL DEVELOPMENT

A. The Initial Susceptibility

From measurements of the permeability spectrum using particle sizes down to the order of single domains, Rado, Wright, and Emerson[5] have shown convincingly that the low-frequency initial susceptibility of ferrites is caused primarily by wall movement rather than by rotational processes. It is therefore of interest to note how this susceptibility must depend upon the forces to which the wall is subject.

A plot of the energy of a ferromagnetic body as a function of position x of a given wall would be, over a small region, an irregular curve with many hills and valleys. When no field is present the wall will be found at a minimum position x_1. If the energy is assumed to be a continuous function of x, then near x_1,

$$V(x) = V(x_1) + (1/2\rho_r)(x-x_1)^2 + \cdots,$$

* Work supported by the Signal Corps Engineering Laboratories, Fort Monmouth, New Jersey.
[1] R. Gans, Z. Physik. **12**, 1053 (1911).
[2] R. S. Tebble and W. D. Corner, Proc. Phys. Soc. (London) **63**, 1005 (1950).
[3] Grimes, Orr, and Winsnes, Phys. Rev. **91**, 435 (1953).
[4] W. F. Brown, Jr., Phys. Rev. **52**, 325 (1937); Phys. Rev. **53**, 482 (1938); Phys. Rev. **54**, 279 (1938). These will be referred to as Parts I, II, and III, respectively.
[5] Rado, Wright, and Emerson, Phys. Rev. **80**, 273 (1950).

where ρ_r is the radius of curvature of $V(x)$ at $x=x_1$. When a reversible field dH is applied, the potential of the wall becomes

$$V^*(x)=V(x)-\gamma M_s x dH,$$

for a wall of unit area. γ is a constant depending upon the type of wall. The wall must move to the minimum of $V^*(x)$, so

$$dM_r=\gamma M_s(x-x_1)=\rho_r\gamma^2 M_s^2 dH,$$
$$\chi_r\equiv dM_r/dH=\rho_r\gamma^2 M_s^2. \quad (3)$$

Since this expression applies to a wall of unit area, the problem of explaining the initial reversible susceptibility becomes that of determining the distribution of the wall area per unit volume located at minima of all possible radii ρ_r, and hence also the distribution of such minima.

B. Reversible Susceptibilities

Gans[1] first suggested the parametric equations,

$$M/M_s=f(\eta), \quad \chi_{rp}/\chi_0=3f'(\eta), \quad (4)$$

where η was an adjustable parameter and $f(\eta)=L(\eta)$, the Langevin function:

$$L(\eta)=[\coth\eta-(1/\eta)].$$

The prime indicates $d/d\eta$.

These equations were found to fit quite well the data for iron and nickel. They were first derived by Brown[4] in 1938 by assuming ferromagnetic material to consist of N domains per unit volume all of fixed and equal volume. These domains were considered to be subjected to random but fixed forces in such a manner that the ordinary techniques of statistical mechanics could be applied.

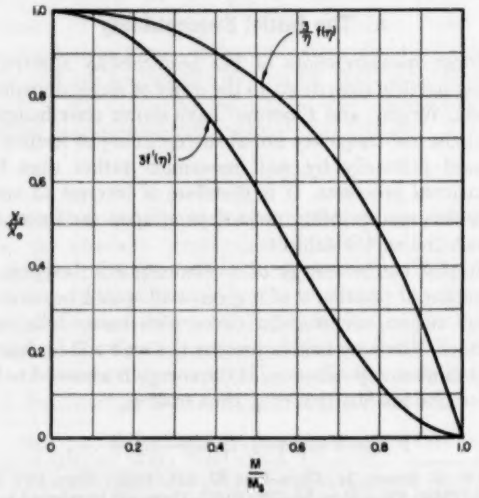

FIG. 1. The parallel and transverse reversible susceptibilities *versus* magnetization for $f(\eta)=\coth\eta-1/\eta$.

If the parallel reversible susceptibility is given by Eq. (4), where $f(\eta)$ is a continuous function of η, χ_{rt}/χ_0 can be developed[6] by assuming that the change in magnetization dM accompanying a change dH_r is such as to keep the total magnetization always parallel to the total field. Then

$$\chi_{rt}\equiv dM/dH_{rt}=M/H_r,$$

where H_r is defined by

$$H_r=\int_0^M \frac{dM}{\chi_{rp}}$$

and is proportional to η. ($\eta=AM_sH_r$.) Therefore,

$$\frac{1}{\chi_{rp}}\equiv\frac{dH_r}{dM}=\frac{d}{dM}\left(\frac{M}{\chi_{rt}}\right).$$

Upon substituting for M and χ_{rp} from Eq. (4) and integrating,

$$\chi_{rt}/\chi_0=3f(\eta)/\eta, \quad (5)$$

since $\chi_{rt}=\chi_{rp}=\chi_0$, when $M=0$.

Brown obtains Eq. (4), from which Eq. (5) follows, for spherical and cubic symmetries. The form of $f(\eta)$ varies with the exact anisotropy type. He found $f(\eta)=\coth\eta-1/\eta$ for isotropic material, and more complicated expressions for [111] and [100] anisotropies. These three expressions, when expanded for small values of η, are identical up to the seventh order. For the specialized anisotropy types the magnetization vectors are assumed to lie only in the specific easy directions of magnetization. Experimental data should approximate this case only for rather small applied fields, for at higher fields domains will begin to leave these directions to become more nearly aligned with the field. The resulting behavior approaches that of the isotropic case so the isotropic equations should be a good approximation throughout. χ_{rp}/χ_0 and χ_{rt}/χ_0 are plotted *vs* M/M_s in Fig. 1; the data are given in Table I, column (*a*).

Brown[7] later derived Eq. (4) by using a model allowing wall movement and a variation in domain size.

C. Extension of Reversible Theory

For a perfect single crystal with zero demagnetizing factor the application of a small field parallel to an easy direction of magnetization should result in an infinite susceptibility. That it is not infinite in polycrystalline material can be considered to be a result of two different types of forces acting to retard wall movements: reversible and irreversible.

The reversible forces can be considered to arise from intragranular potential minima and from intergranular demagnetizing factors. In the discussion of Sec. A the forces were described in terms of an energy function that was a continuous function of spatial coordinate. The exact nature of this force distribution cannot be known.

[6] W. F. Brown, Jr. (private communication).
[7] W. F. Brown, Jr., Phys. Rev. **55**, 568 (1939).

It would be desirable to be able to predict the qualities of the material which do not depend upon the precise distribution.

That Brown's[8] W of Part I is very stable with respect to different distributions can be seen by observing that in the neighborhood of the extremum value given by $\partial \ln W/\partial N_\gamma=0$ higher derivatives of $\ln W$ with respect to N_γ form a polynomial in negative powers of N_γ. An illustration of the stability of this equation would be an application of the equations for isotropic material to [111] or [100] oriented material. The equality to high values of η can be directly attributed to the slowly varying character of W.

We therefore consider the distribution of magnetic moments in a ferromagnetic material when only random reversible forces are applied to be described by Brown's[4] Eq. (9) of Part I without further definition of the specific "randomness" involved. The resulting magnetic disorder could be considered analogous to a magnetic entropy and should be considered when dealing with magnetic energy problems.

We now wish to discuss susceptibility using statistical arguments to describe the irreversible trapping of domain walls in metastable positions by potential holes. Each hole is to be characterized by a single number, loosely called its "depth" f. A wall encountering such a hole will be trapped if the total net force of the field plus reversible forces on the wall is less than f, but will break free irreversibly if this force exceeds f. Actually these potential minima must surely, for finite wall areas, have a finite radius of curvature. However, for purposes of this discussion we consider them to be infinitely sharp "snags," i.e., a wall is held rigidly when trapped by a potential hole. A wall thus held would contribute nothing to the susceptibility. The true behavior of a ferromagnet must lie somewhere between this model and the model assuming only reversible behavior.

We define n_j to be the fraction of the total number of atoms whose permanent dipole moments are oriented in the direction of the unit vector $\bar{\gamma}_j$. (This is not the same definition Brown uses for $n_\sigma{}^r$.)

If no potential holes are present when a field $\mathbf{H}$ is applied, according to the reversible equations:

$$n_j=\exp[AM_s(\mathbf{H}\cdot\bar{\gamma}_j)]/\textstyle\sum_i \exp[AM_s(\mathbf{H}\cdot\bar{\gamma}_j)]. \quad (6)$$

In terms of wall positions, this must also be equal to

$$n_j=\frac{1}{\sum_i \bar{\gamma}_i{}^2}+\sum_i \sum_\sigma a_{ij}{}^\sigma x^\sigma, \quad (7)$$

where $a_{ij}{}^\sigma$ is the area of a particular wall separating domains oriented in the directions $\bar{\gamma}_i$ and $\bar{\gamma}_j$, respectively, x is the spatial coordinate of the wall relative to a position at which the total net magnetization is zero and Brown's[4] Eq. (9) Part I is an extremum, and $\sum_\sigma$ is a sum over all walls of class ij in unit volume.

[8] See reference 4, part I, p. 326.

TABLE I. Parallel and transverse reversible susceptibilities *versus* magnetization for (*a*) isotropic material, (*b*) all atoms either parallel or antiparallel with the applied field, and (*c*) no atoms making angles greater than $\pi/2$ with respect to the applied field.

M/M_s	$\chi_{\parallel}/\chi_0$ (a)	(b)	(c)	$\chi_{\perp}/\chi_0$ (a)	(b)	(c)
0.0	1.000	1.000	···	1.000	1.000	···
0.2	0.929	0.960	···	0.967	0.983	···
0.4	0.724	0.838	···	0.900	0.946	···
0.5	0.581	0.745	1.000	0.837	0.908	∞
0.6	0.421	0.640	0.923	0.750	0.826	5.67
0.7	0.259	0.526	0.728	0.637	0.804	3.24
0.8	0.119	0.373	0.410	0.480	0.725	1.98
0.9	0.030	0.182	0.012	0.270	0.614	1.08
1.0	0	0	0	0	0	0

If there were no snags, x would be a function, for a given wall, only of the pressure which the applied field exerts, given by

$$p^{ij}=M_s[\mathbf{H}\cdot(\bar{\gamma}_i-\bar{\gamma}_j)].$$

The wall would find an equilibrium position for which the reversible forces just balanced this pressure.

When snags are present walls will become trapped in them, and x will no longer be a simple function of pressure. We can express the average x for a large number of walls in terms of the size distribution of these snags by arguments of the nature of a "mean free path" discussion.

Let the number of snags per unit volume whose depth lies between f and $f+df$ be given by $\xi(f)df$. Let there be an initial state in which there is a field $\mathbf{H}_0$ present, and all the walls occupy positions x_0 determined only by this field and the reversible forces, i.e., no walls are snagged in metastable positions. When the field is changed to $\mathbf{H}_1$, there will be a net force on each wall which will diminish again to zero when the wall reaches a new equilibrium position x_1. As a wall of area a moves over an interval dx, it sweeps over a volume adx. And if this volume contains a snag "deeper" than the net force of the field plus reversible forces at that place, then the wall will be caught and held there.

Of all the walls in unit volume, let us select for attention the group consisting of all walls of class ij with area between $a_{ij}{}^\sigma$ and $a_{ij}{}^\sigma+da_{ij}{}^\sigma$. By choosing the coordinates so that x_0 is zero for each wall, then in first approximation the final "reversible" position x_1 of every wall of this select group is equal to the average value $\bar{x}_1$, and the net force $f(x)$ of field plus reversible force at each value of x for every wall is equal to some $\bar{f}(x)$ averaged over all the walls.

Let $N_0{}^\sigma$ be the number of walls in this group, and $N^\sigma(x)$ the number not yet caught after moving a distance x from x_0. Then clearly

$$dN^\sigma(x)=-N^\sigma(x)a_{ij}{}^\sigma dx\int_{\bar{f}(x)}^{\infty}\xi(f)df,$$

$$N^\sigma(x)=N_0{}^\sigma\exp\left[-a_{ij}{}^\sigma\int_0^x dx'\int_{\bar{f}(x')}^{\infty}\xi(f)df\right].$$

The fraction of the original group of walls that becomes snagged in the interval x to $x+dx$ is then

$$\Psi^{\sigma}(x)dx=|dN^{\sigma}(x)|/N_0{}^{\sigma}=\left(\exp\left[-a_{ij}{}^{\sigma}\int_0^x dx'\right.\right.$$
$$\left.\left.\times\int_{\bar{f}(x')}^{\infty}\xi(f)df\right]a_{ij}{}^{\sigma}\int_{\bar{f}(x)}^{\infty}\xi(f)df\right)dx,$$

and the average position at which the walls of the group considered become snagged and stop is

$$\bar{x}^{\sigma}=\int_0^{\bar{x}_1}x\Psi^{\sigma}(x)dx. \tag{8}$$

Apart from the idealization of the potential holes as sharp snags, the most tenuous point of the above discussion is the use of the average net force function $\bar{f}(x)$. The reversible forces actually may vary greatly from wall to wall. In keeping with the original idealization, all local irregularities in the $f(x)$ of any individual wall may be lumped in with the snags, leaving only a smooth curve which decreases from a maximum at $x=0$ to zero at x_1. There still remains the possibility of large differences in $f(0)$ from wall to wall. But this is no difficulty in principle, for one could merely further subdivide the groups of walls into subgroups according to the value of $f(0)$, assume a distribution in numbers of walls in the subgroups, and sum the results over the subgroups. The same comments apply to the use of the average $\bar{x}_1$ in the calculation.

The point is that if the sole object of the formula were the explicit calculation of magnetization curves, one could undoubtedly build enough assumptions and parameters into it by refinements of this type to fit any amount of experimental data. It is surely doubtful if this would be sensible in view of the extreme idealization of the model. It remains of some interest to see if some rough quantitative agreement could not be obtained with the expression in its simplest form, using reasonable assumptions for $\xi(f)$. Such a check is desirable to see if this type of analysis does have any real validity, but this has not yet been done.

However, one important conclusion follows from the form of Eq. (8) independent of these details. To the same approximation as that contained in Eq. (8), the quantity x^{σ} to be used in Eq. (7) for the strictly reversible case is exactly the average "final reversible" coordinate $\bar{x}_1$ that appears as the upper limit in Eq. (8). Now $\bar{x}_1$ must have a certain (perhaps quite complicated) dependence on the relative directions of $\bar{\gamma}_i$, $\bar{\gamma}_j$, and the applied field $\mathbf{H}$ that is consistent with the existence of Eq. (6) for the reversible case. Without any detailed analysis it is clear that $\bar{x}^{\sigma}$ has additional dependence on these directions arising in the expression for $\Psi^{\sigma}(x)$. So the distribution in numbers of atoms oriented in the various possible directions, in the presence of "snags" and metastable wall positions, is different from that implied by an expression of the form of Eq. (6). This amounts to saying that it is not possible to define any simple vector "effective field" $\mathbf{H}'$ that allows a description of the system in terms of Eq. (6). Brown[9] has shown that only if such a vector field exists do the parametric Eqs. (4) hold. Therefore we do not expect them to be strictly true.

The understanding that the affect of the irreversible forces on Eqs. (4) and (5) arises through a redistribution of populations in the various possible directions suggests a simplified approach. One can say that effectively the material has certain peculiar unsymmetrical anisotropy properties that will also lead to a redistribution of atomic moments. It is shown below that certain qualitative features can be correctly predicted very simply in this way for a few special circumstances for which the direction of this redistribution is apparent.

D. Modifications of the Reversible Model

Contribution of Metastable Volume

The reversible susceptibility of a ferromagnetic material is decreased from the value predicted by the reversible equations by the presence of intragrain potential holes. In general, the greater the depth of a minimum the smaller is its radius of curvature, and therefore the less a wall occupying it will contribute to the susceptibility. The decrease should become larger as the peak M reached during a cycle increases, causing walls to cross potential barriers capable of retaining them in deep metastable states. In general, it would not be the same holes that would decrease the two different susceptibilities.

High M/M_s, Decreasing $|\mathbf{M}|$

When $|\mathbf{M}|/M_s=1$, all the material is necessarily aligned with the applied field. As $|\mathbf{M}|$ is decreased from M_s the metastable volume will be predominantly oriented in the direction of M_s. The remainder we take to be oriented in accordance with the reversible equations. Since the number of atoms with their magnetic moments parallel with the biasing field is increased by the action of the potential holes, at a specified value of M there must also be more atoms aligned antiparallel than would otherwise be the case. Since the number of atoms is fixed this must also mean that the number of atoms oriented in all other directions is diminished.

To find qualitatively how this affects the susceptibilities, consider an extreme case where all magnetic moments are oriented either parallel or antiparallel with the field. Brown's[4] Eq. (3) of II then becomes

$$M/M_s=\tanh\eta,$$

where, as usual, $\eta=AM_sH_r$.

[9] See reference 7, p. 574.

This leads to:[10]

$$\chi_{rp}/\chi_0=\operatorname{sech}^2\eta;\quad \chi_{rt}/\chi_0=\tanh\eta/\eta. \tag{9}$$

Values of χ_{rp}/χ_0 and χ_{rt}/χ_0 *vs* M/M_s are given in Table I. Both curves are higher than the corresponding curve for isotropic material, but are of the same order and of the same general form.

High M/M_s, Increasing $|\mathbf{M}|$

In the randomly oriented state, none of the volume is in a metastable condition, but after the application of an external field a finite fraction of the material will be. Those domain walls which are located between atoms with moments parallel and antiparallel to the field will move the farthest when a field is applied. Therefore the fraction of the atoms which find themselves in metastable positions should be greatest for those atoms oriented antiparallel to the field, and zero for those oriented parallel. As the magnetization increases, however, the amount of material available to be held in these metastable states is least for antiparallel and greatest for parallel alignment. Therefore at all values of magnetization greater than a certain minimum, the number of atoms whose magnetic moments are held in metastable positions must go through a maximum at some angle between 0 and π, and so for a given η the normal component of magnetization is increased. It then follows that for a specified M the total magnetic moment both parallel and antiparallel with the field is decreased, while the difference remains constant.

In the limiting case, the number of atoms antiparallel decreases to zero, i.e., no atoms possess magnetic moments making angles greater than $\pi/2$ with the applied field. For this case the magnetization would be given by:

$$\frac{M}{M_s}=\left(\frac{e^\eta}{e^\eta-1}-\frac{1}{\eta}\right).$$

For small fields,

$$M/M_s=\tfrac{1}{2}+\eta/12+\cdots.$$

The resulting susceptibilities are given by:[11]

$$\frac{\chi_{rp}}{\chi_0}=12\left\{\frac{1}{\eta^2}-\frac{e^\eta}{(e^\eta-1)^2}\right\},$$
$$\frac{\chi_{rt}}{\chi_0}=\frac{12}{\eta}\left\{\frac{e^\eta}{e^\eta-1}-\frac{1}{\eta}\right\}. \tag{10}$$

χ_0 is the value of the parallel reversible susceptibility when $\eta=0$. From this model, $\chi_{rt}\neq\chi_{rp}$, when $\eta=0$. Values of M/M_s, χ_{rp}/χ_0, and χ_{rt}/χ_0 are given in Table I.

Obviously χ_{rt}/χ_0 is much greater for this model than for the isotropic model.

[10] The integration constant in χ_{rt}/χ_0 must be zero for symmetry to exist about $\eta=0$.

[11] To evaluate the integration constant note that χ_{rt} must become infinite at some value of M/M_s. It will be positive above that value and negative below. The only point where such a discontinuity can exist is for $\eta=0$. Thus the integration constant must be zero.

III. EXPERIMENTAL METHOD

Experimental data were taken to (*a*) check the validity of the equations describing χ_{rt} *vs* M, and (*b*) to see if deviations from the predicted values of χ_{rp} and χ_{rt} *vs* M using $f(\eta)=L(\eta)$ can be explained in terms of the discussion of the previous section.

The gross magnetization of the samples is excited by a battery-powered dc field, and is measured by the change of flux through windings on the sample when this "bias field" is abruptly changed. This measurement is made with a General Electric fluxmeter. Susceptibility was measured by observing, with a vacuum tube voltmeter the voltage developed across a winding on the sample when a 5 kc/sec current of small known amplitude was driven in the same winding. The flux is assumed to be in phase with the current, so that the induced voltage lags the ohmic voltage by 90°.

A toroidal specimen shape was chosen so that the conflicting requirements for both the parallel and transverse susceptibility measurements could be met by the same sample as far as possible. Closed flux paths around the ring eliminate demagnetizing effects for fields in this direction, while the lateral extent of the specimen is confined so that homogeneous transverse fields may be more readily applied. Susceptibility is measured in both cases around the ring using a toroidal winding. For the parallel case, the bias field is applied by a second toroidal winding, while for the transverse case it is applied along the toroidal axis by an external electromagnet.

Magnetization Measurements

In the parallel case, the applied field varies with position but its average value can be accurately calculated, except for small leakage effects, from the current. The sensing winding detects the total change in flux which is proportional to the average induction. The difference is 4π times the average magnetization. There is considerable difficulty in the determination of the saturation magnetization. The plot of M is still increasing at fields over 200 oersteds, at which value leakage is becoming important and ohmic heat excessive. We obtained the plot this far, and then fitted a Langevin function to the last two points to obtain an estimate of M_s that is believed good to 10 percent. Error in this value affects the normalization of the abscissas of the χ_{rp} *vs* M curves.

In the transverse case the applied field is not known from the bias current, here applied to the electromagnet, because of reluctance and hysteresis of the magnet. It is taken equal to the flux density through the hole in the center of the toroid. This value is measured relative to a

reproducible starting point by observing as the magnet current is cycled, the flux changes in a search coil which embraces the hole. The total flux through the core volume is measured using a girdle winding placed snugly about the inner and outer peripheries of the toroid.

The difference of these two readings we call the apparent magnetization M_a. By an elementary calculation $M_a=(1-N/4\pi)M$, where $N/4\pi$ is the demagnetizing factor. If the geometry is such that the magnetization is homogeneous, then $N/4\pi$ will be constant independent of M, and the ratio of M_a to the apparent saturation value M_{sa} will be strictly equal to the true ratio M/M_s. We thus obtain the properly normalized abscissa without having to determine the demagnetizing factor or the true M_s. To this end, the magnet was built with accurately parallel plane pole faces and a continuously adjustable gap that can be fitted snugly against the windings of the sample. The magnet readily provides very high fields that yield a well defined value of the apparent saturation M_{sa}.

Susceptibility Measurements

In the transverse case the bias magnetization is assumed to be homogeneous, so that the susceptibility is constant throughout the sample. In the parallel case, however, the bias field varies inversely as the radius from the axis of the toroid, so the magnetization and the susceptibility also vary. The observed average of the susceptibility is $4\pi\bar{\chi}=(\bar{\mu}_\Delta-1)$, where $\bar{\mu}_\Delta$ is proportional to the ratio of an induced voltage to a current, and hence

$$\bar{\mu}_\Delta=\overline{\Delta B}/\overline{\Delta H}=\int \mu\Delta H dr \Big/ \int \Delta H dr.$$

Since ΔH is applied by a toroidal winding, it varies as $1/r$, so

$$\bar{\mu}_\Delta=\int \frac{\mu}{r}dr \Big/ \int \frac{1}{r}dr.$$

Thus,

$$\bar{\chi}=\frac{1}{\ln(r_2/r_1)}\int_{r_1}^{r_2}\frac{\chi(r)}{r}dr, \tag{11}$$

where r_1 and r_2 are the inner and outer radii of the toroid, respectively.

It is necessary to calculate this average from the theoretical curves in order to compare with experiment. Because the theory gives only the dependence of χ on M, one must know how M depends on H, which varies as $1/r$, to evaluate the integral. We have made two different simplified assumptions for the $M-H$ loop which represent opposite extremes of observed behaviors. We calculated the integral (11) numerically for each, using the theoretical $\chi-M$ relation. The resulting $\bar{\chi}$ *vs* $\bar{M}$ curves are found to be much alike, and each differs from the uncorrected curve in essentially the same way. Since the result is so insensitive to the details of this assumption, and in view of the uncertainties in our data, it is felt that the labor of preparing a separate curve especially fitted to the experimental $M-H$ loop of each sample would be excessive, particularly since this latter curve is itself only a relation of averages. Therefore a compromise curve displaying the general features of the two special cases has been used for comparison with experiment in all cases.

This compromise curve appears as the theoretical transverse curve in Fig. 2. The two cases for which it represents the average are:

(1) The $M-H$ loop is a parallelogram:

$$M=\beta M_s(H/H_c\pm 1);\quad -M_s<M<M_s.$$

(2) The $M-H$ loop is two displaced Langevin functions:

$$M=M_sL[K(H/H_c\pm 1)],$$

where H_c is the coercive force. The free parameters β and K are given the values 0.2 and 0.615, respectively,

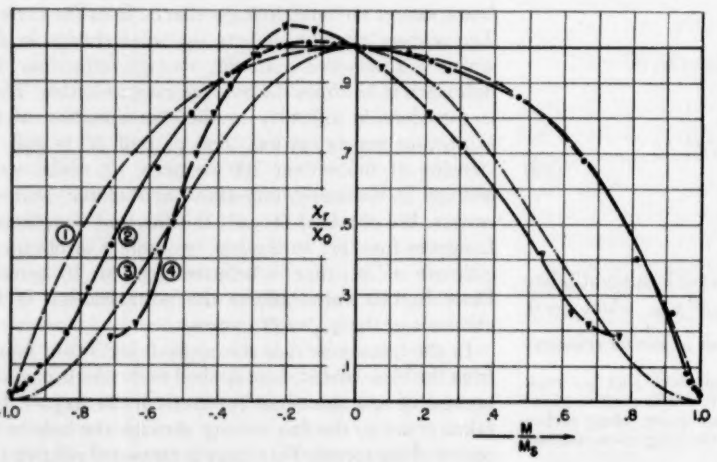

FIG. 2. Parallel and transverse reversible susceptibility *vs* magnetization. The dashed curves are the theoretical curves, with $f(\eta)=\coth\eta-1/\eta$. The solid curves represent experimental measurements. (Core E-3, 25°C.) Curves ① and ③ are for transverse, ② and ④ for parallel susceptibility. Curve ③ incorporates the corrections due to geometric averaging (Sec. III).

to fit these assumptions to the criterion that remanent magnetization $M_R=0.2M_s$. The result is further specialized in that the ratio r_1/r_2 is taken as 0.5.

IV. EXPERIMENTAL RESULTS AND COMPARISON WITH THEORY

Data were taken mainly on three cores purchased from the General Ceramics and Steatite Corporation, Keasby, New Jersey, representing their types *E*, *G*, and *I* ferrites. Most measurements were made at room temperature, but some were made up to 100°C. The interesting features of the data were virtually identical in all cases.

For two of the samples the apparent saturation magnetization was about 20 percent less than the extrapolated parallel value, indicating an effective demagnetizing factor of about 0.2 for the transverse geometry. The third sample was about 50 percent thicker than the others, and gave equal values of M_s for both cases. Evidently the increased thickness sharply reduces the demagnetizing factor. As expected, this produces no noticeable effect on the normalized χ_{rt} *vs* M curve.

In Fig. 2 are shown the parallel and transverse curves for a typical case compared with the corresponding theoretical curves. In Fig. 4 the same curves are shown separately plotted on a folded abscissa for comparison of the ascending and descending branches of each, together with a similar plot of χ_{rp} *vs* the applied field. In Fig. 3 are shown the parallel curves from three different minor loops, in which the peak value of M reached in the cycle is varied.

The curves of Fig. 2 are normalized to the value of χ at $M=0$ on the loop in question, for convenience in comparison with the theoretical curves. The actual χ_0 obtained when the sample is fully demagnetized is always larger than this, and in fact always exceeds the peak values of all these curves as expected. Note that the experimental curves lie generally below the theoretical curves, although with this normalization they lie higher in the region of the maximum. This is in keeping with the previous remark that potential irregularities always act to decrease the susceptibility.

In Fig. 2, the maximum in both cases lies to the left of zero, on the side of decreasing $|\mathbf{M}|$. We can understand this in terms of the trapping of walls by snags. The contribution to the reversible susceptibility of any wall caught by a snag is always diminished. Idealizing this, imagine that on a given loop a certain fraction D of the volume of the sample be held in metastable condition by snags, and contributes nothing to χ_r. Then the total susceptibility of the sample will be maximum when the magnetization of the remaining free volume $(1-D)$ is zero. The metastable volume D will, however, still contribute a net magnetization in the direction of the last previous maximum of M.

The shifting of the susceptibility peak with M_{max} of

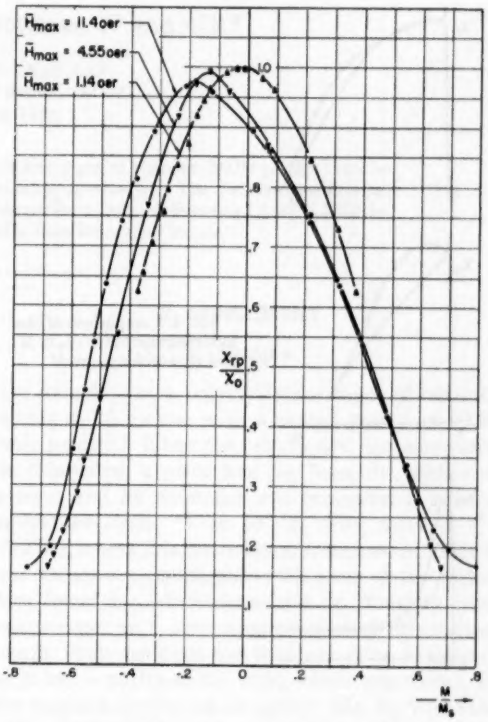

FIG. 3. Variation with peak $|\mathbf{M}|$ of the value of M/M_s at which maximum χ_{rp} occurs. (Core E-3, 25°C.)

Fig. 3 can be understood in the same way. As the peak M of the cycle is increased, the fraction D which is forced over into deep metastable positions would evidently also increase. This will obviously shift the susceptibility peak further to the left and diminish its height, as observed. The given curves apply to the parallel case. The same behavior is expected for the transverse case, but minor loop curves could not be accurately obtained with our procedures.

The location of the susceptibility peak on the decreasing $|\mathbf{M}|$ branch causes this whole branch to lie generally higher than the ascending $|\mathbf{M}|$ branch. In Fig. 4 it is seen that this is true everywhere for the parallel case, and also at low values of magnetization in the transverse case. However, the discussion of Sec. II indicates that for the transverse case, larger values of χ are to be expected on the ascending branch than on the descending branch. In Fig. 4 one sees that the curves do cross over at high M/M_s. The location of this crossover would be expected to shift to lower M/M_s as M_{max} was decreased.

According to Tebble and Corner,[2] the peak in susceptibility occurs at values of M less than remanence. Thus, a plot of χ *vs* the applied field H has its maximum where H is increasing from zero, but is less than the coercive force. Our data for the parallel case, illustrated by the last graph of Fig. 4, agree with this. Note in the

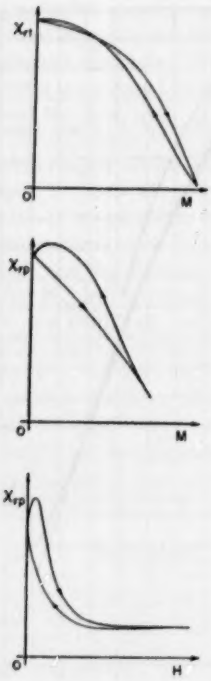

FIG. 4. Comparison of the hysteresis loops for χ_{rp} *vs* M and H, and for χ_{rt} *vs* M.

figure that although the χ *vs* M and χ *vs* H loops look much alike, the directions of travel around them are opposite.

In the transverse case we know the net applied field only very uncertainly, as a small difference of very large terms. Therefore we do not have any good measure of transverse remanence. For two of the samples the transverse susceptibility peak occurs at a value of M/M_s less than the corresponding parallel remanence, but for the third sample the peak is broad and occurs at an M/M_s equal to or perhaps a little greater than the parallel remanence.

The accuracy of our susceptibility measurements was limited by the noise reading on our instrument for measuring the voltage drop across the toroid, (Hewlett Packard 400C VTVM) and our ability to read the meter. The normalized data are considered accurate within ± 5 percent, the absolute values accurate within ± 8 percent.

With the exception of the parallel field measurement of M_s, our magnetization data are limited in accuracy by fluxmeter drift and errors in meter reading. These are considered to be well within ± 5 percent.

V. SUMMARY AND CONCLUSIONS

As far as the authors are aware, the statistical approach to the dependence of macroscopic magnetization on magnetic history that is presented herein has not been suggested previously. While the result quoted is still too general to permit any direct evaluation against experiment, it is felt that it might form a worth-while basis for more detailed analysis. Of more immediate interest is the fact that the general arguments provide basis and motivation for the simple special models devised to predict various general features of the behavior of a ferromagnet. The quoted experimental results indicate that, idealized though they are, these models do provide a qualitative basis for understanding.

While the experimental results presented were all obtained from ferrites, the general theory of course applies to all ferromagnets. However, the more special parts of the discussion would not apply to crystals of lower symmetry without modification.

The authors wish to acknowledge the aid of Professor E. Katz during early stages of the work, Professor H. W. Welch, Jr., for his aid and encouragement, and to Mr. John Newton and Mr. Ralph Olson for their assistance in gathering data.

Atomic Heat of Bismuth between 1° and 4°K*

P. H. KEESOM AND N. PEARLMAN
Purdue University, West Lafayette, Indiana
(Received July 19, 1954)

Between 0.96 and 2.3°K the atomic heat of a polycrystalline ingot of bismuth (99.99 percent) can be represented by: $c=(1.213\pm0.006)T^3+(0.078\pm0.03)T$ millijoules/mole deg. The lattice contribution, given by the cubic term, corresponds to 117°K for the low-temperature Debye θ. Between 2.3 and 4.2°K θ decreases to 105°K. The electronic contribution is much smaller than for normal metals.

I. INTRODUCTION

BISMUTH is unique among the metals in the variety of electric and magnetic properties for which it exhibits anomalously large effects. Among these are resistivity, Hall constant and change of resistivity in a magnetic field, diamagnetic susceptibility, magnetic anisotropy and its magnetic field dependence (de Haas-van Alphen effect). The large diamagnetism can be accounted for at least qualitatively by a theory proposed by Jones.[1,2]

Jones' band picture can be summarized briefly as involving an overlap between the fifth and sixth bands, the latter containing a small number of electrons and the former, a small number of holes. This structure implies that the nonlattice contribution to the atomic heat at very low temperatures will be a very small linear term. However, it was not possible to determine whether such a term is present from the measurements of Keesom and van den Ende[3] in the liquid helium temperature region. We have therefore repeated these measurements, carrying them to somewhat lower temperatures, in order to determine the magnitude of this contribution to the atomic heat.

The scatter of the earlier data makes the calculation of the Debye θ uncertain below 4°K. We were therefore also interested in determining an accurate value for θ_0, the constant value for θ in the "true T^3 region." From the calculations of Blackman,[4] which show that the true T^3 region extends from 0°K to $\theta/100$ or $\theta/50$, and the rough values measured by Keesom and van den Ende,[3] this region would be expected to have its upper limit around 1° or 2°K. The variation of θ with T immediately above the true T^3 region is also of interest because of its connection with the vibration spectrum, which has not yet been calculated theoretically for the lattice in which bismuth crystallizes.

II. EXPERIMENT

A. Sample

The sample was a polycrystalline ingot of bismuth weighing 521.8 grams, with a stated purity of 99.99 atomic percent.[5] When the calorimetric measurements were completed, a piece was cut from the middle of the ingot and its resistance was measured at several temperatures from 4° to 273°K. The ratio $R(T)/R(273°K)$, where R is the resistance, is given in Table I. These values are comparable with some of the higher values found by Schubnikow and de Haas[6] in their measurements on a large number of single crystals of bismuth. Since our ingot was polycrystalline, it appears that it had a purity of the order which was stated. In order to check further on its purity, Mr. R. Van Veld of this department made a spectrographic analysis which could have detected metallic impurities present in concentrations as low as 10^{-5}. No impurities were found.

B. Apparatus and Procedure

The bismuth ingot was hung by nylon thread in a vacuum can. Cigarette paper was glued to the ingot with Glyptal varnish, and on it were wound a constantan heater wire and a phosphor-bronze thermometer wire.[7] In part of the calibrating procedure, the measurements were carried out in the manner reported previously,[8] except for a difference, described below.

Since it was anticipated that the linear term in the atomic heat, if present at all, would be small relative to the cubic lattice term, we added a booster pump[9] in the bath pumping line, so as to be able to reach lower bath temperatures. At the lowest temperature reached,

TABLE I. Resistivity ratio for bismuth sample.

T (°K)	77.3	20.0	14.2	4.2
$R/R_{0°C}$	0.383	0.154	0.135	0.112

* This work was supported by Signal Corps Contract.
[1] H. Jones, Proc. Roy. Soc. (London) **A147**, 396 (1934).
[2] N. F. Mott and H. Jones, *The Theory of the Properties of Metals and Alloys* (Oxford University Press, London, 1936), p. 212.
[3] W. H. Keesom and J. N. van den Ende, Communs. Kamerlingh Onnes Lab. Univ. Leiden, No. 203d: Proc. Koninkl. Ned. Akad. Wetenschap. **33**, 243 (1930); Leiden Communs. 213c, Proc. Koninkl. Ned. Akad. Wetenschap. **34**, 210 (1931).
[4] M. Blackman, Repts. Progr. Phys. **8**, 11 (1951).
[5] Kindly supplied by J. Crawford of the Oak Ridge National Laboratory.
[6] L. Schubnikow and W. J. de Haas, Communs. Kamerlingh Onnes Lab. Univ. Leiden, No. 207c (1930): Proc. Koninkl. Ned. Akad. Wetenschap. **33**, 350 (1930).
[7] Kindly supplied by Dr. K. Taconis of the Kamerlingh Onnes Laboratory, University of Leiden.
[8] N. Pearlman and P. H. Keesom, Phys. Rev. **88**, 398 (1952).
[9] Distillation Products Model KB100.

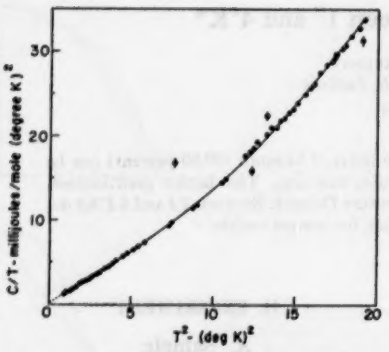

FIG. 1. C/T *vs* T^2 for bismuth in liquid helium region. ●—our results; points with vertical line are those of Keesom and van den Ende.

0.95°K, the evaporation rate was 30 liters of helium at NTP per hour.

Because of the viscous gas flow, a pressure drop will arise in the cryostat, so that vapor pressures measured at the top of the cryostat according to our usual practice will be significantly lower than the corresponding pressures at the surface of the liquid, at the lowest temperatures. The existence of this pressure drop can be seen from the following observation. The lowest bath temperature obtainable without using the booster pump was about 1.2°K, and this temperature could also be reached with the booster pump by heating the bath. The pressure at the top of the cryostat was found to be smaller in the latter case for a given thermometer resistance, corresponding to the fact that since the gas flow was larger due to the higher evaporation rate, the pressure drop in the cryostat was greater.

The correction for this pressure drop is not easy to calculate, since it depends on the temperature distribution of the gas in the cryostat, which is not known. To overcome this difficulty, we condensed some helium in the vacuum can and measured its vapor pressure with a sloping oil manometer. The pressure drop mentioned above, between liquid surface and manometer, does not occur with this arrangement because the vapor is not being pumped away. The liquid helium film, however, creeps up the sides of the container and the connecting tube, evaporates, and condenses at a lower point. This effect will lead to a higher measured pressure than the vapor of the liquid, but calculation shows that for our connecting tube (14-mm i.d.) the difference is negligible. Above 1.2°K the pressure measured at the top of the cryostat was equal to that inside the vacuum can. The differences below this temperature increased as the temperature was lowered, and corresponded to 0.04°K at the lowest temperature.

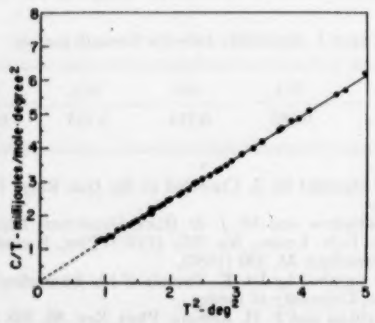

FIG. 2. C/T *vs* T^2 for bismuth in true T^2 region.

The thermometer resistance between 1.3° and 2°K could be represented to within 0.001°K by a parabola. This parabola also agreed with the calibration points below 1.3°K with the same accuracy, if temperatures based on vacuum can pressures were used. The parabola was therefore used below 2°K to convert resistance to temperature. Another parabola, which joined on smoothly to the first at about 2°K and represented the calibration points to within several thousandths of a degree between 2° and 4.2°K, was used in the higher-temperature interval.

III. RESULTS

The results of our measurements are collected in Table II. From these data, we have plotted, in Fig. 1, C_v/T *versus* T^2, together with the points of Keesom and van den Ende[3] in the helium region. It can be seen that their points scatter around ours in a random fashion. Below $T^2=5$ or $T=2.3$°K a straight line can be fitted to our points. In Fig. 2 the data below $T^2=5$ are plotted on a larger scale, again in the form of C_v/T *versus* T^2. The line drawn in Fig. 2 was calculated by the method of least squares; it gives for the atomic heat the expression:

$$C_v=(1.213\pm0.006)T^3+(0.078\pm0.013)T \times\text{millijoules/mole degree.} \quad (1)$$

The errors given in Eq. (1) are standard errors, calculated on the assumption that all errors in the measurement are random. A possible source of systematic error is the vapor pressure curve, which is based on thermodynamic arguments below 1.6°K,[10–12] where the probable error is estimated to be ±0.003°K. Taking this into account, we estimate the total standard error in the linear term to be about 0.03 millijoule/mole degree.[2]

IV. DISCUSSION

A. Lattice Atomic Heat

From the coefficient of the cubic term in Eq. (1) we calculate the value (117±1)°K for θ_0, the constant value of the Debye θ in the temperature region im-

[10] R. Bleaney and F. Simon, Trans. Faraday Soc. **35**, 1205 (1939).

[11] W. H. Keesom and W. P. J. Lignac, Communs. Kamerlingh Onnes Lab. Univ. Leiden, Suppl. 90c (1939): See also *Temperature*, AIP Symposium (Reinhold Publishing Corp., New York, 1941), p. 757.

[12] J. Kistemaker, Communs. Kamerlingh-Onnes Lab., Leiden, No. 269c (1946); Physica **12**, 272 (1946).

TABLE II. Data on atomic heat of bismuth.

Point	T (°K)	ΔT (°K)	C_v $\left(\frac{\text{millijoules}}{\text{mole deg K}}\right)$
	27 April 1953		
2	1.299	0.04877	2.982
3	1.301	0.05007	2.839
4	1.300	0.04978	2.817
5	1.302	0.04986	2.811
6	1.299	0.04877	2.849
7	1.297	0.04856	2.885
8	1.549	0.03009	4.586
9	1.562	0.05325	4.778
10	1.562	0.05305	4.758
11	1.688	0.04120	6.172
12	1.712	0.03997	6.236
13	1.913	0.02872	8.700
14	1.921	0.02821	8.792
15	2.128	0.04019	11.84
16	2.159	0.03910	12.15
17	2.385	0.02804	17.01
18	2.409	0.05506	17.88
19	2.704	0.03800	25.27
20	2.731	0.03640	26.38
21	2.960	0.04737	33.81
22	3.009	0.04491	35.70
23	3.246	0.03416	46.88
24	3.282	0.03307	48.67
25	3.453	0.04258	60.88
26	3.497	0.04098	63.29
27	3.534	0.03948	65.73
28	3.576	0.03762	69.05
29	3.640	0.03550	73.14
30	3.679	0.03373	77.06
31	3.716	0.03314	78.39
32	3.751	0.03180	81.59
33	3.782	0.03112	83.43
34	3.817	0.02986	87.08
35	3.850	0.03689	88.84
36	3.888	0.03534	92.85
37	3.952	0.03307	99.01
38	3.989	0.03182	103.1
39	4.019	0.04058	105.3
40	4.060	0.03817	111.8
41	4.106	0.03657	116.8
42	4.146	0.03575	119.4
43	4.183	0.03434	124.6
44	4.220	0.03327	128.4
45	4.252	0.03287	129.9
46	4.287	0.03128	136.6
47	4.347	0.03000	142.5
48	4.376	0.02885	148.5
49	4.485	0.02592	165.1
50	4.507	0.02534	169.0
51	4.601	0.02363	181.2
52	4.635	0.04586	186.4
53	4.781	0.04062	210.6
54	4.819	0.03893	219.8
55	5.008	0.03303	259.1
56	5.036	0.03141	272.4
	18 May 1953		
8	1.344	0.04041	3.121
9	1.358	0.04075	3.095
10	1.371	0.04000	3.153
11	1.374	0.03986	3.163

Point	T (°K)	ΔT (°K)	C_v $\left(\frac{\text{millijoules}}{\text{mole deg K}}\right)$
	18 May 1953—*Continued*		
12	1.374	0.03979	3.169
13	1.363	0.03993	3.158
16	1.410	0.05096	3.525
17	1.434	0.04979	3.608
18	1.462	0.04726	3.801
19	1.469	0.04685	3.835
20	1.530	0.03713	4.839
21	1.572	0.03713	4.839
22	1.611	0.03471	5.177
23	1.659	0.06392	5.598
24	1.689	0.06107	5.863
25	1.710	0.05944	6.027
	1 June 1953		
1	1.026	0.05574	1.483
2	1.029	0.05716	1.446
3	1.056	0.10794	1.532
4	1.036	0.05844	1.415
5	1.028	0.03580	1.373
6	1.034	0.03596	1.366
7	1.053	0.03342	1.470
8	1.062	0.05400	1.531
9	1.079	0.05248	1.573
10	1.090	0.04947	1.671
11	1.095	0.04867	1.699
12	1.111	0.04728	1.749
13	1.129	0.04575	1.807
14	1.138	0.04401	1.879
15	1.167	0.04086	2.024
16	1.190	0.03881	2.131
17	1.193	0.03903	2.119
18	1.215	0.03688	2.242
19	1.221	0.03692	2.239
20	1.255	0.06853	2.437
21	1.291	0.06264	2.666
22	1.295	0.06209	2.690
23	1.319	0.05880	2.842
24	1.346	0.05506	3.036
25	1.357	0.05435	3.075
26	1.396	0.04943	3.381
27	1.437	0.04534	3.689
28	1.470	0.04264	3.923
29	1.505	0.04020	4.162
30	1.533	0.03727	4.492
31	1.606	0.04404	5.148
32	1.639	0.04096	5.535
33	1.710	0.05238	6.203
34	1.752	0.04836	6.719
35	1.804	0.04477	7.262
36	1.839	0.04203	7.736
37	1.907	0.05834	8.638
38	1.958	0.05368	9.388
39	1.987	0.05191	9.714
40	2.027	0.04878	10.336
45	0.953	0.01951	1.150
46	0.968	0.04097	1.206
47	0.982	0.03882	1.272
48	0.994	0.03790	1.303
49	1.008	0.03605	1.370
51	1.023	0.03659	1.350

mediately above θ°K. The variation of θ with T at higher temperatures is given in Fig. 3, in the form of a plot of θ/θ_0 *versus* T/θ_0, in which the data of Keesom and van den Ende,[3] of Armstrong and Grayson-Smith,[13] and of Anderson[14] are included. These variations in θ correspond to deviations from parabolic form of the vibration spectrum. They occur as a result of the discrete nature of real lattices, as contrasted with the continuum considered by Debye. Hence these devia-

[13] L. D. Armstrong and H. Grayson-Smith, Can J. Research A27, 9 (1949).

[14] C. T. Anderson, J. Am. Chem. Soc. 52, 2720 (1930).

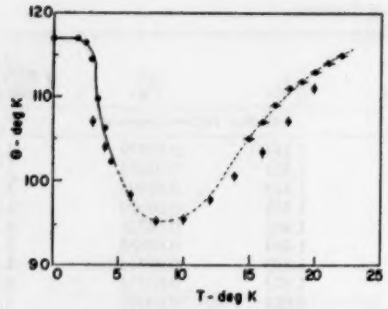

FIG. 3. θ/θ_0 *vs* T/θ for bismuth. ●—our results; points with vertical line, those of Keesom and van den Ende; points with horizontal line, those of Armstrong and Grayson-Smith.

tions will depend on the specific character of the interatomic forces in particular lattice.

Unfortunately, the calculation of the vibration spectrum for a lattice is a very tedious task, which has been accomplished for only a small number of lattices. Much useful information is provided by such calculations, however. For instance, it makes possible the determination of the lattice contribution to the total atomic heat of a metal so that the electronic contribution can be found by subtraction (see, e.g., the recent work of Clement and Quinnell[15] on indium). Hence, information about the general form of vibration spectra, which can be obtained without detailed calculation on the basis of lattice theory, is of interest. Blackman has suggested [16] that the general form of the initial deviations from the parabolic spectrum will be the same for all three-dimensional lattices. This suggestion, which has apparently never been confirmed in the general case, is that the spectrum may be written in the form

$$g(\nu)=a_2\nu^2+a_4\nu^4, \tag{2}$$

so that the Debye parabolic spectrum is a valid approximation at very low frequencies. This form of the spectrum has been verified by Blackman[16] for the simple cubic lattice and by Leighton[17] for the face-centered cubic lattice (f.c.c.). This was done by considering the form of the secular determinant (from which the frequencies are calculated) when its elements are approximated by expressions valid for long wavelengths.

When Eq. (2) is a good approximation for the vibration spectrum at low frequencies, C_v(lattice) can be approximated by

$$C_v(\text{lattice})=\alpha_3T^3+\alpha_5T^5, \tag{3}$$

in which the α's depend on the a's and hence on the nature of the lattice. Blackman has defined, as the "true T^3 region,"[16] temperatures immediately above 0°K for which the second term in Eq. (3) is less than two percent of the first. Thus T_3, the upper limit of the true T^3 region, is given by

$$T_3^2=0.02(\alpha_3/\alpha_5). \tag{4}$$

For bismuth we find that (T_3/θ_0) is 0.019. Blackman found[16] that in the simple cubic lattice (T_3/θ_0) is 0.01, while Leighton found[17] that (T_3/θ_0) is 0.021 in the f.c.c. lattice with nearest neighbor forces only, and 0.025 when the force constant for second-nearest neighbors is one-tenth that for nearest neighbors.

In order to see the extent to which Eq. (3) describes the low-temperature atomic heat of the bismuth lattice, our data are plotted in Fig. 4 in the form C_v(lattice)$/T^3$ *versus* T^2. It is clear that while there does appear to be a term proportional to T^5 in the atomic heat, the coefficient of this term is not constant over the entire range plotted, but increases rather abruptly at a temperature which corresponds roughly to the upper limit of the true T^3 region. Hence Eq. (3) is not a good approximation in this case.

Exact calculations for various spectra show (as has recently been pointed out by de Launay[18] in another connection) that Eq. (2) can be expected to apply over only a limited range of frequencies. Equation (3) will therefore be limited in its applicability to a restricted temperature range. The reason for this limitation is that the vibration spectra have maxima at frequencies much below the cut-off frequency, and these maxima are preceded by a frequency range in which $g(\nu)$ may increase much faster than ν^4. At any rate, Eq. (2) cannot apply at frequencies near the peak in the spectrum.

Although no simple expression such as Eq. (2) is available for this part of the spectrum, the position of the maximum can be estimated by the method of Katz.[19] He treats vibration spectra as being made up of Einstein frequencies with positive or negative weights superimposed upon a parabolic Debye spectrum. No physical basis is claimed for this mode of description; it is proposed, to quote Katz,[19] ". . . as a way of describing mathematically any empirical $C(T)$ in a rapidly converging series." The positions and magnitudes of the Einstein frequencies having positive weights can be found from the dips, and of those having negative weights from the peaks, in the graph of θ/θ_0 *versus* T/θ_0, the pertinent relation being $\nu=5kT/h$. Katz shows that this may be done with reasonable accuracy for T/θ_0 less than 0.1. It is then reasonable to suppose that the positions of the fictitious Einstein frequencies correspond to those of the maxima of the peaks and dips in the vibration spectra. For bismuth, the minimum in $\theta(\theta/\theta_0=0.81)$ at $8°\text{K}(T/\theta_0=0.068)$ thus corresponds to a peak in the spectrum at $\nu/\nu_{\max}$ equal to 0.34. From Leighton's calculated spectra for the f.c.c. lattice we find the value 0.70 in the case of nearest-neighbor forces

[15] J. R. Clement and E. H. Quinnell, Phys. Rev. **92**, 258 (1953).
[16] M. Blackman, Proc. Roy. Soc. (London) **A159**, 416 (1937).
[17] R. B. Leighton, Revs. Modern Phys. **20**, 165 (1948).
[18] J. de Launay, Phys. Rev. **93**, 661 (1954).
[19] E. Katz, J. Chem. Phys. **19**, 488 (1951).

only, and the value 0.65 for the case in which the second-nearest-neighbor force constant is one-tenth as large as the nearest-neighbor force constant. The latter value agrees fairly well with 0.61, the value found from the minimum in the θ *versus* T curve for silver, which Leighton calculated with a somewhat smaller ratio of second-nearest-neighbor to nearest-neighbor force constants. Fine's calculation of the vibration spectrum of tungsten[20] (body-centered cubic lattice, b.c.c.) gives the first peak at ν/ν_{max} equal to 0.57. Hence, in the bismuth vibration spectrum, the distance between the end of the low-frequency parabolic region and the first peak is only about half that in the other spectra discussed. It is likely that this circumstance is responsible for the fact that the atomic heat of bismuth makes an abrupt transition from the true T^3 region to one in which its variation with T is dominated by the approach to a maximum in the vibration spectrum, without an intervening region in which the second term (and perhaps higher terms) in Eq. (2) can be seen.

As has been pointed out, it appears that the form of the vibration spectrum immediately above the low-temperature parabolic portion depends strongly on the nature of the lattice. Although all the vibration spectra calculated so far have a peak in this region, it is not inconceivable that in some cases a dip might precede this peak. Such a spectrum would, for instance, account for the behavior of the atomic heat of niobium (b.c.c.), which has been found[21] to increase more slowly than T^3 immediately after the true T^3 region.

B. Nonlattice Atomic Heat

Since the coefficient of the linear term in Eq. (1) is only between two and three times its total standard error, it is significant only in setting an upper limit to the carrier contribution to the heat capacity. The carrier contribution depends on the density of states at the Fermi level, which can be related to the concentration of carriers and their effective masses. This relation can be written

$$\gamma T = 0.137\mu(V^2 n_a)^{\frac{1}{3}} T \text{ millijoules/mole degree}, \quad (5)$$

where μ is the ratio of effective carrier mass to free electron mass, V is the atomic volume (21.4 cm³/mole for bismuth), and n_a is the number of carriers per atom. From the value of γ in Eq. (1), we find

$$n_a\mu^3 = 4.0\times10^{-4}. \quad (6)$$

This expression assumes the presence of only one kind of carrier. In the case of overlapping bands such as postulated by Jones,[1,2] however, the thermal excitation of electrons in the sixth band will result in a shift of the Fermi level, so that the number of holes and electrons is changed as well. This leads to an additional contribution to the heat capacity, which can be taken into account by replacing μ in Eqs. (5) and (6) by $\bar{\mu}$, defined by

$$\bar{\mu} = 1.2(\mu_e + \mu_h), \quad (7)$$

where μ_e and μ_h are the effective mass ratios for electrons and holes, respectively. Since Jones estimated[2] that n_a is of the order of 10^{-4}, it would follow from Eq. (6) that $\bar{\mu}$ is of the order of unity. However, he also estimated that μ_e is about 1/30. Although he could not make a quantitative estimate of μ_h, data on the magnetic anisotropy led him to surmise that it is even smaller than μ_e. If this is the case, the theoretical value of $n_a\bar{\mu}^3$ is much smaller than the right-hand side of Eq. (6).

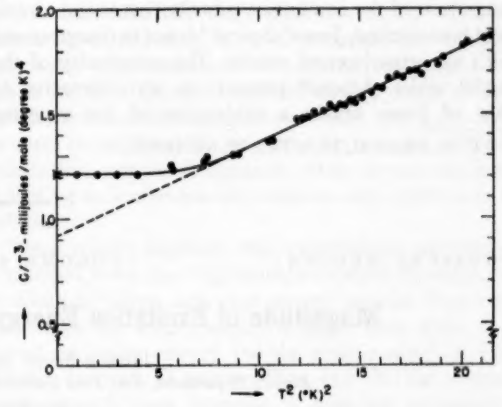

FIG. 4. C/T^3 *vs* T^2 for bismuth in liquid helium region.

It should be emphasized, however, that the latter is an upper limit to the true value for bismuth, not only because it is not large compared with its standard error, but also because the possibility exists that part, or all, of the observed linear term in the atomic heat is due to impurities in the bismuth. If the impurity atoms enter the lattice substitutionally, the electrons or holes they contribute would be expected to have the small effective masses associated with this lattice. Therefore, they could not greatly increase the value of $n_a\bar{\mu}^3$. On the other hand, if the impurities were among those whose solubility in bismuth is very low, such as copper, tin, or iron, so that they did not enter the lattice appreciably, even small concentrations with $\bar{\mu}$ equal to unity (or greater, as for iron) could account for the relatively large value of $n_a\bar{\mu}^3$. The spectrographic analysis mentioned earlier sets an approximate upper limit of 10^{-5} on n_a from metallic impurities, so that it is not impossible that at least part of the value given in Eq. (6) can be accounted for in this way. A more quantitative investigation of this point would require an even purer sample, and also the attainment of lower temperatures.

We can therefore conclude only that, as far as the

[20] J. C. Fine, Phys. Rev. **56**, 355 (1939).
[21] Brown, Zemansky, and Boorse, Phys. Rev. **86**, 134 (1952).

magnitude of the non-lattice contribution to the atomic heat is concerned, Jones' theory[1,2] is not in disagreement with our experimental results. The complexity of the model which Adams[22] presents as an alternative to that of Jones makes a calculation of the expected carrier contribution to the heat capacity very difficult. Such a calculation might, however, offer a useful test of its applicability.

[22] E. N. Adams II, Phys. Rev. 89, 633 (1953).

We would like to express our appreciation for the support and encouragement provided by Dr. K. Lark-Horovitz during the course of this work.

PHYSICAL REVIEW VOLUME 96, NUMBER 4 NOVEMBER 15, 1954

Magnitude of Excitation Energy and Energy Transfer by Collision*

MILTON FURST AND HARTMUT KALLMANN
Physics Department, New York University, Washington Square, New York, New York

(Received July 23, 1954)

Energy transfer by collision in fluorescent solutions is found to drop sharply when the excitation energy of the solute molecule is very close to or below that of the transferring molecule. The results indicate that energy is transferred only when molecules are close to each other as in collision.

HIGH-ENERGY-INDUCED fluorescence in liquid solutions has been shown to be associated with a transfer of energy from an excited solvent molecule to a solute molecule.[1,2] We are now reporting a special instance where such energy transfer takes place between added napthalene and various solute molecules. Napthalene is a solid at room temperature, but it can effectively be used as a solvent for high-energy fluorescence by dissolving large amounts of it in a solvent which may by itself have only mediocre ability to transfer energy. About 300 grams per liter of napthalene in *n*-butylphosphate is such a system.[3] Various highly efficient solutes (in xylene) such as α, α'-binaphthyl, 2, 5-diphenyloxazole and 9, 10-diphenylanthracene were studied in this "solvent" combination. The energy transfer to the solute takes place almost exclusively from the excited napthalene molecules; such a "solvent" combination is found to be almost as effective as xylene for the solutes mentioned. *p*- and *m*-terphenyl behave quite differently; when these substances are put into this "solvent" combination, only small fluorescence occurs, although in xylene both of these materials are highly efficient. This result is interpreted by assuming that no energy transfer takes place from napthalene to *p*- or *m*-terphenyl. If one of these latter molecules is added to a fluorescent solution containing one of the above-mentioned solute molecules, the light output is scarcely changed. This result can be interpreted in the same way.

The explanation proposed here for this behavior is based on the assumption that the energy jump from the ground state to the first singlet state in the terphenyls is slightly too great to enable frequent transfer from napthalene. Judging by the published absorption curves of napthalene and *m*- and *p*-terphenyl one can only say that their lowest excited states are very close.[4] α, α'-binaphthyl, to which a very good energy transfer occurs in this "solvent" combination, also has an absorption edge close to that of napthalene. From the absorption curves, one concludes that the lowest excitation energy for α, α'-binaphthyl probably does not differ by more than 1/10 of an electron volt from the respective excitation energy of napthalene.

The difference in behavior between the terphenyls and α, α'-binaphthyl would be understandable if the absorption curve of the α, α'-binaphthyl extended to longer wavelengths than those of the terphenyls. Therefore, by means of a monochromator and photomultiplier arrangement, a more complete check of the absorption curves of *m*-terphenyl and α, α'-binaphthyl was made in a range where pertinent data were not previously available. (*M*-terphenyl was chosen because of its greater solubility.) The concentrations were chosen in such a way that both the *m*-terphenyl and the α, α'-binaphthyl solutions had practically equal absorption at shorter wavelengths where a maximum in the absorption curve occurs. Then the relative absorption was observed at a series of longer wavelengths. These experiments showed that the absorption spectrum of α, α'-binaphthyl extends to slightly longer wavelengths than that of *m*-terphenyl, which in turn shows that the lowest excitation energy of *m*-terphenyl is greater than that of α, α'-binaphthyl. This supports our explanation that energy transfer to terphenyl from napthalene does not occur because the excitation energy of terphenyl is too high. The occurrence of the small fluorescence of *m*-terphenyl in the solvent combination

* This work was supported by the Signal Corps Engineering Laboratories, Evans Signal Laboratory, Belmar, New Jersey.

[1] H. Kallman and M. Furst, Phys. Rev. 79, 857 (1950).

[2] M. Furst and H. Kallman, Phys. Rev. 94, 503 (1954).

[3] A more complete discussion of this system will be given in a paper now in preparation.

[4] R. A. Friedel and M. Orchin, *Ultraviolet Spectra of Aromatic Compounds* (John Wiley and Sons, Inc., New York, 1951).

shows that the energy level of terphenyl may nevertheless be slightly above that of napthalene.

From these experiments, two conclusions may be drawn. First, a sharp drop in energy transfer only occurs when the excitation energy of the solute molecule is very close to (or below) that of the transferring molecule. α, α'-binaphthyl and napthalene have lowest energy levels which are fairly close to each other; however, despite this small energy difference the energy transfer is just as efficient as to other solute molecules which have much lower energy levels, e.g., 2, 5-diphenyloxazole. If the energy level of the molecule is below the energy level of the solvent molecule (or perhaps extremely close), the energy transfer ceases to occur. Second, these experiments show that the lowest (singlet) state of the napthalene molecule is responsible for the energy transfer; otherwise the terphenyls would be excited by the excited napthalene molecule. It is known both from theoretical considerations and from absorption curves that the lowest singlet state of napthalene has only a very small transition probability to its ground state.[5] The dipole moment associated with this transition in napthalene is about 100 times smaller than that for many other molecules of this type. In spite of this low dipole moment, the energy transfer from napthalene to various solute molecules is almost as efficient as that from molecules which have larger dipole moments associated with the transitions from their lowest excited singlet states. If one now assumes that the true lifetime of these excited solvent molecules is not determined by their transition dipole moment (since these molecules in large concentration display only very little emission), then these results may be taken as an indication that the energy transfer between excited molecules in these liquid systems is not so much caused by a dipole interaction but rather by an interaction over small distances when the excited and accepting molecules are very close to each other as in a collision.

These results together with experiments previously performed show that high-energy-induced fluorescence in dilute solutions, and thus energy transfer from the solvent to the solute, occurs strongly only when the lowest excitation energy (of the singlet state) of the solvent molecule is greater than that of the solute. Even in such cases, however, it does not necessarily occur since the transfer also depends upon the lifetime of the excited solvent molecule. These results (that such transfer drops sharply when the excitation energies come close to each other, and that it is always very small, if it occurs at all, when the solute excitation energy is smaller than that of the solvent) are in agreement with our theory[1] that the energy transfer comes about by a transfer of the lowest excitation energy. These experiments again show[2] that a theory based on energy transfer by means of short-wave radiation[6] is not suitable to account for the observed phenomena.

[5] M. Kasha and R. V. Nauman, J. Chem. Phys. **17**, 516 (1949).

[6] J. B. Birks, *Scintillation Counters* (Pergamon Press, London; McGraw Hill Book Company Inc., New York, 1953); Phys. Rev. **94**, 1567 (1954); **95**, 277 (1954).

Lifetime of Positrons in Superconducting Lead and Tin*

ROBERT STUMP AND HARRY E. TALLEY†
Department of Physics, University of Kansas, Lawrence, Kansas
(Received July 12, 1954; revised manuscript received August 23, 1954)

The mean life of positrons was measured in superconducting lead and tin. Consistent results were obtained with the lead sample giving an average value for the mean life of $(0.57\pm0.07)\times10^{-9}$ sec. A null result was obtained with tin; the measured value of the lifetime was $(0.15\pm0.09)\times10^{-9}$ sec, as compared with the room temperature value of 0.15×10^{-9} sec. The data indicate that the lifetime change in lead is a superconductive phenomenon and not due simply to the low temperature of the sample. Conjectures are made to explain the different results obtained with lead and tin.

INTRODUCTION

NUMEROUS investigations have recently been made to measure the mean life of positrons in condensed materials. The work of Bell and Graham[1] provides the most extensive list of sample materials and allows certain general conclusions to be drawn. Two of these apply particularly to the work being reported upon here. First, the mean life in metals appears, within experimental error, to be constant at about 1.5×10^{-10} second. Second, the mean life measured in insulators varies considerably for different materials, but is almost always longer than that observed in metals by a factor of two or three. In some insulators, about 30 percent of all positrons appear to decay with a longer mean life than the others. The mean life of the longer-lived component decreases as the temperature decreases.

Now superconductors, in spite of their anomalous conductivity, in some ways more nearly resemble insulators than conductors. The infinite conductivity results from the presence of a certain number of electrons, termed superelectrons, which do not interact with their environment. Among the other superconductive effects, one would expect an increase in the positron life time due to the presence of the superelectrons which would not interact strongly with positrons or positronium, and hence not contribute to the annihilation. Dresden[2] indicates two processes which may cause the mean life of positrons in superconductors to differ from the mean life in normal materials. First, the wave function of an electron in a superconductor is certainly much different from that in a normal conductor, and the wave function of a positron may also be different. These differences should lead to an increase in the mean life of all positrons in superconductors. A crude estimate of the amount of this effect by Dresden (unpublished) indicated that a mean life of as much as 3×10^{-9} second for positrons in superconducting lead at 4.2°K might be expected. The second process indicated by Dresden gives rise to a complex lifetime, due to the formation of positronium. Positronium, formed in the triplet state, should not be converted to the singlet state by the superelectrons, and hence might remain much longer than in normal metals. However, it should be noted that all mechanisms, other than the interaction with conduction electrons, which convert triplet to singlet positronium in solids, will probably also be present in superconductors. The magnitude of both effects, on the basis of a superconductivity theory alone, is, of course, a function of how far below the transition temperature the sample is maintained, since thereby is determined the number of superelectrons.[3]

Investigations were then initiated to see whether or not any lifetime change could be observed. Lead was chosen as the first sample material, not only because calculations had been made in terms of it, but also its transition temperature (7.2°K) was sufficiently high to give a relatively large number of superelectrons at the boiling point of liquid helium.

EXPERIMENTAL DETAIL

The customary technique of delayed coincidences was used in carrying out the measurements. The coincidence circuit used initially was a modification of that proposed by de Benedetti and Richings.[4] The modifications consisted, principally, of the use of a negative high-voltage supply and the elimination of the limiter circuit. Stilbene crystals mounted on 5819 phototubes were used as detectors and RG 88/*u*, 185-ohm, cable was employed to secure the necessary delays. The resolving times obtained with this coincidence circuit were, approximately, 1.5×10^{-9} sec.

In later experiments, the coincidence circuit described by Bell *et al.*[5] was adopted, and the 5819 photomultiplier used instead of the 1P21. The circuit requires output of approximately three volts from the phototubes, and necessitates applying, therefore, voltages of about 1500 volts to the 5819. At these voltages

* Part of a dissertation submitted by Harry E. Talley in partial fulfillment of the requirements for the degree of Doctor of Philosophy at the University of Kansas.
† Present Address: Bell Telephone Laboratories, Inc., Transitor Development Division, Allentown, Pennsylvania.
[1] R. E. Bell and R. L. Graham, Phys. Rev. **90**, 644 (1953).
[2] M. Dresden, Phys. Rev. **93**, 1413 (1954).
[3] F. London, *Superfluids* (John Wiley and Sons, Inc., New York, 1950).
[4] S. de Benedetti and H. J. Richings, Rev. Sci. Instr. **23**, 37 (1952).
[5] Bell, Graham, and Petch, Can. J. Phys. **30**, 35 (1952).

the tubes exhibited a form of breakdown characterized by excessive noise and the disappearance of the output pulses. The reason for this was found to be connected with the amplification characteristics of the particular phototube, and the fault could be eliminated by applying stabilizing voltages to the last two dynodes. More complete details are to be published elsewhere.

In each case, both counters were allowed to accept both the nuclear and the annihilation radiations; therefore the delay curves are symmetric about zero delay.

The sample was a solid cylinder along the axis of which a hole had been drilled. $Na^{22}Cl$ in a HCl solution, as obtained from the Oak Ridge National Laboratory, was evaporated in the cylinder. Virtually all of the measurements in which the sample was to be superconducting were made with the cylinder placed in the bottom of a glass Dewar into which had been put liquid helium. The data for liquid nitrogen temperature were obtained from the same arrangement, except that now the sample was either submerged in liquid nitrogen or the chamber between the helium and nitrogen containers was filled with air, thus putting the sample at the nitrogen temperature. Because it was necessary to surround the helium Dewar with liquid nitrogen, the counters were about two inches from the sample, so that the coincidence counting rate was low. For this reason, accurate data for long delay times could not be obtained.

RESULTS

A preliminary experiment was carried out in order to ascertain whether any difference in the mean life between the normal and superconducting states of lead could be observed. The sample was submerged in liquid helium and the delays following the counters were adjusted to correspond to the peak of the delayed coincidence curve. Then the coincidence rate as a function of time was taken. If the mean life of the positron in the superconducting state were longer, the coincidence rate would be lower than the rate taken at a temperature above the transition point. With the lead at the temperature of liquid helium, then, the rate would be low, and would increase very rapidly when the helium in the Dewar had entirely evaporated.

The data are shown in Fig. 1 and clearly follow the indicated behavior. For about thirty minutes, while helium surrounded the lead, the rate was low; at the end of that time, when the helium was gone, the coincidence rate suddenly increased.

Obviously these results may be due to either of the processes described by Dresden. The change could be due to a small increase in the mean life of all positrons, or it could be due to a large increase in the mean life of about 30 percent of the positrons. Assuming that the change is due to a change in the mean life of all positrons, the amount of the lifetime change may be calculated. Such a calculation indicates a mean life of $(0.50\pm0.09)\times10^{-9}$ second. (The uncertainties given here are essentially the standard deviations due to the number of counts involved.) Although the statistics of the experiment are poor, the experiment indicates fairly conclusively that there is a lifetime change. Also, the method serves to give a quick and simple means of detecting lifetime changes of the type being discussed here. Surprisingly, in view of the statistics, the result given above checks quite well with the much more reliable results to be given below.

Satisfied that a change in the mean life could be measured and using the same experimental arrangements, we took several complete decay curves corresponding to the temperatures of liquid helium, liquid nitrogen, and the laboratory. The liquid helium and liquid nitrogen curves are shown in Fig. 2; the curves have been normalized to the same included area. The shape of the delay curves was the same for the liquid nitrogen and room temperature data. Assuming various

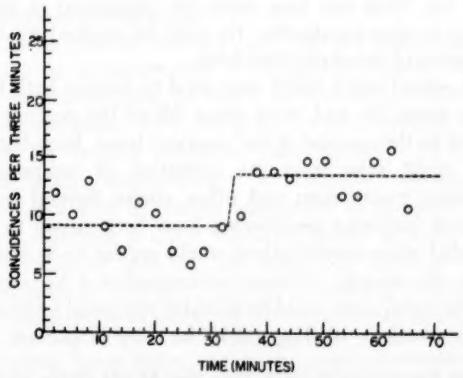

FIG. 1. Plot of coincidences-*vs*-time taken at the peak of a symmetric delayed-coincidence curve for a lead sample.

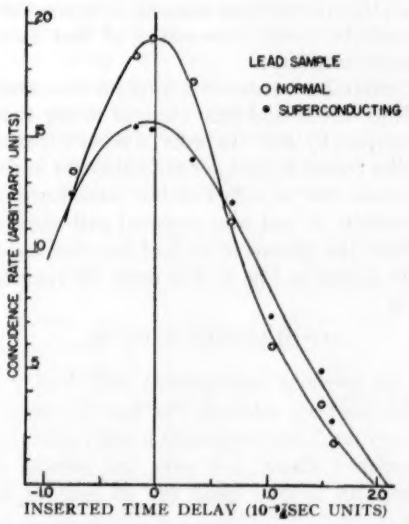

FIG. 2. Delayed-coincidence curves taken for a lead sample at liquid helium and liquid nitrogen temperatures.

single mean lifetimes, the corresponding exponential curves were "smeared-out" with the known shape of the prompt curve and fitted to the liquid helium data. The best fit was given by a mean life of 0.58 ± 0.09 second.

The integrated coincidence rates over the range of delays from -1.5×10^{-9} to $+1.5\times10^{-9}$ second were the same for the liquid nitrogen, liquid helium, and room temperature data. Thus, if a complex life time occurs, a lower limit may be set on the fraction of the positron having the longer mean life if the mean life is known; or an upper limit may be set on the mean life if the fraction of the positrons having that mean life is known. If it is assumed that 30 percent of the positrons have the longer mean life, then the mean life cannot be over about 10^{-9} second. Likewise, if a mean life of 3×10^{-9} second is assumed,[6] then less than 10 percent of the positrons are annihilated with this mean life. This is in agreement with the results of Madansky (private communication) who sets an upper limit of 1 percent on a long-lived component.

The use of lead as sample material has the obvious disadvantage that its transition temperature, 7.2°K, is so high there is no practical way of taking it just out of the superconducting state. Tin, on the other hand, with a transition temperature of 3.26°K presents no such difficulty. Consequently, delayed coincidence measurements were made with tin as the material in which the positrons decayed. Three sets of curves were taken: one with tin at room temperature; one at 4.2°K; and one at 2.4°K, obtained by reducing the pressure in the helium chamber.

Within the accuracy of the experiment, there was no change in the mean life of the positrons with temperature, and no superconducting effect occurred. Calculations of the number of superelectrons indicated, however, that the positron mean life in superconducting tin should be about nine-tenths of that found for superconducting lead.

Just before the measurements on tin were made, the coincidence circuit had been changed to one similar to that described by Bell.[5] In order to be sure that neither the earlier results in lead nor the later ones in tin were due to some sort of failure of the coincidence circuit, measurements of lead were repeated with same circuit with which the lifetime in tin had been measured. The data are similar to Fig. 2. The mean life computed as before is

$$\tau=(0.62\pm0.07)\times10^{-9}\text{ sec.}$$

As in the previous measurement with lead, a single mean life has been assumed. The limit on the presence of a longer mean life component is essentially the same as mentioned above; not over ten percent of the positrons can have a mean life as long as 3×10^{-9} second.

[5] W. E. Millett, Phys. Rev. 94, 809 (1954).

DISCUSSION

The experiments reported here establish with little doubt that there is a change in the mean life of positrons in lead when the lead becomes superconducting, and that there is at most only a very small change in the case of tin. The time distribution of the annihilation of positrons in lead may be explained by a simple exponential decay with a mean life of $(0.57\pm0.07)\times10^{-9}$ second. However, the results are also consistent with a complex lifetime, provided that both components of the decay have a mean life of less than 10^{-9} second, or if only a small fraction of the positrons contribute to the longer mean life.

The behavior of positrons in solids is not at all well understood, but certain speculations can be made which may allow an explanation for the apparent disagreement between the results given above for superconducting lead and tin. The constancy and shortness of the lifetimes in metals are plausible on the basis of the abundance of free electrons in metals, these electrons being available to annihilate with the positrons either directly or through the formation of singlet positronium and to quench the longer-lived triplet state of positronium. In insulators a somewhat longer time is required before the formation of singlet positronium or the direct annihilation of positrons. Furthermore, triplet positronium is not so rapidly converted to the singlet state so that a second mean life, that of the triplet positronium, is observed. However, there are several mechanisms which can shorten the mean life of positrons in insulators. Two in particular might be mentioned.

The quenching of triplet positronium by external magnetic fields is well-known.[7,8] Crystalline fields could, however, also give rise to a quenching action, and one which would be dependent on the lattice structure. For example, there can be no fields or field gradients at lattice points or at the center of the unit cell in a cubic crystal (such as lead), whereas they can be present in more complicated crystals (such as tin). This may give a partial explanation for the results observed in lead and tin. Thus any long mean life component of positrons in superconducting tin may be masked by the presence of the crystalline fields.

A second effect which may tend to shorten both the long mean life and short mean life of the positron is allied to the concept of the covalent bond. Such bonding could arise from the formation of compounds between positronium and other atoms. Several compounds involving positronium have been shown to be stable,[8] while several others would appear to be stable from the analogy between positronium and hydrogen. In the latter class could be included the metal hydrides. This covalent binding could be very important in

[7] M. Deutsch and E. Dulit, Phys. Rev. 84, 601 (1951).

[8] M. Deutsch, *Progress in Nuclear Physics* (Academic Press, Inc., New York, 1953), Vol. 3.

explaining the shortness of the lifetime observed in insulators and provide another means by which triplet positronium may be rapidly converted to singlet positronium. The length of the covalent bond when compared with the lattice parameters could also provide criteria determining whether or not such compounds could be formed.

Clearly a great deal of work must be done to be sure that the effects reported here are reproduced in other superconductors. The dependence of the observed lifetime change on the crystal structure of the superconductor could, for example, be checked. There are many other such problems immediately presented. Experiments are being continued here along these and other lines relating to positron life times in solids.

The authors are deeply indebted to Professor M. Dresden for many valuable discussions of the problem. They are also grateful to Dr. G. G. Wiseman and Mr. J. D. Wackerle for the considerable time spent in maintaining a supply of liquid helium.

PHYSICAL REVIEW VOLUME 96, NUMBER 4 NOVEMBER 15, 1954

Critical Field Phenomena in an Isotropic Paramagnetic Crystal

E. AMBLER AND R. P. HUDSON
National Bureau of Standards, Washington, D. C.

(Received July 9, 1954)

Measurements have been made of the variation of magnetic moment with applied field, at constant entropy, for a spherically-ground single crystal of chromic methylammonium alum. Steady fields up to 500 oersteds were applied along a cubic axis of the crystal and the differential susceptibility measured ballistically by reversing a field of 1.7 oersteds in the primary of a mutual inductance surrounding the specimen. The total magnetic moment was obtained by integration. At entropies below that of the "Curie point" the differential susceptibility showed a pronounced maximum in a field of about one hundred oersteds. This behavior is compared with that observed in earlier measurements on the same specimen in transverse fields. The magnetic moment at constant external magnetic field H, plotted as a function of entropy, shows a maximum for small values of H. The locus of these maxima is evidently a transition curve separating regions of paramagnetic and antiferromagnetic behavior.

1. INTRODUCTION

SINCE the earliest investigations of the behavior of paramagnetic salts at very low temperatures, reached by means of the technique of adiabatic demagnetization, considerable interest has been centered on the phenomena associated with the appearance of a susceptibility maximum.[1] These include hysteresis and remanence observed in dc measurements, a complex ac susceptibility (ac losses), and a negative magnetocaloric effect—evidence of cooperative effects which have been generally ascribed to the onset of antiferromagnetic behavior.[2]

More recently Garrett[3] has reported measurements made on an anisotropic paramagnetic crystal, cobalt ammonium sulfate, in which an interesting effect was observed below the Curie point for fields applied along the K_1 (strong magnetic) axis—namely, that the differential susceptibility at constant entropy S *increased* with increasing magnitude of the polarizing field, reaching a fairly sharp maximum in fields of a few hundred oersteds. By measuring absolute temperatures in zero field, and by calculating increments of temperature as a function of field along an isentropic, using the thermodynamic formula

$$(\partial T/\partial H)_S = -(\partial M/\partial S)_H \qquad (1)$$

(where M is the magnetic moment of the specimen), Garrett was able to plot on a $T-H$ diagram a lattice of isentropic and isomomental curves. The locus of the minima of both sets of curves described a phase boundary which was identified as delineating the transition from antiferromagnetic to paramagnetic behavior, since the features of the diagram showed striking similarity to the predictions of a theory due to Sauer and Temperley[4] postulating antiparallel ordering at very low temperatures through dipole-dipole interaction.

In a recent investigation of the low-temperature magnetic properties of chromic methylammonium alum, a salt which is magnetically isotropic in the region of 1°K, Hudson and McLane[5] obtained indications of similar behavior of the susceptibility below the Curie point. The measurements were made with a transverse polarizing field, the measured susceptibility being assumed to be equal to M/H, as is true for an isotropic material. The indications were, however, that the salt was definitely not isotropic, at least in fields greater

[1] Kurti, Laine, Rollin, and Simon, Compt. rend. **202**, 1576 (1936).
[2] N. Kurti, J. phys. et radium **12**, 281 (1951).
[3] C. G. B. Garrett, Proc. Roy. Soc. (London) **A206**, 242 (1951).
[4] J. A. Sauer and H. N. V. Temperley, Proc. Roy. Soc. (London) **A176**, 203 (1940).
[5] R. P. Hudson and C. K. McLane, Phys. Rev. **95**, 932 (1954).

than 100 oersteds, and it was thought worth while to repeat these measurements with the same crystal in longitudinal fields, measuring a differential susceptibility and obtaining the magnetic moment M by integration. The present paper describes these latter experiments.

2. APPARATUS AND PROCEDURE

The method of mounting the crystal within the cryostat and the details of the measuring equipment have been described in an earlier publication[6] and need not be repeated here. The transverse field measurements had been made with a small ac measuring field of 210 cps frequency. To avoid the strong coupling effects between the coaxial solenoid and "measuring coil," ballistic determinations of the differential susceptibility were made. It is not unlikely that by making ac measurements (with reduced coupling by suitable design of the measuring coil)[6] somewhat different values of the susceptibility would be obtained.

After adiabatic demagnetization, the cryostat was swung out of the magnet into a framework which supported earth's field compensating coils and a small solenoid capable of producing fields up to 500 oersteds. Susceptibility measurements were commenced within thirty seconds, the throw of a ballistic galvanometer being observed for a reversal of a 1.72 oersteds measuring field in the primary coil of the cryostat mutual inductance. The sensitivity of measurement was increased by the familiar procedure of compensating by means of an external mutual inductance the greater part of that in the cryostat and observing the effect of the remainder on the galvanometer, which could then be used at full sensitivity. [The response was found by calibration to be 0.568-mm deflection per microhenry. The uncompensated part of the mutual inductance was generally of the order of 100 microhenries; galvanometer deflections could be read with an accuracy better than 0.2 mm. The total mutual inductance to be measured varied, in general, between 400 and 700 microhenries, but fell as low as 30 microhenries for measurements of the differential susceptibility in fields of the order of 500 oersteds. The period of the galvanometer was 5.6 seconds.] The polarizing field was increased in steps, three or four susceptibility determinations being made for each value of the field. By plotting all the readings as a function of time and extrapolating to time zero, values were obtained for the differential susceptibility as a function of polarizing field for the particular entropy of that demagnetization.

The stray heat leak to the specimen, estimated to be about 50 ergs per minute, proved to be sufficiently small to ensure a small probable error in the aforementioned extrapolation despite the necessity of pursuing the measurements for some twelve minutes after demagnetization.

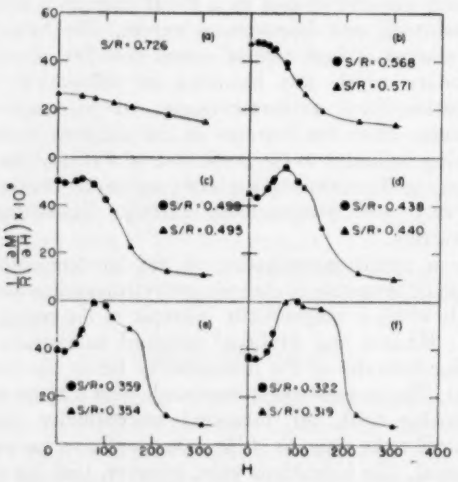

FIG. 1. Isentropic differential susceptibility as a function of external field at various entropies, for chromic methylammonium alum.

[6] Casmir, Bijl, and du Pré, Physica 8, 449 (1941).

3. RESULTS

As a check on the quality of the specimen, which had been stored in a closed vessel at 0°C for seven months, the $S-T^*$ relation was measured over the range 0.077 to 0.476 degree T^*. Exact agreement was obtained with previously published data (reference 5, Single Crystal II). In the immediate neighborhood of the Curie point, however, the zero-field susceptibility appeared to be some five percent too small to fit in with the series of ballistic measurements (using rather higher measuring fields) made when this crystal was placed in the cryostat for the first time. The values were very close, in fact, to those obtained for another specimen (Single Crystal I) with the same measuring field. As noted in reference 5, this degree of nonreproducibility of χ in the region of χ_{max} appears to be associated with differences in the rates of precooling.

The variations of isentropic differential susceptibility $(\partial M/\partial H)_S$ with field H for various entropies is shown in Fig. 1.[7] For entropy greater than that of the Curie point (i.e., S/R greater than 0.53), normal saturation behavior is observed and $(\partial M/\partial H)_S$ decreases continuously as H is increased. Just below the Curie point, however, the behavior is strikingly different; up to about 20 oersteds the susceptibility decreases slightly with increasing field; beyond this point it increases rapidly and then goes through a maximum. As the entropy is progressively lowered, the initial dip in $(\partial M/\partial H)_S$ tends to disappear while the subsequent maximum becomes more pronounced and a side peak develops.

[7] In this paper the not uncommon practice is adopted of dividing magnetic and caloric quantities, scaled to 1 gram ion of salt, by the gas constant R. It is however, frequently convenient to omit the "R" when employing a symbol as an abbreviation for the name of a quantity in the text.

By integrating the curves of Fig. 1 one may obtain the magnetic moment as a function of field at the corresponding entropies and the $M-H$ curves are shown in Fig. 2. In some cases, measurements of M at almost identical entropies had been obtained in the earlier transverse field measurements (but using an ac measuring field) and these are represented in Fig. 2 by the broken lines. Since these latter curves were derived on the assumption of isotropic behavior, that is, by assuming that the apparent susceptibility was equal to M/H, any marked differences in a pair of curves at a given entropy should be evidence of a breakdown of the relation due to *anisotropic* behavior. It would seem, therefore, from our results that the salt is markedly anisotropic at low entropies in fields greater than about

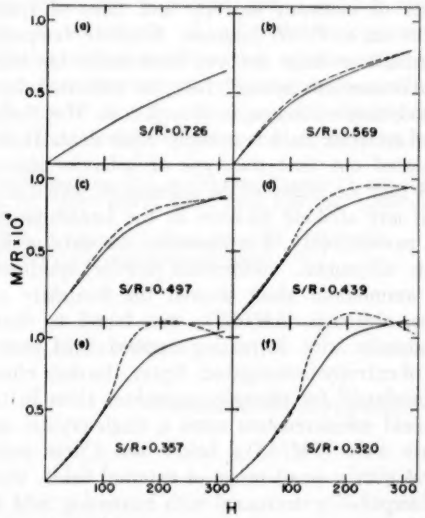

FIG. 2. Magnetic moment as a function of external field at various entropies, obtained by integration of curves of Fig. 1. Full lines, measurements in longitudinal field; broken lines, transverse-field results at corresponding entropies taken from reference 5.

100 oersteds. As the Curie point is approached, anisotropy is evidenced in progressively smaller fields, and the measurements suggest that a detectable anisotropy exists for all values of H at entropies close to and on either side of the Curie point.

The results may be presented in yet a third manner, namely, a plot of magnetic moment M *versus* entropy S for constant values of the static field H. This is given in Fig. 3. For fields up to 120 oersteds, the magnetic moment is seen to go through a maximum. Within the area bounded by the dashed curve, which is the locus of the magnetic moment maxima, the magneto caloric effect—or temperature change upon isentropic change of magnetic field—is negative, since $(\partial M/\partial S)_H$ is positive in this region [see Eq. (1)]. For all points outside this boundary curve, the reverse is true and

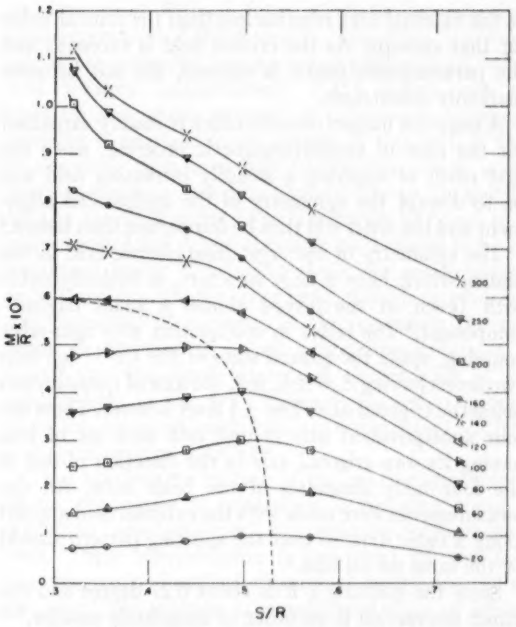

FIG. 3. Magnetic moment as a function of entropy for various values of the applied field. The broken curve is the locus of the maxima and encloses a region of antiferromagnetic behavior.

the magnetocaloric effect is positive, corresponding with normal paramagnetic behavior. At any entropy less than that of the normal Curie point a critical field H_c may be defined—namely, the value of H at that entropy as the boundary curve is crossed. It is apparent that the maxima in $(\partial M/\partial H)_S$ occur at fields slightly less than the critical values.

Since the maximum value of the critical field is so small in this salt (120 oersteds), one can readily make measurements well outside the transition curve, even at the lowest entropies. For fields greater than 120 oersteds the magnetic moment does not go through a maximum with decreasing entropy, but a tendency to do so persists up to fields of 300 oersteds (Fig. 3). This could be evidence that some type of short-range order persists after the destruction of antiferromagnetism. At the lowest entropy—highest field (upper left) portion of Fig. 3 the magnetic moment is seen to be increasing quite rapidly with decreasing entropy and it would be of considerable interest to extend these measurements to much lower entropies in order to obtain, by extrapolation, data on the variation of magnetic moment with external field at the absolute zero.

4. DISCUSSION

On comparing Figs. 2 and 3, it is seen that at entropies below that of the normal Curie point the salt is apparently isotropic—as deduced from the agreement between the present longitudinal field measurements and the earlier transverse field measurements—so long

as the external field remains less than the critical value for that entropy. As the critical field is exceeded and the paramagnetic region is entered, the salt becomes markedly anisotropic.

A negative magnetocaloric effect is readily explained for the case of antiferromagnetic ordering, since the first effect of applying a steadily increasing field will be to disrupt the symmetry of the antiparallel alignment and the order will then be *less* perfect than before.[2]

The symmetry of the crystalline electric field in the alums, which have a *f.c.c.* structure, is basically cubic with (even in the β-type alums) a small trigonal-component.[8] The latter in conjunction with spin-orbit coupling, splits the ground state of the Cr^{+++} ion into two levels having $S_z=\pm\frac{1}{2}, \pm\frac{3}{2}$, the axis of quantization being the trigonal axis. The $\pm\frac{3}{2}$ level is lower. There are four nonequivalent ions in unit cell, each set of ions having its own trigonal axis in the direction of one of the four body diagonals of the basic cube. All the measurements were made with the external field applied along a cubic axis, so that the splitting pattern should be the same for all ions.[9]

Since the splitting δ/K is about 0.27 degree and the direct interaction is an order of magnitude smaller,[5,10] there will be no appreciable overlap of the two sets of levels corresponding to $S_z=\pm\frac{1}{2}$ and $\pm\frac{3}{2}$, and one may use the following rough model. One retains the concept of a quantum number S_z, and as the temperature approaches the Curie point essentially all ions will have $S_z=\pm\frac{3}{2}$, i.e., they will be aligned along their trigonal axes. The ions are then behaving in a very anisotropic way, and for H less than about 200 oersteds can be described by an effective spin $\frac{1}{2}$ with a g-value given by $6\cos\theta$, where θ is the angle between H and the trigonal axis. Thus for all ions, in the present case, the level splits according to $W=\pm\sqrt{3}\beta H$. With $H=200$ oersted, for example, the splitting is equivalent to 0.05 degree.

On the above picture, when cooperative ordering occurs the spins will remain aligned with respect to their own trigonal axes, but there will be presumably a correlation between the directions of neighboring spins. Upon application of a small (but greater than critical) magnetic field, the ions will be largely concentrated in the lowest level $S_z=\pm\frac{3}{2}$. Hence at low entropies and in fields between 120 and (say) 200 oersteds, the spins should be polarized along their own trigonal axes, resulting in a net magnetic moment in the direction of H given by $M/R=\sqrt{3}\beta/K=1.163\times10^{-4}$ degree·oersted^{-1}. [Since the process is isentropic there will be a temperature rise but one finds that up to fields of the order of 200 oersted the effect is small and would not invalidate the above reasoning.] The actual experimental results (Fig. 2) are not inconsistent with this picture. After its steep rise in the region of the critical field the magnetic moment M increases quite slowly for further increase of H. The "knee" in the curve becomes more pronounced with decreasing entropy, and the value of M at this point appears to approach a limiting value of about the magnitude derived above.

The results presented here are similar to those obtained by Garrett[3] for measurements along the K_1 axis of a single crystal of cobalt ammonium sulfate. Garrett observed a maximum in $(\partial M/\partial H)_S$ which was smooth and single, in contrast to the double-peak effect, visible in Fig. 1. These results were presented as lines of constant entropy and lines of constant moment on a $T-H$ diagram. Absolute temperature determinations have not yet been made for chromic methylammonium alum,[10] but, as indicated by the thermodynamic relation in Eq. (1), an $M-S$ plot of lines of constant field is entirely equivalent. It should be pointed out that the type of behavior shown in Fig. 3 may be observed in substances which do not exhibit any striking features in the isentropic differential susceptibility. For example, the data of Kurti[2] for an ellipsoidal, compressed powder specimen of ferric ammonium alum showed the boundary curve feature, although $(\partial M/\partial H)_S$ was found to decrease continuously with increasing applied field over the range of entropy investigated. Again, the data obtained by Steenland[11] for chromic potassium alum in transverse field measurements upon a single-crystal sphere indicate that $(\partial M/\partial S)_H$ below the Curie point is positive over a small range of external fields, whereas the susceptibility decreased with increasing field at all entropies.

The theory of Sauer and Temperley[4] yields the following expressions for the end points of the boundary curve:—the critical temperature in zero field (normal Curie point), T_c, $=3.6\mu^2N/k$, and the critical field at the absolute zero, H_0, $=1.8\mu N$, where N is the number of magnetic ions per cm^3, k is the Boltzmann constant, and μ is the magnetic moment of one ion. The theory, however, included the simplification of a unique direction of alignment with the external field applied parallel to that direction. In the experimental case we have the complicated situation of alignment taking place with respect to each of the four trigonal axes, while the external field is directed along a cubic axis.

For an order-of-magnitude calculation, however, one may take the component of the external field along a trigonal axis, i.e., $H/\sqrt{3}$. Substituting numerical values in the Sauer-Temperley formulas one obtains $T_c=0.04°$ and $H_0=100$ oersteds. The "parallel component" of the H_0 indicated by Fig. 3 (120 oersteds) is 70 oersteds, and T_c is probably about 0.02°K.[5,10] Thus $kT_c/\mu H_0$

[8] J. H. Van Vleck, J. Chem. Phys. **7**, 61 (1939); D. M. S. Bagguley and J. H. E. Griffiths, Proc. Roy. Soc. (London) **A204**, 188 (1950).

[9] L. J. F. Broer, Physica **9**, 537 (1942).

[10] W. E. Gardner and N. Kurti have recently reported [Proc. Roy. Soc. (London) **A223**, 542 (1954)] absolute temperature measurements with this salt in the range 0.013°–0.396°K; the Curie point is given as 0.02°K. These results were not available to the authors at the time of original preparation of this report.

[11] M. J. Steenland, Thesis, Leiden, 1952 (unpublished), p. 44.

$=1.4$, whereas the theory predicts the value 2 for this ratio. In view of the inadequacies of the theoretical model applied to the present case, the agreement between prediction and experience is quite good. For comparison, the results of Steenland suggest that for potassium chromic alum $H_0 \sim 15$ oersteds, and it was found by de Klerk, Steenland, and Gorter[12] that $T_e = 0.004°K$. [The value of T_e obtained by Daniels and Kurti[13] was, however, 0.011°K.]

Garrett[14] has recently extended Van Vleck's exchange-interaction theory of the antiferromagnetic state and obtained the interesting result that, on this model too, a critical curve is to be expected which is not very different in form from that predicted by the Sauer-Temperley dipole-interaction theory. Garrett's theory, however, predicts unity for the ratio $kT_e/\mu H_0$. Whereas dipole interaction is present and of roughly the same order of magnitude in all low-temperature paramagnetics, exchange interaction appears only in some cases and varies greatly in magnitude in these. Kurti has pointed out[15] that the discrepancy in values of δ/k, the crystalline field splitting, in chromic methylammonium alum derived from adiabatic demagnetization experiments,[5] 0.269 degree, and from the most recent paramagnetic resonance measurements of Baker and Bleaney (unpublished), 0.255 degree, can be resolved if a small amount of anisotropic exchange coupling is assumed to be present in this salt. If this is the case, then exchange contributes about seven times as much as does dipole-interaction to the specific heat in the $1/T^2$ region [$b = CT^2/R = 7\times10^{-3}$ and 10^{-3}, respectively] and might therefore be deduced to be an important factor in bringing about the antiferromagnetic transition. On the other hand, there is no evidence (yet reported) of exchange in the potassium chromic alum. In the case of cobalt ammonium sulfate it is found[3] that the dipole-interaction contribution to the specific heat in the $1/T^2$ region is somewhat greater than the exchange contribution: $b(\text{dipole}) = 1.9\times10^{-3}$ and $b(\text{exchange}) = 0.8\times10^{-3}$.

Thus no clear-cut picture of the relative importance of the two types of interaction in bringing about a transition emerges from the existing experimental data. Their interpretation is hampered by the fact that the much simplified theoretical models treated so far bear little relation to complicated state of affairs existing in actual crystals, where both exchange and dipole-dipole interactions may be present and where the ions themselves are magnetically anisotropic.

[12] de Klerk, Steenland, and Gorter, Physica **15**, 649 (1949).
[13] J. M. Daniels and N. Kurti, Proc. Roy. Soc. (London) **A122**, 243 (1954).
[14] C. G. B. Garrett, J. Chem. Phys. **19**, 1154 (1951).
[15] N. Kurti (private communication).

PHYSICAL REVIEW VOLUME 96, NUMBER 4 NOVEMBER 15, 1954

Fluorescent Response of NaI(Tl) to Nuclear Radiations*†

F. S. Eby‡ and W. K. Jentschke
University of Illinois, Urbana, Illinois

(Received July 26, 1954)

The dependence on thallium concentration of the fluorescent response of NaI(Tl) to gamma rays and charged particles has been examined for crystals containing known mole fractions of Tl in the range from 0.00006 to 0.008. Scintillations were detected with a photomultiplier tube and pulses were displayed on an oscilloscope and recorded photographically. Plots of integrated pulse height *vs* energy for alpha-particle excitation show a region of nonlinearity which decreases with increasing Tl concentration. At sufficiently high alpha-particle energies a linear relation is approached for all crystals. No deviations from linearity were observed in plots of pulse height *vs* energy for deuterons or protons in crystals containing a Tl mole fraction of 0.0013. The fluorescent efficiency increases sharply with Tl concentration for mole fractions smaller than about 0.0015 and decreases for higher concentrations, this behavior being more pronounced for deuteron than for alpha-particle excitation. Four separate decay processes characterize the pulse shapes. In addition to the main part of the pulse, which has a rise time (mean life) of about 5.9×10^{-8} sec and a long, concentration dependent, exponential decay (decay constant 2.3 to 3.5×10^{-7} sec, independent of exciting radiation), there are two faster decays: 1, an emission with a decay constant of 1.2×10^{-8} sec from crystals containing Tl mole fractions less than about 0.0002; and 2, a 1.5×10^{-8} sec decay from high Tl content crystals excited by particles having a large specific energy loss. The emission spectrum consists of two bands centered at about 3500 A and 4100 A, their exact positions depending upon the Tl concentration and shifting toward longer wavelengths with increasing Tl concentration. The 1.2×10^{-8} sec emission is from the short wavelength band, and the other emissions are from the band at 4100 A. The dependence of the integrated pulse height on the Tl concentration and specific energy loss of the exciting particle are discussed, and possible explanations of the various decay processes are suggested.

I. INTRODUCTION

An important factor in determining the fluorescent response of a thallium activated sodium iodide crystal, or more generally any activated alkali halide phosphor, is the magnitude and uniformity of the activator concentration. There is often a considerable variation in the Tl concentration throughout a large

* This investigation was supported jointly by the U. S. Atomic Energy Commission and the Office of Naval Research.
† A preliminary report of some of the results was given at the Washington meeting of the American Physical Society in May, 1953, Phys. Rev. **91**, 495 (1953).
‡ Now at the University of California Radiation Laboratory, Livermore, California.

NaI(Tl) scintillation crystal, and that this may in some cases materially effect the total fluorescent response for gamma-ray excitation has been shown by the group at the Harshaw Chemical Company.[1]

In the present work we have investigated the Tl concentration dependence of the response for heavy particle and gamma-ray excitation of crystals containing mole fractions of Tl in the range from 0.00006 to 0.008 mole Tl/mole NaI as a function of the energy of the exciting radiation. Previous measurements have shown that the fluorescent response of commercially available NaI(Tl) crystals resulting from excitation by gamma rays, fast electrons, protons, or deuterons increases linearly with the energy of the bombarding particles[2] but that the response to energetic alpha particles deviates from linearity over an energy range of at least 10 Mev.[2,3] In order to determine the Tl concentration dependence of this nonlinearity and to obtain information about the luminescent efficiency for excitation by particles having a high specific energy loss, most of the present measurements of the total fluorescent response were performed using alpha particles.

Measurements of the characteristic decay times and emission spectra for crystals containing different Tl concentrations provide information about the processes taking place within the crystal which are responsible for its luminescence. Decay-time measurements were made for 23-Mev and 4.7-Mev alpha-particle, 11.5-Mev deuteron, and Ni^{60} gamma-ray excitation of the crystals. Radioactive sources were used for gamma rays and low-energy alpha particles. The University of Illinois cyclotron provided a source of high-energy protons, deuterons, and alpha particles.

All measurements were carried out at room temperature and only prompt ($<10^{-6}$ sec) radiations were observed. Previous accounts of the long-lived radiations from NaI(Tl) have been given by Bonanomi and Rossel[4] and more recently by Emigh and Megill.[5]

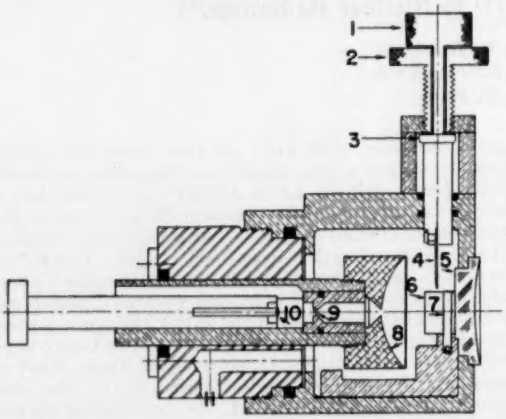

FIG. 1. Chamber used in measurements of scintillation response to low-energy alpha particles. 1, 2—knurled knobs, 3—key, 4—razor edge, 5—Lucite window, 6—NaI(Tl) crystal, 7—retaining strap, 8—hemispherical mirror, 9—foil, 10—Po alpha source, 11—pump-out port. Rotating knurled knob 2 forces piston down and presses razor into the upper edge of crystal cleaving it in two.

II. EXPERIMENTAL PROCEDURE

For the investigation of the response to low-energy alpha particles clear crystals of dimensions 1.2 cm×1.0 cm×0.8 cm were inserted in the chamber shown in Fig. 1. The chamber was evacuated to a pressure of about 10^{-2} mm Hg and the crystals cleaved, exposing a fresh surface to the incident collimated beam of particles from a polonium alpha source. The source was moved along a tube at atmospheric pressure, and the energy of the particles incident on the crystal was determined by the distance of the source from a foil separating the tube and the evacuated chamber and the thickness of the foil. Range-energy curves given by Bethe[6] for alpha particles in air were used in obtaining the energy from the known equivalent air path.

Scintillations from the crystal were observed through a Lucite window with a selected RCA 5819 photomultiplier tube. A hemispherical mirror behind the crystal served to increase the efficiency of light collection, and a drop of oil (Dow Corning 703 fluid) between the crystal surface and the window was used to increase the optical contact between these surfaces. Output pulses from the photomultiplier tube were integrated with an *RC* time constant of 5×10^{-6} sec and fed into a Los Alamos type model 100 pluse amplifier[7] whose gain settings were selected to maintain the output pulse heights in the known linear regions of amplification. Data were recorded by making time exposures of the pulses displayed on the triggered sweep of an oscilloscope (Tektronix 511). Each film was exposed to pulse heights corresponding to several different energies at a common amplifier gain setting and a series of ten voltage calibration lines extending from the base line to 100 volts. A Po alpha source deposited on the vacuum side of the foil furnished particles having an energy of 5.3 Mev, and the resulting pulse heights served as a constant check on the stability of the apparatus.

In order to observe the response to alpha particles of higher energy the chamber was connected directly to the vacuum system at the cyclotron exit port. The magnetically analyzed beam from the cyclotron was collimated by a set of slits 2 mm in diameter and passed through an absorber section containing several movable aluminum absorbers before entering the chamber

[1] Harshaw, Kremers, Stewart, Warburton, and Hay, Atomic Energy Commission Report NYO-1577, September 10, 1952 (unpublished).
[2] Taylor, Jentschke, Remley, Eby, and Kruger, Phys. Rev. **84**, 1034 (1951).
[3] R. H. Loveberg, Phys. Rev. **84**, 852 (1951).
[4] J. Bonanomi and J. Rossel, Helv. Phys. Acta **25**, 725 (1952).
[5] C. R. Emigh and L. R. Megill, Phys. Rev. **93**, 1190 (1954).
[6] H. A. Bethe, Revs. Modern Phys. **22**, 213 (1950).
[7] W. C. Elmore and M. Sands, *Electronics* (McGraw-Hill Book Company, Inc., New York, 1949).

containing the crystal. The response of the crystals to alpha particles of 10, 15, and 23 Mev was observed relative to Po alpha particles from the chamber foil. A more detailed examination of the response of a crystal containing a mole fraction of Tl of 0.0013 was carried out by mounting the crystal directly on the photomultiplier tube which was positioned inside a large evacuated chamber behind an absorber wheel containing 15 different aluminum absorbers. The range-energy curves of Aron, Hoffman, and Williams[8] were used in the determination of the particle energies.

For the observation of luminescent decay times, the crystals and photomultiplier tube were located in a dry air chamber immediately in front of the beam port of the cyclotron. The beam was brought out of the port through a one-mm hole covered by a 1.15 mg/cm² polyethylene terephthalate foil and traversed about two cms of air before striking the crystals. A thin Lucite light pipe was employed in front of the 5819 tube to provide a flat surface for mounting the crystals, which were freshly cleaved immediately preceding the data runs. Dow Corning 200 fluid was used between the crystals and Lucite and between the Lucite and photomultiplier tube for improving optical contact. The signal taken from the last dynode of the 5819 was fed directly into the amplifier of a high-speed triggered sweep oscilloscope (Tektronix 517), and the *RC* time constant (about 2×10^{-9} sec) was determined by the 170-ohm input impedance of the oscilloscope and the interdynode and stray capacitances. Pulses appearing on the face of the oscilloscope tube were recorded photographically. Time calibration was provided by a 51-Mc sinusoidal signal from a crystal-controlled oscillator.

For decay-time measurements using gamma-ray excitation the large statistical fluctuations on the pulses made the use of time exposures impractical. The luminescent decay times of a crystal containing a mole fraction of Tl of 0.00095 were obtained for excitation by Ni^{60} gamma rays and Po alpha particles by photographing single pulses on the face of a Tektronix 517 oscilloscope with an oscillograph record camera (Du Mont type 295). Smoothed-out "average" pulses were constructed for gamma rays and for alpha particles by adding together a large number of single pulses.

Emission spectra of the crystals for excitation by 12-Mev H_2^+ ions were observed with a Hilger quartz spectrograph. Freshly cleaved crystals were mounted in a bracket in front of the beam port of the cyclotron. A beam density of about 2×10^{-8} ampere/cm² over a circular area of one mm diameter produced sufficient light in the crystals to obtain photographs of the spectra for exposure times of the order of a minute with the spectrograph slit 10 cm in front of the crystal. A wavelength calibration was furnished by a Hg arc source which was positioned between the crystal bracket and the spectrograph.

[8] Aron, Hoffman, and Williams, Atomic Energy Commission Report AECU-663 (UCRL-121, Second Revision) September 26, 1950 (unpublished).

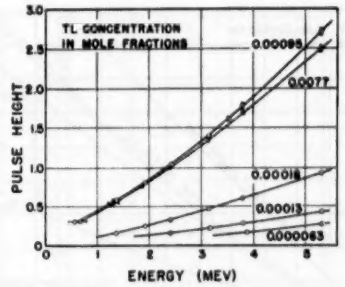

FIG. 2. Pulse heights resulting from low-energy alpha-particle excitation of NaI(Tl) crystals containing various Tl concentrations. The ordinate scale is the same as in Fig. 3.

Approximate values for the Tl concentrations of the crystals, as determined by semiquantitative spectrographic analysis, were obtained from the Larco Nuclear Instrument Company from whom the crystals were purchased. More exact values for the crystals used in the experiments were obtained by several different chemical methods. A tracer technique similar to that discussed by Moreau *et al.*[9] was used in which the Tl was chemically separated from the crystals and later recombined with radioactive I^{131} which was counted. Another and more convenient method of comparable accuracy which was used is the Thionalid method described by Prodinger[10] and others[11,12] in which the crystalline thallium complex ($C_{12}H_{10}ONS$) is precipitated quantitatively from solutions containing tartrate and cyanide. This method is specific for thallium and has a sensitivity of one part in 10^7.

In spite of the fact that high accuracy is possible in determining the total amount of Tl in the samples which are analyzed chemically, the determinations of the Tl concentrations associated with the volumes actually used in the measurements (on the average about 1/50th of the volumes which were analyzed chemically) may be somewhat in error as a result of local variations in the concentration within the crystals.

III. EXPERIMENTAL RESULTS

Pulse Height *vs* Energy and Tl Concentration

The dependence of the mean integrated pulse height on the energy of incident alpha particles having energies of 5.3 Mev or less is shown in Fig. 2 for crystals with five different Tl concentrations. Data for crystals with Tl mole fractions of 0.0025 and 0.0045 were also obtained and lie between the curves shown for crystals with Tl mole fractions of 0.0077 and 0.00095. Pulse heights

[9] Moreau, Chovin, and Daudel, Compt. rend. **219**, 127 (1944).
[10] W. Prodinger, *Organic Reagents Used in Quantitative Inorganic Chemistry* (Elsevier Publishing Company, Inc., New York, 1940).
[11] R. Berg and E. S. Fahrenkamp, Z. Anal. Chem. **112**, 162 (1938).
[12] R. Fresenius and G. Jander, Haundbuch der Analytischen Chemie (Springer-Verlag, Berlin, 1942), Vol. 3.

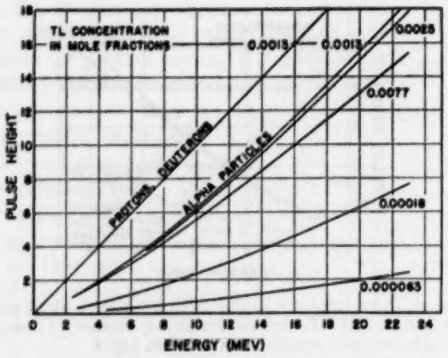

FIG. 3. Pulse heights resulting from alpha-particle and deuteron excitation of NaI(Tl) crystals containing various Tl concentrations.

were measured for two different crystals from the same melt for each Tl concentration. No deviations greater than experimental uncertainties were observed in these measurements, and each of the curves shown has been constructed from the combined data for both crystals.

The uncertainties in pulse heights associated with the points were assigned on the basis of the spread in pulse heights resulting from the finite resolution of the crystal and photomultiplier tube and the spread in alpha-particle energy caused by straggling. Knowledge of the energy coordinate was limited by the accuracy of the experimental determination of the air-equivalent thickness of the chamber foil. Unfortunately, the large uncertainties associated with the low-energy data prevent an accurate overlapping with the measurements of Allison and Casson[13] who determined the response for alpha particles with energies below 0.3 Mev.

Figure 3 shows the response of the various crystals to higher-energy alpha particles, protons, and deuterons. Data for a commercial scintillation crystal (mole fraction of Tl, about 0.0013) were obtained for 15 alpha-particle energies between 4 Mev and 23 Mev. The individual measurements of mean pulse height

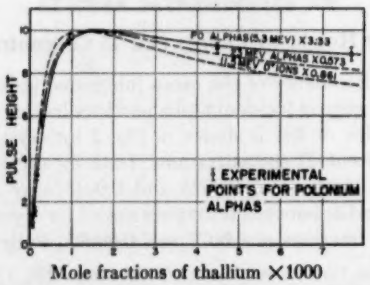

FIG. 4. Variation in pulse height resulting from alpha-particle and deuteron excitation of NaI(Tl) crystals as a function of the Tl concentration.

[13] S. K. Allison and H. Casson, Phys. Rev. **90**, 880 (1953).

were in all cases within one percent of the curve shown. The energy values of the incident cyclotron particles overlap the energy of Po alpha particles which serves as a check point on the low energy side. The response to protons and deuterons was found to be linear within the accuracy of the measurements, in agreement with previous work.[2] The curves for the other crystals were drawn on the basis of the ratios of the measured pulse heights for alpha particles of 10, 15, and 23 Mev relative to Po alpha particles and indicate that the response of NaI(Tl) to alpha particles increases with Tl concentration for mole fractions smaller than about 0.0013 and decreases for higher concentrations. The linearity, however, shows a steady improvement with Tl concentration. This is apparent from plots of the specific fluorescent *vs* the specific energy loss of the particle which are presented later.

A plot of pulse height *vs* Tl concentration for alpha particles of two different energies and deuterons of 11.5 Mev is shown in Fig. 4. The points on the curve

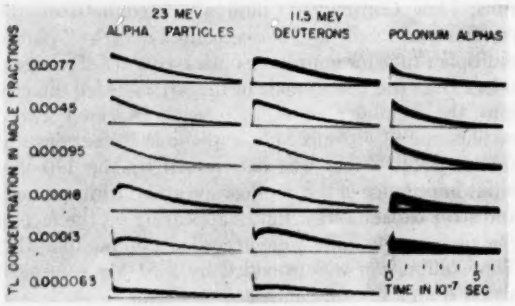

FIG. 5. Oscillograms of pulses (time exposures) resulting from the excitation of NaI(Tl) crystals by deuterons and high- and low-energy alpha particles.

for Po alpha particles are average values obtained for two different crystals from the same melt. The uncertainties associated with the points are based upon the reproducibility of the measurements which is limited by such factors as the crystal geometry, optical coupling, and slight variations in the Tl concentration. The curves for 23-Mev alphas and 11.5-Mev deuterons were derived from the measured ratios of the pulse heights for the energetic particles relative to pulse heights for Po alpha particles. Since pulse heights due to alpha-particle excitation vary in a more nearly proportional manner with the particle energy for high Tl content crystals than for low, the alpha-particle pulse heights in Fig. 4 tend to increase relative to deuteron pulse heights with increasing Tl concentration. The deuteron curve is in agreement with the data obtained by the Harshaw group[1] for Cs^{137} gamma-ray excitation within the accuracy of the respective experiments. This is to be expected in view of the similarity of the pulse heights *vs* energy relations for deuterons and gamma rays.

Luminescent Decay Times and Emission Spectra

Figure 5 shows oscillograms of pulses resulting from the excitation of crystals containing different concentrations of Tl by 23-Mev alpha particles, 11.5-Mev deuterons, and Po alpha particles. Each of the oscillograms represents a time exposure of the oscilloscope face and is made up of between 5000 and 30 000 individual pulses. The pulse heights were adjusted to a convenient size by changing the magnitude of the photomultiplier tube high voltage and were all taken with the same amplifier gain. The ripples superimposed on the 23-Mev alpha and deuteron pulses are due to pick-up from the cyclotron oscillator which was in synchronism with the particle bursts. The leading edges of the pulses are limited by the rise time (approximately 7×10^{-9} sec) of the amplifier, and the pulses can be relied upon to represent quantitatively the rate of light emission from the crystals only for times greater than about 3×10^{-8} sec. For times shorter than this the pulse shapes are to some extent influenced by the characteristics of the amplifier and have only qualitative validity.

Four separate decay processes characterize the pulse shapes: 1, that giving rise to the spike appearing on the leading edges of pulses from crystals with low Tl concentrations; 2, the initial rapid decay of Po alpha pulses for crystals abundant in Tl; 3, the rise of the main pulse; and 4, the relatively long decay of the main pulse. Figure 6 shows the measured exponential rise and decay times (mean lives) of the main pulse as a function of the Tl concentration. The points shown are average values obtained from several sets of data. Times were measured by making enlargements of oscillograms and transferring the ordinates of the traces to semilog paper. The uncertainties indicated in the figure were assigned on the basis of the widths of the traces and reproducibility of measurements made on different crystals from the same melt and represent the extreme values which could reasonably be assigned from any of the oscillograms. The rise-time characteristic of the main pulse is clearly evinced on semilog plots of pulses from both the 23-Mev alphas and the deuterons and, within the accuracy of the measurements is independent of Tl concentration and equal to 5.9×10^{-8} sec. The decay times for a given Tl concentration are the same for alpha particles and deuterons for times greater than about 2×10^{-7} sec after the start of the pulse. No indication was found of the presence of after-pulses on the segments of the curves which were used in the measurements. After-pulses generally do not appear until more than a microsecond after the start of the main pulse in the 5819 tube.[14]

The spike characteristic of low Tl concentration crystals has a decay time (mean life) of about 1.2×10^{-8} sec and the initial fast decay of the Po alpha pulses has a decay time of approximately 1.5×10^{-8} sec.

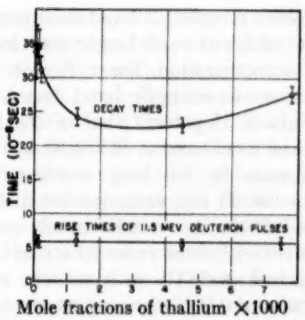

FIG. 6. Rise and decay times (mean-lives) of the main pulse resulting from deuteron excitation of NaI(Tl) crystals as a function of the Tl concentration. The decay times are the same as for excitation by other heavy particles.

The luminescent decay time of a crystal containing a mole fraction of Tl of 0.00095 was determined for Ni^{60} gamma-ray excitation from a smoothed-out "average" pulse which was obtained by numerically adding together a number of single pulses. Figure 7 shows a typical pulse due to a single gamma ray and below it an "average" pulse representing the sum of 75 single pulses. The irregularities of the gamma-ray pulse are the result of statistical fluctuations in the rate of light emission from the crystal. The shape of the smoothed pulse is similar to that observed for deuteron excitation, and the measured decay time is the same within the accuracy of the measurement.

The total emission spectrum, including phosphorescent components as well as prompt radiations, was measured for 11.5-Mev H_2^+ ion excitation of crystals containing various Tl concentrations and was found to consist of two broad bands. For crystals containing a mole fraction of Tl of 0.000063 the emission occurs in a band centered at 4100±50 A with a full width at half maximum of 800±50 A and a band (with about 60 percent of the maximum intensity of the first) centered at 3200±50 A and having a width of 450

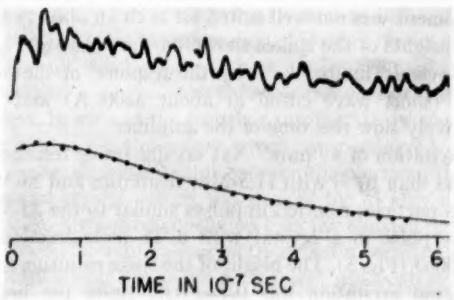

FIG. 7. Oscillogram of a single pulse from a NaI(Tl) crystal (containing a mole fraction of Tl of 0.00095) excited by a gamma ray from a Ni^{60} source and an "average" pulse obtained by adding together 75 single pulses.

[14] J. S. Allen, Los Alamos Report LA-1459, Aug., 1952 (unpublished). See also Mueller, Best, Jackson, and Singletary, Nucleonics **10**, No. 6, 53 (1952).

±50 A. The short wavelength band decreases in relative intensity and shifts toward longer wavelengths with increasing Tl concentration. For a Tl mole fraction of 0.0045 the short wavelength band has a maximum intensity of about 35 percent that of the long wavelength band and is centered at 3430±50 A. The position of the maximum in the long wavelength band is insensitive to the Tl concentration for mole fractions smaller than 0.0045. Our measurements on this band are in agreement with those reported earlier by Hofstadter[15] who excited NaI(Tl) with gamma rays. For a Tl mole fraction of 0.0077 the long-wavelength band is centered about 4400±50 A and has a width at half-maximum of 900±50 A. The short-wavelength band has a relative maximum intensity about 20 percent as great and is centered at about 3450 A. A shift in the wavelength of the emission spectrum with Tl concentration has been found in other alkali halide phosphors and has been described by Pringsheim.[16]

By inserting an appropriate optical filter between the crystal and photomultiplier tube it is possible to observe practically unattenuated the prompt radiation from the short wavelength band and to greatly reduce contributions from the long wavelength band. Pulses were observed from crystals excited by 23-Mev alpha particles alternately with and without a Corning 7–54 Red Purple Corex A filter (89 percent transmission at 3200 A decreasing to 10 percent at 2400 A and at 4000 A). The insertion of the filter between a crystal with a mole fraction of Tl of 0.000063 and the photomultiplier tube resulted in about a 10 percent decrease in the height of the spike on the leading edge and a decrease in the height of the rest of the pulse by a factor of about five with no detectable change in the decay times. The insertion of the filter between the photomultiplier tube and crystals containing mole fractions of Tl greater than 0.00095 decreased the pulse heights by a factor of five or more without detectable changes in either the shapes of the pulses or the decay times. In particular there is no apparent indication of a fast spike component of the pulses from crystals containing Tl mole fractions greater than 0.00018. It should be noted, however, that our experimental equipment was not well suited for such an observation. The heights of the spikes shown on the pulses of Fig. 5 are severely limited both by the response of the 5819 tube (short wave cutoff at about 3100 A) and the relatively slow rise time of the amplifier.

Excitation of a "pure" NaI crystal (mole fraction of Tl less than 10^{-7}) with 11.5-Mev deuterons and 23-Mev alpha particles resulted in pulses similar to the 23-Mev alpha pulse in a crystal with a Tl mole fraction of 0.000063 (Fig. 5). The height of the spike resulting from deuteron excitation was 0.77±0.06 times the height resulting from alpha particle excitation. The two lowest Tl concentration crystals also showed about this ratio. There was no evidence that the decay time of the spike depends upon either the Tl concentration or the specific energy loss of the particle. The intensity of the long component was about the same for deuteron as for alpha particle excitation, as is also the case for crystals with a Tl mole fraction of 0.000063. The maximum intensity of the long component relative to the spike was about one-half that of the pulse shown in Fig. 5 and the decay time of the long component about twice as long as the pulse in Fig. 5.

Two alternative possibilities suggest themselves to account for the absence of the spike component from crystals with high Tl concentrations. Either the processes which give rise to this emission are not present in high Tl content crystals, or the processes are present but the light is absorbed by the Tl before it escapes from the crystal. The long-wave absorption band in NaI(Tl) peaks at 2930 A.[17] In order to decide between these possibilities, experiments were performed with two crystals, one as a scintillator and one as a filter. The use of an RCA type C7140 A end-window photomultiplier tube (short wave cutoff at about 2100 A, relative sensitivity of 55 percent at 3200 A) enhanced the response to the short wavelength radiation by a factor of 2 or 3 relative to the long wavelength component. 23-Mev alpha particles and 11.5-Mev deuterons were used to excite the spike in a "pure" crystal. The pulses were essentially unchanged by the insertion of another pure crystal (about 3 mm thick) between the phototube and the crystal being bombarded. After the insertion of a crystal containing a Tl mole fraction of about 0.001 (also about 3 mm thick) between the phototube and the pure crystal which was bombarded, the spike component was decreased in intensity by a factor of about 3 and the long component remained essentially unchanged.

The fact that the spike was not entirely removed in this case indicates that its absence from crystals with Tl concentrations greater than 0.00018 must be explained by assuming the processes which give rise to this radiation are not present, or are at least not important, in high Tl content crystals. The accuracy of the experiment was not sufficient to ascertain whether or not the energy absorbed by the filter crystal appeared in the long component.

Prolonged bombardment of the crystals by 23-Mev alpha particles (integrated flux of about 10^{14} particles/cm^2) produced no measurable change in the intensity or decay time of the spike component.

IV. DISCUSSION

The response of Tl-activated alkali halide phosphors to excitation by light in the visible and ultraviolet regions has been the subject of numerous experimental

[15] R. Hofstadter, Phys. Rev. 75, 796 (1949).
[16] P. Pringsheim, Revs. Modern Phys. 14, 132 (1942).

[17] See, for example, P. Pringsheim, *Fluorescence and Phosphorescence* (Interscience Publishers, Inc., New York, 1949).

investigations, and in an early theoretical study based on the experimental work of Pohl and his co-workers Seitz[18] interpreted the absorption and emission spectra of these phosphors in terms of the excitation of the thallous ions which were assumed to occur substitutionally in the lattice. Later, Williams[19] succeeded in describing quantitatively the behavior of KCl containing dilute concentrations of Tl and was able to calculate the absorption and emission spectra at various temperatures.

Charged particles, however, lose their energy almost completely to the base material, and very little is known about the details of the mechanism for the transfer of the absorbed energy through the crystal. In addition, it appears that once the luminescent centers have been excited in crystals containing high activator concentrations the radiative processes do not occur in a manner in all ways similar to that exhibited for the optical excitation of crystals containing only small amounts of the activator.

In the following we shall consider the various prompt decay processes ($<10^{-6}$ sec) evident in NaI(Tl), the specific fluorescence as a function of the specific energy loss of the particle, and the dependence of the light emission on the Tl concentration and type of particle responsible for the excitation.

Energy Transfer and Decay Processes

Upon entering the crystal a fast charged particle loses its energy principally to the electronic system producing excitons and free electrons with a wide range of energies, and toward the end of its range a non-negligible fraction of its energy is expended in exciting lattice vibrations. The migration of free electrons, holes, and excitons and certain resonance processes appear as possible mechanisms responsible for the transfer of energy within the crystal. The number and types of centers which are excited evidently depends upon their concentrations and their relative cross sections for intercepting the carriers. During the period of energy migration several different types of excited levels are created whose characteristic de-excitation times can be observed in the pulses.

As was noted earlier the main part of the light pulse is characterized by a rise time of about 5.9×10^{-8} sec and a decay time which depends upon the Tl concentration and varies between 2.3×10^{-7} and 3.5×10^{-7} sec. A minimum of two excited states is necessary to describe this behavior, one state of the luminescent centers (radiative state) and at least one other state, not necessarily associated with luminescent centers, which decays nonradiatively into it. An approximate ratio for the relative initial (before appreciable light is emitted) populations of these states can be estimated by fitting to the deuteron pulses of Fig. 5 curves describing the ordinary radioactive decay law for the radiation of the daughter substance when both the mother and daughter levels are populated at zero time.

The question as to whether the rise or the relatively long decay of the pulse is characteristic of the radiative state cannot be definitely resolved on the basis of the present results. If it is assumed that the rise is characteristic of the radiative state the ratio of the initial populations of the radiative state to the nonradiative state which decays into it varies between about 0.1 and 0.2 having a maximum for a Tl mole fraction of about 0.002. If the alternative assumption is made the ratio ranges between 1 and 3, again with a maximum for a Tl mole fraction of about 0.002.

The fact that in either case the relative initial population of the radiative state increases with Tl concentration for low concentrations, seems to support the supposition that the Tl is indeed the luminescent center. It has been suggested that the function of the Tl is restricted to the trapping process and nonradiative transition.[4] It is difficult to see why, if this is so, the initial population of excited luminescent centers should increase with increasing Tl concentration, unless the actual process is somewhat more complicated than has been assumed here and three states are involved: a nonradiative state, an excited state in Tl, and a short-lived light-emitting state not in Tl.

The dependence of the integrated pulse height on the Tl concentration, which is discussed later, indicates that the rise time of the main pulse (5.9×10^{-8} sec) is probably the one associated with the radiative state and that the relatively long decay is apparently characteristic of the nonradiative state. In this case it must be supposed that most of the energy which is emitted in prompt radiations has passed through the nonradiative state and that the process giving rise to the main part of the pulse is a type of host-sensitized luminescence.[20]

The initial (approximately 1.5×10^{-8} sec) decay characteristic of Po alpha pulses from crystals with Tl mole fractions of 0.00095 and greater apparently represents an additional emission which exists under the conditions of high Tl concentration and large specific energy loss of the primary particle and suggests the possibility that another excited state of the luminescent center can be formed, perhaps by the capture of more than a single carrier during the energy transfer process. In view of the fact that this fast decay was not accentuated on the pulses which were observed after placing an ultraviolet filter between the photomultiplier tube and crystal, which was excited by 23-Mev alpha particles, it must be concluded that the emitted light is not much different in energy than that associated with the level giving rise to the main pulse. Although precise measurements could not be made of the magnitude of the contribution of this emission to the integrated

[18] F. Seitz, J. Chem. Phys. **6**, 150 (1938).
[19] F. E. Williams, J. Chem. Phys. **19**, 457 (1951).
[20] D. L. Dexter, J. Chem. Phys. **21**, 836 (1953) contains references to previous work.

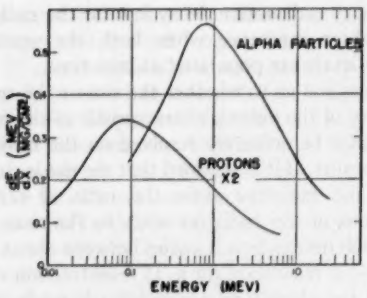

FIG. 8. Specific energy loss for alpha particles and protons in NaI.

pulse height it appears probable that it is to a large extent responsible for the increased linearity of the pulse height *vs* energy relation for high Tl content crystals.

Pulses from crystals containing Tl mole fractions of 0.00018 or smaller are characterized by an additional fast decay not apparent from crystals with higher Tl concentrations. This emission, which lies on the short wavelength side of the main band, is relatively less sensitive to the specific energy loss of the primary particle than the main pulse and is more prominant the lower the Tl concentration. Its presence in a "pure" crystal indicates that it has its origin in the base material. Since the decay time, 1.2×10^{-8} sec, is comparable to the lifetime expected for an exciton in a crystal containing this concentration of impurity atoms[21,22] it seems possible that this emission is associated with the extinction of excitons generated along the particle track. The fact that no strong characteristic luminescence has been observed when an alkali halide crystal is irradiated in the first fundamental band (presumably the most direct means of producing excitons) makes this explanation seem unlikely, however.§ Also the fact that the decay time is insensitive to the Tl concentration and remains essentially unchanged after the crystal has been exposed to prolonged particle bombardment is not in accord with this explanation. The efficiency for the production of this radiation is greater for deuterons than for alpha particles (which have a higher specific energy loss) which suggests that it does not owe its existence to imperfections created by heavily ionizing radiations.‖ Although this radiation was present from crystals containing low Tl concentrations which were obtained from the Larco Nuclear Instrument Co. as well as a "pure" NaI crystal obtained from the Harshaw Chemical Co., the possibility that it arises as a result of some impurity in the crystal cannot be definitely ruled out.

Specific Fluorescence *vs* Specific Energy Loss

The extent to which the specific energy loss of the incident particle influences the efficiency of light production in the crystal may be observed by plotting the specific fluorescence, dL/dx, obtained by differentiating a curve of pulse height *vs* residual range of the particle in NaI, as a function of the specific energy loss, dE/dx, of the incident particle. Unfortunately, the ranges of the particles and values of dE/dx in NaI have not been measured and must be inferred from existing data on other materials.

Figure 8 shows a plot of dE/dx *vs* energy for alpha particles and protons in NaI which has been calculated on the basis of stopping power and range-energy measurements of several different investigators and the assumption of the additivity law for combining the individual values of the stopping powers of Na and I. The dE/dx values for alpha particles with energies less than 2 Mev were constructed from the measured stopping powers of different substances relative to air[23] and the dE/dx values for air as given by Bethe.[24] In the region from 2 to 8.77 Mev the values were found by interpolation of dE/dx *vs* E curves based on ThC′ alpha particle range-energy measurements of Rosenblum.[25] For energies higher than 8.77 Mev Bethe's theoretical expression[24] was used for calculating the stopping powers using experimental values of the mean excitation potentials given by Mano.[26] Values of dE/dx for protons with energies below 2 Mev were obtained by interpolation of available experimental data on the rate of energy loss of protons in various metals,[27] and a point at 6.3 Mev was found by interpolation of the measured stopping power values of Marmier.[28] Values of dE/dx for alpha particles inferred from Aron's[29] theoretical dE/dx values for protons agree within ±5 percent with the values obtained by use of Mano's

[21] D. L. Dexter and W. R. Heller, Phys. Rev. **84**, 377 (1951).
[22] F. Seitz, Revs. Modern Phys. **26**, 7 (1954) mentions calculations of the lifetime of an exciton by Toyozawa.
§ *Note added in proof.*—No evidence was found of a similar fast fluorescent response from crystals of KI, KCl, or NaCl which were subjected to bombardment by 23-Mev alpha particles. These crystals were all observed to fluoresce weakly when exposed to a 10^{-8} ampere/cm² beam of 6-Mev protons (violet in the case of KI, green for KCl and NaCl, and an intense coloration was produced in the crystals after an exposure of about 15 sec (green in KI, violet in KCl, and yellow in NaCl). This behavior is strikingly different from that of NaI which fluoresces brilliantly (blue) and exhibits no perceptible coloration as a result of the bombardment.

‖ *Note added in proof.*—Subsequent work has shown that this radiation is excited by gamma rays and that the fluorescent efficiency is very nearly the same as for proton or deuteron excitation.
[23] Landolt-Börnstein and Roth-Scheel, *Physikalisch-Chemische Tabellen* (Springer Verlag, Berlin, 1936), fifth edition, Third Supplementary Volume, Second Part.
[24] See for example, E. Segrè, *Experimental Nuclear Physics* (John Wiley and Sons, Inc., New York, 1953), Vol. 1, Part II.
[25] S. Rosenblum, Ann. phys. **10**, 408 (1928).
[26] G. Mano, Ann. phys. **1**, 407 (1934).
[27] S. K. Allison and S. D. Warshaw, Rev. Modern Phys. **25**, 779 (1953).
[28] F. P. Marmier, Helv. Phys. Acta **24**, No. 1 (1951).
[29] W. A. Aron, thesis; University of California (UCRL 1325) (unpublished).

values for the excitation potentials in Bethe's formula for the region of alpha particle energies above 16 Mev. At 25 Mev the dE/dx values for alphas in NaI calculated from the works of Aron, Marmier, and Mano are in agreement to within 2 percent. The dE/dx values for alpha particles with energies greater than about 3 Mev seem to be consistent with those shown for protons. For lower energies dE/dx values for alpha particles are smaller than, and not directly comparable with, values for protons because of electron pickup and consequent change in the effective charge of the alpha particle. The curves for protons and for alpha particles with energies greater than 2 Mev are thought to be reliable to within ± 8 percent. The curve for alpha particles with energies less than 2 Mev is not more certain than about ± 10 percent.

Curves of dL/dx *vs* dE/dx are shown in Fig. 9 for crystals with three different Tl concentrations and indicate the amount of light dL emitted as a result of the particle's losing energy dE in traversing a path dx within the crystals. The relative uncertainties associated with the individual curves range from about 5 percent for low values of dE/dx to about 15 percent for the highest dE/dx values.

The straight portions of the curves occurring for low dE/dx values correspond to the region of linear pulse height *vs* energy response. Although the curve representing the Tl mole fraction 0.00018 is nonlinear throughout the energy range in which data were obtained, it seems probable that at sufficiently high alpha particle energies a region of linear response is approached for all the crystals. The range in dE/dx for the curve with a Tl mole fraction of 0.0013 has been extended by the inclusion of data for protons with energies up to 6 Mev. The maximum dE/dx value for protons is approximately that for 18-Mev alpha particles. The extent to which dL/dx is independent of the details of the way in which particle energy is lost is illustrated by the accuracy with which the response of the crystal to low energy alpha particles can be predicted from a knowledge of dE/dx and the dL/dx curve of Fig. 9. Figure 10 shows the measured pulse-height values of Allison and Casson[13]

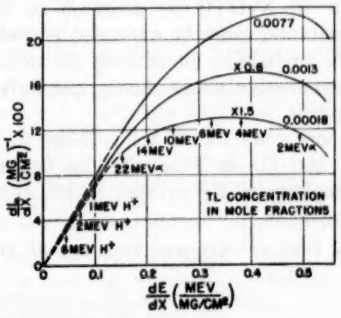

FIG. 9. Variation of the specific fluorescence, dL/dx, of NaI(Tl) with the specific energy loss, dE/dx, of the incident particles. L is in the same units as in Figs 2–4. dx is in mg/cm² of NaI.

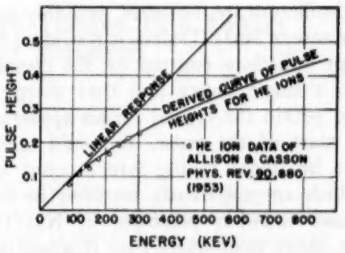
PULSE HEIGHT
ENERGY (KEV)
LINEAR RESPONSE
DERIVED CURVE OF PULSE HEIGHTS FOR HE IONS
• HE ION DATA OF ALLISON & CASSON PHYS. REV. 90, 880 (1953)

FIG. 10. Pulse heights resulting from excitation of a commercial NaI(Tl) crystal by alpha particles with energies below 350 kev. Pulse height scale is the same as in Figs. 2–4.

and a derived curve using data from Fig. 8 and the curve for a Tl mole fraction of 0.0013 from Fig. 9 with the assumption that dL/dx depends only on dE/dx. Because of the relatively large uncertainties in the low energy region of Fig. 8, the derived curve is probably not more accurate than ± 10–15 percent. Comparison of the pulse heights from low-energy alpha particles and the line representing linear response suggests that the thermal spike[30] produced in the wake of a slow alpha particle can have only slight, if any, deleterious effect on the fluorescent efficiency.

Although the Tl concentration exerts a strong influence on the absolute values of the specific fluorescence, the dependence on dE/dx is relatively insensitive to Tl concentration, and the number of activator ions present within the range of migration of the energy is clearly not the dominant factor responsible for the bending over of the curves for high values of dE/dx in NaI(Tl). The saturation of the specific fluorescence with increasing dE/dx is a characteristic of most of the common scintillators[31] and is usually somewhat more pronounced in organic materials. That the behavior of dL/dx is indeed a property of the bulk material and is not to be associated with "surface effects" has been demonstrated for NaI(Tl) by der Mateosian and Yuan.[32]

For reasons which will be mentioned later, it appears that most of this effect is tracable to processes taking place during the time in which the energy is transferred from the neighborhood of the particle track to the various trapping centers. Simple models of the type which have been used with some success to describe quantitatively the behavior of dL/dx *vs* dE/dx in

[30] A short discussion and references are given in the book by Shockley, Hollomon, Maurer, and Seitz, *Imperfections in Nearly Perfect Crystals* (John Wiley and Sons, Inc., New York, 1952).

[31] Reference 2; see also G. T. Wright and G. F. J. Garlick, Brit. J. Appl. Phys. 5, 13 (1954); W. T. Link and D. Walker, Proc. Phys. Soc. (London) **A66**, 767 (1953) have given a curve for KI(Tl). The situation in the case of KI(Tl) is somewhat confused. Link and Walker report a deviation from linearity in the pulse height *vs* energy curves for protons and deuterons. The paper by Franzen, Peele, and Sherr, Phys. Rev. **79**, 742 (1950) and preliminary unpublished results of the group at Chalk River (private communication) indicate a linear response.

[32] E. der Mateosian and L. C. L. Yuan, Phys. Rev. **90**, 868 (1953).

organic scintillators are, however, probably not applicable to the case of NaI(Tl) since it is evident that all of the prompt radiations emitted by the crystal do not arise from a single source and that energy is being transferred within the crystal for an appreciable time after the start of the pulse. It would seem that a theoretical treatment taking into account all of the factors which are apparently involved in the energy transfer and emission processes in NaI(Tl) would contain so many parameters that it would not easily lend itself to convincing experimental verification by curves of the type shown in Fig. 9.

Dependence of Light Emission on Tl Concentration and dE/dx of the Primary Particle

The increase in the integrated pulse height with Tl concentration for crystals containing mole fractions of Tl less than about 0.0015 (Fig. 4) is evidently the result of the greater probability for exciting luminescent centers due simply to their increased abundance. The pulse heights resulting from a given excitation tend to decrease, however, for mole fractions greater than about 0.0015. In view of the fact that the emission spectrum shifts toward longer wavelengths with increasing Tl concentration and more nearly matches the response of the photomultiplier tube, the decrease in light intensity for high Tl concentrations is possibly somewhat greater than is indicated by the pulse heights.

In order to explain the decreased fluorescence of phosphors with high activator concentrations, several theories have been proposed[33,34] which postulate that concentration dependent quenching mechanisms compete with the process of light emission in the de-excitation of the luminescent centers. Such processes, if present, might be expected to alter the decay times of the excited centers and to result in faster decays the higher the activator concentration. Although evidence of this behavior is definitely not present in the measured decay times of the pulses (Fig. 6), a decrease in the rise times with Tl concentration sufficient to account for the decrease in the pulse heights, while not obvious, (Fig. 6) is not inconsistent with the present measurements. A concentration-dependent quenching process which takes place before appreciable light has been emitted from the crystals would not be apparent in either the rise or the decay times of the pulses. As has been mentioned previously, the ratio of the initial populations of the radiative to the nonradiative state which decays into it decreases with Tl concentration for mole fractions greater than about 0.002. Although this decrease could be explained by assuming that fewer luminescent centers are excited during the energy transfer process, it is perhaps more plausible to assume that a concentration dependent quenching mechanism operates to deplete the radiative level before appreciable light is emitted.

It seems probable that the pulses rise with a time constant characteristic of the luminescent centers and that the decays of the pulses are determined by the nonradiative states. This assumption is to some extent supported by the fact that the long decay has been found to be present in the luminescence of NaI crystals which were supposedly free of Tl, both in the present work and in the earlier observations of Bonanomi and Rossel.[4] No rise component was apparent in the pulses from pure crystals observed in the present work. The existence of the long decay from pure crystals presumably indicates that the "nonradiative" state may either luminesce weakly or lose its energy to some other imperfections in the crystal which later radiate. It is not entirely clear why the decay time of this state should depend on the Tl concentration in the manner shown in Fig. 6. It seems probable that the decay time decreases with increasing Tl concentration for mole fractions less than about 0.003, mainly as a result of the increased probability for the state's transferring its energy to the luminescent centers as these become more abundant. The subsequent increase in decay time with Tl concentration, however, indicates that other factors must also be considered.

There is no evidence from the present work that the magnitude of the specific energy loss of the primary particle exerts an influence on the decay times of either the radiative or the nonradiative states, as seems to be the case for certain organic phosphors.[35] Although the time constant associated with the rise of the main pulse could not be measured for Po alpha excitation, it was found to be the same, within the accuracy of the measurements, for deuteron and 23-Mev alpha excitation. The decay time (after about 2×10^{-7} sec) is the same for alpha particle and deuteron excitation. Apparently the difference in the relative efficiencies for fluorescence in NaI(Tl) by deuteron or by alpha-particle excitation must be explained entirely on the basis of the probability of exciting the radiative and various nonradiative states during the initial energy transfer process.

The authors would like to acknowledge their indebtedness to Mr. G. de Pasquali who performed the chemical analyses of the crystals which were used in the measurements.

[33] P. D. Johnson and F. E. Williams, J. Chem. Phys. **18**, 1477 (1950).

[34] H. Kallman and M. Furst, Phys. Rev. **79**, 857 (1950).

[35] Bittman, Furst, and Kallmann, Phys. Rev. **87**, 83 (1952).

Theory of Electric Breakdown in the High-Temperature Region and Its Relation to Thermionic Emission

KURT LEHOVEC
Sprague Electric Company, North Adams, Massachusetts
(Received August 5, 1954)

The decrease of von Hippel's breakdown field caused by random fluctuations of electron energy is estimated from consideration of the distribution function of electrons in strong fields. This decrease of breakdown field is appreciable at ordinary temperatures in case of the interaction of electrons with optical modes of lattice vibrations in ionic lattices and this may account for the observed decrease of breakdown field with increasing temperatures at elevated temperatures.

The rate of formation of "fast" electrons from "slow" electrons is used to estimate the deviations from thermal equilibrium distribution of electrons at the surface of a thermionic cathode. Deviations from Richardson's equation are expected if $E(h\nu)/(kT)^2 \lesssim (3/16)^{\frac{1}{2}}$, where E is the height of energy barriers at the surface above the bottom of the conduction band in semiconductors, $h\nu$ is the phonon energy, and kT is the energy equivalent of temperature. A strong increase of the thermionic emission current with the field in the cathode is predicted for semiconductors at fields of the order of the breakdown field.

INTRODUCTION

ELECTRIC breakdown in insulators may arise by two different processes: (1) At high field-strength electrons from the filled band may enter the empty band by the wave mechanical tunnel effect (Zener effect).[1] (2) Electrons in the nearly empty band may acquire sufficient energy to release secondary electrons from the filled band by collision, these in turn release tertiary electrons, etc. (breakdown by electron avalanches).[2]

In this paper, we are concerned with the breakdown by electron avalanches only. The early theoretical work in this field[3] was based on considerations of the rate at which an average electron reaches sufficient energy to create a secondary electron. Seitz[4] has considered the effect of deviations from the average behavior of an electron on the breakdown field. More recently, Fröhlich,[5] Heller,[6] Franz,[7] and Yamashita and Watanabe[8] have discussed breakdown phenomena in terms of the distribution function of electrons over the energy states. In this work, the breakdown field is derived from the condition that the rate of creation of secondary electrons exceeds the rate of recombination of electrons excited by impact. Kawamura[9] has used an expression derived by Franz[7] for a comparison of the effect of random processes on breakdown field as obtained from the theory based on the distribution function with the expression derived by Seitz.[4]

In this paper, we would like to use considerations of the distribution function in strong fields for a discussion of (1) the relation of the breakdown theory based on the distribution function to the older one, based on the behavior of an individual electron; (2) the temperature dependence of the breakdown field at elevated temperatures; (3) a relation between breakdown field and thermionic emission. Instead of specializing the rather complicated expressions derived by Heller,[6] for our purposes it may be permissible to present a simplified derivation which involves a boundary condition of the distribution function at the ionization energy which differs from that of previous workers. For a justification of some of the applications made, the reader will be referred frequently to the paper by Heller.[6]

THE BEHAVIOR OF THE ELECTRONS AND THE EFFECT OF RANDOM PROCESSES

The release of a secondary electron by impact of a fast electron is pictured schematically in Fig. 1. A fast electron of energy E in the conduction band of the crystal excites an electron from the filled band to the conduction band and loses its own energy in this process. Thus by the impact of a fast electron, two slow electrons

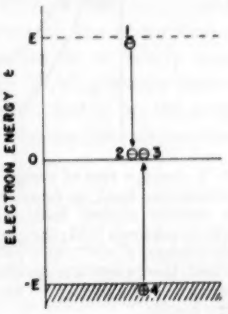

FIG. 1. Production of a secondary electron by impact. (1) Fast electron before impact. (2) Same electron after having lost its kinetic energy by impact. (3) Secondary electron excited by impact from the filled band into the conduction band. (4) Hole left behind in the filled band. $\epsilon > 0$: electron conduction band; $\epsilon < -E$: filled band.

[1] C. M. Zener, Proc. Roy. Soc. (London) **A145**, 523 (1934); W. Franz, Z. Physik **113**, 607 (1939); W. V. Houston, Phys. Rev. **57**, 184 (1940).

[2] See A. von Hippel, Trans. Faraday Soc. **A42**, 78 (1946), and A. von Hippel and R. S. Alger, Phys. Rev. **76**, 127 (1949) for recent accounts of this point of view and for a more complete bibliography.

[3] H. Fröhlich, Proc. Roy. Soc. (London) **A160**, 230 (1937); **A172**, 94 (1939); **A178**, 493 (1941); **A188**, 521 (1947); R. J. Seeger and E. Teller, Phys. Rev. **54**, 515 (1939); **56**, 352 (1939); H. Callen, Phys. Rev. **76**, 1394 (1940). F. Seitz, Phys. Rev. **76**, 1376 (1949).

[4] F. Seitz, Phys. Rev. **76**, 1376 (1949).

[5] H. Fröhlich, Proc. Roy. Soc. (London) **A188**, 532 (1947).

[6] W. R. Heller, Phys. Rev. **84**, 1130 (1951).

[7] W. Franz, Z. Physik **132**, 285 (1952).

[8] J. Yamashita and M. Watanabe, Repts. Inst. Sci. Tech. Univ. Tokyo **6**, III (1952).

[9] H. Kawamura, J. Phys. Soc. (Japan) **8**, 424 (1953).

of energy $\epsilon \approx 0$ are created, whereas one fast electron of energy $\epsilon \approx E$ disappears. The slow electron may either become a fast electron and create another pair of slow electrons by impact, or it may disappear from the conduction band by recombination. Breakdown occurs if the rate at which slow electrons become fast electrons is larger than the rate of recombination. Therefore, the breakdown theory is concerned with (a) the rate at which slow electrons become fast electrons, and (b) the rate of recombination.

An electron exchanges energy with the crystal lattice at an average rate $\langle d\epsilon/dt\rangle_L$, which is a function of its energy ϵ.[4] A typical curve of $\langle d\epsilon/dt\rangle_L$ *versus* ϵ is shown schematically in Fig. 2, case $F=0$. Except for electrons of very low energy $\epsilon \lesssim kT$, the electrons lose energy on the average by interaction with lattice vibrations. On the other hand, the electron gains (kinetic) energy from an applied field F at an average rate of $\langle d\epsilon/dt\rangle_F > 0$. The average rate of energy change from both field and lattice,

$$d\epsilon/dt = \langle d\epsilon/dt\rangle_L + \langle d\epsilon/dt\rangle_F, \qquad (1)$$

is shown schematically in Fig. 2 for three different fields. For sufficiently strong fields, $F \geq F^*$, we have $d\epsilon/dt \geq 0$ for all electron energies. For fields $F < F^*$, there exists an energy region where $d\epsilon/dt < 0$; this region will be referred to as "energy barrier" in what follows.

If the rate of energy change of each electron of energy ϵ would equal the average rate $d\epsilon/dt$, a slow electron could never become a fast electron, capable of forming a secondary electron, at a field $F < F^*$, and no breakdown could occur. Von Hippel identifies F^* with the breakdown field. Calculations of the breakdown field on this basis give a reasonable order of magnitude and predict an increase of the breakdown field with increasing temperature.

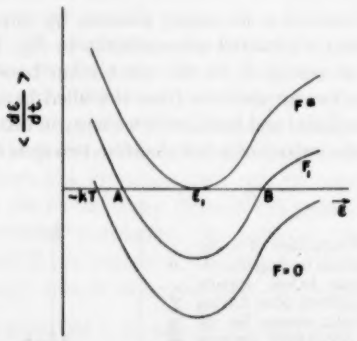

FIG. 2. Average rate of energy change $\langle d\epsilon/dt\rangle$ of an electron in the conduction band as function of its energy (schematically). $F=0$: without applied field; $\langle d\epsilon/dt\rangle = \langle d\epsilon/dt\rangle_L$; $F=F^*$: at von Hippel's breakdown field; the electrons of any energy gain energy on the average; $F_1 < F^*$: at a field less than von Hippel's breakdown field, there exists a range of energy $A \leq \epsilon \leq B$, where electrons lose energy on the average. This range will be referred to as an "energy barrier."

Experiments show that the breakdown field passes through a maximum with increasing temperature.[10] A possible explanation[11] of the decrease of the breakdown field with increasing temperature in the high-temperature region may be sought along the following lines. The energy change of an electron by interaction with the lattice is a statistical process, the elements of which are the absorption and emission, respectively, of a vibrational energy quantum $h\nu$ (phonon). At a sufficiently high temperature ($kT \gg h\nu$) and for electrons of energy $\epsilon \gg kT$, the rate of emission is larger than the rate of absorption; however, this difference is small as compared to either rate and arises from the "spontaneous emission." Hence, the change of energy of an electron by interaction with the lattice vibrations consists of large random fluctuations with a resultant small average energy. This is similar to the motion of an electron in a crystal in an electric field where there is a large random movement with a small superimposed directed movement. It is well known that the random movement leads

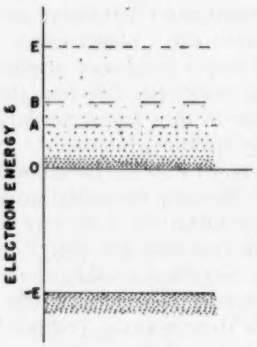

FIG. 3. Distribution of electrons (black dots) over the energy states of the crystal. Zero level of energy is the bottom of the electron conduction band. The top of the filled band lies at $-E$. The dotted line at $+E$ marks the electron energy necessary for production of secondary electrons by impact. In the range between A and B, the electrons lose energy on the average. This range is referred to as "energy barrier." A and B depend on the applied field.

to a diffusion current in case of a variation of concentration of electrons with position. Accordingly, in the case of a variation of electron concentration with energy (e.g., in the case of a Boltzmann distribution), the random fluctuation of energy leads to a diffusion current in energy space. Since there are more electrons of low energy than of high energy (see Fig. 3), the diffusion current is directed from low-energy values to high-energy values. We conclude that even in the case of $F \leq F^*$, a certain number of electrons may cross the "energy barrier" by diffusion processes.

It is obvious that the theory of electric breakdown which is based on "average electrons" does not take into account the crossing of the energy barrier by diffusion. The diffusion process enhances the number of fast electrons capable of producing secondaries and thus enhances electric breakdown. Hence one may suspect

[10] A. von Hippel and G. M. Lee, Phys. Rev. **59**, 824 (1941); A. M. Thomas and M. V. Griffith, J. Inst. Elect. Engrs. (London) **89**, 487 (1942).

[11] Another explanation has been proposed by H. Fröhlich, Proc. Roy. Soc. (London) **A188**, 521 (1947).

that the diffusion process, which increases with temperature, may be responsible for the observed decrease of the breakdown field at high temperatures.

By comparing the rates of crossings of the energy barrier due to the field and due to the diffusion, it is possible to modify the old breakdown theory[2] (which does not consider diffusion). This procedure, though only approximate, is attractive because it does not necessitate any assumptions about recombination processes. A detailed theory of breakdown must be based on knowledge of the distribution function of electrons over the energy states of the empty band and necessitates detailed assumption regarding their recombination with holes in the filled band.[6,7]

RATE OF FLOW OF ELECTRONS IN WAVE VECTOR SPACE

Consider the number of electrons per unit time which change from energy less than ϵ to larger than ϵ. This number represents a flow rate $S(\epsilon)$ in wave vector space through the surface $\epsilon=$const. Let $0\leq f(\epsilon)\leq 1$ be the probability that an energy state ϵ is occupied by an electron. In what follows we shall express $S(\epsilon)$ in terms of the distribution function $f(\epsilon)$ of the electrons. The calculation will be based on the following assumptions:

(1) Spherically symmetrical energy surfaces in wave vector space

$$\epsilon=h^2k^2/2m \tag{2}$$

(h Planck's constant, k wave vector of the electron, m effective electron mass). For such surfaces the density of energy states is[12]

$$D(\epsilon)=2(2\pi/h^3)(2m)^{\frac{3}{2}}\epsilon^{\frac{1}{2}}. \tag{3}$$

(2) The distribution function $f(\epsilon)$ can be expanded in terms of Legendre polynomials with the field direction as axis. All terms except the first will be neglected. Thus we set

$$f(k,\vartheta)=f_0(\epsilon)+f_1(\epsilon)k_z, \tag{4}$$

where $k_z=|k|\cos\vartheta$ is the wave vector component in field direction.

(3) A detailed analysis of the scattering process and of the influence of the field on the electron distribution shows that at sufficiently weak fields

$$f_1\sim-\tau(eF/m)h(df_0/d\epsilon), \tag{5}$$

where

$$1/\tau=-(1/k_z)\langle dk_z/dt\rangle_L \tag{6}$$

is the "transport collision frequency." τ is a function of energy in a manner which depends on details of the scattering mechanism of electrons and lattice vibrations. In what follows, we shall assume that Eq. (5) is valid for field strengths up to the breakdown field.

(4) The electrons interact with lattice vibrations of a single frequency ν (Einstein distribution), which are assumed to be thermally fully excited; i.e., $n=kT/h\nu\gg 1$ (k Boltzmann constant).

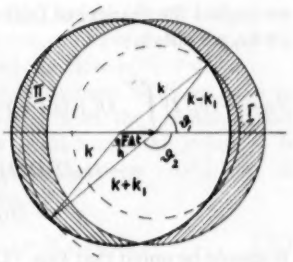

FIG. 4. A shift of the electron distribution by $eF\Delta t/h$ in the k_z direction causes the electrons of wave vectors in area I to flow out of the energy surface $\epsilon=(h^2k^2/2m)$ (thickly drawn circle) and the electrons of wave vectors in area II to flow into the energy surface.

(5) Collisions between electrons are neglected (see Heller[6]).

There are three contributions to the flow of electrons in k-space $S(\epsilon,F)$ through the energy surface $\epsilon=$constant:

$$S=S_F+S_L+S_D. \tag{7}$$

S_F arises from the change of wave vector with time due to the electric field

$$(dk_z/dt)_F=eF/h. \tag{8}$$

We have (see Fig. 4)[13]

$$S_F dt=4\pi\int_0^{eFdt/h}\left\{\int_0^{\vartheta_1(k_1)} f(k-k_1,\vartheta)(k-k_1)^2\sin\vartheta d\vartheta - \int_{\vartheta_2(k_2)}^{\pi} f(k+k_1,\vartheta)(k+k_1)^2\sin\vartheta d\vartheta\right\}dk_1. \tag{9}$$

Considering a sufficiently short time interval dt so that $(eF/h)dt\ll k$, we obtain from Fig. 4: $\cos\vartheta_1=-\cos\vartheta_2\cdot k_1/(eF/hdt)$. If we introduce Eq. (4) into Eq. (9), the terms containing f_0 cancel and we obtain

$$S_F=(8\pi/3)(eF/h^4)(2m)^{\frac{3}{2}}f_1(\epsilon)\epsilon^{\frac{1}{2}}. \tag{10}$$

Combining Eqs. (10), (3), and (5), we have

$$S_F=-\tfrac{2}{3}D(\epsilon)(eF)^2\epsilon(df_0/d\epsilon)/m. \tag{11}$$

S_L arises from the average change of energy due to collisions with lattice vibrations,

$$S_L=Df_0\langle d\epsilon/dt\rangle_L. \tag{12}$$

In the temperature region where $n=kT/h\nu\gg 1$, and for energies $\epsilon\gg h\nu$, the occurence of the absorption and emission of vibrational quanta $h\nu$ is nearly equally frequent. The energy change $\langle d\epsilon/dt\rangle_L$ results then only from the spontaneous emission and is on the average $-h\nu/(2n+1)$ per collision, whereas the random energy change per collision is $\pm h\nu$. Thus,

$$\langle d\epsilon/dt\rangle_L=-\nu_c h\nu/(2n+1)\approx-\nu_c(h\nu)^2/2kT, \tag{13}$$

where ν_c is the collision frequency. S_D results from the random changes $\pm h\nu$ of electron energy per collision; if

[12] $D(\epsilon)$ includes a factor 2 from the two spin possibilities.

[13] A factor 2 accounting for the two spin possibilities is included.

we neglect the changes of $D(\epsilon)$ with ϵ in the range $\epsilon-h\nu$, $\epsilon+h\nu$, we obtain:

$$S_D=-(\nu_c/2)\int_0^{h\nu} D[f_0(\epsilon+\epsilon_1)-f_0(\epsilon-\epsilon_1)]d\epsilon_1$$
$$\approx-(\nu_c/2)D(df_0/d\epsilon)(h\nu)^2$$
$$=D(df_0/d\epsilon)\mathrm{k}T\langle d\epsilon/dt\rangle_L. \quad (14)$$

It should be noted that Eqs. (13) and (14) are valid only if $h\nu\ll\epsilon$.

By substituting Eqs. (11), (12), and (14) into Eq. (8), we obtain:[5]

$$S(\epsilon,F)=Df_0\langle d\epsilon/dt\rangle_L$$
$$+Ddf_0/d\epsilon[\mathrm{k}T\langle d\epsilon/dt\rangle_L-(2/3)\tau\epsilon(eF)^2/m]. \quad (15)$$

$\langle d\epsilon/dt\rangle_L$ and τ are functions of ϵ, which may be derived from considerations of the type of interaction of electrons with lattice vibrations. For the purposes of this paper, we need not specify these functions in detail, except that $\langle d\epsilon/dt\rangle_L$ is negative for $\epsilon\geq kT$, and that there is a maximum of $-(\langle d\epsilon/dt\rangle_L/\tau)$ at an energy ϵ_1, (see Fig. 2).[14]

COMPARISON WITH THE OLD BREAKDOWN THEORY

According to Eqs. (16) and (8), the average change of wave vector component in the x direction is

$$dk_x/dt=\langle dk_x/dt\rangle_F+\langle dk_x/dt\rangle_L=(eF/h)-(k_x/\tau). \quad (16)$$

The ordinary breakdown theory[4,15] considers an "average electron," defined by having a wave vector component in the x-direction which does not change, on the average, because of the field or lattice vibrations, i.e., $dk_x/dt=0$. Hence the x-component of wave vector of the average electron is

$$k_x=(eF/h)\tau. \quad (17)$$

The average rate of change of energy due to the field is obtained from Eqs. (2) and (8):

$$\langle d\epsilon/dt\rangle_F=(d\epsilon/dk_x)\langle dk_x/dt\rangle_F=hk_x(eF/m). \quad (18)$$

From Eqs. (18) and (17), the average rate of change of energy of the "average electron" is obtained:

$$d\epsilon/dt=\langle d\epsilon/dt\rangle_L+[(eF)^2/m]\tau. \quad (19)$$

According to von Hippel,[2] the breakdown field F^* is determined by

$$d\epsilon/dt=\langle d\epsilon/dt\rangle_L+[(eF^*)^2/m]\tau=0, \quad (20)$$

where the right side is to be taken at its maximum value (the corresponding energy will be designated by ϵ_1; see Fig. 2).

If we take the flow rate $S_{F=F^*}$ at $\epsilon=\epsilon_1$ as determining the breakdown, then the inclusion of the diffusion flow rate S_D would lead to a breakdown field G^*, defined by

$$S_{F=F^*}=S_{F=G^*}+S_D, \quad (21)$$

with all values taken at $\epsilon=\epsilon_1$. Equations (11) and (14) indicate that $S_F\rightarrow S_F+S_D$ by the substitution $(eF)^2/m=(eF)^2/m-\frac{3}{2}(\mathrm{k}T/\epsilon)\langle d\epsilon/dt\rangle_L/\tau$. Hence the breakdown field F^* as given by the ordinary breakdown theory [Eq. (20)] should be corrected to give the breakdown field G^* defined by Eq. (21) by setting:

$$G^{*2}=F^{*2}+\tfrac{3}{2}(m/e^2)\langle d\epsilon/dt\rangle_L/(\mathrm{k}T/\epsilon_1)$$
$$=F^{*2}[1-\tfrac{3}{2}(\mathrm{k}T/\epsilon_1)]. \quad (22)$$

If F^{*2} increases proportionally to T, G^* has a maximum $F^*/2$ at the temperature $T_m=\epsilon_1/(3\mathrm{k})$.

In the case of interaction of electrons with the optical modes of lattice vibrations in ionic crystals, we have $\epsilon_1\sim0.1-0.2$ ev (e.g., most of the alkali halides) corresponding to $T_m\sim400-800°\mathrm{K}$. Therefore, at ordinary temperatures, the term $\frac{3}{2}\mathrm{k}T/\epsilon_1$ is not negligible compared to unity in the case of interaction with the optical modes of lattice vibrations. In the case of interaction with the acoustical modes of lattice vibrations, ϵ_1 is of the order of an electronvolt. Hence the term $\frac{3}{2}\mathrm{k}T/\epsilon_1$ should be negligible compared to unity in the case of interaction with the acoustical modes, in agreement with the estimate by Seitz.[3]

In ionic crystals either the interaction with the optical modes of lattice vibrations or that with the acoustical modes of lattice vibrations may be the cause of the "energy barrier," determining the breakdown field.[4] It is usually assumed[15] that the interaction with the optical modes determines the breakdown field, though this is not necessarily the case.

GENERAL TREATMENT OF BREAKDOWN BASED ON THE DISTRIBUTION FUNCTION

The breakdown criterion of the simple theory is unsatisfactory because it does not compare the rate of generation of secondary electrons with the rate of their recombination. The breakdown criterion should be based on the condition that no stationary electron distribution can be maintained for fields $F\geq H$ (where H is the breakdown field). In order to obtain a quantitative formulation, assumptions about (a) the ionization process, and (b) the recombination process, have to be made.

With regard to the ionization process, we shall assume that each electron creates a secondary electron and loses its own energy as soon as it acquires the ionization energy E.[16] This means that (1) fast electrons disappear at a rate $S(E)$, (2) slow electrons are created at a rate $2S(E)$, and (3) that $f(\epsilon)=0$ for $\epsilon>E$.

With regard to the recombination process, we shall assume:

[14] Since $\tau\approx1/\nu_c$ and since ν_c is proportional to $\langle d\epsilon/dt\rangle_L$, $\langle d\epsilon/dt\rangle_L/\tau$ is essentially the function $\langle d\epsilon/dt\rangle_L^2$.

[15] H. Callen, Phys. Rev. 76, 1394 (1949).

[16] As is shown by Heller (see reference 6) the delay of the distribution function for energies $\epsilon>E$ is extremely rapid.

(1) Only "slow electrons" of energy $\epsilon<\epsilon_0$ recombine. This assumption seems justified since only slow electrons remain sufficiently long in the neighborhood of recombination centers to recombine. We shall choose $\epsilon_0 \gtrsim kT \gg h\nu$, so that $\langle d\epsilon/dt\rangle_L<0$ for $\epsilon \gtrsim \epsilon_0$ (see Fig. 2, case $F=0$).

(2) The rate of recombination is a given function R of $f(\epsilon_0)$, which we shall not specify closer. At first sight it appears preferable to consider the recombination as a function of the number of "slow electrons"

$$N=\int_0^{\epsilon_0} Df_0(\epsilon)d\epsilon.$$

However, if ϵ_0 is of the order kT, $f_0(\epsilon)$ will be nearly a constant in the range $\epsilon_0 \leq \epsilon \leq E_0$ and N will be proportional to $f_0(\epsilon_0)$.

Since there is no recombination in the range $\epsilon_0 \leq \epsilon \leq E$, we have $f_0(\epsilon)=$ constant in this range in a stationary state, and we obtain from Eq. (15):

$$f_0(\epsilon)=f_0(E)\exp\left(+\int_\epsilon^E p d\epsilon\right) - S\left[\int_\epsilon^E p\left[\frac{\exp\left(-\int_\epsilon^E p du\right)}{D\langle d\epsilon/dt\rangle_L}\right]d\epsilon\right] \times\left[\exp\left(+\int_\epsilon^E p d\epsilon\right)\right], \quad (23)$$

where

$$p=[kT-(2/3)(\tau\epsilon/\langle d\epsilon/dt\rangle_L)(eF)^2/m]^{-1}. \quad (24)$$

If one recalls that $\langle d\epsilon/dt\rangle_L<0$ for the energy range considered, and that $0<p\leq(kT)^{-1}$, Eq. (23) may be interpreted as follows: The first term on the right hand side is a generalized Boltzmann distribution with a "temperature" p/k depending on energy and field as expressed by Eq. (24). The second term is the modification of the Boltzmann distribution by the flow S. It will be shown in the Appendix, that $f_0(E)$ is proportional to S, the proportionality constant being a function of the applied field:

$$f_0(E)=a(F)S. \quad (25)$$

If we introduce the Eq. (25) into the Eq. (23), written for $\epsilon=\epsilon_0$, we obtain

$$b(F)=S/f_0(\epsilon_0) = \left\{a(F)-\int_{\epsilon_0}^E p\left[\frac{\exp\left(-\int_\epsilon^E p du\right)}{D\langle d\epsilon/dt\rangle_L}\right]d\epsilon\right\}^{-1} \times\exp\left(-\int_{\epsilon_0}^E p d\epsilon\right). \quad (26)$$

Since $a(F)>0$ (see Appendix) and $\langle d\epsilon/dt\rangle<0$ (for $\epsilon \gtrsim \epsilon_0$), we have $b(F)>0$. For $F\to\infty$, we have $p\to 0$ [Eq. (24)] and $a\to 0$ (Appendix), and therefore $b(F)\to\infty$.

In order to obtain the breakdown field, we have to compare the flow $S=bf(\epsilon_0)$ with the recombination $Rf_0(\epsilon_0)$. At fields below breakdown, the value f_0 is determined by the balance between production of secondaries and recombination:

$$b(F)f_0(\epsilon_0)=R[f_0(\epsilon_0)]. \quad (27)$$

The breakdown field H is determined by the condition that no solution $f_0(\epsilon_0)\leq 1$ of the Eq. (27) exists for $F\geq H$, whereas such a solution exists for $F<H$. Any extension of the above theory requires more detailed knowledge of the recombination process.

RELATION TO THE THEORY OF THERMIONIC EMISSION

It will be noticed that for $F=0$, Eq. (26) leads to a finite rate of ionization S_0 and Eq. (23) gives then an electron distribution which differs from that of thermal equilibrium. The reason for the failure of Eq. (23) in the case of thermal equilibrium ($F=0$) is the following: Our treatment was based on the creation of two slow electrons and the disappearance of one fast electron in the process of the ionization by impact (see Fig. 1). The reverse process, disappearance of two electrons and simultaneous creation of one fast electron, was neglected. However, in thermal equilibrium the rate of each process equals that of its reversed process. Hence we cannot keep one process and neglect its reverse process in thermal equilibrium.

A finite flow rate S in the case of $F=0$ and the corresponding deviation from thermal equilibrium distribution of electrons are of interest for the theory of thermionic emission. The thermionic emission current results from the few electrons which have by thermal agitation acquired sufficient energy to overcome the potential wall at the surface of the solid. In the theory of breakdown fast electrons are removed by ionization processes. In the theory of thermionic emission fast electrons are removed irreversibly over the surface barrier of the solid (Fig. 5).

The calculations of thermionic emission are usually based on the assumption of a thermal equilibrium distribution of electrons within the solid. Clearly this assumption is justified only if the rate at which fast electrons leave the solid is small compared to the rate at which fast electrons can be replenished in the boundary of the solid.

Fast electrons can be replenished in the boundary by slow electrons gaining energy near the surface of the cathode and by fast electrons from the bulk of the solid entering the boundary zone (Fig. 5). A detailed discussion of these electron currents would require the consideration of a distribution function $f_0(\epsilon,x)$, which

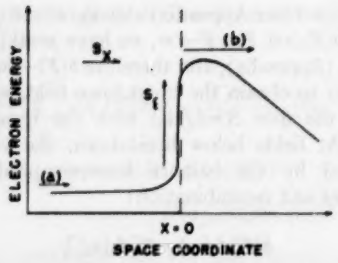

FIG. 5. Energy profile along a line perpendicular to the surface ($x=0$) of a cathode with a field applied. Electrons of low energy are supplied from the bulk of the cathode (arrow a); the thermionic emission removes electrons of high energy from the surface of the cathode (arrow b). These electrons are replenished by slow electrons gaining energy (vertical arrow S_ϵ) or fast electrons moving toward the boundary (horizontal arrow S_x).

depends on both, energy ϵ and position.[17] From the distribution function a flow vector $\mathbf{S}(\epsilon,x)$ can be derived. In a stationary state one has

$$(\partial S_\epsilon/\partial\epsilon)+(\partial S_\psi/\partial x)=0, \tag{28}$$

where S_ϵ and S_x are, respectively, vertical and horizontal components of the flow vector in a diagram such as in Fig. 5. The component S_x can be represented as the sum of a spacial field current and of a spacial diffusion current. If the expressions for S_ϵ [Eq. (15)] and S_x are introduced into Eq. (28), a partial differential equation for the function $f_0(\epsilon,x)$ is obtained. Boundary conditions are: The quasithermal equilibrium distribution, modified by a field, in the bulk of the cathode ($x=-\infty$) and the thermionic emission current resulting from $f_0(\epsilon,0)$ at the surface of the cathode.[18]

In absence of a solution of the two-dimensional problem mentioned above, we shall attempt to estimate an upper limit of thermionic emission, imposed by the rate at which slow electrons can gain energy near the surface of a cathode. The emission current is

$$I=e\int_{-\infty}^{0} S_\epsilon(E,x)dx. \tag{29}$$

In order to estimate this integral we shall replace the gradual decrease of $S_\epsilon(E,x)$ toward the inside of the cathode by a step function (see Fig. 6); i.e.,

$$S_\epsilon(E,x)=S, \quad \text{for} \quad -L\leq x\leq 0;$$
$$S_\epsilon(E,x)=0, \quad \text{for} \quad x<-L.$$

We have then

$$I\sim eLS. \tag{30}$$

[17] The component S_ϵ cannot be considered as being independent of x any more.

[18] In studying emission by the tunnel effect, the boundary condition at $x=0$ has to take into account the emission of electrons through the surface barrier by tunneling.

In the case of a negligible electric field,[19] $F=0$ in the cathode, the value of L can be obtained by considering the diffusion of electrons of energy $\epsilon>E$ toward the surface in a layer of thickness L with a source density S of electrons of energy $\epsilon\geq E$. The continuity equation for the concentration,

$$n=\int_{\epsilon}^{\infty} f_0(\epsilon,x)D(\epsilon)d\epsilon, \tag{31}$$

of electrons of energy $\epsilon\geq E$ reads

$$-\mathfrak{D}(d^2n/dx^2)e=Se, \tag{32}$$

where $\mathfrak{D}$ is the (average) diffusion constant of electrons of energy $\epsilon\geq E$. The solution of Eq. (32) with the boundary conditions $n=n^*$ (n^* is the thermal equilibrium value) at $x=-L$ and $n=n_0$ at $x=0$ reads

$$n=n_0-(n^*-n_0)x/L-(S/2\mathfrak{D})x(x+L). \tag{33}$$

The condition that

$$dn/dx=0 \quad \text{at} \quad x=-L \tag{34}$$

yields

$$L=[(n^*-n_0)2\mathfrak{D}/S]^{\frac{1}{2}}. \tag{35}$$

Therefore, from the Eqs. (30) and (35), we obtain

$$I<e(2n^*\mathfrak{D}S)^{\frac{1}{2}}. \tag{36}$$

By writing Eq. (28) for $\epsilon=E$ and $F=0$,[20] we obtain

$$f_0(E)\approx f_0(\epsilon_0)\exp[-(E-\epsilon_0)/kT]+S/\langle d\epsilon/dt\rangle_L. \tag{37}$$

It will be noticed that $S(>0)$ is less than the value,

$$S_M=-f_0(\epsilon_0)\exp[-(E-\epsilon_0)/kT]\langle d\epsilon/dt\rangle_L D, \tag{38}$$

obtained from Eq. (37) by setting $f_0(E)=0$. Therefore, from Eq. (36) with (38), $f_0(\epsilon_0)\approx\exp-[(\epsilon_0-\zeta)/kT]$ and $n^*=D(E)kT\exp[-(E-\zeta)/kT]$ [where $D(E)$ is

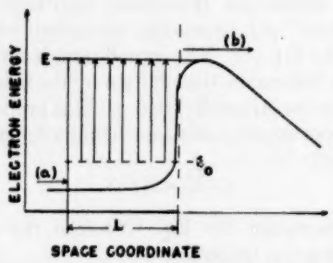

FIG. 6. Approximation of the electron flow for sake of obtaining an order of magnitude estimate of its effect on thermionic emission.

[19] The charges induced in semiconducting cathodes by the applied voltage may extend over many interatomic distances into the cathode [N. D. Morgulis, J. Phys. (U.S.S.R.) **11**, 67 (1947)], and the neglection of the electric field in the cathode may not be justified then; the considerations of the text apply to a metal cathode.

[20] Use of Eq. (28) implies that $\partial S_x/\partial x$ for $\epsilon<E$ is negligible *versus* $\partial S_\epsilon/\partial\epsilon$; it follows then that $S_\epsilon(\epsilon,x)$ is independent of ϵ, and that Eq. (28) is valid.

defined by Eq. (3)]; we obtain

$$I<AT^2\exp[-(E-\zeta)/kT]\times[(16\mathfrak{D}mE\langle d\epsilon/dt\rangle_L)/(kT)^3]^{\frac{1}{2}}, \quad (39)$$

where

$$A=4\pi mek^2/h^3 \quad (40)$$

is the Richardson constant, and $E-\zeta$ is the "work function." Therefore, deviations from the Richardson equation should be expected, if

$$(16\mathfrak{D}mE\langle d\epsilon/dt\rangle_L)/(kT)^3\lesssim 1. \quad (41)$$

Condition (41) can be transformed into

$$Eh\nu/(kT)^2\lesssim(3/16)^{\frac{1}{2}} \quad (42)$$

by using the values of Eq. (13) for $\langle d\epsilon/dt\rangle_L$ and[21]

$$\mathfrak{D}\approx 2E/(3m\nu_e). \quad (43)$$

Since our considerations were based on the assumption $E\gg kT\gg h\nu$, it is not obvious whether the condition (42) is fulfilled or not.

The simple estimate presented above was based on the assumption that all electrons of energy $\epsilon>E$ have the same ("average") velocity. No conclusion can be drawn therefore from these considerations about the energy distribution of the emitted electrons. Deviations from a Boltzmann distribution of emitted electrons have been observed.[22]

In the above discussion we have neglected the influence of the electric field in the cathode on the emission. At high fields, the effect of the electric field on the factor S of Eq. (30) is stronger than the effect of the electric field on the factor L. Therefore, it may be permissible for an order of magnitude estimate of the field dependence to consider L in Eq. (30) as a constant.[23] Using the value of S from Eq. (23) (written for $\epsilon=E$) and expressing $f_0(E)$ by $I\approx AT^2f_0(E)$,[24] we obtain from Eq. (30):

$$I=\frac{AT^{*2}f_0(\epsilon_0)\exp-(E-\epsilon_0)/kT}{1+d}c, \quad (44)$$

where c and d are numerical values, given by

$$c=\exp\left[-\int_{\epsilon_0}^{E}\langle p-(kT)^{-1}\rangle d\epsilon\right]\geq 1, \quad (45)$$

$$d=-AT^2\int_{\epsilon_0}^{E}\left[\frac{p\exp\left(-\int_{\epsilon_0}^{E}pdu\right)}{LeD\langle d\epsilon/dt\rangle_L}\right]d\epsilon>0. \quad (46)$$

[21] According to E. H. Kennard [*Kinetic Theory of Gases* (McGraw-Hill Book Company, Inc., New York, 1938), p. 188] the diffusion current of gas particles of concentration gradient dn/dx and of average velocity $\bar{v}$ is $\frac{1}{3}(\bar{v})^2\tau(dn/dx)$. Accordingly, the diffusion coefficient is $\mathfrak{D}=\frac{1}{3}(\bar{v})^2\tau$. We are dealing with electrons of energy $\geq E$, velocity $\bar{v}\approx(2E/m)^{\frac{1}{2}}$, and collision time $1/\nu_e$. Insertion of these values into Kennard's formula gives the diffusion coefficient of Eq. (43).

[22] W. B. Nottingham, Phys. Rev. **49**, 78 (1936).

[23] In case of strong fields the divergence of the field current has to be added to Eq. (32), and Eq. (33) is then no longer valid.

[24] Strictly, the temperature T of the factor T^2 should be replaced by $T^*=(L/k)f_0(\epsilon)/[df_0(\epsilon)/d\epsilon]$ at $\epsilon=E$.

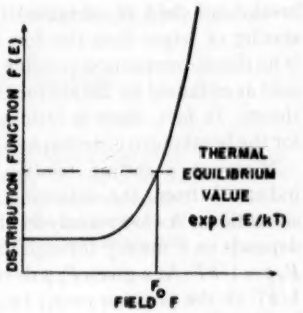

FIG. 7. Probability of occupation by an electron for an energy state near the top of the surface barrier of a cathode from which a saturation current is drawn as function of the field in the cathode. The thermionic emission current is proportional to $f(E)$.

In the case of $F=0$, we have

$$c_0=1, \quad (47)$$

and

$$d_0=-AT^{*2}\int_0^E\frac{\exp[-(E-\epsilon)/kT]}{kTDLe\langle d\epsilon/dt\rangle_L}d\epsilon \approx-(AT^{*2}/Le)[1/(D\langle d\epsilon/dt\rangle_L)], \quad (48)$$

where the values of L, D and $d\epsilon/dt$ are to be taken at $\epsilon=E$. With increasing F, d increases and c decreases. However, the change of d and c with F becomes noticeable only when $p(\epsilon)$ differs appreciably from $1/kT$. If E is larger than the peak ϵ_1 of the friction barrier (see Fig. 2), the difference between $1/kT$ and $p(\epsilon,F)$ will be largest at $\epsilon=\epsilon_1$. Thus the appreciable change of c and d commences at a field F_0 which is determined by the value of $(1/kT)-p_{\epsilon=\epsilon_1}$, but does not depend critically on the height of the surface barrier E (if $E\gg\epsilon_1$). For F larger than F_0, the thermionic emission rises rapidly, because the concentration of electrons of energy E rises rapidly, as shown schematically in Fig. 7.

In the literature, the increase of the thermionic emission current at strong fields is usually attributed to a decrease of the surface barrier E with the field[25] or to tunneling of electrons through the surface barrier. The above considerations indicate an additional effect, caused by deviations of the electron distribution from thermal equilibrium at fields of the order of F_0.

CONCLUSIONS

We have defined at various points of this paper characteristic fields which are of importance for breakdown (F^*,H) and for a rapid increase in thermionic emission with the field (F_0). The question arises whether there exists a relation between these fields.

F^* is the field at which the electron of any energy gains energy on the average as required by von Hippel's breakdown condition, Eq. (20). If we introduce F^* into the Eq. (26), a flow rate $S(F^*)$ would be obtained. Depending on the assumption made for the recombination process, the flow rate $S(H)$, corresponding to the

[25] W. Schottky, Z. Physik **15**, 872 (1914); H. Morgulis, J. Phys. (U.S.S.R.) **11**, 67 (1947); D. A. Wright, Proc. Phys. Soc. (London) **B65**, 134 (1952); K. Lehovec, Phys. Rev. **85**, 705 (1952).

breakdown field H, obtained from Eq. (27), may be smaller or larger than the flow rate $S(F^*)$. Thus, there is no direct comparison possible between the breakdown field as obtained by the simple theory and by the refined theory. In fact, there is little quantitative justification for the breakdown criterion as used in the simple theory.

However, a certain relation between H and F^* is indicated from the following more qualitative considerations. A closer analysis of Eq. (26) shows that S depends on F mainly through the parameter p. At small F, $p \approx 1/kT$. At a given F, p deviates most strongly from $1/kT$ at the position $\epsilon=\epsilon_1$; i.e., the top of the friction barrier. Thus, $S(F)$ becomes strongly dependent on F, if $(\lambda/kT)-p(F,\epsilon_1)=\Delta$ differs appreciably from $1/kT$. For von Hippel's breakdown field F^* [Eq. (20)]: $\Delta=(kT)^{-1}[1+3kT/(2\epsilon_1)]^{-1}$.

Similar considerations apply to a discussion of the field F_0, at which thermionic emission rises rapidly, since this rise depends on F again through the parameter p. Since the strongest deviation of p from $1/kT$ occurs at $\epsilon=\epsilon_1$ (if $E \gg \epsilon_1$) and not at E, the field F_0 characteristic for a rapid rise of thermionic emission is rather insensitive to the height of the surface barrier. Similarly, the field H at which breakdown occurs should be rather insensitive to the ionization energy in accordance with the wellknown "low-energy criterion." In conclusion, thermionic emission should rise rapidly with the field, at fields of the same order of magnitude as the breakdown field, if both the ionization energy and the height of the surface barrier are larger than the energy corresponding to the top of the friction barrier.

In this paper, only a stationary state has been considered. Since most of the breakdown experiments are carried out under pulse conditions in order to avoid heating as much as possible, a stationary state may not be reached in these experiments and breakdown field may then depend on pulse duration as discussed by Franz.[7]

APPENDIX

Relation between $f_0(E)$ and S

Consider the flow of electrons through the energy surface $\epsilon=E$. Since there are no electrons of energy $\epsilon>E$, we have no flow from the outside through the energy surface $\epsilon=E$. Thus the flow through the energy surface $\epsilon=E$ is only due to (a) energy gain of electrons in the field, (b) absorption of phonons by electrons (see Fig. 4):

$$S_F dt = 4\pi \int_0^{eFdt/h} \int_0^{\vartheta_1(k)} f(k-k_1,\ \vartheta)(k-k_1)^2 \sin\vartheta d\vartheta dk_1$$
$$= 2\pi[f_0(E)(2mE/h^2) + \tfrac{2}{3} f_1(E)(2mE/h^2)^{\frac{1}{2}}]eFdt/h. \quad \text{(A-1)}$$

Expressing $f_1(E)$ by $df_0/d\epsilon/_{\epsilon=E}$, and using Eq. (5), we obtain from Eq. (23),

$$(df_0/d\epsilon)_{\epsilon=E} = p[(S/D)\langle d\epsilon/dt\rangle_L - f_0(E)]. \quad \text{(A-2)}$$

Combining the Eqs. (A-1), (5), and (A-2) and replacing D by the value given in Eq. (3), we have

$$S_F = f_0(E)[4\pi mEeF/h^3 + (4/3)(p\tau e^2F^2/m)(2mE/h^2)^{\frac{1}{2}}] - (SpE\tau e^2F^2)/(3m\langle d\epsilon/dt\rangle_L). \quad \text{(A-3)}$$

The right hand side is to be taken at $\epsilon=E$. The flow of electrons through the energy surface $\epsilon=E$, caused by the absorption of phonons, is

$$S_A = (\nu_c/2)[h\nu D f_0(E)]. \quad \text{(A-4)}$$

We may express ν_c by $\langle d\epsilon/dt\rangle_L$, using Eq. (13), and obtain from the Eqs. (A-3) and (A-4):

$$S = f_0(E)\{4\pi mEeF/h^3 + (4/3)(p\tau e^2F^2/m)(2mE/h^2)^{\frac{1}{2}} - (kT\langle d\epsilon/dt\rangle_L D)/(h\nu)\} - (SpE\tau e^2F^2)/(3m\langle d\epsilon/dt\rangle_L). \quad \text{(A-5)}$$

Therefore,

$$a(F) = \frac{f_0(E)}{S} = \frac{[1+(pE\tau e^2F^2)/(3m\langle d\epsilon/dt\rangle_L)]}{[4\pi mEeF/h^3 + (4/3)(p\tau e^2F^2/m)(2mE/h^2)^{\frac{1}{2}} - (kT\langle d\epsilon/dt\rangle_L D/(h\nu)]}. \quad \text{(A-6)}$$

The values of $a(F)$ for the two boundary cases $F=0$ and $F\to\infty$ are as follows: In the case $F=0$, one has $p=1/kT$ and

$$a(0) = -h\nu/(kT\langle d\epsilon/dt\rangle_L D)_{\epsilon=E}, \quad \text{(A-7)}$$

and in the case $F\to\infty$, one has $p \approx -\frac{3}{2}m\langle d\epsilon/dt\rangle_L/\tau Ee^2F^2$, and Eq. (A-6) becomes

$$a(\alpha) \approx h^3/(8\pi mEeF). \quad \text{(A-8)}$$

ACKNOWLEDGMENT

The author is indebted to Miss Alma Marcus and Mr. Kurt Schoeni for helpful discussions.

Effects of Anisotropy on Thermodynamic Properties of Antiferromagnets*

J. A. Eisele and F. Keffer
Sarah Mellon Scaife Radiation Laboratory, University of Pittsburgh, Pittsburgh, Pennsylvania

(Received August 13, 1954)

In antiferromagnets, because of interplay with exchange energy, a small anisotropy can have a huge effect on thermodynamic properties. Detailed calculations are given, using spin-wave theory, of this effect on sublattice magnetization, specific heat, and parallel susceptibility of a cubic or uniaxial antiferromagnet. Specific heat data are discussed and experiments are suggested on the relatively large spin specific heats of antiferromagnets with low Curie points. The theory is extended to orthorhombic symmetry, and reasonable agreement found with existing experimental data on $CuCl_2 \cdot 2H_2O$.

I. INTRODUCTION

RECENTLY Anderson[1] has revived interest in the spin-wave theory of antiferromagnetism, first introduced in 1936 by Hulthén.[2] In this theory it is assumed that the antiferromagnetic ground state may be described in terms of a two-sublattice picture, the spins of one sublattice all pointing up, those of the other all pointing down. Since the actual ground state is a highly degenerate spin-zero state, it is by no means clear that a two-sublattice treatment is at all adequate. However, by a careful study of the zero-point spin-wave energy, Anderson has shown that the ground state of a three-dimensional antiferromagnet approaches closely the presumed two-sublattice arrangement. Several authors[3–7] have extended Anderson's theory to higher temperatures, and in particular Kubo[3,8] has presented a detailed discussion of the abnormal fluctuations inherent in the spin-wave approach.

Whether these fluctuations are real properties of antiferromagnets or are dissembled by the approximate nature of the theory is not clear at present. Real or fictitious, the fluctuations are subdued by the introduction of crystalline anisotropy into the theory; and probably all antiferromagnets have some anisotropy. Furthermore, neutron diffraction experiments[9] indicate that the spins of antiferromagnets are actually arrayed in sublattices, at least for times longer than 10^{-13} second.

The two most-studied single crystals, MnF_2 and $CuCl_2 \cdot 2H_2O$, are believed to have anisotropy energies of the order of one percent of their respective exchange energies. Other antiferromagnets seem to have similar anisotropies.[10] Thus the thermodynamic properties of antiferromagnets at temperatures low with respect to their Curie points should be accounted for by spin-wave theory, if this theory is at all meaningful.

In this paper we examine theoretically the expected temperature dependence of three measurable properties of antiferromagnets: (1) the magnetization of a sublattice, which may be detected most accurately by its effect on nuclear resonance;[11] (2) the spin-system specific heat, which swamps the lattice specific heat if the Curie point is well below the Debye temperature; and (3) the parallel susceptibility, or susceptibility of a single crystal in a magnetic field oriented along the preferred spin axis. We show that the presence of a small anisotropy, through a coupling of anisotropy and exchange energies, has a marked effect on these thermodynamic properties, and we consider this effect in some detail.

II. EFFECTS OF ANISOTROPY

The size of the anisotropy constant K is conveniently measured in terms of

$$\alpha = 2K/z|J|, \tag{1}$$

where $J/2$ is the exchange integral and z is the number of nearest neighbors.

Although α may be only a few percent, it appears in the spin-wave energy as $\alpha^{\frac{1}{2}}$. This tremendous enhancement of the effects of anisotropy comes about through a subtle coupling of anisotropy and exchange energies, the nature of which has been discussed in detail elsewhere.[7]

We define a temperature T_{AE} to measure this strong effect of anisotropy-exchange interplay:

$$kT_{AE} = z|J|S(2\alpha)^{\frac{1}{2}} = 2(z|J|K)^{\frac{1}{2}}S, \tag{2}$$

where S is the spin quantum number of a single atom.

The energy of a spin wave for small wave number $\mathbf{k}$ is

$$E_{\mathbf{k}} = z|J|S(b\mathbf{k}^2 + 2\alpha + \alpha^2)^{\frac{1}{2}}. \tag{3}$$

Here $\mathbf{k}$ is referred to the first Brillouin zone of the sublattice, and the constant b is a structure factor depending upon the type of lattice considered. Equation (3) is

* This research was supported by the U. S. Air Force under a contract monitored by the Office of Scientific Research of the Air Research and Development Command.

[1] P. W. Anderson, Phys. Rev. **86**, 694 (1952).
[2] L. Hulthén, Proc. Roy. Acad. Sci. Amsterdam **39**, 190 (1936).
[3] R. Kubo, Phys. Rev. **87**, 568 (1952).
[4] T. Nakamura, Progr. Theoret. Phys. (Japan) **7**, 539 (1952).
[5] J. R. Tessman, Phys. Rev. **88**, 1132 (1952).
[6] J. M. Ziman, Proc. Phys. Soc. (London) **A65**, 540, 548 (1952); **A66**, 89 (1953).
[7] Keffer, Kaplan, and Yafet, Am. J. Phys. **21**, 250 (1953).
[8] R. Kubo, Revs. Modern Phys. **25**, 344 (1953).
[9] Shull, Strauser, and Wollan, Phys. Rev. **83**, 333 (1951).
[10] See, for example, J. W. Stout and L. M. Matarrese, Revs. Modern Phys. **25**, 338 (1953).
[11] N. J. Poulis and G. E. G. Hardeman, Physica **19**, 391 (1953). Neutron diffraction may also be used to detect sublattice magnetization, but with less accuracy. See R. A. Erickson, Phys. Rev. **90**, 779 (1953).

derived by Anderson[1] and by Kubo.[3] The total spin-wave energy is obtained by summing E_k over over Bose distributions in the (equivalent) first Brillouin zones of both sublattices. For small $\mathbf{k}$ this sum is approximated by an integral to infinity; and by proper normalization, the variable $b\mathbf{k}^2$ can be replaced by a single parameter λ^2. A similar approximation is used to obtain both the magnetization of a sublattice and the parallel susceptibility from the free energy. The procedure is given in detail in Kubo's 1952 paper,[3] which we use as a standard reference.

Thus Kubo finds for the temperature-dependent part of the total spin-wave energy of N spins:

$$E_T=NkTA_l\int_0^\infty \beta_\lambda(e^{\beta_\lambda}-1)^{-1}\lambda^{D-1}d\lambda, \tag{4}$$

where

$$\beta_\lambda=(z|J|S/kT)(\lambda^2+2\alpha+\alpha^2)^{\frac{1}{2}}. \tag{5}$$

Here A_l, the normalization factor discussed above, depends on the lattice structure; D is the dimensionality of the lattice, which we shall take as 3.

It should be noted that anisotropy is introduced into this theory as a crystalline field, that is, as involving the direction cosines between single spins and the crystal axes. A large part of the anisotropy, however, will originate in dipole-dipole and in anisotropic exchange forces, and hence involve the mutual orientation of pairs of spins. Ziman[6] has shown that such terms in the Hamiltonian lead to severe algebraic complications; and we shall not consider them in this paper. In making quantitative comparison of theory and experiment this limitation should be kept in mind.

Furthermore, we have restricted ourselves to calculations of sublattice magnetization and specific heat in the absence of an applied field.

A. Magnetization of a Sublattice

The temperature-dependent part of the sublattice magnetization, M_{ST}, in terms of the magnetization for complete alignment, M_∞, is given by:[3]

$$M_{ST}=-M_\infty(z|J|/kT)A(1+\alpha)\times\int_0^\infty \beta_\lambda^{-1}(e^{\beta_\lambda}-1)^{-1}\lambda^{D-1}d\lambda. \tag{6}$$

We may evaluate Eq. (6) by expanding the Bose function,

$$(e^{\beta_\lambda}-1)^{-1}=\sum_{n=1}^\infty e^{-n\beta_\lambda},$$

and integrating term by term. Dropping α^2 as small compared to 2α, we make the substitution

$$(2\alpha)^{\frac{1}{2}}\cosh y=(\lambda^2+2\alpha)^{\frac{1}{2}}.$$

Thus, for $D=3$,

$$\frac{M_{ST}}{(M_\infty/S)}\approx-2\alpha A_l\sum_{n=1}^\infty\int_0^\infty \exp[-(nT_{AE}/T)\cosh y]\sinh^2 y dy$$

$$=-2\alpha A_l\sum_{n=1}^\infty\frac{K_1(nT_{AE}/T)}{(nT_{AE}/T)}. \tag{7}$$

Here K_1 is a Hankel function and the summation, which converges rapidly, is known as a Schlömilch series.

We now introduce the variable

$$\theta=kT/z|J|S\approx\tfrac{1}{3}(S+1)(T/T_c), \tag{8}$$

where the exchange integral $J/2$ is approximated from Van Vleck's[12] molecular field theory of the Curie temperature, T_c. Equation (7) may be written

$$\frac{M_{ST}}{(M_\infty/S)}=-A_l\theta^3(\pi^2/6)M(T/T_{AE}), \tag{9}$$

with

$$M(T/T_{AE})=\frac{6}{\pi^2}\frac{T_{AE}}{T}\sum_{n=1}^\infty\frac{1}{n}K_1\left(\frac{nT_{AE}}{T}\right). \tag{10}$$

Equation (9) is also given, but not plotted, in Kubo's paper;[3] we have derived it here to make clear some new relations which follow. In the absence of anisotropy $M(T/T_{AE})$ goes to 1, and Eq. (9) reduces to the T^3 law given by Kubo. The variation of $M(T/T_{AE})$ with T/T_{AE} is plotted as the dashed line in Fig. 1.

B. Specific Heat

By the same process which led from Eq. (6) to Eq. (7), we may bring Eq. (4) into the form (for $D=3$):

$$\frac{E_T}{Nz|J|S}=4\alpha^2A_l\sum_{n=1}^\infty\frac{d^2}{d(nT_{AE}/T)^2}\left\{\frac{K_1(nT_{AE}/T)}{(nT_{AE}/T)}\right\}$$

$$=4\alpha^2A_l\sum_{n=1}^\infty\left\{\frac{K_3(nT_{AE}/T)}{(nT_{AE}/T)}-\frac{K_2(nT_{AE}/T)}{(nT_{AE}/T)^2}\right\}. \tag{11}$$

The specific heat, C_T, is the derivative of (11) with respect to θ and has the value

$$C_T/Nk=A_l\theta^3(4\pi^4/15)C(T/T_{AE}), \tag{12}$$

with

$$C(T/T_{AE})=\frac{15}{8\pi^4}\left(\frac{T_{AE}}{T}\right)^4\sum_{n=1}^\infty\{K_2(nT_{AE}/T)+K_4(nT_{AE}/T)\}. \tag{13}$$

In the absence of anisotropy $C(T/T_{AE})$ goes to 1, and Eq. (12) reduces to the T^3 law given by Kubo.[3] The variation of $C(T/T_{AE})$ with T/T_{AE} is plotted as the solid line in Fig. 1.

[12] J. H. Van Vleck, J. Chem. Phys. 9, 85 (1941).

C. Parallel Susceptibility

In calculating the parallel susceptibility $\chi_{\parallel}$ one must restrict the applied field H_0 to values less than $kT_{AE}/g\mu_0$. Otherwise the spins can lower their free energy by flopping over to the hard axis, and one will find oneself confronted with $\chi_{\perp}$.

As shown by Kubo[3]

$$\chi_{\parallel}=(Ng^2\mu_0^2/4kT)A_l\int_0^{\infty}(\coth^2\tfrac{1}{2}\beta_\lambda-1)\lambda^{D-1}d\lambda. \quad (14)$$

The integrand is equal to

$$\coth^2\tfrac{1}{2}\beta_\lambda-1=\frac{4e^{\beta\lambda}}{(e^{\beta\lambda}-1)^2}=-4\frac{\partial}{\partial(zJS/kT)} \times[(e^{\beta\lambda}-1)^{-1}(\lambda^2+2\alpha+\alpha^2)^{-1}],$$

and comparison with Eq. (6) shows that

$$\frac{\chi_{\parallel}}{(Ng^2\mu_0^2/kT)}=\frac{1}{(1+\alpha)}\frac{\partial}{\partial(zJS/kT)}\left(\frac{M_{ST}}{M_\infty/S}\right) =\frac{(2\alpha)^{\frac{1}{2}}}{(1+\alpha)}\frac{\partial}{\partial(T_{AE}/T)}\left(\frac{M_{ST}}{M_\infty/S}\right). \quad (15)$$

Applying the above to Eq. (9) we find

$$\frac{\chi_{\parallel}}{(Ng^2\mu_0^2/kT)}=A_l\frac{\pi^2}{3}\theta^3\chi\left(\frac{T}{T_{AE}}\right), \quad (16)$$

with

$$\chi\left(\frac{T}{T_{AE}}\right)=\frac{3}{\pi^2}\left(\frac{T_{AE}}{T}\right)^2\sum_{n=1}^{\infty}K_2\left(\frac{nT_{AE}}{T}\right). \quad (17)$$

In the absence of anisotropy $\chi(T/T_{AE})$ goes to 1, and Eq. (16) reduces to the T^2 law given by Kubo. The variation of $\chi(T/T_{AE})$ with (T/T_{AE}) is plotted as the dotted line in Fig. 1. For temperatures well below T_{AE} the susceptibility rises exponentially, a result obtained by Tessman.[5]

Equation (15) gives a general relation between the parallel susceptibility and the magnetization of a sublattice. It is interesting to compare this with the general relation given by Van Vleck's molecular field theory:[12]

$$\frac{\chi_{\parallel}}{(Ng^2\mu_0^2/kT)}=\frac{S^2B_S'(y_0)}{1+(S/\theta)B_S'(y_0)}. \quad (18)$$

Here, for comparison, the Brillouin function represents

$$SB_S(y_0)=(M_{S0}+M_{ST})/(M_\infty/S),$$

with

$$y_0=SB_S/\theta.$$

Thus, Van Vleck's relation may be brought into the form

$$\frac{\chi_{\parallel}}{(Ng^2\mu_0^2/kT)}=\frac{[\partial/\partial(1/\theta)][SM_{ST}/M_\infty]}{\{[(M_{S0}+M_{ST})/M_\infty] +(2/S\theta)[\partial/\partial(1/\theta)][SM_{ST}/M_\infty]\}}. \quad (18')$$

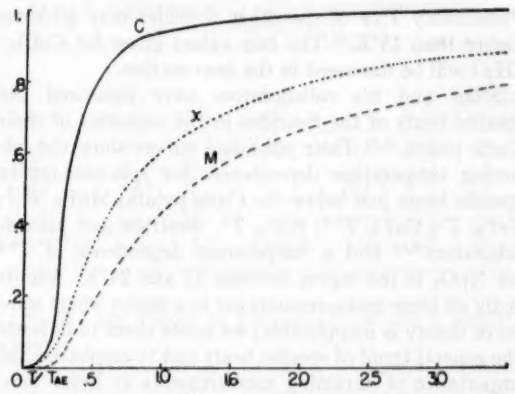

FIG. 1. The temperature variation of the three thermodynamic quantities for cubic or uniaxial symmetry showing the effect of anisotropy. The solid line is the specific heat $C(T/T_{AE})$, the dashed line is the magnetization $M(T/T_{AE})$, and the dotted line is the susceptibility $\chi(T/T_{AE})$.

At low temperatures (small θ) the denominator of Eq. (18′) is approximately 1 and, in the absence of anisotropy, Van Vleck's relation agrees with the spin-wave Eq. (15). (The correction for anisotropy is negligible.) Since the molecular field approximation is more accurate near the Curie point, Eq. (18′) might be valid at all temperatures.

III. DISCUSSION OF SPECIFIC HEATS

Postponing until the next section the interesting case of $CuCl_2\cdot 2H_2O$, we discuss here the specific heats of a few antiferromagnetic salts. First, the condition under which the spin-wave specific heat will be larger than the lattice specific heat should be pointed out. In the usual Debye approximation the lattice specific heat at low temperature is given by

$$C_L/N'k=(12/5)\pi^4(T/\Theta)^3, \quad (19)$$

where Θ is the Debye temperature. Comparison with Eq. (12) yields

$$C_T/C_L=(A_l/243)(S+1)^3(\Theta/T_c)^3 \times C(T/T_{AE})(N/N'). \quad (20)$$

Here N/N' is the ratio of paramagnetic ions to total number of ions.

In Table I we apply Eq. (20) to a few antiferromagnetic salts with low Curie points. It is seen that, as a general rule of thumb, the spin-wave contribution to the specific heat will be larger than that of the lattice if

$$T_c<\sim\Theta/5. \quad (21)$$

However, in the region $T<T_{AE}$ the spin-wave specific heat will be sharply reduced by $C(T/T_{AE})$ [see Fig. 1]. Values of T_{AE} simply are not known at present. The value given in Table I for MnF_2 is a theoretical estimate[13] based chiefly on magnetic-dipole anisotropy.

[13] F. Keffer, Phys. Rev. 88, 608 (1952).

Presumably T_{AE} of the other fluorides may go even higher than 15°K.[10] The two values given for $CuCl_2 \cdot 2H_2O$ will be discussed in the next section.

Stout and his collaborators have measured the specific heats of the fluorides in the vicinities of their Curie points.[14,15] Their published curves show the following temperature dependences for spin-plus-lattice specific heats just below the Curie points: MnF_2, $T^{1.7}$; FeF_2, T^2; CoF_2, $T^{2.9}$; NiF_2, T^3. Westrum and his collaborators[16,17] find a temperature dependence of $T^{3.2}$ for NpO_2 in the region between 15 and 24°K. Admittedly all these measurements are in a region where spin-wave theory is inapplicable; we quote them to indicate the general trend of specific heats and to emphasize the importance of obtaining measurements at lower temperatures. The measurements on MnF_2 were carried down to 15°K (vicinity of T_{AE}) with no appreciable change in the curious $T^{1.7}$ dependence. However, NpO_2 in the region between 15 and 11°K shows a marked drop in specific heat, perhaps indicating effects of anisotropy.

Mention should be made of $FeCl_2$, $CoCl_2$, and particularly $MnCl_2$ which have very low Curie points and should have large spin specific heats.

IV. ORTHORHOMBIC SYMMETRY

In an orthorhombic crystal, taking the z axis as preferred, the anisotropy is different for displacements towards the x and the y axes. As a measure of these anisotropies we introduce $\alpha(1)$ and $\alpha(2)$, to which correspond the two temperatures $T_{AE}(1)$ and $T_{AE}(2)$. The spin waves split into two sets, with approximate energies

$$E_k(i) \cong z|J|S[bk^2+2\alpha(i)]^{\frac{1}{2}}, \tag{22}$$

as shown by Nakamura.[4]

The magnetization of a sublattice is obtained by a summation over all spin waves, and we now merely sum over the two independent sets. Thus

$$\frac{M_{ST}}{(M_\infty/S)} = -\tfrac{1}{2}A\beta^{\frac{3}{2}}\left(\frac{\pi^2}{6}\right) \times\left[M\left(\frac{T}{T_{AE}(1)}\right)+M\left(\frac{T}{T_{AE}(2)}\right)\right]. \tag{23}$$

Similarly, the specific heat is given by

$$\frac{C_T}{Nk} = \tfrac{1}{2}A\beta^{\frac{3}{2}}\left(\frac{4\pi^4}{15}\right)\left[C\left(\frac{T}{T_{AE}(1)}\right)+C\left(\frac{T}{T_{AE}(2)}\right)\right]. \tag{24}$$

One might expect the parallel susceptibility to be obtained on applying Eq. (15) to Eq. (23), but it turns out to be a much more complicated expression. Introducing

$$\epsilon = g\mu_0 H_0/z|J|S \tag{25}$$

as a measure of the applied field H_0, we may distinguish two cases:

$$(A) \quad \epsilon^2 > \alpha(2)-\alpha(1).$$

Here the applied field is large compared to the difference between the two anisotropy-exchange fields, and hence the normal modes of the spin waves are essentially determined by the applied field. The two sets of spin waves may be thought of as precessing, respectively, clockwise and counterclockwise about H_0. The energies of the spin waves are given approximately by[4]

$$E_k \cong z|J|S\{[bk^2+\alpha(1)+\alpha(2)]^{\frac{1}{2}} \pm \epsilon\}. \tag{26}$$

Accordingly, $\chi_\parallel$ will be given by Eq. (16) with T_{AE} replaced by $\frac{1}{2}[T_{AE}(1)+T_{AE}(2)]$.

$$(B) \quad E^2 < \alpha(2)-\alpha(1)$$

Here the normal modes are essentially determined by the two widely different anisotropy-exchange fields. The spin-wave energies are given by adding terms in ϵ^2 to Eq. (22). The parallel susceptibility is field dependent in a complicated way. In the absence of a more precise introduction of anisotropy terms (especially since we are here dealing with a large difference in anisotropies), it hardly seems worthwhile to go further.

A remarkable series of measurements has recently been made at Leiden on single crystals of the orthorhombic $CuCl_2 \cdot 2H_2O$. From susceptibility measurements[18] it is possible to deduce values of $T_{AE}(1)$ and $T_{AE}(2)$. The smaller of these may be found from the critical field, that is, from the value of H_0 which is suf-

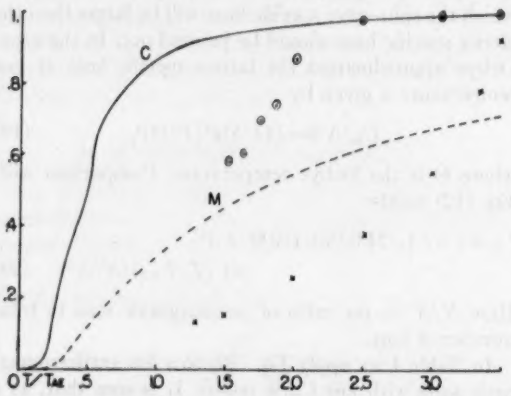

FIG. 2. The temperature variation of the two thermodynamic quantities for orthorhombic symmetry showing the effect of anisotropy. The solid line is the specific heat $C(T/1)+C(T/2)$, and the circles are the experimental points (see reference 19). The dashed line is the magnetization $M(T/1)+M(T/2)$, and the crosses are the experimental points (see reference 11).

[14] J. W. Stout and H. E. Adams, J. Am. Chem. Soc. **64**, 1535 (1942).
[15] J. W. Stout and E. Catalano, Phys. Rev. **92**, 1575 (1953).
[16] Westrum, Hatcher, and Osborne, J. Chem. Phys. **21**, 419 (1953).
[17] D. W. Osborne and E. F. Westrum, Jr., J. Chem. Phys. **21**, 1884 (1953).
[18] Van den Handel, Gijsman, and Poulis, Physica **18**, 862 (1952).

ficient to overcome the anisotropy-exchange energy holding the spins to the preferred axis and to allow them to flop to the second-preferred xais. This is detected by an immediate jump of susceptibility from $\chi_{\parallel}$ to $\chi_{\perp}$. Inserting the measured value of 6500 oersteds for the critical field into

$$kT_{AE}(1)=g\mu_0(H_0)_{\text{crit}}, \tag{27}$$

we obtain $T_{AE}(1)\approx 1°\text{K}$.

There exists a critical field for flop from the preferred to the third-preferred axis, and $T_{AE}(2)$ is given by this field. Since the spins will have flopped to the second-preferred axis before this field is reached, it cannot be measured directly, but must be inferred from measurement of the flop from the second- to the third-preferred axis when H_0 is along the second axis. This flop takes place at 10 690 oersteds. Now from Eq. (2) we see that the anisotropy is proportional to the square of the critical field, and since to first order the anisotropy constant for first- to third-preferred axis is the sum of the constants first- to second-preferred and second- to third-preferred, the critical fields will sum in the square. This yields a field of 12 500 oersteds corresponding to $T_{AE}(2)\approx 2°\text{K}$.

The Curie point of $CuCl_2\cdot 2H_2O$ is 4.3°K; thus the values of T_{AE} are very large, and effects of anisotropy will be strong. In Fig. 2 we have plotted $M(T/1)+M(T/2)$ as the dashed line and $C(T/1)+C(T/2)$ as the solid line. Experimental measurements of Poulis and Hardeman[11] on sublattice magnetization and of Friedberg[19] on specific heat are indicated; in plotting these points we have used the value $5/(2\pi^2)$ for the geometrical factor A_l, and we have evaluated J from molecular field theory, Eq. (8). Slight changes in J move all the points large distances up or down, but have little effect on the shape of the curves. None of the data are at sufficiently low temperatures for one to expect the spin-wave theory to be valid; nevertheless the general trend of things is encouraging. It is interesting to note the much stronger effect of anisotropy on sublattice magnetization than on specific heat.

Poulis and Hardeman[11] find that the sublattice magnetization closely follows a T^4 law over most of their range. We are unable to account for any such simple behavior.

[19] S. A. Friedberg, Physica **18**, 714 (1952).

TABLE I. Application of Eq. (20) to some representative antiferromagnetic salts.

Salt	Θ (°K) approx.	T_c (°K)	T_{AE} (°K)	S	N/N'	C_T/C_L from Eq. (20) (for $T>T_{AE}$)
MnF_2	450	70	15	5/2	1/3	7
FeF_2	420	78		2	1/3	3
CoF_2	360?	37		3/2	1/3	8
NiF_2	450	73		1	1/3	1
NpO_2	360	25		3/2?	1/3	10
$CuCl_2\cdot 2H_2O$	250	4.2	1 and 2	1/2	1/9	70

The anisotropy in $CuCl_2\cdot 2H_2O$ is due partly to anisotropic exchange, partly to magnetic dipole interactions, and partly to the anisotropy of the g factor (crystalline fields).[20] As noted in Sec. II, the theory used in this paper assumes the anisotropy can be represented as a sum of terms involving single spins only. Some of the detailed behavior of the thermodynamic properties may be lost in this simplification. However, since we have used the experimentally determined critical fields in the above, and these represent a sort of activation energy for spin waves, we doubt that a more involved treatment would change things significantly. We should note that one can obtain the critical fields from antiferromagnetic resonance frequencies, that is, from the activation energies of $\mathbf{k}=0$ spin waves. Using the data of Ubbink *et al.*,[21] Nagamiya[22] has deduced fields of 7200 and 13 000 oersteds, in good agreement with the susceptibility determination.

On the other hand the detailed nature of the anisotropy may be of considerable importance in the theory of parallel susceptibility, especially for applied fields of the same order of magnitude as the critical fields. The measurements[18] are in fields of this size and furthermore are all at 1.6°K or higher. Because of this, and since the susceptibility is field-dependent in such a complicated way, we shall drop the problem at this point.

[20] T. Moriya and K. Yosida, Progr. Theoret. Phys. (Japan) **9**, 663 (1953). See also discussion remark of F. Keffer, Revs. Modern Phys. **25**, 337 (1953).
[21] Ubbink, Poulis, Gerritsen, and Gorter, Physica **18**, 361 (1952).
[22] T. Nagamiya (private communication).

Thermodynamics of the Thomas-Fermi Atom at Low Temperature

J. J. GILVARRY
The Rand Corporation, Santa Monica, California
(Received June 1, 1954)

It is shown that an expression for the Helmholtz function on the Thomas-Fermi atom model permits one, in the limit of low temperature T, to expand the total energy as an asymptotic series in T^2. The leading term of the expansion is a known analytic expression for the energy at $T=0$, from which one can calculate the pertinent thermodynamic functions for this case in their dependence on the atom radius and on the boundary and initial parameters associated with a solution of the zero-temperature Thomas-Fermi equation. Published values of these parameters are fitted by functions of the atom radius having the correct asymptotic behavior in the two limiting cases of an infinitesimal and an infinite atom. This procedure makes thermodynamic functions in this case directly available. Thermodynamic functions for the case of a first-order temperature perturbation are derived from the corresponding term in the asymptotic expansion of the energy. They depend (in addition to dependence on parameters of the unperturbed atom) on two parameters derived from solution of the differential perturbation equation. These parameters differ according as the differential perturbation equation is solved under a condition of fixed atomic volume or of zero initial slope (which is computationally more convenient and corresponds to published solutions). The asymptotic forms of the parameters in the first case are determined for the two limits of an infinitesimal and an infinite atom. The boundary and initial parameters corresponding to fixed atomic volume are expressed in terms of the parameters corresponding to a solution under zero initial slope, and are evaluated in three cases from published solutions. These values are fitted by functions of the atom radius which have the proper limiting behavior for an infinitesimal and an infinite atom. Thus, approximate values of the first-order temperature perturbations of thermodynamic functions become directly available.

THE statistical theory of Thomas[1] and Fermi,[2] generalized to arbitrary temperature, contains implicitly a complete thermodynamic specification of the atom model. Brachman[3] has derived expressions on this model for the Helmholtz function, the entropy, and the heat capacity at constant volume. This paper shows that Brachman's results permit one to expand the energy as an asymptotic series in powers of the temperature. With this expansion available, it is possible to exhibit explicitly the thermodynamics of the Thomas-Fermi atom model for the case of a first-order temperature perturbation. The thermodynamic functions for the case of zero temperature can be obtained directly from an analytic expression due to Milne[4] for the energy. In this case, the thermodynamic functions can be made directly accessible by fitting semi-empirically as a function of atom radius the pertinent parameters derived from solution[5-7] of the Thomas-Fermi equation. A corresponding procedure can be carried out in the temperature-perturbed case.[5] The effect of exchange[8] will be neglected throughout, which makes the results valid only in the limit of high atomic number at sufficiently high compression.

[1] L. H. Thomas, Proc. Cambridge Phil. Soc. **23**, 542 (1927).
[2] E. Fermi, Z. Physik **48**, 73 (1928).
[3] M. K. Brachman, Phys. Rev. **84**, 1263 (1951).
[4] E. A. Milne, Proc. Cambridge Phil. Soc. **23**, 794 (1927).
[5] Feynman, Metropolis, and Teller, Phys. Rev. **75**, 1561 (1949) (referred to hereafter as FMT).
[6] J. C. Slater and H. M. Krutter, Phys. Rev. **47**, 559 (1935) (referred to hereafter as SK).
[7] P. Gombas, *Die Statistiche Theorie des Atoms und ihre Anwendungen* (Springer Verlag, Vienna, 1949), pp. 53, 357.
[8] P. A. M. Dirac, Proc. Cambridge Phil. Soc. **26**, 376 (1930).

1. INTRODUCTION

By the generalized Thomas-Fermi equation shall be meant Poisson's equation $\nabla^2V=4\pi e\rho$ for the potential $V(r)$, at a point r in a spherically symmetric atom and due to electrons of charge $-e$ and a number density $\rho(r)$ which is a function of the temperature T:

$$\rho=(4\pi/h^3)(2m)^{\frac{3}{2}}(kT)^{\frac{3}{2}}I_{\frac{1}{2}}(eV/kT+\eta). \tag{1}$$

Here m is the electron mass, $kT\eta$ is the chemical potential, h and k are the Planck and Boltzmann constants, respectively. The function $I_{\frac{1}{2}}(\lambda)$ is defined by

$$I_k(\lambda)=\int_0^\infty y^k[\exp(y-\lambda)+1]^{-1}dy. \tag{2}$$

The kinetic energy $E_{\rm kin}$ on this model corresponds to a kinetic energy density $\epsilon_{\rm kin}(r)$ given by

$$\epsilon_{\rm kin}=(4\pi/h^3)(2m)^{\frac{3}{2}}(kT)^{5/2}I_{\frac{3}{2}}(eV/kT+\eta). \tag{3}$$

The potential energy $E_{\rm pot}$ consists of two terms, E_{ee} and E_{en}, where E_{ee} corresponding to the electron-electron interaction equals the integral $-(e/2)\int_v\rho V_e d\tau$ over the volume v of the atom ($d\tau=4\pi r^2dr$), and $E_{en}=-e\int_v\rho V_n d\tau$ corresponding to the electron-nucleus interaction is

$$E_{en}=ZeV_e(0)=Ze[d(Vr)/dr]_{r=0}, \tag{4}$$

if $V_e(r)$ and $V_n(r)=Ze/r$ are the potentials due to the electrons and the nucleus, respectively. If one of the energies $E_{\rm kin}=\int_v\epsilon_{\rm kin}d\tau$, $E_{\rm pot}$ or the total energy $E=E_{\rm kin}+E_{\rm pot}$ is known, the other two energies can be determined directly from the virial theorem,

$$E=\tfrac{3}{2}Pv+\tfrac{1}{2}E_{\rm pot}, \tag{5}$$

where P is the pressure given by

$$P=\tfrac{2}{3}\epsilon_{\rm kin}(a), \tag{6}$$

in which a is the atom radius.

Brachman[3] has shown by an explicit temperature integration of the Gibbs-Helmholtz equation, that the Helmholtz function F on the Thomas-Fermi model is given by

$$F=-\tfrac{2}{3}E_{\rm kin}-E_{ee}+ZkT\eta, \tag{7}$$

from which the entropy S and heat capacity C_v at constant volume follow directly. His expression for the heat capacity C_v can be written

$$TC_v=(7/4)E+\tfrac{3}{4}T^2(\partial/\partial T)_v[(Pv+E_{en}+ZkT\eta)/T], \tag{8}$$

by means of Eqs. (4) and the virial theorem (5).

2. GENERAL PERTURBATION METHOD

Brachman's Eq. (8) for C_v will be made the basis in this section of a perturbation calculation of the total energy E. All the thermodynamic functions can be obtained once the energy is available.

It is convenient to define a Φ (generalizing in the manner of MB[9] the usual Thomas-Fermi function ϕ corresponding to zero temperature) by

$$Ze^2\Phi/\mu x=eV+kT\eta, \tag{9}$$

where x is defined by $r=\mu x$, and μ equals $a_0(9\pi^2/128Z)^{\frac{1}{3}}$ in terms of the radius a_0 of the first Bohr orbit for hydrogen. By means of an asymptotic expansion[10] for $I_{\frac{1}{2}}(\lambda)$ applied to ρ of Eq. (1), which is valid for $\lambda=Ze^2\Phi/\mu xkT\gg1$, the asymptotic form of the generalized Thomas-Fermi equation for low temperatures becomes

$$\partial^2\Phi/\partial x^2=(\Phi^{\frac{1}{2}}/x^{\frac{1}{2}})\left[1+\sum_{n=1}^{N}\zeta_n(kTx/\Phi)^{2n}\right], \tag{10}$$

in which $n\geq1$,

$$\zeta_n=(\mu/Ze^2)^{2n}a_n, \tag{11}$$

and the coefficients a_n are defined and tabulated by McDougall and Stoner.[10] Equation (10) reduces to the usual Thomas-Fermi equation for $T=0$ (where $kT\eta$ approaches a constant η'). The function Φ is subject to a boundary condition at the radius x_b of the atom which makes it a function $\Phi(x,x_b)$ of the two variables x and x_b. The initial and boundary conditions on $\Phi(x,x_b)$ are, respectively,

$$\Phi(0,x_b)=1, \tag{12a}$$

$$\Phi_b=x_b\left[\frac{\partial\Phi(x,x_b)}{\partial x}\right]_{x=x_b}, \tag{12b}$$

where $\Phi_b=\Phi(x_b,x_b)$ is the boundary value of Φ. The distinction implied by the partial derivative notation in Eqs. (10) and (12b) will be germane later. It is possible to show[11] that Φ/x is a monotone-decreasing function of x for any neutral atom solution of the generalized Thomas-Fermi equation; hence the domain of validity $\lambda\gg1$ of Eq. (10) becomes

$$kT\ll(Ze^2/\mu)\Phi_b/x_b. \tag{13}$$

The asymptotic series on which Eq. (10) is based is divergent for N sufficiently large, so that an optimum N exists for a given accuracy when the inequality (13) is fulfilled for a given λ.

For this same domain of validity, the corresponding asymptotic expansion of $I_{\frac{1}{2}}(\lambda)$ yields for the pressure P from Eq. (6),

$$P=\frac{Z^2e^2}{10\pi\mu^4}\left(\frac{\Phi_b}{x_b}\right)^{5/2}\left[1+\sum_{n=1}^{N}\frac{5\zeta_n}{5-4n}\left(\frac{kTx_b}{\Phi_b}\right)^{2n}\right], \tag{14}$$

where the chemical potential $kT\eta$ has been evaluated from Eq. (9) as

$$kT\eta=(Ze^2/\mu)\Phi_b/x_b \tag{15}$$

(since $V=0$ at the atom boundary). From Eqs. (4) and (9), the energy E_{en} can be evaluated as

$$E_{en}=(Z^2e^2/\mu)(\Phi_i'-\Phi_b/x_b), \tag{16}$$

where Φ_i' is the initial slope $[\partial\Phi/\partial x]_{x=0}$. The volume v of the atom is determined by the boundary condition (12b) as $v=(4\pi/3)\mu^3x_b^3$. These thermodynamic functions are the ones given directly by solution of the differential Eq. (10).

With use of Eqs. (15) and (16), Brachman's Eq. (8) for C_v yields

$$T\left(\frac{\partial E}{\partial T}\right)_v-\frac{7}{4}E=\tfrac{3}{4}T^2\left(\frac{\partial}{\partial T}\right)_v\left\{T^{-1}\left[Pv+\frac{Z^2e^2}{\mu}\Phi_i'\right]\right\}, \tag{17}$$

where the right-hand side contains no terms depending on integrals over the volume. This equation is a first-order partial differential equation in T for the total energy E. Its solution is

$$E=\tfrac{3}{4}T^{7/4}\int_0^T T^{-\frac{1}{4}}(\partial/\partial T)_v \times\{T^{-1}[Pv+(Z^2e^2/\mu)\Phi_i']\}dT, \tag{18}$$

where the integration is carried out at constant volume. For $T=0$, in which case the integrand appearing is singular, this equation gives correctly the result of Milne[4] for the energy.

Since P is expressed by Eq. (14) as an asymptotic series in T^2 whose coefficients depend on Φ only through boundary values, the integral on the temperature in

[9] R. E. Marshak and H. A. Bethe, Astrophys. J. **91**, 239 (1940) (referred to hereafter as MB).

[10] J. McDougall and E. C. Stoner, Trans. Roy. Soc. (London) **A237**, 67 (1938).

[11] This result has been shown by Dr. R. Latter by means of an integral equation formulation of the generalized Thomas-Fermi equation.

Eq. (18) can be evaluated if Φ_i' can be obtained as a function of T^2. This can be done by expanding Φ as an asymptotic series

$$\Phi=\phi+\sum_{n=1}^{N}\zeta_n\chi_n(kT)^{2n}, \tag{19}$$

in T^2, where ϕ is the Thomas-Fermi function corresponding to $T=0$, and the coefficients χ_n are functions only of x and x_b, determined by solution of the asymptotic Thomas-Fermi Eq. (10). Determination of the χ_n requires the solution of N separate differential equations, whose analytical form can be found by substituting Eq. (19) into Eq. (10). The differential equation for χ_n is an inhomogeneous linear equation involving ϕ and all perturbations of lower order. With the functions χ_n available, Φ_i' becomes

$$\Phi_i'=\phi_i'+\sum_{n=1}^{N}\zeta_n\chi_{n,i}'(kT)^{2n}, \tag{20}$$

where ϕ_i' and $\chi_{n,i}'$ are the initial slopes corresponding to ϕ and χ_n, respectively. Since the integrand in Eq. (18) then depends on Φ only through boundary and initial parameters, the equation yields an asymptotic series for the energy E in powers of T^2 through T^{2N}, which is analogous to the corresponding expansion in the case of a degenerate Fermi-Dirac gas.[12]

In the literature, two methods of solving the differential perturbation equations (for the case $N=1$) have been used. In the method of MB, the radius of the atom is kept at its unperturbed value x_b, and the boundary condition (12b) is met by requiring

$$\chi_{n,b}=x_b\left[\frac{\partial\chi_n(x,x_b)}{\partial x}\right]_{x=x_b}, \tag{21}$$

where $\chi_{n,b}$ is the boundary value of χ_n at the atom boundary x_b. In this case, the initial slope of the perturbation must be selected (by trial) so that Eq. (21) is met at the boundary. In the method of FMT, the initial slope is set equal to zero, and a perturbed radius x_b^* of the atom is determined at which the boundary condition (12b) is met. The method of FMT is computationally far more convenient, but the method of MB avoids the complication of introducing a perturbation in the volume. In any event, solutions of the differential perturbation equation of any order by the two methods can differ only by a solution of the corresponding homogeneous equation. Thus it is possible to express the pertinent parameters on the method of MB in terms of corresponding parameters derived by the computationally more convenient method of FMT; in Sec. 4b, this process is carried out explicitly for the case $N=1$.

For the subsequent development of the thermodynamics, it is convenient to modify the total energy E by subtraction of the energy of a standard state to obtain a total energy U which is always positive. The standard state is taken as a neutral atom of infinite radius at zero temperature, for which the energy is $(3/7)(Z^2e^2/\mu)\phi_{i,\infty}'$, where $\phi_{i,\infty}'$ is the corresponding initial slope of ϕ. Accordingly, one has

$$U=E-(3/7)(Z^2e^2/\mu)\phi_{i,\infty}'. \tag{22}$$

In terms of U, a parameter γ can be defined at this point by

$$U=Pv/(\gamma-1). \tag{23}$$

Further, it is convenient to introduce two differential parameters:

$$\epsilon_S=-(\partial\ln P/\partial\ln v)_S,\quad \epsilon_T=-(\partial\ln P/\partial\ln v)_T, \tag{24}$$

which are the (negative) slopes of the pressure-volume curves in log-log coordinates for constant entropy and for constant temperature respectively. These parameters are connected by the relation[13]

$$\epsilon_S/\epsilon_T=C_P/C_v, \tag{25}$$

where C_P is the heat capacity at constant pressure. The energy equation of thermodynamics[13] provides a connection

$$\epsilon_S=\gamma-[\partial\ln(\gamma-1)/\partial\ln v]_S \tag{26}$$

between ϵ_S and γ. An integral relation between ϵ_S and γ can be derived directly from the first law of thermodynamics; it is[14]

$$\gamma=U^{-1}\int_0^U\epsilon_S dU=\langle\epsilon_S\rangle_U, \tag{27}$$

which one can show by direct mathematical processes to be an integral of Eq. (26). An integration by parts on the integral in Eq. (27) shows that $\gamma\geq\epsilon_S$.

3. CASE OF ZERO TEMPERATURE

In this section, the thermodynamic functions corresponding to the case $T=0$ will be developed. For reasons that will become clear in the next section, thermodynamic variables corresponding to this case will be distinguished by a special notation.

For the case $T=0$, the Thomas-Fermi Eq. (10) becomes

$$\partial^2\phi/\partial x^2=\phi^{\frac{1}{2}}/x^{\frac{1}{2}}. \tag{28}$$

The initial value $\phi(0,x_b)$ of ϕ is unity, and the boundary value ϕ_b satisfies the condition (12b) at the atom radius x_b. Since the entropy is zero, the isothermal and isentropic equations of state are identical in this case; the common value of ϵ_S and ϵ_T will be denoted by ϵ_0, and the value of γ by γ_0. For the other thermodynamic

[12] J. E. Mayer and M. G. Mayer, *Statistical Mechanics* (John Wiley and Sons, Inc., New York, 1940), p. 374.

[13] M. W. Zemansky, *Heat and Thermodynamics* (McGraw-Hill Book Company, Inc., New York, 1937), first edition, pp. 222, 225, 227.

[14] This result for zero temperature was derived by the author; the generalization to nonzero temperature, by Dr. W. G. McMillan.

functions, the values corresponding to the case $T=0$ will be distinguished by use of lower case letters.

The basic thermodynamic function is the total energy u [corresponding to U of Eq. (22)], evaluated by Milne[4] and SK as

$$u=(Z^2e^2/\mu)[(3/7)(\phi_i'-\phi_{i,\infty}')+(2/35)x_b^{\frac{1}{2}}\phi_b^{5/2}]. \quad (29)$$

The pressure p is

$$p=(Z^2e^2/10\pi\mu^4)(\phi_b/x_b)^{5/2}, \quad (30)$$

from Eq. (14). The enthalpy h is accordingly

$$h=(Z^2e^2/\mu)[(3/7)(\phi_i'-\phi_{i,\infty}')+(4/21)x_b^{\frac{1}{2}}\phi_b^{5/2}]. \quad (31)$$

The Helmholtz function is identical, of course, with the total energy, and the Gibbs function is identical with the enthalpy. The connection between the three variables x_b, ϕ_b and ϕ_i' which enter the functions is provided by $p=-du/dv$, which yields the differential relation

$$x_b^{\frac{1}{2}}d\phi_i'/dx_b=-\phi_b^{5/2}-\tfrac{1}{3}x_b\phi_b^{\frac{1}{2}}d\phi_b/dx_b. \quad (32)$$

The parameter ϵ_0 can be evaluated directly from Eq. (30) as

$$\epsilon_0=(5/6)[1-d\ln\phi_b/d\ln x_b], \quad (33)$$

and the parameter γ_0 can be evaluated from Eqs. (29) and (30) as

$$(\gamma_0-1)^{-1}=(3/7)[1+(15/2)(\phi_i'-\phi_{i,\infty}')/(x_b^{\frac{1}{2}}\phi_b^{5/2})]. \quad (34)$$

For the case $T=0$, the partial derivative in Eq. (26) becomes a total derivative, so that ϵ_0 and γ_0 are equal whenever either is constant. A lower bound on γ_0 can be written immediately from the virial theorem in the form (5); since E_{pot} is necessarily negative, it follows that[15] $\gamma_0\geq 5/3$ at $T=0$.

The limiting values of the thermodynamic functions for high and low pressures can be evaluated if the corresponding asymptotic forms of ϕ_b and ϕ_i' as a function of x_b can be determined for $x_b\to 0$ and $x_b\to\infty$. For sufficiently high pressures, the Thomas-Fermi atomic model must pass over into the degenerate Fermi-Dirac gas, since the kinetic energy (varying as $1/r^2$ in the limit of small volume) dominates the potential energy (varying as $1/r$). Accordingly, the potential inside the atom for this limiting case is

$$V=(Ze/\mu)[x^{-1}+\tfrac{1}{2}x_b^{-3}x^2-\tfrac{3}{2}x_b^{-1}], \quad (35)$$

which corresponds to the sum of the nuclear potential and the potential due to a uniform distribution of Z electrons within the atomic volume. The corresponding value of ϕ is thus

$$\phi=1+\tfrac{1}{2}(x/x_b)^3-\tfrac{3}{2}(x/x_b)+3^{\frac{1}{2}}x/x_b^2, \quad (36)$$

where the last term arises by evaluating the chemical potential $\eta'=\lim_{T\to 0}kT\eta$ for the Thomas-Fermi atom from the expression[12] $\eta'=(h^2/8m)(3Z/\pi v)^{\frac{1}{3}}$ for the chemical potential of a Fermi-Dirac gas of Z electrons in the atomic volume v, as

$$\eta'=3^{\frac{1}{3}}Ze^2/\mu x_b^2 \quad (37)$$

in terms of x_b. Since the last term of Eq. (36) dominates in ϕ for x_b small, one obtains

$$\phi_b=3^{\frac{1}{2}}/x_b, \quad \phi_i'=3^{\frac{1}{2}}/x_b^2, \quad (38)$$

in the limit $x_b\to 0$. With these asymptotic forms for x_b small, all the thermodynamic functions derived reduce to the corresponding functions for a Fermi-Dirac gas,[12] as one can verify. The common limiting value of ϵ_0 and γ_0 in this case is 5/3.

The corresponding forms for the limit of low pressure (infinite atom) can be obtained from an asymptotic formula due to Sauvenier[16] (derived from a result of Sommerfeld,[17]), which represents an approximate solution of the Thomas-Fermi Eq. (28) which is perturbed slightly from the solution for an infinite atom. The solution is

$$\phi=(1+z)^{-\lambda_1/2}\left[1+\frac{4z_b+1}{(\lambda_1-4)z_b+1}\left(\frac{1+z}{1+z_b}\right)^{\lambda_1/\lambda_2}\right], \quad (39)$$

where

$$z=(x/12^{\frac{1}{3}})^{\lambda_2}, \quad z_b=(x_b/12^{\frac{1}{3}})^{\lambda_2}, \quad (40)$$

and

$$\lambda_1=\tfrac{1}{2}[73^{\frac{1}{2}}+7], \quad \lambda_2=\tfrac{1}{2}[73^{\frac{1}{2}}-7]. \quad (41)$$

This expression yields[16]

$$\phi_b=16(3+2\lambda_1)x_b^{-3}[1-(3+8\lambda_1)12^{\frac{1}{3}\lambda_2}/18x_b^{\lambda_2}] \quad (42)$$

as the asymptotic form of ϕ_b for $x_b\to\infty$. The corresponding asymptotic form of ϕ_i follows from Sauvenier's result, by means of Eq. (32), as

$$\phi_i'=\phi_{i,\infty}'+(256/9)(2+3\lambda_2)(3+2\lambda_1)^{5/2}12^{\frac{1}{3}\lambda_2}x_b^{-\lambda_1}, \quad (43)$$

and is determined only by the second term of Eq. (42). The common limiting value of ϵ_0 and γ_0 is 10/3 from these asymptotic forms. It is possible to show[11] that ϕ_b and $d\phi_b/dx_b$ are monotonic functions of x_b, which shows that ϵ_0 and γ_0 between the limits 5/3 and 10/3 are monotonic functions of x_b.

To determine thermodynamic functions for a given volume v, one needs values of ϕ_b and ϕ_i' (and their derivatives) corresponding to $x_b=(3v/4\pi)^{\frac{1}{3}}/\mu$. Fourteen values of ϕ_b and $\phi_i'-\phi_{i,\infty}'$ corresponding to values of x_b are available from numerical results[18] of FMT and

[15] This result was derived by Dr. W. G. McMillan. The lower limit in question does not hold for temperatures other than zero, because of the presence in the definition of U by Eq. (22) of the energy of a standard state corresponding to $T=0$.

[16] H. Sauvenier, Bull. Soc. Roy. Sci. Liege 8, 313 (1939).

[17] A. Sommerfeld, Z. Physik 78, 19 (1932).

[18] The data consists of results from six solutions of FMT (Table III of their paper), and from eight solutions of SK, as tabulated in Table V of Gombas (see reference 7). The value of $\phi_{i,\infty}'(-1.58875)$ given by FMT was associated with their data, and the value (-1.58808) given by SK was associated with theirs, in obtaining the difference $\phi_i'-\phi_{i,\infty}'$. In the region of x_b, where they overlap, the results of FMT and SK are discrepant; the discrepancy is more significant in $\phi_i'-\phi_{i,\infty}'$ than in ϕ_b. The data was smoothed in this region with major weight given to the data of FMT. For this reason, and because insufficient significant figures apparently appear in the difference $\phi_i'-\phi_{i,\infty}'$, results of a seventh and eighth solution of SK corresponding to the largest volumes, as given by Gombas, have been ignored in showing data points in Figs. 1, 2, and 3. The discrepancy in question has been noted by K. Umeda [Phys. Rev. 83, 651 (1951)].

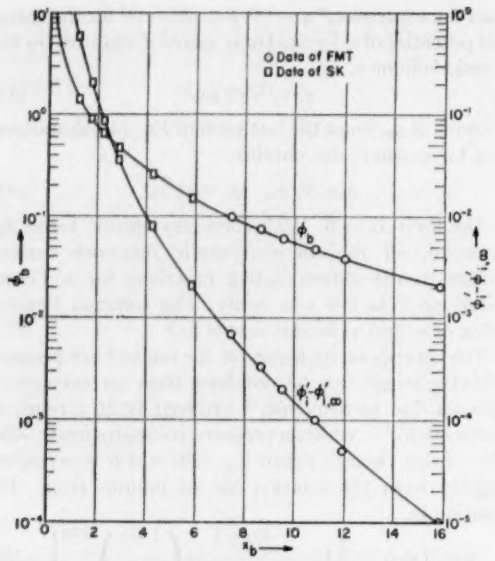

FIG. 1. Fitted functions for ϕ_b and $\phi_i'-\phi_{i,\infty}'$ against boundary radius in zero-temperature case.

SK. To reduce the labor of interpolation, and in the interest of direct accessibility of the data, it is convenient to fit these results by empirical formulae chosen to have the correct asymptotic forms in the two limits $x_b \to 0$ and $x_b \to \infty$. A fitting function for ϕ_b yielding the correct asymptotic forms can be written as

$$\phi_b = [\sum A_n x_b^{n/2}]^{-1}, \tag{44}$$

if n ranges over the sequence $n=2, 3, \cdots, 6$ and if the coefficients A_2 and A_6 are chosen to agree with the corresponding coefficients in the asymptotic forms (38) and (42), respectively. It has been found possible to choose the intermediate coefficients A_n to represent the smoothed data[18] of FMT and SK within about 1.5 percent. The coefficients A_n are tabulated in Table I; since they are all positive, the fitted function is monotone, as is[11] ϕ_b. The fitted function ϕ_b is shown in Fig. 1 for comparison with the data points.

The corresponding fitted function for $\phi_i'-\phi_{i,\infty}'$ could be determined, in principle, from Eq. (32), but it is simpler to fit the data for $\phi_i'=\phi_{i,\infty}'$ directly. A reasonable fitting function is

$$\phi_i'-\phi_{i,\infty}' = [\sum B_n x_b^n]^{-1}, \tag{45}$$

in which n ranges over the sequence $n=2, 3, \cdots 7, \lambda_1$, and the coefficients B_2 and B_{λ_1} are chosen to agree with the corresponding coefficients in the asymptotic forms (38) and (43), respectively. The smoothed data[18] of FMT and SK for the difference $\phi_i'-\phi_{i,\infty}'$ can be reproduced within about 1.5 percent by means of the coefficients B_n tabulated in Table I. It is possible to show[11] that ϕ_i' is a monotonic function of x_b; the fitted function has this property likewise.[19] The fitted function and the data points are shown in Fig. 1.

With these fitted functions for ϕ_b and ϕ_i', all the thermodynamic functions discussed previously can be determined by direct algebraic or differential processes. In the range covered by the data of FMT and SK, thermodynamic functions can be obtained with an accuracy of the order of a few percent, on the basis of the data[18] employed. Outside this range the fitted functions yield results which are correct in both asymptotic limits, and their monotonic character gives some assurance of approximate validity, at least, outside of the regions fitted directly. The fitted function for ϕ_b yields the equation of state

$$p^{2/5} \sum_{n=2}^{6} A_n (3v/4\pi\mu^3)^{(n+2)/6} = (Z^2e^2/10\pi\mu^4)^{2/5}. \tag{46}$$

Pressures from this equation are shown in Fig. 2 for comparison with the corresponding quantities as calculated directly from the data of FMT and SK. The energy u from Eq. (29) is shown likewise; the unit of energy is the Rydberg, $R=e^2/2a_0$. A similar comparison with directly calculated values is shown in Fig. 3 for γ_0 (directly calculated values are not given for ϵ_0 since it is a differential parameter). Note that pressure and energy scale as $Z^{10/3}$ and $Z^{7/3}$, respectively, while the volume scales as Z^{-1}.

4. FIRST-ORDER TEMPERATURE PERTURBATION

In this section, the thermodynamic functions derived for the case $T=0$ will be generalized to include terms in T^2. The procedure corresponds to retaining terms through T^2 in the expansion of the right-hand side of the asymptotic Thomas-Fermi Eq. (10). Setting $\chi_1=\chi$ and $\zeta_1=\zeta$ in Eq. (19), one can write

$$\Phi = \phi + \chi\zeta(kT)^2 \tag{47}$$

as a solution of the resulting equation, where ϕ is an unperturbed solution corresponding to $T=0$, and the perturbation χ satisfies

$$\partial^2\chi/\partial x^2 = \tfrac{3}{2}(\phi/x)^{\frac{1}{2}}\chi + x^{\frac{1}{2}}/\phi^{\frac{1}{2}} \tag{48}$$

TABLE I. Coefficients[a] of fitted functions, zero-temperature case.

n	A_n	B_n
2	4.8075×10^{-1}	4.8075×10^{-1}
3	7.009×10^{-2}	4.3462×10^{-1}
4	7.003×10^{-2}	6.9203×10^{-2}
5	8.901×10^{-2}	5.9472×10^{-2}
6	3.3704×10^{-3}	-4.9688×10^{-3}
7		4.3386×10^{-4}
$\lambda_1=7.77200$		1.5311×10^{-6}

[a] The coefficients are given to four or five figures to minimize round-off error and to yield smoothness in computational work.

[19] The coefficient B_6 is negative, but one can show that ϕ_i' and $d\phi_i'/dx_b$ from the tabulated coefficients have no zeros for x_b positive.

under the initial condition $\chi(0,x_b)=0$. The coefficient ζ can be evaluated (with $a_1=\pi^2/8$) as $\pi^2\mu^2/8Z^2e^4$, or as $(2.034Z^{4/3}R)^{-2}$ in terms of the Rydberg. The limitation (13) on the temperature can be written

$$Z^{-4/3}kT/R\ll 8(2/9\pi^2)^{\frac{1}{2}}\phi_b/x_b. \tag{49}$$

A particular perturbation χ always corresponds to a definite $\phi(x,x_b)$; the atom corresponding to this ϕ will be referred to as the unperturbed atom to which the perturbation χ corresponds.

In Sec. 4a following, the thermodynamic functions will be developed in terms of parameters corresponding to the method of MB. In Sec. 4b following, these parameters will be expressed in terms of parameters on the method of FMT, in order to yield the thermodynamic functions in that case. In a final section, numerical results will be presented.

a. Method of MB

In this case, the perturbation leaves the volume v unchanged. The boundary value $\chi_b=\chi_{1,b}$ satisfies the boundary condition (21) at the radius x_b of the unperturbed atom. The initial slope $\chi_i'=\chi_{1,i}'$ must be selected by trial so that this condition is met.

It is convenient to introduce two parameters,

$$\sigma=\chi_b/\phi_b,\quad \omega=\chi_i'/(x_b^{\frac{1}{2}}\phi_b^{5/2}), \tag{50}$$

in terms of which the boundary value Φ_b and initial slope Φ_i' of Φ can be written

$$\Phi_b=\phi_b[1+\sigma\zeta(kT)^2], \tag{51a}$$

$$\Phi_i'=\phi_i'+x_b^{\frac{1}{2}}\phi_b^{5/2}\omega\zeta(kT)^2, \tag{51b}$$

respectively. With use of Eq. (51a), the pressure P of the perturbed atom follows directly from Eq. (14), by retention only of terms through T^2, as

$$P=p[1+(5/2)(\sigma+2\tau)\zeta(kT)^2], \tag{52}$$

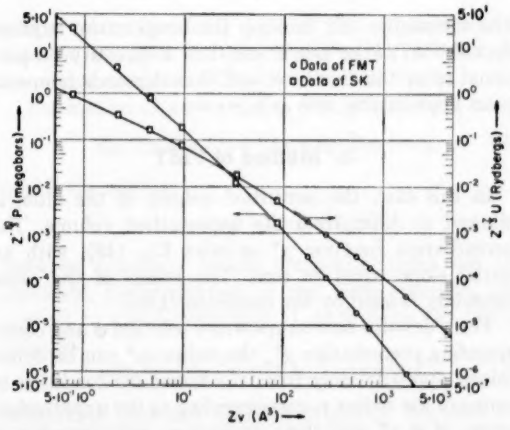

FIG. 2. Scaled pressure and energy from fitted functions for ϕ_b and $\phi_i'-\phi_{i,\infty}'$, against scaled volume in cubic angstroms; zero-temperature case.

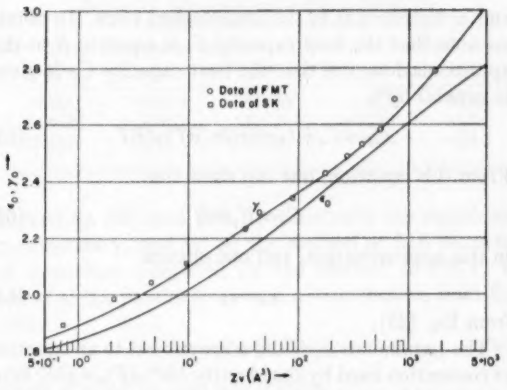

FIG. 3. Parameters γ_0 and ϵ_0 from fitted functions for ϕ_b and $\phi_i'-\phi_{i,\infty}'$, against scaled volume in cubic angstroms; zero-temperature case.

where p is the pressure of Eq. (30) corresponding to the unperturbed atom, and

$$\tau=(x_b/\phi_b)^2. \tag{53}$$

The parameters σ, τ, and ω are functions of x_b, and thus of v.

Equations (52) and (51b) provide expansions through terms in T^2 of P and Φ_i', respectively, so that the total energy can be evaluated from Eq. (18). The energy U is

$$U=u+(15/2)pv(\sigma+2\tau+3\omega)\zeta(kT)^2, \tag{54}$$

where u is the energy of the unperturbed atom, given by Eq. (29). The entropy S is

$$S=15pv(\sigma+2\tau+3\omega)\zeta k^2T, \tag{55}$$

from the relation $T(\partial S/\partial T)_v=(\partial E/\partial T)_v$. The enthalpy H is

$$H=h+(5/2)pv(4\sigma+8\tau+9\omega)\zeta(kT)^2, \tag{56}$$

where h is the enthalpy of the unperturbed atom. The Helmholtz function F is

$$F=u-(15/2)(\sigma+2\tau+3\omega)\zeta(kT)^2, \tag{57}$$

and the Gibbs function G is

$$G=h-(5/2)(2\sigma+4\tau+9\omega)\zeta(kT)^2. \tag{58}$$

One can verify (with the aid of the virial theorem) that F satisfies the Brachman relation (7).

The parameter γ is determined by

$$\gamma=\gamma_0-(5/2)(\gamma_0-1)\times[(3\gamma_0-4)(\sigma+2\tau)+9(\gamma_0-1)\omega]\zeta(kT)^2, \tag{59}$$

where γ_0 corresponds to the unperturbed atom. The differential parameter ϵ_T can be obtained from the definition as

$$\epsilon_T=\epsilon_0-[(5/6)d\sigma/d\ln x_b+4\epsilon_0\tau]\zeta(kT)^2, \tag{60}$$

where use has been made of the relation

$$d\tau/d\ln x_b=(12/5)\epsilon_0\tau, \tag{61}$$

and ϵ_0 corresponds to the unperturbed atom. To obtain ϵ_S, note that the heat capacity C_v is equal to S in this approximation, and that the heat capacity C_P is given in general by[13]

$$C_P=C_v+(\epsilon_T/v)(\partial v/\partial T)_P PT. \tag{62}$$

From this equation, one can show that

$$C_P=C_v=S \tag{63}$$

in this approximation, and one obtains

$$\epsilon_S=\epsilon_T \tag{64}$$

from Eq. (25).

The parameters σ, τ, and ω are subject to an equation of connection fixed by the identity $(\partial P/\partial T)_v=(\partial S/\partial v)_T$, which yields the differential relation

$$d(\sigma+3\omega)/d\ \ln x_b=(3\epsilon_0-2)\sigma +[(6/5)\epsilon_0-4]\tau+9(\epsilon_0-1)\omega. \tag{65}$$

As one can verify, this relation is necessary and sufficient for the differentials of U, H, F and G, as derived above, to be exact differentials of their arguments, and for the Maxwell relations to be satisfied. Equation (65) implies a differential relation between χ_b, χ_i' and ϕ_b which is the analog of Eq. (32) in the zero-temperature case.

In the limit $x_b\rightarrow 0$ of vanishing atomic volume, the thermodynamic functions derived must reduce to the corresponding functions for a degenerate Fermi-Dirac gas through terms of order T^2. Substitution in the differential equation (48) for χ of the dominant terms of Eq. (36) for ϕ in the Fermi-Dirac limit, solution of the resulting equation, and imposition of the boundary condition (21) yields

$$\chi_i'=-(2/3^{5/3})x_b^2 \tag{66}$$

for the initial slope. The corresponding solution for χ in the Fermi-Dirac limit is

$$\chi=-(2/3^{5/3})x_b^2x, \tag{67}$$

which is a straight line in x. The boundary value of χ is thus

$$\chi_b=-(2/3^{5/3})x_b^3 \tag{68}$$

and the parameters σ and ω become

$$\sigma=-(2/3^{7/3})x_b^4,\quad \omega=-(2/3^{10/3})x_b^4, \tag{69}$$

with use of the first of Eqs. (38). The parameter τ is

$$\tau=(1/3^{4/3})x_b^4. \tag{70}$$

One can verify that, with these asymptotic forms, all the thermodynamic functions derived reduce to the corresponding functions for a degenerate Fermi-Dirac gas through terms of order T^2. The inequality (49) in this case requires that $Z^{-4/3}kT/R$ be less than a quantity proportional to x_b^{-2}, so that large temperatures are permitted.

In the opposite limit of an infinite atom, for $x_b\rightarrow\infty$, the corresponding asymptotic forms can be obtained from the differential equation (48) by substitution of the approximation for ϕ in this case,

$$\phi=(144/x^3)(1-\lambda_1 12^{\frac{1}{2}\lambda_2}/2x^{\lambda_2}), \tag{71}$$

which corresponds, in Eq. (39), to replacing the square bracket by unity and expanding the factor $(1+z)^{-\lambda_1/2}$. The solution for χ in this limit is

$$\chi=Ax^{\lambda_1-3}\left[1+\frac{3\lambda_1 12^{\frac{1}{2}\lambda_2}}{4x^{\lambda_2}}\right]+\frac{x^5}{24}\left[1+\frac{(4+5\lambda_1)12^{\frac{1}{2}\lambda_2}}{6x^{\lambda_2}}\right], \tag{72}$$

where the constant A is fixed by the boundary condition (21) as

$$A=-[(\lambda_1-3)/108]x_b^{8-\lambda_1}[1+(\lambda_1-1)12^{\frac{1}{2}\lambda_2}/6x_b^{\lambda_2}]. \tag{73}$$

This solution yields

$$\chi_b=-[(2\lambda_2-1)/216]x_b^5[1+\lambda_1 12^{\frac{1}{2}\lambda_2}/2x_b^{\lambda_2}] \tag{74}$$

for the boundary value of χ. The value of σ follows as

$$\sigma=-[(4\lambda_2-3)/2^7 3^4]\times x_b^5[1+(3+17\lambda_1)12^{\frac{1}{2}\lambda_2}/6x_b^{\lambda_2}], \tag{75}$$

with use of Eq. (42), and the value of τ is

$$\tau=[(33-40\lambda_2)/2^8 3^6]x_b^8. \tag{76}$$

The parameter ω is determined by the differential identity (65), and is independent of the first-order terms of σ and τ in x_b^8. With inclusion of a second-order term in ϵ_0 by

$$\epsilon_0=(10/3)[1-(\lambda_1+9)12^{\frac{1}{2}\lambda_2}/24x_b^{\lambda_2}], \tag{77}$$

integration of Eq. (65) yields

$$\omega=-[(30+7\lambda_2)/2^9 3^7]12^{\frac{1}{2}\lambda_2}x_b^{8-\lambda_2}. \tag{78}$$

The corresponding value of the initial slope χ_i' is

$$\chi_i'=-(2/3^7)(30+7\lambda_2)(3+2\lambda_1)^{5/2}12^{\frac{1}{2}\lambda_2}x_b^{1-\lambda_2}. \tag{79}$$

The inequality (49) limiting the temperature requires that $Z^{-4/3}kT/R$ be much less than a quantity proportional to x_b^{-4} in this case, and thus demands temperatures approaching zero as $x_b\rightarrow\infty$.

b. Method of FMT

In this case, the perturbed volume of the atom is allowed to differ from the unperturbed volume. The perturbation function χ^* satisfies Eq. (48), with an initial slope equal to zero. The radius of the atom boundary is fixed by the condition (12b).

For a definite zero-temperature solution ϕ and corresponding perturbation χ^*, the radius x_b^* can be determined approximately from the boundary condition in terms of the radius x_b corresponding to the unperturbed atom, if ϕ, χ^* and their derivatives are expanded in Taylor series about the point $x=x_b$. Making use of the differential Eqs. (28) and (48) and the boundary con-

dition on ϕ, one obtains in first order

$$x_b^* = x_b[1+\nu\zeta(kT)^2], \tag{80}$$

where the parameter ν is defined by

$$\nu = (\chi_b^* - x_b\chi_b^{*\prime})/(x_b\phi_b)^{\frac{1}{2}}, \tag{81}$$

in which ϕ_b is the value of ϕ at the boundary $x=x_b$ of the unperturbed atom, and χ_b^* and $\chi_b^{*\prime}$ are the values of χ^* and $\partial\chi^*/\partial x$, respectively, evaluated at the same point $x=x_b$. The volume v^* of the perturbed atom is accordingly

$$v^* = v[1+3\nu\zeta(kT)^2], \tag{82}$$

in terms of the volume v of the corresponding unperturbed atom.

To relate χ^* with χ for the same volume v^*, where χ is the perturbation function computed by the method of MB, one notes that χ must satisfy Eq. (48) with a $\phi=\phi^*$ chosen to correspond to the perturbed atom radius x_b^*. The value of ϕ^* is, accordingly,

$$\phi^* = \phi(x,x_b) + [\partial\phi(x,x_b)/\partial x_b](x_b^* - x_b), \tag{83}$$

where $\phi(x,x_b)$ is the unperturbed solution to which χ^* corresponds. Substitution of ϕ^* into the perturbation Eq. (48) to obtain the differential equation for χ, and comparison of the result with the differential equation for χ^*, yields

$$\chi^* = \chi + \nu x_b \partial\phi/\partial x_b \tag{84}$$

with use of Eq. (80).

The function $\partial\phi/\partial x_b$ is a solution of the homogeneous equation,

$$\partial^2(\partial\phi/\partial x_b)/\partial x^2 = \tfrac{3}{2}(\phi/x)^{\frac{1}{2}}\partial\phi/\partial x, \tag{85}$$

corresponding to the inhomogeneous perturbation equation, as one can verify by differentiating the zero-temperature Eq. (28) with respect to x_b. At the origin, the function vanishes and its slope satisfies the initial condition,

$$[\partial(\partial\phi/\partial x_b)/\partial x]_{x=0} = d\phi_i'/dx_b, \tag{86}$$

where ϕ_i' is the initial slope of the zero-temperature solution $\phi(x,x_b)$. The function ϕ^* then satisfies the boundary condition (12b) at x_b^* automatically.

Evaluation at $x=x_b$ of Eq. (84) for χ^*, with use of

$$d\phi_b/dx_b = \phi_b/x_b + [\partial\phi(x,x_b)/\partial x_b]_{x=x_b}, \tag{87}$$

yields the relation

$$\chi_b = \chi_b^* + (6/5)\epsilon_0\nu\phi_b \tag{88}$$

between boundary values computed under the two methods. Differentiation of the same equation with respect to x and evaluation at $x=0$ yields the further relation

$$x_b^{\frac{1}{2}}\phi_b^{\frac{1}{2}}\chi_b + 3\chi_i' = x_b^{\frac{1}{2}}\phi_b^{\frac{1}{2}}\chi_b^* + 4\nu x_b^{\frac{1}{2}}\phi_b^{5/2}, \tag{89}$$

when Eqs. (86) and (32) are employed. The last two equations give

$$\chi_i' = [4/3-(2/5)\epsilon_0]\nu x_b^{\frac{1}{2}}\phi_b^{5/2}. \tag{90}$$

TABLE II. Boundary and initial parameters, temperature-perturbed case.

x_b	x_b^*	$x_b^{*\prime}$	χ_b	χ_i'
9.5651	1747.3	834.82	−812	−13.4
10.8038	3068.2	1315.7	−1320	−15.7
15.8698	18731.	5689.1	−6420	−24.8

Equations (88) and (90) fix completely the significant parameters χ_b and χ_i' on the method of MB in terms of quantities computed by the method of FMT. In terms of the parameters σ and ω, one obtains, from Eq. (88),

$$\sigma = \sigma^* + (6/5)\epsilon_0\nu, \tag{91}$$

where $\sigma^* = \chi_b^*/\phi_b$, and one obtains

$$\omega = [4/3-(2/5)\epsilon_0]\nu, \tag{92}$$

from Eq. (90).

Thermodynamic functions for the volume v are available from preceding results in terms of the parameters σ and ω corresponding to the method of MB. To determine a thermodynamic function for the volume v^* in terms of the parameters σ^* and ν corresponding to the method of FMT, it is necessary merely to take account of the perturbation in the temperature-independent term due to the volume change, v^*-v, and to transform σ and ω into σ^* and ν by the preceding equations. Thus, if P^* is the pressure corresponding to the volume v^*, one has

$$P^* = P + (dp/dv)(v^*-v), \tag{93}$$

if P corresponds to v. With use of Eq. (82) for v^*-v and the defining equation for ϵ_0, one obtains

$$P^* = p[1+(5/2)(\sigma^*+2\tau)\zeta(kT)^2]. \tag{94}$$

In a similar manner, it can be shown that the energy U^* corresponding to v^* is

$$U^* = u + \tfrac{3}{2}pv(5\sigma^*+10\tau+18\nu)\zeta(kT)^2, \tag{95}$$

and that the entropy S^* is

$$S^* = 15pv(\sigma^*+2\tau+4\nu)\zeta k^2T. \tag{96}$$

It is clear that these results are easily modified to take account of the use of an arbitrary initial slope (rather than zero) in the method of FMT.

c. Numerical Results

Three solutions by their method of the first-order temperature-perturbation equation have been tabu-

TABLE III. Coefficients[a] of fitted functions, temperature-perturbed case.

n	C_n	n	D_n
3	-3.205×10^{-1}	$1-\lambda_3=0.22800$	-5.805×10^{-3}
4	-4.021×10^{-2}	1	-3.755×10^{-1}
5	-2.519×10^{-3}	2	−3.120

[a] The coefficients are given to four figures to minimize round-off error and to yield smoothness in computational work.

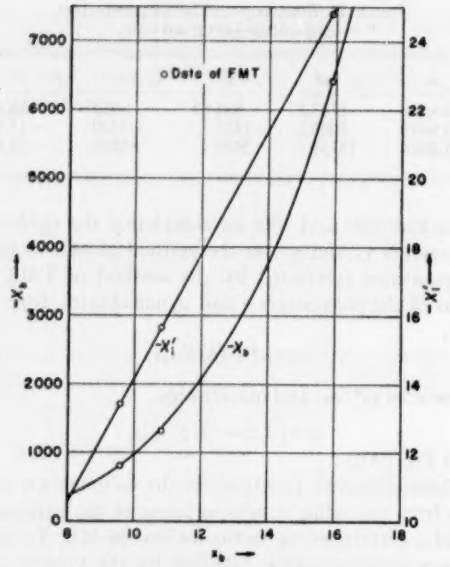

FIG. 4. Fitted functions for χ_b and χ_i' against boundary radius in temperature-perturbed case.

lated by FMT. The corresponding values of χ_b^* and $\chi_b^{*\prime}$ have been determined by quartic interpolation from their data and are tabulated in Table II against the unperturbed radius x_b to which they correspond. The corresponding values of χ_b and χ_i' on the method of MB have been determined by use of Eqs. (88) and (90) respectively and tabulated likewise. Since these equations involve the differential parameter ϵ_b, which has been determined from the fitted function (44) for ϕ_b, the accuracy of χ_b and χ_i' cannot be guaranteed as better than a few percent.

As in the zero-temperature case, it is desirable to represent the pertinent quantities, which the differential equation yields, by fitted functions having the proper asymptotic behavior in the two limits $x_b \to 0$ and $x_b \to \infty$. It is convenient to use parameters corresponding to the method of MB, in order to avoid the complication of a perturbation in the volume. The quantity χ_b can be represented by

$$\chi_b = \sum C_n x_b^n, \tag{97}$$

if $n = 3, 4, 5$, and the coefficients C_3 and C_5 are chosen to agree with the corresponding coefficients in the asymptotic forms (68) and (74), respectively. Similarly χ_i' can be represented by

$$\chi_i' = [\sum D_n x_b^{-n}]^{-1}, \tag{98}$$

if n ranges over the sequence $1-\lambda_2$, 1, 2 and the coefficients D_2 and $D_{1-\lambda_2}$ are fixed by Eqs. (66) and (79), respectively. The coefficients C_n and D_n tabulated in Table III reproduce[20] the values of Table II within about 1 percent in the case of χ_b and within about 3 percent in the case of χ_i'. It can be shown that χ_b and χ_i' are monotonic functions of x_b, as are the fitted functions. The fitted functions and the data points are

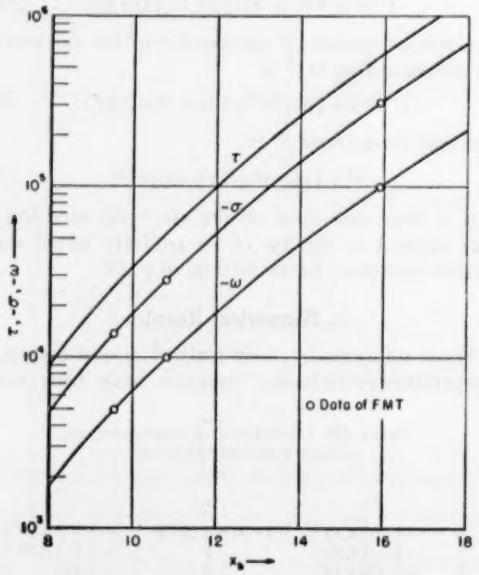

FIG. 5. Perturbation parameters σ, τ, and ω from fitted functions for χ_b, χ_i' and ϕ_b, against boundary radius in temperature-perturbed case.

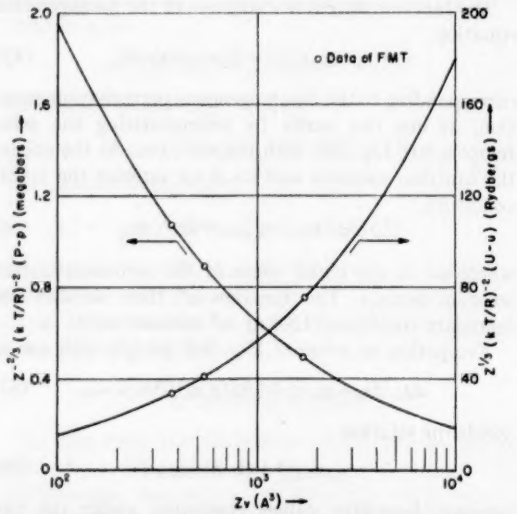

FIG. 6. Scaled pressure perturbation and energy perturbation from fitted functions for χ_b, χ_i' and ϕ_b, against scaled volume in cubic angstroms; temperature-perturbed case.

[20] By adjusting the exponent as well as the coefficient of the middle term in Eqs. (97) and (98), one can obtain a much closer fit. The accuracy obtained is considered sufficient, however, since χ_b and χ_i' are perturbation parameters. Note further that τ (known only to a few percent from the fitted function for ϕ_b) exceeds $-\sigma$ by a factor of about two and $-\omega$ by a factor of five or six, over the range of x_b corresponding to the data (Fig. 5).

shown in Fig. 4. Values of the parameters σ and ω computed from the fitted functions, as well as values of τ, are shown in Fig. 5 with directly computed values (omitted in the case of τ).

In Fig. 6, the effect of the first-order temperature perturbation on the equation of state is shown graphically by plotting $Z^{-\frac{1}{3}}(kT/R)^{-2}(P-p)$, which is independent of T, as a function of Zv. The energy perturbation $U-u$ in units of the Rydberg is shown similarly. The entropy S is not shown, since the value of $Z^{\frac{1}{3}}(kT/R)^{-1}S$ in $R/°K$ differs from $Z^{\frac{1}{3}}(kT/R)^{-2}(U-u)$, as plotted, by the numerical factor 1.27×10^{-5}. The parameters ϵ_T and γ are shown in similar fashion in Fig. 7. The quantity $8(2/9\pi^2)^{\frac{1}{2}}\phi_b/x_b$, relative to which $Z^{-4/3}kT/R$ must be small, is shown by the dashed curve in Fig. 7. Note that the perturbation in a thermodynamic function scales with Z differently than does the unperturbed function (for fixed temperature).

5. CONCLUSION

As mentioned in the Introduction, neglect of exchange makes the results obtained valid only in the limit of high Z and high compression. It is hoped to extend this work by including exchange to remove this limitation. Since initiation of this work, extensive numerical results obtained by Dr. R. Latter indicate some systematic errors in the published data used; it is planned in the future to give fitted functions for the solution parameters which are based on more accurate data.

The author wishes to thank Professor W. G. McMillan of the University of California, Los Angeles, and Dr. R. Latter of the Rand Corporation, for the use of a number of their results and for helpful discussions. He acknowledges with appreciation the helpful advice of Professors M. G. Mayer and J. E. Mayer of the University of Chicago, and of Professor R. P. Feynman of the California Institute of Technology. Thanks are due to Mr. R. H. Johnson and Miss E. Force for the computational work.

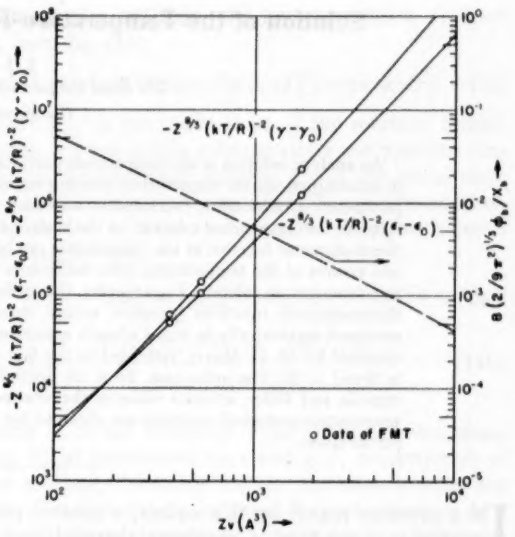

FIG. 7. Scaled perturbations in parameters γ and ϵ_T from fitted functions, against scaled volume in cubic angstroms; temperaturel perturbed case. The scaled temperature $Z^{-4/3}kT/R$ must be smalrelative to the quantity shown by the dashed curve.

Solution of the Temperature-Perturbed Thomas-Fermi Equation

J. J. GILVARRY
The Rand Corporation, Santa Monica, California

(Received July 30, 1954)

An analytic solution of the temperature-perturbed Thomas-Fermi equation of nth order is given in terms of quadratures on the unperturbed solution corresponding to zero temperature. The boundary and initial parameters corresponding to a solution, necessary for the thermodynamics, are given as explicit integrals in terms of the unperturbed solution, on the basis of a boundary condition for fixed atomic volume. Thus, every thermodynamic function at low temperature can be written as an asymptotic series, either in the even or the odd powers of the temperature, with coefficients which can be expressed in terms of quadratures on the zero-temperature solution. In particular, the coefficients of the asymptotic series corresponding to the basic thermodynamic functions (pressure, energy, entropy, enthalpy, Helmholts and Gibbs functions) can be expressed algebraically in terms of such quadratures. These results extend and generalize a similar result obtained by M. G. Mayer, restricted to the first-order temperature-perturbed case. The theory is applied in detail to the first-order case. From six neutral-atom zero-temperature solutions due to Feynman, Metropolis, and Teller, accurate values of the corresponding boundary and initial parameters of the first-order temperature-perturbed equation are obtained for the case of fixed atomic volume under the temperature perturbation.

IN a previous paper[1] by this author, a general perturbation procedure of obtaining thermodynamic functions at low temperature for the temperature-perturbed Thomas-Fermi atom was outlined. The method was applied in detail to obtain the thermodynamic functions corresponding to a first-order temperature perturbation. The numerical results were based on three numerical solutions of the first-order perturbation equation due to FMT.[2]

This paper gives an analytic solution of the temperature-perturbed Thomas-Fermi equation of nth order in terms of quadratures on the unperturbed solution corresponding to zero temperature. Further, the boundary and initial parameters corresponding to a solution, necessary for the thermodynamics, can be written as explicit integrals on the basis of a boundary condition for fixed volume. Hence, one can show that all the basic thermodynamic functions (pressure, energy, entropy, enthalpy, Helmholtz and Gibbs functions) can be expressed as asymptotic series, either in the even or the odd powers of the temperature, with coefficients which can be written algebraically in terms of quadratures on the zero-temperature Thomas-Fermi function. A result similar to the last has been given by Mayer[3] for the first-order case, but with the salient difference that the pressure cannot be obtained except by a numerical differentiation with respect to volume.

This quadrature solution has been applied to six zero-temperature solutions of FMT to obtain accurate values of the boundary and initial parameters for the corresponding first-order temperature-perturbed cases, on the basis of a fixed atom volume. The temperature-perturbation solutions of FMT correspond to an atomic volume which is a function of temperature; the process in I of transforming (for convenience in the thermodynamics) the pertinent parameters derived from these solutions into parameters corresponding to a fixed volume degraded the accuracy to a few percent. This loss of accuracy is avoided in the direct solutions for fixed volume given here.

1. INTRODUCTION

The Thomas-Fermi function Φ is connected with the electrostatic potential V at a point r in an atom of atomic number Z by

$$Ze^2\Phi/\mu x = eV + kT\eta, \tag{1}$$

where e is the electronic charge, k is Boltzmann's constant, T is the temperature, $kT\eta$ is the chemical potential, and x is defined by $r=\mu x$, where $\mu=a_0(9\pi^2/128Z)^{\frac{1}{3}}$ in terms of the radius a_0 of the first Bohr orbit for hydrogen. The asymptotic form for low temperature of the generalized Thomas-Fermi equation which Φ satisfies is

$$d^2\Phi/dx^2 = (\Phi^{\frac{1}{2}}/x^{\frac{1}{2}})[1+\textstyle\sum_n \zeta_n (kTx/\Phi)^{2n}], \tag{2}$$

in which $n \geq 1$,

$$\zeta_n = (\mu/Ze^2)^{2n} a_n, \tag{3}$$

and the coefficients a_n are defined and tabulated by McDougall and Stoner.[4]

The function Φ can be expanded as an asymptotic series,

$$\Phi = \phi + \textstyle\sum_n \chi_n \zeta_n (kT)^{2n}, \tag{4}$$

where ϕ is the Thomas-Fermi function corresponding to $T=0$, and the perturbation χ_n of order n is a function of x. The function ϕ satisfies the differential equation

$$d^2\phi/dx^2 = \phi^{\frac{1}{2}}/x^{\frac{1}{2}}, \tag{5}$$

[1] J. J. Gilvarry, preceding paper [Phys. Rev. 96, 944 (1954)], referred to hereafter as I.
[2] Feynman, Metropolis, and Teller, Phys. Rev. 75, 1561 (1949), referred to hereafter as FMT.
[3] M. G. Mayer (private communication).
[4] J. McDougall and E. C. Stoner, Trans. Roy. Soc. (London) A237, 67 (1939).

and each perturbation χ_n satisfies an inhomogeneous linear differential equation of the form

$$d^2\chi_n/dx^2=\tfrac{3}{2}(\phi/x)^{\frac{1}{2}}\chi_n+f_n, \tag{6}$$

where f_n is a function of x, ϕ and the perturbations χ_1, χ_2, $\cdots$, χ_{n-1}. The form of f_n can be found by substituting the series (4) into the differential equation (2). The initial and boundary conditions on $\chi_n(x)$ are

$$\chi_n(0)=0, \tag{7a}$$

$$\chi_{n,b}=x_b[d\chi_n/dx]_{x=x_b}, \tag{7b}$$

where $\chi_{n,b}$ is the boundary value of χ_n at the boundary x_b of the unperturbed atom. The atomic volume corresponding to the boundary condition (7b) is $v=(4\pi/3)(\mu x_b)^3$; thus, the volume is unperturbed.

Fermi[5] has shown that one solution of the homogeneous equation corresponding to Eq. (6) is $\xi_1=\phi+\frac{1}{3}xd\phi/dx$ if ϕ satisfies Eq. (5). It follows that a second solution of the homogeneous equation is $\xi_2=\xi_1\int\xi_1^{-2}dx$. By the method of variation of parameters, one can then obtain the general solution of Eq. (6) in terms of integrals on ϕ and f_n. It is convenient to define four integrals, of which the first,

$$J_1(x)=\int_0^x[\phi+\tfrac{1}{3}x'd\phi/dx']^{-2}dx', \tag{8}$$

is a function only of x, and the three,

$$J_2(f,x)=\int_0^x f(x')[\phi+\tfrac{1}{3}x'd\phi/dx']dx', \tag{9a}$$

$$J_{12}(f,x)=\int_0^x J_1(x')f(x')[\phi+\tfrac{1}{3}x'd\phi/dx']dx', \tag{9b}$$

$$J_{21}(f,x)=\int_0^x J_2(f,x')[\phi+\tfrac{1}{3}x'd\phi/dx']^{-2}dx', \tag{9c}$$

are functionals of a function f of x. These four integrals satisfy the identity

$$J_{12}(f,x)+J_{21}(f,x)=J_1(x)J_2(f,x). \tag{10}$$

The general solution of Eq. (6) is then

$$\chi_n=[c_1+c_2J_1(x)+J_{21}(f_n,x)][\phi+\tfrac{1}{3}xd\phi/dx], \tag{11}$$

where c_1 and c_2 are constants.

2. FIRST-ORDER TEMPERATURE PERTURBATION

a. Quadrature Solution

The first-order differential perturbation equation corresponds to Eq. (6) with

$$f_1=x^{\frac{1}{2}}/\phi^{\frac{1}{2}}. \tag{12}$$

[5] E. Fermi, Mem. reale accad. Italia Classe sci. fis. mat. e nat. 1, 1 (1930).

The solution satisfying the initial condition $\chi_1(0)=0$ is, from Eq. (11),

$$\chi_1=[\chi_{1,i}'J_1(x)+J_{21}(f_1,x)][\phi+\tfrac{1}{3}xd\phi/dx], \tag{13}$$

where $\chi_{1,i}'$ is the initial slope of the solution. Substitution of $x=x_b$ in this solution yields one equation connecting the boundary value $\chi_{1,b}$ with the initial slope $\chi_{1,i}'$, and the boundary condition (7b) provides another. The solution of these two equations yields, with use of the identity (10),

$$\chi_{1,b}=-12\phi_bJ_{12}(f_1,x_b)[9+4x_b^{\frac{1}{2}}\phi_b^{5/2}J_1(x_b)]^{-1}, \tag{14a}$$

$$\chi_{1,i}'=-\frac{9J_2(f_1,x_b)+4x_b^{\frac{1}{2}}\phi_b^{5/2}J_{21}(f_1,x_b)}{9+4x_b^{\frac{1}{2}}\phi_b^{5/2}J_1(x_b)}, \tag{14b}$$

where ϕ_b is the boundary value of ϕ. The boundary and initial parameters ($\chi_{1,b}$ and $\chi_{1,i}'$, respectively) of the solution, necessary for the thermodynamics, are thus obtained directly in terms of quadratures on ϕ.

In I, thermodynamic functions for the first-order temperature-perturbed case were given in a form in which the coefficient of T^2 or T was expressed in terms of the parameters σ, τ, and ω, of which

$$\tau=(x_b/\phi_b)^2 \tag{15}$$

depends on the solution of the zero-temperature equation, and

$$\sigma=\chi_{1,b}/\phi_b, \quad \omega=\chi_{1,i}'/(x_b^{\frac{1}{2}}\phi_b^{5/2}), \tag{16}$$

depend on the solution of the corresponding differential perturbation equation. Thus, the pressure P from I is

$$P=p[1+(5/2)(\sigma+2\tau)\zeta_1(kT)^2], \tag{17}$$

where p is the pressure

$$p=(Z^2e^2/10\pi\mu^4)(\phi_b/x_b)^{5/2}, \tag{18}$$

corresponding to the unperturbed atom of the same volume. By means of Eqs. (14), the parameters σ and ω can be written directly in terms of quadratures on ϕ. Hence, one obtains Mayer's result[3,6]: the coefficient of T^2 or T in the first-order perturbation of every thermodynamic function can be expressed in terms of quadratures on ϕ. This statement does not imply that the coefficient of T^2 or T may not contain a derivative with respect to x_b (or volume), as is necessarily the case, for example, in the differential parameter ϵ_T defined by

$$\epsilon_T=-(\partial\ \ln P/\partial\ \ln v)_T, \tag{19}$$

[6] M. G. Mayer derived this result independently of (and prior to) the considerations of this paper. It follows directly from the quadrature expression (22) for the entropy, since every thermodynamic function can be derived from the entropy. There is a slight difference between the result obtained by the method of Mayer and the result by the method of this paper: in the former case, thermodynamic functions are expressed in terms of quadratures on ϕ, while the method of this paper expresses them in terms of quadratures on ϕ and $d\phi/dx$ (since ϕ is given in tabular form for a solution, $d\phi/dx$ is also directly available). The pressure obtained by Mayer's method contains an integral on the function $\partial\phi/\partial x_b$, which is not obtained usually in a solution.

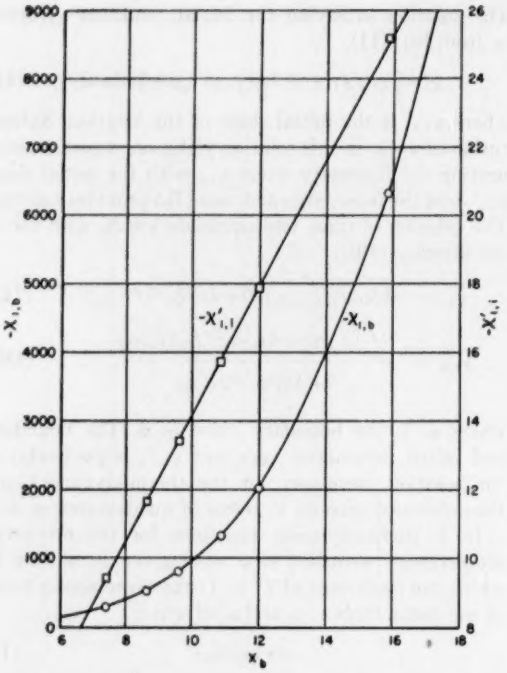

FIG. 1. Fitted functions for $\chi_{1,b}$ and $\chi_{1,i}'$ against boundary radius; first-order temperature-perturbed case.

and evaluated in I as

$$\epsilon_T=\epsilon_0-[(5/6)d\sigma/d\ \ln x_b+4\epsilon_0\tau]\zeta_1(kT)^2, \qquad (20)$$

where $\epsilon_0=(5/6)(1-d\ \ln\phi_b/d\ \ln x_b)$ corresponds to zero temperature.

The basic thermodynamic functions do not involve σ, τ, or ω differentially. In such a case, the coefficient of T^2 or T in the first-order perturbation can be evaluated algebraically in terms of quadratures on ϕ. Thus, the pressure P from Eq. (17) becomes

$$P=p\left\{1+5\left[\frac{x_b^2}{\phi_b^2}-\frac{6J_{12}(f_1,x_b)}{9+4x_b^{\frac{1}{2}}\phi_b^{5/2}J_1(x_b)}\right]\zeta_1(kT)^2\right\}. \qquad (21)$$

Computation of the entropy S in this manner yields the result of Mayer[3]

$$S=4(Z^2e^2/\mu)\zeta_1k^2T\int_0^{x_b}x^{\frac{1}{2}}\phi^{\frac{1}{2}}dx, \qquad (22)$$

where the special result

$$J_2(f_1,x)=\frac{2}{3}\left[x^{5/2}\phi^{\frac{1}{2}}-\int_0^x x^{\frac{1}{2}}\phi^{\frac{1}{2}}dx\right] \qquad (23)$$

for a first-order perturbation has been used. The energy U is

$$U=u+2(Z^2e^2/\mu)\zeta_1(kT)^2\int_0^{x_b}x^{\frac{1}{2}}\phi^{\frac{1}{2}}dx, \qquad (24)$$

where u is the energy at zero temperature corresponding to the unperturbed atom of the same volume, given by

$$u=(Z^2e^2/\mu)[(3/7)(\phi_i'-\phi_{i,\infty}')+(2/35)x_b^{\frac{1}{2}}\phi_b^{5/2}], \qquad (25)$$

in terms of the initial slope ϕ_i' and boundary value ϕ_b of $\phi(\phi_{i,\infty}'$ is the initial slope corresponding to an infinite atom). The quadrature expressions of the enthalpy, and of the Helmholtz and Gibbs functions follow directly. The method of Mayer[3,6] does not yield the pressure, enthalpy, or Gibbs function in the form of an algebraic function of quadratures on ϕ, since the pressure must be determined from Eq. (22) by means of the relation $(\partial P/\partial T)_v=(\partial S/\partial v)_T$.

The statement made without proof in I that $\chi_{1,b}$ and $\chi_{1,i}'$ are monotonic functions of the radius x_b follows directly from Eqs. (14).

b. Numerical Results

The quadrature expressions (14) have been applied to the six neutral-atom zero-temperature solutions available from the work of FMT to obtain accurate values by numerical integration of the corresponding parameters $\chi_{1,b}$ and $\chi_{1,i}'$. The results are tabulated in Table I against the radius of the unperturbed atom to which they correspond, with those of I for comparison. The tabulated results have been fitted by expressions of the form

$$\chi_{1,b}=\sum_n C_n x_b^n, \quad \chi_{1,i}'=[\sum_m D_m x_b^{-m}]^{-1}, \qquad (26)$$

in which $n=3$, n', 5, and $m=1-\lambda_2$, m', 2, where $\lambda_2=[(73)^{\frac{1}{2}}-7]/2$ and n', m' are disposable exponents. The pair of coefficients C_3, D_2 and the pair C_5, $D_{1-\lambda_2}$ are chosen (with the corresponding exponents) to yield the proper asymptotic behavior of the fitted functions in the two limits $x_b\to 0$ and $x\to\infty$, respectively; thus $C_{n'}$ and $D_{m'}$ are the only disposable coefficients. The values of $C_{n'}$ and $D_{m'}$ (and their corresponding exponents) are tabulated in Table II, in conjunction with the values of the other coefficients from I. The tabulated coefficients yield fitted functions which reproduce the data of Table I within less than 0.4 percent in the cases of both $\chi_{1,b}$ and $\chi_{1,i}'$. The fitted functions and the data points are shown in Fig. 1.

Values of the parameters σ and ω computed from these fitted functions and from the fitted function for ϕ_b given in I are shown in Fig. 2 with the directly com-

TABLE I. Boundary and initial parameters, first-order temperature perturbation.

x_b	$-\chi_{1,b}$	$-\chi_{1,i}'$	$-\chi_{1,b}$ (from I)	$-\chi_{1,i}'$ (from I)
7.3851	$297._9$	9.41_5		
8.5880	$532._7$	11.6_2		
9.5651	$810._6$	13.4_2	$81_{2.}$	$13._4$
10.8038	$131_{7.}$	15.7_4	$13_{20.}$	$15._7$
11.9634	$198_{5.}$	17.9_1		
15.8698	$634_{7.}$	25.1_3	$64_{20.}$	$24._8$

puted values for comparison (the parameter τ from results of I is shown likewise). In Fig. 3, the effect of the first-order temperature perturbation on the equation of state is shown graphically by plotting $Z^{-\frac{1}{2}}(kT/R)^{-2}\times(P-p)$, which is independent of T, as a function of Zv (R is the Rydberg); the energy perturbation $U-u$ in units of R is shown similarly. The value of $Z^{\frac{1}{2}}(kT/R)^{-\frac{1}{2}}S$ in $R/°K$ differs from $Z^{\frac{1}{2}}(kT/R)^{-2}(U-u)$, as plotted, by the numerical factor 1.27×10^{-5}. The dimensionless parameters ϵ_T and γ, defined by Eq. (19) and by $U=Pv/(\gamma-1)$, respectively, are shown in similar fashion in Fig. 4 (γ_0 corresponds to zero temperature).

3. GENERAL TEMPERATURE PERTURBATION

The functions f_n of Eq. (6) are

$$f_2=(x\phi)^{-\frac{1}{2}}\left\{\frac{x^4}{\phi^2}-\frac{a_1^2}{a_2}\left[\frac{1}{2}\frac{x^2}{\phi}\chi_1-\tfrac{3}{8}\chi_1^2\right]\right\}, \tag{27a}$$

$$f_3=(x\phi)^{-\frac{1}{2}}\left\{\frac{x^6}{\phi^4}+\frac{a_1^3}{a_3}\left[\frac{3}{8}\frac{x^2}{\phi^2}\chi_1^2-\frac{1}{16\phi}\chi_1^3\right]-\frac{a_1a_2}{a_3}\left[\frac{5}{2}\frac{x^4}{\phi^3}\chi_1+\frac{1}{2}\frac{x^2}{\phi}\chi_2-\tfrac{3}{4}\chi_1\chi_2\right]\right\}, \tag{27b}$$

for $n=2, 3$. A general (but rather complex) formula can be given for arbitrary n. The general solution of the differential perturbation equation of nth order is, from Eq. (11),

$$\chi_n=[\chi_{n,i}'J_1(x)+J_{21}(f_n,x)][\phi+(1/3)xd\phi/dx], \tag{28}$$

where $\chi_{n,i}'$ is the initial slope of the solution. It has been shown in the preceding that χ_1 can be expressed in terms of quadratures on ϕ. It follows by induction that f_n (which in the first instance is a function of x, ϕ and $\chi_1, \chi_2, \cdots, \chi_{n-1}$) and thus χ_n can be so expressed. The boundary value $\chi_{n,b}$ and initial slope $\chi_{n,i}'$ of χ_n are then obtainable from the equations derived by replacing f_1 with f_n in Eqs. (14a) and (14b), respectively. Thus the solution of the perturbation equation of nth order and the associated boundary and initial parameters can all be expressed in terms of quadratures on ϕ.

The thermodynamic functions that are available directly from a solution of the Thomas-Fermi equation are essentially the pressure and the volume. The pressure P is given by the asymptotic series,

$$P=\frac{Z^2e^2}{10\pi\mu^4}\left(\frac{\Phi_b}{x_b}\right)^{5/2}\left[1+\sum_n\frac{5\zeta_n}{5-4n}\left(\frac{kTx_b}{\Phi_b}\right)^{2n}\right], \tag{29}$$

where Φ_b, given by

$$\Phi_b=\phi_b+\sum_n\chi_{n,b}\zeta_n(kT)^{2n}, \tag{30}$$

is the boundary value of Φ. Thus, the pressure can be expressed as an asymptotic series in T^2, with coefficients which can be evaluated in terms of quadratures on ϕ. From I, the energy[7] E is given by

$$E=\tfrac{3}{4}T^{7/4}\int_0^T T^{-\frac{1}{2}}(\partial/\partial T)_v\times\{T^{-1}[Pv+(Z^2e^2/\mu)\Phi_i']\}dT, \tag{31}$$

where the integration is carried out at constant volume, and Φ_i', defined by

$$\Phi_i'=\phi_i'+\sum_n\chi_{n,i}'\zeta_n(kT)^{2n}, \tag{32}$$

is the initial slope of Φ. If this series for Φ_i' and the series (29) for P are substituted into Eq. (31), E can

TABLE II. Coefficients[a] of fitted functions, first-order temperature perturbation.

n	C_n	m	D_m
3	-3.205×10^{-1}	$1-\lambda_2=0.2280$	-5.805×10^{-3}
$n'=4.059$	-3.424×10^{-2}	$m'=0.8159$	-2.325×10^{-1}
5	-2.519×10^{-3}	2	-3.120

[a] The coefficients are given to four figures to minimize round-off error.

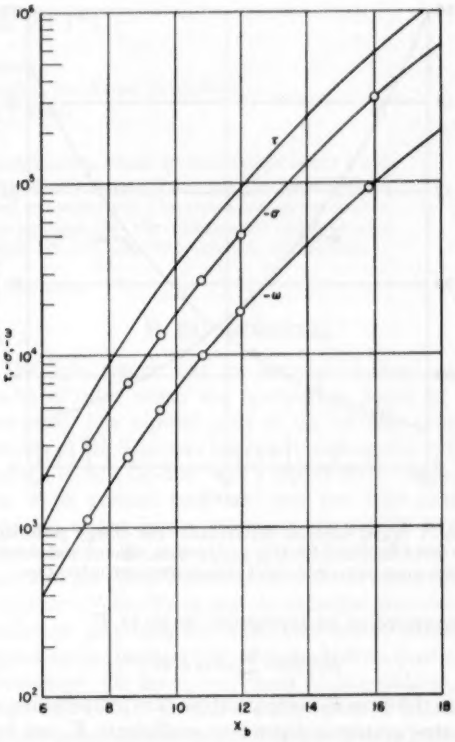

FIG. 2. Perturbation parameters σ, τ, and ω from fitted functions for $\chi_{1,b}$, $\chi_{1,i}'$, and ϕ_b, against boundary radius; first-order temperature-perturbed case.

[7] The energy E differs from U introduced previously by the energy corresponding to a standard state (an infinite atom at zero temperature).

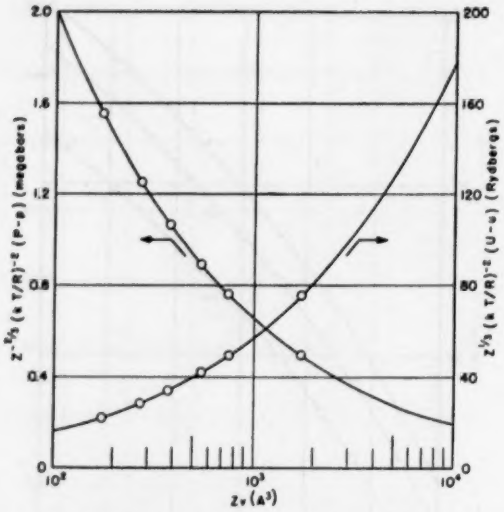

FIG. 3. Scaled pressure perturbation and energy perturbation from fitted functions for $\chi_{1,b}$, $\chi_{1,i}'$, and ϕ_b, against scaled volume in cubic angstroms; first-order temperature-perturbed case.

be expressed as an asymptotic series in T^2,

$$E=E_0+\sum_n E_n\zeta_n(kT)^{2n}, \tag{33}$$

where the term E_0 corresponds to zero temperature, and the temperature-independent coefficients E_n are functions in the first instance of x_b, ϕ_b; $\chi_{1,b}$, $\cdots$, $\chi_{n,b}$; $\chi_{1,i}'$, $\cdots$, $\chi_{n,i}'$. Thus, the energy likewise can be expressed as an asymptotic series in T^2, with coefficients in terms of quadratures on ϕ. This expansion is analogous to the corresponding result[8] in the case of a degenerate Fermi-Dirac gas. From the energy, one can obtain every thermodynamic function by algebraic, differential, or integral processes. Hence the result follows: every thermodynamic function at low temperature can be written as an asymptotic series, either in the even or the odd powers of the temperature, with coefficients in terms of quadratures on ϕ. This statement is the generalization to a perturbation of nth order of Mayer's result for the case $n=1$ cited previously.

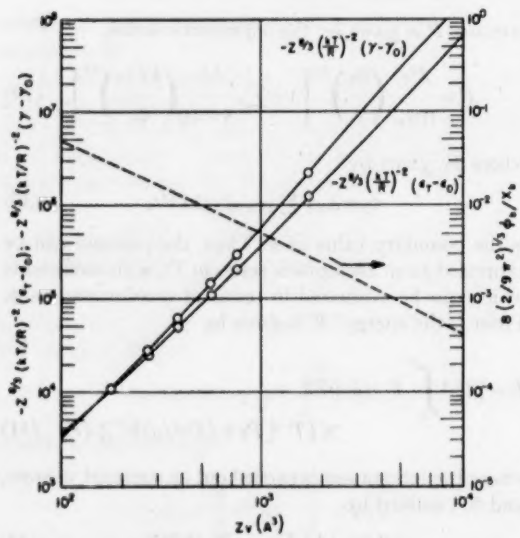

FIG. 4. Scaled perturbations in parameters γ and ϵ_T from fitted functions, against scaled volume in cubic angstroms; first-order temperature-perturbed case. The scaled temperature $Z^{-4/3}kT/R$ must be small relative to the quantity shown by the dashed curve.

The coefficients of the asymptotic series corresponding to the basic thermodynamic functions can be written in algebraic form in terms of quadratures on ϕ. This statement is obvious in the case of the pressure and the energy, from which it follows for the enthalpy. The entropy S, from Eq. (33) and the relation $T(\partial S/\partial T)_v=(\partial E/\partial T)_v$, is

$$S=\sum_n[2n/(2n-1)]E_n\zeta_n k^{2n}T^{2n-1}, \tag{34}$$

from which the statement follows for the corresponding coefficients. The result for the Helmholtz and Gibbs functions then follows directly.

The method of this paper of solving the temperature-perturbed Thomas-Fermi equation can be used likewise to obtain a solution of the Thomas-Fermi-Dirac[2] equation in powers of the parameter $\epsilon=(3/32\pi^2)^{\frac{1}{3}}Z^{-\frac{1}{3}}$. The corresponding approximation improves for higher Z and for higher compressions. To a degree depending on the powers of ϵ retained, it should be valid except at the immediate boundary of the limiting atom (atom of largest radius); the type of difficulty that enters at this boundary is the same as appears in Sommerfeld's perturbation treatment of the positive ion.[9] This approximation yields a method of determining the exchange correction to the binding energy of an atom, alternative to that of Scott[10] or March.[11] Difficulties associated with the boundary of the atom should be unimportant in this application, since the boundary region of the limiting atom contributes little to the energy.

The author wishes to thank Professor M. G. Mayer of the University of Chicago for the communication of a number of results prior to publication. He is indebted to Dr. G. H. Peebles of the Rand Corporation, who carried out the numerical integrations with the computational assistance of Miss E. Force. Thanks are due to Dr. A. L. Latter of the Rand Corporation for a number of discussions.

[8] J. E. Mayer and M. G. Mayer, *Statistical Mechanics* (John Wiley and Sons, Inc., New York, 1940), p. 374.
[9] A. Sommerfeld, Z. Physik **78**, 283 (1932).
[10] J. M. C. Scott, Phil. Mag. **43**, 859 (1952).
[11] N. H. March, Phil. Mag. **44**, 1193 (1952).

Isotope Shift in Hf I*†

J. A. COLLINSON‡
Sloane Physics Laboratory, Yale University, New Haven, Connecticut

(Received August 5, 1954)

The hyperfine structure in $_{74}$Hf I lines has been resolved and found to consist of either a single line or a well resolved doublet. The components of the doublets are attributed to isotopes 178 and 180. The magnitudes of these shifts have been determined using several independent measurements. The typical size of the doublet separations is about 0.035 K. The arrangement of the shifts indicates that the configuration responsible for seven low-energy levels is $5d^26s^2$. The structure due to isotopes 176, 177, and 179 is nowhere well resolved.

I. INTRODUCTION

SPECTROSCOPIC isotope shift at the heavy end of the periodic table is, in the main, the product of the change in the average extension of nuclear charge between isotopes of a given element. The effect has therefore been recognized for some time as a source of information on nuclear properties. Several anomalies, however, appear when the data are compared to the simple volume theory.[1] Perhaps the most troublesome of these is the average smallness[2] of shifts as compared to the values predicted by the theory, taking the nuclear radius to be given by $1.4\times10^{-13}A^{\frac{1}{3}}$. A smaller coefficient in the expression could give agreement, but this possibility was not advanced very firmly for some time. Now, however, recent work on high energy electron scattering and on the gamma-ray spectrum of the μ-mesonic atom points to a nuclear radius substantially smaller than the previously accepted value. This has served to underscore the potential value of isotope shift data.

Isotope shift can further be of assistance in the assignment of terms to electron configurations in the spectrum under examination. Wilets and Bradley emphasize this in their study[3] of isotope shift in Er, where the work was carried out partly to further the analysis of the Er spectra. The latest published analysis[4] of the Hf I spectrum is incomplete and private communication with Meggers revealed that this spectrum has been persistently difficult. Meggers expressed a hope that the data which follow would be of aid.

A survey of the literature showed an obvious gap in knowledge of isotope shift at Hf. Rasmussen[5] reports only on nine lines and, of these, on only two quantitatively. The present work was undertaken, therefore, to extend the data on Hf as far as possible.

II. EXPERIMENTAL

The light source was the standard hollow cathode discharge tube, which was operated at liquid air temperatures. The exposed area of the cathode consisted entirely of Hf. This was machined from a solid cylinder $\frac{1}{4}$ in.$\times\frac{3}{8}$ in. to a taper fit with a copper shell. The sample was 98.98 percent pure and was the very generous donation of the Foote Mineral Company of Berwyn, Pennsylvania. This sample produced a brilliant, clean spectrum for many hundreds of hours of operation.

A quartz Fabry-Perot was the principal instrument of resolution. For this, the flats were kindly loaned by Dean George Harrison of the Massachusetts Institute of Technology. On these, very good Al-Mg surfaces were prepared by O. H. Arroe of the University of Wisconsin; for this generous service the writer is greatly indebted. Six spacers were fabricated from quartz tubing of approximate lengths 2, $2\frac{1}{2}$, 3, $3\frac{1}{2}$, 4, and $4\frac{1}{2}$ cm. Auxiliary dispersion was provided by a large Hilger prism Littrow mounting spectrgoraph. Quartz and glass elements were used to cover the range 2900 to 7000A.

III. RESULTS

The structure consisted of a singlet in 11 lines and of a well resolved doublet on an unresolved background in 63 others. In view of the isotopic composition of natural hafnium, the doublets are expected to correspond to appreciable shifts between isotopes 178 and 180. The isotopic abundances in the naturally occurring material are the following:

Isotope	174	176	177	178	179	180
Abundance (%)	0.18	5.2	18.4	27.1	13.8	35.3

In most cases the relative intensities of components in the doublets made possible simple and unambiguous identification of direction of shift. In a number of lines, however, early examination of structure which had been produced by the lower resolution of smaller spacers revealed relative intensities which appeared to be very nearly equal. Improvement of the resolution later showed the correct directions in these cases and furthermore made it clear that all cases of apparent "negative" direction were in fact all instances of the more common "positive" direction.

* Part of a dissertation presented for the degree of Doctor of Philosophy at Yale University.

† Supported in part by the U. S. Atomic Energy Commission.

‡ Now at Photo Products Research Division, E. I. du Pont de Nemours and Company, Inc., Parlin, New Jersey.

[1] J. H. Bartlett, Nature **128**, 408 (1931); G. Racah, Nature **129**, 723 (1932); J. E. Rosenthal and G. Breit, Phys. Rev. **41**, 459 (1932); G. Breit, Phys. Rev. **42**, 348 (1932).

[2] See, principally, M. F. Crawford and A. L. Schawlow, Phys. Rev. **76**, 1310 (1949); P. Brix and H. Kopfermann, Z. Physik **126**, 344 (1949).

[3] L. Wilets and L. C. Bradley, Phys. Rev. **87**, 1018 (1952).

[4] W. F. Meggers and B. F. Scribner, J. Research Natl. Bur. Standards **4**, 169 (1930).

[5] E. Rasmussen, Naturwiss. **23**, 69 (1935).

When the resolution had been improved enough to show that all resolved shifts were positive, the source of the previous misidentification of direction was fully revealed. Generally in these cases the magnetic splitting of the odd isotopes was sufficiently small that, with relatively poor resolution, the blackening of the plate from the radiation of isotopes 177 and 179 caused the 178 component to appear very definitely more intense. Improved resolution characteristically revealed a pronounced shoulder on the short wavelength side of the true 178 component, and it also reversed the *apparent* relative intensities.

Nowhere was the resolution of the components from isotopes 177 and 179 good enough to permit any conclusions regarding either the character of the possible magnetic splitting or the separation of the center of the 177 "shoulder" from the 178 component.

The magnitudes of the measured shifts between isotopes 178 and 180 are listed in Table I for each line in the Hf I spectrum in which the structure was resolved. An effort was made to obtain values for each shift by using four spacer sizes, but often the exposures with a certain spacer size were not resolved for some line. The number of independent values obtained for any shift is therefore given. The values of shifts listed represent averages of the quantities obtained by using the different spacers. The errors indicate simply the spreads of measured values; a good deal of systematic error from alterations in the pattern caused by the magnetic splitting might not be represented by the errors stated. The lines marked by asterisks were assigned to the Hf I spectrum according to the relative arc and spark intensities given by Meggers,[6] since the lines do not appear in any analysis.

TABLE I. Isotope shifts in Hf I (1 K = 1 kayser = 1 cm^{-1}).[a]

λ(A)[a]	Mean shift, $\Delta\nu_{178-180}(10^{-3}$ K)	No. of values	λ(A)[a]	Mean shift, $\Delta\nu_{178-180}(10^{-3}$ K)	No. of values
6818.94	Single		3858.30	37.0±1.9	4
6789.27	30.8±1.5	4	3849.17	45.2±1.6	4
6386.23	29.4±1.0	4	3820.74	33.3±0.5	4
6238.58	Single		3811.76	37.9±2.5	4
6098.67	33.2±1.6	4	3800.39	31.1±2.0	2
5902.94	27.1±1.6	4	3785.46*	37.2±2.3	4
5719.18	Single		3777.64	Single	
5613.27	28.5±1.1	4	3733.78	37.5±1.4	4
5552.12	Single		3717.80	39.3±2.4	4
5550.60	27.9±2.4	3	3696.52	32.8±1.6	3
5452.92*	40.2±1.3	3	3682.25	33.2±1.3	3
5438.74	Single		3649.09	39.7±1.9	3
5373.86	29.6±3.0	4	3630.86	23.1±1.2	2
5294.87	27.9±3.1	4	3616.89	33.1±0.9	4
5243.99	42.8±0.8	3	3615.05	37.4±1.6	4
5181.86	22.6±1.4	4	3536.62	35.5±1.9	3
5112.13	42.8±1.5	3	3523.02	31.6±2.0	3
4975.25	37.5±1.1	5	3497.49	33.4±0.6	4
4837.24	23.6±7.0	1	3472.38	28.6±0.8	2
4800.50	Single		3417.35	43.9±1.6	4
4773.72	Single		3332.73	31.6±1.5	3
4655.19	40.1±2.8	4	3312.87	42.4±1.5	4
4620.87*	36.5±4.5	4	3306.12	45.2±0.6	4
4565.94	27.9±1.7	4	3206.11	38.7±1.9	3
4540.92	34.1±1.1	4	3189.63	32.5±3.5	2
4461.17	35.0±4.0	2	3172.94	43.7±3.8	4
4457.35*	37.4±1.3	4	3168.39	Single	
4438.02	38.9±3.2	3	3162.57	39.2±4.0	4
4356.29*	37.0±3.7	4	3156.68	45.8±3.2	4
4294.77	33.7±2.2	4	3131.81	53.4±4.8	4
4228.08	Single		3080.84	41.2±1.0	3
4174.33	29.8±0.7	4	3072.88	37.9±4.4	3
4145.76	36.2±4.9	4	3067.41	35.7±2.2	3
4062.84*	Single		3057.02*	41.5±2.2	4
4032.27	35.5±5.0	3	3050.76	46.3±3.9	4
3951.81	37.3±2.3	4	2964.88	44.6±6.8	2
3899.93	31.0±1.4	4	2950.68	48.5±4.4	3

[a] The lines marked by asterisks were assigned to the Hf I spectrum according to the relative arc and spark intensities given by Meggers (see reference 6).

An examination of the data in terms of the energy level scheme for Hf I is not possible since the analysis for the first Hf spectrum is not complete. It is therefore not possible to calculate the isotope shift constant for Hf nor even to determine the shifts produced in a given term by the presence of a 6*s* electron.

Meggers and Scribner,[4] in their tentative analysis of the Hf I spectrum, give a matrix arrangement which displays the wave number positions of seven low energy levels, the wave number positions of 63 high energy levels and the wave numbers and wavelengths of various transitions between low and high levels. The form is such that any horizontal line across the matrix will select transitions from a single high energy level to the various low levels. Now the electron configurations which can produce the terms evidently responsible for the seven low levels are $5d^26s^2$ and $5d^36s$. And each configuration could produce any or all of these terms, which are ^3F, ^1D, and ^3P. But comparison of these isotope shifts with the matrix shows that without exception the shift is of essentially the same character for every line contained in a single horizontal row. Where the shifts have been resolved, every line in a single row is either single or else every line is double. Hence, a single electron configuration must be responsible for each low energy level, since the configurations have different numbers of 6*s* electrons and would produce different shifts in the low levels. This configuration is, presumably, the $5d^26s^2$ of the ground state.

In the only previous work on the isotope shift in Hf, Rasmussen[5] reported the structure in nine lines. The lines λλ5550, 5452, 5373, 5243, and 4655 were given as double, with the intervals in λλ5550 and 5452 of the respective sizes 0.035 K and 0.043 K. These are somewhat larger than the values obtained here. λλ5613, 5552, 4837, and 4800 were all reported as single, while λ5613 and λ4837 here very definitely appeared double. Rasmussen states that, on the basis of the observed number of components apparently produced by magnetic splitting of the odd isotopes, the spins of both the 177 nucleus and the 179 nucleus are probably either ½ or

[6] W. F. Meggers, J. Research Natl. Bur. Standards **1**, 151 (1928).

$\frac{3}{2}$. It is impossible to confirm this from the structure observed in any line.

Further work is being done on samples enriched in the isotopes 174 and 176 in order to determine the shifts 174–176 and 176–178. The interference systems on hand at this writing do not warrant even qualitative conclusions, however.

Professor W. W. Watson provided assistance and encouragement throughout this work, and this is gratefully acknowledged.

PHYSICAL REVIEW VOLUME 96, NUMBER 4 NOVEMBER 15, 1954

Electronic Polarizabilities of Ions from the Hartree-Fock Wave Functions*†

R. M. STERNHEIMER
Brookhaven National Laboratory, Upton, New York

(Received August 9, 1954)

The electronic polarizability α has been calculated for several ions by obtaining the perturbation of the wave functions by an external field from a numerical solution of the differential equation satisfied by the perturbation. For the helium-like ions an analytic solution was obtained by using the wave functions of Löwdin. The calculated values of α are, in general, between 1 and 1.5 times the observed values. For several ions values have been calculated for the quadrupole polarizability which measures the quadrupole moment induced in the ion by an external charge. The effect of the dipole moment induced in the ion on the electric field at the nucleus is discussed.

I. INTRODUCTION

THE electronic polarizability of ions has been determined by a number of different methods. The polarizability can be obtained from the index of refraction of the ion in solutions or in crystals. An independent method consists in a consideration of the Rydberg-Ritz correction for the spectral series of atoms. Following Born and Heisenberg,[1] the deviation of the spectral terms of the alkalis from hydrogenic levels is attributed to the polarization of the core by the valence electron. This procedure to obtain the polarizability was also used by Mayer and Mayer.[2] The determination of the polarizability from the index of refraction of solutions was first carried out by Heydweiller[3] and by Fajans and Joos.[4] While the present work was in progress, there appeared a paper by Tessman, Kahn, and Shockley[5] who made a determination of the ionic polarizabilities from the experimental refraction data of crystals containing the ions considered.[6]

In contrast to the variety of experimental determinations of the polarizability α, there exist comparatively few theoretical treatments which attempt to explain the values of α in terms of the electronic structure of the ion. Pauling[7] derived an analytic expression for α for electrons which move in a pure Coulomb field (hydrogenic wave functions). He used this expression with appropriate screening constants for the helium-like ions and obtained good agreement with the observed values of α. This method is not expected to give accurate results for medium and heavy ions since the electronic wave functions are very different from hydrogenic wave functions in this case. Buckingham[8] obtained an expression relating α to the average values of r^2 for the various electron shells, where r is the distance between the nucleus and an electron of the core. This expression was derived from a variational calculation in which the perturbed wave function for each shell was taken as a preassigned function times a parameter which was varied to minimize the energy. Although different parameters were used for the different subshells, this procedure probably does not always give a good approximation to the actual perturbed function, because only a single parameter for each subshell is available in the variational calculation.

In the present paper, values of α are obtained for nine ions from F^- to Cs^+ by means of a numerical solution of the differential equation for the perturbation of the electronic wave functions for the various shells. For the unperturbed wave functions, the Hartree-Fock functions of the ions are used. For the helium-like ions an approximate analytic solution for the perturbation based on the wave functions of Löwdin[9] will be employed. The calculated values of α lie, in general, between 1 and 1.5 times the experimental values. Thus the calculations are in reasonable agreement with ex-

* Work done under the auspices of the U. S. Atomic Energy Commission.

† A preliminary account of this work was presented at the April 29–May 1, 1954 Meeting of the American Physical Society in Washington, D. C. [Phys. Rev. 95, 594 (1954)].

[1] M. Born and W. Heisenberg, Z. Physik 23, 388 (1924).

[2] J. E. Mayer and M. G. Mayer, Phys. Rev. 43, 605 (1933).

[3] A. Heydweiller, Physik. Z. 26, 526 (1925).

[4] K. Fajans and G. Joos, Z. Physik. 23, 1 (1924).

[5] Tessman, Kahn, and Shockley, Phys. Rev. 92, 890 (1953).

[6] An extensive discussion of the work on polarizabilities is given by J. H. Van Vleck, *The Theory of Electric and Magnetic Susceptibilities* (Oxford University Press, London, 1932), first edition, Chap. VIII.

[7] L. Pauling, Proc. Roy. Soc. (London) A114, 181 (1927).

[8] R. A. Buckingham, Proc. Roy. Soc. (London) A160, 94 (1935).

[9] P. O. Löwdin, Phys. Rev. 90, 120 (1953).

periment. The tendency for the calculated values to be somewhat too large is probably due to the fact that the Hartree-Fock wave functions give less binding and are more external than the actual wave functions. An increase of the binding would be accompanied by a decrease of α. The agreement of the present values of α with experiment is on the whole better than that obtained by Buckingham.[8]

Besides the dipole polarizability α, it is of interest to consider the quadrupole polarizability which will be defined as the ratio of the quadrupole moment induced in the ion by the field of an external charge to the field gradient at the nucleus produced by the charge. The quadrupole polarizability α_q was first introduced by Mayer and Mayer.[2] In the present paper, values of α_q have been calculated analytically for the helium-like ions and numerically for the Na^+ and Cs^+ ions. The last section of this paper gives a discussion of the electric field at the nucleus due to the dipole moment induced in the ion by the field of an external charge.

II. EXPRESSION FOR THE POLARIZABILITY

Assume that the electric field is produced by a unit charge $+e$ at a large distance R from the nucleus along the positive X axis. If R is in units of the Bohr radius a_H, the dipole part of the potential energy (in Rydberg units) is given by

$$H_1=-(2/R^2)r\cos\theta, \tag{1}$$

where θ is the angle between the X axis and the radius vector (of length r) from the nucleus to an electron in the core. The unperturbed wave function times r for a core electron will be denoted by u_0. Let u_1 denote r times the perturbation of the wave function due to H_1, and let E_1 by the first-order perturbation of the energy. H_0 and E_0 will denote the unperturbed Hamiltonian and energy, respectively. The Schrödinger equation to the first order in H_1 is given by

$$(H_0+H_1)(u_0+u_1)=(E_0+E_1)(u_0+u_1). \tag{2}$$

E_1 is given by

$$E_1=\int_0^\infty\int_0^\pi\int_0^{2\pi}H_1u_0^2dr\,\sin\theta d\theta d\varphi, \tag{3}$$

where φ is the azimuthal angle. Since H_1 is linear in $\cos\theta$ while u_0^2 is an even function of $\cos\theta$, the integral over θ vanishes, so that $E_1=0$. By subtracting from Eq. (2) the unperturbed Schrödinger equation,

$$H_0u_0=E_0u_0, \tag{4}$$

one obtains the equation for u_1:

$$(H_0-E_0)u_1=-H_1u_0. \tag{5}$$

In the following, u_0 will be normalized according to

$$\int_0^\infty\int_0^\pi\int_0^{2\pi}u_0^2dr\,\sin\theta d\theta d\varphi=1. \tag{6}$$

u_0 will be written

$$u_0=(2\pi)^{-\frac{1}{2}}u'_0\Theta_l^m\exp(im\varphi), \tag{7}$$

where u'_0 is the radial wave function (times r), l=azimuthal quantum number, m=magnetic quantum number, Θ_l^m is the angular eigenfunction with the choice of phases as given in Condon and Shortley.[10] u_0' and Θ_l^m are normalized according to

$$\int_0^\infty u'^2_0dr=\int_0^\pi|\Theta_l^m|^2\sin\theta d\theta=1. \tag{8}$$

The first-order perturbation of the density $[(u_0+u_1)^2]$ is given by $2u_0u_1$ for each core electron. Hence, the induced dipole moment which will be called $p_{\text{ind. }X}$ is given by

$$p_{\text{ind. }X}=-2e\sum_{nlm}\int_0^\infty\int_0^\pi\int_0^{2\pi}(u_0u_1)_{nlm}r\times\cos\theta dr\,\sin\theta d\theta d\varphi, \tag{9}$$

where n is the principal quantum number, and the sum extends over all electrons of the core. Since the density $2u_0u_1$ depends on n, l, and m, it has been labeled $2(u_0u_1)_{nlm}$. The field E_X is $-e/R^2$, so that the polarizability is given by

$$\alpha=p_{\text{ind. }X}/E_X=2R^2\sum_{nlm}\int_0^\infty\int_0^\pi\int_0^{2\pi}(u_0u_1)_{nlm}r\times\cos\theta dr\,\sin\theta d\theta d\varphi. \tag{10}$$

We will now obtain an expression for α in terms of the radial functions by integrating over θ and φ, and performing the sum over the magnetic quantum numbers m for each shell.

The contribution of the s shells will be considered first. Since $\Theta_0^0=2^{-\frac{1}{2}}$, u_0 can be written

$$u_0=(2\pi)^{-\frac{1}{2}}2^{-\frac{1}{2}}u'_0. \tag{11}$$

Thus the right hand side of (5) becomes in view of (1),

$$-H_1u_0=(2\pi)^{-\frac{1}{2}}2^{\frac{1}{2}}R^{-2}u'_0r\cos\theta. \tag{12}$$

If Rydberg units are used, H_0 is given by

$$H_0=-\nabla^2+V_0, \tag{13}$$

where V_0 is the unperturbed potential in which the electron moves. Equation (12) shows that u_1 is a p wave. u_1 can be written

$$u_1=(2\pi)^{-\frac{1}{2}}2^{\frac{1}{2}}R^{-2}u'_{1,0\to1}\cos\theta, \tag{14}$$

where $u'_{1,0\to1}$ is the radial function which is determined by

$$\left(-\frac{d^2}{dr^2}+\frac{2}{r^2}+V_0-E_0\right)u'_{1,0\to1}=u'_0r. \tag{15}$$

[10] E. U. Condon and G. H. Shortley, *The Theory of Atomic Spectra* (Macmillan Company, New York, 1935), p. 52.

Here and in the following the notation $u'_{1,l\to l'}$ denotes the radial function for the excitation of a state with azimuthal quantum number l into states with azimuthal quantum number l'. Upon inserting Eqs. (11) and (14) into Eq. (10) one obtains for the contribution of both ns electrons to α:

$$\alpha(ns\to p)=4R^2\int_0^\infty\int_0^\pi\int_0^{2\pi}u_0u_1r\cos\theta dr\sin\theta d\theta d\varphi \tag{16}$$
$$=(8/3)\int_0^\infty u'_0u'_{1,0\to1}rdr.$$

The procedure of the numerical solution of Eq. (15) will be described in Sec. III. Here we note that for the $1s$ shell, if u'_0 is assumed to be a hydrogenic wave function, Eq. (15) has an exact solution, as was shown previously.[11] Thus if the unperturbed function is taken as

$$u'_0=2Z^{\frac{1}{2}}r\exp(-Zr) \tag{17}$$

with an appropriate value of the effective atomic number Z (including screening), then $u'_{1,0\to1}$ is given by

$$u'_{1,0\to1}=Z^{-\frac{1}{2}}r^2\exp(-Zr)[1+(Z/2)r], \tag{18}$$

as can be verified by substitution in Eq. (15). Upon inserting (17) and (18) into (16), one obtains

$$\alpha(1s\to p)=(9/Z^4)a_{\mathrm{H}}{}^3. \tag{19}$$

This is a well-known result which has been derived previously by Pauling[7] and others.[6]

The contribution of the p shells to α will now be obtained. The electrons with $m=0$ will be considered first. The unperturbed function is given by

$$u_0{}^{(0)}=(2\pi)^{-\frac{1}{2}}(3/2)^{\frac{1}{2}}u'_0\cos\theta. \tag{20}$$

Here and in the following the superscript of $u_0{}^{(m)}$ indicates the magnetic quantum number. In view of Eqs. (1) and (20), $-H_1u_0{}^{(0)}$ is given by

$$-H_1u_0{}^{(0)}=(2\pi)^{-\frac{1}{2}}(2/3)^{\frac{1}{2}}R^{-2}u'_0[(3\cos^2\theta-1)+1], \tag{21}$$

where the square bracket is written as the sum of a d function and an s function; these terms give rise to excited d waves and s waves, respectively. The $np\to d$ excitation will be considered first. In view of (5) and (13), the excited wave function is given by

$$u_{1,1\to2}{}^{(0)}=(2\pi)^{-\frac{1}{2}}(2/3)^{\frac{1}{2}}R^{-2}u'_{1,1\to2}(3\cos^2\theta-1), \tag{22}$$

where the radial function $u'_{1,1\to2}$ is determined by

$$\left(-\frac{d^2}{dr^2}+\frac{6}{r^2}+V_0-E_0\right)u'_{1,1\to2}=u'_0r. \tag{23}$$

In Eq. (22) and in the following, $u_{1,l\to l'}{}^{(m)}$ denotes r times the wave function for the excitation of an electron with azimuthal quantum number l and magnetic quantum number m into states with azimuthal quantum number l'. The details of the numerical solution of Eq. (23) are given in Sec. III. Upon inserting Eqs. (20) and (22) into (10), one obtains for the contribution of both $m=0$ electrons to α,

$$\alpha^{(0)}(np\to d)=4R^2\int_0^\infty\int_0^\pi\int_0^{2\pi}u_0{}^{(0)}u_{1,1\to2}{}^{(0)}r\times\cos\theta dr\sin\theta d\theta d\varphi \tag{24}$$
$$=(32/15)\int_0^\infty u'_0u'_{1,1\to2}rdr.$$

The np states with $m=\pm1$ will now be considered. The unperturbed function is given by

$$u_0{}^{(\pm1)}=\mp(2\pi)^{-\frac{1}{2}}(3^{\frac{1}{2}}/2)u'_0\sin\theta\exp(\pm i\varphi). \tag{25}$$

We have

$$-H_1u_0{}^{(\pm1)}=\mp(2\pi)^{-\frac{1}{2}}3^{\frac{1}{2}}R^{-2}u'_0\sin\theta\cos\theta\exp(\pm i\varphi). \tag{26}$$

Since the right hand side of (26) is a pure d function, the $m=\pm1$ electrons do not contribute to the $np\to s$ excitation. The perturbation is given by

$$u_{1,1\to2}{}^{(\pm1)}=\mp(2\pi)^{-\frac{1}{2}}3^{\frac{1}{2}}R^{-2}u'_{1,1\to2}\sin\theta\cos\theta\exp(\pm i\varphi). \tag{27}$$

Upon inserting (26) and (27) into (10), one obtains for the contribution of the four $m=\pm1$ electrons to α,

$$\alpha^{(\pm1)}(np\to d)=8R^2\int_0^\infty\int_0^\pi\int_0^{2\pi}u_0{}^{(\pm1)}u_{1,1\to2}{}^{(\pm1)}r\times\cos\theta dr\sin\theta d\theta d\varphi \tag{28}$$
$$=(16/5)\int_0^\infty u'_0u'_{1,1\to2}rdr.$$

In view of (24) and (28), the $np\to d$ contribution of the complete p shell to α is given by

$$\alpha(np\to d)=(16/3)\int_0^\infty u'_0u'_{1,1\to2}rdr. \tag{29}$$

The $np\to s$ term due to the $m=0$ electrons is obtained in the same manner as $np\to d$. From (21) one finds for the perturbation,

$$u_{1,1\to0}{}^{(0)}=(2\pi)^{-\frac{1}{2}}(2/3)^{\frac{1}{2}}R^{-2}u'_{1,1\to0}, \tag{30}$$

where the radial function $u'_{1,1\to0}$ is determined by

$$\left(-\frac{d^2}{dr^2}+V_0-E_0\right)u'_{1,1\to0}=u'_0r. \tag{31}$$

Upon inserting (20) and (31) into (10) one obtains for both $m=0$ electrons,

$$\alpha(np\to s)=(8/3)\int_0^\infty u'_0u'_{1,1\to0}rdr. \tag{32}$$

[11] Foley, Sternheimer, and Tycko, Phys. Rev. **93**, 734 (1954).

Here and in the following, $\alpha(nl\to l')$ denotes the contribution to α of the complete subshell nl.

The contributions of the d shells to α can be found in the same manner as for np. The d electrons are excited into p and f states. The complete derivation will not be given here, but the various excited wave functions will be listed together with the final results. The $nd\to f$ waves will be considered presently. The excited wave functions are given by

$$u_{1,2\to3}^{(0)}=(2\pi)^{-\frac{1}{2}}(3/10^{\frac{1}{2}})R^{-2}u'_{1,2\to3}(5\cos^3\theta-3\cos\theta), \quad (33)$$

$$u_{1,2\to3}^{(\pm1)}=\mp(2\pi)^{-\frac{1}{2}}(3/5)^{\frac{1}{2}}R^{-2}u'_{1,2\to3} \times(5\sin\theta\cos^2\theta-\sin\theta)\exp(\pm i\varphi), \quad (34)$$

$$u_{1,2\to3}^{(\pm2)}=(2\pi)^{-\frac{1}{2}}(15^{\frac{1}{2}}/2)R^{-2}u'_{1,2\to3}\sin^2\theta \times\cos\theta\exp(\pm2i\varphi), \quad (35)$$

for the $m=0$, ±1, and ±2 electrons, respectively. Similarly to Eqs. (15), (23), and (31), the radial function $u'_{1,2\to3}$ is determined by

$$\left(-\frac{d^2}{dr^2}+\frac{l'(l'+1)}{r^2}+V_0-E_0\right)u'_{1,l\to l'}=u'_0r, \quad (36)$$

in which $l=2$, $l'=3$, and u'_0 is the unperturbed radial nd function. Upon inserting Eqs. (7) and (33)–(35) into (10), one obtains

$$\alpha(nd\to f)=8\int_0^\infty u'_0u'_{1,2\to3}r\,dr. \quad (37)$$

The $nd\to p$ excited wave functions are given by

$$u_{1,2\to1}^{(0)}=(2\pi)^{-\frac{1}{2}}(8/5)^{\frac{1}{2}}R^{-2}u'_{1,2\to1}\cos\theta, \quad (38)$$

$$u_{1,2\to1}^{(\pm1)}=\mp(2\pi)^{-\frac{1}{2}}(3/5)^{\frac{1}{2}}R^{-2}u'_{1,2\to1} \times\sin\theta\exp(\pm i\varphi), \quad (39)$$

and $u_{1,2\to1}^{(\pm2)}=0$. The radial function $u'_{1,2\to1}$ is determined by Eq. (36) with $l=2$ and $l'=1$. From Eqs. (10), (38), and (39), one obtains

$$\alpha(nd\to p)=(16/3)\int_0^\infty u'_0u'_{1,2\to1}r\,dr. \quad (40)$$

The f electrons are excited into d and g states. The excited wave functions for $nf\to g$ are given by

$$u_{1,3\to4}^{(0)}=(2\pi)^{-\frac{1}{2}}14^{-\frac{1}{2}}R^{-2}u'_{1,3\to4} \times(35\cos^4\theta-30\cos^2\theta+3), \quad (41)$$

$$u_{1,3\to4}^{(\pm1)}=\mp(2\pi)^{-\frac{1}{2}}(75/56)^{\frac{1}{2}}R^{-2}u'_{1,3\to4} \times(7\sin\theta\cos^3\theta-3\sin\theta\cos\theta)\exp(\pm i\varphi), \quad (42)$$

$$u_{1,3\to4}^{(\pm2)}=(2\pi)^{-\frac{1}{2}}(15/28)^{\frac{1}{2}}R^{-2}u'_{1,3\to4} \times(7\sin^2\theta\cos^2\theta-\sin^2\theta)\exp(\pm2i\varphi), \quad (43)$$

$$u_{1,3\to4}^{(\pm3)}=\mp(2\pi)^{-\frac{1}{2}}(35/8)^{\frac{1}{2}}R^{-2}u'_{1,3\to4} \times\sin^3\theta\cos\theta\exp(\pm3i\varphi), \quad (44)$$

where $u'_{1,3\to4}$ is determined by Eq. (36) with $l=3$, $l'=4$, and u'_0 taken as the unperturbed f function. From Eqs. (10) and (41)–(44), one obtains

$$\alpha(nf\to g)=(32/3)\int_0^\infty u'_0u'_{1,3\to4}r\,dr. \quad (45)$$

The excited wave functions for $nf\to d$ are as follows,

$$u_{1,3\to2}^{(0)}=(2\pi)^{-\frac{1}{2}}(3/14^{\frac{1}{2}})R^{-2}u'_{1,3\to2}(3\cos^2\theta-1), \quad (46)$$

$$u_{1,3\to2}^{(\pm1)}=\mp(2\pi)^{-\frac{1}{2}}(24/7)^{\frac{1}{2}}R^{-2}u'_{1,3\to2} \times\sin\theta\cos\theta\exp(\pm i\varphi), \quad (47)$$

$$u_{1,3\to2}^{(\pm2)}=(2\pi)^{-\frac{1}{2}}(15/28)^{\frac{1}{2}}R^{-2}u'_{1,3\to2} \times\sin^2\theta\exp(\pm2i\varphi), \quad (48)$$

where $u'_{1,3\to2}$ is determined by Eq. (36) with $l=3$, $l'=2$. From Eqs. (10) and (46)–(48), one finds

$$\alpha(nf\to d)=8\int_0^\infty u'_0u'_{1,3\to2}r\,dr. \quad (49)$$

From Eqs. (16), (29), (32), (37), (40), (45), and (49), one obtains the following expression for α,

$$\alpha=\sum_n\left(\frac{8}{3}I_{0\to1}\right)_{ns}+\sum_n\left(\frac{8}{3}I_{1\to0}+\frac{16}{3}I_{1\to2}\right)_{np} +\sum_n\left(\frac{16}{3}I_{2\to1}+8I_{2\to3}\right)_{nd}+\sum_n\left(8I_{3\to2}+\frac{32}{3}I_{3\to4}\right)_{nf}, \quad (50)$$

where the sums extend over the occupied s, p, d, and f shells, and $I_{l\to l'}$ is defined as

$$I_{l\to l'}\equiv\int_0^\infty u'_0u'_{1,l\to l'}r\,dr, \quad (51)$$

where $u'_{1,l\to l'}$ is the perturbation considered. It may be noted that the coefficients of $I_{l\to l'}$ and $I_{l'\to l}$ in Eq. (50) are equal. This was expected because the transition from nlm to $n'l'm$ (n' = principal quantum number of excited state) has the same matrix element as the transition from $n'l'm$ to nlm. Since the angular factors do not depend on n and n', the equality of the coefficients of the $I_{l\to l'}$ follows. We note that Eq. (50) gives α in units a_H^3 and must be multiplied by a factor $0.529^3=0.148$ to obtain α in units A^3.

III. CALCULATIONS OF THE POLARIZABILITY

In this section the calculation of the radial functions $u'_{1,l\to l'}$ is described and the resulting values of α, as obtained from Eq. (50), are compared with experiment.

The $u'_{1,l\to l'}$ are determined by Eq. (36), of which Eqs. (15) for $ns\to p$, (23) for $np\to d$, and (31) for $np\to s$ are special cases. The calculations of α for the helium-like ions, which were done analytically, will be discussed below. In the numerical calculations for the medium

and heavy ions, the unperturbed functions u'_0, were taken as the Hartree-Fock or Hartree wave functions. For Na^+, Cl^-, K^+, Ca^{++}, and Cu^+, the Hartree-Fock functions[12–16] (including exchange) were used, while for F^-, Al^{3+}, Rb^+, and Cs^+ only Hartree functions[17–18] (without exchange) are available. The function on the left hand side of Eq. (36) was obtained directly from the tabulated Hartree-Fock functions, in the manner shown previously.[11] Thus, let $P(r)$ be defined as

$$P(r)\equiv[l(l+1)/r^2]+V_0(r)-E_0, \tag{52}$$

where l is the azimuthal quantum number for the unperturbed state. If r_n is a selected radius and δ is the interval at which u'_0 is tabulated, $P(r_n)$ is given by

$$P(r_n)=[u'_0(r_n+\delta)-2u'_0(r_n)+u'_0(r_n-\delta)]/[\delta^2u'_0(r_n)]. \tag{53}$$

The function which appears on the left hand side of Eq. (36) is

$$P'(r)\equiv P(r)+[l'(l'+1)-l(l+1)]/r^2. \tag{54}$$

If I denotes the inhomogeneity $I=u'_0r$, the equation used for the numerical integration with the same interval δ is given by

$$u'_1(r_n+\delta)=u'_1(r_n)\{2+\delta^2[P'(r_n)-I(r_n)/u'_1(r_n)]\}-u'_1(r_n-\delta). \tag{55}$$

Equation (55) is appropriate for outward integration starting near $r=0$. The equation for inward integration is obtained from (55) by reversing the sign of δ.

For $ns\rightarrow p$ and $np\rightarrow s$, Eq. (36) was integrated outward with starting values obtained as follows. Near $r=0$, the $ns\rightarrow p$ function $u'_{1,0\rightarrow1}(ns)$ is approximately proportional to the unperturbed np function $u'_0(np)$ for the same n, as will now be shown. Here and in the following $u'_0(nl)$ denotes the unperturbed function for nl, and $u'_{1,l\rightarrow l'}(nl)$ denotes the perturbation of the state nl. From Eq. (15) it is seen that the inhomogeneity u'_0r acts in the same manner as an additional potential $\delta V=-u'_0r/u'_{1,0\rightarrow1}$. Near $r=0$, $u'_0(ns)\propto r$, $u'_{1,0\rightarrow1}(ns)\propto r^2$, so that δV is constant and therefore much smaller than the terms $2/r^2$ and V_0. Thus the right hand side of (15) can be neglected near $r=0$ and the equation for $u'_{1,0\rightarrow1}(ns)$ is the same as the equation for $u'_0(np)$, except for the small difference between the unperturbed energies E_0 for ns and for np. However, the term E_0 plays a negligible role near $r=0$, so that $u'_{1,0\rightarrow1}(ns)$ is approximately proportional to $u'_0(np)$. The integration [Eq. (55)] was started at two values of r near $r=0.05a_H$; the starting values $u'_1(r_n)$ and $u'_1(r_n+\delta)$ were taken proportional to the values of $u'_0(np)$ at these radii. Thus $u'_1=\beta_1u'_0(np)$, where β_1 is a proportionality constant to be determined. The integrations were carried out with several values of β_1. The correct β_1 is that for which the resulting $u'_{1,0\rightarrow1}$ is well behaved (i.e., exponentially decreasing) at infinity. In practice, β_1 and $u'_{1,0\rightarrow1}$ were found by interpolation. For two choices of β_1 which enclose the correct value, the functions diverge slowly, the one to positive values, the other to negative values as $r\rightarrow\infty$. However, they agree quite well (in general within $\sim$15 percent) in the region of importance for α, between $r\sim1a_H$ and $r\sim3a_H$, where the outermost maximum of u'_0 occurs. Figure 1 shows the $3s\rightarrow p$ function $u'_{1,0\rightarrow1}$ for Cl^-, together with twice the unperturbed $3s$ function $2u'_0$.

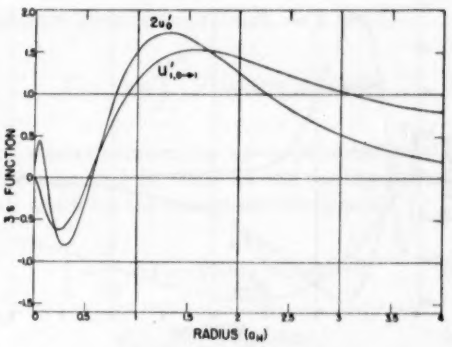

FIG. 1. $3s$ function u'_0 and $3s\rightarrow p$ perturbation $u'_{1,0\rightarrow1}$ for Cl^-.

For the $np\rightarrow s$ excitation essentially the same procedure was used as for $ns\rightarrow p$. Near $r=0$, the perturbation $u'_{1,1\rightarrow0}(np)$ is proportional to $u'_0(ns)$ since the extra potential $\delta V=-u'_0(np)r/u'_{1,1\rightarrow0}(np)$ which corresponds to the inhomogeneity of Eq. (31) is negligible near the nucleus. This follows from the fact that $u'_0(np)\propto r^2$, $u'_{1,1\rightarrow0}(np)\propto r$, so that $\delta V\propto r^2$ near $r=0$, in contrast to V_0 which goes as $1/r$. The difference between the values of E_0 for ns and for np can also be neglected, so that Eq. (31) is approximately the same as the equation for $u'_0(ns)$. The numerical integration [Eq. (55)] was started near $r=0.05a_H$, using for $u'_{1,1\rightarrow0}$ the values of $\beta_2u'_0(ns)$ where β_2 is a proportionality constant. Similarly to $ns\rightarrow p$, the integrations were carried out for several values of β_2 until a value was found by interpolation for which the resulting $u'_{1,1\rightarrow0}$ is well behaved at $r=\infty$. Figure 2 shows the $3p\rightarrow s$ perturbation $u'_{1,1\rightarrow0}$ for Cl^-, together with twice the unperturbed $3p$ function $2u'_0$.

For $np\rightarrow d$, an inward method of integration was used in most cases, starting at a large radius r_1. For this purpose, Eq. (23) was written as follows,

$$d^2u'_{1,1\rightarrow2}/dr^2=Nu'_{1,1\rightarrow2}, \tag{56}$$

[12] V. Fock and M. Petrashen, Physik. Z. Sowjetunion **6**, 368 (1934).
[13] D. R. Hartree and W. Hartree, Proc. Roy. Soc. (London) **A156**, 45 (1936).
[14] D. R. Hartree and W. Hartree, Proc. Roy. Soc. (London) **A166**, 450 (1938).
[15] D. R. Hartree and W. Hartree, Proc. Roy. Soc. (London) **A164**, 167 (1938).
[16] D. R. Hartree and W. Hartree, Proc. Roy. Soc. (London) **A157**, 490 (1936).
[17] D. R. Hartree, Proc. Roy. Soc. (London) **A151**, 96 (1935).
[18] D. R. Hartree, Proc. Roy. Soc. (London) **A143**, 506 (1934).

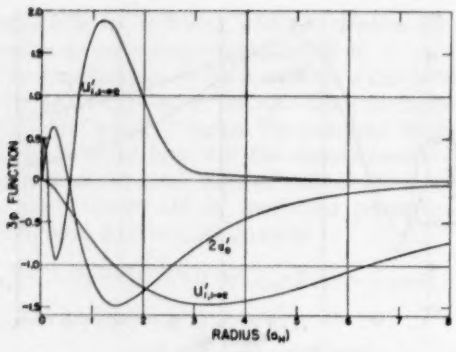

FIG. 2. $3p$ function u'_0, $3p\to s$ perturbation $u'_{1,1\to 0}$, and $3p\to d$ perturbation $u'_{1,1\to 2}$ for Cl^-.

where N is given by [see Eqs. (52) and (54)]:

$$N=P'-[u'_0r/u'_{1,1\to 2}]. \tag{57}$$

Note that for large r, N is constant and given by $-E_0$. Several integrations were carried out with different starting values $u'_{1,1\to 2}(r_1)$. It was assumed that N is constant for $r>r_1$; for a given $u'_{1,1\to 2}(r_1)$, $N(r_1)$ is calculated from (57), and $u'_{1,1\to 2}(r_1+\delta)$ is obtained from

$$u'_{1,1\to 2}(r_1+\delta)=u'_{1,1\to 2}(r_1)\exp\{-[N(r_1)]^{\frac{1}{2}}\delta\}. \tag{58}$$

The numerical integration is then started with the values $u'_{1,1\to 2}(r_1)$ and $u'_{1,1\to 2}(r_1+\delta)$. The correct value of $u'_{1,1\to 2}(r_1)$ is that for which the resulting $u'_{1,1\to 2}$ is zero at $r=0$. This requirement is appropriate since the actual perturbation goes as r^3 near $r=0$. In practice, the actual $u'_{1,1\to 2}(r_1)$ and the solution were found by interpolation. For two choices of $u'_{1,1\to 2}(r_1)$ which enclose the correct value, the solutions $u'_{1,1\to 2}(r)$ diverge slowly, the one to positive values, the other to negative values, near $r=0$. However, they agree closely (in general within 15 percent) in the region of importance for $\alpha(r\sim 1a_H-3a_H)$. Figure 2 shows the $3p\to d$ perturbation $u'_{1,1\to 2}$ for Cl^-. The contribution to α is determined by $(16/3)u'_0u'_{1,1\to 2}r$ [see Eq. (29)]. Since $u'_{1,1\to 2}$ and u'_0 have the same sign for $r>0.55a_H$, the contribution to $\alpha(3p\to d)$ from this region is positive. For $r<0.55a_H$, $u'_{1,1\to 2}$ and u'_0 have opposite sign because of the node of u'_0, so that the region inside $0.55a_H$ makes a negative contribution to $\alpha(3p\to d)$. However, this contribution is negligible compared to that made by $r>0.55a_H$, because the values of u'_0, $u'_{1,1\to 2}$, and r are considerably smaller than in the region[19] $r>0.55a_H$. The sign of the terms of α due to $3s\to p$ and $3p\to s$ is discussed below.

For Cu^+, $3d\to f$, and inward method of integration was used, similar to that for $np\to d$, while the $3d\to p$ wave of Cu^+ was obtained by outward integration, similar to $ns\to p$ and $np\to s$.

After the $u'_{1,l\to l'}$ are obtained, the integrals $I_{l\to l'}$ [Eq. (51)] are evaluated and α is calculated from Eq. (50). It is estimated that the inaccuracy of the values of α due to the interpolation procedure to obtain the $u'_{1,l\to l'}$ is less than ± 20 percent. In many cases the values of $\alpha(nl\to l')$ are probably accurate to ± 10–15 percent.

It was found that the polarizability α is almost entirely due to the outermost shell whose principal quantum number will be called n_0. The contribution of the shells with $n<n_0$ is negligible in all cases. This result was already obtained by Pauling[7] from the hydrogenic wave functions and by Buckingham.[8] The results of the calculations are presented in Table I. The first five rows list the term $\alpha(n_0l\to l')$ due to the various modes of excitation of the outermost shell. The last two rows give the resulting calculated value of α and the experimental values. The fact that the inner shells $(n<n_0)$ make a negligible contribution to α was established by calculating $\alpha(2p\to d)$ for Cl^-, $\alpha(3d\to f)$ for Rb^+, and $\alpha(4d\to f)$ for Cs^+. These represent the largest terms for the shell with $n=n_0-1$, and were found to be $0.01A^3$, $0.03A^3$, and $0.16A^3$, respectively. Even for Cs^+, this term represents only 3 percent of the contribution due to $n_0=5$, and is therefore appreciably smaller than the uncertainty of the calculations. The reason why the inner shells make only a negligible contribution is that both the right hand side of Eq. (36) for $u'_{1,l\to l'}$ and the integrand of $I_{l\to l'}$ [Eq. (51)] contain a factor r, so that the contribution to α depends essentially on the average value of r^2 for the shell considered.[8] Since $\langle r^2\rangle_{nl}$ decreases very considerably as n is decreased by 1, only the outermost shell contributes effectively to α.

The experimental values α(exp) given in the last row of Table I correspond to the values obtained by Born and Heisenberg,[1] Mayer and Mayer,[2] Fajans and Joos,[4] Pauling,[7] and Tessman, Kahn, and Shockley.[5] The range of α(exp) is due to the fact that different experimental methods give appreciably different values of α in some instances. These discrepancies can probably be attributed to uncertainties in corrections which enter into the determination of α from the experimental data. As an example of these corrections, the quadrupole polarizability and the effect of penetration of the core enter into the spectral level method.[2] Similarly, the values of α obtained from the index of refraction of

[19] While the contribution of $r<0.55a_H$ is negligible for the polarizability, it may be important for properties which depend strongly on the region of the electron cloud near the nucleus. Thus as shown below (Sec. V) the induced charge distribution contributes to the electric field at the nucleus. The term in the electric field due to $3p\to d$ is given by $(16e/3R^3)\int_0^r u'_0u'_{1,1\to 2}r^{-2}dr$. The fact that the dependence on r is r^{-2} rather than r as for the polarizability results in a strong dependence on the values of $u'_0u'_{1,1\to 2}$ near the nucleus. It may also be noted that the antishielding correction to the nuclear quadrupole coupling (reference 11) is an effect similar to the one discussed here. In this case, the perturbed wave functions are such as to shield the atom from the electric field gradient of the external charge in the vicinity of that charge, i.e., in the region of the outermost maximum of the atomic wave functions. However, near the nucleus, the effect is in some cases an antishielding because of nodes and changes of sign of the unperturbed and perturbed wave functions.

crystals[1,5] may be affected by distortion of the ion by interatomic forces.[6]

Table I shows that $\alpha(n_0s\to p)$ and $\alpha(n_0p\to s)$ cancel each other approximately, so that $\alpha(n_0p\to d)$ makes the major contribution to α for the cases where n_0p is the outermost subshell. A similar near-cancellation takes place for $3p\to d$ and $3d\to p$ of Cu^+, so that the $3d$ subshell through $\alpha(3d\to f)$ makes the largest contribution to α for Cu^+. This cancellation will now be explained for the case of $n_0s\to p$ and $n_0p\to s$. For this purpose, Eq. (15) for $u'_{1,0\to1}$ and Eq. (31) for $u'_{1,1\to0}$ will be solved in terms of eigenfunctions. We expand $u'_{1,0\to1}$ in terms of the np eigenfunctions for the potential V_0. Thus

$$u'_{1,0\to1}=\sum_n a_n u'_0(np), \tag{59}$$

where a_n is a coefficient and $u'_0(np)$ is the normalized solution of

$$\left[-\frac{d^2}{dr^2}+\frac{2}{r^2}+V_0-E_0(np)\right]u'_0(np)=0, \tag{60}$$

where $E_0(np)$ is the energy eigen value for np. In (59) the sum extends over all of the discrete states allowed by (60) and over the continuum states with $E_0(np)>0$. In Eq. (15) E_0 will be written more explicitly as $E_0(n_0s)$ and u'_0 will be written as $u'_0(n_0s)$. Upon inserting (59) into (15), one obtains

$$\left[-\frac{d^2}{dr^2}+\frac{2}{r^2}+V_0-E_0(n_0s)\right]\sum_n a_n u'_0(np)=u'_0(n_0s)r. \tag{61}$$

In view of (60), Eq. (61) becomes

$$\sum_n[E_0(np)-E_0(n_0s)]a_n u_0'(np)=u_0'(n_0s)r. \tag{62}$$

Upon multiplying both sides of (62) by $u'_0(np)$ and integrating over r, one obtains

$$a_n=\left[\int_0^\infty u'_0(n_0s)ru'_0(np)dr\right]\Big/[E_0(np)-E_0(n_0s)]. \tag{63}$$

Since the energy denominator is smallest for $n=n_0$, the largest a_n is expected to be a_{n0}, so that $u'_{1,0\to1}$ is approximately given by $a_{n0}u'_0(n_0p)$. As a result,

$$I_{0\to1}\sim a_{n0}\int_0^\infty u'_0(n_0s)ru'_0(n_0p)dr. \tag{64}$$

In a similar manner, the $np\to s$ perturbation $u'_{1,1\to0}$ will be expanded in terms of the ns eigenfunctions $u'_0(ns)$ which are the normalized solutions of

$$\left[-\frac{d^2}{dr^2}+V_0-E_0(ns)\right]u'_0(ns)=0. \tag{65}$$

Thus,

$$u'_{1,1\to0}=\sum_n b_n u'_0(ns), \tag{66}$$

where b_n is a coefficient. In Eq. (31) E_0 will be written more explicitly as $E_0(np_0)$ and u'_0 as $u'_0(n_0p)$. Upon inserting (66) into (31) and using (65), one obtains

$$\sum_n[E_0(ns)-E_0(n_0p)]b_n u'_0(ns)=u'_0(n_0p)r. \tag{67}$$

Upon multiplying both sides of (67) by $u'_0(ns)$ and integrating over r, one finds

$$b_n=\left[\int_0^\infty u'_0(n_0p)ru'_0(ns)dr\right]\Big/[E_0(ns)-E_0(n_0p)]. \tag{68}$$

Again the smallest energy denominator is obtained for $n=n_0$, and a comparison of (63) and (68) shows that $b_{n0}=-a_{n0}$. In the approximation in which the terms $n\neq n_0$ are neglected, we have

$$I_{1\to0}\sim-a_{n0}\int_0^\infty u'_0(n_0s)ru'_0(n_0p)dr, \tag{69}$$

so that $I_{0\to1}$ and $I_{1\to0}$ would exactly cancel each other.

These results have a simple physical interpretation. In the absence of the Pauli principle, the major part of the $n_0s\to p$ excitation would be n_0p, and the major part of the $n_0p\to s$ excitation would be n_0s. However, since both the n_0s and n_0p shells are filled, the two terms just cancel each other, so that only excitations of n_0s into higher p states ($n>n_0$) and excitations of n_0p into higher s states ($n>n_0$) are possible. This leaves $n_0p\to d$

TABLE I. Calculated and experimental values of the polarizability α. The rows above α(calc) list the contributions to α of the various modes of excitation of the (outermost) shell with highest principal quantum number n_0. All values are in units A^3.

Ion	F^-	Na^+	Al^{3+}	Cl^-	K^+	Ca^{++}	Cu^+	Rb^+	Cs^+
$\alpha(n_0s\to p)$	0.39	0.125	0.061	1.33	0.57	0.40	0.077	0.98	2.15
$\alpha(n_0p\to s)$	−0.30	−0.101	−0.054	−0.97	−0.44	−0.36	−0.069	−0.89	−1.71
$\alpha(n_0p\to d)$	3.11	0.121	0.043	5.28	1.13	0.69	0.096	2.61	4.43
$\alpha(n_0d\to p)$							−0.084		
$\alpha(n_0d\to f)$							0.450		
α(calc)	3.20	0.145	0.050	5.65[a]	1.26	0.73	0.470	2.73[b]	5.03[c]
α(exp)	0.76–1.04	0.17–0.26	0.052–0.067	2.97–3.66	0.80–1.20	0.47–1.1	1.6	1.4–1.8	2.35–3.14

[a] Includes a term $0.01A^3$ due to $2p\to d$.
[b] Includes a term $0.03A^3$ due to $3d\to f$.
[c] Includes a term $0.16A^3$ due to $4d\to f$.

as the major contribution to α, since the energy difference between n_0p and n_0d is fairly small and the n_0d states are unoccupied. A similar explanation applies to the approximate cancellation of the $3p\rightarrow d$ and $3d\rightarrow p$ terms for Cu^+ and the predominance of the $3d\rightarrow f$ term, involving the excitation into the unoccupied f states.

The preceding results are illustrated by Figs. 1 and 2. Figure 1 shows that the $3s\rightarrow p$ excitation $u'_{1,0\rightarrow 1}$ of Cl^- and the $3s$ function $u'_0(3s)$ have the same sign throughout most of the range of r (for $r>0.12a_H$), resulting in a positive contribution to α since $u'_0u'_{1,0\rightarrow 1}>0$ [see Eq. (16)]. By contrast the $3p\rightarrow s$ wave $u'_{1,1\rightarrow 0}$ and the $3p$ function have in general opposite sign (see Fig. 2) so that $\alpha(3p\rightarrow s)$ is negative. It is also seen that $u'_{1,0\rightarrow 1}$ for $3s\rightarrow p$ has the same node as $u'_0(3p)$ at $r=0.55a_H$ and is approximately proportional to $u'_0(3p)$ inside $r=2a_H$. Similarly, $u'_{1,1\rightarrow 0}(3p\rightarrow s)$ and $u'_0(3s)$ have the same nodes and are approximately proportional for $r<2a_H$.

From Table I it is seen that the calculated values of α are, in general, between 1 and 1.5 times the experimental values. As mentioned above, a discrepancy in this direction is expected because the Hartree-Fock functions provide less binding than the actual wave functions and should, therefore, tend to give values of α which are too large. For Cl^-, Rb^+, and Cs^+, the disagreement is a factor of $\sim$1.5. However, for K^+, the calculated α is barely above the experimental range, and for Na^+, Al^{3+}, and Ca^{++}, the calculated α is either within the experimental range or slightly below the experimental values. This agreement can be understood by virtue of the fact that for small positive ions or ions with net charge greater than 1, the wave functions of the outermost electrons have a relatively strong binding, and the calculated polarizability should be insensitive to small inaccuracies of the potential for the external electrons and of the zero-order wave functions. The fact that for Na^+, $\alpha(\text{calc})=0.145A^3$ is below the experimental values is somewhat disturbing. A difference in this direction has already been noted by Buckingham.[8] However, it should be pointed out that the experimental values are subject to uncertainties, and the discrepancy $(0.17-0.145=0.025A^3)$ is smaller than the difference between the experimental values $(0.26-0.17=0.09A^3)$. We also note that the value of α derived in Sec. IV from the spectral term defect including the quadrupole polarizability is $0.138A^3$ which is smaller than $\alpha(\text{calc})$. For F^-, $\alpha(\text{calc})$ is larger than $\alpha(\text{exp})$ by a factor of 3. This disagreement is probably due to the fact that only Hartree functions[17] were available for the calculation. Since F^- is a negative ion, the binding of the $2p$ electrons is very sensitive to small changes of the potential in which these electrons move. Since the wave function was obtained from the Hartree equations,[17] the exchange correlation which would provide additional binding is not included. Thus, the rather large discrepancy is not surprising. The fact that there is better agreement for Cl^- than for F^- is probably due to the use of Hartree-Fock functions[13] for Cl^-. For Cu^+, Table I shows that $\alpha(\text{calc})=0.47A^3$ is appreciably smaller than $\alpha(\text{exp})=1.6A^3$. The experimental value was obtained by Tessman, Kahn, and Shockley[5] from the index of refraction of CuCl, CuBr, and CuI for the wavelength λ_D of the sodium D line. While the values of α obtained from the 3 compounds agree quite well (1.47, 1.67, and $1.71A^3$) it is likely that α for infinite wavelength $\lambda=\infty$ is appreciably smaller than α for $\lambda=\lambda_D$. This trend is shown by all of the positive ions investigated by Tessman *et al.*[5] However, it seems unlikely that it can account for all of the discrepancy. Thus for Rb^+, $\alpha(\lambda_D)-\alpha(\infty)$ is $0.182A^3$. For Ca^{++} and Ba^{++} the difference between $\alpha(\lambda_D)$ determined by Tessman *et al.*[5] and the largest value of α obtained by the other authors[1-4] is $0.59A^3$ and $0.82A^3$. Hence it cannot be excluded that the difference $\alpha(\text{exp})-\alpha(\text{calc})$ is due to the inaccuracy of the experimental determination and the fact that $\alpha(\text{exp})$ pertains to λ_D rather than $\lambda=\infty$. Another possible explanation is that part of the discrepancy is due to the use of a single radial wave function for the $3d$ electrons of Cu^+. This wave function was obtained by Hartree[16] from the Hartree-Fock method which treats the ten $3d$ electrons as a single group. It is possible that in a more accurate treatment the $3d$ electrons would fall into two groups, some being closer to the nucleus than predicted by the Hartree-Fock function, while the remainder would be more loosely bound since they are shielded more effectively from the nucleus. Such a distribution of two $3d$ groups could have a lower total energy, because of the presence of the tightly bound group of electrons, and at the same time, the distribution could have a larger polarizability because of the loosely bound electrons, each of which may give a considerably larger contribution than an electron which is described by the Hartree-Fock function.

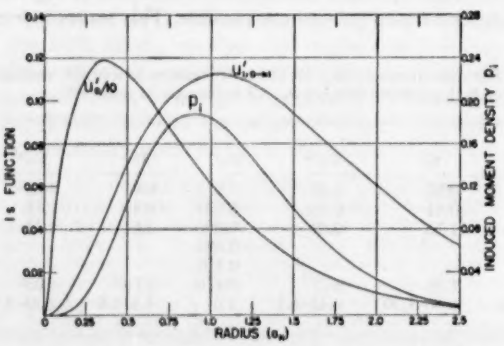

FIG. 3. $1s$ function u'_0, $1s\rightarrow p$ perturbation $u'_{1,0\rightarrow 1}$, and induced moment density $p_i=(8/3)u'_0u'_{1,0\rightarrow 1}r$ for Li^+.

It can be concluded that with the exception of F^- and Cu^+, the calculated values of α are in reasonable agreement with experiment. In 4 out of 9 cases, $\alpha(\text{calc})$ is essentially within the range of the observed values. In 3 other cases, $\alpha(\text{calc})$ exceeds $\alpha(\text{exp})$ by a factor of order 1.5.

The calculations for the helium-like ions will now be

described. For the unperturbed $1s$ functions we used the Slater-type functions of Löwdin[9] which can be written as follows,

$$u'_0 = c_1[2Z_1^{\frac{1}{2}} r \exp(-Z_1 r)] + c_2[2Z_2^{\frac{1}{2}} r \exp(-Z_2 r)], \quad (70)$$

where Z_1 and Z_2 are two effective values of the atomic number Z; c_1 and c_2 are coefficients. If there were no overlap between the two functions in square brackets, we would have $c_1^2+c_2^2=1$. In Sec. II, the $1s \rightarrow p$ perturbed function $u'_{1,0\rightarrow 1}$ was obtained for an arbitrary Z [Eq. (18)]. Therefore, it seems reasonable to use for the perturbation corresponding to (70) the following expression,

$$u'_{1,0\rightarrow 1} = c_1\{Z_1^{-\frac{1}{2}} r^2[1+(Z_1/2)r] \exp(-Z_1 r)\} + c_2\{Z_2^{-\frac{1}{2}} r^2[1+(Z_2/2)r] \exp(-Z_2 r)\}. \quad (71)$$

Thus the polarizability (in units a_H^3) is given by

$$\alpha = (8/3)\int_0^\infty u'_0 u'_{1,0\rightarrow 1} r\, dr, \quad (16)$$

in which u'_0 and $u'_{1,0\rightarrow 1}$ are given by Eqs. (70) and (71), respectively.

It may be noted that the expression of Eq. (71) is not exact, because it assumes that the $1s$ electrons are in a superposition of two states in which they experience slightly different potentials. Thus if the energy is E_0, the potential pertaining to Z_1 which is implied by Eq. (71) is

$$V_1 = -(2Z_1/r) + Z_1^2 + E_0, \quad (72)$$

while the potential pertaining to Z_2 is

$$V_2 = -(2Z_2/r) + Z_2^2 + E_0, \quad (73)$$

both in Rydberg units. However, the error made by this approximation is very small, as was verified by a calculation for Li^+. Thus the exact perturbed function can be found by solving Eq. (15) numerically by means of the function P [Eq. (52)] which can be obtained directly from the Löwdin function u'_0 according to Eq. (53). For the case of Li^+ the function $u'_{1,0\rightarrow 1}$ obtained numerically was found to differ from (71) by less than 6 percent throughout the range of r, and the resulting value of α is $0.0306A^3$ as compared to $0.0316A^3$ obtained from (70) and (71). This difference is probably well within the uncertainty which arises from the inaccuracy of the Löwdin wave function u'_0 due to neglect of the correlation between the $1s$ electrons. Figure 3 shows the perturbed wave function $u'_{1,0\rightarrow 1}$ for Li^+, as calculated from (71), together with the unperturbed $1s$ function [Eq. (70)], and the density of induced moment $p_i = (8/3)u'_0 u'_{1,0\rightarrow 1} r$, i.e., the integrand of α [see Eq. (16)]. The constants c_i and Z_i for Li^+ as obtained from Löwdin's[9] work, are:

$$Z_1 = 2.435, \quad Z_2 = 4.425,$$
$$c_1 = 6.664/(2Z_1^{\frac{1}{2}}) = 0.877, \quad c_2 = 2.562/(2Z_2^{\frac{1}{2}}) = 0.138.$$

TABLE II. Calculated and experimental values of α for helium and the helium-like ions. The calculated values were obtained from the Löwdin wave functions. All values are in units A^3.

Ion	α(calc)	α(exp)
H^-	16.1	
He	0.236	0.203
Li^+	0.0316	0.025–0.08
Be^{++}	0.0083	0.007–0.04
B^{3+}	0.00308	0.003–0.02
C^{4+}	0.00139	0.0013–0.012

Table II gives the calculated values of α for helium and the helium-like ions from H^- to C^{4+}. The experimental values are also listed.[1–5] It is seen that the calculated values are generally in good agreement with experiment. This agreement was expected for the positive ions, since for these ions the $1s$ electrons have a relatively strong binding, and hence α should be insensitive to small inaccuracies of the potential and of the zero-order Löwdin wave functions, in the same manner as was discussed above for Na^+, Al^{3+}, and Ca^{++}.

IV. QUADRUPOLE POLARIZABILITY

When an ion is placed in the field of an external charge, the quadrupole part of the field of the charge induces a quadrupole moment in the charge distribution of the ion. The quadrupole field is closely connected with the electric field gradient at the nucleus. If the external charge is at $X=R$, the term in the potential energy is given by

$$V_q = -(r^2/R^3)(3\cos^2\theta - 1), \quad (74)$$

in Rydberg units. Equation (74) is valid for $r<R$. The field gradient at the nucleus in the X direction is

$$\partial E_X/\partial X = -2e/R^3. \quad (75)$$

The induced quadrupole moment Q_{ind} is given by

$$Q_{\text{ind}} = \int \rho_{\text{ind},q} r^2(3\cos^2\theta - 1)dV, \quad (76)$$

where dV = volume element, and $\rho_{\text{ind},q}$ is the density induced in the ion by the potential V_q. It is convenient to define the quadrupole polarizability as follows,

$$\alpha_q = \frac{-eQ_{\text{ind}}}{\partial E_X/\partial X}. \quad (77)$$

The quadrupole polarizability was first discussed by Mayer and Mayer[2] in their calculations on the spectral term defect of the alkalis. A problem related to α_q was also treated by Foley, Sternheimer, and Tycko[11] who calculated the perturbation of the electric field gradient at the nucleus produced by the density $\rho_{\text{ind},q}$ due to an external charge. In view of (76) and (77) α_q is given by

$$\alpha_q = (R^3/2)\int \rho_{\text{ind},q} r^2(3\cos^2\theta - 1)dV. \quad (78)$$

We now obtain an expression for α_q similar to Eq. (50) for the dipole polarizability α. The derivation follows closely the same lines as for α. The results of Foley, Sternheimer, and Tycko[11] will be used. These authors showed that V_q results in an excitation of s electrons into excited d states, and of p electrons into p and f states. Similarly the d electrons are excited into s, d, and g states. The $ns\rightarrow d$ wave will now be considered. If the zero-order ns function (times r) is denoted by u_0, and if u_1 denotes r times the $ns\rightarrow d$ perturbation, then u_1 is determined by Eq. (2) in which H_1 is now defined as V_q and E_1 is the first-order perturbation of the energy due to H_1. By subtracting Eq. (4) from Eq. (2), one obtains

$$(H_0-E_0)u_1=(E_1-H_1)u_0. \tag{79}$$

E_1 is zero for s states. Upon inserting Eq. (11) for u_0 and Eq. (74) for H_1 into (79), one obtains

$$(H_0-E_0)u_{1,0\rightarrow 2}=(2\pi)^{-\frac{1}{2}}2^{-\frac{1}{2}}R^{-3}u'_0r^2(3\cos^2\theta-1). \tag{80}$$

Here and in the following $u_{1,l\rightarrow l'}$ denotes the wave function for the quadrupole excitation of a state with azimuthal quantum number l into states with azimuthal quantum number l'. Upon inserting (13) into (80), one obtains

$$u_{1,0\rightarrow 2}=(2\pi)^{-\frac{1}{2}}2^{-\frac{1}{2}}R^{-3}u'_{1,0\rightarrow 2}(3\cos^2\theta-1), \tag{81}$$

where the radial function $u'_{1,0\rightarrow 2}$ is determined by

$$\left(-\frac{d^2}{dr^2}+\frac{6}{r^2}+V_0-E_0\right)u'_{1,0\rightarrow 2}=u'_0r^2. \tag{82}$$

Here and in the following the subscript notation for $u'_{1,l\rightarrow l'}$ is the same as for $u_{1,l\rightarrow l'}$. In view of (78) the contribution to α_q from the $ns\rightarrow d$ wave is given by

$$\alpha_q(ns\rightarrow d)=4(R^3/2)\int_0^\infty\int_0^\pi\int_0^{2\pi}u_0u_{1,0\rightarrow 2}r^2\times(3\cos^2\theta-1)dr\sin\theta d\theta d\varphi, \tag{83}$$

where the factor 4 arises from the fact that the perturbed density $\rho_{\text{ind},q}$ is $2u_0u_{1,0\rightarrow 2}$ for each ns electron. Upon inserting Eqs. (11) and (81) into (83) and performing the integrations over θ and φ, one obtains

$$\alpha_q(ns\rightarrow d)=(8/5)\int_0^\infty u'_0u'_{1,0\rightarrow 2}r^2dr. \tag{84}$$

We will next consider the excitation of p electrons into p states. For the states with $m=0$ the perturbation energy E_1 is given by

$$E_1=-R^{-3}\int_0^\infty\int_0^\pi\int_0^{2\pi}[u_0^{(0)}]^2r^2\times(3\cos^2\theta-1)dr\sin\theta d\theta d\varphi, \tag{85}$$

where $u_0^{(0)}$ is the unperturbed np function as given by Eq. (20). Upon substituting this expression in (85), one obtains

$$E_1=-(4/5)\langle r^2\rangle_{nl}R^{-3}, \tag{86}$$

where $\langle r^2\rangle_{nl}$ is the average value of r^2 over the radial function u'_0:

$$\langle r^2\rangle_{nl}=\int_0^\infty u'_0{}^2r^2dr. \tag{87}$$

Upon inserting Eqs. (20), (74), and (86) into Eq. (79), one obtains

$$(H_0-E_0)u_1^{(0)}=-(2\pi)^{-\frac{1}{2}}\frac{4}{5}\left(\frac{3}{2}\right)^{\frac{1}{2}}\frac{\langle r^2\rangle_{nl}}{R^3}u_0\cos\theta+(2\pi)^{-\frac{1}{2}}\left(\frac{3}{2}\right)^{\frac{1}{2}}\frac{r^2}{R^3}u'_0\left[\frac{4}{5}\cos\theta+\left(3\cos^3\theta-\frac{9}{5}\cos\theta\right)\right], \tag{88}$$

where the angular factor in the square brackets has been written as the sum of a p and a f function. The p part contributes to the excited p wave function $u_{1,1\rightarrow 1}{}^{(0)}$ which can be written

$$u_{1,1\rightarrow 1}{}^{(0)}=(2\pi)^{-\frac{1}{2}}(24/25)^{\frac{1}{2}}R^{-3}u'_{1,1\rightarrow 1}\cos\theta, \tag{89}$$

where the radial function $u'_{1,1\rightarrow 1}$ is determined by the following equation,

$$\left(-\frac{d^2}{dr^2}+\frac{2}{r^2}+V_0-E_0\right)u'_{1,1\rightarrow 1}=u'_0(r^2-\langle r^2\rangle_{nl}). \tag{90}$$

The contribution to α_q due to the excitation of the $m=0$ electrons is given by

$$\alpha_q{}^{(0)}(np\rightarrow p)=4(R^3/2)\int_0^\infty\int_0^\pi\int_0^{2\pi}u_0{}^{(0)}u_{1,1\rightarrow 1}{}^{(0)}\times r^2(3\cos^2\theta-1)dr\sin\theta d\theta d\varphi \tag{91}$$

$$=(32/25)\int_0^\infty u'_0u'_{1,1\rightarrow 1}r^2dr,$$

where the factor 4 has the same origin as in Eq. (83).

For the np electrons with $m=\pm 1$, E_1 is given by

$$E_1=\int_0^\infty\int_0^\pi\int_0^{2\pi}[u_0{}^{(\pm 1)}]^2V_qdr\sin\theta d\theta d\varphi=(2/5)\langle r^2\rangle_{nl}R^{-3}, \tag{92}$$

where Eq. (25) for $u_0{}^{(\pm 1)}$ has been used. Upon inserting Eqs. (25), (74), and (92) into Eq. (79), one obtains

$$(H_0-E_0)u_1^{(\pm 1)}=\pm(2\pi)^{-\frac{1}{2}}\left(\frac{3^{\frac{1}{2}}}{5}\right)\frac{\langle r^2\rangle_{nl}}{R^3}u'_0\sin\theta\times\exp(\pm i\varphi)\pm(2\pi)^{-\frac{1}{2}}\left(\frac{3^{\frac{1}{2}}}{2}\right)\frac{r^2}{R^3}u'_0\left[-\tfrac{2}{5}\sin\theta+(3\cos^2\theta\sin\theta-\tfrac{2}{5}\sin\theta)\right]\exp(\pm i\varphi). \tag{93}$$

The square bracket has been written as a sum of p and f functions. Upon using the p part, one obtains the following expression for the perturbed p wave,

$$u_{1,1\to1}^{(\pm1)}=\mp(2\pi)^{-\frac{1}{2}}(3^{\frac{1}{2}}/5)R^{-3}u'_{1,1\to1}\times\sin\theta\exp(\pm i\varphi), \quad (94)$$

where $u'_{1,1\to1}$ is determined by Eq. (90). The contribution to α_q from the four electrons with $m=\pm1$ is given by

$$\alpha_q^{(\pm1)}(np\to p)=8(R^3/2)\int_0^\infty\int_0^\pi\int_0^{2\pi}u_0^{(\pm1)}\times u_{1,1\to1}^{(\pm1)}r^2(3\cos^2\theta-1)dr\sin\theta d\theta d\varphi \quad (95)$$

$$=(16/25)\int_0^\infty u'_0u'_{1,1\to1}r^2dr.$$

From Eqs. (91) and (95) one obtains for the complete np shell,

$$\alpha_q(np\to p)=(48/25)\int_0^\infty u'_0u'_{1,1\to1}r^2dr. \quad (96)$$

In order to obtain the terms of α_q for the excitation of np electrons into f states and the excitation of the d electrons, we make use of the results previously derived[11] for the perturbation of the electric field gradient at the nucleus. This quantity, which will be called $\Delta(\partial E_X/\partial X)$, is given by

$$\Delta(\partial E_X/\partial X)=e\int\rho_{\text{ind},q}r^{-3}(3\cos^2\theta-1)dV. \quad (97)$$

Results were obtained for the ratio of $-\Delta(\partial E_X/\partial X)$ to the field gradient $-2e/R^2$ produced by the external charge. In view of Eq. (97), this ratio which was called γ_∞ is given by

$$\gamma_\infty=(R^3/2)\int\rho_{\text{ind},q}r^{-3}(3\cos^2\theta-1)dV. \quad (98)$$

By comparing (78) with (98), it is seen that α_q differs from γ_∞ only by having r^2 instead of r^{-3} in the integrand. Thus the integration over θ and φ, and the summation over the magnetic substates in Eq. (78) give the same coefficients as for γ_∞.

The radial wave functions $u'_{1,l\to l'}$ are determined by the following equation similar to Eq. (14) of reference 11,

$$\left[-\frac{d^2}{dr^2}+\frac{l'(l'+1)}{r^2}+V_0-E_0\right]u'_{1,l\to l'}=u'_0(r^2-\langle r^2\rangle_{nl}\delta_{ll'}), \quad (99)$$

where $\langle r^2\rangle_{nl}$ is given by Eq. (87). Obviously, Eqs. (82) and (90) are special cases of (99). The term $\langle r^2\rangle_{nl}\delta_{ll'}$ arises from the E_1u_0 term of Eq. (79) [see Eqs. (88) and (93)]. For the case $l=l'$ that solution $u'_{1,l\to l}$ of Eq. (99) must be chosen which is orthogonal to u'_0.

As is seen from Eqs. (84) and (96), $\alpha_q(nl\to l')$ involves the integral.

$$J_{l\to l'}\equiv\int_0^\infty u'_0u'_{1,l\to l'}r^2dr. \quad (100)$$

The coefficients of the $J_{l\to l'}$ can be obtained from the expression for γ_∞, as was mentioned above. For this purpose, we note that γ_∞ also occurs in the calculation of the quadrupole moment $Q_{\text{ind},Q}$ induced in the core by the nuclear quadrupole moment[20] Q. γ_∞ is equal to this induced moment expressed in units of Q. Thus the coefficients of the $J_{l\to l'}$ must be proportional to the coefficients which occur in the expression for $Q_{\text{ind},Q}$ as given by Eqs. (3) and (7) of reference 20. In fact, with the present normalization of the radial wave functions $u'_{1,l\to l'}$ [Eq. (99)] the coefficients for $Q_{\text{ind},Q}$ and for α_q turn out to be equal; e.g., the contribution to $Q_{\text{ind},Q}$ from $ns\to d$ is given by $(8/5)Q\int_0^\infty u'_0u'_{1,Q}r^2dr$, where $u'_{1,Q}$ is the appropriate perturbation; the coefficient 8/5 is equal to that which appears in Eq. (84) for $\alpha_q(ns\to d)$. Hence the coefficients of the $J_{l\to l'}$ can be obtained directly from Eqs. (3) and (7) of reference 20. One finds

$$\alpha_q=\sum_n\left(\frac{8}{5}J_{0\to2}\right)_{ns}+\sum_n\left(\frac{48}{25}J_{1\to1}+\frac{72}{25}J_{1\to3}\right)_{np}+\sum_n\left(\frac{8}{5}J_{2\to0}+\frac{16}{7}J_{2\to2}+\frac{144}{35}J_{2\to4}\right)_{nd}, \quad (101)$$

where the sums extend over the occupied s, p, and d shells, respectively. The terms $J_{1\to1}$ and $J_{1\to3}$ for np pertain to the $np\to p$ and $np\to f$ excitations, respectively. The terms for nd pertain to the $nd\to s$, $nd\to d$, and $nd\to g$ waves. Equation (101) gives α_q in units a_H^5 and must be multiplied by $0.529^5=0.0415$ to obtain α_q in units A^5.

For $1s\to d$, it is easily verified that if u'_0 is a hydrogenic wave function Eq. (82) has an exact solution which is given by

$$u'_{1,0\to2}=(Z^{-\frac{1}{2}}/2)r^2[1+\tfrac{2}{3}Zr]\exp(-Zr). \quad (102)$$

Upon inserting (17) and (102) into (84) one finds for both $1s$ electrons,

$$\alpha_q(1s\to d)=(30/Z^6)a_H^5. \quad (103)$$

Thus for the hydrogen atom, $\alpha_q=15a_H^5=0.622A^5$.

In order to obtain values of α_q for helium and the helium-like ions, the Löwdin[9] wave functions will again be used [Eq. (70)]. For the perturbation $u'_{1,0\to2}$ we will use an expression similar to Eq. (71) for the $1s\to p$ perturbation. In view of (102), $u'_{1,0\to2}$ will be taken as follows,

$$u'_{1,0\to2}=c_1\{(Z_1^{-\frac{1}{2}}/2)r^2[1+\tfrac{2}{3}Z_1r]\exp(-Z_1r)\}+c_2\{(Z_2^{-\frac{1}{2}}/2)r^2[1+\tfrac{2}{3}Z_2r]\exp(-Z_2r)\}. \quad (104)$$

[20] R. M. Sternheimer, Phys. Rev. 95, 736 (1954).

By inserting Eqs. (70) and (104) into (84) one obtains the values of α_q listed in Table III.

Besides the calculations for the helium-like ions, values of α_q were obtained for the cases of Na^+ and Cs^+ by numerical integration of Eq. (99). The results are listed in Table III. For Na^+, the contributions to $\alpha_q(=0.058A^5)$ are as follows: $0.013A^5$ from $2s\rightarrow d$, $0.020A^5$ from $2p\rightarrow p$, and $0.025A^5$ from $2p\rightarrow f$. The unperturbed functions u'_0 used in these calculations are the Hartree-Fock functions obtained by Fock and Petrashen.[12] As an illustration of the numerical procedure, in order to obtain the $2p\rightarrow p$ wave, $\langle r^2\rangle_{2p}$ is calculated from $u'_0(2p)$ and the resulting value $0.78a_H^2$ is inserted in Eq. (99) in which l and l' are taken as 1. $P(r_n)$ is obtained from the tabulated values of[12] u'_0 by means of (53), and $u'_{1,1\rightarrow 1}$ is calculated by outward integration by means of (55) in which

$$I(r)=u'_0(r^2-\langle r^2\rangle_{2p}).$$

After a function $u'_{1,1\rightarrow 1}$ is thus obtained, a suitable multiple of u'_0 is subtracted, so as to make the resulting function orthogonal to u'_0. From Eq. (103) the $1s\rightarrow d$ term for Na^+ is $0.0415\times(30/Z^6)\approx 0.8\times 10^{-6}A^5$ which is negligible.

For Cs^+ the wave functions obtained by Hartree[19] were used. The terms of $\alpha_q(=7.62A^5)$ are as follows: $0.90A^5$ for $5s\rightarrow d$, $1.56A^5$ for $5p\rightarrow p$, and $5.16A^5$ for $5p\rightarrow f$. The largest term is due to the $5p\rightarrow f$ waves, because the overlap of $5p$ with the $5p\rightarrow f$ function $u'_{1,1\rightarrow 3}$ is greatest for large values of r which in turn make large contributions to $J_{1\rightarrow 3}$ through the factor r^2 [see Eq. (100)]. The contribution of the inner shells is expected to be negligible because of the relatively small values of $\langle r^2\rangle_{nl}$ for these shells. This was verified by calculating the $4d\rightarrow g$ wave which gives one of the largest $n=4$ terms. The result was $\alpha_q(4d\rightarrow g)=0.019A^5$ which is negligible compared to the $n_0=5$ terms. Note that r^2 enters twice, namely in Eq. (99) for $u'_{1,l\rightarrow l'}$ and in the integral $J_{l\rightarrow l'}$. Since $\langle r^2\rangle_{nl}$ decreases rapidly as n is decreased, this explains why only the outermost shell contributes to α_q. The situation is similar to that for the dipole polarizability α. In fact, the relative contribution of the inner shells is even smaller for α_q than for α, because α_q depends essentially on $[\langle r^2\rangle_{nl}]^2$ as compared to the dependence of α on $\langle r^2\rangle_{nl}$.

TABLE III. Calculated values of the quadrupole polarizability (in units A^5).

Ion	α_q
H^-	71.1
He	0.101
Li^+	4.77×10^{-3}
Be^{++}	6.40×10^{-4}
B^{3+}	1.40×10^{-4}
C^{4+}	4.31×10^{-5}
Na^+	0.058
Cs^+	7.62

As was first shown by Mayer and Mayer,[2] the values of α_q enter into the term defect of the energy levels of the valence electron in the alkalis and the alkali-like atoms. The term defect ΔT is defined as the difference between the energy E of the level and the corresponding hydrogenic value which is $E_H=-R_AZ^2/n^2$, where R_A is the value of the Rydberg constant for the atom considered, Z is the net charge of the ion in whose field the valence electron moves, and n is the principal quantum number. Thus

$$\Delta T=E_H-E. \tag{105}$$

As is well known, ΔT has been interpreted by Born and Heisenberg[1] as due to the dipole moment induced in the electron core by the series electron. However, as pointed out by Mayer and Mayer,[2] the induced quadrupole moment makes an additional contribution to ΔT. The dipole part ΔT_d of ΔT is given by $\alpha\langle r^{-4}\rangle$ Rydberg, where α is the polarizability in units a_H^3 and $\langle r^{-4}\rangle$ is the average value of r^{-4} over the valence wave function, where r is in units a_H. The quadrupole part ΔT_q of ΔT is obtained in the same manner as[1,2] ΔT_d. For the following derivation we assume that all lengths are in cm. When the valence electron is at a distance r, the electric field gradient at the nucleus is $2e/r^3$, and hence the induced quadrupole moment is given by

$$Q_{\text{ind}}=2\alpha_q/r^3. \tag{106}$$

Q_{ind} gives rise to the following potential at the position of the valence electron,

$$\bar{V}_q=Q_{\text{ind}}e/(2r^3). \tag{107}$$

The resulting field is given by

$$E_q=-\partial\bar{V}_q/\partial r=3Q_{\text{ind}}e/(2r^4)=3\alpha_qe/r^7, \tag{108}$$

where the last equality follows from (106). From (108) one obtains for the potential due to E_q,

$$\delta V_q=e\int_r^\infty E_q\,dr'=-\alpha_qe^2/(2r^6). \tag{109}$$

Hence δV_q equals $-\alpha_q/r^6$ rydbergs, if α_q and r are units a_H^5 and a_H, respectively. Thus

$$\Delta T_q=\alpha_q\langle r^{-6}\rangle R_A, \tag{110}$$

where $\langle r^{-6}\rangle$ is the average of r^{-6} over the valence wave function.

It was shown by Mayer and Mayer[2] that the observed ΔT includes, besides ΔT_d and ΔT_q, a term ΔT_{pen} which is due to the penetration of the core by the series electron. The zero-order (spherical) part of the potential is larger than $2Z/r$ when the series electron is inside the core. ΔT_{pen} has been calculated by Mayer and Mayer.[2] Thus we have

$$\Delta T-\Delta T_{\text{pen}}=R_A[\alpha\langle r^{-4}\rangle+\alpha_q\langle r^{-6}\rangle]. \tag{111}$$

Mayer and Mayer[2] have made a study of the term defects by means of Eq. (111) in order to obtain values of α. In this treatment, they used estimates of α_q based on an expansion of the quadrupole perturbation of the core in terms of eigenfunctions of the unperturbed problem [similar to Eqs. (59)–(69) of Sec. III]. It was assumed that all of the excitations have the same energy denominator, so that the completeness properties of the eigenfunctions could be used. The expectation value of r^4 for the core electrons which enters into the resulting expression for α_q was not calculated directly, but was estimated from the values of $\langle r^2\rangle_{nl}$. The present values of α_q lead to a quadrupole term ΔT_q of the order of twice as large as that obtained by Mayer and Mayer.[2] It therefore seems worth while to repeat their calculations using the values of α_q of Table III. The discrepancy of the α_q is probably due in part to the approximations made by Mayer and Mayer.[2] On the other hand, the present values of α_q are subject to uncertainties, because α_q is rather sensitive to the zero-order wave functions, since it depends on the external part of the ion core through the factor r^2 in $J_{l\to l'}$. However, this reservation probably does not apply to the α_q for Be^{++}, B^{3+}, and C^{4+} because of the large binding of the 1*s* electrons for these ions.

Following Mayer and Mayer,[2] Eq. (111) will be written as follows,

$$\Delta T-\Delta T_{\text{pen}}=R_A\alpha_0\langle r^{-4}\rangle=R_A\alpha C_q\langle r^{-4}\rangle, \quad \text{(111a)}$$

where α_0 and C_q are constants; in view of (111), C_q is given by

$$C_q=1+\alpha_q\langle r^{-6}\rangle/(\alpha\langle r^{-4}\rangle). \quad (112)$$

In order to calculate C_q, $\langle r^{-4}\rangle$ is obtained from the formula of Waller[21] and $\langle r^{-6}\rangle$ is obtained from the work of Van Vleck.[22] For convenience the values of $\langle r^{-6}\rangle/\langle r^{-4}\rangle$ will be listed here; they are $0.222Z^2$, $0.271Z^2$, $0.291Z^2$ for 3*d*, 4*d*, 5*d*, respectively; and $0.0208Z^2$, $0.0267Z^2$, $0.0295Z^2$ for 4*f*, 5*f*, 6*f*, respectively. As has been mentioned previously by several authors,[1,2] $\langle r^{-6}\rangle/\langle r^{-4}\rangle$ and hence C_q-1 is approximately constant within a given series, but is considerably smaller for *nf* than for *nd*. For the *p* electrons $\langle r^{-6}\rangle$ diverges so that the present treatment is inapplicable.[2] C_q is obtained from the above $\langle r^{-6}\rangle/\langle r^{-4}\rangle$ together with values of α_q obtained from Table III and of α from Tables I and II. Note that α_q and α must be expressed in units $a_H{}^5$ and $a_H{}^3$, respectiively, for use in Eq. (112). The resulting values of C_q are listed in Table IV. The third column in this table lists the values of α_0 as obtained by Mayer and Mayer[2] from $\Delta T-\Delta T_{\text{pen}}$. The last column gives the resulting dipole polarizability $\alpha=\alpha_0/C_q$. By comparing Table IV with the results of Mayer and Mayer,[2] it is seen that the present values of C_q are appreciably larger. As a result, the values of α of Table VI are about 10–20 percent smaller than those given in reference 2.

TABLE IV. Values of the polarizability α as obtained from spectral term defects. The second column gives the state of the valence electron in the field of the ion. The values of the constant α_0 were calculated by Mayer and Mayer.[2] C_q is the factor which corrects for the quadrupole polarizability. α and α_0 are in units A^3.

Ion	State	α_0	C_q	α
Li^+	3*d*	0.0258	1.12	0.0230
	4*d*	0.0273	1.14	0.0239
	5*d*	0.005	1.16	0.0043
Be^{++}	3*d*	0.00841	1.24	0.00678
	4*d*	0.00746	1.30	0.00574
	5*d*	0.00696	1.32	0.00527
B^{3+}	3*d*	0.00361	1.32	0.00273
	4*d*	0.00405	1.40	0.00289
	5*d*	0.00421	1.43	0.00294
C^{4+}	3*d*	0.00185	1.40	0.00132
	4*d*	0.00193	1.48	0.00130
	5*d*	0.00198	1.52	0.00130
Na^+	3*d*	0.184	1.32	0.139
	4*d*	0.192	1.39	0.138
	5*d*	0.194	1.42	0.137
Cs^+	4*f*	2.58	1.11	2.32
	5*f*	2.61	1.14	2.29
	6*f*	2.56	1.16	2.21

In Table IV, values are given only for the *d* series, except for Cs, where the *d* levels are too strongly penetrating so that the *f* series must be used to calculate α. The "best" values of α as obtained by averaging the values[23] of Table IV are (in units A^3):

$$\alpha(Li^+)=0.0235,\quad \alpha(Be^{++})=0.0059,\quad \alpha(B^{3+})=0.0029,$$
$$\alpha(C^{4+})=0.0013,\quad \alpha(Na^+)=0.138,\quad \text{and}\quad \alpha(Cs^+)=2.27.$$

It is of interest that all of these values are somewhat smaller than those calculated from the perturbed wave functions, as was expected from the discussion of Sec. III.

V. ELECTRIC FIELD AT THE NUCLEUS

It was pointed out by Foley[24] that the electric field at the nucleus of an ion in the presence of an external electric field is known and can therefore be used as an additional test of the perturbed wave functions u_1. Taking first the example of a neutral atom, the total electric field at the nucleus $\mathbf{E}_{\text{tot}}(0)$ must be zero since the nucleus does not move. This means that the induced density must give rise to a field at the nucleus $\mathbf{E}_{\text{ind}}(0)$ which just cancels the external field. In the present discussion it is assumed that the external field is weak enough so that it does not cause ionization; this, of course, is implied in the assumption that $u_1\ll u_0$ so that first-order perturbation theory can be used. The external field will again be considered as due to a unit positive external charge $+e$ at a distance $X=R$ from the

[21] I. Waller, Z. Phys. 38, 635 (1926).

[22] J. H. Van Vleck, Proc. Roy. Soc. (London) A143, 679 (1934). The values of $\langle 1/r^4\rangle$ for *nd* states as given in this paper are too large by a factor of 10.

[23] The 5*d* level of Li will be excluded because the Li *nd* series is strongly perturbed starting with 5*d*, as can be seen from the fact that for $6d-9d$, E_H-E is negative, i.e., the valence electron is bound less strongly than for a hydrogenic level [see R. F. Bacher and S. Goudsmit, *Atomic Energy States* (McGraw-Hill Book Company, Inc., New York, 1932), first edition, p. 265].

[24] Professor H. M. Foley (private communication).

nucleus. For an ion of net charge qe, $E_{\text{tot},X}(0)$ must be $-qe/(ZR^2)$ since the force on the nucleus in the X direction is $-qe^2/R^2$. Thus the field due to the induced density is given by

$$E_{\text{ind},X}(0)=-\frac{qe}{ZR^2}+\frac{e}{R^2}=\frac{e}{R^2}\left(1-\frac{q}{Z}\right), \tag{113}$$

where the term e/R^2 in the first equality is minus the external field. By calculating $E_{\text{ind},X}(0)$ from the perturbed wave functions u_1 and comparing with Eq. (113) one obtains an additional check on the u_1. It may be noted that the preceding considerations can also be used for the total force on the electrons in the presence of an external field. Since the acceleration of the electrons is the same as that of the nucleus, the force must be smaller by a factor of order m/M, where m and M are the mass of the electron and of the proton, respectively.[25] In the present approximation this means that the total force on the electrons must be zero both for neutral atoms and ions, i.e., the force due to the induced distribution cancels the effect of the external field e/R^2.

If Eq. (113) is satisfied, then it follows that the total force F_X on the electrons is zero, so that the condition $F_X=0$ does not lead to a further test of the perturbed wave functions u_1. In order to prove this result, we note that $E_{\text{ind},X}(0)$ is given by

$$E_{\text{ind},X}(0)=e\int\rho_{\text{ind}}r^{-2}\cos\theta dV, \tag{114}$$

where ρ_{ind} is the electron density induced by the field e/R^2 of the external charge $+e$ at $X=R$. The force on the electrons F_X consists of two parts: (1) the force $F_{\text{ext},X}$ due to the external charge which is

$$F_{\text{ext},X}=(Z-q)e^2/R^2, \tag{115}$$

since there are $Z-q$ electrons; (2) the force $F_{\text{ind},X}$ due to the electric field of the nucleus acting on ρ_{ind}. Since the component of electric field along X is $Ze\cos\theta/r^2$, $F_{\text{ind},X}$ is given by

$$F_{\text{ind},X}=-Ze^2\int\rho_{\text{ind}}r^{-2}\cos\theta dV=-ZeE_{\text{ind},X}(0), \tag{116}$$

where the last equality follows from Eq. (114). Thus in order that $F_X=0$, we must have

$$F_{\text{ext},X}+F_{\text{ind},X}=-Ze\left[E_{\text{ind},X}(0)-\left(1-\frac{q}{Z}\right)\frac{e}{R^2}\right]=0, \tag{117}$$

which leads to the condition of Eq. (113) for $E_{\text{ind},X}(0)$.

In order to obtain an expression for $E_{\text{ind},X}(0)$ in terms of the u_0 and u_1, we note that the induced dipole moment is given by

$$\alpha e/R^2=e\int\rho_{\text{ind}}r\cos\theta dV. \tag{118}$$

Since (114) and (118) involve the same angular factor, the integration over θ and φ, and the summation over the magnetic substates give the same coefficients as for α, and hence $E_{\text{ind},X}(0)$ is given by the following expression similar to Eqs. (50) and (51),

$$E_{\text{ind},X}(0)=\frac{e}{R^2}\left\{\sum_n\left(\frac{8}{3}K_{0\to1}\right)_{ns}+\sum_n\left(\frac{8}{3}K_{1\to0}+\frac{16}{3}K_{1\to2}\right)_{np}+\sum_n\left(\frac{16}{3}K_{2\to1}+8K_{2\to3}\right)_{nd}+\sum_n\left(8K_{3\to2}+\frac{32}{3}K_{3\to4}\right)_{nf}\right\}, \tag{119}$$

where $K_{l\to l'}$ is defined by

$$K_{l\to l'}\equiv\int_0^\infty u'_0u'_{1,\,l\to l'}r^{-2}dr. \tag{120}$$

The sums of Eq. (119) extend over the filled s, p, d, and f shells. Before proceeding to the calculations for the helium-like ions by means of the Löwdin wave functions, we note the result of Eq. (119) for the $1s$ electrons when the hydrogenic wave functions of Eqs. (17) and (18) are used. If one considers an ion with a single $1s$ electron (e.g., He^+, Li^{++}, etc.) one obtains for the field due to ρ_{ind} by substituting (17) and (18) into (119):

$$E_{\text{ind},X}(0)=(4/3)(e/R^2)K_{0\to1}=e/(ZR^2). \tag{121}$$

This agrees with Eq. (113) since $q=Z-1$ when only one $1s$ electron is present.

In obtaining $E_{\text{ind},X}(0)$ for the helium-like ions using the Löwdin[9] wave functions, $K_{0\to1}$ [Eq. (120)] was evaluated using Eq. (70) for u'_0 and Eq. (71) for $u'_{1,0\to1}$. The results are given in the second column of Table V. The values listed are $E_{\text{ind},X}(0)/(e/R^2)$ which will be denoted by $\bar{E}_{\text{ind},X}(0)$. Thus $\bar{E}_{\text{ind},X}(0)$ was calculated from

$$\bar{E}_{\text{ind},X}(0)=(8/3)\int_0^\infty u'_0u'_{1,0\to1}r^{-2}dr. \tag{119a}$$

The third column gives the actual values of $\bar{E}_{\text{ind},X}(0)$, i.e., $1-q/Z$ [see Eq. (113)]. The fourth column gives the ratio ρ of the calculated to the actual values. It is seen that ρ is always larger than 1, as was expected from the similar result for the polarizability α. Thus since the calculated wave functions give too little

[25] If the mass of the electrons is not neglected, $-qe/ZR^2$ in Eq. (113) is replaced by $-(qe/ZR^2)(1-M_e/M_i)$, where M_e = mass of all electrons and M_i = mass of ion. The force on the electrons is then $F_X=-(qe^2/R^2)(M_e/M_i)$.

binding, they are expected to give values for the induced density which are too large, and hence an overestimate of $\bar{E}_{\text{ind},X}(0)$. ρ decreases with increasing state of ionization in passing from H^- to C^{4+}. This result can be explained as follows. As the field due to the nucleus becomes relatively more important in comparison with the repulsion between the electrons, the wave function becomes less sensitive to small inaccuracies of the binding, and hence the calculated $E_{\text{ind},X}(0)$ should become closer to the actual value.

Besides the calculations for the helium-like ions, $E_{\text{ind},X}(0)$ was also calculated numerically from the perturbed wave functions $u'_{1,l\to l'}$ for the cases of F^-, Na^+ and Al^{3+}. The integrals involved in (120) were carried out numerically, using the functions $u'_{1,l\to l'}$ obtained in Sec. III. However, the $2p\to d$ wave functions $u'_{1,1\to 2}$ for Na^+ and Al^{3+} were recalculated by outward integration starting with a power series near $r=0$, so that accurate values could be obtained near the nucleus which is the region of importance for $E_{\text{ind},X}(0)$, because of the $1/r^2$ factor in $K_{1\to 2}$. This recalculation was necessary because the function $u'_{1,1\to 2}$ determined in Sec. III for the calculation of α was obtained by inward integration starting from a large r. This procedure does not give reliable values of $u'_{1,1\to 2}$ near the nucleus. For F^-, the function $u'_{1,1\to 2}$ determined in Sec. III to calculate α had been obtained by outward integration from the nucleus so that a recalculation was not necessary. The resulting values of $\bar{E}_{\text{ind},X}(0)$ are listed in Table V. The contributions to $\bar{E}_{\text{ind},X}(0)$ from $1s\to p$, $2s\to p$, $2p\to s$, and $2p\to d$ are as follows for F^-: 0.23, 1.42, -1.29, and 1.91, respectively. For Na^+ the contributions in the same order are: 0.19, 1.06, -0.95, and 1.05. For Al^{3+} the corresponding terms are 0.16, 0.82, -0.74, and 0.80. We note that for the $1s$ shells a numerical calculation was not carried out, since the term of $\bar{E}_{\text{ind},X}(0)$ is given to a good approximation by $2/Z_{\text{eff}}$ [see Eq. (121)] where Z_{eff} is an effective Z obtained by subtracting from the atomic number a correction for shielding of 0.30 as obtained from Slater's[26] screening constants. We note that the $2s\to p$ and $2p\to s$ terms nearly cancel each other, as was expected in view of the behavior of the wave functions $u'_{1,0\to 1}$ and $u'_{1,1\to 0}$ and of the corresponding terms for α. The values of ρ again decrease with increasing binding in going from F^- to Al^{3+}. The large value of ρ for F^- arises for the same reason as the similar discrepancy for α (see Table I), namely the use of Hartree wave functions (without exchange) which give considerably too little binding for $2p$. We note, however, that the discrepancy $\rho=2.05$ is less than the corresponding discrepancy for α, presumably because the wave functions are less sensitive to binding near $r=0$ than in the region of large r which is of importance for α.

The values of ρ are of interest in connection with previous calculations of the electric field gradient at the nucleus due to the charge distribution induced in the core by an external charge or valence electron.[11,20] This effect is of importance in the determination of nuclear quadrupole moments, since it enters into the nuclear quadrupole coupling q. An estimate of the reliability of this calculated correction Δq to q can be obtained from the accuracy of $E_{\text{ind},X}(0)$, i.e., from the values of ρ. The calculation of $E_{\text{ind},X}(0)$ should be better suited for this estimate than the calculated α, since the integrand of $K_{l\to l'}$ for $E_{\text{ind},X}(0)$ has a factor $1/r^2$ and involves therefore the region near the nucleus in a manner similar to $\Delta q\,[=\Delta(\partial E_X/\partial X)$, see Eq. (97)] which involves $1/r^3$, and in contrast to α for which the integrand of $I_{l\to l'}$ has a factor r and depends essentially on the behavior of the wave functions at large r. We may conclude that the calculated Δq is probably overestimated by $\sim$10–50 percent, except possibly for negative ions, where the overestimate may be larger if the calculations are based on Hartree wave functions (without exchange). This estimate of the accuracy of Δq is actually not very different from that which would have been obtained from a comparison of the calculated values of α with the experimental values. However, it should be noted that the values of the overestimate given above neglect two differences between Δq and $E_{\text{ind},X}(0)$. $E_{\text{ind},X}(0)$ was calculated for the field of an external charge, whereas Δq is determined by the field of the valence electron which penetrates the core during an appreciable part of the time. This fact reduces Δq considerably and may tend to make the error for Δq smaller than that for $E_{\text{ind},X}(0)$ since the region near the nucleus (which is insensitive to binding) becomes more emphasized. The second difference is that Δq involves a different perturbation than $E_{\text{ind},X}(0)$, namely a perturbation in which l changes by 0 or 2 units, whereas $E_{\text{ind},X}(0)$ involves $\Delta l=\pm 1$. The perturbation which gives rise to $E_{\text{ind},X}(0)$ is probably more related to the modes of excitation with $\Delta l=\pm 2$ (shielding modes) for Δq than to those with $\Delta l=0$ (radial or antishielding modes).[20]

It seems of interest to calculate $E_{\text{ind},X}(0)$ from the Thomas-Fermi model, in order to compare with the wave function results. The calculation follows the same

TABLE V. Values of the field at the nucleus due to the induced charge distribution. $\bar{E}_{\text{ind},X}(0)$ is the induced field (in units of e/R^2) as obtained from wave function calculations. $1-q/Z$ is the actual value of $\bar{E}_{\text{ind},X}(0)$, and ρ is the ratio of the calculated to the actual value.

Ion	$\bar{E}_{\text{ind},X}(0)$	$1-q/Z$	ρ
H^-	3.81	2	1.91
He	1.32	1	1.32
Li^+	0.792	0.667	1.19
Be^{++}	0.566	0.5	1.13
B^{3+}	0.441	0.4	1.10
C^{4+}	0.361	0.333	1.08
F^-	2.27	1.11	2.05
Na^+	1.35	0.909	1.49
Al^{3+}	1.04	0.769	1.35

[26] J. C. Slater, Phys. Rev. 36, 57 (1930).

lines as the Thomas-Fermi calculation[27] of Δq. The momentum p of an electron in the presence of an external charge $+e$ at $X=R$ is given by

$$\frac{p^2}{2m}=\frac{Z\chi e^2}{r}+\frac{e^2 r\cos\theta}{R^2}, \tag{122}$$

where χ is the Thomas-Fermi function. If p_0 denotes the momentum in the absence of the external charge, and $\Delta p=p-p_0$, we have

$$p_0\Delta p=me^2 r\cos\theta/R^2, \tag{123}$$

$$p_0=(2mZ\chi e^2/r)^{\frac{1}{2}}. \tag{124}$$

The change of density $\Delta\rho$ corresponding to Δp is given by

$$\Delta\rho=8\pi p_0^2\Delta p/h^3. \tag{125}$$

The field at the nucleus produced by $\Delta\rho$ is

$$E_{\text{ind},x}(0)=2\pi e\int_0^\infty\int_0^\pi \Delta\rho\cos\theta dr\sin\theta d\theta. \tag{126}$$

Upon inserting Eqs. (123), (124), and (125) into (126) and integrating over θ one obtains

$$E_{\text{ind},x}(0)=\frac{e}{R^2}\left[\frac{32\pi^2 2^{\frac{1}{2}}m^{\frac{1}{2}}Z^{\frac{1}{2}}e^3}{3h^3}\int_0^\infty(\chi r)^{\frac{1}{2}}dr\right]. \tag{127}$$

Upon using the Thomas-Fermi variable

$$x=2Z^{\frac{1}{2}}r(3\pi/4)^{-\frac{1}{2}}a_H^{-1},$$

one finds

$$E_{\text{ind},x}(0)=(e/2R^2)\int_0^\infty(\chi x)^{\frac{1}{2}}dx. \tag{128}$$

The integral over $(\chi x)^{\frac{1}{2}}$ diverges logarithmically at the upper limit, because χ falls off only as $1/x^3$ for large x, instead of exponentially, as required by the wave functions. This result is associated with the inadequacy of the statistical model for large x. Thus we can conclude that the Thomas-Fermi model (without exchange) cannot be used to discuss the distribution induced by an external charge.[28]

In contrast to the function χ, the Thomas-Fermi-Dirac potential χ_{exch} which includes exchange vanishes for large x. Since the difficulties encountered above are associated with this region, it appears possible that the Thomas-Fermi-Dirac potential will give reasonable results for $E_{\text{ind},x}(0)$. A derivation of $E_{\text{ind},x}(0)$ using the potential χ_{exch} will now be given.

The maximum momentum p_0 in the Thomas-Fermi-Dirac model is determined by[29]

$$\frac{p_0^2}{2m}-\frac{2e^2p_0}{h}+e(E_0-V_0)=0, \tag{129}$$

where E_0 is the maximum energy of the electrons, and V_0 is the electrostatic potential; the second term $-2e^2p_0/h$ takes into account the exchange. If V_0 is varied by an amount

$$\Delta V=er\cos\theta/R^2, \tag{130}$$

the resulting change of p_0 called Δp is determined by

$$\frac{p_0\Delta p}{m}-\frac{2e^2\Delta p}{h}-e\Delta V=0, \tag{131}$$

which gives

$$\Delta p=e\Delta V\Big/\left(\frac{p_0}{m}-\frac{2e^2}{h}\right). \tag{132}$$

The solution of Eq. (129) for p_0 is given by[29]

$$p_0=\frac{2e^2m}{h}+\left[\frac{4e^4m^2}{h^2}+2em(V_0-E_0)\right]^{\frac{1}{2}}. \tag{133}$$

The change of the density $\Delta\rho$ is again given by Eq. (125). Upon using the definition of χ_{exch} given by Slater and Krutter,[29]

$$Z\chi_{\text{exch}}e/r=V_0-E_0+2me^3/h^2, \tag{134}$$

p_0 can be written as follows,

$$p_0=4(4\pi^2/3)^{\frac{1}{2}}me^2h^{-1}[\epsilon+(\chi_{\text{exch}}/x)^{\frac{1}{2}}], \tag{135}$$

where $\epsilon=0.2118Z^{-\frac{1}{2}}$ and x is the Thomas-Fermi variable defined after Eq. (127). We also have

$$\frac{p_0}{m}-\frac{2e^2}{h}=\frac{me^2}{h}\left(\frac{\chi_{\text{exch}}}{x}\right)^{\frac{1}{2}}. \tag{136}$$

---

[27] R. M. Sternheimer, Phys. Rev. **80**, 102 (1950).

[28] The same integral over $(\chi x)^{\frac{1}{2}}$ also occurs in the expression for the quadrupole moment induced by the nuclear quadrupole moment Q. The total induced quadrupole moment is given by

$$Q_{\text{ind},Q}=(3/10)Q\int_0^\infty(\chi x)^{\frac{1}{2}}dx, \tag{128a}$$

and its sign is such as to shield the nuclear Q. [Note that the factor 0.2998 in Eq. (8) of reference 27 should be 3/10.] The divergence of the integral for large x does not affect the calculation of Δq for atomic ground states since Δq depends only on the values of $(\chi x)^{\frac{1}{2}}$ near the nucleus [see reference 20 and discussion at the end of this section]. From Eq. (128a) one can also conclude that the electric field gradient at the nucleus produced by an external charge is changed by an amount

$$\Delta\left(\frac{\partial Ex}{\partial x}\right)=\frac{2e}{R^3}\left[\frac{3}{10}\int_0^\infty(\chi x)^{\frac{1}{2}}dx\right], \tag{128b}$$

due to the perturbation of the core by the external change [R. M. Sternheimer and H. M. Foley, Phys. Rev. **92**, 1460 (1953)]. Thus the Thomas-Fermi model is inadequate both for the electric field and the electric field gradient at the nucleus due to an external charge.

[29] J. C. Slater and H. M. Krutter, Phys. Rev. **47**, 559 (1935).

The rest of the derivation is identical with that given in Eqs. (126)–(129) for the Thomas-Fermi model. From Eqs. (132), (135), and (136), one obtains

$$E_{\text{ind},\chi}(0)=(e/2R^2)\int_0^{x_0}[\epsilon+(\chi_{\text{exch}}/x)^{\frac{1}{2}}]^2 \times(\chi_{\text{exch}}/x)^{-\frac{1}{2}}x\,dx, \quad (137)$$

where x_0 is the value of x beyond which $\chi_{\text{exch}}=0$. Equation (137) differs from (128) only through the replacement of χ by χ_{exch} and the presence of ϵ.

Values of χ_{exch} throughout the range of Z have been obtained by Metropolis and Reitz.[30] We have carried out calculations of $E_{\text{ind},\chi}(0)$ using the tabulated χ_{exch} for $Z=18$ and 57, to correspond approximately to the cases of Cl and Cs, respectively. For each value of Z, Metropolis and Reitz[30] have calculated several functions χ_{exch} which are obtained by using different slopes at $x=0$ and lead to different values of x_0. Solutions with a relatively large downward slope at $x=0$ become zero at a finite $x=x_0$ and correspond to positive ions. Solutions with a less negative slope at $x=0$ go through a minimum at large x and correspond to neutral atoms; they are cut off at the value of $x=x_0$ for which

$$\left(\frac{d\chi_{\text{exch}}}{dx}\right)_{x=x_0}=\left(\frac{\chi_{\text{exch}}}{x}\right)_{x=x_0}.$$

Equation (137) was evaluated for nine cases. The results are given in Table VI. The first two columns list the value of Z and the number labeling the function χ_{exch} as given by Metropolis and Reitz[30] (e.g., $Z=18$, 1 is "case 1" for $Z=18$ in their paper). The third column lists the values of x_0; the unit of x is $0.338a_{\text{H}}$ for $Z=18$ and $0.230a_{\text{H}}$ for $Z=57$. The fourth column gives the net charge $Z_i(=q)$ of the ion if the solution is ionic; the other cases where no value is listed correspond to neutral atoms of various radii. The next column gives $\bar{E}_{\text{ind},\chi}(0)$ which is one-half the integral of Eq. (137), while the last column lists the values of $\bar{E}_{\text{ind},\chi}(0)/x_0$. It may be noted that for ionic solutions where χ_{exch} becomes zero at x_0, the integrand of (137) has a singularity at $x=x_0$. However, since the integrand goes as $(x_0-x)^{-\frac{1}{2}}$ near x_0, the integral is finite, and in fact, the region near x_0 makes only a very small contribution.

It is seen that the calculated $\bar{E}_{\text{ind},\chi}(0)$ are considerably too large, since the actual value is 1 for neutral atoms and $1-Z_i/Z$ for ions [see Eq. (113)]. Except for $Z=57$, case 7, the disagreement is by a factor larger than 2 with values ranging up to 4.6 for $Z=57$, case 3. These values of ρ may be compared with those obtained from the wave function calculations (see Table V) which are generally in the range 1–1.5. It may be noted that the values of $\bar{E}_{\text{ind},\chi}(0)/x_0$ are nearly constant. Thus the Thomas-Fermi-Dirac values of $\bar{E}_{\text{ind},\chi}(0)$ depend primarily on the radius x_0. For ions the general decrease of $\bar{E}_{\text{ind},\chi}(0)$ with increasing Z_i and decreasing x_0 is in the right direction, but the values of $\bar{E}_{\text{ind},\chi}(0)$ for the small Z_i of interest are too large. For neutral atoms one could obtain a value of $\bar{E}_{\text{ind},\chi}(0)$ close to 1 by assuming a small value for the radius x_0. However, as is shown by the example of $Z=57$, case 7, the required x_0 would be unreasonably small, since $x_0=3.81$ for $Z=57$, case 7, corresponds to a radius of $3.81\times0.230=0.88a_{\text{H}}$, which is considerably smaller than the radius of the outermost maximum of the $5p$ distribution which occurs at $r=1.9a_{\text{H}}$.

TABLE VI. Values of $\bar{E}_{\text{ind},\chi}(0)$ from the Thomas-Fermi-Dirac model.

Z	Case	x_0	Z_i	$\bar{E}_{\text{ind},\chi}(0)$	$\bar{E}_{\text{ind},\chi}(0)/x_0$
18	1	6.00	3.047	2.19	0.365
18	2	9.20	0.976	3.99	0.434
18	3	7.25		2.98	0.411
18	4	6.66		2.73	0.409
18	5	5.46		2.22	0.406
57	1	5.17	14.80	1.59	0.306
57	3	12.80	2.303	4.41	0.345
57	4	9.66		3.50	0.362
57	7	3.81		1.47	0.385

It should be emphasized that the preceding discussion of the inadequacy of the statistical model for the field at the nucleus produced by an external charge does not apply to the correction Δq to the quadrupole coupling for atomic states. Δq can be regarded as due to the interaction of the valence electron with the quadrupole moment $Q_{\text{ind},Q}$ induced in the core by the nuclear Q. The Thomas-Fermi expression for the density of induced moment is[27,28]

$$Q_{\text{ind},Q}dr=(3/10)Q(\chi x)^{\frac{1}{2}}(x/r)dr. \quad (138)$$

For the atomic ground states and first excited states the statistical model can be used to calculate the shielding because the result depends only on the values of $(\chi x)^{\frac{1}{2}}$ near the nucleus, by virtue of the penetration of the valence electron. Thus in the expression[27] for Δq, $(\chi x)^{\frac{1}{2}}$ is essentially multiplied by v^2, where v is r times the valence wave function. As a result of the exponential decrease of v^2 at large r, the contribution of this region to Δq becomes negligible. As was shown in reference 20, the Thomas-Fermi values of Δq divided by 1.5 give a good estimate of the contribution of the shielding modes of excitation of the core to the quadrupole coupling. The factor 1.5 by which the Thomas-Fermi model overestimates these shielding terms arises primarily because $Q_{\text{ind},Q}$ is too large near the nucleus.

In the same manner as in the derivation of (137), one can show that the density of induced moment according to the Thomas-Fermi-Dirac model is given by

$$Q_{\text{ind},Q}dr=(3/10)Q\{[\epsilon+(\chi_{\text{exch}}/x)^{\frac{1}{2}}]^2 \times(\chi_{\text{exch}}/x)^{-\frac{1}{2}}x\}(x/r)dr. \quad (139)$$

The previous calculations[20] of Δq from the statistical

[30] N. Metropolis and J. R. Reitz, J. Chem. Phys. 19, 555 (1951).

model were carried out using the Thomas-Fermi expression (138). However, the values given by (139) differ from (138) by less than 12 percent (for $Z \geqq 18$) in the region of importance near the nucleus (i.e., for $x \lesssim 2$). Thus at $x=2$, the curly bracket of (139) which replaces $(\chi x)^{\frac{1}{2}}$ in Eq. (138) has the value 0.779 for $Z=18$ and 0.732 for $Z=57$, as compared to $(\chi x)^{\frac{1}{2}}=0.698$. These differences are even smaller for $x<2$ and vanish as $x \to 0$. Hence the previous conclusions[20] about the Thomas-Fermi values of Δq are essentially unaffected by the inclusion of exchange in the statistical model.

I would like to thank Professor H. M. Foley for suggesting this problem and for several helpful and stimulating discussions.

PHYSICAL REVIEW VOLUME 96, NUMBER 4 NOVEMBER 15, 1954

Rotational Spectra of RbCl by the Molecular Beam Electric Resonance Method*

J. W. TRISCHKA† AND R. BRAUNSTEIN‡
Columbia University, New York, New York

(Received August 2, 1954)

The rotational transitions for which $J=0 \to 1$ were studied by the molecular beam electric resonance method for the first three vibrational states, $v=0, 1, 2$, of $Rb^{85}Cl^{35}$ and the ground vibrational state, $v=0$, of $Rb^{87}Cl^{35}$. The molecular constants are:

	$Rb^{85}Cl^{35}$	$Rb^{87}Cl^{35}$
Y_{01} (Mc/sec)	2627.394 ±0.002	2609.779±0.003
$-Y_{11} \approx \alpha_e$ (Mc/sec)	13.601 ±0.005	13.464±0.005
$Y_{21} \approx \gamma_e$ (Mc/sec)	0.021 ±0.002	0.021±0.002
B_e (Mc/sec)	2627.414 ±0.010	
r_e (A)	2.78670±0.00006	

The quadrupole (eqQ) and spin-rotation (c) interaction constants of $Rb^{85}Cl^{35}$ are:

	$v=0$	$v=1$	$v=2$
$(eqQ)_{Rb}$ (Mc/sec)	−52.675±0.005	−52.306±0.030	−51.903±0.040
$(eqQ)_{Cl}$ (Mc/sec)	+ 0.774±0.009	+ 0.612±0.013	+ 0.470±0.017
c_{Rb} (kc/sec)	+ 0.3 ±0.3		
c_{Cl} (kc/sec)	0.0 ±0.8		

For the $v=0$ state of $Rb^{87}Cl^{35}$, $(eqQ)_{Rb}=-25.485\pm0.006$ Mc/sec. The ratio of the Rb quadrupole moments is $Q_{85}/Q_{87}=2.0669\pm0.0005$. The mass ratio of the Rb isotopes is $M_{85}/M_{87}=0.9770163\pm0.0000045$.

I. INTRODUCTION

THROUGH their studies of KCl and KBr Carlson, Fabricand, Lee, and Rabi[1,2] initiated an investigation by the molecular beam electric resonance method[1,3] of the rotational spectra of the alkali halide molecules in their ground $^1\Sigma$ electronic states. We have continued this work by studying the $J=0 \to 1$ transitions of $Rb^{85}Cl^{35}$ in its three lowest vibrational states and of $Rb^{87}Cl^{35}$ in its ground vibrational state.

We selected RbCl in order to clarify further the nature of the Cl quadrupole interaction which shows unusual variations with vibration in KCl.[2] Also, at the outset of our work, the mass ratio of the Rb isotopes had not been determined with the accuracy made possible by the electric resonance method. Since then Honig, Mandel, and Townes, using microwave absorption measurements of the rotational spectra of RbBr and RbI, have obtained this mass ratio with an accuracy equal to ours,[4] while Collins, Johnson, and Nier have made mass spectrometric measurements which give a mass ratio of much greater accuracy.[5]

The hyperfine structure of the spectra yielded the Rb and Cl quadrupole and spin-rotation interaction constants, the ratio of the quadrupole moments of the Rb isotopes and the frequencies of the unperturbed rotational lines. The last-named frequencies gave the first three rotational constants of the molecules, the equilibrium internuclear distance and the mass ratio of the Rb isotopes. Of the above quantities the following have been measured by other methods: the magnitudes of the quadrupole and spin-rotation interactions of Rb^{87} in $Rb^{87}Cl$,[6] the ratio of the quadrupole moments of the Rb isotopes,[7] the internuclear distance,[8] and the mass ratio of the Rb isotopes.[4,5] These constants, with the

* This research was supported in part by the Office of Naval Research and by the Army Signal Corps.

† On leave of absence from Syracuse University, Syracuse, New York, 1952–1953.

‡ Now at RCA Laboratories, Princeton, New Jersey.

[1] Lee, Fabricand, Carlson, and Rabi, Phys. Rev. **91**, 1395 (1953).

[2] Fabricand, Carlson, Lee, and Rabi, Phys. Rev. **91**, 1403 (1953).

[3] H. K. Hughes, Phys. Rev. **72**, 614 (1947).

[4] Honig, Mandel, and Townes (private communication).

[5] Collins, Johnson, and Nier, Phys. Rev. **94**, 398 (1954).

[6] D. I. Bolef and H. J. Zeiger, Phys. Rev. **85**, 799 (1952).

[7] V. Hughes and L. Grabner, Phys. Rev. **79**, 314 (1950).

[8] Maxwell, Hendricks, and Mosley, Phys. Rev. **52**, 968 (1937).

exception of the Rb spin-rotation interaction and Rb mass ratio, have been determined by us with much greater accuracy.

The apparatus and procedure used in our experiments has been described by others.[1,2]

II. THEORY

The first order Hamiltonian used to explain and to make calculations from the hyperfine structure of the observed rotational spectra of RbCl is

$$\begin{aligned}\mathcal{H}=&-(eqQ)_{\mathrm{Rb}}[3(\mathbf{I}_1\cdot\mathbf{J})^2+\tfrac{3}{2}(\mathbf{I}_1\cdot\mathbf{J})\\&-\mathbf{I}_1^2\mathbf{J}^2]/2I_1(2I_1-1)(2J-1)(2J+3)\\&-(eqQ)_{\mathrm{Cl}}[3(\mathbf{I}_2\cdot\mathbf{J})^2+\tfrac{3}{2}(\mathbf{I}_2\cdot\mathbf{J})\\&-\mathbf{I}_2^2\mathbf{J}^2]/2I_2(2I_2-1)(2J-1)(2J+3)\\&+c_{\mathrm{Rb}}(\mathbf{I}_1\cdot\mathbf{J})+c_{\mathrm{Cl}}(\mathbf{I}_2\cdot\mathbf{J}).\quad(1)\end{aligned}$$

The first two terms in Eq. (1) are the operators for the quadrupole interactions, while the last two terms are the operators for the spin-rotation interactions. The nuclear spin-spin interaction is negligible. The quadrupole interaction constant defined by Bardeen and Townes is eqQ.[9] I_1 and I_2, the Rb and Cl nuclear spins, have the values 5/2, 3/2, and 3/2 for Rb^{85}, Rb^{87}, and Cl^{35}, respectively. J is the rotational quantum number.

The observed spectral lines can be explained without the use of the last term in Eq. (1); i.e., $c_{\mathrm{Cl}}=0$ within experimental error. However, it is not permissible to omit this term from the Hamiltonian since it cannot be concluded that $c_{\mathrm{Cl}}\equiv 0$. Therefore, while only the first three terms in Eq. (1) were used to determine the interaction constants for these terms, all four terms were used to determine the errors in these constants and in c_{Cl}.

Because $(eqQ)_{\mathrm{Rb}}\gg(eqQ)_{\mathrm{Cl}}$, the energy levels obtained by the use of the first three terms in Eq. (1) are, in the notation of Bardeen and Townes,[9,10]

$$\begin{aligned}W(F_1,F)=&E(F_1)+A(F_1,F_1)\\&+\sum_{F_1'\neq F_1}[A(F_1,F_1')]^2/[E(F_1)-E(F_1')]\\&+(c_{\mathrm{Rb}}/2)[F_1(F_1+1)-I_1(I_1+1)-J(J+1)].\quad(2)\end{aligned}$$

F_1 and F are defined by $\mathbf{F}_1=\mathbf{I}_1+\mathbf{J}$ and $\mathbf{F}=\mathbf{I}_2+\mathbf{F}_1$. The first term in Eq. (2) is the first-order energy of the Rb quadrupole interaction, while the second and third terms are the first and second order energies of the Cl quadrupole interaction. The last term is contributed by the Rb spin-rotation interaction.

The Rb quadrupole interaction is large enough to produce an observable mixing of rotational states. When the matrix elements of Bardeen and Townes were used to calculate this second order effect,[11] the first order energy levels of $Rb^{85}Cl^{35}$ were shifted by the following amounts: ($J=0$, $F_1=5/2$), −6.2 kc/sec; (1, 3/2), −0.6 kc/sec; (1, 5/2), −2.2 kc/sec; (1, 7/2), −3.0 kc/sec.

The rotational constants were calculated from equations most conveniently found in reference 2 and originally derived by Dunham.[12]

III. SPECTRA

The total beam, refocused beam, and line intensities were of the same order as those observed with KBr.[3] For the weakest line which could be observed, the decrease in refocused beam produced a change of 3×10^{-15} amp in the ion current. The corresponding change for the strongest line was 10×10^{-15} amp. The sensitivity of the dc amplifier, expressed in terms of galvanometer deflection, was 10^{-15} amp/cm.

The measured line width was usually 16 kc/sec, while the predicted width was 8 kc/sec.[13] The discrepancy between the observed and predicted line widths suggests that the radiofrequency (rf) power was too high. However, when the rf power was reduced, it was usually found that the line intensity decreased with no corresponding decrease in line width. On the other hand, it was found for a few lines, observed under conditions for which the signal-to-noise ratio was exceptionally high, that when the rf power was reduced sufficiently the lines split symmetrically into two lines about 8 kc/sec wide, separated at their peaks by a frequency of 12 kc/sec. No satisfactory explanation of this effect has been found and further confirmation and study of it seems necessary. It is believed that this line splitting is a consequence of some structural feature of the apparatus and is not a feature of the spectra of RbCl. The position of a line for which this splitting was observed was taken as midway between the peaks of the two lines into which it was split.

All of the lines observed were for the transition $J=0\rightarrow1$. Since there is no hyperfine structure when $J=0$, the hyperfine structure of the spectrum for a given vibrational state is identical with that for the rotational state $J=1$ and is conveniently labeled with the (F,F_1) values for the levels of this state. The numbers of experimentally distinct lines predicted for one vibrational state are eleven for $Rb^{85}Cl^{35}$ and eight for $Rb^{87}Cl^{35}$.

Table I is a list of all of the lines observed for $Rb^{85}Cl^{35}$ and $Rb^{87}Cl^{35}$. The largest number of lines was observed for the ground vibrational state $v=0$ of $Rb^{85}Cl^{35}$ because these lines had the greatest intensities. The only missing line in this spectrum, the one for which $F=0$ and $F_1=3/2$, was too weak to observe. No effort was made to study the lines of $Rb^{85}Cl^{35}$ designated by $F_1=5/2$ and $v=1,2$. The lines of the $Rb^{87}Cl^{35}$ spectrum specified by $F_1=3/2$ and $F=0,2$ were too weak to

[9] J. Bardeen and C. H. Townes, Phys. Rev. **73**, 97 (1948).
[10] The first three terms in Eq. (2) are given in reference 1 in different notation. The last term comes from V. Hughes and L. Grabner, Phys. Rev. **79**, 829 (1950).
[11] J. Bardeen and C. H. Townes, Phys. Rev. **73**, 627 (1948).
[12] J. L. Dunham, Phys. Rev. **41**, 721 (1932).
[13] H. C. Torrey, Phys. Rev. **59**, 293 (1941).

TABLE I. Frequencies in Mc/sec of observed lines for $J=0\rightarrow1$ transitions in RbCl. The numbers in parentheses designate the hyperfine structure levels (F,F_1) of the $J=1$ state.

Vibrational state	$Rb^{85}Cl^{35}$	$Rb^{87}Cl^{35}$
0	5248.596 (2, 3/2)	5212.474 (1, 2; 1/2)
	5248.566 (1, 3; 3/2)	
	5243.905 (4, 7/2)	5207.389 (2, 5/2)
	5243.855 (3, 7/2)	5207.332 (4, 5/2)
	5243.788 (5, 7/2)	
	5243.745 (2, 7/2)	
	5232.889 (1, 5/2)	5201.032 (1, 3; 3/2)
	5232.809 (4, 5/2)	
	5232.750 (2, 5/2)	
	5232.671 (3, 5/2)	
1	5221.421 (2, 3/2)	
	5221.395 (1, 3; 3/2)	
	5216.752 (4, 7/2)	
	5216.712 (3, 7/2)	
	5216.660 (5, 7/2)	
	5216.630 (2, 7/2)	
2	5194.306 (1, 3; 3/2)	
	5189.681 (4, 7/2)	
	5189.656 (3, 7/2)	
	5189.616 (5, 7/2)	
	5189.587 (2, 7/2)	

observe. No attempt was made to find all of the four lines of this spectrum for which $F_1=5/2$. The two lines of this group shown in the table were identified by their consistency with the other measured lines in the spectrum.

The remarks which follow constitute all that can be said with certainty about the relative intensities of the observed lines within a given vibrational state. The ratio of the intensities of the $Rb^{85}Cl^{35}$ lines designated by (1, 3; 3/2) and (2, 3/2) was 2:1. For the same molecule the lines for which $F_1=5/2$ were noticeably weaker than those for which $F_1=7/2$.

Since no spectra of $RbCl^{37}$ were observed, it is necessary to prove that the spectra found can in fact be ascribed to $RbCl^{35}$. Since the nuclear spins of Cl^{35} and Cl^{37} are the same, the hyperfine structure gives no clue to the identity of the Cl isotope, and the electron diffraction value of the internuclear distance is not sufficiently reliable to act as a check on the present measurements. However, the calculated mass ratio of the Rb isotopes would have been significantly different from the value found from mass spectrometer measurements,[5] which was not the case, had the spectra been those of $RbCl^{37}$.

The experimental probable error in the determinations of line positions was 2.0 kc/sec for all lines except the $v=2$ lines of $Rb^{85}Cl^{35}$. For these lines the error was 2.5 kc/sec.

TABLE II. Quadrupole and spin-rotation interaction constants of RbCl.

Quantity	$Rb^{85}Cl^{35}$	$Rb^{87}Cl^{35}$
$(eqQ)_{Rb}$ $(v=0)$ (Mc/sec)	-52.675 ± 0.005	-25.485 ± 0.006
$(v=1)$	-52.306 ± 0.030	
$(v=2)$	-51.903 ± 0.040	
$(eqQ)_{Cl}$ $(v=0)$ (Mc/sec)	$+0.774\pm0.009$	
$(v=1)$	$+0.612\pm0.013$	
$(v=2)$	$+0.470\pm0.017$	
c_{Rb} $(v=0)$ (kc/sec)	$+0.3\pm0.3$	
c_{Cl} $(v=0)$ (kc/sec)	0.0 ± 0.8	

IV. CALCULATIONS AND RESULTS

A least-squares analysis was made of the hyperfine structure lines to determine the constants given in Table II and the unperturbed rotational frequencies shown in Table III. Not only the magnitudes, but also the signs of the interaction constants in Table II were determined uniquely by the relative positions of the spectral lines. The errors in the two tables are probable errors.

In the calculations made from the $v=1,2$ spectra of $Rb^{85}Cl^{35}$ use was made of the values of c_{Rb} and c_{Cl} determined from the $v=0$ spectrum of this molecule. When $(eqQ)_{Rb}$ was calculated from the $Rb^{87}Cl^{35}$ spectrum it was assumed that $(eqQ)_{Cl}$ and c_{Cl} had the values determined from the $v=0$ spectrum of $Rb^{85}Cl^{35}$ and that c_{Rb} for Rb^{87} was equal to this constant for Rb^{85} multiplied by the ratio of the nuclear g values of the two isotopes.

TABLE III. Calculated frequencies of the unperturbed rotational transitions, $J=0\rightarrow1$, of RbCl.

Molecule	Freq. (Mc/sec)
$Rb^{85}Cl^{35}$ $(v=0)$	5241.1919 ± 0.0006
$(v=1)$	$5214.074\ \pm0.003$
$(v=2)$	$5187.039\ \pm0.004$
$Rb^{87}Cl^{35}$ $(v=0)$	5206.0987 ± 0.0012

The quadrupole interactions of Rb and Cl for $Rb^{85}Cl^{35}$ may be summarized by empirical equations which show their variation with vibrational state. These equations are, for Rb^{85} in $Rb^{85}Cl^{35}$,

$$(eqQ)_{Rb}(\text{Mc/sec})=-52.675+0.38v; \tag{3}$$

and for Cl^{35} in $Rb^{85}Cl^{35}$,

$$(eqQ)_{Cl}(\text{Mc/sec})=0.744-0.155v, \tag{4}$$

where v is the vibrational quantum number.

The ratio of the nuclear quadrupole moments of the Rb isotopes is, to the present accuracy, equal to the ratio of the quadrupole interactions for these isotopes, since the effect of the differences in zero point vibrations is negligible. From the data for $v=0$,

$$Q_{85}/Q_{87}=2.0669\pm0.0005. \tag{5}$$

Calculations based on the rotational frequencies in Table III gave the rotational constants and the equilibrium internuclear distance listed in Table IV. The calculation of the Y's in Table III required, in addition to the frequencies in Table II, the quantity $Y_{02}=-4B_e^3/\omega_e^2$. The vibrational constant, determined by Barrow and Caunt from the ultraviolet absorption spectra of RbCl,[14] is 270 cm^{-1}. $Y_{02}=-1.1$ kc/sec for $Rb^{85}Cl^{35}$. The information in Table III did not permit an independent calculation of the Y's for $Rb^{87}Cl^{35}$. Therefore, use was made of the well established relationships between the Y's of different isotopic species.[12] Within experimental error γ_e for $Rb^{87}Cl^{35}$ is the same as γ_e for $Rb^{85}Cl^{35}$, while $\alpha_e^{87}=(\mu_{85}/\mu_{87})^{3/2}\alpha_e^{85}$, where μ is the reduced mass of the molecule. The calculation of Y_{01} for $Rb^{87}Cl^{35}$ then required these values of γ_e and α_e, the above value of Y_{02}, and the rotational frequency for $v=0$ in Table III.

The quantity B_e differs from Y_{01} by a small correction term[1] which involves all of the Y's in Table III and the vibrational constants ω_e and $\omega_e x_e$.

$$B_e(\text{Mc/sec})=Y_{01}+(0.020\pm0.010), \tag{6}$$

where the error is almost entirely the result of the errors in ω_e and $\omega_e x_e$. For the calculation of r_e from B_e the additional quantities required were the masses[5,15] of Rb and Cl and the fundamental constants h/e and F.[16] The error in r_e is entirely the result of the errors in h/e and F.

Within the present experimental accuracy the ratio of the reduced masses of $Rb^{85}Cl^{35}$ and $Rb^{87}Cl^{35}$ is

$$\mu_{85}/\mu_{87}=(Y_{01})_{87}/(Y_{01})_{85}. \tag{7}$$

When Eq. (7) was used in conjunction with the formula[1,2] for the atomic mass ratio, the mass ratio of the Rb isotopes was found to be

$$M_{85}/M_{87}=0.9770163\pm0.0000045. \tag{8}$$

V. DISCUSSION

Bolef and Zeiger,[6] using the molecular beam magnetic resonance method at zero field, found $|eqQ|_{87}$ (Mc/sec) $=25.37\pm0.04$ for the Rb quadrupole interaction in the ground vibrational state of $Rb^{87}Cl$. This disagrees by more than the experimental errors with the present value of 25.485 ± 0.004 Mc/sec. If the source of this disagreement is sought in the present experiments, it may be suggested that the observed lines for $Rb^{87}Cl^{35}$ may not be properly identified since measurements were not made on all of the eight lines predicted. However, any different identification of these lines makes them inconsistent among themselves by more than their experimental errors and also causes a serious disagreement between the mass ratio of the Rb isotopes determined from the present experiments and the ratio calculated from the mass spectrometric measurements. In Table V the quadrupole constants obtained by the zero field magnetic resonance method and by the electric resonance method are compared. Although all of the differences shown in the last column of the table have the same sign, only the difference for RbCl is greater than the experimental errors.

In the presentation of their results Bolef and Zeiger use the equation

$$eqQ=eQ\bar{q}+eq^{(v)}Qv+eq^{(J)}QJ(J+1). \tag{9}$$

They find $eq^{(v)}Q/h=-0.230\pm0.050$ Mc/sec for Rb^{87} in $Rb^{87}Cl$. When the coefficient of the second term in Eq. (3) of the present paper is multiplied by the ratio of the Rb quadrupole interactions a value of 0.18 ± 0.03 Mc/sec is obtained for $eq^{(v)}Q/h$ for Rb^{87}. It is seen that the two values agree within experimental error. Bolef and Zeiger found that $eQ\bar{q}$ and $eq^{(v)}Q$ have opposite signs, in agreement with the present results shown in Eq. (3).

The magnitude of the spin-rotation constant for Rb obtained in the present experiments agrees within experimental error with the more accurate value for Rb^{87}, 1.0 ± 0.1 kc/sec, found by Bolef and Zeiger who could not determine the sign of this constant.

The ratio of the quadrupole moments of the Rb isotopes found by Hughes and Grabner for RbF, 2.07 ± 0.01,[7] agrees within the range of experimental errors with the more accurate value found in the present experiments.

The mass ratio of the Rb isotopes, 0.9770191 ± 0.0000022, computed from the masses given by Collins, Johnson, and Nier[5] agrees within experimental error with the less accurate value obtained in the present experiments. Possible difficulties in the in-

TABLE IV. Molecular constants of RbCl.

Constant	$Rb^{85}Cl^{35}$	$Rb^{87}Cl^{35}$
Y_{01} (Mc/sec)	2627.394 ± 0.002	2609.779 ± 0.003
$-Y_{11}\approx\alpha_e$ (Mc/sec)	13.601 ± 0.005	13.464 ± 0.005
$Y_{21}\approx\gamma_e$ (Mc/sec)	0.021 ± 0.002	0.021 ± 0.002
B_e (Mc/sec)	2627.414 ± 0.010	
$r_e=2.78670\pm0.00006$ A		

TABLE V. Comparison of quadrupole interaction constants determined by the magnetic resonance method at zero field and by the electric resonance method. The constants are given for the ground vibrational state.

Constant	Magnetic (Mc/sec)	Electric (Mc/sec)	Difference (El.-Mag.)
$\|eqQ\|_{Cl}$ of $TlCl^{35}$	15.788 ± 0.020	15.795 ± 0.004	$+0.007$
$\|eqQ\|_{Cl}$ of $TlCl^{37}$	12.425 ± 0.020	12.446 ± 0.003	$+0.021$
$\|eqQ\|_{Rb}$ of $Rb^{87}F$	33.96 ± 0.02	34.00 ± 0.06	$+0.04$
$\|eqQ\|_{Rb}$ of $Rb^{87}Cl$	25.37 ± 0.04	25.485 ± 0.004	$+0.115$

[14] R. F. Barrow and A. D. Caunt, Proc. Roy. Soc. (London) **A219**, 120 (1953).
[15] Collins, Nier, and Johnson, Phys. Rev. **84**, 717 (1951).
[16] J. W. M. DuMond and E. R. Cohen, Revs. Modern Phys. **25**, 691 (1953).

TABLE VI. Comparison of the alkali quadrupole interactions in the alkali halides. The interactions in the alkali fluorides are taken as standards for each row.

	Halogen			
Alkali	F	Cl	Br	I
Li	1.00	0.47	0.45	0.42
Na	1.00	0.67	0.57	0.48
K	1.00	0.71	0.63	—
Rb	1.00	0.75	—	—

terpretation of the mass ratio computed from the molecular constants of the alkali halides are discussed in reference 1.

The most remarkable feature of the quadrupole interactions in RbCl is the positive sign of the Cl^{35} interaction. Since the quadrupole moment of Cl^{35} is negative, q_{Cl}, the electric field gradient at the Cl nucleus, must be negative in RbCl. This sign of q is the opposite of that found experimentally for q at the halogen nuclei of KCl and KBr;[1,2] it is also the opposite of the sign predicted by the theory of Inglis[17] and the theory of Foley, Sternheimer, and Tycko.[18] The antishielding effect, which is the central effect considered by the latter authors, is apparently so submerged by other effects in RbCl that a reversal in the sign of q results. Finally, the negative sign of q in RbCl contradicts the empirically based conjecture made by Logan, Cote, and Kusch that q at each nucleus is positive in every diatomic molecule.[19]

It is of interest to note that the second term in Eq. (4), giving the variation of the Cl interaction constant with vibration in RbCl, has not only the same algebraic sign as it does in KCl,[1] but also nearly the same magnitude.

The sign of the Rb quadrupole interaction in RbCl has been determined for the first time in the present experiments. That this sign is the same as that found for the Rb interaction in RbF gives further support to the suggestion made by Logan, Cote, and Kusch that the signs of the alkali interactions are the same in all alkali halides having a common alkali atom.

Some interesting regularities in the magnitudes of the alkali quadrupole interactions in the alkali halides can be shown with the aid of Table VI. Each number in the table is the ratio of the alkali quadrupole interaction in a given alkali halide to the interaction in the fluoride of the same alkali. The alkali halide for which each ratio is given is specified by the row and column headings for that ratio.[20] An examination of Table VI shows that the ratios decrease monotonically from left to right and increase monotonically from top to bottom.

VI. ACKNOWLEDGMENTS

We wish to express our thanks to Professor I. I. Rabi and Professor P. Kusch for the opportunity to use the electric resonance apparatus at Columbia University and for their aid and advice while the present work was being performed. We are also indebted to Dr. Charles Lee for many helpful discussions during the performance of this work.

[17] D. R. Inglis, Revs. Modern Phys. **25**, 390 (1953).
[18] Foley, Sternheimer, and Tycko, Phys. Rev. **93**, 734 (1954).
[19] Logan, Cote, and Kusch, Phys. Rev. **86**, 280 (1952).

[20] The values of the quadrupole interactions in RbCl, KCl, and KBr come from the present paper and from references 1 and 2, respectively. All other values are tabulated in reference 19 where references to the original papers are given.

Charge States of Heavy-Ion Beams Passing through Gases

P. M. Stier, C. F. Barnett, and G. E. Evans*
Oak Ridge National Laboratory, Oak Ridge, Tennessee

(Received July 19, 1954)

Measurements are reported of the fraction of an ion beam in the various charge states $(-1, 0, +1, +2)$ after equilibrium has been established between competing electron capture and loss reactions. The ions H^+, He^+, N^+, Ne^+, and A^+ were passed through the gases hydrogen, helium, nitrogen, oxygen, air, neon, and argon. The energy range studied was 20 kev to 250 kev. Under conditions of equilibrium between the singly ionized and neutral states, the velocity dependence of the charge ratios is given by $\sigma_{01}/\sigma_{10}=K_1v^m$, where σ_{if} is the cross section for the transition between initial charge i and final charge f, v is the velocity, and K_1 and m are constants for each ion-stopping gas combination. The corresponding charge ratio for equilibrium between doubly and singly ionized states is given by $\sigma_{12}/\sigma_{21}=K_2(v-v_c)^m$, where K_2, v_c, and m are constants for each ion-stopping gas combination. The values of the constants v_c and m are tabulated. Negative ions are detectable only in the hydrogen beams. They constitute approximately 1 percent of the beam at 30 kev, and decrease in number rapidly at higher energies.

I. INTRODUCTION

An important process by which low-energy heavy particles lose energy in passing through matter is charge exchange. For each electron capture and subsequent loss, the minimum energy loss by the incident particle is the ionization energy of the atoms of the stopping material. Also, the average charge of the particle beam (determined by charge exchange) influences the rate of energy loss by ionization and excitation because of the charge dependence of these cross sections.

The subject of charge exchange has been reviewed by Ruchardt[1] and more recently very useful summaries have appeared by Massey and Burhop[2] and by Allison and Warshaw.[3] The capture and loss of electrons by protons have been studied in gases[3] and in metal foils,[4,5] and the electron capture and loss cross sections have been measured in hydrogen[6,7] and air.[8] Also, the charge exchange reactions have been studied for helium ions at high energies using natural alpha-particle sources,[9,10] and at low energies by Meyer,[11] Rudnick,[12] and others.[3] More recently, charge exchange for helium ions in gases has been investigated by Snitzer[13] in the energy range 100 to 480 kev, and in metals by Dissanaike[14] from 0.13 to 1.1 Mev. Measurements of charge exchange for ions heavier than helium are restricted almost entirely to energies less than 10 kev,[2] except for the work with fission fragments at much higher energies.

The present paper reports the results of measurements made of the fraction of a particle beam in each of the possible charge states after passage through a gas target which is sufficiently thick for equilibrium to be established between competing capture and loss reactions. These measurements have been made for each of the ions H^+, He^+, N^+, Ne^+, and A^+ passing through the stopping gases hydrogen, helium, nitrogen, oxygen, neon, and argon. Subsequent papers will report

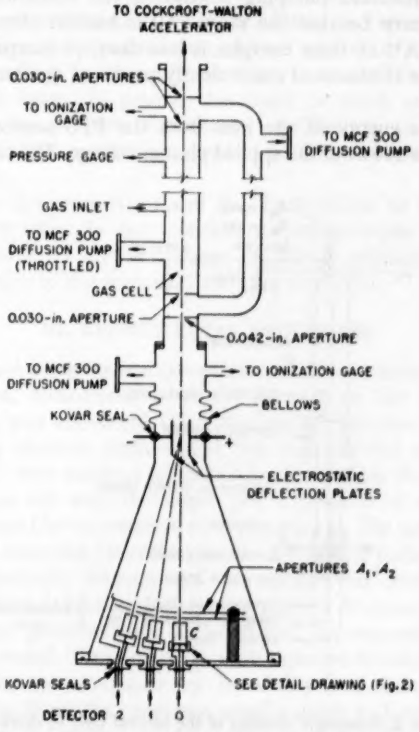

FIG. 1. Schematic drawing of the experimental apparatus.

* On leave to National Carbon Company, Cleveland, Ohio.

[1] E. Ruchardt, *Handbuch der Physik* (J. Springer, Berlin, 1933), Vol. 22, No. 2, p. 103.

[2] H. S. W. Massey and E. H. S. Burhop, *Electronic and Ionic Impact Phenomena* (Oxford University Press, London, 1952), Chap. VIII, Sec. 6.

[3] S. K. Allison and S. D. Warshaw, Revs. Modern Phys. **25**, 779 (1953).

[4] T. Hall, Phys. Rev. **79**, 504 (1950).

[5] J. A. Phillips, Phys. Rev. **91**, 455(A) (1953).

[6] J. H. Montague, Phys. Rev. **81**, 1026 (1951).

[7] F. L. Ribe, Phys. Rev. **83**, 1217 (1951).

[8] H. Kanner, Phys. Rev. **84**, 1211 (1951).

[9] G. H. Henderson, Proc. Roy. Soc. (London) **A109**, 157 (1925).

[10] E. Rutherford, Phil. Mag. **47**, 277 (1924).

[11] H. Meyer, Ann. Physik **37**, 69 (1940).

[12] P. Rudnick, Phys. Rev. **38**, 1342 (1931).

[13] E. Snitzer, Phys. Rev. **89**, 1237 (1953).

[14] G. A. Dissanaike, Phil. Mag. **44**, 1051 (1953).

measurements of the separate electron loss and capture cross sections for these incident ions and stopping gases. It is the purpose of this series of experiments to present a unified, consistent set of data from which an interpretation of the phenomena of charge exchange may be given in terms of the various pertinent parameters (mass, velocity, ionization potential, etc.).

II. DESCRIPTION OF APPARATUS

A. General

The output of a Phillips Ionization Gauge type ion source[15] was accelerated in the ORNL heavy-ion Cockcroft-Walton accelerator. The desired ion mass was deflected by a stabilized analyzing magnet through an angle of 15 degrees and passed through the windowless gas cell shown schematically in Fig. 1. The gas cell was 18.0 inches in length and had an inside diameter of 1.13 inches. The beam entrance apertures were 0.030 inch and the exit apertures were 0.030 inch and 0.042 inch, as shown. The differential pumping properties allowed pressures of 0.2 mm Hg to be established in the gas cell without appreciably altering the pressure in the accelerator or electrostatic analyzer. The pressure in these regions was ordinarily between 0.8 and 1.0 $\times 10^{-5}$ mm Hg. The closely collimated particle beam which emerged from the gas cell, was electrostaticly analyzed into the various charged components.

Differential pumping instead of foil windows was necessary because the range of the heavier ions used (e.g. A^+) at these energies is less than, or comparable to, the thickness of conveniently produced and handled foils.

The energy of the ions from the PIG source was within 100 ev of the applied plasma voltage. The current through a precision 600-megohm high-voltage resistor connected from the ion source anode to ground was used to measure the incident particle energy. The overall ion energy was held constant to within 0.02 percent of the desired value over long periods of time by a regulator in the high-voltage terminal. In principle, this circuit is equivalent to a conventional regulator used in most constant-voltage supplies at low voltage. The plate resistance of a triode in series with the supply load is controlled through a high-gain stabilized dc amplifier by the error between a reference voltage and the voltage developed in a fraction of the precision 600-megohm resistor by the bleeder current.

In these experiments, only the approach and attainment of charge equilibrium in the particle beam is measured. Since the fraction of the beam in the various charge states is pressure independent at equilibrium, the pressure measurement need not be absolute. An Alphatron Gage[16] was used for convenient, approximate pressure measurements.

In order to reduce evacuation time and permit continuous flushing of the gas cell, a liquid nitrogen trapped diffusion pump was connected to the gas cell through a throttling valve (Fig. 1). During many of the charge equilibrium measurements the stopping gas flowed through the charge exchange chamber at a rate of approximately one cc/min by appropriate adjustment of the throttling valve. This procedure acted as a test for impurities in the stopping gas arising from inleakage or chamber outgassing.

As shown in Fig. 1, the detector chamber was connected to the analyzer by means of a bellows section. This allowed the neutral (No. 0) detector to be aligned with the neutral beam. Also, the short section of the vacuum chamber, through which the analyzer Kovar seals pass, could be rotated about the axis of the neutral beam (this detail is not shown in Fig. 1). The vacuum seal was maintained by a peripheral O-ring at each end. Thus, after correct alignment of the neutral detector, the analyzing plates were positioned so that the charged beams struck the center of detectors No. 1 and No. 2.

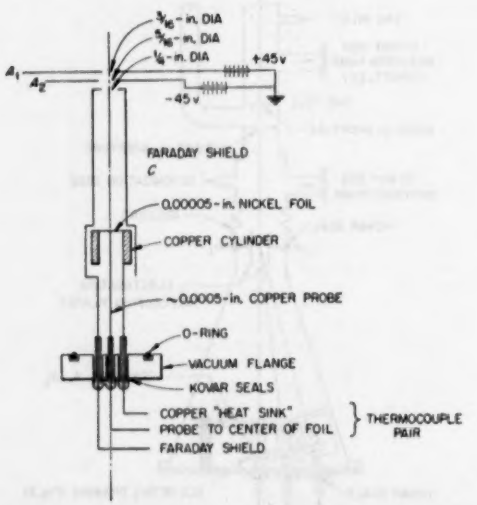

FIG. 2. Schematic drawing of the neutral (No. 0) detector.

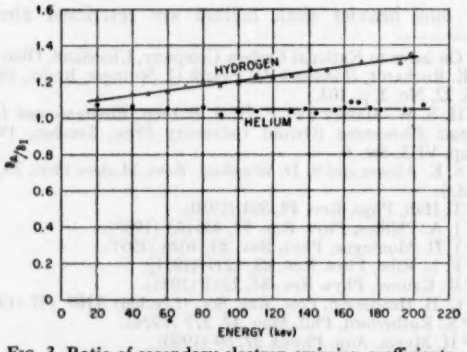

FIG. 3. Ratio of secondary electron emission coefficients for atoms to that for ions.

[15] Barnett, Stier, and Evans, Rev. Sci. Instr. 24, 394 (1953).

[16] National Research Company, Cambridge, Massachusetts.

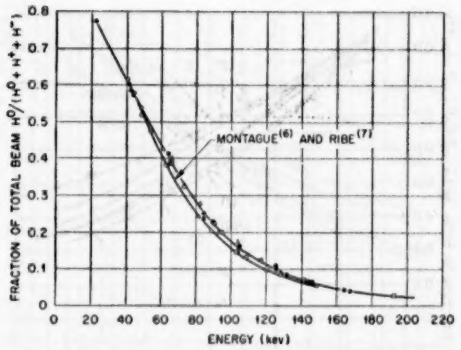

FIG. 4. Equilibrium fraction of hydrogen beam which is neutral in hydrogen gas. The following point designations are used: ○ = the results of Ribe (Ref. 7) and Montague (Ref. 6). ● = data taken with the apparatus shown in Figs. 1 and 2. □ = data taken using apparatus described in Sec. IVB. ■ = data taken using apparatus described in Sec. IVB, with only neutrals incident on second charge exchange chamber. △ = data taken with apparatus described in Sec. II (Fig. 1) but using slow detectors described in Sec. IVA.

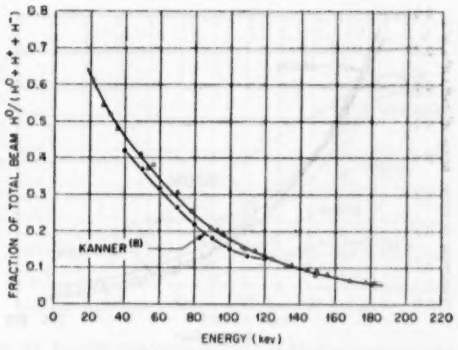

FIG. 5. Equilibrium fraction of hydrogen beam which is neutral in air. The point designations used are: ● = the results of Kanner (Ref. 8). △ = data taken with apparatus shown in Figs. 1 and 2. ○ = data taken with the apparatus described in Sec. IVB.

B. The Detectors

The neutral or undeflected particle beam impinges on a foil differential thermocouple similar to that described recently by Gardon.[17] A schematic drawing of this detector is shown in Fig. 2. The thickness of the nickel foil was 0.00005 inch, yielding sensitivities of several microvolts per milliwatt with a time constant of about one second. As indicated, the collimated beam strikes near the center of the foil at the "hot" junction. The temperature of the relatively massive copper heat sink was independent of the beam because of the good conduction of the support structure. For the beam currents used in these experiments the temperature difference between the center of the foil and the heat sink was a few degrees. The output of this differential thermocouple was measured by a high-gain dc amplifier.

By applying appropriate potentials to the electrodes, the detector may be used either to measure the total incident charge (as a Faraday cup), or to measure the number of secondary electrons emitted by the foil (as a secondary electron detector). By using the thermocouple as a charge insensitive detector, the relative secondary emission for ions and atoms of the same mass and energy has been measured for this detector. The secondary electron emission for helium and hydrogen atoms was found to be somewhat higher than that for the corresponding ions, as shown in Fig. 3. These data are representative of the many simultaneous measurements of thermocouple response and secondary electron emission taken during the course of these experiments. They represent data taken under widely different experimental conditions of beam intensity, gas cell pressure, and alignment. Although the individual measurements deviate by several percent from the mean, no systematic change in the relative response for ions and atoms could be detected. Corresponding plots for the ions and atoms of argon, neon, and nitrogen showed that within the limits of measurement, the secondary electron emission was independent of the particle charge. It should be pointed out that this observed relative secondary electron emission is for the foil surface conditions present in this experimental apparatus and may not be characteristic of a clean metal.

The secondary electron emission was found useful as a measure of the beam at the lower energies (less than 60 kev) where it was difficult to get sufficient response of the thermocouple. For calibration of the secondary emission, the pressure in the gas cell needed only to be high enough to neutralize an easily measured fraction of the beam. In general this could be much smaller than the pressure for charge equilibrium, so that attenuation caused by elastic scattering was not as severe.

The detectors No. 1 and No. 2 are similar to No. 0 except they do not contain a thermocouple. The apertures $A1$ and $A2$, shown in Fig. 2, improve the efficiency of the secondary electron collection.

III. EXPERIMENTAL PROCEDURE

When using the equipment described in the preceding section, measurements of the fraction of the beam which was uncharged (after equilibrium between competing electron capture and loss reaction was established) were made as follows: After thoroughly flushing the gas cell with the target gas, a pressure of about 0.01 mm Hg was established in the gas cell. The particle beam emerging from the gas was allowed to strike the thermocouple detector and its response was recorded. Sufficient deflection voltage was applied to remove all charged particles from the beam and the response was again noted. These readings were repeated to minimize random errors caused by instability and errors in reading. Since the beam was usually stable to 1 percent during consecutive readings, results from successive

[17] R. Gardon, Rev. Sci. Instr. 24, 366 (1953).

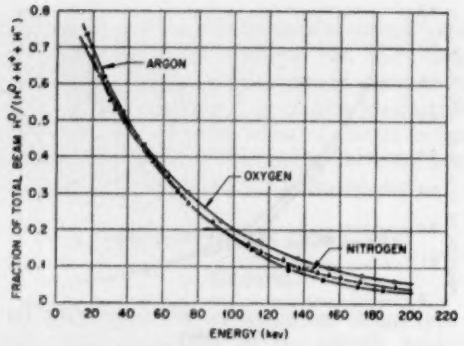

FIG. 6. Equilibrium fraction of hydrogen beam which is neutral in nitrogen, oxygen, and argon.

measurements agreed within 2 percent. All measurements were then repeated at a substantially different pressure and the results compared. If agreement was not within experimental error, additional gas cell pressures were established until the equilibrium charge distribution was attained. These steps were repeated at a sufficient number of incident ion energies to determine the dependence of the fraction of the particle beam which is neutral on the incident ion energy.

The measurement of the ratio of the number of doubly charged ions to the number of singly charged ions was made in one of two ways. For most of the measurements, the current to Faraday cup No. 1 was recorded as the analyzing voltage was varied to bring the charge one and charge two beams alternately into this detector. The other procedure was to read detectors No. 1 and No. 2 simultaneously. The results obtained by these two methods agreed within 2 percent. Repetition of the measurements at different pressures was again used as the test of equilibrium.

After completing the study of the positively charged components of the ion beams, it was felt that a search should also be made for negative ions in the beam emerging from the gas cell. This was accomplished by applying the deflection voltage necessary to bring the

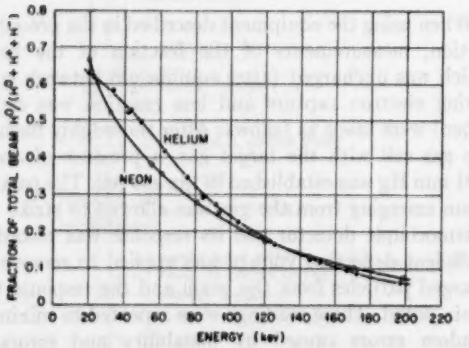

FIG. 7. Equilibrium fraction of hydrogen beam which is neutral in helium and neon.

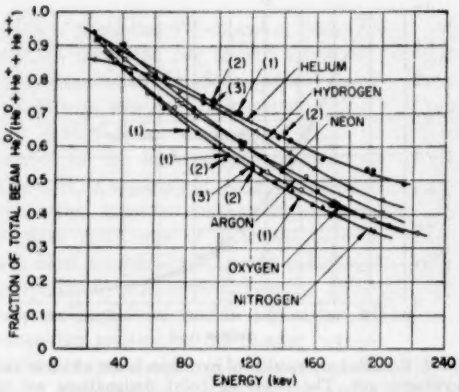

FIG. 8. Equilibrium fraction of helium beam which is neutral in various gases. The numbered points on the helium and nitrogen curves represent data taken by following methods: (1) using two slow thermocouples described in Sec. IVA, (2) using apparatus described in Sec. IVB, (3) using apparatus described in Sec. IVB with only neutral atoms incident on the second charge exchange chamber. All other points taken with apparatus described in Sec. II.

beam of charge+1 ions to detector No. 1 and then reversing the polarity of the deflecting voltage.

In this type of experiment it is assumed that the gas cell pressure is high enough so that equilibrium is established between competing capture and loss reactions (that is, the beam assumes an average, pressure-independent charge), but is low enough so that the energy degradation of the beam may be neglected. That this assumption is justified is evident from the fact that, particularly for H^+ and He^+ ions where elastic scattering is small, the pressure may be varied over a factor of ten with no change in charge distribution. For the heavier ions, where attenuation of the beam caused by elastic scattering is large, one finds that the average charge is pressure independent over a factor of three or four change in pressure. However,

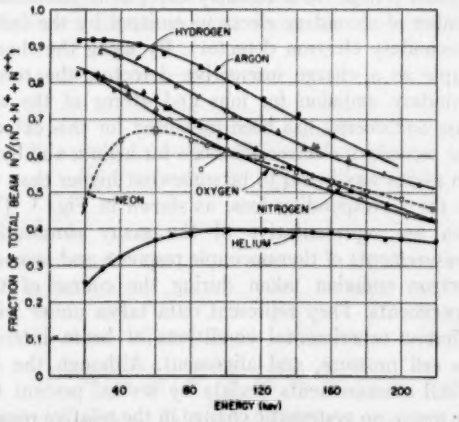

FIG. 9. Equilibrium fraction of nitrogen beam which is neutral in various gases.

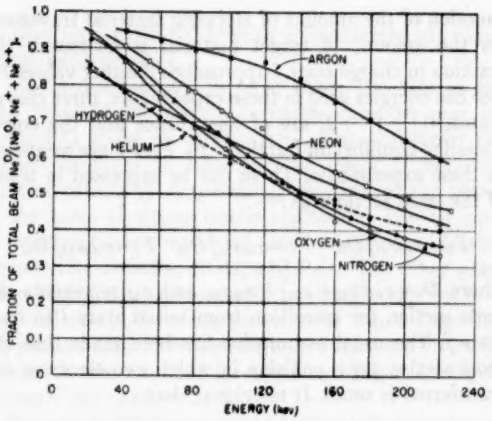

FIG. 10. Equilibrium fraction of neon beam which is neutral in various gases.

as the gas cell pressure is further increased, the fraction of the beam which is neutral begins to decrease slightly. This is in contrast to the expected behavior for a beam degraded in energy. This decrease may be associated with the relative elastic scattering of ions and atoms.

IV. OTHER EQUIPMENT AND PROCEDURES

In view of the rather large differences which often exist between the results of different workers in this field, it was felt that it would be wise to test for systematic errors because of the type of detector, gas cell geometry, and experimental procedure. For this purpose, during preliminary experiments, several such variations were made.

A. Detector Changes

The detectors No. 1 and No. 0 described in Sec. IIB were replaced with simple 0.003-inch copper-constantan wire thermocouples spotwelded to platinum foils $\frac{3}{8}$ inch

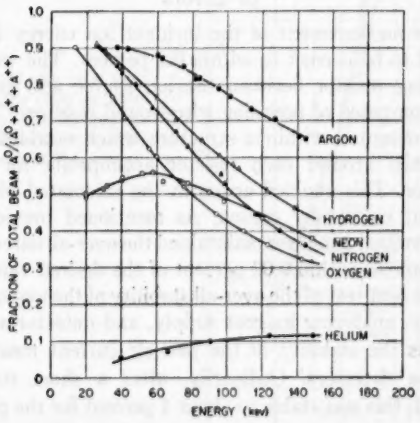

FIG. 11. Equilibrium fraction of argon beam which is neutral in various gases.

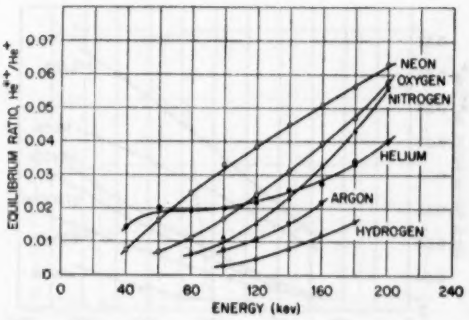

FIG. 12. Equilibrium ratio of He^{++} to He^{+} in various gases.

in diameter and 0.001 inch thick. These thermocouples required approximately five minutes to reach equilibrium and proved to be identical in response to within 3 percent, the accuracy of measurement. This sensitivity measurement was made with the gas cell at high vacuum so that nearly all the beam was singly charged. As described above, the method of support of the detector chamber was such that either thermocouple could be placed at the "neutral beam position" to record the total beam, and by applying the analyzing voltage in the correct polarity, the singly charged component could be measured on the other thermocouple. This versatility allowed the equivalence of these thermocouples to be established and thus served as a test of the detectors described in Sec. IIB, which were used for most of the work described in this paper. Sample results obtained with these slow thermocouples are displayed in Figs. 4 and 8 for comparison with the results measured with the fast differential thermocouple.

B. Geometry Changes

In order to test for possible systematic errors caused by gas cell geometry or differential pumping apertures, a series of measurements of the neutral component of the beam were made on apparatus being assembled for measurements of electron loss cross sections to be described in a subsequent paper. This equipment con-

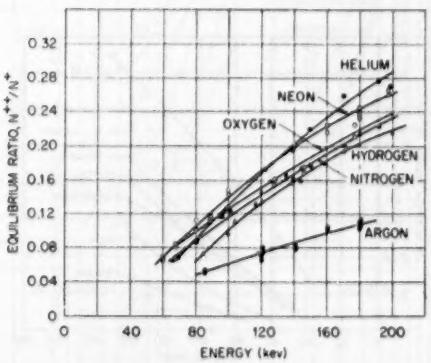

FIG. 13. Equilibrium ratio of N^{++} to N^{+} in various gases.

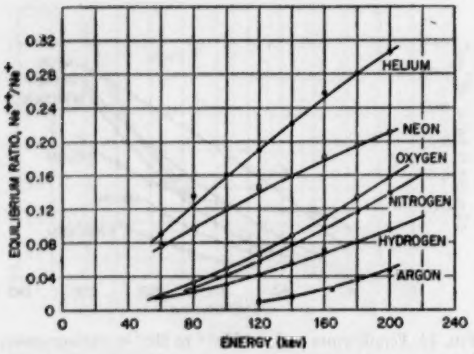

FIG. 14. Equilibrium ratio of Ne^{++} to Ne^{+} in various gases.

sisted of two differentially pumped gas cells, each of which was followed by an electrostatic analyzer. With this arrangement, it was possible to make the particle beam incident on the second charge exchange chamber entirely uncharged, so that charge equilibrium is approached from an initially neutral beam rather than the customary singly charged beam. By definition, the results should be identical if equilibrium is established. For both of these gas cells, instead of using a differentially pumped "window," as described above, the entrance and exit apertures were canals, $\frac{1}{2}$ inch in length and $\frac{1}{16}$ inch in diameter. The pumping speed from the analyzing chambers was sufficient to maintain pressures of about 5×10^{-5} mm Hg. Only one detector was used since only the fraction of the particle beam, which was neutral, was measured. This was a differential thermocouple and Faraday cup similar to the described in Sec. IIB. For comparison, a few data taken with this apparatus are plotted in Figs. 4, 5, and 8.

V. ANALYSIS OF EXPERIMENTAL RESULTS

A. Relation of Charge Equilibrium to the Capture and Loss Cross Sections

The differential equations representing transitions between the possible charge states can be solved for the fraction of the particle beam in each state as a function of the amount of stopping material traversed. As the amount of target material is increased, the fraction in charge state i approaches limiting values F_i. For the energies used in these experiments, three charge states, 0, +1, +2, are of importance and the corresponding equilibrium fractions, F_0, F_1, F_2, are measured in these experiments. These can be expressed in terms of the cross sections as:[18]

$$F_0=\sigma_{10}\sigma_{21}/D_0,\quad F_1=\sigma_{01}\sigma_{21}/D_0,\quad F_2=\sigma_{01}\sigma_{12}/D_0,$$

where $D_0=\sigma_{01}(\sigma_{12}+\sigma_{21})+\sigma_{10}\sigma_{21}$ and σ_{if} represents the cross section for transition from initial state i to final state f. The usual assumption has been made that the cross section for a collision in which two electrons are transferred is small. It is evident that

$$F_1/F_0=n^{+}/n^{0}=\sigma_{01}/\sigma_{10};\quad F_2/F_1=n^{2+}/n^{+}=\sigma_{12}/\sigma_{21}.$$

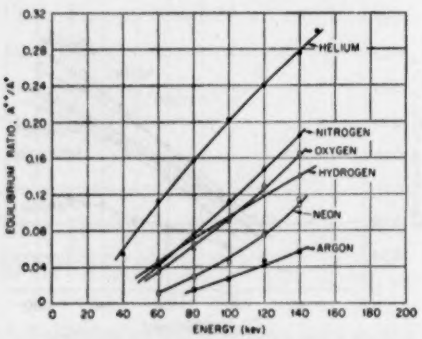

FIG. 15. Equilibrium ratio of A^{++} to A^{+} in various gases.

B. Experimental Results

The results of the determinations of the fraction of the particle beam which was neutral at charge equilibrium are displayed in Figs. 4–11. In Figs. 4 and 5, the data for protons passing through hydrogen and air are compared with the results of other observers. The ratio of charge 2 to charge 1 components are given in Figs. 12–15.

The number of negative ions formed in the charge exchange chamber was below the detectable limit (about 0.1 percent of the total beam at 30 kev, 0.01 percent at 100 kev) for the incident ions He^{+}, N^{+}, Ne^{+}, and A^{+}. The energy dependence of the H^{-} component formed by the passage of protons through nitrogen is shown in Fig. 16.

The study of the negative component was only extensive enough to establish that, for the energy range investigated, no serious error was introduced by neglecting it in the computation of the neutral or positive fractions.

C. Errors

The measurement of the incident ion energy is believed to be correct to within 0.2 percent. The voltage dividing resistor between the ion source and ground was composed of precision wire-wound resistors. These were mounted within a structure which established a potential around each resistor appropriate for that resistor. This avoided errors in the calculated bleeder current caused by corona. As mentioned previously, the terminal regulator maintained the over-all ion energy constant to within 0.02 percent of the desired value.

The best test of the over-all stability of the ion source, energy, analyzing magnet supply, and detector amplifiers is the stability of the particle current measured at the detectors. Ordinarily, after a short startup period, this was stable to about 1 percent for the period

[18] See, e.g., reference 3 for a rather complete derivation and discussion of these equations.

of time required for the series of measurements taken at each energy point.

As discussed above, in most cases, the rate of gas flow through the charge exchange chamber was increased to about an atmospheric cubic centimeter per minute in order to minimize the effect of impurity buildup caused by outgassing, inleakage, or the beam, in the cases of strong elastic scattering. The air used as stopping gas was dried and the carbon dioxide removed by Drierite, KOH, and P_2O_5. The other gases were good-grade compressed gas and were used as supplied except for being passed over a cold trap. For oxygen and argon the trapping agent was a dry ice-butyl cellusolve mixture, and for the remaining gases liquid nitrogen was used.

The search for errors caused by gas cell geometry or detector properties has been described in Sec. IV. It should also be noted that during most of the experiments the cross section of the particle beam at the detector position was approximately $\frac{1}{8}$ inch in diameter, whereas the detector aperture and sensitive area were $\frac{5}{16}$ inch. Thus, a very definite plateau existed in a response *versus* detector position curve when secondary electron or positive ion detection was used. The corresponding curve for the differential thermocouple was of course somewhat rounded at the top. As described above, by appropriate detector positioning and adjustment of the deflecting voltage, a beam of particles of charge +1 could be moved to each of the detectors. The agreement was within 2 percent.

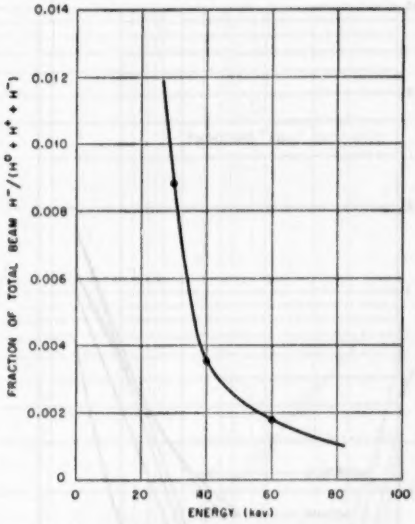

FIG. 16. Equilibrium fraction of hydrogen beam which is H^- in nitrogen.

The linearity of the electrometers used was measured to be within 1 percent and the thermocouple was linear to 1 percent over the very limited temperature range

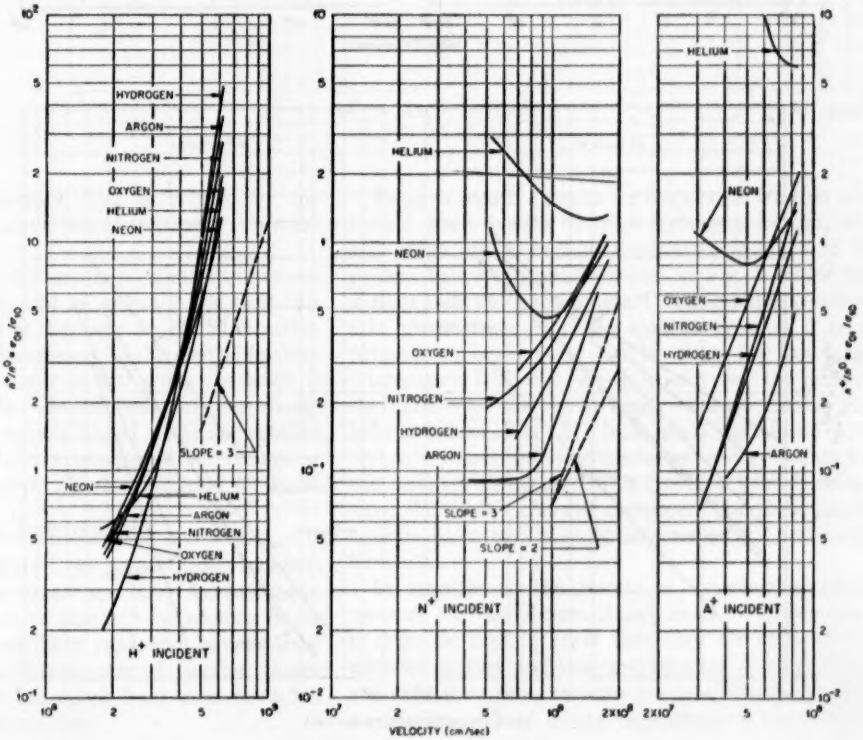

FIG. 17. Ratio of loss to capture cross sections (σ_{01}/σ_{10}) for hydrogen, nitrogen, and argon ions in various gases.

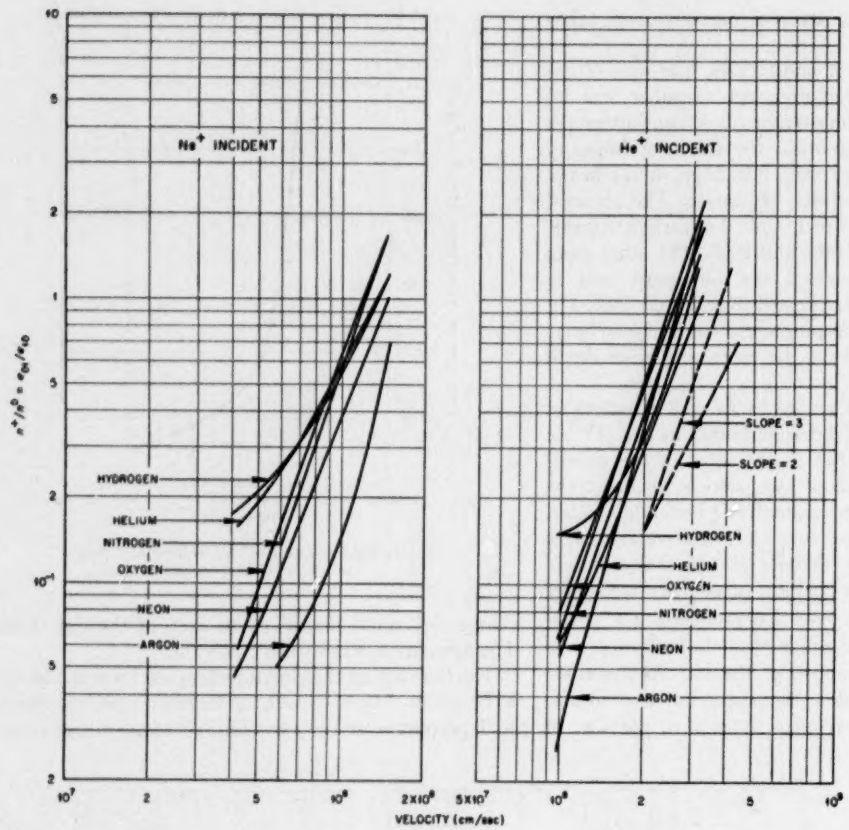

FIG. 18. Ratio of loss to capture cross sections (σ_{01}/σ_{10}) for helium and neon ions in various gases.

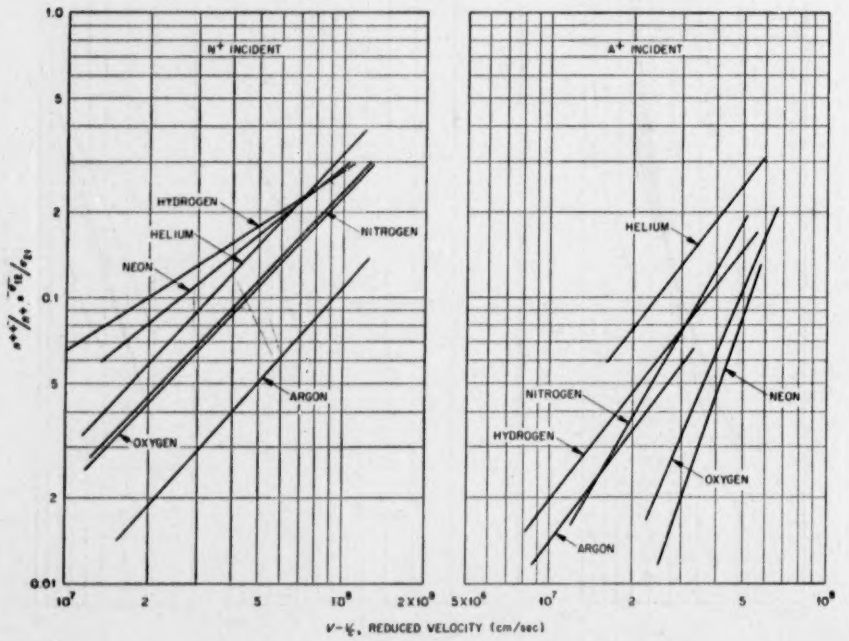

FIG. 19. Ratio of second loss to capture cross sections (σ_{12}/σ_{21}) for nitrogen and argon ions in various gases.

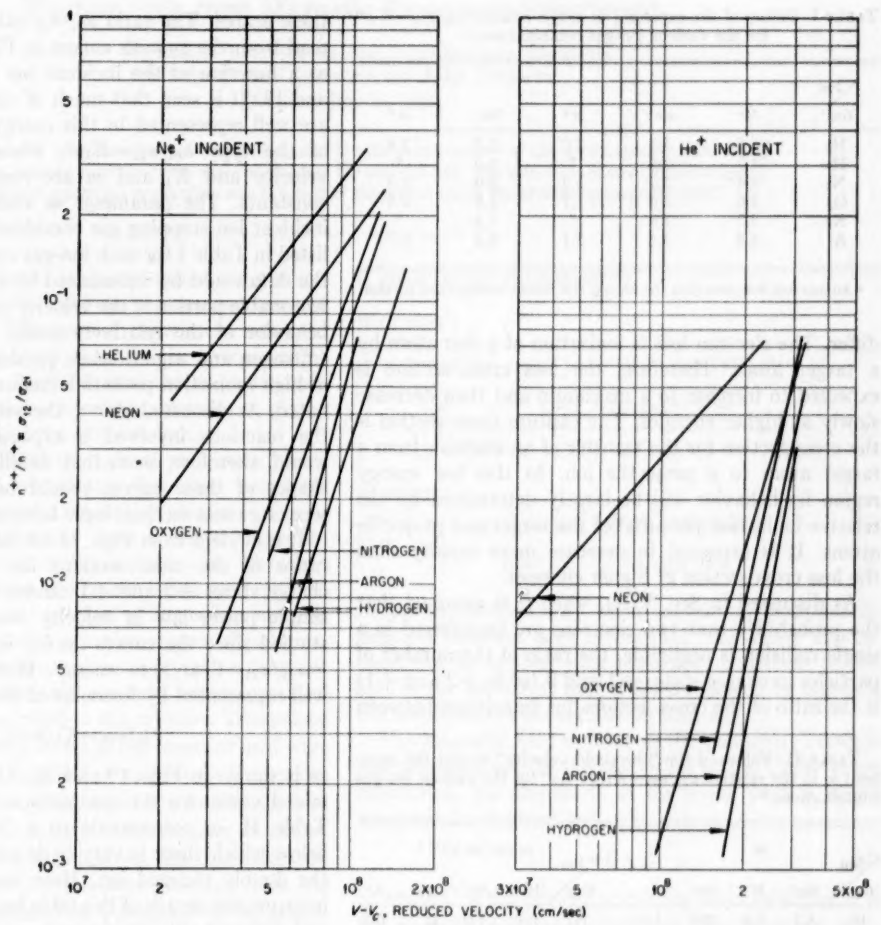

FIG. 20. Ratio of second loss to capture cross sections (σ_{12}/σ_{21}) for helium and neon ions in various gases.

used in these experiments. This is verified by the agreement between data taken for very different intensity ion beams.

The over-all error in the results is estimated to be not larger than 5 percent, and is probably less than this for much of the data. Because of the subtraction technique used for measurement of the neutral fraction of the beam, the accuracy is best when the beam is approximately equally divided between the charge states. In general the error is largest at the low energies because of decreased beam intensity and the consequent reliance on the secondary electron emission for beam measurements.

VI. DISCUSSION

The agreement between the present measurements and the results of Montague[6] and Ribe[7] for protons in hydrogen (Fig. 4) and of Kanner[8] for protons in air (Fig. 5), while not exceedingly good, may be considered satisfactory. The equilibrium neutral fraction shown in Figs. 4 and 5 are calculated from their measured capture and loss cross sections.

Snitzer's reported results for the neutral fraction of a helium beam passing through hydrogen, helium, air, and argon are in each of these cases from 20 to 30 percent below the results shown in Fig. 8. Since the various tests described in Sec. IV indicated no systematic errors larger than the random error of 2 or 3 percent, no explanation can be given for this large discrepancy. It should be pointed out that the ratio of the number of doubly to singly charged ions in the helium beams (Fig. 12) is in good agreement with Snitzer's values, provided his lowest energy points for this ratio are disregarded. This provision seems justified since the doubly charged component for these points appears to be only slightly larger than his detectable limit.

In interpreting the results of experiments which measure the equilibrium charge ratio for heavy ions, it must be kept in mind that only the ratio of the electron capture and loss cross sections is determined, and that these cross sections are for different types of interactions, whose energy dependence is expected to

TABLE I. Values of the exponent m in the relation $\sigma_{01}/\sigma_{10}=K_1v^m$ for the various ion-gas combinations.*

Gas \ Ion	H^+	He^+	N^+	Ne^+	A^+
H_2	6.5	3.3	2.0	2.2	2.8
He	4.7	2.6	*	1.9	*
N_2	5.4	2.9	2.2	2.9	3.3
O_2	4.6	2.6	1.7	2.8	2.5
Ne	3.7	2.8	*	2.5	*
A	5.8	3.5	3.1	4.3	3.7

* An asterisk indicates that the log-log plot has no straight line portion

differ. The electron loss is ionization of a fast atom by a target atom. Therefore, the loss cross section is expected to increase to a maximum and then decrease slowly at higher energies. The capture cross section is the cross section for the transfer of an electron from a target atom to a projectile ion. In this low energy region its behavior will be largely determined by the relative ionization potential of the target and projectile atoms. It is expected to decrease more rapidly than the loss cross section at higher energies.

As discussed in Sec. V(A), when it is assumed that the probability that two electrons are transferred in a single collision is negligible, the ratio of the number of particles in charge states +1 and 0 (or in +2 and +1) is the ratio of the cross sections for transitions between these states. The ratio σ_{01}/σ_{10} calculated from values read from the smooth curves in Figs. 4–11 are plotted as a function of the incident ion velocity in Figs. 17 and 18. It is seen that much of the experimental data are well represented in this energy range by formulas of the type $\sigma_{01}/\sigma_{10}=K_1v^m$, where v is the particle velocity and K_1 and m are empirically determined constants. The parameter m varies for the different incident ion-stopping gas combinations, and values are listed in Table I for each ion-gas combination for which the data could be represented by a straight line over a reasonable portion of the velocity range. The interesting behavior of the relatively easily ionized, heavy ions (nitrogen and argon) when passing through the gases of high ionization potential (helium and neon) is to be noted. As discussed above, the velocity dependence of the reactions involved is expected to differ and it would, therefore, seem that detailed discussion of the shapes of these curves should be deferred until the separate cross sections have been measured.

It is evident from Figs. 12–15 that in many cases the ratios of the cross sections for transitions between charge states +2 and +1 cannot be represented by a simple power law in velocity over the energy range studied since the curves do not extrapolate to $n^{2+}/n^+=\sigma_{12}/\sigma_{21}=0$ at zero energy. However, the data are well represented by formulas of the type

$$\sigma_{12}/\sigma_{21}=K_2(v-v_e)^m,$$

as is shown in Figs. 19 and 20. The empirically determined values for the constants m and v_e are shown in Table II. v_e corresponds to a "threshold velocity," below which there is very little probability of forming the doubly charged ion. Here again it is difficult to interpret the details of this table because of the unknown and different velocity dependence of the cross sections involved.

TABLE II. Values of the "threshold velocity" v_e and the exponent m in the relation $\sigma_{12}/\sigma_{21}=K_2(v-v_e)^m$ for the various ion-gas combinations.*

Gas \ Ion	m He^+	N^+	Ne^+	A^+	v_e, cm/sec $\times10^{-8}$ Gas \ Ion	He^+	N^+	Ne^+	A^+
H_2	5.7	0.6	3.0	1.3	H_2	0.2	1.0	0	0.3
He	*	1.1	1.3	1.3	He	*	0.7	0.4	0.3
N_2	4.7	1.0	2.8	1.7	N_2	0.1	0.7	0.2	0.3
O_2	3.4	1.0	2.7	2.3	O_2	0	0.6	0.3	0.2
Ne	1.1	0.8	1.4	2.9	Ne	1.1	0.8	0.2	0.3
A	4.7	1.0	3.8	1.3	A	0	0.6	0.5	0.5

* An asterisk indicates that the log-log plot has no straight line portion.

The authors wish to acknowledge helpful discussions with Doctors A. H. Snell and E. O. Wollan of the Oak Ridge National Laboratory physics staff, and with Dr. S. K. Allison of the University of Chicago.

Neutron Spin from Magnetic Resonance Experiment

C. P. STANFORD,* T. E. STEPHENSON,† AND SEYMOUR BERNSTEIN
Oak Ridge National Laboratory, Oak Ridge, Tennessee

(Received July 26, 1954)

The magnetic resonance type of experiment used for the measurement of the gyromagnetic ratio of the neutron has been extended to give a demonstration of the neutron spin. The spin ($\frac{1}{2}$) is demonstrated uniquely by the measured transition probability as a function of the amplitude of the oscillating magnetic field.

THE molecular beam magnetic resonance method was developed by Rabi[1] for the measurement of gyromagnetic ratio. This type of experiment was used by Alvarez and Bloch[2] to measure the gyromagnetic ratio of the neutron. We have used the magnetic resonance method with monochromatic neutrons to give a direct demonstration of the neutron spin.

Two magnetized single crystals of magnetite whose polarizing properties were closely the same[3] were used as neutron polarizer and analyzer, as shown in Fig. 1. The use of Bragg reflection from a single magnetite crystal for the selection of a particular spin state has distinct advantages over the transmission method used by Alvarez and Bloch,[2] in that a monoergic neutron beam is produced which has a high degree of polarization.[3,4] Between these two magnetite crystals a constant field H_1 of several hundred oersteds was maintained parallel to the field applied to the crystals. Transitions between neutron energy levels in the constant field were induced by an oscillating field of amplitude H_0 perpendicular to H_1. The frequency ω_0 of the oscillating field was adjusted so as to satisfy the resonance condition $\omega_0=\omega_1=(\mu/S)H_1$, in which $\mu/S=g$, the gyromagnetic ratio of the neutron. The intensity reflected from the two crystals was measured as a function of the amplitude of the oscillating field. The oscillating magnetic field was produced by a variable frequency oscillator whose output was continuously variable. A maximum oscillating field strength of about 65 oersteds was produced in an oval-shaped 80-turn solenoid of about 6 cm maximum height, 4 cm maximum width, and 8 cm length. Neutrons of energy 0.075 ev were used.

The transition probability in a rotating magnetic field is a function of the frequency ω_r, the strength of the field H_r and the length of time t spent by the particle in the field. It depends also upon the angular momentum j of the particle and upon its initial and final magnetic quantum numbers, m and m'. The transition probability is given by the expression[5,6]:

$$W(j,m,m') = (j+m)!(j-m)!(j+m')!(j-m')!(\sin\tfrac{1}{2}\alpha)^{4j} \times\left|\sum_{\rho=0}^{2j}\frac{(-1)^{\rho}(\cot\tfrac{1}{2}\alpha)^{m+m'+2\rho}}{(m+m'+\rho)!(j-m'-\rho)!(j-m-\rho)!\rho!}\right|^2, \quad (1)$$

in which

$$\alpha=2\arcsin[(gH_r/L)\sin(\tfrac{1}{2}Lt)] \quad (2)$$

and

$$L=[(\omega_r-\omega_1)^2+(gH_r)^2]^{\frac{1}{2}}. \quad (3)$$

In the summation, any term containing factorials of negative numbers is to be omitted. The above expressions can be applied with good approximation to the case of the oscillating field if H_r is replaced by one-half the amplitude of the oscillating field H_0.

The magnetic field applied to the magnetite crystals was perpendicular to the scattering plane. Under these conditions, the amplitude of scattering from a single magnetic ion is given by[7]

$$a=C+D, \quad (4)$$

in which C is the nuclear scattering amplitude and D is the magnetic scattering amplitude. The magnetic scattering amplitude is given by

$$D=(2e^2/mc^2)S'fg'jm, \quad (5)$$

in which S' is the effective atomic angular momentum in units of $\hbar$, f is the atomic magnetic form factor, j and m are the neutron spin total and magnetic quantum numbers, (e^2/mc^2) is the classical electron radius, and g' is defined as the ratio of the neutron magnetic moment

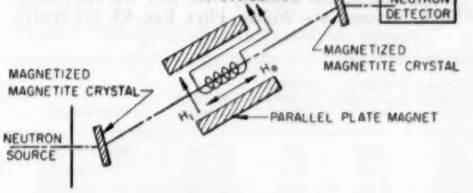

FIG. 1. Schematic diagram of apparatus.

* Now at Westinghouse Research Laboratories, East Pittsburgh, Pennsylvania.
† Now with Consolidated Vultee Aircraft Corp., Ft. Worth, Texas.
[1] Rabi, Zacharias, Millman, and Kusch, Phys. Rev. **53**, 318 (1938).
[2] L. W. Alvarez and F. Bloch, Phys. Rev. **57**, 111 (1940).
[3] Stanford, Stephenson, Cochran, and Bernstein, Phys. Rev. **94**, 374 (1954).
[4] C. G. Shull, Phys. Rev. **81**, 626 (1951).
[5] E. Majorana, Nuovo cimento **9**, 43 (1932).
[6] F. Bloch and I. I. Rabi, Revs. Modern Phys. **17**, 237 (1945).
[7] O. Halpern and M. H. Johnson, Phys. Rev. **55**, 898 (1939).

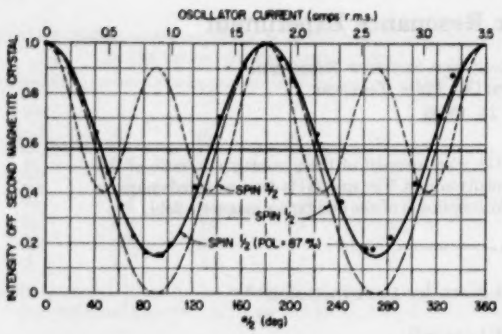

FIG. 2. Relative neutron intensity *vs* amplitude of oscillating field. Points are measured values; long dash curve calculated for neutron spin $\frac{1}{2}$, short dash curve calculated for spin $\frac{3}{2}$; solid curve, calculated for spin $\frac{1}{2}$ and 87 percent polarization.

in nuclear Bohr magnetons to its angular momentum in units of $\hbar$.

In this work we used reflection from the 220 planes of magnetite. The crystal structure of magnetite is such that the amplitude of scattering A from a single unit cell for the 220 reflection depends only upon the eight tetrahedral Fe^{+++} ions in the cell. It is given in centimeters by

$$A_{220}=7.65\times10^{-13}-31.0\times10^{-13}jm. \qquad (6)$$

To obtain (6) from (4) and (5) we have used the values[8,9] $C=0.956\times10^{-12}$ cm, $f=0.72$, with $S'=5/2$ and $g'=-3.83$. The intensity of reflection is proportional to $(A_{220})^2$.

Using values of the transition probability calculated from Eq. (1), and values of the magnetite crystal reflectivity calculated from Eq. (6), we have calculated the neutron intensity reflected from the two crystals as a function of the amplitude of the oscillating magnetic field, for different values of the neutron spin. With $\omega_0=\omega_1$, the transition probability for spin $\frac{1}{2}$ is of the form $W=\sin^2(\frac{1}{2}\alpha)$, where α is proportional to the amplitude H_0 of the oscillating field. The intensity I coming off the second crystal is then proportional to $[1-B\sin^2(\frac{1}{2}\alpha)]$, in which B is a function of the polarization P produced by either crystal alone: $B=(2P^2)/(1+P^2)$. The measured and calculated values for neutron intensity as a function of amplitude of oscillating field are compared in Fig. 2. The points of Fig. 2 represent the measured values. The long dash curve represents the calculated intensity *vs* amplitude of oscillating field for spin $\frac{1}{2}$. For purpose of comparison, the calculated intensity for spin $\frac{3}{2}$ is shown by the short dash curve. These curves are based upon numerical values of the nuclear and magnetic scattering amplitudes of Eq. (6). The calculated value of the polarization P of spin $\frac{1}{2}$ neutrons reflected from our magnetite crystal, when these amplitudes are used, is very close to 100 percent. However, we have measured the polarization of the reflected beam[3] and found it to be 87 percent. The solid curve of Fig. 2 has been calculated with $P=87$ percent for spin $\frac{1}{2}$. It fits the measured values very well. The minimum at oscillator current of 0.9 amperes should correspond to $\alpha/2=\pi/2$. For $\omega_0=\omega_1$, $\alpha/2=gH_1t/2$. The value of $\alpha/2$ at this minimum was calculated to be $\pi/2$ from the measured current in the solenoid, the geometrical properties of the solenoid, and the known neutron velocity. Also, the calculated ordinates in the region of the minimum and maximum intensities pass through the measured values. The value of $P=0.87$ corresponds to a value of the amplitude C (or D) different by 50 percent from the value derived from neutron diffraction data. The reason for our low value of P is not known. (Two single crystals of magnetite giving widely different neutron polarizations were found to be closely the same on chemical analysis.)

A similar attempt to fit the data with neutron spin $\frac{3}{2}$, by varying the parameter C, was much less successful. For C up to twice the accepted value, the first minimum occurs at a value of α about $\frac{1}{2}$ of the measured value and at an ordinate a factor of two above the measured value of 0.16; the first maximum occurs at $\alpha/2=90°$ instead of 180°, with an ordinate of only about 0.7 instead of 1. The character of the curve for spin $\frac{3}{2}$ can be forced to approach the measured curve, only by changing C by about a factor of 10. Such a change from the accepted value seems hardly likely. Other neutron spin values are equally unsatisfactory.

The straight line of Fig. 2 is drawn through the measured values of the intensity when the neutron beam is depolarized between the two crystals by the insertion of a thin sheet of iron in a region of near zero field. The fact that the best-fit calculated curve is symmetrical about this line demonstrates that the maximum transition probability was 100 percent.

We are grateful to Dr. A. Simon for helpful discussions.

[8] Shull, Wollan, and Koehler, Phys. Rev. **84**, 912 (1951).
[9] Shull, Strauser, and Wollan, Phys. Rev. **83**, 333 (1951).

Total Cross Section of Li^6 for Neutrons*

C. H. JOHNSON, H. B. WILLARD, AND J. K. BAIR
Oak Ridge National Laboratory, Oak Ridge, Tennessee

(Received August 13, 1954)

The total cross section of Li^6 for neutrons has been measured for neutron energies from 0.035 to 4.2 Mev. A resonance was observed with its maximum at 0.255±0.010 Mev, which corresponds to 7.46-Mev excitation energy in Li^7. The observed width of the resonance at half-maximum is 100 kev. It is interpreted according to the nuclear dispersion theory as resulting from p neutrons forming a state of total angular momentum 5/2. The cross section rises gradually in the region from 1.5 Mev to 4.2 Mev.

I. INTRODUCTION

CONSIDERABLE attention has been devoted to the level structure of Li^7 because it is one of the simplest of the light nuclei.[1] In particular, a level at 7.46 Mev in Li^7 was found from a resonance in the $Li^6(n,\alpha)H^3$ reaction.[2] Later it became questionable that this resonance should be attributed to interaction of neutrons with Li^6 since the total cross section of Li^7 shows a resonance at about the same neutron energy.[3] Protons, deuterons, and α particles inelastically scattered from Li^7 have given no indication of the 7.46-Mev level;[1,4] however, a group of α particles from the bombardment of Be^9 with deuterons probably results from Li^7 being left in this excited state.[1] The $Li^7(\gamma,\alpha)H^3$ reaction shows a peak at 7.25 Mev which was interpreted as resulting from this level.[5] The mirror level in Be^7 was found by bombarding Li^6 with protons[6] and also from the neutron spectrum of the $Li^7(p,n)Be^7$ reaction.[7] In the present paper the neutron total cross section of Li^6 was measured in order to study this state in Li^7 and to extend the level survey to higher energies.

II. EXPERIMENTAL METHOD

The total cross section of Li^6 for neutrons was measured by a transmission experiment. Scattering samples were prepared from isotopically enriched lithium metal produced by the Stable Isotopes Division at Oak Ridge. Dr. P. S. Baker of the Stable Isotopes Division supervised the casting of the lithium into cylindrical thin-walled stainless steel cans. To test the casting procedure several cylinders were made using limited quantities of normal lithium. The density of these samples was correct within 0.5 percent. Table I describes the five Li^6 samples that were made. The chemical purity shown in the table is the percent by weight of lithium metal. Samples 1, 2, and 3, which were used for the first measurement in 1952, had several percent by weight of impurity which a quantitative spectroscopic analysis showed to be Na, Mg, Al, Si, K, and Cu. Since the atomic weight of the impurities is several times that of lithium, these percentages correspond to less than one atomic percent of impurity. The number of atoms/cm² shown in the table is the number of atoms of all types including the small atomic percent of impurity. If these numbers of atoms/cm² were reliable, the impurity would cause a negligible error in cross section; however, the densities of the three samples as given in Table I were not consistent with the quoted impurities. This is not surprising since the spectroscopic analysis is not accurate for the alkalies and gives no analysis for the halides. It was estimated that the number of atoms/cm² may be five percent high for these three samples. For this reason samples 4 and 5 were made with high purity and used for a repeat measurement in 1954. The atoms/cm² for these samples is believed accurate to one percent. In the measurement of cross sections, scatterers were chosen to give about 50 percent transmission.

Various neutron sources and detectors were used to cover the energy range from 0.035 to 4.2 Mev. Protons from the Oak Ridge National Laboratory 5.5-Mev Van de Graaff bombarded a lithium target of 15-kev stopping power to produce neutrons with energy up to 1.5 Mev. Neutrons of greater energy were obtained from the $T(p,n)$ reaction by use of a Zr-T target[8] with 35-kev stopping power at threshold. Because of the decrease in stopping power with energy the tritium target was less than 20 kev thick for most of the measurement.

TABLE I. Description of the Li^6 scattering samples.

Sample No.	Atoms/cm²	Chemical purity	Percent error in density	Isotopic percentage of Li^6	Sample diameter (cm)
1	0.0708×10^{24}	96.72	8.0	89.0	2.2
2	0.1086	95.49	0.5	88.9	3.0
3	0.2223	98.14	6.0	89.7	3.0
4	0.0641	99.97	1.0	93.8	2.0
5	0.1280	99.97	1.7	93.8	2.0

* This document is based on work performed for the U. S. Atomic Energy Commission at the Oak Ridge National Laboratory.

[1] H. E. Gove and J. A. Harvey, Phys. Rev. **82**, 658 (1951). This includes references to previous work.

[2] J. M. Blair and R. E. Holland, data reproduced in *Neutron Cross Sections*, Atomic Energy Commission Report AECU 2040 (Office of Technical Services, Washington, D. C., 1952).

[3] R. K. Adair, Phys. Rev. **79**, 1018 (1950).

[4] W. Franzen and J. G. Likely, Phys. Rev. **87**, 667 (1952).

[5] P. Stoll and M. Wächter, Nuovo cimento **10**, 347 (1953).

[6] S. Bashkin and H. T. Richards, Phys. Rev. **84**, 1124 (1951).

[7] D. M. Thompson, Phys. Rev. **88**, 954 (1952).

[8] The tritium target was loaned to us by T. W. Bonner of Rice Institute.

In the energy region from 0.035 to 0.18 Mev, a BF_3 detector similar to that described by Seagondollar and Barschall[9] was placed with its axis at 97 degrees to the proton beam and with its front face 30 cm from the neutron source. The transmission of samples 2 plus 3 when placed 8 cm from the source was determined relative to that of identical empty cans, and the total cross section was found assuming exponential attenuation of the neutron flux. Since in this geometry 2.0 percent of the scattered neutrons would reach the detector if the scattering were isotropic in the center-of-mass system, a 2.0 percent scattering-in correction was applied. From 0.14 to 0.20 Mev sample 3 was used in this same scattering geometry at zero degrees to the proton beam.

For neutron energies of 0.18 to 1.5 Mev the detector was a propane-filled proportional recoil counter 2.5 cm in diameter and 10 cm long, placed with its axis coincident with that of the proton beam and with its center 30 cm from the neutron source. The amplifier bias was set to discriminate against the low-energy neutron group from the $Li^7(p,n)Be^7$ reaction.[10] Scatterers were placed midway between source and detector so that the scattering-in correction was 1.6 percent for samples 2 and 3 and 1.0 percent for sample 1. A second run was made near the resonance by using samples 4 and 5 with the counter 37 cm from the source. The scattering-in correction was then 0.45 percent. Within 50 kev of the resonance all of these scattering-in corrections were multiplied by 1.3 to give an approximate correction for the nonisotropic scattering[11] from Li^6.

For energies above 1.5 Mev, a high-pressure hydrogen chamber 2.5 cm in diameter and 13 cm long replaced the propane counter. It operated as an electron collection chamber using a 0.02-inch central wire. The filling was 100 atmos of electrolytic hydrogen further purified by passing over hot magnesium for several hours. To obtain a good signal-to-noise ratio the chamber was shock-mounted and the pulses were amplified with a slow amplifier[12] with rise and decay time constants each adjusted to 30 microseconds. The counter had an efficiency of about 6 percent.

Background corrections, measured by interposing a paraffin shadow cone 25 cm long between source and detector, were appreciable for the BF_3 counter but were negligible (less than 1 percent) for the recoil counters. For all measurements, current integration of the proton beam served to monitor the neutron flux.

The total cross section of the lithium was determined by assuming the total number of atoms given in Table I to be the number of lithium atoms and the total cross section of Li^6 was found by correcting for the presence of Li^7 using the known cross sections.[13–15] Near the resonance we used the 5-kev resolution data[14] on Li^7 by correcting for the energy resolution of the present measurements and assuming the resonances in the two isotopes coincide. Since the Li^6 and Li^7 cross sections are similar, the Li^7 correction was of the order of 1 percent, except on the sides of the resonance where it is as large as 6 percent.

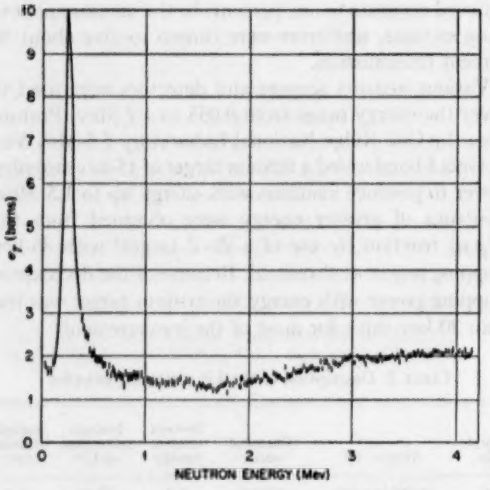

FIG. 1. Total cross section of Li^6 for neutrons, measured by a transmission experiment using a scatterer of enriched Li^6 metal.

III. RESULTS

Figure 1 shows the total cross section of Li^6 as a function of the neutron energy which has been corrected for target thickness. The lengths of the vertical lines indicate standard statistical errors of the data points. Our best estimate of the error arising from the sample impurities is that the observed cross section is 3 percent low off-resonance. It is interesting that the entire curve is nearly identical to the total cross section of Li^7. Both cross sections show a resonance at nearly 255 kev, although the widths of the two resonances differ by about a factor of two. In addition, a slow rise in cross section at high energies is observed for both nuclei. The upper curve of Fig. 2 shows the details of the resonance which was observed with various scatterers and detectors. Samples 1, 2, and 3 are shown with open symbols in an attempt to de-emphasize these results near the peak. It is estimated that the effect of unknown impurities in those three samples could make the cross section 5 to 10 percent low at the peak. The high-purity samples 4 and 5 are shown as solid symbols. The resonance has a maximum of 10.2 barns and an observed width at half-maximum of 100 kev. The peak lies at 255±10 kev in

[9] L. W. Seagondollar and H. H. Barschall, Phys. Rev. **72**, 439 (1947).
[10] Johnson, Laubenstein, and Richards, Phys. Rev. **77**, 413 (1950).
[11] Willard, Bair, and Kington (to be published).
[12] P. R. Bell Model A-2 Amplifier (private communication).
[13] Bockelman, Miller, Adair, and Barschall, Phys. Rev. **84**, 69 (1951).
[14] P. H. Stelson and W. M. Preston, Phys. Rev. **84**, 162 (1951).
[15] Published curves extend to 3.4 Mev. Measurements at this laboratory show that the cross section of normal lithium rises smoothly to 2.5 barns at 4.2 Mev.

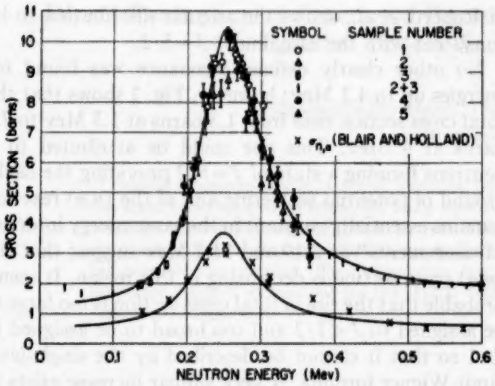

FIG. 2. The upper curve is the total cross section of Li^6 for neutrons as determined using five different scattering samples. Table I describes the five samples. The lower curve presents the data of Blair and Holland[2] on the $Li^6(n,\alpha)H^3$ reaction. The solid curves are calculated from the nuclear dispersion theory by assuming the resonance results from p neutrons forming a state of $J=5/2$.

agreement with the $Li^6(n,\alpha)$ peak found at 250 kev.[2] According to known mass values,[16] the peak corresponds to 7.46-Mev excitation in the Li^7 nucleus.

IV. DISCUSSION

According to the nuclear dispersion theory, the total cross section near an isolated resonance consists of resonant scattering and absorption of neutrons in addition to potential elastic scattering. It will be shown that the magnitude of the resonance is too large to be ascribed to s-wave resonant interaction; hence, the resonance scattering will not interfere coherently with the potential scattering which is predominantly s wave for these neutron energies.[17] The total cross section near the isolated resonance may then be written as the sum of a resonance term, plus a potential term,[17,18]

$$\sigma_T=\frac{\pi}{k^2}\frac{2J+1}{6}\frac{\Gamma_n(\Gamma_n+\Gamma_\alpha)}{(E_\lambda+\Delta_\lambda-E)^2+(\Gamma_n+\Gamma_\alpha)^2/4}+\frac{4\pi}{k^2}\sin^2\delta_0, \quad (1)$$

where J is the total angular momentum of the λth level in the compound nucleus Li^7; k is the neutron wave number corresponding to the energy E; Γ_n and Γ_α are the neutron and α-particle widths; E_λ and Δ_λ are the characteristic energy and energy shift of the level; and δ_0 is the s-wave potential phase shift. If one assumes the potential scattering is hard sphere, then $\delta_0=-ka_n$, where a_n is the radius of interaction of the neutron and Li^6. All energies refer to center-of-mass coordinates.

In Eq. (1) it is assumed the only process of significance other than elastic scattering is the $Li^6(n,\alpha)H^3$ reaction. The ×'s in Fig. 2 show the preliminary (n,α) data of Blair and Holland.[2] Since the Breit-Wigner formula as written above cannot account for the observed off-resonance (n,α) cross section, it is necessary to add another term which presumably results from tails of other distant resonances. A simple addition which gives an approximate description of the data near resonance is a constant equal to 0.5 barn. To describe the off-resonance total cross section, which includes this constant plus potential scattering, we have chosen $a_n=1.4\times6^{\frac{1}{3}}\times10^{-13}$ cm $=2.54\times10^{-13}$ cm.

At resonance the observed total cross section corrected for energy resolution is 10.3 barns and the (n,α) cross section is 3.2 barns. By choosing the ratio Γ_n/Γ_α at resonance in Eq. (1) to fit the total cross section, one finds that for $J=3/2$, $5/2$, and $7/2$ the (n,α) cross section (resonant term $+0.5$ barn) should be 0.52, 3.65, and 5.12, respectively. Only $J=5/2$ agrees within experimental error with the observed cross section; therefore, it is assumed in the following discussion that the resonance results from a single compound state with $J=5/2$.

In forming this state, total angular momentum can be conserved by neutrons of orbital angular momentum from $J-\frac{1}{2}$ to $J+\frac{1}{2}$ so that the resonance cannot result from s-wave neutrons. Orbital angular momentum enters the Breit-Wigner formula through the level shift and partial widths which may be written[18,19]

$$\Delta_\lambda=\sum_s\Delta_{\lambda s}=-\sum_{sl}\gamma_{sl}^2a_s^{-1}\times[l+d\ln(F_{sl}^2+G_{sl}^2)^{\frac{1}{2}}/d(\ln k_sa_s)], \quad (2)$$

$$\Gamma_{sl}=\sum_l 2k_s\gamma_{sl}^2(F_{sl}^2+G_{sl}^2)^{-1},$$

where γ^2 is an energy-independent reduced width; $(F^2+G^2)^{-1}$ is a barrier penetration factor; and l and s refer to the relative orbital angular momentum l of the pair of particles s. In the reaction being considered, s includes two possible pairs which have been denoted by subscripts n and α. Since the α-particle energy is large compared to the energy range considered, Γ_α and $\Delta_{\lambda\alpha}$ are approximately constant. As stated above, four possible l values may be considered for the neutron; however, the penetration factor decreases so rapidly with increasing l that only the lowest l value for each parity need be considered, namely, $l=1$ and 2. For d neutrons the resonance could not have a width exceeding 10 kev even if $\gamma_n^2\to\infty$, so that the resonance must result from p-wave neutrons. For p neutrons it was possible to choose Γ_n and Γ_α at resonance (114 kev and 60 kev in the center-of-mass system) to give a good description of the total cross section. In Fig. 2 the upper solid curve is the fit to the total cross-section data and the lower curve is the corresponding fit to the preliminary (n,α) data of Blair and Holland.

[16] Li, Whaling, Fowler, and Lauritsen, Phys. Rev. **83**, 512 (1951).
[17] Feshbach, Peaslee, and Weisskopf, Phys. Rev. **71**, 142 (1947).
[18] E. P. Wigner and L. Eisenbud, Phys. Rev. **72**, 29 (1947).
[19] R. G. Thomas, Phys. Rev. **81**, 148 (1951).

TABLE II. Parameters to describe the resonance shown in Fig. 2.

Resonance energy in the lab system	255 kev
Total angular momentum	$J=5/2$
Neutron orbital angular momentum	$l=1$
Interaction radius	2.54×10^{-13} cm
Constant (n,α) cross section	0.5 barn
Neutron width in the center-of-mass system at resonance	114 kev
α-Particle width in the center-of-mass system	60 kev

The reduced neutron width is then 11.8×10^{-13} Mev-cm which is 42 percent of the sum-rule limit, $3\hbar^2/2\mu a$, where μ is the reduced neutron mass. The single-particle model of this level is, therefore, approximately valid[20] even though the excitation energy is several Mev. An estimate of the α-particle reduced width and level shift was obtained from Eq. (2) by assuming a radius of 3.5×10^{-13} cm and f-wave interaction. This gave $\gamma_n^2/\gamma_\alpha^2\cong10^3$ and $\Delta_{\lambda n}\gg\Delta_{\lambda\alpha}$. The total level shift is then essentially $\Delta_{\lambda n}$, so that the characteristic energy E_λ is $E_\lambda=7.46$ Mev$+\Delta_{\lambda n}=7.70$ Mev. Table II summarizes the parameters used to describe this resonance.

Additional evidence exists that this resonance results from p neutrons. Bashkin and Richards[21] concluded that this state and a level at $E_\lambda=7.31$ Mev in Be^7 are mirror levels formed by p-wave neutrons or protons on Li^6. Roberts *et al.*[22] found that the angular distribution of the $Li^6(n,\alpha)H^3$ reaction indicates primarily p-wave interaction at the resonance. Peshkin and Siegert[23] presented an analysis which, when applied to the more recent data of Roberts *et al.*, shows the angular distribution to be consistent with the assignment $J=5/2$.

No other clearly defined resonance was found for energies up to 4.2 Mev; however, Fig. 1 shows that the total cross section rises from 1.3 barns at 1.5 Mev to 2.1 barns at 4 Mev. This rise could be attributed to p neutrons forming a state of $J=5/2$ providing the background of potential scattering and of the (n,α) reaction remains essentially constant in the same energy interval. Measurements[24] at 2.49 and 14.2 Mev suggest that the (n,α) cross section is decreasing in this region. It seems probable that the rise in total cross section is too large to be assigned to $J<7/2$ and too broad to be assigned to $l>1$ so that it cannot be described by the single-level Breit-Wigner formula. A very similar increase exists in the total cross section of Li^7 which cannot be described by the single-level formula.

Recent observations[25,26] of the differential elastic scattering for neutrons on light nuclei are not well described using phase shifts predicted for hard-sphere potential scattering. An analysis of the high-energy cross section should await data on the scattering phase shifts. It may also be that the potential scattering near the resonance should not be calculated for hard sphere scattering as was done above. In any case, the data near the resonance are well described by assuming an approximately constant s-wave potential scattering of 0.75 barn.

ACKNOWLEDGMENTS

The authors are indebted to Dr. P. S. Baker and G. F. Wells of the Stable Isotope Division for the preparation of the Li^6 samples, to J. D. Kington for aid in performing the experiment, and to Dr. A. Simon and Dr. L. C. Biedenharn for helpful discussions.

[20] T. Teichmann and R. P. Wigner, Phys. Rev. **87**, 123 (1952).

[21] See reference 6. Since these authors used a larger interaction radius than that of the present paper, their γ^2 and Δ_λ are smaller than those found here; however, their final conclusions do not depend critically upon the assumed radius.

[22] Roberts, Darlington, and Haugsnes, Phys. Rev. **82**, 299 (1951); W. O. Solano and J. H. Roberts, Phys. Rev. **89**, 829(A) (1953); Darlington, Haugsnes, Mann, and Roberts, Phys. Rev. **90**, 1049 (1953).

[23] Murray Peshkin and A. J. F. Siegert, Phys. Rev. **87**, 735 (1952).

[24] R. L. Ribe, Phys. Rev. **87**, 205 (1952).

[25] Willard, Bair, and Kington, Phys. Rev. **94**, 786 (1954).

[26] C. H. Johnson and J. L. Fowler, Phys. Rev. **95**, 637 (1954).

Direct Evaluation of Fractional Parentage Coefficients Using Young Operators. General Theory and $<4|2,2>$ Coefficients

H. A. JAHN
Mathematics Department, The University, Southampton, England

(Received June 1, 1954)

General expressions for $\langle n|m,n-m\rangle$ fractional parentage coefficients are derived, for the special case where the state vectors are all different, by using normalized Young symmetry operators constructed out of permutation operators acting on the state vectors. The coefficients are given directly in terms of matrix elements of the permutations characterizing the cosets of the subgroup $S_m \times S_{n-m}$ of S_n multiplied by the corresponding permutation operator. The permutation operators themselves are expressible in terms of Racah W functions. Explicit expressions for the $\langle 4|2,2\rangle$ coefficients are given also for cases where some of the state vectors are identical.

1. INTRODUCTION

PROGRESS in the theory of nuclear structure requires, with the shell model, the setting up of energy matrices between many different single-particle configurations. The most direct way of setting up the energy matrices is by use of n-particle wave functions expressed as linear combinations of totally antisymmetric states of the first $n-2$ particles, vector coupled to totally antisymmetric states of the last two particles. Reduction in the size of energy matrices determining ground state properties requires the construction of states belonging to definite irreducible representations of the group of permutations of the space coordinates alone, so that the energy matrices can, in the first instance, be set up between states of maximum or near maximum orbital symmetry characteristic of the ground state. The coefficients of those linear combinations of vector coupled orbital states of $n-2$ and 2 particles of definite orbital symmetry, which give rise to states of definite orbital symmetry for n particles, are the $\langle n|n-2, 2\rangle$ orbital coefficients of fractional parentage. It is with the calculation of these, in mixed single-particle configurations, that we are mainly concerned.

2. PERMUTATIONS OF STATES AND PARTICLES. NORMALIZED YOUNG OPERATORS

If

$$\Phi_0=\Phi(j_1(1)\,j_2(2)J_2,\ j_3(3)J_3,\ \cdots,\ j_{n-1}(n-1)J_{n-1},\ j_n(n)JM) \quad (1)$$

is an n-particle vector coupled orbital state, with $j_1, j_2, \cdots, j_n$ all different, the numbers in parentheses being the particle numbers, we may form $n!$ distinct states from it by either permuting the particle numbers keeping the order of the states fixed, or by permuting the order of the states keeping the particle order unaltered. The relation between these two operations is the following. If P is a permutation of the particle nunbers, P^{-1} its inverse, then we define the corresponding permutation $\bar{P}$ of the states by

$$\begin{aligned}\bar{P}\Phi_0&=P^{-1}\Phi_0\\&=\Phi(j_1(P^{-1}1)\,j_2(P^{-1}2)J_2,\ j_3(P^{-1}3)J_3,\ \cdots\\&\qquad J_{n-1},\ j_n(P^{-1}n)JM)\\&=\sum_{J_2'J_3'\cdots J_{n-1}'}\langle j_1j_2J_2j_3J_3\cdots J_{n-1}j_nJ|\\&\quad j_{P1}j_{P2}J_2'j_{P3}J_3'\cdots J_{n-1}'j_{Pn}J\rangle\\&\quad\times\Phi(j_{P1}(1)\,j_{P2}(2)J_2',\ j_{P3}(3)J_3',\ \cdots,\\&\qquad J_{n-1}',\ j_{Pn}(n)JM).\end{aligned} \quad (2)$$

This is the basic operation of fractional parentage coefficient theory, where the particle order is always maintained.

There are now two distinct ways of operating on the state $\bar{P}\Phi_0$ by a further permutation, depending upon whether we take this to be (a) a permutation of the state vectors, or (b) a permutation of the particle numbers. These two operations commute and we have

$$\text{(a)}\qquad \bar{Q}(\bar{P}\Phi_0)=\overline{QP}\Phi_0=\bar{Q}\bar{P}\Phi_0, \quad (3)$$

$$\text{(b)}\qquad Q(\bar{P}\Phi_0)=\bar{P}Q\Phi_0=\bar{P}\bar{Q}^{-1}\Phi_0. \quad (4)$$

We see that the permutation of the state vectors $\bar{Q}$ operates by multiplication on the left of the operator $\bar{P}$, while the permutation Q of the particle numbers operates as $\bar{Q}^{-1}$ on the right of $\bar{P}$. We may say therefore that the $n!$ functions $\bar{P}\Phi_0$ can be subject to two commuting groups of permutations and it is possible to choose linear combinations of them so that they belong simultaneously to a definite row of a definite irreducible representation of each group.[1]

The linear combinations required are given directly by operating on Φ_0 by the $n!$ linear combinations of the permutations $\bar{P}$ characterizing the $n!$ distinct normalized Young tableau operators,[2]

$$\bar{\omega}_{rs}{}^{[\lambda]}=(f_\lambda/n!)^{\frac{1}{2}}\sum_P\theta_{rs}{}^{[\lambda]}(P)\bar{P}, \quad (5)$$

[1] Compare the analogous problem in molecular theory, where the rotational wave functions may be transformed by the two commuting groups of rotations (a) about axes fixed in space, (b) about axes fixed in the molecule; see, for instance, H. A. Jahn, Ann. Physik 23, 529 (1935).

[2] The relation with the unnormalized orthogonal Young units $o_{rs}{}^{[\lambda]}$ as commonly defined [e.g., by D. E. Rutherford, *Substitutional Analysis* (University Press, Edinburgh, 1948)] is $\omega_{rs}{}^{[\lambda]}=(n!/f_\lambda)^{\frac{1}{2}}o_{rs}{}^{[\lambda]}$.

associated with the irreducible orthogonal matrix representations $\theta_{rs}^{[\lambda]}(P)$ of the symmetric group S_n, f_λ being the dimension of the representation. With the Young operators normalized in this way, the inverse relation,

$$\bar{P}=\sum_{\lambda rs}(f_\lambda/n!)\theta_{rs}^{[\lambda]}(P)\tilde{\omega}_{rs}^{[\lambda]}, \tag{6}$$

expressing the $n!$ permutations in terms of the

$$\sum_\lambda (f_\lambda)^2=n! \tag{7}$$

symmetry operators, has the same coefficients as (5), showing that these transformation coefficients,

$$T_{\lambda rs,P}=(f_\lambda/n!)^{\frac{1}{2}}\theta_{rs}^{[\lambda]}(P), \tag{8}$$

describe an orthogonal transformation satisfying the relations:

$$\sum_{\lambda rs} T_{\lambda rs,P}T_{\lambda rs,Q}=\sum_{\lambda rs}(f_\lambda/n!)\theta_{rs}^{[\lambda]}(P)\theta_{rs}^{[\lambda]}(Q)$$
$$=\delta(P,Q), \tag{9}$$

$$\sum_P T_{\lambda rs,P}T_{\lambda' r's',P}=\{(f_\lambda f_{\lambda'})^{\frac{1}{2}}/n!\}\sum_P\theta_{rs}^{[\lambda]}(P)\theta_{r's'}^{[\lambda']}(P)$$
$$=\delta(\lambda,\lambda')\delta(r,r')\delta(s,s'). \tag{10}$$

We may then form, for given $j_1j_2\cdots j_nJ_2J_3\cdots J_{n-1}JM$, the following $n!$ states,

$$\Phi_{rs}\equiv\Phi(r|\,j_1j_2J_2j_3J_3\cdots j_{n-1}J_{n-1}j_nJM\,|s)$$
$$=\tilde{\omega}_{rs}^{[\lambda]}\Phi_0, \tag{11}$$

with the following properties:

(I) If Φ_0 is normalized and the state vectors $j_1, j_2, \cdots, j_n$ are all different, then the states Φ_{rs} are normalized and orthogonal.

(II) A permutation $\bar{P}$ of the state vectors acting as operator on Φ_{rs} transforms the first index r, leaving the second index s invariant:

$$\bar{P}\Phi_{rs}=\sum_t\Phi_{ts}\theta_{tr}^{[\lambda]}(P). \tag{12}$$

(III) A permutation P of the particle numbers acting as operator on Φ_{rs} transforms the second index s and leaves the first index unaltered:

$$P\Phi_{rs}=\sum_t\Phi_{rt}\theta_{ts}^{[\lambda]}(P). \tag{13}$$

The first property follows from the fact that under the conditions stated the $n!$ states $\bar{P}\Phi_0$ are all normalized and orthogonal. The second and third properties may be deduced easily from the following properties of the Young orthogonal units:

$$P=\sum_{\lambda rs}\theta_{rs}^{[\lambda]}(P)o_{rs}^{[\lambda]}, \tag{14}$$

$$o_{rs}^{[\lambda]}o_{r's'}^{[\lambda']}=\delta(\lambda,\lambda')\delta(s,r')o_{rs'}^{[\lambda]}. \tag{15}$$

In cases where some or all of the state vectors are identical it may be simpler to regard the Young operators as built up in the first place out of permutations of the particle numbers, rather than out of permutations of the state vectors. In this connection we may note that if we define for an orthogonal representation

$$\omega_{sr}^{[\lambda]}\Phi_0=(f_\lambda/n!)^{\frac{1}{2}}\sum_P\theta_{sr}^{[\lambda]}(P)P\Phi_0, \tag{16}$$

we will have simply

$$\tilde{\omega}_{rs}^{[\lambda]}\Phi_0=\omega_{sr}^{[\lambda]}\Phi_0. \tag{17}$$

It is then in accordance with our notation to define

$$\Phi_{rs}^{[\lambda]}=N_r\omega_{sr}^{[\lambda]}\Phi_0, \tag{18}$$

the second label s describing as before the transformation properties with respect to permutation of the particle numbers. The factor N_r is introduced to allow of the renormalization that will be required when some of the state vectors are identical. Some of the state labels r may also become redundant, as the corresponding states may vanish identically or become identical with other states.

3. THE $\langle n|n-1,1\rangle$ FRACTIONAL PARENTAGE COEFFICIENTS

We choose the orthogonal matrix representation $\theta_{rs}^{[\lambda]}(P)$ to have the standard Young-Yamanouchi form[3] appropriate to the regular partition,

$$[\lambda]=[\lambda_1\lambda_2\cdots\lambda_k], \tag{19}$$

of n:

$$n=\lambda_1+\lambda_2+\cdots+\lambda_k,\quad \lambda_1\geqslant\lambda_2\geqslant\cdots\geqslant\lambda_k. \tag{20}$$

We may then take the row and column indices r, s to be Yamanouchi symbols,[3]

$$(r)=(r_1r_2\cdots r_n),\quad (s)=(s_1s_2\cdots s_n), \tag{21}$$

where (r) is an arrangement of λ_1 integers 1, λ_2 integers 2, $\cdots$, λ_k integers k, such that, read from left to right,[4] the number of times the integer p has occurred at any stage is never less than the number of times the integer $p+1$ has occurred. Similarly for (s). The matrices of the transpositions P_{12}, P_{23}, $\cdots P_{n-1,n}$ can then be written down immediately by the Young-Yamanouchi rules and the matrix of any other permutation calculated.

We may then write

$$(s)=(s'\sigma), \tag{22}$$

where

$$\sigma=s_n \tag{23}$$

and

$$(s')=(s_1s_2\cdots s_{n-1}) \tag{24}$$

is a Yamanouchi symbol of a definite representation,

$$R[\lambda']=R[\lambda_1'\lambda_2'\cdots\lambda_{k'}'], \tag{25}$$

of S_{n-1}.

[3] H. A. Jahn, Proc. Roy. Soc. (London) **A205**, 192 (1951); H. A. Jahn and H. van Wieringen, Proc. Roy. Soc. (London) **A209**, 502 (1951).

[4] We have found it convenient to retain the natural order here, rather than the reverse of natural order previously used in reference 3.

We wish to express $\tilde{\omega}_{r,s'\sigma}^{[\lambda]}$ in terms of the normalized Young operators $\tilde{\omega}_{t's'}^{[\lambda']}$ of S_{n-1}, (t') being another Yamanouchi symbol for $R[\lambda']$. To do this we express the general permutation P of S_n as the product of a permutation R of S_{n-1} and a permutation Q taken from one of the $n-1$ cosets in S_n of the subgroup S_{n-1}. There is considerable arbitrariness in the choice of the permutations Q; we could for instance take simply

$$Q_1=I, \quad Q_2=P_{1n}, \quad Q_3=P_{2n}, \quad \cdots, \quad Q_n=P_{n-1,n}. \tag{26}$$

With such a choice of the Q's made, we have the unique expression,

$$P=QR, \tag{27}$$

for any permutation P of S_n. It follows that

$$\begin{aligned}\tilde{\omega}_{r,s'\sigma}^{[\lambda]}&=(f_\lambda/n!)^{\frac{1}{2}}\textstyle\sum_P \theta_{r,s'\sigma}^{[\lambda]}(P)\bar{P}\\&=(f_\lambda/n!)^{\frac{1}{2}}\textstyle\sum_t[\sum_Q \theta_{rt}^{[\lambda]}(Q)\bar{Q}]\\&\qquad\times[\textstyle\sum_R \theta_{t,s'\sigma}^{[\lambda]}(R)\bar{R}]\\&=(f_\lambda/n!)^{\frac{1}{2}}\textstyle\sum_t[\sum_Q \theta_{rt}^{[\lambda]}(Q)\bar{Q}]\\&\qquad\times[\textstyle\sum_R \delta(t,t'\sigma)\theta_{t's'}^{[\lambda']}(R)\bar{R}]\\&=(f_\lambda/nf_{\lambda'})^{\frac{1}{2}}\textstyle\sum_{t'}[\sum_Q \theta_{r,t'\sigma}^{[\lambda]}(Q)\bar{Q}]\\&\qquad\times\{[f_{\lambda'}/(n-1)!]^{\frac{1}{2}}\textstyle\sum_R \theta_{t's'}^{[\lambda']}(R)\bar{R}\}\\&=(f_\lambda/nf_{\lambda'})^{\frac{1}{2}}\textstyle\sum_{t'}\sum_Q \theta_{r,t'\sigma}^{[\lambda]}(Q)\bar{Q}\tilde{\omega}_{t's'}^{[\lambda']}.\end{aligned} \tag{28}$$

The coefficients,

$$\langle rs'\sigma|Qt's'\rangle\bar{Q}\equiv\langle r|Qt'\rangle\bar{Q}=(f_\lambda/nf_{\lambda'})^{\frac{1}{2}}\theta_{r,t'\sigma}^{[\lambda]}(Q)\bar{Q}, \tag{29}$$

define the $\langle n|n-1,1\rangle$ fractional parentage coefficients of type $\langle[\lambda]|[\lambda']\times[1]\rangle$. It is seen that they are independent of the particular value of the Yamanouchi symbol (s'). Normalization and orthogonality require, for given s,

$$\begin{aligned}&\textstyle\sum_Q\sum_{t'}\langle r|Qt'\rangle\langle p|Qt'\rangle\\&=(f_\lambda/nf_{\lambda'})\textstyle\sum_Q\sum_{t'}\theta_{r,t'\sigma}^{[\lambda]}(Q)\theta_{p,t'\sigma}^{[\lambda]}(Q)=\delta(r,p).\end{aligned} \tag{30}$$

This follows of course from the derivation, it may be deduced also directly from (10).

We have then

$$\begin{aligned}&\Phi(r|\,j_1j_2J_2j_3J_3\cdots J_{n-1}j_nJM|\,s'\sigma)\\&=\tilde{\omega}_{r,s'\sigma}^{[\lambda]}\Phi(j_1(1)j_2(2)J_2,\ j_3(3)J_3,\ \cdots J_{n-1},\ j_n(n)JM)\\&=(f_\lambda/nf_{\lambda'})^{\frac{1}{2}}\textstyle\sum_{t'}\sum_Q\theta_{r,t'\sigma}^{[\lambda]}(Q)\bar{Q}\tilde{\omega}_{t's'}^{[\lambda']}\\&\qquad\times\Phi(j_1(1)\cdots J_{n-1},\ j_n(n)JM)\\&=(f_\lambda/nf_{\lambda'})^{\frac{1}{2}}\textstyle\sum_{t'}\sum_Q\theta_{r,t'\sigma}^{[\lambda]}(Q)\bar{Q}\\&\qquad\times\Phi((t'|\,j_1j_2J_2j_3\cdots j_{n-1}J_{n-1}|\,s'),\ j_n(n)JM),\end{aligned} \tag{31}$$

expressing an n-particle state of definite permutation symmetry as a linear combination of states of definite permutation symmetry of $n-1$ particles, vector coupled to the states of the nth particle.

4. THE $\langle n|m,\ n-m\rangle$ COEFFICIENTS

The determination of the $\langle n|m,\ n-m\rangle$ coefficients of type $\langle[\lambda]|[\lambda']\times[\lambda'']\rangle$ proceeds in a similar manner. Instead of the standard Young-Yamanouchi representation of S_n, in which the subgroups $S_{n-1}, S_{n-2}, \cdots, S_2$ appear in standard form, we use a transformed representation in which the matrices of the group S_m of permutations R of the first m integers appear in standard Yamanouchi form and the group S_{n-m} of permutations S of the last $n-m$ integers appears also in standard form. In place of the labels r, s of the original representation, we may use modified labels,

$$(r)=(\alpha,\beta), \quad (s)=(\rho,\sigma), \tag{32}$$

built up out of the same set of integers as the original labels, with

$$(\alpha)=(r_1r_2\cdots r_m) \quad \text{and} \quad (\rho)=(s_1s_2\cdots s_m) \tag{33}$$

being standard Yamanouchi symbols associated with a definite row and a definite column of the representation $R[\lambda']$ of S_m (this is a property of the original Young-Yamanouchi representation), and with

$$(\beta)=(r_{m+1}r_{m+2}\cdots r_n) \quad \text{and} \quad (\sigma)=(s_{m+1}s_{m+2}\cdots s_n) \tag{34}$$

involving the remaining integers. Although these latter symbols are not necessarily of the form of standard Yamanouchi symbols, they may nevertheless be used, by prescription, to specify a definite row and a definite column of a definite representation $R[\lambda'']$ of S_{n-m}. The reason that such a prescription is always possible is that the total number of states before and after the transformation is the same, and after the transformation each state belongs to a definite row of a definite representation of each group.

The permutations RS form the subgroup $S_m\times S_{n-m}$ of S_n of dimension $m!(n-m)!$, and, as before, we may introduce

$$\binom{n}{m}=n!/[m!(n-m)!] \tag{35}$$

permutations Q characterizing the cosets of this subgroup (taking again $Q_1=I$, counting the subgroup itself as coset). We may then express any permutation P of S_n in the form

$$P=QRS, \tag{36}$$

and we have

$$\begin{aligned}\tilde{\omega}_{\alpha\beta,\rho\sigma}^{[\lambda]}&=(f_\lambda/n!)^{\frac{1}{2}}\sum_{QRS}\theta_{\alpha\beta,\rho\sigma}^{[\lambda]}(QRS)\bar{Q}\bar{R}\bar{S}\\&=(f_\lambda/n!)^{\frac{1}{2}}\sum_{uvxy}[\textstyle\sum_Q\theta_{\alpha\beta,uv}^{[\lambda]}(Q)\bar{Q}]\\&\qquad\times[\textstyle\sum_R\theta_{uv,xy}^{[\lambda]}(R)\bar{R}][\sum_S\theta_{xy,\rho\sigma}^{[\lambda]}(S)\bar{S}]\\&=(f_\lambda/n!)^{\frac{1}{2}}\sum_{uvxy}[\textstyle\sum_Q\theta_{\alpha\beta,uv}^{[\lambda]}(Q)\bar{Q}]\\&\qquad\times[\delta(v,y)\textstyle\sum_R\theta_{ux}^{[\lambda']}(R)\bar{R}]\\&\qquad\times[\delta(x,\rho)\textstyle\sum_S\theta_{y\sigma}^{[\lambda'']}(S)\bar{S}]\\&=\left\{f_\lambda\Big/\left[\binom{n}{m}f_{\lambda'}f_{\lambda''}\right]\right\}^{\frac{1}{2}}\sum_{uvQ}\theta_{\alpha\beta,uv}^{[\lambda]}(Q)\bar{Q}\\&\qquad\times\tilde{\omega}_{u\rho}^{[\lambda']}\tilde{\omega}_{v\sigma}^{[\lambda'']}.\end{aligned} \tag{37}$$

The coefficients $\langle n|m, n-m\rangle$ of fractional parentage of type $\langle[\lambda]|[\lambda']\times[\lambda'']\rangle$ are hence given by

$$\langle\alpha\beta\rho\sigma|Quv\rho\sigma\rangle\bar{Q}\equiv\langle\alpha\beta|Quv\rangle\bar{Q}$$
$$=\left\{f_\lambda\Big/\left[\binom{n}{m}f_{\lambda'}f_{\lambda''}\right]\right\}^{\frac{1}{2}}\theta_{\alpha\beta,\,uv}{}^{[\lambda]}(Q)\bar{Q}, \quad (38)$$

and are independent of the value of the Yamanouchi symbols ρ and σ. We have then

$$\Phi(\alpha,\beta|(j_1j_2J_2j_3J_3\cdots J_{m-1}j_mJ_m),$$
$$(j_{m+1}j_{m+2}J_{m+2}j_{m+3}J_{m+3}\cdots j_nJ_n),JM|\rho,\sigma)$$
$$=\tilde{\omega}_{\alpha\beta,\,\rho\sigma}{}^{[\lambda]}\Phi\{((j_1(1)j_2(2)J_2,\cdots j_m(m)J_m),$$
$$(j_{m+1}(m+1)j_{m+2}(m+2)$$
$$J_{m+2},\cdots,j_n(n)J_n),JM\}$$
$$=\left\{f_\lambda\Big/\left[\binom{n}{m}f_{\lambda'}f_{\lambda''}\right]\right\}^{\frac{1}{2}}\sum_{uv}\sum_{Q}\theta_{\alpha\beta,\,uv}{}^{[\lambda]}(Q)\bar{Q}$$
$$\times\Phi((u|j_1j_2J_2\cdots j_mJ_m|\rho),$$
$$(v|j_{m+1}j_{m+2}J_{m+2}\cdots J_n|\sigma),JM), \quad (39)$$

which expresses the n-particle state of definite permutation symmetry as a linear combination of states of definite permutation symmetry of the first m particles, vector coupled to states of definite permutation symmetry of the last $n-m$ particles. Orthogonality and normalization require

$$\left\{f_\lambda\Big/\left[\binom{n}{m}f_{\lambda'}f_{\lambda''}\right]\right\}\sum_{Q}\sum_{uv}\theta_{\alpha\beta,\,uv}{}^{[\lambda]}(Q)\theta_{\alpha'\beta',\,uv}{}^{[\lambda]}(Q)$$
$$=\delta(\alpha,\alpha')\delta(\beta,\beta'), \quad (40)$$

which also, as before, may be deduced directly from (10).

5. THE $\langle n|n-2, 2\rangle$ COEFFICIENTS

In the important case of the $\langle n|n-2, 2\rangle$ coefficients, some simplification is possible since the group S_2 has only two irreducible representations each of which is one dimensional. Hence, in (39) applied to this case the summation over v is not required, since we must have here $v=\sigma$. Taking then the $n(n-1)/2$ operators Q to be

$$I,\ P_{k,n-1},\ P_{kn},\ P_{k,n-1}P_{ln},\ (l>k=1,2,\cdots n-2), \quad (41)$$

we have the general $\langle n|n-2, 2\rangle$ fractional parentage coefficients given us by

$$\Phi(\alpha,\beta|j_1j_2J_2j_3J_3\cdots j_{n-2}J_{n-2},\ j_{n-1}j_nJ_n,JM|\rho,\sigma)$$
$$=\left\{f_\lambda\Big/\left[\binom{n}{2}f_{\lambda'}\right]\right\}^{\frac{1}{2}}\sum_{u}\sum_{Q}\theta_{\alpha\beta,\,uu}{}^{[\lambda]}(Q)\bar{Q}$$
$$\times\Phi((u|j_1j_2J_2\cdots j_{n-2}J_{n-2}|\rho),(\sigma|j_{n-1}j_nJ_n|\sigma),JM)$$
$$=\left\{f_\lambda\Big/\left[\binom{n}{2}f_{\lambda'}\right]\right\}^{\frac{1}{2}}\sum_{u}\Big\{\delta(\alpha,u)\delta(\beta,\sigma)$$
$$+\sum_{l>k=1}^{n-2}\theta_{\alpha\beta,\,uu}{}^{[\lambda]}(P_{k,n-1}P_{ln})\bar{P}_{k,n-1}\bar{P}_{ln}$$
$$+\sum_{k=1}^{n-2}[\theta_{\alpha\beta,\,uu}{}^{[\lambda]}(P_{k,n-1})\bar{P}_{k,n-1}+\theta_{\alpha\beta,\,uu}{}^{[\lambda]}(P_{kn})\bar{P}_{kn}]\Big\}$$
$$\times\Phi\{(u|j_1j_2J_2j_3J_3\cdots j_{n-2}J_{n-2}|\rho),$$
$$(\sigma|j_{n-1}j_nJ_n|\sigma),JM\}, \quad (42)$$

where the effect of the permutations $\bar{P}$ of the state vectors can be expressed in terms of Racah W functions.

For normalized two-particle states of definite symmetry, such as occur here, it is convenient to introduce the following special notation

$$\Phi(j_a(i)j_b(k)\sigma JM)\equiv\Phi(\sigma|j_a(i)j_b(k)JM|\sigma)$$
$$=(1/\sqrt{2})[I+(-1)^\sigma P_{ik}]\Phi(j_a(i)j_b(k)JM), \quad (43)$$

with the convention

$$\begin{aligned}&(-1)^\sigma=+1, \text{ when } \sigma \text{ denotes a symmetrical two-particle state,}\\ &(-1)^\sigma=-1, \text{ when } \sigma \text{ denotes an antisymmetrical state.}\end{aligned} \quad (44)$$

It is easy to verify that

$$\Phi(j_a(i)j_b(k)\sigma JM)$$
$$=(-1)^\sigma(-1)^{j_a+j_b-J}\Phi(j_b(i)j_a(k)\sigma JM). \quad (45)$$

Further, in the standard $(P_{n-1,n})$-diagonalized Young-Yamanouchi representation,[5] we may make the prescription mentioned in connection with (34) so that $(\beta)=(r_{n-1}r_n)$ is interpreted in the following simple form:

$$\begin{aligned}&\text{(i) if } r_{n-1}<r_n \text{ then } \beta \text{ describes an antisymmetrical state,}\\ &\text{(ii) if } r_{n-1}\geqslant r_n \text{ then } \beta \text{ describes a symmetric state.}\end{aligned} \quad (46)$$

That this is so may be seen as follows.

(A) If $|r_1r_2\cdots r_{n-2}rs\rangle$ and $|r_1r_2\cdots r_{n-2}sr\rangle$, with $r<s$, are both allowed Yamanouchi symbols, we may define[5] the orthogonal transformation diagonalizing $P_{n-1,n}$ by means of

$$|r_1r_2\cdots r_{n-2},rs\rangle=[(\mu-1)/(2\mu)]^{\frac{1}{2}}|r_1r_2\cdots r_{n-2}sr\rangle$$
$$-[(\mu+1)/(2\mu)]^{\frac{1}{2}}|r_1r_2\cdots r_{n-2}rs\rangle,$$
$$|r_1r_2\cdots r_{n-2},sr\rangle=[(\mu+1)/(2\mu)]^{\frac{1}{2}}|r_1r_2\cdots r_{n-2}sr\rangle \quad (47)$$
$$+[(\mu-1)/(2\mu)]^{\frac{1}{2}}|r_1r_2\cdots r_{n-2}rs\rangle,$$

with

$$\mu=\lambda_r-\lambda_s+s-r, \quad (48)$$

[5] Elliott, Hope, and Jahn, Trans. Roy. Soc. (London) **A246**, 241 (1953).

so that, for $r<s$, we have

$$\langle r_1r_2\cdots r_{n-2}, rs|P_{n-1,n}|r_1r_2\cdots r_{n-2}, rs\rangle=-1,$$
$$\langle r_1r_2\cdots r_{n-2}, sr|P_{n-1,n}|r_1r_2\cdots r_{n-2}, sr\rangle=+1. \quad (49)$$

(*B*) If $|r_1r_2\cdots r_{n-2}rs\rangle$ is an allowed symbol, but not $|r_1r_2\cdots r_{n-2}sr\rangle$, then we must have $r<s$ and we may put here

$$|r_1r_2\cdots r_{n-2}, rs\rangle=|r_1r_2\cdots r_{n-2}rs\rangle$$
$$\text{(when } |r_1r_2\cdots r_{n-2}sr\rangle \text{ not allowed).} \quad (50)$$

(*C*) Finally we write

$$|r_1r_2\cdots r_{n-2}, rr\rangle=|r_1r_2\cdots r_{n-2}rr\rangle. \quad (51)$$

It follows then from the properties of the standard Young-Yamanouchi representation[3,4] that the prescription (46) is valid in all cases. This process and prescription can be extended to the case where $P_{n-1,n}$, $P_{n-3,n-2}$, $\cdots$, P_{12} (n even) or P_{23} (n odd) are taken to be diagonal matrices, thus defining the $(\cdots P_{n-3,n-2}, P_{n-1,n})$-diagonal Young-Yamanouchi representation with standard phases.

6. EXPLICIT EXPRESSIONS FOR THE $\langle 4|2,2\rangle$ COEFFICIENTS

In the particular case of the $\langle 4|2,2\rangle$ coefficients the sum over both u and v in (39) become unnecessary and we have simply, $f_{\lambda'}$ and $f_{\lambda''}$ being here both unity,

$$\begin{aligned}\Phi(\alpha,\beta|\,j_1j_2J_1j_3j_4J_2JM|\,\rho,\sigma)&=(f_\lambda/6)^{\frac12}[\delta(\alpha,\rho)\delta(\beta,\sigma)+\theta_{\alpha\beta,\rho\sigma}{}^{[\lambda]}(P_{13}P_{24})\bar P_{13}\bar P_{24}\\&+\theta_{\alpha\beta,\rho\sigma}{}^{[\lambda]}(P_{13})\bar P_{13}+\theta_{\alpha\beta,\rho\sigma}{}^{[\lambda]}(P_{14})\bar P_{14}\\&+\theta_{\alpha\beta,\rho\sigma}{}^{[\lambda]}(P_{23})\bar P_{23}+\theta_{\alpha\beta,\rho\sigma}{}^{[\lambda]}(P_{24})\bar P_{24}]\\&\times\Phi(j_1(1)j_2(2)\rho J_1,\ j_3(3)j_4(4)\sigma J_2,\ JM). \quad (52)\end{aligned}$$

From (47), (48), (50), and (51) the basic vectors,

$$|\alpha,\beta\rangle\equiv|r_1r_2, r_3r_4\rangle, \quad (53)$$

of the standard (P_{12}, P_{34})-diagonal Young-Yamanouchi representation are given in terms of the vectors $|r_1r_2r_3r_4\rangle$ of the standard Young-Yamanouchi representation by

$[\lambda]=[4]$: $|11,11\rangle=|1111\rangle$;

$[\lambda]=[1111]$: $|12,34\rangle=|1234\rangle$,

$[\lambda]=[31]$: $|11,21\rangle=(2/3)^{\frac12}|1121\rangle+(1/3)^{\frac12}|1112\rangle$,
$|11,12\rangle=(1/3)^{\frac12}|1121\rangle-(2/3)^{\frac12}|1112\rangle$,
$|12,11\rangle=|1211\rangle$, (54)

$[\lambda]=[211]$: $|12,13\rangle=(1/3)^{\frac12}|1231\rangle-(2/3)^{\frac12}|1213\rangle$,
$|12,31\rangle=(2/3)^{\frac12}|1231\rangle+(1/3)^{\frac12}|1213\rangle$,
$|11,23\rangle=|1123\rangle$,

$[\lambda]=[22]$: $|11,22\rangle=|1122\rangle$; $|12,12\rangle=|1212\rangle$.

Since then, with the convention of (44), we have

$$P_{12}|\alpha,\beta\rangle=(-1)^\alpha|\alpha,\beta\rangle;\quad P_{34}|\alpha,\beta\rangle=(-1)^\beta|\alpha,\beta\rangle, \quad (55)$$

it follows that the matrices of P_{13}, P_{14}, and P_{24} are simply expressible as follows in terms of the matrices of P_{23}.

$$\begin{aligned}\theta_{\alpha\beta,\rho\sigma}{}^{[\lambda]}(P_{13})&=\theta_{\alpha\beta,\rho\sigma}{}^{[\lambda]}(P_{12}P_{23}P_{12})\\&=(-1)^{\alpha+\rho}\theta_{\alpha\beta,\rho\sigma}{}^{[\lambda]}(P_{23}),\\\theta_{\alpha\beta,\rho\sigma}{}^{[\lambda]}(P_{14})&=\theta_{\alpha\beta,\rho\sigma}{}^{[\lambda]}(P_{12}P_{34}P_{23}P_{12}P_{34})\\&=(-1)^{\alpha+\beta+\rho+\sigma}\theta_{\alpha\beta,\rho\sigma}{}^{[\lambda]}(P_{23}),\\\theta_{\alpha\beta,\rho\sigma}{}^{[\lambda]}(P_{24})&=\theta_{\alpha\beta,\rho\sigma}{}^{[\lambda]}(P_{34}P_{23}P_{34})\\&=(-1)^{\beta+\sigma}\theta_{\alpha\beta,\rho\sigma}{}^{[\lambda]}(P_{23}).\end{aligned} \quad (56)$$

In order, however, to obtain a simple general expression for the matrix element of $P_{13}P_{24}$, it is desirable to make an additional phase change: we change the sign of the representation vector $|12,31\rangle$. We may do this by using in place of the vector $|12,31\rangle$ a non-standard vector $|23,11\rangle$ defined by

$$|23,11\rangle\equiv-|12,31\rangle, \quad (57)$$

this still being in agreement with the prescription (46). It may be verified then that

$$\theta_{\alpha\beta,\rho\sigma}{}^{[\lambda]}(P_{13}P_{24})=S(\lambda)\delta_p(\alpha,\sigma)\delta_p(\beta,\rho), \quad (58)$$

where

$$S(\lambda)=+1 \text{ for } [\lambda]=[4],\ [22],\ [1111],$$
$$=-1 \text{ for } [\lambda]=[31],\ [211], \quad (59)$$

and

$$\delta_p(x,y)=\tfrac12[1+(-1)^{x+y}]$$
$$=+1, \text{ when } x \text{ and } y \text{ have the same parity,}$$
$$\text{zero otherwise.} \quad (60)$$

We may call the representation with this modification the modified (P_{12},P_{34})-diagonal representation and it may be verified that in this representation the matrix elements of P_{23} are as follows:

$[\lambda]$: $[4]$ $[22]$ $[1111]$ $[31]$ $[211]$

$\theta_{\alpha\beta,\rho\sigma}{}^{[\lambda]}(P_{23})$:

$[4]$: $11,11\ [1]$

$[22]$:

	$11,22$	$12,12$
$11,22$	$-\frac12$	$\sqrt{3}/2$
$12,12$	$\sqrt{3}/2$	$\frac12$

$[1111]$: $12,34\ [-1]$

$[31]$:

	$11,21$	$11,12$	$12,11$
$11,21$	0	$-\sqrt{\frac12}$	$\sqrt{\frac12}$
$11,12$	$-\sqrt{\frac12}$	$\frac12$	$\frac12$
$12,11$	$\sqrt{\frac12}$	$\frac12$	$\frac12$

$[211]$:

	$12,13$	$23,11$	$11,23$
$12,13$	0	$\sqrt{\frac12}$	$-\sqrt{\frac12}$
$23,11$	$\sqrt{\frac12}$	$-\frac12$	$-\frac12$
$11,23$	$-\sqrt{\frac12}$	$-\frac12$	$-\frac12$

(61)

Using this representation, we obtain from (52), on evaluating the transformations $\bar{P}$ of the state vectors, the general $\langle 4|2,2\rangle$ expansion as follows:

$$\Phi(\alpha,\beta|\,j_1j_2J_1j_3j_4J_2JM|\,\rho,\sigma)$$

$$=(f_\lambda/6)^{\frac{1}{2}}\Big\{\delta(\alpha,\rho)\delta(\beta,\sigma)\Phi(j_1j_2\rho J_1j_3j_4\sigma J_2JM)+S(\lambda)\delta_p(\alpha,\sigma)\delta_p(\beta,\rho)(-1)^{J_1+J_2-J}\Phi(j_3j_4\rho J_2j_1j_2\sigma J_1JM)$$

$$+2\theta_{\alpha\beta,\rho\sigma}{}^{[\lambda]}(P_{23})\times\tfrac{1}{2}\Big[\sum_{J_3J_4}\chi\begin{pmatrix}j_1j_2J_1\\j_3j_4J_2\\J_3J_4J\end{pmatrix}(\Phi(j_1j_3\rho J_3j_2j_4\sigma J_4JM)+(-1)^{\alpha+\beta+J_3+J_4-J}\Phi(j_2j_4\rho J_4j_1j_3\sigma J_3JM)$$

$$+\sum_{J_5J_6}\chi\begin{pmatrix}j_1j_2J_1\\j_4j_3J_2\\J_5J_6J\end{pmatrix}\Big[(-1)^{\alpha+j_3+j_4-J_2+J_5+J_6-J}\Phi(j_2j_3\rho J_6j_1j_4\sigma J_5JM)$$

$$+(-1)^{\beta+j_3+j_4-J}\Phi(j_1j_4\rho J_5j_2j_3\sigma J_6JM)\Big]\Big]\Big\}, \quad (62A)$$

where

$$\chi\begin{pmatrix}abe\\cdf\\ghk\end{pmatrix}=[(2e+1)(2f+1)(2g+1)(2h+1)]^{\frac{1}{2}}\begin{Bmatrix}abe\\cdf\\ghk\end{Bmatrix}=\langle(ab)e,(cd)f,kq|\,(ac)g,(bd)h,kq\rangle \quad (63)$$

is the Hope χ function.[6] The normalization of the function (62A) is assured by the relation

$$(f_\lambda/6)[\delta(\alpha,\rho)\delta(\beta,\sigma)+\delta_p(\alpha,\sigma)\delta_p(\beta,\rho)+4\{\theta_{\alpha\beta,\rho\sigma}{}^{[\lambda]}(P_{23})\}^2]=1, \quad (64)$$

which follows from (10) and may be verified also directly from (61).

It is easy to deduce from (62A) the corresponding expansions when some or all of the state vectors become equal. This may be done by removing, for the time being, the labels ρ and σ in the functions on the right-hand side by inserting the corresponding factors

$$(1/\sqrt{2})[I+(-1)^\rho P_{12}], \quad (1/\sqrt{2})[I+(-1)^\sigma P_{34}] \quad (65)$$

and then making the vectors equal. Then on reapplying the operators (65) allowance has to be made for the renormalization that may be required. In the process of collecting together identical states use is made of the fundamental symmetry relation of the Hope χ function:[6]

$$\chi\begin{pmatrix}abe\\cdf\\ghk\end{pmatrix}=(-1)^{a+b-e+c+d-f+g+h-k}\chi\begin{pmatrix}cdf\\abe\\ghk\end{pmatrix}. \quad (66)$$

Equations (62B, C, D, and E) below give the resulting $\langle 4|2,2\rangle$ expansions for the configurations $j_1j_2j_3^2$, $j_1^2j_2^2$, $j_1^3j_2$, and j^4, respectively. For the last two cases the over-all normalizing factor is not here determined,[7] for the first two normalization is assured by (64).

$$\Phi(\alpha,\beta|\,j_1j_2J_1j_3^2J_3JM|\,\rho,\sigma)$$

$$=\delta_p(\beta,2j_3-J_2)(f_\lambda/6)^{\frac{1}{2}}\Big\{\delta(\alpha,\rho)\delta(\beta,\sigma)\Phi(j_1j_2\rho J_1j_3^2J_2JM)+S(\lambda)\delta_p(\alpha,\sigma)\delta_p(\beta,\rho)(-1)^{J_1+J_2-J}\Phi(j_3^2J_2j_1j_2\sigma J_1JM)$$

$$+2\theta_{\alpha\beta,\rho\sigma}{}^{[\lambda]}(P_{23})\sum_{J_3J_4}\chi\begin{pmatrix}j_1j_2J_1\\j_3j_3J_2\\J_3J_4J\end{pmatrix}(1/\sqrt{2})[\Phi(j_1j_3\rho J_3j_2j_3\sigma J_4JM)+(-1)^{\alpha+\beta+J_3+J_4-J}\Phi(j_2j_3\rho J_4j_1j_3\sigma J_3JM)]\Big\}, \quad (62B)$$

[6] H. A. Jahn and J. Hope, Phys. Rev. 93, 318 (1954).
[7] It has been evaluated by M. J. Englefield (to be published).

$$\Phi(\alpha,\beta|\, j_1^2 J_1 j_2^2 J_2 JM|\,\rho,\sigma)$$

$$=\delta_p(\alpha,\,2j_1-J_1)\delta_p(\beta,\,2j_2-J_2)(f_\lambda/6)^{\frac{1}{2}}\Big[\delta(\alpha,\rho)\delta(\beta,\sigma)\Phi(j_1^2 J_1 j_2^2 J_2 JM)+S(\lambda)\delta_p(\alpha,\sigma)\delta_p(\beta,\rho)(-1)^{J_1+J_2-J}$$

$$\times\Phi(j_2^2 J_2 j_1^2 J_1 JM)+2\theta_{\alpha\beta,\,\rho\sigma}{}^{[\lambda]}(P_{23})\sum_{J_3J_4}\chi\begin{pmatrix} j_1 j_1 J_1\\ j_2 j_2 J_2\\ J_3 J_4 J\end{pmatrix}\Phi(j_1 j_2\rho J_3 j_1 j_2\sigma J_4 JM)\Big], \quad (62C)$$

$$\Phi(\alpha,\beta|\, j_1^2 J_1 j_1 j_2 J_2 JM|\,\rho,\sigma)$$

$$=N_{\alpha\beta}(f_\lambda/6)^{\frac{1}{2}}\delta_p(\alpha,\,2j_1-J_1)\Big\{\delta(\alpha,\rho)\delta(\beta,\sigma)\Phi(j_1^2 J_1 j_1 j_2\sigma J_2 JM)+S(\lambda)\delta_p(\alpha,\sigma)\delta_p(\beta,\rho)(-1)^{J_1+J_2-J}$$

$$\times\Phi(j_1 j_2\rho J_2 j_1^2 J_1 JM)+2\theta_{\alpha\beta,\,\rho\sigma}{}^{[\lambda]}(P_{23})\sum_{J_3J_4}\chi\begin{pmatrix} j_1 j_1 J_1\\ j_1 j_2 J_2\\ J_3 J_4 J\end{pmatrix}\Big[\delta_p(\rho,\,2j_1-J_3)\Phi(j_1^2 J_3 j_1 j_2\sigma J_4 JM)$$

$$+\delta_p(\sigma,\,2j_1-J_3)(-1)^{\alpha+\beta+J_3+J_4-J}\Phi(j_1 j_2\rho J_4 j_1^2 J_3 JM)\Big]\Big\}, \quad (62D)$$

$$\Phi(\alpha,\beta|\, j^2 J_1 j^2 J_2 JM|\,\rho,\sigma)$$

$$=N_{\alpha\beta}(f_\lambda/6)^{\frac{1}{2}}\delta_p(\alpha,\,2j-J_1)\delta_p(\beta,\,2j-J_2)\Big\{\delta(\alpha,\rho)\delta(\beta,\sigma)\Phi(j^2 J_1 j^2 J_2 JM)+S(\lambda)\delta_p(\alpha,\sigma)\delta_p(\beta,\rho)(-1)^{J_1+J_2-J}$$

$$\times\Phi(j^2 J_2 j^2 J_1 JM)+2\theta_{\alpha\beta,\,\rho\sigma}{}^{[\lambda]}(P_{23})\sum_{J_3J_4}\chi\begin{pmatrix} jjJ_1\\ jjJ_2\\ J_3J_4J\end{pmatrix}\Big[\delta_p(\rho,\,2j-J_3)\delta_p(\sigma,\,2j-J_4)\Phi(j^2 J_3 j^2 J_4 JM)$$

$$+\delta_p(\sigma,\,2j-J_3)\delta_p(\rho,\,2j-J_4)(-1)^{\alpha+\beta+J_3+J_4-J}\Phi(j^2 J_4 j^2 J_3 JM)\Big]\Big\}. \quad (62E)$$

CONCLUSION

We may note finally that it is not always simpler to construct all the states required by means of Young operators: when one state has been constructed, others may be obtained from it by operating on it by a suitably chosen permutation. Using this mixed method and the standard (P_{12},P_{34},P_{56})-diagonal representation the writer has constructed, using the $\langle 4|2,2\rangle$ expansion given here, a complete set of $\langle 6|4,2\rangle$ coefficients for states of maximum symmetry [42] arising from the mixed configurations s^4l^2, $s^4l_1l_2$ and $s^3l_1^2l_2$. These are being used,[8] in conjunction with numerical tables[5] of charge and spin coefficients and numerical tables of $\langle 6|4,2\rangle$ coefficients for s^2p^4 previously obtained, to set up the energy matrix, with central and tensor forces, for Li^6 with ten S states, six P states, and fifteen D states, all of symmetry type [42], even parity, $T=0$, $S=1$, $J=1$, obtained from the assumed lowest configuration s^4p^2 under the restriction of not more than two quanta of single-particle excitation. It is considered that it will be of some interest to see how much binding energy can be obtained for the ground state of Li^6 using this 31×31 matrix with the charge symmetric Pease-Feshbach or Hu-Massey mixture of central and tensor forces with oscillator well wave functions.

[8] This work is being undertaken mainly by P. G. Wakely, A. E. Lee, and R. Fielder.

Proton Groups from the Reaction $O^{18}(d,p)O^{19}$

CURT MILEIKOWSKY AND KATARINA AHNLUND
Nobel Institute of Physics, Stockholm 50, Sweden

(Received June 28, 1954)

Separated targets of O^{18} on thick and thin backings have been used in a search for proton groups from the reaction $O^{18}(d,p)O^{19}$. Three proton groups due to this reaction were found. Their energies were measured with a double focusing magnetic spectrometer which in this case was calibrated with known particle group energies from $B^{10}(d,p)B^{11}$ and $N^{14}(d,p)N^{15}$. The Q values of $O^{18}(d,p)O^{19}$ are $Q_1=1730\pm8$ kev, $Q_2=1636\pm8$ kev, and $Q_3=262\pm6$ kev.

INTRODUCTION

IN an earlier paper[1] we reported two particle groups from $O^{18}(d,p)O^{19}$. It was not possible, however, to make a systematic search for particle groups over a large energy region, because the target backings were thick and a proton background from d-D protons masked large regions. In the present paper the proton spectra from deuteron bombardment of O^{18} targets are reported for the energy region 1.6–4.1 Mev, at the observation angle 61.0°, and for 0.7–3.9 Mev at the angle 134.7°. This work was performed by means of a target technique using thin foil backings.

We have found altogether three proton groups belonging to $O^{18}(d,p)O^{19}$. We cannot definitely say that we have found the ground-state transition, because one narrow energy region is masked, at both angles, by the unavoidable parasite proton group from carbon-12.

APPARATUS AND TARGET TECHNIQUE

The targets were produced by magnetic separation in the 1.6-meter isotope separator of the Nobel Institute.[2] The targets were prepared in two different ways. For one type, water was used that had been

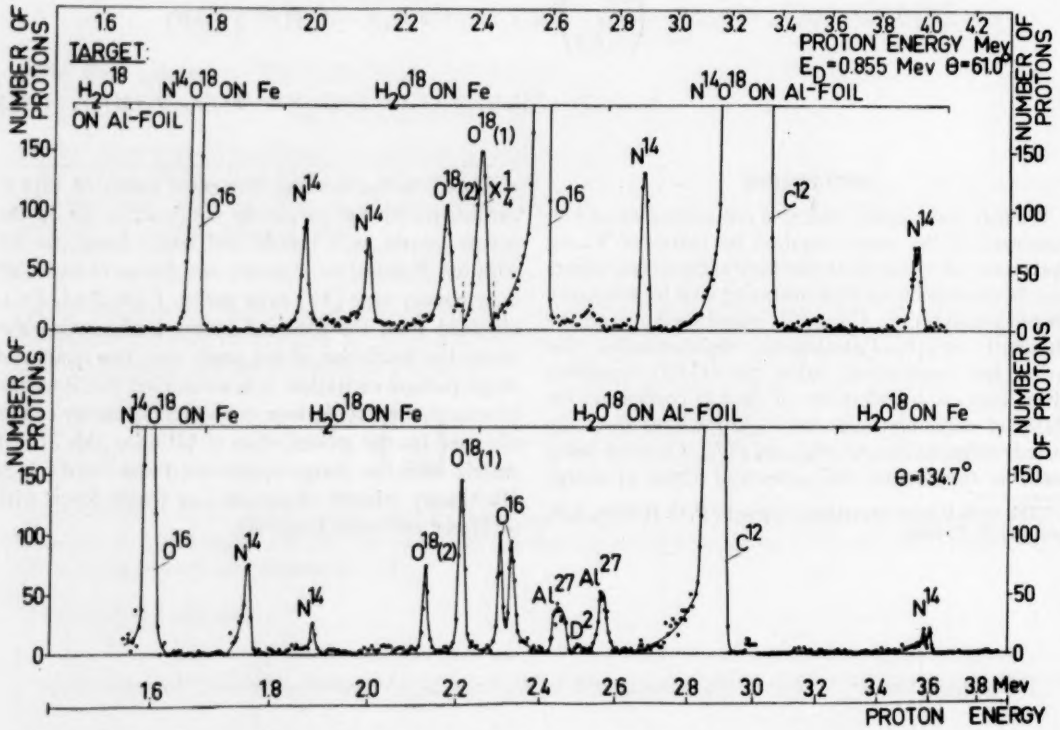

FIG. 1. The proton spectra from deuteron bombardment of O^{18} targets. The upper curve was obtained at the observation angle 61.0°, the lower curve at the angle 134.7°. The deuteron bombarding energy was 855 kev. The targets and target backings used at different energy regions are marked in the figure.

[1] K. Ahnlund and C. Mileikowsky, Arkiv. Fysik. (to be published).
[2] Bergström, Thulin, Svartholm, and Siegbahn, Arkiv. Fysik. 1, 281 (1950).

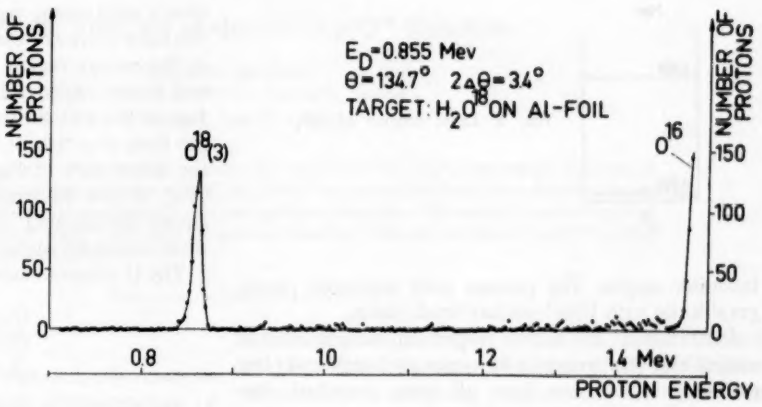

FIG. 2. Low-energy part of the proton spectrum at 134.7°. Deuteron bombardment energy 855 kev.

enriched in oxygen-18 at A.E.R.E., Harwell, and the H_2O^{18}-beam of mass number 20 was collected. The second type was produced from a sample of oxygen and nitrogen, presented to our laboratory by Professor K. Clusius, Zürich. In this case the $N^{14}O^{18}$ beam was collected.

The beams were collected on thick plates of steel or on thin foils of aluminum. The foils were about 20 kev thick for a single passage of deuterons of 850 kev.

The deuteron bombardment was performed with the stabilized Cockcroft-Walton accelerator at the Nobel Institute.[3] The primary beam passes an analyzing magnet and its energy is also calibrated by means of this magnet. The energy calibration of deuterons of 850 kev ultimately depends on the well-known proton resonance in F^{19} at proton energy 873.5 kev. The link from proton to deuteron calibration is obtained by scattering protons and deuterons against aluminum and beryllium[4] into the particle spectrometer, which is held at a given magnetic field.

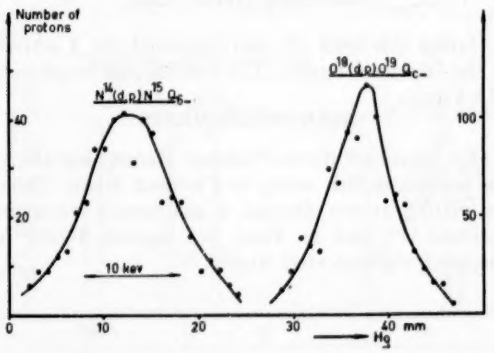

FIG. 3. The proton spectrum from $O^{18}(d,p)O^{19}$ and $N^{14}(d,p)N^{15}$ at a deuteron bombarding energy of 855 kev in the region of Q_3. The calibration peak of $N^{14}(d,p)N^{15}$ is due to Q_8=300 kev. The observation angle is 134.7°. Target backing: Al foils.

[3] C. Mileikowsky and R. T. Pauli, Arkiv. Fysik. **4**, 287 (1952).
[4] C. Mileikowsky, Arkiv. Fysik. **7**, 117 (1953).

In the present case, however, the absolute deuteron energy calibration is not very critical. This is because the energies of the proton groups from $O^{18}(d,p)O^{19}$ are compared with the close-lying proton groups of known energies from the reactions $B^{10}(d,p)B^{11}$ and $N^{14}(d,p)N^{15}$.[5,6] The final measurement of a Q value is performed in such a way that both the calibration group and the particle group to be measured fall on the photographic plate close together in the same magnetic field.

The particle spectrometer[7] is double focusing (40-cm radius) and stands on a rotating table so that it can accept the secondary particles at any angle to the primary beam from zero up to 135°. The incident beam path is screened over the important parts of its length by iron tubing. By this arrangement any significant displacement of the beam spot caused by the stray field from the spectrometer is avoided also at un-

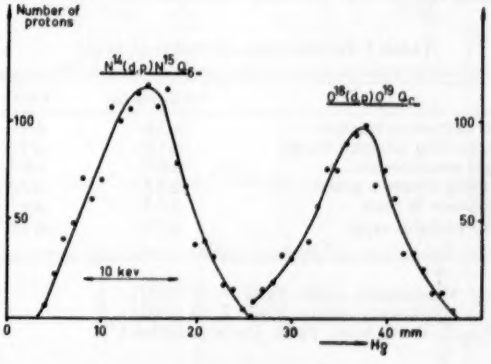

FIG. 4. The proton spectrum from $O^{18}(d,p)O^{19}$ and $N^{14}(d,p)N^{15}$ at a deuteron bombarding energy of 855 kev in the region of Q_3. The calibration peak of $N^{14}(d,p)N^{15}$ is due to Q_8=300 kev. The observation angle is 134.7°. Target backing: Al foils. The N^{14} targets are different in Figs. 3 and 4.

[5] van Patter, Buechner, and Sperduto, Phys. Rev. **82**, 248 (1951).
[6] R. Malm and W. W. Buechner, Phys. Rev. **80**, 771 (1950).
[7] C. Mileikowsky, Arkiv. Fysik. **4**, 337 (1952).

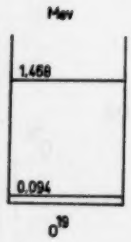

FIG. 5. Level scheme of O^{19}.

favorable angles. The protons were registered photographically with Ilford nuclear track plates.

Instrumental line widths, dispersion, measurement of angles, and arrangements for target exchange and plate exchange in vacuum have all been described elsewhere.[8–10]

RESULTS

The proton spectra at spectrometer angles 61.0° and 134.7° are shown in Figs. 1 and 2. For 61.0° the energy region is from 1.55 Mev to 4.10 Mev and for 134.7° the energy region is from 0.70 Mev to 3.90 Mev. Three of the proton peaks are the result of the reaction $O^{18}(d,p)O^{19}$. They are absent in runs on target backings which were not hit by the separator beam. Also, their energy change with spectrometer angle corresponds to target mass number 18. The other proton peaks correspond to different parasite reactions. Many of them are transitions in $N^{14}(d,p)N^{15}$, two are from $O^{16}(d,p)O^{17}$, and one is from $C^{12}(d,p)C^{13}$. The carbon peak is so strong and broad at both angles that no search for other groups can be successful within this region of about 100 kev, at least not with the bombarding energies available to us.

During bombardment, deuterons stick in the target, giving rise to d-D protons, which are very disturbing over a large energy region, if the target backing is thick. We have therefore used thin foil backings of aluminum in the energy region 2.8–4.1 Mev at the angle 61.0°, and in the region 2.25–3.25 Mev at the angle 134.7°, Fig. 1. We still get the d-D protons, now, however, in the form of a definite and rather small peak, as seen in the lower part of Fig. 1. In the region 0.7–1.5 Mev (Fig. 2) foil backings were also used to reduce the strong background of scattered deuterons. This was more successful at the angle 134.7° than at 61.0°.

TABLE I. Partial errors, referred to Q, in kev.

	For Q_1 and Q_2	For Q_3
Q of calibration reaction	±5.6	±4.0
Bombarding deuteron energy	±1.8	±0.8
Angle measurement	±0.5	±0.1
Reading of proton peaks	±3.6	±3.5
Dispersion in plate	±3.2	±1.5
Total probable error	±7.6	±5.6

The Q values obtained for $O^{18}(d,p)O^{19}$ are

$$Q_1 = 1730 \pm 8 \text{ kev},$$
$$Q_2 = 1636 \pm 8 \text{ kev},$$
$$Q_3 = 262 \pm 6 \text{ kev}.$$

The first two of these were obtained with $B^{10}(d,p)B^{11}$, $Q_6 = 1937$ kev, as a calibration of the spectrometer. This group is known to ±6 kev and falls conveniently between the two $O^{18}(d,p)O^{19}$ groups. An evaporated natural boron target was used.

A group of $N^{14}(d,p)N^{15}$, $Q = 300$ kev, served to calibrate the spectrometer in the case of the third Q value. Two spectra taken in different runs on different targets are shown in Figs. 3 and 4. Each spectrum contains the calibration peak and the $O^{18}(d,p)$ peak to be measured.

The total probable errors are calculated from the partial errors, referred to Q, listed in Table I. The partial errors for reading of proton peaks given in this table also include uncertainties in layers on targets.

If we assume that Q_1 corresponds to the ground-state transition of $O^{18}(d,p)O^{19}$—which is not necessarily true—we obtain the level scheme in Fig. 5 for O^{19}. There is one low excited state at 94 kev, and one state at 1468 kev. With this assumption, and using the masses 18.004848, 2.014735, and 1.008142 amu for O^{18}, D^2 and H^1, we obtain the following mass for O^{19}:

$$19.009583 \pm 0.000025 \text{ amu}.$$

During this work we also registered the β activity of the O^{19} nuclei formed. The half-life was found to be 31 ± 4 sec.

ACKNOWLEDGMENTS

Our thanks are due to Professor Manne Siegbahn for his interest in this work, to Professor Klaus Clusius for placing at our disposal a gas sample containing enriched O^{18}, and to Tekn. lic. Sigvard Thulin for preparing the separated targets.

[8] C. Mileikowsky, Arkiv. Fysik. **7**, 33 (1953).
[9] C. Mileikowsky, Arkiv. Fysik. **7**, 89 (1953).
[10] R. T. Pauli, Arkiv. Fysik. (to be published).

Magnetic Analysis of the $O^{17}(d,p)O^{18}$ Reaction

KATARINA AHNLUND
Nobel Institute of Physics, Stockholm, Sweden

(Received June 28, 1954)

Separated isotopic targets of O^{17} were used to study the reaction $O^{17}(d,p)O^{18}$. The energy spectrum of protons from this reaction has been analyzed at 61.0° and 134.7° to the incident 0.855-Mev deuteron beam, using a double focusing magnetic spectrometer and photographic detection. The survey covers a range of excitation in O^{18} from 0 to 4.8 Mev. Two proton groups were identified with the reaction $O^{17}(d,p)O^{18}$, giving $Q_0=5821\pm10$ kev and $Q_1=3835\pm8$ kev.

INTRODUCTION

OXYGEN-17 has not been reported elsewhere as target nucleus for precision measurements of nuclear energy levels—its isotopic abundance is only 0.04 percent. An earlier paper[1] described the separation method used for thin O^{17} targets and reported a measurement of the reaction energy of $O^{17}(d,p)O^{18}$. This systematic survey over the energy region below this proton group has been undertaken in order to obtain information about the hitherto unknown level scheme of O^{18}.

APPARATUS AND EXPERIMENTAL PROCEDURE

The apparatus and experimental procedure used in the investigation are essentially similar to those described in earlier papers.[2,3] The apparatus consisted of the Nobel Institute 1.4-Mev Cockcroft-Walton accelerator, a deflecting magnet and slit system to define the energy of the deuteron beam, and a double focusing magnetic spectrometer to analyze the particles leaving the target. The spectrometer is movable in the angle interval 0° to 135° to the incident beam. Ilford nuclear track plates were used to detect the particles deflected by the spectrometer.

Two series of plates were taken, at the observation angles 61.0° and 134.7° to the incident beam. This was done in order to diminish the chance that a O^{17} group with low intensity would be masked by some contaminant group at the same time as it was used to identify the various groups.

The O^{17} targets used were all produced from gaseous

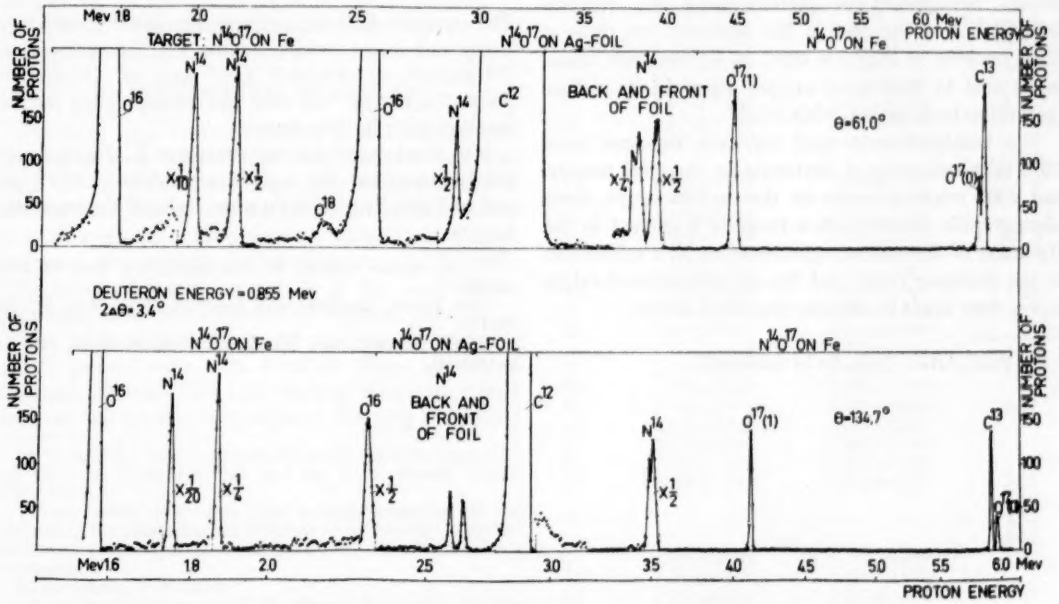

FIG. 1. Spectra of protons from O^{17} target bombarded with 0.855-Mev deuterons. The upper curve is obtained at the observation angle $\theta=61.0°$ and the lower at $\theta=134.7°$. Each point in the figure stands for the mean of two measured points. The types of target used in different energy regions are indicated in the figure.

[1] Ahnlund, Thulin, and Pauli, Arkiv. Fysik. (to be published).
[2] C. Mileikowsky and R. Pauli, Arkiv. Fysik **4**, 287 (1952).
[3] C. Mileikowsky, Arkiv. Fysik. **7**, 89 (1953).

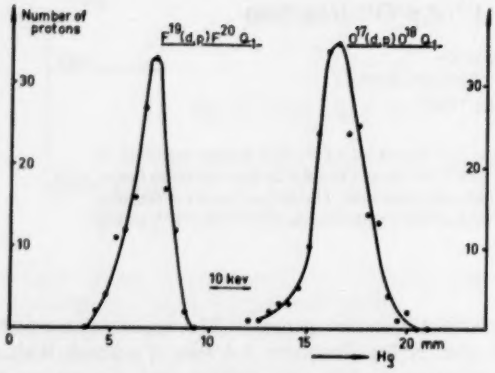

FIG. 2. Spectrum of short-range protons from $O^{17}(d,p)O^{18}$ compared to the proton spectrum from $F^{19}(d,p)F^{20}$, Q_1. Deuteron energy = 0.855 Mev, $\theta = 134.7°$, $2\Delta\theta = 3.4°$. Both targets were on thick backings.

oxygen enriched by thermal diffusion in O^{17} and O^{18} by a factor of about one hundred. This was accomplished by Professor K. Clusius of Zürich. By electromagnetic isotope separation at the Nobel Institute, thin O^{17} targets were collected from $N^{14}O^{17}$ ions. Two types of target backing were used. For the work in the region $E_p = 2.0-4.0$ Mev the O^{17} nuclei were collected on a thin 0.28-mg/cm² Ag foil. In this energy region a thick target backing could not be used, because of a serious background of protons from the reaction $D(d,p)H^3$. For the rest of the spectrum we chose a thick backing of stainless steel, as Fe has been found to be able to hold more oxygen atoms in its surface than other backing materials tried.[4]

The bombardments used for each exposure were 2400 microcoulombs of deuterons on the steel targets, and 4000 microcoulombs on the Ag-foil target. Each photographic plate covers a range of 4 percent in the $H\rho$ value of the nuclear spectrometer. The calibration of the deuteron beam and the measurement of target layers were made in the way described earlier.

[4] R. Pauli, Arkiv. Fysik. (to be published).

RESULTS AND DISCUSSION

Figure 1 shows the spectrum of protons, observed from the bombardment of the O^{17} target with 0.855-Mev deuterons, as a function of their energy. The groups of protons marked $O^{17}(0)$ and $O^{17}(1)$ refer to particles which have left the residual nucleus O^{18} in the ground state and first excited state, respectively. Other groups resulting from reactions with contaminant elements are marked according to the target nuclei. One region is masked at both angles by the intense group from $C^{12}(d,p)C^{13}$. At 134.7° its width is about 150 kev. The corresponding region in O^{18} can only be covered by use of a deuteron beam of 6–8 Mev. The energies of the O^{17} groups have been calculated using the high energy edges, minimum observation angle, and external layer correction. The long-range group was calibrated[1] with α particles from ThC giving $Q_0 = 5821 \pm 10$ kev, while the short-range group was compared with protons from $F^{19}(d,p)F^{20}$, $Q_1 = 3721 \pm 6$ kev[5] at the observation angle $\theta = 134.7°$ as shown in Fig. 2 giving $Q_1 = 3835 \pm 8$ kev. An earlier determination of Q_1 was made by use of a less intense oxidized O^{17} target. The protons from O^{17} were compared with protons from $B^{10}(d,p)B^{11}$, $Q_3 = 4201 \pm 8$ kev[6] at $\theta = 134.7°$, giving the result $Q_1 = 3835 \pm 10$ kev.

We adopt the values:

$$O^{17}(d,p)O^{18}: \quad Q_0 = 5821 \pm 10 \text{ kev}, \quad Q_1 = 3835 \pm 8 \text{ kev}.$$

The corresponding excitation energy in O^{18} is 1986 kev. Using our latest values for the reaction energies of $O^{18}(p,\alpha)N^{15}$, $Q = 3967 \pm 9$ kev,[3] and of $O^{17}(d,\alpha)N^{15}$, $Q = 9807 \pm 12$ kev,[7] we close the corresponding nuclear reaction cycle by 19 ± 18 kev.

My thanks are due to Professor K. Clusius who kindly presented the sample of enriched $O^{17}O^{18}$ gas and to Tekn. lic. S. Thulin who produced the separated targets.

[5] H. A. Watson and W. W. Buechner, Phys. Rev. **88**, 1324 (1952).

[6] Van Patter, Buechner, and Sperduto, Phys. Rev. **82**, 248 (1951).

[7] Pauli, Ahnlund, and Mileikowsky, Arkiv. Fysik. (to be published).

Magnetic Analysis of the $Co^{59}(d,p)Co^{60}$ Reaction*†

G. M. Foglesong‡ and D. G. Foxwell‡
Physics Department and Laboratory for Nuclear Science, Massachusetts Institute of Technology, Cambridge, Massachusetts

(Received July 21, 1954)

Proton groups from cobalt targets bombarded with 5-Mev deuterons from the MIT-ONR electrostatic generator have been analyzed with a 180-degree focusing magnetic spectrograph. The ground-state Q value for the $Co^{59}(d,p)Co^{60}$ reaction was found to be 5.283 ± 0.008 Mev. The 60-kev metastable state and thirty-four additional excited states were observed and their Q values measured.

I. INTRODUCTION

TO date, the best information on the binding energy of the last neutron in Co^{60} and the excited states of Co^{60} is found in the (n,γ) work of Bartholomew and Kinsey.[1] However, they could not determine whether the most energetic gamma ray seen (7.486 Mev) was attributable to a transition to the ground state or to the known metastable state[2] at 58.9 ± 0.5 kev, inasmuch as both transitions were not observed. Earlier cobalt (d,p) analyses, by Bateson and Pollard,[3] Hoesterey,[4] and Harvey,[5] had resulted in binding energies which were, in general, consistent with the results of Bartholomew and Kinsey, but were not of sufficient precision to permit a resolution of the above-mentioned indeterminancy or to make possible the construction of a definite energy-level diagram for Co^{60}.

The present work was undertaken in order to clarify the position of the ground state of Co^{60} in relation to Co^{59}, with the secondary purpose of studying the region of excitation covered in the (n,γ) work.

II. EXPERIMENTAL PROCEDURE

Platinum- and Formvar-backed cobalt targets were bombarded with magnetically analyzed deuteron beams from the MIT-ONR electrostatic generator, and the protons emerging at 90 degrees to the incident beam were analyzed by a 180-degree focusing, 35-cm radius, magnetic spectrograph and photographically detected. This installation and the details of the experimental technique have been described in a recent paper.[6]

The targets were made by vacuum evaporating cobalt pellets onto thin Formvar films and clean platinum sheets. The high boiling point of cobalt required the use of a technique of clamping the pellets between sharpened carbon electrodes.[7] A spectrochemical analysis of the cobalt used showed impurities between 0.1 and 10 percent nickel, 0.01 and 1 percent magnesium and copper, and less than 0.1 percent of other metals. Cobalt is naturally monoisotopic.

III. RESULTS

A typical proton spectrum, obtained at a deuteron energy of 5.0 Mev, is shown in Fig. 1. The numbered

TABLE I. Q values for $Co^{59}(d,p)Co^{60}$ and excited states of Co^{60}. Excitation energy in Mev.

Group	Q value in Mev	Present work	Bartholomew and Kinsey[a]
0	5.283 ± 0.008	0	
1	5.223 ± 0.009	0.060 ± 0.003	
2	4.997 ± 0.009	0.286 ± 0.003	0.285
3	4.838 ± 0.009	0.445 ± 0.003	0.445
4	4.770 ± 0.009	0.513 ± 0.003	0.512
5	4.726 ± 0.009	0.557 ± 0.005	
6	4.661 ± 0.009	0.622 ± 0.004	0.619
7	4.491 ± 0.009	0.792 ± 0.003	0.796
8	4.271 ± 0.009	1.012 ± 0.003	1.012
9	4.046 ± 0.009	1.237 ± 0.005	1.236
10	3.889 ± 0.009	1.394 ± 0.004	1.376
11	3.750 ± 0.010	1.533 ± 0.006	1.520
12	3.620 ± 0.010	1.663 ± 0.006	
			1.760
13	3.458 ± 0.010	1.825 ± 0.006	1.840
14	3.278 ± 0.010	2.005 ± 0.006	
15	3.218 ± 0.010	2.065 ± 0.006	
16	3.129 ± 0.010	2.154 ± 0.006	2.135
17	2.988 ± 0.010	2.295 ± 0.006	2.307
18	2.913 ± 0.015	2.370 ± 0.013	
19	2.673 ± 0.010	2.610 ± 0.006	2.583
20	2.659 ± 0.010	2.624 ± 0.006	
21	2.497 ± 0.012	2.786 ± 0.009	
22	2.413 ± 0.015	2.870 ± 0.013	
23	2.359 ± 0.012	2.924 ± 0.009	2.90
24	2.245 ± 0.012	3.038 ± 0.009	
25	2.163 ± 0.012	3.120 ± 0.009	3.12
26	2.145 ± 0.012	3.138 ± 0.009	
27	2.075 ± 0.012	3.208 ± 0.009	
28	1.995 ± 0.012	3.288 ± 0.009	
29	1.979 ± 0.012	3.304 ± 0.009	3.30
			3.46
			3.80
			4.13
30	1.062 ± 0.012	4.221 ± 0.009	
31	0.981 ± 0.013	4.302 ± 0.010	
32	0.862 ± 0.013	4.421 ± 0.010	
33	0.789 ± 0.015	4.494 ± 0.013	
34	0.750 ± 0.015	4.533 ± 0.013	
35	0.712 ± 0.015	4.571 ± 0.013	

[a] See reference 1.

* This work has been supported in part by the joint program of the Office of Naval Research and the U. S. Atomic Energy Commission.

† These results were taken from a thesis submitted by the authors to the Massachusetts Institute of Technology in partial fulfillment of the requirements for the degree of Master of Science in Physics.

‡ Lieutenants, U. S. Navy.

[1] G. A. Bartholomew and B. B. Kinsey, Phys. Rev. **89**, 386 (1953).

[2] R. L. Caldwell, Phys. Rev. **78**, 407 (1950).

[3] W. D. Bateson and E. Pollard, Phys. Rev. **79**, 241 (1950).

[4] D. C. Hoesterey, Phys. Rev. **87**, 216 (1952).

[5] J. A. Harvey, Phys. Rev. **81**, 353 (1951).

[6] Buechner, Sperduto, Browne, and Bockelman, Phys. Rev. **91**, 1468 (1953).

[7] J. E. Schwager and L. A. Cox, Rev. Sci. Instr. **24**, 986 (1953).

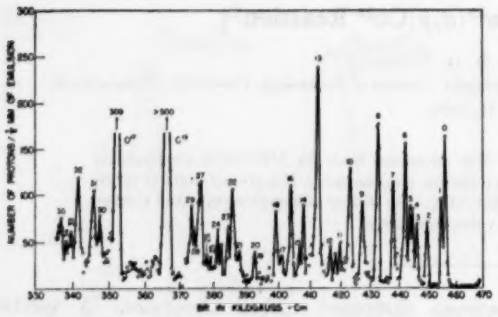

FIG. 1. Typical proton spectrum from a solid-backed cobalt target bombarded with 5-Mev deuterons. The ground-state groups from the $O^{16}(d,p)O^{17}$ and $C^{12}(d,p)C^{13}$ reactions are labeled with the residual nucleus. The numbered groups are presumed to arise from the $Co^{59}(d,p)Co^{60}$ reaction.

peaks were assigned to cobalt primarily on the basis of the reproducibility of the Q values calculated on this assumption as the bombarding energy was changed from 5.0 to 5.8 Mev. For each of the numbered peaks, the Q values thus obtained agreed to within 10 kev. Actually, this is equivalent to stating that the mass of the target nucleus responsible for any peak lies between 50 and 80. However, since the spectrochemical analysis showed that in this range of masses the only impurities present were small amounts of nickel and copper and since there was no evidence for any groups which correspond to known levels in these nuclei, it is probable that the assignment of these groups is correct. It is also probable that some of the weaker groups from cobalt have not been detected in these experiments.

The Q values for these groups are listed in Table I, together with the corresponding energies of excitation in Co^{60}. The ground-state Q value is based on three separate observations, at different bombarding energies, which agreed to within 3 kev. The energy of the first excited state in Co^{60} was determined from these observations to be 60 ± 3 kev, in excellent agreement with the value 58.9 ± 0.5 kev found by Caldwell[2] for the metastable level.

Also included in Table I are the energies obtained for certain of the excited states in Co^{60} calculated on the assumption that each of the gamma rays observed by Bartholomew and Kinsey originated in a transition direct from the capturing state to the state in question, and that this highest-energy gamma ray is associated with a transition direct to the ground state. It is seen that there is generally good agreement between the two sets of values, the only serious discrepancy being in the region between groups 29 and 30, where it is possible that the assumption regarding the gamma-ray assignments is incorrect or that weak groups might have been missed in the present work because of background from the carbon and oxygen groups. In view of this agreement, it is surprising that the Q value for the $Co^{59}(d,p)Co^{60}$ reaction, derived by subtracting the deuteron-binding energy from the value for the most energetic gamma ray, is 5.260 ± 0.007 Mev, which differs by 23 kev from the present measurement.

This work was carried out while the authors were assigned to duty at Massachusetts Institute of Technology as part of the program of the U. S. Naval Postgraduate School, Monterey, California. The authors are indebted to Professor W. W. Buechner, C. K. Bockelman, C. P. Browne, C. M. Braams, and A. Sperduto for guidance and assistance during the course of this work, and to Mr. W. A. Tripp, Miss Janet Frothingham, and Miss Sylvia Darrow for their careful reading of the nuclear-track plates.

Neutron-Deficient Activities of Praseodymium

THOMAS H. HANDLEY AND ELMER L. OLSON
Oak Ridge National Laboratory, Oak Ridge, Tennessee
(Received August 12, 1954)

Neutron-deficient radionuclides of praseodymium were produced by proton bombardment of enriched isotopes of cerium and neodymium. Two unreported activities were found, 22-min Pr^{135} and 70-min Pr^{136}; the gamma and beta spectra of each were determined. Further study of 2.0-hr Pr^{138} and 4.5-hr Pr^{139} was also made, and gamma spectra of each are shown. The half-life of Pr^{137} is shown to be <5 min or >1 year. Confirmation of assignment of 3.4-min Pr^{140} is made.

PRASEODYMIUM-135

AN enriched stable isotope of Ce^{136} was bombarded with 22.4-Mev protons in the Oak Ridge National Laboratory 86-inch cyclotron. Ion exchange methods were used to separate the products.[1] Following separation, the praseodymium fraction was found to contain a 22-min activity, a 70-min activity, 4.5-hr Pr^{139}, and 19.3-hr Pr^{142}. A second bombardment was made with the energy of the incident proton beam adjusted to 9.5 Mev by use of aluminum absorbers. Following separation the praseodymium fraction was found to contain a 70-min activity and 19.3-hr Pr^{142}; thus the 22-min activity was produced by either a $(p,2n)$ or $(p,3n)$ reaction. The 22-min activity was not observed as a result of bombarding enriched stable Ce^{138} or natural cerium with either 22.4 or 9.5-Mev protons, thus eliminating its assignment to a mass higher than 136. In another bombardment of enriched Ce^{136} with 22.4-Mev protons the praseodymium fraction from an initial separation was permitted to decay; then, after a second separation, 22-hr Ce^{135} was found to be present in the cerium fraction. Thus, the 22-min activity is the parent of Ce^{135} and is assigned to Pr^{135}. A gamma-ray spectrum as measured with a NaI(Tl) scintillation spectrometer is shown in Fig. 1. The spectrum shows the presence of positron emission with gammas of 0.080, 0.22, and 0.30-Mev energy. Because of problems of counting efficiency and internal conversion it was not practical to distinguish between the x-rays due to electron capture and those due to internal conversion. However, it is reasonably certain that the activity decays by both electron capture and positron emission. The 0.033-Mev peak is the x-ray and the 0.51-Mev the annihilation peak. More energetic radiation was not observed. The gamma-ray spectrum was determined once every 20 minutes for ten half-lives and the contribution of the longer lived components of the praseodymium fraction subtracted in order to obtain a spectrum for the 22-min activity.

The maximum energy of the positron emitted was determined by use of a scintillation spectrometer consisting of a cylindrical anthracene crystal $1\frac{1}{2}$ in. in diameter and 1 in. in thickness mounted on top of a DuMont type 6292 photomultiplier. Pulses from the photomultiplier tube were fed into a preamplifier. These were further amplified by a linear amplifier and fed into a single-channel pulse height analyzer and a scaler. The beta spectrum was determined several times over a period of ten half-lives. Decay of each experimental point was plotted and the decay curve analyzed for the 22-min component. The gamma background was determined in a similar manner, by using an appropriate absorber, and subtracted. The results were plotted with counting rate *versus* pulse height as coordinates. A Kurie plot indicated a value of 2.5 ± 0.1 Mev. Comparison with a phosphorus-32 curve obtained under identical conditions gave agreement with this value. An aluminum absorption curve also agreed within these limits.

PRASEODYMIUM-136

As stated in the previous section, bombardment of enriched stable isotope Ce^{136} with 9.5-Mev protons followed by ion exchange separation gave praseodymium activities with half-lives of 70 min and 19.3 hr. The 3.4-min Pr^{140} had decayed by the end of the chemical separation and there was not enough Ce^{138} present to produce a detectable amount of 2.0-hr Pr^{138}. The

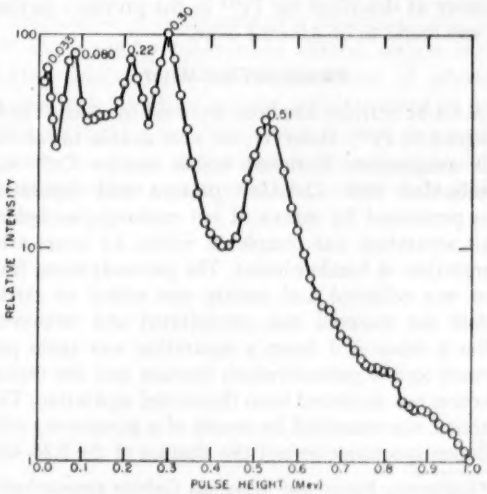

FIG. 1. Gamma-ray spectrum of 22-min Pr^{135}.

[1] B. H. Ketelle and G. E. Boyd, J. Am. Chem. Soc. **69**, 2800 (1947).

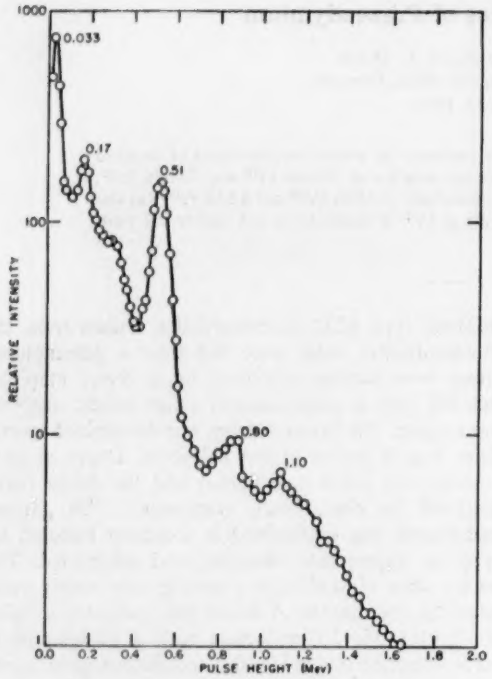

FIG. 2. Gamma-ray spectrum of 70-min Pr^{136}.

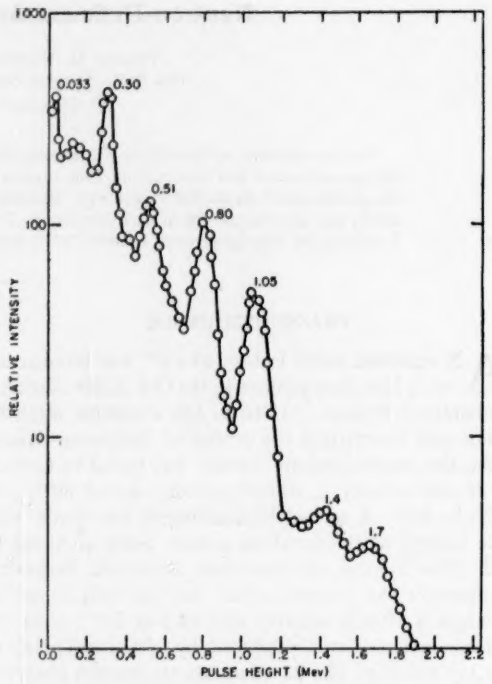

FIG. 3. Gamma-ray spectrum of 2.0-hr Pr^{138}.

19.3-hr Pr^{142} was produced by a (p,n) reaction on Ce^{142}. The 70-min activity was not observed as a result of bombarding enriched Ce^{138} or natural Ce with 9.5-Mev protons. This assigns the 70-min activity to Pr^{136}. A gamma-ray spectrum, Fig. 2, shows it to decay by positron emission with a gamma of 0.17-Mev energy, and with possibly more energetic gammas of low intensity with energies of 0.80 and 1.1 Mev. The energy of the positron was determined in the same manner as described for Pr^{135} in the previous section. It was found to be 2.0±0.1 Mev.

PRASEODYMIUM-137

A 1.4-hr activity has been reported by others[2] to be assigned to Pr^{137}. However, we were unable to confirm this assignment. Enriched stable isotope Ce^{138} was bombarded with 22.4-Mev protons and separation was performed by means of ion exchange, as before. This separation was completed within 2.5 hours after completion of bombardment. The praseodymium fraction was collected and cerium was added as carrier before the material was precipitated and recovered. After a delay of 7 hours a separation was again performed on the praseodymium fraction and the cerium fraction was recovered from the second separation. This fraction was examined by means of a gamma-ray scintillation spectrometer and the absence of the 0.26-Mev gamma ray associated with 36-hr Ce^{137} was confirmed. The x-ray peak and a 0.17-Mev peak were the only radiations observed, both of which are associated with 140-day Ce^{139}. The Ce^{139} is present because of the decay of 4.5-hr Pr^{139}. Decay of the cerium fraction has also been followed for 90 days and at this time shows a slope corresponding to a half-life of 140 days, thus proving that the 1.4-hr activity previously reported is not the parent of Ce^{137}. Since the unknown Pr^{137} and 4.5-hr Pr^{139} activities would be produced with approximately the same cross section, it is possible to calculate, with corrections for time of bombardment, dilution factors, chemical yields, and isotopic abundance of the Ce^{138} and Ce^{140} in the enriched sample of Ce^{138}, the maximum half-life of activities longer than 4.5 hours. From these results it can be said that the half-life of Pr^{137} is >1 year. In other short bombardments an upper limit of <5 min can be placed on the half-life of Pr^{137}. In summation, limits of >1 year or <5 min may be placed on the half-life of Pr^{137}.

PRASEODYMIUM-138

Bombardment of enriched stable isotope Ce^{138} with 9.5-Mev protons followed by ion exchange separations yielded two activities in the praseodymium fraction, 2.0-hr Pr^{138} and 19.3-hr Pr^{142}. Previous reports[2,3] on the half-life of Pr^{138} were confirmed with a value of 2.0±0.1 hr. The 2.0-hr activity was not observed by

[2] Dahlstrom, Foster, and Thompson [private communication to J. M. Hollander (October 1952)]; Hollander, Perlman, and Seaborg, Revs. Modern Phys. **25**, 469 (1953).

[3] B. J. Stoner, Phys. Rev. **81**, 8 (1951).

bombarding natural cerium with 9.5-Mev or 22.4-Mev protons. This would assign to it a mass lower than 139 and, since it is produced by 9.5-Mev protons on enriched Ce^{138}, confirmation of assignment to Pr^{138} is also made. A gamma-ray spectrum, Fig. 3, shows the presence of positron emission. Gamma rays of 0.30-, 0.80-, and 1.05-Mev energy are in disagreement with values obtained by others.[3] The 0.033-Mev peak is the x-ray and the 0.51-Mev is the annihilation peak. Here again the fraction of x-rays associated with electron capture and internal conversion was not determined. There is also the possibility of more energetic gamma rays of 1.4- and 1.7-Mev energy and of a very low intensity relative to the others. Energy of the positron was measured with a scintillation spectrometer as previously described and by aluminum absorption curves. A value of 1.4 ± 0.1 Mev was found, which is in agreement with that previously reported.

PRASEODYMIUM-139

Bombardment of natural cerium with 22.4-Mev protons followed by chemical separation yielded two praseodymium activities, 4.5-hr Pr^{139} and 19.3-hr Pr^{142}; the 3.4-min Pr^{140} decayed before completion of the separation. The 4.5-hr activity was not observed as a result of 9.5-Mev proton bombardment of natural cerium. It was also shown, in the section of this paper on Pr^{137}, to be the parent of Ce^{139}. Thus, its half-life and assignment are confirmed.[2] To obtain a sample containing less 19.3-hr Pr^{142}, neodymium enriched in mass 142 was bombarded with 17.5-Mev protons; the 4.5-hr Pr^{139} was produced by the (p,α) reaction on Nd^{142}. At this energy, the $(p,\alpha n)$ reaction is eliminated. The neodymium contained 93.0 percent Nd^{142} and 0.4 percent Nd^{145}. The 19.3-hr Pr^{142} would be produced from Nd^{145} by the reaction $Nd^{145}(p,\alpha)Pr^{142}$. However, calculations show it to be much less from this bombardment than from the (p,n) reaction on natural cerium. A gamma-ray spectrum, Fig. 4, shows the presence of positron emission with gamma rays of 0.17-, 1.3-, and 1.6-Mev energy. The 0.17-Mev gamma ray is the same as that associated with Ce^{139}. The fraction of x-rays due to electron capture was not determined. A gamma-ray spectrum of Pr^{139} produced by the reaction $Ce^{140}(p,2n)Pr^{139}$ agreed exactly with that shown in Fig. 4, which was produced by $Nd^{142}(p,\alpha)Pr^{139}$. The

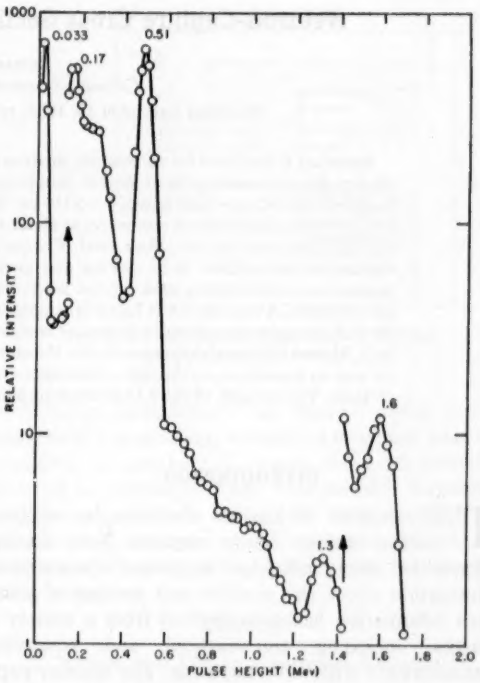

FIG. 4. Gamma-ray spectrum of 4.5-hr Pr^{139}.

values of the gamma-ray energies do not agree with those reported by others.[3] However, since this work shows agreement with two different methods of production, the values are assumed to be correct. The energy of the positron was determined by techniques already described and the 1.0- ±0.1-Mev value obtained is in agreement with that previously reported.

PRASEODYMIUM-140

Confirmation of assignment of a 3.4-min activity to Pr^{140} was made by bombarding natural cerium with 9.5-Mev protons; also by bombardment of praseodymium with 22.5-Mev protons, which resulted in the $Pr^{141}(p,pn)Pr^{140}$ reaction. No further attempt was made to study its decay characteristics because of experimental difficulties encountered due to the short half-life involved.

Neutron-Capture Cross Sections by Capture-Gamma Counting

EDWARD MESERVEY
Columbia University, New York, New York

(Received December 14, 1953; revised manuscript received May 12, 1954)

A method is described for determining neutron capture cross sections and locating capture resonances by capture gamma counting. Breit-Wigner parameters for the strong resonance in cadmium are determined to be $E_0=0.177$ ev, $\sigma_{c0}=7600$ barns, $\Gamma=0.110$ ev. Resonances have been found in cadmium at 19 and 28 ev with evidence of unresolved resonances at about 100 ev and above; $\sigma_{c0}\Gamma\cong 3$ barn-ev for the 19-ev level, and $\sigma_{c0}\Gamma^2\cong 9$ barn(ev)^2 for the 28-ev level. Comparison transmission measurements on cadmium show the capture-gamma method to be quicker and more sensitive under some circumstances than transmission measurements for locating weak capture levels. Factors affecting the relative sensitivity of the two methods are discussed. A resonance was found in strontium at 3.58 ev; its strength ($\sigma_{c0}\Gamma^2$) is approximately 8 barn-(ev)^2. Resonances were found in barium at energies of 25, 93 and 380 ev, with strengths ($\sigma_{c0}\Gamma^2$) estimated to be 8, 90, and 550 barn(ev)^2, respectively. Measurements on a thick silver sample show that the method can be used to measure σ_c/σ_t through a resonance over a fairly large range of values of transmission and cross sections. The strength of the 5.13-ev resonance in silver is determined to be $\sigma_{c0}\Gamma^2=345\pm 30$ barn(ev)^2.

INTRODUCTION

THE analysis of nuclear structure by studying nuclear energy levels requires both detailed information about individual levels and also extensive information about the position and spacing of levels. Such information has been derived from a variety of sources, including transmission[1] and scattering[2] measurements with slow neutrons. The present paper describes a technique for measuring as a function of neutron energy the relative number of gamma rays emitted when a neutron is captured by a nucleus. This technique is applicable to detailed study of neutron capture cross sections in the neighborhood of a resonance, thus providing an independent analysis of the Breit-Wigner resonance shape for comparison with the results of transmission and scattering measurements; it also provides a quick sensitive method of detecting weak capture resonances.

DESCRIPTION OF APPARATUS AND EXPERIMENTAL PROCEDURE

The Columbia University pulsed cyclotron and slow neutron velocity selector which has been adequately described previously[1] were used with a modified sample and detector arrangement. A 2-in.×3-in. rectangular sample was placed in the pulsed neutron beam at a measured distance (about 6 meters) from the neutron source. Above and below the sample were placed stilbene scintillation counters shielded by a special lead-lithium collimating system as shown in Fig. 1. Neutrons captured in the sample produce immediate capture gammas which are detected by the scintillation counters; amplified pulses from these counters are fed into the detection circuits of the velocity-selector; thus, the over-all apparatus records as a function of neutron time-of-flight the relative number of capture-gammas produced in the sample.

For each sample investigated, sample-in and sample-out runs were made. In addition, two standard samples were used: a cadmium standard was used to compare counting rates from one run to the next to take account of possible slight variations in geometry and neutron beam intensity; a Co^{60} source (made in the shape of the samples) was used to calibrate and monitor the operations of the detectors, amplifiers, and pulse-recording system. The following second-order effects have been investigated and found to be negligible in the apparatus used: scattering by the sample of background gammas, capture in detector or structural material of neutrons scattered by sample, and production of capture gammas in aluminum sample-holders.

ANALYSIS OF DATA

After correction for background effects, the experimental data consist of capture-gamma counts as a function of neutron energy. The capture-gamma count for a single detection channel can be represented as the product of a number of factors as in Eq. (1),

$$R=\phi M\tau_d AC\epsilon_\gamma, \tag{1}$$

where R=capture gamma counts in one detection interval, ϕ=neutron flux [neutrons at sample cm^{-2}(monitor count)$^{-1}$(μsec/meter)$^{-1}$], M=cyclotron monitor counts, τ_d=width of velocity selector detection channel (μsec/meter), A=area of neutron beam striking sample, C=fraction of neutrons captured in sample, $\epsilon_\gamma=N_\gamma T_\gamma\Omega$=gamma counts per neutron captured, N_γ=gamma multiplicity factor (includes the combined effect of the number of gammas emitted per neutron captured and the effective detector efficiency for the capture-gamma spectrum, aside from the solid angle factor), T_γ=average transmission of sample for capture-gammas produced in the sample,

[1] W. W. Havens, Jr., and L. J. Rainwater, Phys. Rev. 83, 1123 (1951) (contains references to previous work by the same and other authors). For extensive references, see "Nuclear Data," Natl. Bur. Standards Circ. No. 499 (Government Printing Office, Washington, D. C., 1950).

[2] Jay Tittman and Charles Sheer, Phys. Rev. 83, 746 (1951) (contains further references).

and Ω=effective solid angle between sample and detectors.

The data are analyzed by comparing the counting rate for a given sample with that for a standard; ϕ in Eq. (1) is a function of source and collimator characteristics and can be made equal for the sample and standard; M is directly measured; A is always the same; T_γ is nearly unity in most cases which require accurate analysis and can therefore be estimated theoretically with sufficient accuracy; Ω is the same for samples of equal thickness, and corrections for difference in thickness between sample and standard can be made on the basis of experimental tests using a standard gamma-ray source.

The counting rate depends on the neutron capture and scattering cross section of the sample through the factor C, the fractional capture. In many cases of practical interest, this relation can be accurately approximated by

$$C \cong 1-e^{-N\sigma_c}, \qquad (2)$$

where N=atoms per cm² of sample, and σ_c=capture cross section (cm²).

In other cases (relatively large scattering cross section and transmission considerably less than 1) a more complicated expression is needed, which takes account of multiple scattering in the sample. In these cases an independent transmission measurement is required to determine the capture cross section uniquely.

The factor N_γ of Eq. (1) represents the number of capture gammas emitted per neutron captured multiplied by the efficiency of the detector averaged over the energy spectrum of the emitted gammas. Since the gamma multiplicity and energy spectrum depend on the level structure of the excited compound nucleus, it is not possible to assume that N_γ is the same for sample and standard or even for two different resonances in the same sample. The perfect standard is a slab of the same material as the sample being investigated which is thick enough to be "black" (absorb all incident neutrons, i.e., $C=1$) over the entire energy range of interest and which is physically thin enough to make self-absorption of capture gammas small. In this case, N_γ is the same for standard and sample because they are made of the same material and are being compared at the same neutron energy. In this ideal case, then, the fractional capture of the sample is just equal to the ratio of counting rates for sample and standard (after corrections for M, T_γ, and Ω have been made). In most cases, a slab of the sample material cannot be obtained which absorbs all incident neutrons over the entire energy range of interest. It is often possible, however, to obtain a sample which is essentially "black" at some particular energy—either at the peak of a strong resonance or at the low-energy end of the thermal region; relative cross sections can then be obtained at other energies from the counting rates at those energies if the variation of incident neutron flux with energy is known. If no "black" region can be found or if it is necessary to make comparison from one resonance to another, N_γ must either be measured directly[3] or estimated from "reasonable" theoretical considerations.[4] Such theoretical estimates are not reliable for exact cross section measurements but are adequate for order-of-magnitude estimates of resonance strengths.

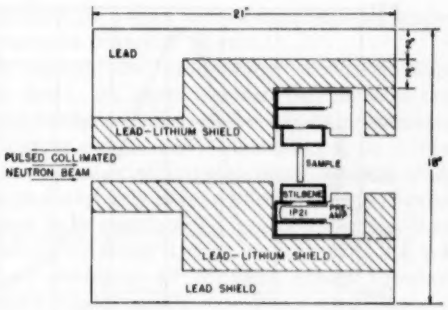

FIG. 1. Capture-gamma apparatus for neutron cross-section measurement.

RESULTS

A. Shape of 0.176-ev Cadmium Resonance

A run was made on cadmium in the region of the well-known resonance at 0.176 ev[5] in order to check the Breit-Wigner formula[6] by direct measurements of the (n,γ) cross section. The sample used was a piece of uniform 1-mil cadmium foil of 0.0195 g/cm²(=0.0001045 atom/barn). A thicker slab of 0.522 g/cm²(=0.00280 atom/barn) of cadmium was used as a standard. (This is an example of the ideal standard discussed above.) Figure 2 shows the experimental values for σ_c plotted against time of flight. The theoretical Breit-Wigner curve is shown for the resonance parameters E_0=0.177 ev, Γ=0.110 ev, and σ_{c0}=7600 barns. The solid curve is corrected for instrument resolution while the dashed curve is uncorrected. Background varied from about 7 percent to about 4 percent of the counting rate due to the sample at the peak. The uncertainties in the above parameters may be taken as the amount by which they must be changed to cause a significant difference between the theoretical curve and the experimental results. These are $\pm$0.005 ev in E_0 and Γ, and $\pm$300 barns in σ_{c0}. Within the estimated

[3] C. O. Muehlhause, Phys. Rev. **79**, 277 (1950); B. Hamermesh, Phys. Rev. **81**, 487 (1951); Kinsey, Bartholomew, and Walker, Phys. Rev. **77**, 723 (1950); Phys. Rev. **78**, 77 (1950); Phys. Rev. **78**, 481 (1950).

[4] For example, J. M. Blatt and V. F. Weisskopf, *Theoretical Nuclear Physics* (John Wiley and Sons, Inc., New York, 1952), Chap. XII, Sec. 7D. Shell structure considerations will in many cases be important in such estimates.

[5] Rainwater, Havens, Wu, Dunning, Phys. Rev. **71**, 65 (1947); W. H. Zinn, Phys. Rev. **81**, 752 (1947); Sawyer, Wollan, Bernstein, and Peterson, Phys. Rev. **72**, 109 (1947); B. N. Brockhouse, Can. J. Phys. **31**, 432 (1953).

[6] G. Breit and E. Wigner, Phys. Rev. **49**, 519 (1936).

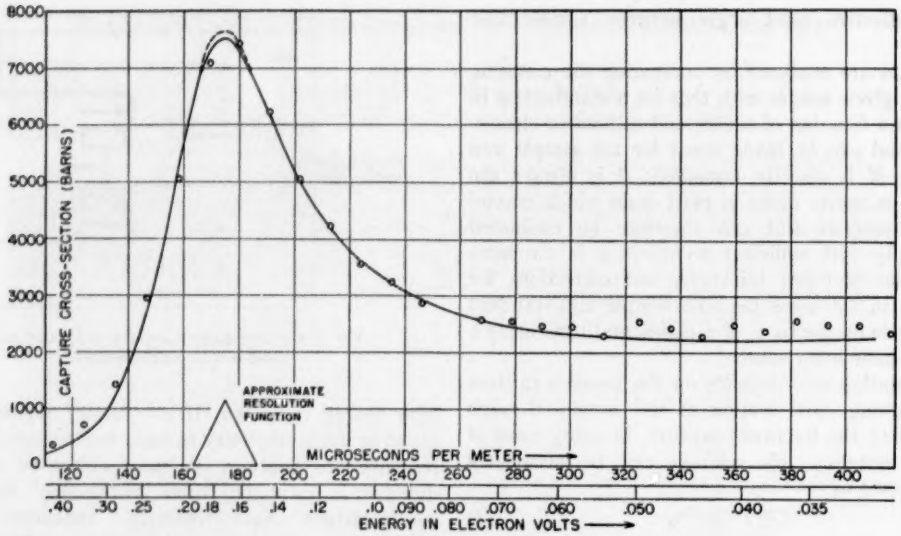

FIG. 2. Capture cross section of cadmium. The points show experimental values of capture cross section calculated from capture-gamma measurements. The full line is a theoretical Breit-Wigner curve (corrected for instrument resolution) calculated using the parameters $E_0=0.177$ ev, $\Gamma=0.110$ ev, and $\sigma_{e0}=7600$ barns.

limits of accuracy these values are consistent with previous measurements.[6]

B. Cadmium: Location of Higher Resonances

Runs were made on a thick sample (0.0622 atom/barn) of cadmium in the resonance region both to look for higher resonances and to compare the sensitivity of this method with that of the transmission measurement method. Figure 3 shows the results obtained. The solid and dashed lines show fractional capture and transmission, respectively. The data for these two curves were taken using the same sample thickness, resolution, and cyclotron running time. The capture curve shows resonances at 19 and 28 electron-volts, with evidence of several unresolved levels in the region of 100 electron-volts and above; dips in the transmission curve occur at essentially the same energies.[7] The scales for the transmission and fractional capture curves of Fig. 3 are chosen so as to make the statistical error bars the same size for the two curves at the 28-ev resonance. The background was about 15 percent of the sample counting rate at the strong peaks, and about 60 percent at the 19-ev peak.

The strengths of the two levels at 19 ev and 28 ev have been estimated by using a second cadmium sample whose thickness was 0.0261 atom/barn (results not shown). The areas under the 28-ev peak for the two samples are approximately proportional to $\sqrt{N}$, where N=atoms/barn; therefore, the "thick" sample approximation is used, and the strength is estimated to be $\sigma_{e0}\Gamma^2=9$ barn(ev)^2. The areas under the 19-ev peak are too small to estimate with any great accuracy, especially that for the thinner sample; the areas appear, however, to be proportional to N instead of $\sqrt{N}$, so the "thin" sample approximation is used to give $\sigma_{e0}\Gamma\cong 3$ barn ev. These values are based on the assumption that the gamma-multiplicity factor for these resonances is the same as that for cadmium in the thermal region.

It is estimated that resonances in the region investigated could have been undetected in the runs on cadmium if their strengths were $(\sigma_{e0}\Gamma)_{\min}\lesssim 0.05E_0$ barn ev if N_γ is the same at the resonances as for the thermal region.

C. Comparison of Sensitivity of Capture-Gamma Measurements and Ordinary Transmission Measurements for Locating Resonances

The obvious difference in the peak-to-hollow ratio for the two curves of Fig. 3 indicates that the capture-gamma method may be more sensitive than the transmission method for locating capture resonances. A quantitative comparison of the sensitivities can be obtained by estimating the minimum resonance strength detectable by the two methods. This comparison is made below by assuming

(1) equal cyclotron intensity and running time, i.e., equal number of cyclotron monitor counts,

(2) optimum sample thickness for the transmission method and a reasonably practical sample thickness for the capture gamma method,

(3) very little time is spent in either method on

[7] Higher-resolution transmission measurements by Bollinger *et al.* at Argonne National Laboratory show resonances at 18.0, 27.2, 66.6, 88.2, and 122 ev. See U. S. Atomic Energy Commission Report AECU-2040 (Technical Information Service, Department of Commerce, Washington, D. C., 1952).

open-beam, background, or standard sample runs. This assumption is a fair one if the purpose is merely to detect weak resonances quickly. If a quantitative measurement of resonance strength is then to be made, some time must be spent on calibration and background runs, and the conclusions obtained below would have to be modified accordingly.

In the capture-gamma method a resonance is detectable if it produces a peak in the sample-in curve of gamma counts *vs* time-of-flight which is significant compared with peaks due to statistical fluctuations in the gamma background; in the transmission method a resonance is detectable if it produces a dip in the sample-in curve of neutron counts *vs* time-of-flight, which is significant compared with dips due to statistical fluctuations in the counting rate on either side of the resonance energy where the cross section is approximately constant. The following analysis assumes a "thin" sample case throughout. The results would be changed in a fairly obvious way for the thick sample case, but would not be changed qualitatively. The strength $(\sigma_{e0}\Gamma)$ of a resonance can be determined in terms of the area of capture-gamma peak by integrating Eq. (1) over the resonance by using Eq. (2) for C and the Breit-Wigner formula for σ_e. The minimum detectable resonance can then be determined by setting this integral equal to a statistical fluctuation area proportional to the square root of background counts. A similar expression can be derived for the minimum resonance strength detectable by the transmission method. The ratio of these two minimum strengths defines the relative sensitivity S of the capture-gamma detection method. The expression for S is

$$S=\frac{(\sigma_0\Gamma)_{T\ \min}}{(\sigma_0\Gamma)_{\gamma\ \min}}=\frac{\sigma_{e0}}{\sigma_0}\frac{N}{N_T(T_K)^{\frac{1}{2}}}\frac{\epsilon_\gamma A}{(\epsilon A_T)^{\frac{1}{2}}}\left(\frac{\phi_t\tau_d}{R_B}\right)^{\frac{1}{2}}. \quad (3)$$

Thus the ratio of the sensitivities of the capture gamma method to the transmission method is proportional to the square root of the ratio of $\phi_t\tau_d$ (the average flux of neutrons cm^{-2} sec^{-1} per detection channel) to R_B (the average gamma counter background rate per second per channel). It is proportional to the sample area A times the detection efficiency ϵ_γ for the capture gamma method, but inversely proportional only to the square root of the product of the neutron counter area A_T and the counter efficiency ϵ in the transmission method. It is proportional to the capture gamma sample thickness N (except as ϵ_γ decreases for very thick samples), and is inversely proportional as the product of the sample thickness N_T times $(T_K)^{\frac{1}{2}}$ in the transmission method. (T_K is the sample transmission away from resonance.) $N_T(T_K)^{\frac{1}{2}}$ is a maximum when $\ln T_K=-2$, or $T_K=0.135$. The ratio (σ_{e0}/σ_0) of the capture to total cross sections at resonance appears since only that part of σ_0 due to capture contributes to the capture gamma method (for thin samples). Actually, the factor (σ_{e0}/σ_0) is too small for a thick sample since multiple scattering increases the chance of capture.

To examine the consequences of this equation in more detail, we must consider the practical factors related to the selection of the adjustable parameters. For a given sample area A, increasing ϵ_γ by increasing the amount of scintillation detector material tends to increase R_B roughly in proportion. Similarly, increasing A tends to be counteracted by a decrease in ϵ_γ through the solid angle factor Ω, or an increase in R_B if ϵ_γ is kept fixed. Considering all of these effects together, S increases roughly as $A^{\frac{1}{2}}$.

If BF_3 counters are used in the transmission method, S increases as the neutron energy increases because ϵ varies as $E^{-\frac{1}{2}}$. Although ϵ_γ fluctuates in an irregular way through the factor N_γ, it is certainly constant within an order of magnitude and has no systematic trend as E increases.

The factor $(N/N_T\sqrt{T_K})$ multiplied by the factor T_γ (in ϵ_γ) is usually of the order of unity. The optimum thickness for capture-gamma measurements is not easily determined because the dependence of T_γ and Ω (in ϵ_γ) on thickness cannot be simply expressed. With the apparatus used in the present experiments, however, the sample thickness was generally limited to the width (5 cm) of the scintillation crystals, since Ω decreased rapidly for greater thicknesses. For very dense materials, the optimum thickness would be less than 5 cm because of the decrease in T_γ with increasing thickness. The cadmium sample used for the measurements of Fig. 3 was 1.35 cm thick, and $NT_\gamma/N_T\sqrt{T_K}\approx 1$. If $\sigma_K=5$ barns for Cd, (where σ_K is the constant part of the cross section) the optimum sample thicknesses in this case would be about 5 cm and 10 cm, respectively,

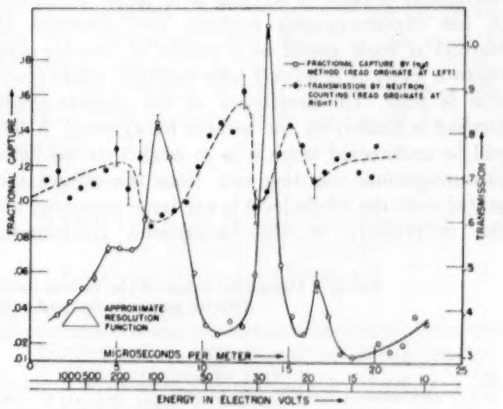

FIG. 3. Cadmium resonances. Open circle points and full line show experimental values of fractional capture (ordinate scale at left) measured by the capture-gamma method; capture resonances occur at 19 and 28 ev, with evidence of several unresolved resonances near 100 ev and above. Solid circle points and dashed line show experimental values of transmission (ordinate scale at right). Same resolution and running time. Vertical scales chosen to make statistical error bars same size at peak of 28-ev resonance.

for the capture gamma and transmission methods giving $NT_\gamma/N_T\sqrt{T_K}\cong 0.5$. If σ_K is 10 barns, the optimum thickness for both transmission and capture-gamma methods is 5 cm and $NT_\gamma/N_T\sqrt{T_K}\cong 1$.

The factor $(\phi_{1T_d}/R_B)^{\frac{1}{2}}$ shows the dependence of S on neutron intensity and gamma background. If the gamma background is directly proportional to neutron intensity, this factor is a constant. There is, however, a gamma background counting rate which is independent of neutron intensity; this adds a term to R_B which is proportional to cyclotron running time instead of monitor counts. This means that S decreases if the cyclotron intensity falls too low. (It has been assumed that there is no analogous background counting rate in the neutron counters used in transmission measurements.) If cyclotron intensity is high, then S will decrease (or increase) with intensity depending on whether gamma background varies more rapidly (or less rapidly) than neutron intensity.

Values for the various parameters and the relative sensitivity at three different energies are given in Table I for the data on cadmium (Fig. 3).

It can be seen that in this particular example the sensitivity of the capture-gamma method is perhaps an order of magnitude greater than the transmission method. The relative sensitivity increases with energy for two main reasons: the decrease in neutron counter sensitivity, and the increase in incident neutron flux relative to gamma background.

In summary it can be stated that since the transmission method measures the total cross-section (scattering plus capture), the relatively constant potential scattering integrated over the whole resolution width may be large enough in some cases to obscure a narrow capture resonance if the resolution of the instrument is poor. Scattering is of minor importance in the capture-gamma method, and therefore the method is most useful as a means of locating weak capture levels at relatively high energies, where resolution is poor. The sensitivity of the capture-gamma method is limited by the gamma background. A level will be undetected when it is so weak that the actual capture-gamma counting rate from the sample integrated over the whole level is not large compared with the uncertainty in the background counting-rate integrated over the detection channel width. Experience in the present investigations has shown that it is difficult to improve the signal-to-background ratio (and hence the sensitivity) beyond a certain point without at the same time cutting the absolute counting rate too much. This is, however, an instrument limitation, not a fundamental limitation of the method.

D. Strontium

Measurements were made using a sample of strontium fluoride, of thickness 0.0317 molecule of SrF_2 per barn, in the region from about 0.025 ev to about 500 ev. A single resonance at about 3.6 ev was found. The survey measurements were made at a sensitivity such that resonances would have been undetected if their strengths were $(\sigma_{c0}\Gamma)_{\min}\lesssim 0.2E_0$. The black circles in Fig. 4 give the experimental values of fractional capture assuming N_γ for the cadmium is 1.7 times that for strontium. The factor 1.7 represents the maximum possible value since larger values would give fractional captures larger than unity. The dashed line in Fig. 4 shows fractional capture (corrected for resolution), with the Breit-Wigner parameters $E_0=3.58$ ev, $\sigma_{c0}=840$ barns, $\Gamma=0.1$ ev. If 1.7 is the correct gamma-multiplicity ratio, the sample is "thick" and the experimental data can be used to obtain a value of $\sigma_{c0}\Gamma^2[=8.4$ barn $(\text{ev})^2]$ but not to separate values of σ_{c0} and Γ.[8] (The curve for $\Gamma=0.2$ and $\sigma_{c0}=210$ falls nearly on the dashed curve of Fig. 4 in the wings of the resonance but falls slightly below it at the peak.) Background was about 10 percent of the counting rate due to the sample at the peak.

It is probable that the factor N_γ is less for strontium[4] than for cadmium because (a) its mass number is smaller and (b) if the resonance is due to capture in Sr^{87}, the compound nucleus is even-even and has a closed shell of 50 neutrons. If it is assumed that N_γ for strontium equals that for cadmium, the fractional capture is as shown by the open circle points in Fig. 4. The solid line on the graph is a theoretical Breit-Wigner curve (corrected for instrument resolution but not Doppler broadening) calculated using the parameters $E_0=3.58$ ev, $\sigma_{c0}=35$ barns, and $\Gamma=0.4$ ev. This gives $\sigma_{c0}\Gamma^2=5.6$ barn$(\text{ev})^2$. The values of 5.6 barn$(\text{ev})^2$

TABLE I. Calculated values of the various factors in the relative sensitivity formula [Eq. (3)] for three different energies, obtained from the data used for the graphs in Fig. 3.

E_0 (ev)	t_0 μsec/meter	$\frac{N}{N_T\sqrt{T_K}}$	$\frac{A}{\sqrt{AT}}$ cm²/cm	ϵ_γ	ϵ	$\frac{\epsilon_\gamma A}{(\epsilon AT)^{\frac{1}{2}}}$	ϕ_{1T_d} neutrons/channel cm² sec	R_B background counts sec channel	$\left(\frac{\phi_{1T_d}}{R_B}\right)^{\frac{1}{2}}$	$\frac{\sigma_0 S}{\sigma_{c0}}$
12.6	20.2	1.16	8.11	0.073	0.027	3.6	0.20	0.027	2.7	11
49.3	10.2	1.16	8.11	0.073	0.014	5.1	0.47	0.035	3.7	22
214	5.2	1.16	8.11	0.073	0.0067	7.2	1.02	0.053	4.4	36

[8] A detailed discussion of the relation between capture-gamma counting rate and resonance parameters is given in the Columbia University PhD thesis on which this paper is based. In many cases the area method will give $\sigma_{c0}\Gamma^2$ to a good approximation with thick samples.

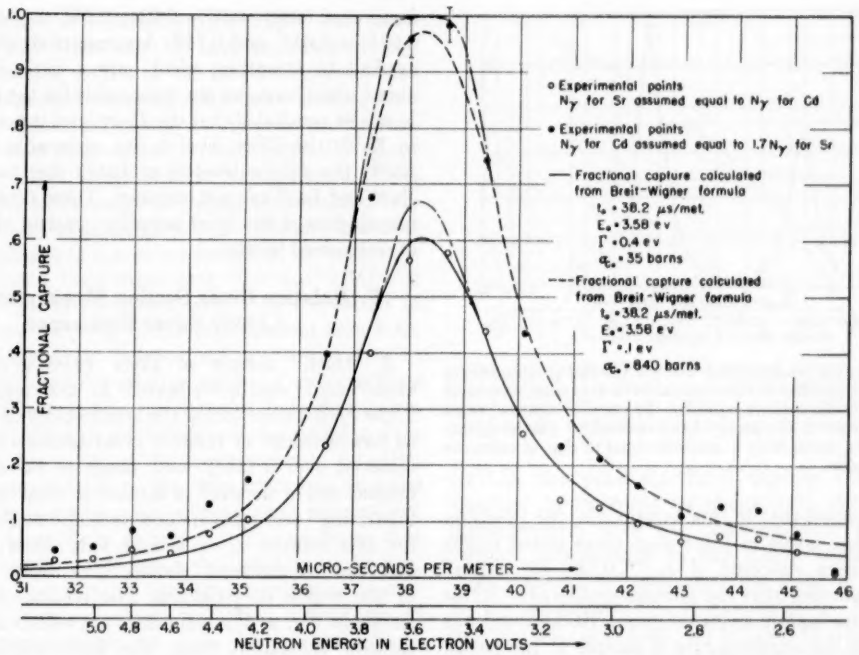
FRACTIONAL CAPTURE
MICRO-SECONDS PER METER
NEUTRON ENERGY IN ELECTRON VOLTS
o Experimental points
N_γ for Sr assumed equal to N_γ for Cd
• Experimental points
N_γ for Cd assumed equal to 1.7 N_γ for Sr
Fractional capture calculated from Breit-Wigner formula
t_0 = 38.2 μs/met.
E_0 = 3.58 ev
Γ = 0.4 ev
σ_{e0} = 35 barns
Fractional capture calculated from Breit-Wigner formula
t_0 = 38.2 μs/met.
E_0 = 3.58 ev
Γ = .1 ev
σ_{e0} = 840 barns

FIG. 4. Neutron capture resonance in strontium (for 0.0317 atom/barn). ○ = experimental values of fractional capture (capture-gamma multiplicity N_γ of strontium assumed equal to that of cadmium), ● = experimental fractional capture (N_γ for Cd assumed equal to 1.7 times N_γ for Sr). Theoretical Breit-Wigner curve (corrected for resolution) with parameters

———— E_0=3.58 ev, Γ=0.4 ev, σ_{e0}=35 barns.
- - - - - - - E_0=3.58 ev, Γ=0.1 ev, σ_{e0}=840 barns.
— · — · — = theoretical curves uncorrected for resolution.

and 8.4 barn(ev)^2 for $\sigma_{e0}\Gamma^2$ represent minimum and maximum values corresponding, respectively, to maximum and minimum values of the gamma-multiplicity factor of strontium relative to that for cadmium.

If the radiation width Γ_γ is assumed to be 0.1 ev, a statistical theory of level spacing[9] predicts spacings of 95, 5.4, 15, and 0.6 ev if the observed level is assigned to strontium isotopes of mass number A=84, 86, 87, and 88, respectively. If the reduced width ($\Gamma_N E_0^{-\frac{1}{2}}$) is assumed constant for levels of the same isotope and spin state, then the experimental sensitivity and the Breit-Wigner formula require minimum level spacings of about 50, 80, 75, and 80 for A=84, 86, 87, and 88, respectively. Otherwise levels at lower energies would have been seen with the sensitivity used. Although the theory is statistical and not accurate for detailed predictions, the two sets of predicted spacings indicate that the resonance is most probably in Sr^{84} and then, in order of decreasing probability, Sr^{87}, Sr^{86}, and Sr^{88}.

E. Location of Resonances—Barium

A sample of barium fluoride of thickness=0.0252 molecule/barn was investigated in the energy range from 12 to about 500 ev. Resonances were found at 25, 93, and 380 ev. Figure 5 shows the fractional capture as a function of time of flight calculated from the capture-gamma counting rate with the assumption that the gamma-multiplicity-factor is the same for the barium resonances as for cadmium in the thermal region. The strengths of these resonances have been estimated from the area under the curves to be the following:

for the 25-volt level

If Γ=0.4 ev, $\sigma_{e0}\Gamma\cong 30$, $\sigma_{e0}\Gamma^2\cong 12$ barn(ev)^2,
Γ<0.4 ev, $12\gtrsim\sigma_{e0}\Gamma^2\gtrsim 8$ barn(ev)^2,
Γ>0.4 ev, $30\gtrsim\sigma_{e0}\Gamma\gtrsim 20$ barn ev;

for the 93-volt level

If $\Gamma\cong$1.3 ev, $\sigma_{e0}\Gamma\cong 100$, $\sigma_{e0}\Gamma^2\cong 130$ barn(ev)^2,
Γ<1.3, $130\gtrsim\sigma_{e0}\Gamma^2\gtrsim 90$,
Γ>1.3, $100\gtrsim\sigma_{e0}\Gamma\gtrsim 70$;

for the 380 volt level

If $\Gamma\cong$3.4 ev, $\sigma_{e0}\Gamma\cong 250$ barn ev, $\sigma_{e0}\Gamma^2\cong 850$ barn(ev)^2,
Γ<3.4 ev, $850\lesssim\sigma_{e0}\Gamma^2\gtrsim 550$ barn(ev)^2,
Γ>3.4 ev, $250\gtrsim\sigma_{e0}\Gamma\gtrsim 170$ barn ev.

[9] Feshbach, Peaslee, and Weisskopf, Phys. Rev. **71**, 145 (1947); Feshbach, Porter, and Weisskopf, Phys. Rev. **90**, 166L (1953).

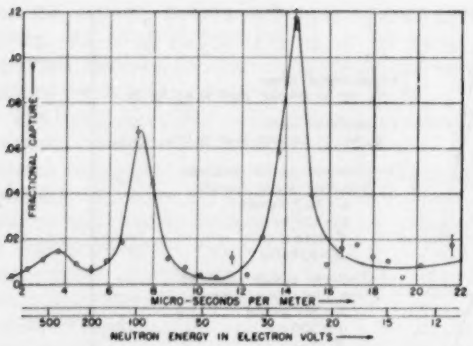

FIG. 5. Capture resonances in barium (as BaF_2). Resonances occur at 25, 93, and 380 ev. Since resolution is very poor, numerical values of fractional capture represent the fraction captured of all incident neutrons in the energy band covered by the resolution width. Gamma multiplicity is assumed equal to that of cadmium in thermal region.

It is estimated that in this barium run, the precision was such that levels in the region investigated might not have been detected if $\sigma_{e0}\Gamma \lesssim 0.1E_0$ for "thin" samples, assuming that the gamma-multiplicity factor is the same for barium as for cadmium. Background was $\frac{1}{3}$ to 1 times the counting rate of sample at the peaks.

Barium has isotopes of mass numbers 130, 132, 134, 135, 136, 137, and 138 with spin-abundance weighting factors of 0.001, 0.001, 0.024, 0.041 or 0.025, 0.078, 0.071 or 0.042, and 0.717. Arguments similar to those applied to strontium yield only a little information about which isotopes are responsible for the resonances. It can be concluded that the 25-ev level is not assignable to Ba^{138}; the 93-ev level is not assignable to Ba^{130} or Ba^{132}; the 380-ev level is probably due to Ba^{138}, but Ba^{136} and Ba^{137} are not excluded. These conclusions are meaningless if the level actually consists of a number of unresolved levels.

F. Relative Cross Section Measurements—5.13-ev Silver Resonance

A "thick" sample of silver (4.08 g/cm^2=0.0228 atom/barn) was investigated in the region of the 5.13-ev resonance[1] to test the applicability of the method to measurement of relative cross sections for a given material over a fairly wide range of values of transmission and of the ratio of capture to total cross section. Scattering[10] and transmission[1] measurements show that for this sample σ_e/σ_T should vary from 0.5 to 0.9 and the transmission should vary from 0.6 to 0.0 in the region investigated. The results obtained are shown in Fig. 6. The solid lines are values of fractional capture calculated from the Breit-Wigner formula using Sheer's parameters $\Gamma_N/\Gamma=0.110$ and $\sigma_p=6$ barns,[2] where Γ_N=neutron width, Γ=total width,

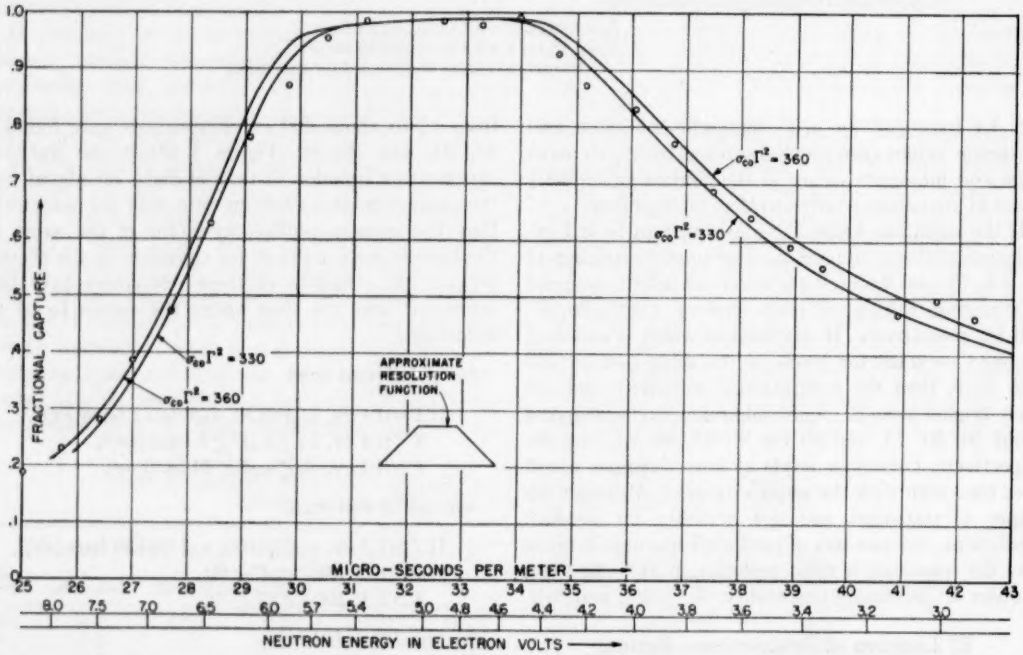

FIG. 6. Fractional capture at 5.13-ev resonance in silver. Thick sample (0.0228 atom/barn). ○=experimental values of fractional capture (normalized by assuming $\Gamma_N/\Gamma=0.110$; see text for discussion). Full lines show fractional capture calculated from Breit-Wigner formula for cross sections. Parameters $\Gamma_N/\Gamma=0.110$, $\sigma_p=6$ barns; $\sigma_{e0}\Gamma^2=360$ and 330 barn (ev)^2 for upper and lower curves, respectively.

[10] C. Sheer (private communication).

and σ_p=potential scattering; the upper and lower curves use $\sigma_{c0}\Gamma^2=360$ and 330 barn(ev)^2, respectively. The experimental points on the graph (obtained from the capture-gamma counting rates) have been normalized to the calculated curves at the peak of the resonance ($C=0.98$ at $T=0$ and $\sigma_c/\sigma_T=0.89$). The shape of the calculated curve fits the experimental points well over the whole range of the measurements. Background in these measurements was less than 10 percent of the counting rate due to the sample at its maximum. It is concluded from these data that $\sigma_{c0}\Gamma^2=345\pm30$ barn(ev)^2; this is consistent with values reported in the literature.[11] In Fig. 6, the experimental points are normalized by using independent scattering data to obtain Γ_N/Γ, and the relative values of cross sections from the capture-gamma measurements are then shown to be consistent with scattering and transmission data throughout the range of the measurements. Actually, a good approximation to the true fractional captures can be made in many cases without using independent scattering data. If the sample is thick enough so that the experimental curve has a flat portion at the top, then it can be concluded that the transmission is zero at the top. Figure 7 shows calculated dependence of the fractional capture on σ_s/σ_t for a semi-infinite zero-transmission sample. (Processes involving up to three collisions were considered.) It can be seen that even at high values of σ_s/σ_t the fractional capture is not very different from unity. If, for all "thick" samples it is assumed that $C=0.95$ at the peak, then the error in normalizing the experimental data would not exceed 5 percent for values of $\Gamma_N/\Gamma(=\sigma_s/\sigma_t$ at the resonance peak) from 0 to 0.45; if $C=0.9$ is assumed, Γ_N/Γ can be anything from 0 to 0.7 without causing a normalization error of more than 10 percent. Since for most cases of interest Γ_N/Γ is expected to be fairly small

[11] W. W. Havens, Jr., and J. Rainwater, Phys. Rev. **70**, 154 (1946); W. Selove, Phys. Rev. **84**, 869 (1951).

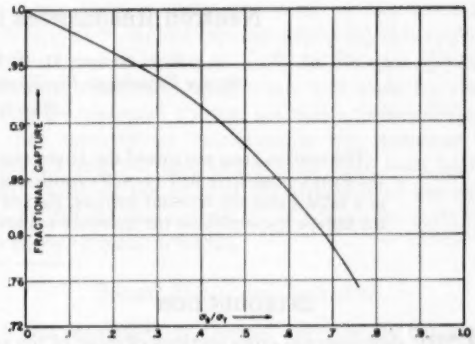

FIG. 7. Calculated value of fractional capture as a function of σ_s/σ_t (ratio of scattering to total cross section) for a "thick" (zero-transmission) sample, taking account of multiple scattering in the sample, neglecting energy change upon scattering.

(<0.5), the peak fractional capture can safely be assumed to be equal to about 0.95. Although such measurements have not been made in this case, a "thick" sample such as this would provide a fairly ideal standard for measurements using a thin sample in the neighborhood of a resonance. The "thick" sample data, of course, can be used to determine only the parameter $\sigma_{c0}\Gamma^2$ since the data are insensitive to Γ_N/Γ and to σ_p.

ACKNOWLEDGMENTS

It is a pleasure to express my thanks to Dr. J. G. Beckerley for suggesting this investigation and to Dr. W. W. Havens, Jr., and Dr. L. J. Rainwater for continued advice and encouragement in doing the research.

Thanks are also due various members of the Columbia cyclotron staff for help in building the apparatus and making the measurements and Mr. Ernest Ashley for helping with some of the calculations.

Neutron Resonances in the Rare Earth Elements*

V. L. Sailor, H. H. Landon, and H. L. Foote, Jr.
Reactor Department, Brookhaven National Laboratory, Upton, New York

(Received July 20, 1954)

The neutron cross sections of the fifteen rare earth elements (excepting $_{61}$Pm) have been measured in the energy range from 0.07 to ~20 ev with a crystal spectrometer. The resonances found are summarized in a table giving the resonant energies, E_0, and a qualitative value of the strength, $\sigma_0\Gamma^2$. For some cases, the isotope responsible for the resonance has been identified and is also listed.

INTRODUCTION

THE slow-neutron cross sections of most of the rare earth elements are characterized by complicated resonance structure. Previous measurements[1–4] with adequate resolution of rare earth cross sections have been limited primarily to energies below 1 ev. Several of the elements in this group have never been studied, mainly because of the difficulty in obtaining suitable samples. During the past two years, the authors have made systematic measurements of the rare earth cross sections over the range of neutron energies from 0.07 to ~20 ev. The objectives of this study were: (1) to locate any resonances that might exist and to assign each of these to the proper element; (2) to assign each resonance to the proper isotope; and, (3) to obtain the Breit-Wigner parameters for each resonance. At the present time, the first objective has been largely completed; however, the second and third objectives have been only partially accomplished and cannot be completed in the foreseeable future. Since a knowledge of the location and approximate "strength" of resonances is of value to many applications, we are presenting a summary of the results in their present status. Some of the measurements presented here have appeared previously,[5–7] but are included in this summary for completeness. Typical experimental cross-section curves appear in references 6 and 7.

Table I. Key to qualitative description of strengths of resonances listed in Table II.

$\sigma_0\Gamma^2$ (barn ev^2)	Qualitative description	Abbreviation
>100	very strong	v.s.
50–100	strong	s.
10– 50	moderate	m.
1– 10	weak	w.
<1	very weak	v.w.

* Research performed under contract with the U. S. Atomic Energy Commission.

[1] Borst, Ulrich, Osborne, and Hasbrouck, Phys. Rev. **70**, 557 (1946).
[2] W. J. Sturm and G. P. Arnold, Phys. Rev. **71**, 556 (1947).
[3] W. J. Sturm, Phys. Rev. **71**, 757 (1947).
[4] Bernstein, Borst, Stanford, Stephenson, and Dial, Phys. Rev. **87**, 487 (1952).
[5] Sailor, Foote, and Landon, Phys. Rev. **89**, 904 (1953).
[6] Foote, Landon, and Sailor, Phys. Rev. **92**, 656 (1953).
[7] Sailor, Landon, and Foote, Phys. Rev. **93**, 1292 (1954).

EXPERIMENTAL DETAILS

Total Cross-Section Measurements

The total cross section as a function of neutron energy was measured with the BNL crystal spectrometer. Procedures have been described in detail previously.[8] The spectrometer resolution function was approximately triangular, having a full width at half-maximum of 0.85 microsecond per meter.[9]

Samples

The quality of the specimens has been of primary importance to these measurements. Because of the large number of resonances in these elements, the presence of impurities, consisting of the other rare earths, can lead to considerable confusion as to the element responsible for an observed "line." The extreme variations of the strength of resonances within any one isotope make more difficult the assignment to the proper element. Thus, an observed "weak" resonance might truly be a weak resonance in the element under study or might possibly be a "strong" resonance in a trace impurity. An effort was made to work only with highly pure materials and wherever possible to verify the observed structure by using samples from two or more independent sources.

Specimens were obtained from three primary sources: (1) samples of Sm, Gd, Dy, Ho, Er, Tm, Yb, and Lu of unusually high purity were obtained on loan from Dr. F. H. Spedding, of the Ames Laboratory; (2) La, Ce, Pr, Nd, Sm, Eu, and Yb were purchased from the Research Chemicals, Inc., Burbank, California; and, (3) Eu, Gd, Tb, Dy, Er, Yb, and Lu were purchased from Jarrell-Ash Company, Boston, Massachusetts (Johnson, Matthey and Company, Ltd.). The neutron measurements constitute a very sensitive "spectroscopic" analysis of these specimens. It was found that samples from these three sources were quite reliable, being within the purity indicated by the supplier as far as the sensitivity of our measurements could determine. Enriched isotopes of samarium were obtained from the Isotope Research and Production Division of the Oak Ridge National Laboratory.

The preparation of samples has been discussed in other papers.[6,7]

[8] L. B Borst and V. L. Sailor, Rev. Sci. Instr. **24**, 141 (1953).
[9] Seidl, Hughes, Palevsky, Levin, Kato, and Sjöstrand, Phys. Rev. **95**, 476 (1954).

DESCRIPTION OF THE TABLES

The resonances which were found are listed for each element in Tables I and II.

Energy Scale

The resonant energy, E_0, is based on the energy scale of the BNL crystal spectrometer which is believed to have a precision of approximately $\delta E = \pm 0.003$ ev at 1 ev and $\delta E = \pm 0.10$ ev at 10 ev. On this energy scale, the prominent resonance in indium[10] occurs at 1.458 ev and in gold[11] at 4.91 ev. In spectra containing many closely spaced resonances it was frequently impossible to obtain E_0 to the usual precision due to the distortion introduced by adjacent resonances.

Resonances Above 20 Ev

In a few cases, unusually prominent resonances were found above 20 ev and occasionally extra time was spent obtaining good counting statistics at these higher energies. A few such resonances have been listed in Table II, but, of course, results above 20 ev are generally incomplete, and many resonances undoubtedly were not observed.

Strength of a Resonance

The "strength" of a resonance may be defined[12] as the product $\sigma_0\Gamma^2$ (barn ev^2). Numerical values of $\sigma_0\Gamma^2$ have been entered in the tables for the few cases which have been carefully analyzed by methods of "shape analysis."[13] For all other resonances, the strength is indicated qualitatively as shown in Table I. The qualitative entries are based on values of $\sigma_0\Gamma^2$ obtained by "area analysis."[12]

Column two of the tables lists the elemental "strength" of each resonance; i.e., the strength in a sample containing the element in its natural isotopic ratios. In cases for which isotopic assignment has been possible, the isotopic strength, $\sigma_0\Gamma^2/F$ is listed in column four, where F is the abundance of the isotope in the natural element.

Isotopic Assignments

The isotopic assignments of the resonances in samarium were made with enriched stable isotopes.[14] It should be noted that it was not possible to make definite assignments to a few of the resonances. The europium resonances were assigned[15] by observing the nine-hour Eu^{152} activity produced in the reaction, $Eu^{151}(n,\gamma)Eu^{152}$. Resonances not producing this activity were assumed to belong to Eu^{153}. In the case of a few individual resonances, assignment was made by comparing the measured thermal activation cross sections[16] to that expected by extrapolating the resonance to thermal energy. A few assignments have been tentatively made on the basis of the strengths of the resonances. Where the assignment is subject to question, the entries appear in italics.

Special Entries and References

A few resonances at thermal energies are listed for completeness. The values were obtained from the literature and appear in parentheses. Also references are made to independent results obtained with other instruments, but such results have not been incorporated in the tables.

DISCUSSION

General Features

The general features of the observed resonant structures are in good agreement with previous conclusions based on other types of data. The importance of the stability of the target nucleus in determining level densities, as was pointed out by Hurwitz and Bethe,[17] is well illustrated by these data. No resonances were found in the closed shell isotopes La^{139}, Ce^{140}, and Pr^{141} within the range of the measurements. Few resonances have been positively identified in even-even target nuclei, and such resonances invariably have been unusually strong, in agreement with previous conclusions by Goldhaber.[18] On the basis of the few isotopic assignments which can be made for resonances in even Z elements, it appears that most of the resonances are in the even-odd isotopes. The spacings of levels in the even-odd and odd-even isotopes appear to be quite similar.

It is interesting to note that in any one isotope the reduced strengths of resonances vary over a large range; extreme values differing by as much as a factor of 100. These variations in strength represent corresponding variations in the neutron width, Γ_n, because there is much evidence that the radiation width, Γ_γ, is not subject to large variations.

Failure to Observe Resonances

Examination of the tables will show immediately that more resonances have been found in the range from 0 to 10 ev than were found from 10 to 20 ev.

[10] V. L. Sailor and L. B. Borst, Phys. Rev. **87**, 161 (1952).
[11] H. H. Landon and V. L. Sailor, Phys. Rev. **93**, 1030 (1954).
[12] Melkonian, Havens, and Rainwater, Phys. Rev. **92**, 702 (1953).
[13] Sailor, Landon, and Foote, Phys. Rev. **93**, 1292 (1954), see p. 1293.
[14] These samples of enriched samarium isotopes were obtained on loan from the Isotope Research and Production Division of the Oak Ridge National Laboratory, Oak Ridge, Tennessee.
[15] R. E. Wood, Phys. Rev. **95**, 453 (1954).
[16] Isotopic thermal activation cross sections have been compiled in "Nuclear Data," Natl. Bur. Standards Circ. No. 499 (U. S. Government Printing Office, Washington, D. C., 1950).
[17] H. Hurwitz, Jr., and H. A. Bethe, Phys. Rev. **81**, 898 (1951).
[18] M. Goldhaber, Brookhaven National Laboratory Report BNL-C-9, 96, 1949 (unpublished).

TABLE II. A summary of resonances in the slow-neutron cross sections of the rare earth elements. A key to the abbreviations appears in Table I. Entries in italics indicate regions in which only the most prominent resonances could be observed.

Element	E_0 (ev)	Strength ($\sigma_0\Gamma^2$)	Isotope	Isotopic strength $\sigma_0\Gamma^2/F$	Other measurements
$_{57}$La	(no resonances observed below 20 ev)				*a*
$_{58}$Ce	(no resonances observed below 20 ev)				
$_{59}$Pr	(no resonances observed below 20 ev)				*b*
$_{60}$Nd	4.38 ±0.04	w.			*c*
$_{61}$Pm	(no stable isotopes)				
$_{62}$Sm[d]	0.0976±0.0005	68±1	149	490±10	*e, f, g*
	0.871 ±0.005	m.	149	v.s.	
	3.43 ±0.02	w.	147	m.	
	4.98 ±0.05	w.	149	m.	
	6.45 ±0.10	w.	149(?)	m.	
	8.2 ±0.1	v.s.	152	v.s.	*h*
	9.1 ±0.2	w.	149(?)	m.	
	12.0 ±0.5	w.			
	15.2 ±0.5	w.	149(?)	m.	
	17.2 ±0.5	w.	149(?)	m.	
	19.1 ±0.5	s.	147	v.s.	
	21.1 ±0.5	s.	150	v.s.	
$_{63}$Eu	(−0.011)[f,j]	m.	151[k]	s.	*e*
	0.327 ±0.001	14.5±0.7	151	30.0± 1.5	*f*
	0.461 ±0.001	102 ±5	151	213 ±10	*f, e*
	1.056 ±0.005	14.5±1.0	151	30.4± 2.0	
	1.76 ±0.02	w.	153	w.	
	2.46 ±0.01	45.2±0.5	153	86 ±10	
	2.73 ±0.05	w.	151(?)	w.	
	3.35 ±0.01	s.	151	v.s.	*l*
	3.84 ±0.02	m.	153	s.	
	6.25 ±0.04	w.	153	m.	
	7.36 ±0.03	s.	151	v.s.	
	8.98 ±0.05	m.	153	s.	
	10.6 ±0.2				
	11.8 ±0.1				
	12.8 ±0.3				
	15.1 ±0.2				
	19.5 ±0.4				
$_{64}$Gd	(0.031)[f] or (0.044)[e]	s.[e]	155 and 157[m]	v.s.[e]	*n*
	2.01 ±0.01	w.			*o*
	2.57 ±0.02	m.			*o*
	2.81 ±0.03	w.			*o*
	6.33 ±0.06	m.			*o*
	7.8 ±0.1	w.			*o*
	11.9 ±0.2				*o*
	16.9 ±0.4				*o*
	21.1 ±0.5				*o, h*
	22.5 ±0.6				*o, h*
	30.5 ±0.8				*o, h*
	34.0 ±1.0				*o, h*
$_{65}$Tb	3.37 ±0.03	m.	159	m.	
	5.4 ±0.2	w.	159	w.	
	10.6 ±0.3	m.	159	m.	
	11.4 ±0.2	s.	159	s.	
	(no data above 13 ev)				

Undoubtedly, many resonances were present which were not observed, particularly at higher energies. The probability of observing a resonance decreases as the resonant energy is increased.

There are several reasons for failing to observe certain resonances. At higher energies, the resolution of the instrument becomes insufficient to separate adjacent resonances, and under such conditions only the stronger resonances can be observed. In elements where the average spacing between resonances is small this situation is aggravated. At high energies, where resolution is poor, even an isolated weak resonance is apt to be unobservable because the poorer resolution tends to flatten and broaden the resonance until it cannot be observed above the background. In most cases, an additional handicap to detecting weak resonances was the lack of enough material to prepare sufficiently thick samples.

Resonances in isotopes having low natural abundance appear very weak superimposed on a background composed of potential scattering and the resonance contributions from the other isotopes. Such resonances can be observed only if the neighboring resonant structure is of favorable shape and the instrument resolution very good. It was possible, for example, to observe several resonances in Lu^{176} (2.6 percent abundance) in

TABLE II.—*Continued.*

Element	E_0 (ev)	Strength ($\sigma_0\Gamma^n$)	Isotope	Isotopic strength $\sigma_0\Gamma^n/F$	Other measurements
$_{66}$Dy	$(-1.01)^t$	v.s.[t]			
	1.72 ±0.01	m.			p
	2.73 ±0.02	w.			
	3.70 ±0.03	w.			
	4.36 ±0.05	w.			
	5.49 ±0.04	v.s.			p
	7.8 ±0.2				
	9.9 *±0.5*	v.w.			
	10.6 ±0.15	m.			
	13.5 *±0.5*				
	16.8 *±0.3*				
	19.5 *±0.5*				
	74 *±5*	s.			
$_{67}$Ho[q]	3.96 ±0.03	77±10	165	77±10	
	12.8 ±0.2	v.s.	165	v.s.	r
	19.0 ±0.3		165		r
	22.0 ±0.4		165		r
	39 ±1		165		r
$_{68}$Er[s]	0.47 ±0.01	m.			t
	0.58 ±0.01	m.			t
	6.10 ±0.06	s.			
	9.62 ±0.09	m.			
	16.2 ±0.2	m.			
	21.2 *±0.3*				
	27.5 *±0.4*				
$_{69}$Tm[q]	3.92 ±0.03	380±40	169	380±40	r
	14.8 ±0.2	s.	169	s.	r
	17.6 ±0.3	m.	169	m.	r
$_{70}$Yb[d]	0.597 ±0.001	1.28±0.10	168	995±90	
	4.55 ±0.03	v.w.			
	8.09 ±0.08	w.			
	13.3 ±0.14	w.			
	18.2 ±0.2	w.			
$_{71}$Lu[q]	0.142 ±0.001	1.4±0.3	176	54±12	
	1.57 ±0.01	v.w.	176	m.	
	2.62 ±0.02	w.	176	v.s.	r
	4.80 ±0.04	w.	176(?)	v.s.	r
	5.30 ±0.05	m.	175	m.	r
	11.4 ±0.2	m.	175	m.	r
	14.4 *±0.3*		175		r
	20.6 *±0.5*		175(?)		r

[a] J. Rainwater and W. W. Havens, Jr. [unpublished, see R. H. Adair, Revs. Modern Phys. **22**, 249 (1950)].
[b] R. S. Carter and J. A. Harvey, Phys. Rev. **95**, 645 (1954).
[c] Reference 2 (no resonances observed).
[d] Reference 5.
[e] Reference 1.
[f] Reference 3.
[g] A. W. McReynolds and E. Andersen, Phys. Rev. **93**, 195 (1954).
[h] Albert, Yeater, and Gaerttner, Phys. Rev. **95**, 644 (1954).
[i] Reference 7.
[j] Norman Holt, JENER, Kjeller, Norway (unpublished).
[k] Isotopic assignments made by R. E. Wood (see reference 15).
[l] M. Goldhaber [unpublished, see reference 20 in W. J. Sturm, Phys. Rev. **71**, 757 (1947)].
[m] Lapp, Van Horn, and Dempster, Phys. Rev. **71**, 745 (1947).
[n] B. N. Brockhouse and D. G. Hurst, Phys. Rev. **83**, 841 (1951).
[o] R. R. Palmer and L. M. Bollinger, Phys. Rev. **91**, 450 (1953).
[p] Reference 2.
[q] Reference 6.
[r] Pilcher, Carter, and Stolovy, Phys. Rev. **95**, 645 (1954).
[s] Foote, Sailor, and Landon, Phys. Rev. **90**, 362 (1953).
[t] Reference 4.

the region below 4 ev, but at higher energies they could not be observed because of poorer resolution. Isotopes such as La^{138} (0.089 percent abundance) were of too low natural abundance to give observable resonances.

Future improvements in instrument resolution and the use of enriched isotopes will unquestionably reveal many new resonances in this group of elements.

ACKNOWLEDGMENTS

The authors are grateful to Dr. F. H. Spedding for making available many extremely valuable samples on a loan basis. We are indebted to R. E. Wood for his isotopic assignments of the Eu resonances and to R. L. Smith and G. J. Weremchuk for continuing assistance in the measurements.

Natural Abundance of the Lithium Isotopes

DWIGHT A. HUTCHISON
Chemistry Division, Argonne National Laboratory, Lemont, Illinois
(Received June 25, 1953; revised manuscript received December 2, 1953)

The natural abundance ratio of the lithium isotope of mass 7 to the isotope of mass 6 has been determined from the density and x-ray data for certain crystals. Consideration of the maximum limits of variation of this ratio in nature and the error assignments of the data used in this calculation have resulted in the value 11.53 ± 0.29. This value disagrees with the mass spectrometric and optical determinations. Some of the possible errors in the mass spectrometric work are considered.

I. INTRODUCTION

EXPERIMENTAL determinations of the natural abundance of the lithium isotopes have yielded a great variation in the ratio Li^7/Li^6. The values of this ratio vary from approximately 11.5 to 13.0. Apparently, the best determinations rest upon mass spectrometric methods applied by Brewer,[1] Lu,[2] White and Cameron,[3] and Hintenberger.[4] From the description of these experimental determinations of the abundance ratio, it seems plausible to conclude that the observed variation does not represent the natural variation of the ratio; rather, the observed variation represents an incomplete knowledge of the isotopic fractionation effects in the experimental preparation of samples for analysis, in evaporation or ionization processes, and in numerous instrumental factors.

From a review of previous work it is apparent that a determination of the lithium isotopic abundance by a method which is independent of the mass spectrometric or optical methods[5] would be highly desirable both to give a reliable value to the abundance ratio, and to serve as a guide in perfecting the various analytical techniques that may be of use in studies of isotopic reactions and separation processes. Such a method fulfilling these requirements exists and has been presented by Hutchison[6] and by the writer[6] in connection with a determination of the atomic weights of calcium and fluorine. In essence, the method consists of a comparison of the molecular weights of two crystalline substances for which there are accurate x-ray and density data available.

The purpose of this paper is to present the application of the x-ray density method to the determination of the natural isotopic abundance of lithium, and to evaluate the reliability of the value thus determined.

[1] A. K. Brewer, J. Chem. Phys. **4**, 350 (1936).
[2] H. Lu, Phys. Rev. **53**, 845 (1938).
[3] J. R. White and A. E. Cameron, Phys. Rev. **74**, 991 (1948).
[4] H. Hintenberger, Naturwiss. **34**, 52 (1947).
[5] Ornstein, Vreeswijk, and Wolfsohn, Physica **53**, 1 (1934); G. Nakamura, Nature **128**, 759 (1931); W. R. v. Wijk and A. J. v. Koeveringe, Proc. Roy. Soc. (London) **A132**, 98 (1931).
[6] C. A. Hutchison, J. Chem. Phys. **10**, 489 (1942); D. A. Hutchison, J. Chem. Phys. **13**, 383 (1945).

II. THE LITHIUM ISOTOPIC RATIO FROM X-RAY AND DENSITY DATA

In the present calculation we wish to compare the molecular weight of lithium fluoride with the molecular weights of calcite, diamond, sodium chloride, and potassium chloride for all of which accurate x-ray and density data exist. By use of the mass values for fluorine and the two lithium isotopes we can arrive at the isotopic composition of the lithium in a highly purified sample of lithium fluoride which was purified by a method shown not to alter its isotopic composition.

The comparison of molecular weights is given by the relation,

$$M_1=M_2(\rho_1/\rho_2)FR_\varrho^3, \tag{1}$$

where subscripts 1 refer to data for LiF and subscripts 2 refer to data on the other four crystals; M is an isotopic, atomic, or molecular weight based on the physical mass scale; ρ is a density in units of g-cm^{-3}; R_ϱ is the ratio of the x-ray grating space of lithium fluoride to that of one of the other four crystals; F is a factor depending on the crystal geometries, and the arrangements and number of ion pairs or molecules in the unit cells.

The R_ϱ is expressed in terms of the observed reflection angles, ϑ_i, by the relation,

$$R_\varrho=\frac{n_1\lambda_1\sin\vartheta_2(1-\delta_2/\sin^2\vartheta_2)\xi}{n_2\lambda_2\sin\vartheta_1(1-\delta_1/\sin^2\vartheta_1)}, \tag{2}$$

which utilizes the Bragg law together with the appropriate refraction corrections. The ξ is a factor which corrects for the fact that x-ray reflection angles are not from corresponding planes in the two crystals; λ is the wavelength of the radiation employed in the determination of the x-ray reflection angles and was computed from the reflection angles for the Cu $K\alpha_1$ and Mo $K\alpha_1$ lines from calcite as obtained by Bearden and Shaw,[7] and Larsson[8]; ϑ is the Bragg reflection angle; n is the order of the reflection; and δ, the unit decrement of the index of refraction of the crystal, is defined by the relation, $\delta=1-\mu$, where μ is the index of refraction. The δ's were computed from the relation, $\delta=(ke^2\lambda^2/2\pi mc^2)$ which assumes the wavelengths used to be much shorter than any critical absorption wavelength of the

[7] J. A. Bearden and C. H. Shaw, Phys. Rev. **48**, 18 (1935).
[8] A. Larsson, Phil. Mag. [7] **3**, 1136 (1927).

TABLE I. Data for the calculation of the natural isotopic abundance of lithium, with estimated maximum errors for various factors expressed in parts per million (ppm).

Substance	Calcite	Diamond	Lithium fluoride	Sodium chloride	Potassium chloride
$\rho_{20°C}$ (g-cm^{-3})	2.71030[a] ±22 ppm	3.51540[b] ±20 ppm	2.64030[c] ±53 ppm	2.16360[d] ±18 ppm	1.98827[e] ±20 ppm
ϑ (radians)	0.117106[f,g] ±12 ppm 0.486229[g] ±30 ppm	0.409016[f] ±5.9 ppm	1.463790[h] ±1.7 ppm	0.276656[i] ±14 ppm	0.112989[f] ±17 ppm
Reflecting plane	Natural cleavage	100	111	100	100
Reflection order	1 4	1	3	1	1
$\delta\times10^6$	1.85 ±5×10^4 ppm	2.39 ±5×10^4 ppm	7.91 ±5×10^4 ppm	1.41 ±5×10^4 ppm	1.32 ±5×10^4 ppm
ξ	1	1	$\sqrt{3}/2$	1	1
F	0.912459 ±9.1 ppm	0.250000 ±0.0 ppm	1.000000 ±0.0 ppm	1.000000 ±0.0 ppm	1.000000 ±0.0 ppm
$\alpha\times10^6$ (°C^{-1}) (linear)	1.04[j] ±2.0×10^4 ppm	0.118[k] ±2.0×10^4 ppm	3.41[l] ±2.0×10^4 ppm	4.05[m] ±2.0×10^4 ppm	3.77[n] ±2.0×10^4 ppm
B	0.151539 ±45 ppm	0.151541 ±37 ppm		0.151540 ±42 ppm	0.151540 ±59 ppm

[a] J. A. Bearden, Phys. Rev. **38**, 2089 (1931).
[b] J. A. Bearden, Phys. Rev. **54**, 698 (1938).
[c] C. A. Hutchison and H. L. Johnston, J. Am. Chem. Soc. **62**, 3165 (1940).
[d] H. L. Johnston and D. A. Hutchison, Phys. Rev. **62**, 32 (1942).
[e] D. A. Hutchison, Phys. Rev. **66**, 144 (1944).
[f] Y. Tu, Phys. Rev. **40**, 622 (1932).
[g] A. Larrsson, Phil. Mag. [7] **3**, 1136 (1927).
[h] Straumanis, Ievins, and Karlsons, Z. physik. Chem. **B42**, 143 (1939).
[i] M. Siegbahn, Ann. Physik **59**, 56 (1919).
[j] A. Larsson, Inaugural-Dissertation, Uppsala, 1929 (unpublished).
[k] *International Critical Tables* (McGraw-Hill Book Company, Inc., New York, 1927), **3**, p. 21.
[l] H. Adenstedt, Ann. Physik **26**, 69 (1936).
[m] M. Straumanis and A. Ievins, Z. Physik **102**, 353 (1936); Straumanis, Ievins, and Karlsons, Z. anorg. u. allgem. Chem. **238**, 175 (1938).
[n] Klemm, Tilk, and Mullenheim, Z. anorg. u. allgem. Chem. **176**, 1 (1928).

crystals. In the latter expression k is the number of electrons per cubic centimeter and other symbols have their usual significance.

By substitution of Eq. (2) in (1) and solving for the atom fraction, $\chi(\mathrm{Li}^6)$, of the mass-6 lithium isotope, we obtain the following expressions used in this calculation:

$$\chi(\mathrm{Li}^6)=C-AB, \tag{3}$$

where

$$C=\frac{M_{\mathrm{Li}^7}+M_F}{M_{\mathrm{Li}^7}-M_{\mathrm{Li}^6}}, \tag{4}$$

$$A=\rho_1\left[\frac{n_1\lambda_1\xi_1}{\sin\vartheta_1(1-\delta_1/\sin^2\vartheta_1)}\right]^3, \tag{5}$$

$$B=\frac{FM_2}{\rho_2}\left[\frac{\sin\vartheta_2(1-\delta_2/\sin\vartheta_2)}{n_2\lambda_2}\right]^3. \tag{6}$$

It will be observed that the calculation summarized in Eq. (3) is independent of the Avogadro number and of $\lambda_\vartheta/\lambda_s$, the ratio of wavelengths on the grating or Ångstrom scale to the wavelengths on the Siegbahn scale. The quantities which are temperature-dependent, i.e., the ρ's and ϑ's, have been reduced to the common temperature of 20°C. The densities were temperature-corrected by use of the appropriate thermal expansion coefficients, and the x-ray reflection angles by means of the relation,

$$\log\sin\vartheta_{20°C}=\log\sin\vartheta_T-\alpha(20-T)/2.303, \tag{7}$$

where T is the centigrade temperature at which the reflection angles were determined.

The atomic, isotopic, or molecular mass values are based on chemical atomic weight determinations except for M_{Li^6}, M_{Li^7}, and M_F which have been derived from nuclear reaction data. It is this very accurate mass value for fluorine that makes possible the application of the x-ray-density method of the calculation of the natural isotopic abundance of lithium.

The value employed to convert from the chemical to the physical mass scale is 1.000272. The values of the quantities used in this calculation together with references to their literature sources are summarized in Tables I and II. With each quantity there is listed in parentheses the estimated maximum error expressed in parts per million (ppm).

The first step of the calculation was to obtain the value of B by Eq. (6) in which the x-ray and density data of all the crystals except lithium fluoride were employed. The individual B values and their errors, propagated from the error assignments of the primary data, are listed in Table I. The value for calcite is a

TABLE II. Atomic masses employed in calculations, with estimated maximum errors expressed in parts per million (ppm).

Element	Mass (physical mass scale)
C	12.0137[a] (±18 ppm)
Ca	40.0959[b] (±130 ppm)
Cl	35.4666[c] (±15 ppm)
K	39.1066[d] (±14 ppm)
Na	23.0033[e] (±23 ppm)
F	19.004456[e] (±0.79 ppm)
Li^7	7.018223[e] (±3.7 ppm)
Li^6	6.017021[e] (±3.7 ppm)

[a] G. P. Baxter and A. H. Hale, J. Am. Chem. Soc. **59**, 506 (1937); A. F. Scott and F. H. Hurley, J. Am. Chem. Soc. **59**, 1905 (1937).
[b] O. Hönigschmid and K. Kempter, Z. anorg. u. allgem. Chem. **163**, 315 (1927); **195**, 1 (1931).
[c] T. W. Richards and R. C. Wells, "A Revision of the Atomic Weights of Sodium and Chlorine," Carnegie Institution of Washington, Publication No. 28 (1905); W. A. Noyes and H. C. P. Weber, J. Am. Chem. Soc. **30**, 13 (1908); E. Zintl and A. Meuwsen, Z. anorg. u. allgem. Chem. **136**, 223 (1924); Hönigschmid, Chan, and Birckenbach, Z. anorg. u. allgem. Chem. **163**, 315 (1927); O. Hönigschmid and R. Sachtleben, Z. anorg. u. allgem. Chem. **178**, 1 (1929); A. F. Scott and C. R. Johnson, J. Phys. Chem. **33**, 1975 (1929); O. Hönigschmid, J. Am. Chem. Soc. **53**, 3012 (1931).
[d] T. W. Richards and A. Stahler, J. Am. Chem. Soc. **29**, 623 (1907); T. W. Richards and E. Mueller, J. Am. Chem. Soc. **29**, 639 (1907); G. P. Baxter and W. M. MacNevin, J. Am. Chem. Soc. **55**, 3185 (1933); O. Hönigschmid and R. Sachtleben, Z. anorg. u. allgem. Chem. **213**, 365 (1933); R. K. McAlpine and E. J. Bird, J. Am. Chem. Soc. **63**, 2960 (1941).
[e] Li, Whaling, Fowler, and Lauritsen, Phys. Rev. **83**, 512 (1951).

weighted average[9] of the two B values from the two reflection angles listed. From the first-order reflection one obtains $B(n=1)=0.151540$ (±69 ppm) and from the fourth-order reflection, $B(n=4)=0.151538$ (±60 ppm). A weighted average[9] of the B values obtained from the four values listed in Table I gives

$$B_{\text{wt'd Av}}=0.151540\ (\pm 22\ \text{ppm}).$$

The value obtained for A from Eq. (5) is

$$A_{\text{LiF}}=170.9885\ (\pm 66\ \text{ppm}).$$

The value obtained for C from Eq. (4) is

$$C=25.99144\ (\pm 34\ \text{ppm}).$$

Finally, combination of B, A, and C according to Eq. (3) yields

$$\chi(\text{Li}^6)=0.0798\ (\pm 2.5\ \text{percent})$$
$$=0.0798\pm 0.0020,$$

and the abundance ratio of mass-7 to mass-6 lithium isotopes becomes

$$R(7/6)=11.53\ (\pm 2.5\ \text{percent})$$
$$=11.53\pm 0.29.$$

The errors stated are obtained by a least-squares propagation of the maximum error assignments given for the quantities in Tables I and II. The relatively large errors of the calculated quantities, $\chi(\text{Li}^6)$ and $R(7/6)$, when compared with the small error of the quantities given in Tables I and II, are due to the fact that in Eq. (3) a small difference is obtained from two accurately determined quantities, i.e., C and AB.

[9] The fractional error obtained for the final weighted B value was obtained from internal consistency. The ratio of errors obtained from external consistency to that from internal consistency is 0.138 indicating that too great allowances have been made for systematic errors in the primary data used in the calculations. For a discussion describing the method of taking the weighted averages, see R. T. Birge, Phys. Rev. **40**, 207 (1932).

III. THE NATURAL ABUNDANCE OF LITHIUM ISOTOPES

The value calculated for the abundance of the mass-7 and mass-6 lithium isotopes represents the abundance for crystals prepared from a particular batch of carefully purified lithium fluoride[10] in which the lithium isotopic composition was not altered within the stated limits of accuracy for its density determination. It is felt reasonable to assume that the $R(7/6)$ determined here represents the best average natural ratio, and that the only question remaining is that concerning the natural variation in the ratio.

There appear to be at least two types of processes that would cause natural variation in the lithium isotopic abundance, that due to chemical reactions and, to a smaller degree, that due to thermal neutron absorption. From Urey's[11] computations of the partition functions for the lithium isotopes, their hydrides and deuterides, the differences predicted in the thermodynamic quantities of the isotopic lithium compounds suggest that some isotopic exchange may occur in nature which would give a small separation of the lithium isotopes. A rough estimate of a maximum figure for the variation in the abundance ratio may be about 0.5 percent. Evidence for thermal neutron capture is to be found in the work of Aldrich and Nier[12] who observed He^3 concentrations in the lithium-containing mineral, spodumene, which were greater than that of other minerals. This fact may be attributed to the $Li^6(n,\alpha)H^3$ reaction. Thode and co-workers[13] have found the ratio of the boron isotopes, $R(11/10)$, to vary from 4.27 to 4.42, or a 3.5 percent variation, depending on the natural source. On the assumption that all of this variation is due to neutron capture by B^{10}, then taking into account the isotopic composition of boron and lithium, the $R(7/6)$ for lithium should vary as the ratio of the thermal neutron absorption cross sections for Li^6 and B^{10}. This would mean that the lithium abundance ratio should vary by only 0.36 percent. However, neutron intensities in the earth's atmosphere, especially in the earth's crust, due to cosmic and other sources would seem too low to account for the observed variation in boron such that the variation expected in the lithium ratio would be less than the 0.36 percent figure.

From the qualitative considerations above concerning the maximum variation of the lithium abundance ratio in nature, we may conclude that the 2.5 percent

[10] C. A. Hutchison and H. L. Johnston, J. Am. Chem. Soc. **62**, 3165 (1940); H. L. Johnston and C. A. Hutchison, J. Chem. Phys. **8**, 869 (1940).
[11] H. C. Urey, J. Chem. Soc. 562 (1947).
[12] L. T. Aldrich and A. O. Nier, Phys. Rev. **74**, 1590 (1948).
[13] Thode, Macnamara, Lossing, and Collins, J. Am. Chem. Soc. **70**, 3008 (1948).

error of the $R(7/6)$ value obtained in this calculation well includes the expected natural variation.

IV. DISCUSSION AND CONCLUSIONS

In the mass spectrometric determinations[1–4] of $R(7/6)$, the workers mentioned in the introduction have employed thermal emission of ions or electron bombardment of vapor from lithium containing compounds placed on a platinum or tungsten substrate which was heated to about 600–900°C. Apparently, in none of these determinations has anyone given consideration to the effect of the process of solution of the lithium compound in the substrate on the possible alteration of $R(7/6)$ in the compound from which the lithium vapor or ions were obtained. For example, Brewer[1] dissolved lithium salt in a platinum disk at red heat, scraped the salt from the platinum, and washed with water. In his theoretical considerations no attention was given to the process of solution of the lithium in the platinum. An isotopic separation certainly must have existed due to different isotopic rates of diffusion. Further, he assumed perfect mixing of Li^7 and Li^6 in the platinum substrate, which seems untenable as his data show. It becomes evident that further experimental and theoretical consideration should be given to the processes of diffusion of lithium into and out from the metal substrate.

Probably more important than the solution processes in the mass spectrometric measurement of ion current ratios of light mass ions are the many instrumental effects. A typical property of instruments employing two parallel plates with slits in the ion source for acceleration of ions without previous ion focusing is the so-called "voltage effect." The observed effect is that the collected ion current increases with ion accelerating voltage until a voltage is reached at which the ion current may remain essentially constant with further increase in voltage. In the case of the molecular ion species of the various isotopic hydrogen molecules, distinct maxima[14] exist in the curves of peak height *versus* accelerating voltage such that, at a given accelerating voltage, measured current ratios may deviate by more than 50 percent from their correct values. For the usual magnetic field intensities employed in mass spectrometers, the ion accelerating voltages for collection of lithium ions will vary from 1000 v to 4000 v over which range the observed "voltage effect" occurs and must have existed in the determinations of $R(7/6)$. This effect in itself could account for the wide range of values found for $R(7/6)$. It becomes apparent that a thorough study of the preparation and handling of lithium-containing samples and of instrumental effects on the collected ion currents is necessary before the mass spectrometric determinations can be considered reasonably trustworthy.

Bainbridge and Nier[15] have adopted Lu's value of 12.29 ± 0.20 for $R(7/6)$, with supporting evidence from a value computed from the chemical atomic weight and the physical isotopic weights. Inherent in the present x-ray density determination of $R(7/6)$ is the result that the atomic weight[16] of lithium is somewhat lower than the value adopted by the Committee on Atomic Weights of the International Union of Chemistry. Hence, a smaller value of $R(7/6)$ is obtained.

The x-ray density determination presented here gives a relatively precise determination of $R(7/6)$ which is independent of mass spectrometric or optical work. Qualitative considerations of the natural variation to be expected in $R(7/6)$ give a variation within the stated probable error of $R(7/6)$ from this calculation. The result obtained here disagrees with the mass spectrometric determinations. However, consideration of the mass spectrometric techniques shows that sample handling and instrumental effects raise many debatable questions concerning the validity of these determinations. The results obtained in the present work are based upon a highly consistent set of data as evidenced by the consistent results obtained through its use by Birge[17] in his determination of the Avogadro number and by the writer[6] in his determination of the atomic weights for calcium and fluorine. Birge has concluded that these crystals must be geometrically perfect to better than 1 part in 10 000 as judged from the consistency of his values of the Avogadro numbers obtained from the data on each of these crystals. In the present calculation the consistency of the quantity B rules out any noticeable effect of crystal imperfections on the stated results. The mass spectrometric and optical determinations of $R(7/6)$ varying from 11.5 to 13.0, however, do not appear to form a consistent set of results. The great consistency of the x-ray and density data collected from many measurements by different observers should lend credence to the present calculation of $R(7/6)$.

The writer wishes to thank Dr. O. C. Simpson for his suggestion of this problem.

Note Added in Proof.—It may be of interest to consider the effect on the present calculations of the changes of the atomic weights of sodium and carbon as adopted by the International Commission on Atomic Weights and given in the American Chemical Society report by E. Wichers [J. Am. Chem. Soc. **76**, 2033 (1954)]. When the new values are employed, there results the weighted average B value, 0.1515400, in exact agreement with the result of this paper. Therefore, the value of $R(7/6)$ remains unchanged.

[14] From unpublished data taken by the writer. The data were taken without the usual magnetic field across the ion source for alignment of the electron beam.

[15] K. T. Bainbridge and A. O. Nier, Prelim. Rep. No. 9, Nuclear Science Series, Div. of Math. and Phys. Sci., Natl. Research Council, December, 1950 (unpublished).

[16] D. A. Hutchison, J. Am. Chem. Soc. **76**, 967 (1954).

[17] R. T. Birge, Am. J. Phys. **13**, 63 (1945).

Gamma-Ray Energies in the Decay of Cs^{134}

M. C. Joshi and B. V. Thosar
Tata Institute of Fundamental Research, Bombay, India
(Received April 12, 1954; revised manuscript received August 23, 1954)

The photoelectric conversion spectrum of gamma rays in the decay of Cs^{134} was studied with a newly installed Siegbahn-Slätis beta-ray spectrometer, using a strong source and thick lead and uranium radiators to bring out weak lines. Lines corresponding to the following gamma rays were found (expressed in kev) 467; 553; 571; 607; 794; 1027; 1164; 1368; 1401.

THE gamma rays emitted in the decay of Cs^{134} of 2.3-year half-life have been studied by recording the photoelectron spectrum, both lead and uranium radiators being used. The instrument used was a Siegbahn-Slätis type intermediate image beta-ray spectrometer which has recently been installed at this Institute. This had a high transmission for a resolution of 1.5 percent used in these experiments. The source, 1.5 mC, was covered with aluminum sufficient in thickness to absorb all beta particles. Figure 1 shows the spectrum of the photoelectric conversion electrons of the gamma rays in lead of thickness 110 mg/cm². Photoelectron lines were observed corresponding to the following gamma-ray energies, expressed in kev: 467±15, 553±7, 571±7, 607±5, 794±3, 1027±15, 1164±10, 1368±5, and 1401±15. The observed relative intensities are $\gamma_1:\gamma_3:\gamma_4:\gamma_6:\gamma_7:\gamma_8::0.035:0.21:1:1:0.04:0.053$.

This confirms the gamma-ray energies reported by Schmidt and Keister[1] and by Waggoner *et al.*,[2] who studied the electron spectrum caused by internal conversion, and gives, in addition, two gamma rays, one at 0.47 Mev and the other at 1.40 Mev. A fairly consistent level scheme for Ba^{134} can be drawn to explain most of the gamma-ray transitions, though the gamma ray of energy 1.036 Mev has been attributed by some observers to an alternative K-capture decay branch. Another suggestion[3] for explaining this gamma ray has been to postulate an excited level at 1.831 Mev below the highest level at 1.956 Mev in Ba^{134}. This level scheme, shown in Fig. 2, also explains the gamma ray of 0.47 Mev, this transition being indicated by a dotted arrow. The line corresponding to the 1401-kev gamma ray is very weak and it is difficult to estimate its relative intensity. From the energy level schemes for Ba^{134}, suggested by previous workers, a gamma ray of this energy could be caused by a cross-over transition from the 1.395-Mev level to the ground state. On the other hand, the spin assignment to this excited level from angular correlation experimental data is 4^+. The intensity of a crossover transition to the ground state 0^+, relative to that of the 0.607-Mev gamma ray which is a transition from the same 4^+ level to an intermediate level 2^+ (0.794 Mev) would be of the order of 10^{-7}. The observed relative intensity is

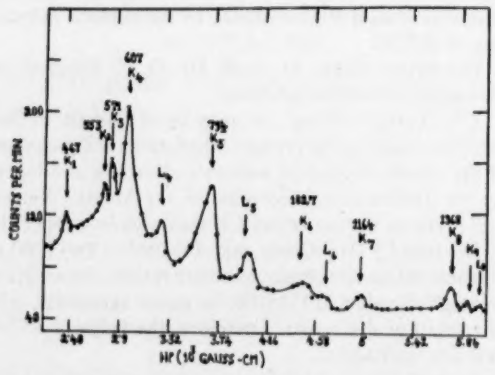

FIG. 1. Spectrum of the photoelectric conversion electrons of the γ rays emitted in the decay of Cs^{134}. Thickness of lead radiator is 110 mg/cm².

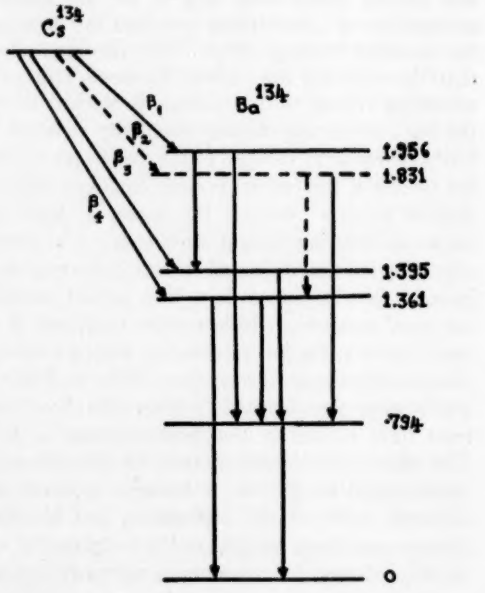

FIG. 2. Proposed decay scheme of Cs^{134}.

[1] F. H. Schmidt and G. L. Keister, Phys. Rev. **86**, 632 (1952).
[2] Waggoner, Moon, and Roberts, Phys. Rev. **80**, 420 (1950).
[3] Hollander, Perlman, and Seaborg, Revs. Modern Phys. **25**, 552 (1953).

of the order of 10^{-3}. It is not possible, therefore, to fit this gamma-ray transition into the decay scheme with any certainty at this stage.

Most of the previous work on gamma rays from this isotope has been concerned with internal conversion lines when thin sources of presumably low total strength are used. The study of the photoelectron spectrum has a greater chance of bringing out weaker gamma rays, as stronger and thicker sources may be used.

The Radiochemical Center, Amersham, England, which supplied the active cesium bromide, gave us the quantitative spectrographic analysis of the material. Consideration of these data and the relevant capture cross sections for neutrons shows that no appreciable radioactive impurity can be present in the sample.

Further work on the details of the decay scheme of Cs^{134} is in progress.

Our thanks are due Dr. H. J. Bhabha, F.R.S. for his keen interest in the work of installation of the new spectrometer and also in the work here described.

PHYSICAL REVIEW VOLUME 96, NUMBER 4 NOVEMBER 15, 1954

Radiative Capture of Deuterons by He^3†

J. M. Blair, N. M. Hintz, and D. M. Van Patter*
Department of Physics, University of Minnesota, Minneapolis, Minnesota
(Received August 9, 1954)

The excitation function of $He^3(d,\gamma)$ capture radiation, measured from $E_d=0.2$ to 2.85 Mev, exhibits a broad resonance at 0.45 ± 0.04 Mev, with a total cross section of 0.05 ± 0.01 mb. Above this energy, the presence of nonresonant capture is observed. At $E_d=0.58$ Mev, the radiation is isotropic from 0° to 90° within ±10 percent. The measured gamma-ray energy of 16.6 ± 0.2 Mev at resonance corresponds to a Q value for the $He^3(d,\gamma)Li^5$ reaction of 16.36 ± 0.2 Mev. The experimental radiation width at resonance is calculated to be 11 ± 2 ev, which is compared to the Weisskopf estimate for $E1$ transitions.

I. INTRODUCTION

THE ground states of each member of the mirror pair, He^5 and Li^5 are unstable against nucleon decay to He^4 by about 1.0 and 1.9 Mev, respectively, with a lifetime $\sim10^{-21}$ sec (Fig. 1). These states have been observed chiefly as resonances in the elastic scattering of neutrons and protons[1,2] by He^4, although there has been some indication from other experiments.[3–5] The results of the experiment reported here give independent evidence for the existence of a virtual ground state of Li^5 together with a measurement of its energy.

For the case of Li^5, a phase shift analysis of the p-He^4 scattering data,[6] together with a measurement of the polarization of the scattered protons,[7] fixes the character of the ground state as $P_{\frac{3}{2}}$, as expected from an independent particle model with spin-orbit coupling.[8] Aside from the rather uncertain $P_{\frac{1}{2}}$ level in the vicinity of 2.5 Mev, the only other known state of Li^5 is the comparatively narrow level at 16.7 ± 0.2 Mev, observed as a resonance in the $He^3(d,p)He^4$ reaction.[9–11] This has been assigned $J=\frac{3}{2}+$ on the basis of the (d,p) cross section at resonance and the observed isotropy of the protons. It occurred to one of us (N.M.H.) that if these assignments are correct, it should be possible to observe radiative capture of deuterons from the state at 16.7 Mev to the virtual ground state by electric dipole transition. This is indicated by a dotted line in Fig. 1. Such a transition would be interesting to detect as it would provide an independent measurement of the ground-state energy and give some information on the character of the states involved. Radiative capture of deuterons has not been reported previously except in the case of the $D(p,\gamma)He^3$ reaction.[12]

With these considerations in mind it was decided to search for a gamma ray of energy ~17 Mev from the deuteron bombardment of a He^3 gas sample.

II. EXPERIMENTAL PROCEDURE

The Minnesota electrostatic generator was used to provide a beam of deuterons or protons up to 2.8 Mev. As indicated in Fig. 2, the beam was defined by tantalum diaphragms, then passed through a thin nickel foil into the target chamber containing the enriched He^3 gas. The stainless steel target chamber was normally 6.17

† Assisted by the joint program of the Office of Naval Research and the U. S. Atomic Energy Commission.
* Present address: Bartol Research Foundation, Swathmore, Pennsylvania.
[1] Freier, Lampi, Sleator, and Williams, Phys. Rev. **75**, 1345 (1949).
[2] R. K. Adair, Phys. Rev. **86**, 155 (1952).
[3] Almqvist, Allen, Dewan, and Pepper, Phys. Rev. **91**, 1022 (1953).
[4] E. W. Titterton and T. A. Brinkley, Proc. Phys. Soc. (London) **A64**, 212 (1951).
[5] R. W. Gelinas and S. S. Hanna, Phys. Rev. **86**, 253 (1952).
[6] C. L. Critchfield and D. C. Dodder, Phys. Rev. **76**, 602 (1949).
[7] M. Heusinkveld and G. Freier, Phys. Rev. **85**, 80 (1952).
[8] D. R. Inglis, Revs. Modern Phys. **25**, 390 (1953).
[9] Bonner, Conner, and Lillie, Phys. Rev. **88**, 473 (1952).
[10] Yarnell, Lovberg, and Stratton, Phys. Rev. **90**, 292 (1953).
[11] G. Freier and H. Holmgren, Phys. Rev. **93**, 825 (1954).
[12] Fowler, Lauritsen, and Tollestrup, Phys. Rev. **76**, 1767 (1949).

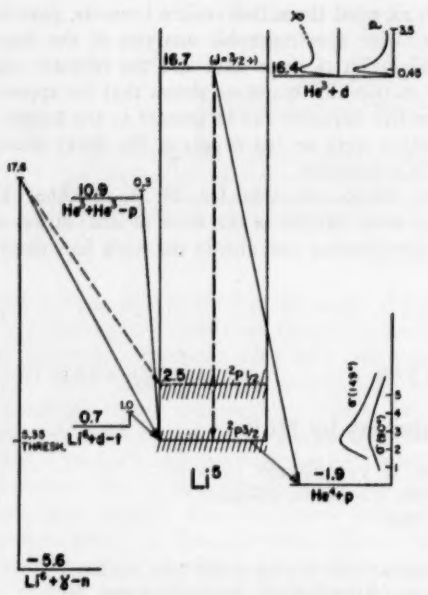

FIG. 1. Energy level diagram for Li^6. Dotted line shows transition reported in this paper.

cm long, with 0.050-in. thick walls. For some parts of the experiment where it was advantageous to have a shorter chamber, a target chamber 3.31 cm long was used. For measurements of the gamma radiation from the proton bombardment of lithium, the gas target chamber was replaced by a chamber which had a thick layer of LiOH at the position indicated in Fig. 2. The lithium gamma rays were used for energy and cross-section calibration.

About 3 cc of helium gas enriched to 94.5 percent He^3 were used in this experiment. The isotopic percentage of He^3 was measured before and after the experiment by mass spectroscopic analysis, and was found to be constant within 0.5 percent.[13] The enriched He^3 was transferred from a storage vessel to the target chamber and back by means of a mercury Toeppler pump. The storage vessel contained activated charcoal, which could be cooled by liquid nitrogen to purify the gas sample. It was demonstrated that any air contamination of the He^3 gas could be quickly removed by this means. To prevent mercury vapor from entering the target chamber, there was a U tube in the gas inlet line, which could be cooled by liquid nitrogen. The gas pressure was measured by means of a Bourdon gauge calibrated to within 0.2 cm Hg. Gas pressures of up to 19 cm Hg were used during the experiment.

To permit measurement of the incident beam, the target cup assembly was insulated from the target tube, and there was an insulating section in the gas inlet line. During each run, the beam current was integrated by means of a circuit developed by Dr. R. J. S. Brown for a previous experiment.[14]

The gamma-ray detector was a scintillation counter consisting of a NaI(Tl) crystal, 4.9 cm in diameter and 3 cm long, encased in a thin-walled aluminum can, having a glass window mounted with a Lucite adapter against the end of a 5819 photomultiplier tube. The pulses from the photomultiplier were amplified using a Model 100 amplifier, and analyzed by a single-channel pulse-height discriminator. During most of the experiment, the distance from the center of the target chamber to the front face of the crystal was 1.6 cm. Larger separations were used for the measurement of the absorption of the gamma rays in lead and their angular distribution.

A calibration of the bombarding energy scale was made from the $Li^7(p,n)Be^7$ threshold at the beginning and end of the experiment, and was found to remain constant within ± 0.15 percent. The ratio between the measured voltage on the electrostatic analyzer and bombarding energy had been found to be constant within ± 0.4 percent in an earlier experiment.[10] The thickness of the nickel entrance window was measured before and after the experiment as 185 ± 4 kev by observing the 441.5-kev $Li^7(p,\gamma)$ resonance, with the window inserted in the proton beam.

In order to estimate the energy loss in the window for various bombarding energies, the proton energy loss curve measured by Kahn[15] was used. Since only the variation in energy loss in nickel with bombarding energy was needed, it was considered that no appreciable error would be introduced by the use of the curve for copper. For the energy loss in helium, the results of Reynolds *et al.*[16] for the atomic stopping cross section of protons in helium were used for proton energies up

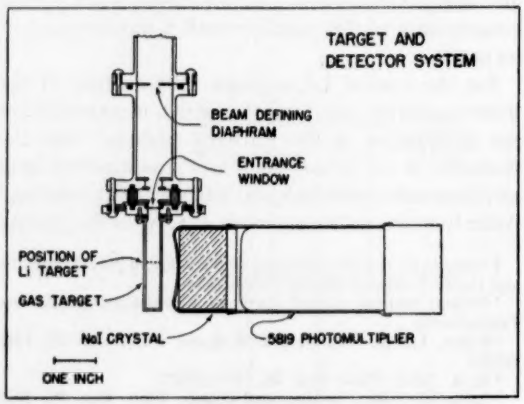

FIG. 2. Experimental arrangement of the target and detector system.

[13] The authors are indebted to Mr. Bailey Donnally of Professor A. O. C. Nier's mass spectrometer group for analyzing the samples of He^3.

[14] R. J. S. Brown, Rev. Sci. Instr. (to be published).
[15] D. Kahn, Phys. Rev. **90**, 503 (1953).
[16] Reynolds, Dunbar, Wenzel, and Whaling, Phys. Rev. **92**, 742 (1953).

to 0.6 Mev. For higher energies, an extrapolation was made using Bethe's formula, normalized to the experimental value at a proton energy of 0.5 Mev. After estimates of various sources of errors, it was concluded that the energy at the center of the chamber was known to ±20 kev.

III. RESULTS

A. Pulse-Height Distribution

When the empty target chamber was bombarded by deuterons, a large background of low-energy pulses was observed. A concerted attempt was made to locate the cause of this background, which led to the conclusion that it originated from all surfaces exposed to the beam. The background was reduced considerably after all the collimators were replaced by freshly cleaned tantalum, and all surfaces exposed to the beam were covered with 1-mil tantalum foil. In the light of later results, it is thought that most of the background of low-energy pulses could be attributed to deuteron bombardment of air adsorbed on the surfaces. In addition, a background of high-energy pulses of about 20 counts/min was observed, which remained constant when the beam was cut off at a point above the target system. This background was attributed to cosmic radiation, and was subtracted from experimental data as a time-dependent background.

A typical differential pulse distribution of the radiation observed from the He^3 enriched gas target bombarded by 0.54-Mev deuterons is shown in Fig. 3. The empty chamber background is shown on the same plot. For comparison, the pulse distribution due to gamma radiation from a LiOH target bombarded by 0.54-Mev protons is also shown. The γ radiation from Li^7+p at this bombarding energy consists of a monoenergetic 17.63-Mev γ ray and a broad 14.8-Mev γ ray, in the ratio of about 2:1.[17] The lack of resolution of the scintillation counter can be attributed to the relatively small crystal used for detection of this high-energy γ radiation.[18]

From comparison with the pulse distribution from Li^7+p, it is concluded that the radiation observed from He^3+d contains a high-energy component, which is not present in the empty chamber background. As will be discussed later, the rapid increase of the distribution for low pulse heights can be largely attributed to a small percentage of air contamination in the He^3 sample.

The end points of the He^3+d and Li^7+p pulse distributions were compared by similar extrapolation of the slope of steepest descent. In order to reduce effects due to gain changes in the photomultiplier and amplifier, comparisons were made as quickly as possible, usually within a few hours. Six comparisons in all were made, which gave an average energy of 16.6±0.2 Mev

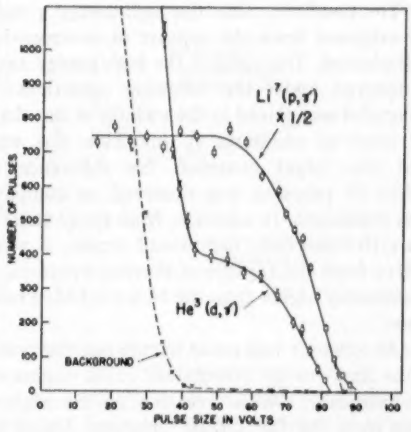

FIG. 3. Pulse-height distributions of the gamma radiation from $d+He^3$, $p+LiOH$, and $d+$empty chamber, at a bombarding energy of 0.54 Mev.

for the extrapolated end point of the He^3+d pulse distribution at a deuteron bombarding energy of 0.45 Mev, assuming a linear relation between quantum energy and pulse height. The error of ±0.2 Mev represents a standard deviation obtained from the differences of the six values from the mean. An outside error of ±0.6 Mev would include all the individual determinations.

B. Identification

Several checks were made to establish the identity of the high-energy radiation observed from enriched He^3 bombarded by deuterons.

(1) It was verified that the pulses observed were caused by high-energy γ radiation emitted from the He^3 target, rather than from neutron capture γ radiation in the NaI crystal. This result was obtained by comparing the absorption in lead of the He^3+d radiation to the absorption of the Li^7+p radiation. The decrease in the number of pulses above 50 volts was measured as a function of lead absorber thickness. The absorption curves observed for both radiations were found to be similar. The experimental results of Adams[19] were used to give the variation of the absorption coefficient in lead as a function of γ-ray energy. After taking into account the presence of the two components in the Li^7+p γ radiation, it was found that the high-energy component of the radiation from He^3+d had an absorption coefficient corresponding to a γ-ray energy of 16±3 Mev.

(2) It was shown that the high-energy γ radiation was emitted from the He^3 contained in the chamber gas. Pulse distributions were observed for deuteron bombardment of the chamber filled with normal helium, hydrogen, and air. In all cases, the high-energy component observed from He^3+d was absent.

[17] R. L. Walker and B. D. McDaniel, Phys. Rev. **74**, 315 (1948).
[18] J. G. Campbell and A. J. F. Boyle, Australian J. Phys. **6**, 171 (1953).
[19] G. D. Adams, Phys. Rev. **74**, 1707 (1948).

(3) The possibility that the high-energy γ radiation might originate from the capture of neutrons by He^3 was eliminated. The yield of the high-energy radiation was observed under the following conditions: (a) 8 lb of paraffin was placed in the vicinity of the chamber; (b) a layer of cadmium $\frac{1}{16}$ in. thick was wrapped around the target chamber. No difference within statistics (2 percent) was observed as compared to normal conditions. In addition, from the Q value of the $He^3(n,\gamma)He^4$ reaction, one would expect a γ ray of 20.5 Mev from the capture of thermal neutrons, which is considerably higher than the 16.6 ± 0.2 Mev radiation observed.

(4) An attempt was made to rule out the possibility that the high-energy γ radiation could originate from some secondary nuclear reaction of the high-energy protons from the $He^3(d,p)He^4$ reaction. Under normal conditions, the protons passed through 1 mil of tantalum, and were stopped in the 0.050-in. stainless steel wall of the target chamber. For this investigation, the target chamber was lined with 0.038 in. of lead, so that the high-energy $He^3(d,p)$ protons were exposed only to lead. The yield of the high-energy γ radiation from He^3+d was observed to be the same as before within 6 ± 5 percent, after correction for the added absorption of the lead lining. Hence the possibility that the γ radiation from He^3+d could be attributed to a secondary reaction becomes very unlikely. Additional evidence for this conclusion comes from the fact that the excitation curve for the He^3+d γ radiation was found to differ from the known excitation curve for the $He^3(d,p)He^4$ protons.[9,10]

(5) The remaining possibility to be eliminated was that the high-energy γ radiation might originate from an excited state of He^4 formed from the $He^3(d,p)He^4$ reaction rather than from the $He^3(d,\gamma)$ capture process. This possibility can be readily investigated, since the energy of a γ ray emitted from an excited state of a product nucleus should be independent of deuteron bombarding energy. On the other hand, one expects the energy of the $He^3(d,\gamma)$ capture radiation observed at 90° to depend on deuteron bombarding energy in the following manner:

$$\Delta E_\gamma = \Delta E_d m_{He^3}/(m_{He^3}+m_{D^2}) = 0.6E_d.$$

The end point of the γ-ray pulse distribution from He^3+d was measured at deuteron energies of 2.59 and 0.58 Mev. The resultant shift was found to be 5.8 ± 1.0 volts, corresponding to a change in γ-ray energy of 1.3 ± 0.2 Mev. The expected change for $He^3(d,\gamma)$ capture radiation is 1.21 Mev. The quoted error in the energy shift comes from estimates of the errors involved in locating the extrapolated end points of the two distributions, and does not take into account any gain change while the machine energy was being lowered. If this error is not underestimated, then this result indicates that the γ radiation can only originate from deuteron capture on a very light element. For instance, the expected shift in γ-ray energy for $C^{12}(d,\gamma)$ would be 1.71 Mev. Since the high-energy radiation was not observed with hydrogen, He^4 or air in the chamber, and one would not expect Li, Be, or B in the chamber, the observed γ-ray energy shift indicates that the only possible assignment is to the $He^3(d,\gamma)$ capture.

An attempt was made to observe the Doppler shift of the γ-ray energy, which would have unambiguously assigned the γ radiation to a reaction involving a very light element. However, with the experimental arrangement used, it was found to be impossible to make a reliable measurement of the Doppler shift, because of difficulties caused by background and gain instability.

It was concluded that most of the rapid rise for pulses below 40 volts (see Fig. 3) could be attributed to air contamination of the He^3 gas. In the case of the $He^3(d,\gamma)$ results shown in Fig. 3, a pressure increase of up to 5 percent was observed, which was attributed to an air leak. The yield of γ radiation from a known amount of air in the target chamber was compared to the He^3+d pulse distribution, after subtraction of the pulses due to the high-energy component. The rapid rise of low-energy pulses could be well fitted by assuming that the pressure increase was caused by air leaking into the target chamber. In another run of 6.5 hours, when there was no indication of an air leak, the low-energy pulses from He^3+d could be accounted for by the presence of 0.9 ± 0.3 percent of air contamination. At the end of the experiment, a sample of He^3 gas was extracted from the target chamber after a two-hour run. Analysis of this sample by a mass spectrometer indicated an air contamination of 0.27 percent to 0.54 percent. It was concluded that an air contamination of this magnitude could account for the low-energy pulses observed from He^3+d, for runs without known air leaks, within the reliability of the data. Evidently this air contamination originated from the outgassing of the target chamber walls and gas inlet, since the He^3 was free from air contamination when first inserted in the chamber. However, because of the high yield of γ rays of energy less than 9 Mev from air contamination, one cannot rule out the possibility that a $He^3(d,\gamma)Li^{5*}$ γ ray of less than 9 Mev may be present with an intensity comparable to that of the high-energy component.

C. Excitation Curve

The yield of the high-energy $He^3(d,\gamma)$ radiation was measured from 0.2 to 2.85 Mev, using the experimental arrangement of Fig. 2. Later, an improved collimating system was inserted which gave current collection reliable to ±3 percent, and the excitation curve was remeasured using the 3.31-cm target chamber for bombarding deuteron energies from 0.17 to 2.42 Mev. The results of this are shown in Fig. 4. From the lowest to the highest bombarding energy, the energy loss in the entrance window varied from 260 to 130 kev,

while the loss in the He^3 gas varied from 100 to 25 kev. The energy scale plotted in Fig. 4 represents the estimated deuteron energy at the center of the chamber, considered reliable to ± 20 kev.

Most of the data for the excitation curve were obtained by counting all the pulses greater than 55 volts (see Fig. 3). However, at energies above 1.7 Mev, it was found that some pulses were being recorded from the tail of the rapid increase of low-energy pulses, amounting to 18 percent at the highest bombarding energy. In order to eliminate this source of uncertainty, pulses above 65 volts were also counted for the higher bombarding energies. After the highest energy point was obtained, repeat runs were made at $E_d=0.91$ and 0.41 Mev, in order to estimate any possible gain changes. No gain change was observed within the combined statistical errors of ± 4 percent.

Several corrections were applied to the original data to obtain the excitation curve plotted in Fig. 4. A background correction, averaging 5 percent, was made, estimated from the background observed from the empty chamber. To the three highest energy points, taken at the integral bias setting of 55 volts, corrections of up to 18 percent have been subtracted to eliminate the contribution of the low-energy rise mentioned above. A correction was also made for the change of the He^3+d capture γ-ray energy with bombarding energy, since the bias setting was not changed for the measurement of the excitation curve.

In addition, a correction was applied for the effect of multiple scattering in the entrance window. The root-mean-square spatial angle was calculated using Molière's theory[20] and was found to be 10° at the lowest bombarding energy. The effective reduction of deuteron path length in the target was estimated by numerical integration, taking the finite area of the beam into account. This resulted in a correction of $+18\pm 5$ percent to the lowest point on the excitation curve; however, this correction rapidly decreased to only $+2$ percent at $E_d=0.49$ Mev. Hence, multiple scattering caused very little effect on the general shape of the observed excitation curve.

The data obtained for pulses greater than 65 volts have been normalized to the points for pulses greater than 55 volts, essentially using the ratio observed at $E_d=0.41$ Mev. In addition to the data shown in Fig. 4, earlier measurements of the excitation curve were made at about 100-kev intervals to a maximum bombarding energy of 2.85 Mev. These data indicate that the yield varied smoothly between the points plotted in Fig. 4, but because of gain changes which occurred during these measurements, the earlier data are not considered to be as reliable as the data shown. A maximum is observed in the excitation curve at a bombarding energy of 0.45 ± 0.04 Mev.

[20] G. Molière, Z. Naturforsch. **3A**, 78 (1948); W. C. Dickenson and D. E. Dodder, Rev. Sci. Instr. **24**, 428 (1953).

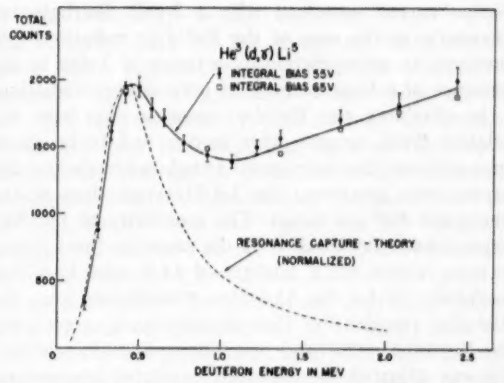

FIG. 4. Excitation curve for the $He^3(d,\gamma)Li^5$ reaction. The solid curve was drawn through the experimental points. The dotted curve shows the contribution expected from resonance capture alone, calculated using dispersion theory with level parameters found for the $He^3(d,p)$ He^4 reaction.

D. Angular Distribution

A rough angular distribution of the high-energy $He^3(d,\gamma)$ radiation was measured using a 66-kev target at $E_d=0.585$ Mev, slightly above the peak of the excitation curve. Measurements were made at laboratory angles of 0°, 45°, and 90° with an angular resolution of about 25°. Corrections were made for the effect on the average value of $1/r^2$ due to the extended target and finite size of the crystal, resulting in a net correction of only 3 percent between points taken at 0° and 90°. The largest uncertainty in the measurements (± 5.5 percent) came from the uncertainty of the gain stability during the run, which was estimated from pulse distributions measured immediately following the angular distribution. The total errors, including statistics (3 percent), amounted to about ± 9 percent. From this data, the angular distribution from 0° to 90° appeared to be isotropic within ± 10 percent.

E. Absolute Cross Section

The absolute cross section for production of the high-energy $He^3(d,\gamma)$ capture γ radiation at $E_d=0.45$ Mev has been computed from the observed yield of γ rays in two ways.

(1) The first method was based on a comparison with the yield of γ rays from the $Li^7(p,\gamma)$ reaction.[21] To obtain the relative number of γ rays counted from the two reactions, differential pulse distributions for both the $He^3(d,\gamma)$ and $Li^7(p,\gamma)$ reactions were measured (Fig. 3). In each case the total number of γ rays producing pulses in the NaI crystal was estimated from the observed integral count above a convenient bias level and the shape of the differential pulse distri-

[21] Fowler, Lauritsen, and Lauritsen, Revs. Modern Phys. **20**, 248 (1948); and revision by W. A. Fowler and C. C. Lauritsen, Phys. Rev. **76**, 314 (1949).

bution curves (obtained with a 3-volt discriminator channel). In the case of the $He^3(d,\gamma)$ radiation, this involved an extrapolation by a factor of 3 due to the presence of a large amount of lower-energy radiation.

In obtaining the $He^3(d,\gamma)$ cross section from the relative yield, several other factors had to be taken into account. The average solid angle subtended by the crystal was greater at the LiOH target than at the elongated He^3 gas target. The sensitivity of the NaI crystal was calculated to be the same for the $Li^7(p,\gamma)$ γ rays, which are a mixture of 14.8- and 17.6-Mev radiation, as for the 16.6-Mev γ radiation from the $He^3(d,\gamma)$ reaction.[17,22] The absolute thick target yield for the 441-kev $Li^7(p,\gamma)$ resonance quoted in reference 21 was adjusted for the contribution of nonresonant radiation to the thick target yield, since the $Li^7(p,\gamma)$ yield in this experiment was measured at a proton energy of 0.54 Mev.

The $He^3(d,\gamma)$ radiation was assumed to be isotropic, in accordance with our rough measurements. On this basis, the total cross section for production of high-energy $He^3(d,\gamma)$ capture radiation at the peak of the excitation curve is calculated to be $(0.57\pm0.10)\times10^{-28}$ cm^2. Individual determinations of this value were consistent to within 10 percent; however, because of uncertainties in the extrapolation of the differential pulse distribution, and in the estimation of the relative solid angle subtended by the crystal at the targets, a larger estimate of error is quoted.

(2) As a check on the first method, a calculation was also made of the absolute sensitivity of the NaI crystal for 16.6-Mev γ rays. This calculation was based on the γ-ray cross sections contained in reference 22. Therefore, it does not depend on the absolute value of the $Li^7(p,\gamma)$ yield, but does contain the same solid angle calculation and extrapolation of the pulse-height distribution to zero pulse height. This method results in a maximum cross section for the $He^3(d,\gamma)$ high-energy γ radiation of $(0.37\pm0.10)\times10^{-28}$ cm^2. Two experimental determinations of this value were consistent to 5 percent, but a larger error is estimated for the same reasons as for the other method.

IV. CONCLUSIONS

The radiative capture of deuterons by He^3 seems to be well estabilshed. The total cross section is measured to be $(0.5\pm0.1)\times10^{-28}$ cm^2 at $E_d=0.45$ Mev. The energy of the γ ray is 16.6 ± 0.2 Mev at this deuteron energy. A rough measurement of the angular distribution indicates isotropy to within ±10 percent slightly above the resonance energy. This is consistent with the formation of the state by s-wave deuterons as is also indicated by the isotropy of the protons from the (d,p) reaction at the same deuteron energy.[10]

[22] C. M. Davisson and R. D. Evans, Revs. Modern Phys. **24**, 79 (1952).

A. Contribution from Resonance Capture

The contribution to the $He^3(d,\gamma)Li^5$ reaction to be expected from resonance capture from the 16.7-Mev level to the $P_{\frac{3}{2}}$ ground state has been calculated using the Wigner-Eisenbud dispersion theory.[23] The parameters a, E_λ; γ_d^2, γ_p^2 have been selected to give a good fit to the (d,p) reaction data of Yarnell *et al.*[10] and Freier and Holmgren[11] in the vicinity of the resonance for this reaction ($E_d=0-1$ Mev). The parameters are:

$$a=7.6\times10^{-13}\text{ cm},\quad \gamma_d^2=5.0\times10^{-10}\text{ kev cm},$$
$$E_\lambda=195\text{ kev},\quad \gamma_p^2=12.8\times10^{-12}\text{ kev cm}.$$

These are the same as used by Bonner *et al.*[9] to fit their $He^3(d,p)He^4$ measurements except for a slightly larger γ_p^2, which was needed to give a total cross section of 0.9 barn at resonance as measured by Freier and Holmgren[11] with somewhat better experimental geometry. Only s-wave deuterons were considered in the calculation. The outgoing protons must be d wave for the breakup of a $J=\frac{3}{2}+$ state. In calculating the level shifts Δ_λ and the total width Γ_λ, the contribution from the radiative width was neglected. For the radiative width Γ_γ, an energy dependence of the form $(\text{const}\times E_\gamma^3)$ was assumed, the constant being adjusted to give a calculated cross section equal to the experimental at $E_d=0.45$ Mev. The calculated resonance contribution to the (d,γ) reaction is plotted as a broken line in Fig. 4.

From Fig. 4 it is apparent that there is a large contribution to the (d,γ) reaction from nonresonant capture above $E_d=0.45$ Mev. As pointed out by Thomas,[24] this is to be expected for such light nuclei, because the large reduced widths of the initial and final states result in a large contribution to the capture cross section from the external region. In fact, the usual perturbation calculation gives an infinite result for the external contribution to the dipole matrix element. This is because both the initial and final state wave functions extend to infinity for virtual states.[25] Further theoretical work is necessary to find a way around this difficulty.

B. Size of the Dipole Matrix Element

The experimental radiative width at the resonance energy deduced from the measured (d,γ) and (d,p) cross sections is $\Gamma_\gamma=11\pm2$ ev. In comparing with the Weisskopf[26] estimate for $E1$ transitions, it is necessary to divide the experimental width by a statistical weight factor of $\frac{1}{3}$ for a $J=\frac{3}{2}\rightarrow\frac{3}{2}$ transition.[27] The

[23] E. P. Wigner and L. Eisenbud, Phys. Rev. **72**, 29 (1947); R. G. Thomas, Phys. Rev. **81**, 148 (1951).

[24] R. G. Thomas, Phys. Rev. **88**, 1109 (1952).

[25] We are indebted to R. G. Thomas for an informative discussion on this point.

[26] J. M. Blatt and V. F. Weisskopf, *Theoretical Nuclear Physics* (John Wiley and Sons, New York, 1952).

[27] D. J. Hughes, Phys. Rev. **94**, 740 (1954).

experimental Γ_γ then corresponds to an electric dipole matrix element 0.043 times the Weisskopf estimate for a radiative transition to the ground state of Li^5. This is of the same order of magnitude as $E1$ matrix elements for other light nuclei.[28] In using Weisskopf's formula, a conventional radius of $R=1.45\times10^{-13}\ A^{\frac{1}{3}}$ cm was used. However, the formula depends on R^2; if $R=a=7.6\times10^{-13}$ cm is used, the experimental Γ_γ is equal to the Weisskopf estimate. In any case, it is not expected that a single-particle model, as used by Weisskopf, would give the correct transition probability for a (d,γ) reaction on such a light nucleus. This is especially true as the 16.7-Mev state of Li^5 appears to be due to an excitation of the α core[8] while the ground state is more nearly a single-particle state.

Transitions from the 16.7-Mev state of Li^5 to a possible $P_{\frac{1}{2}}$ state in the vicinity of 2.5 Mev, relative to transitions to the ground state, should occur in a ratio of $\sim(14.1/16.7)^3\times5=3$ (including the statistical weight factors).[26,27] However, because of the poor resolution inherent in a small NaI crystal and the large background below 9 Mev due to air contamination, nothing can be said experimentally about possible radiative transitions to this $P_{\frac{1}{2}}$ state. It would be interesting to repeat the experiment with a very large NaI crystal and with greater precautions against contamination.

C. The Mass of Li^5

From the measured γ-ray energy, $E_\gamma=16.6\pm0.2$ Mev at $E_d=0.45$ Mev, the Q for the $He^3(d,\gamma)Li^5$ reaction is calculated to be $Q=16.36\pm0.2$ Mev. Using the mass values tabulated by Li *et al.*,[29] this gives the Li^5 ground state at an energy of 1.95 ± 0.2 Mev above He^4+p. The measurements of Almqvist *et al.*[3] on the $He^3(He^3,p)Li^5$ reaction give 1.99 ± 0.15 Mev for the $Li^5-(p+He^4)$ mass difference. The phase-shift analysis of the low-energy $p+He^4$ scattering data[2,6] gives $E_{res}=2.1\pm0.1$ Mev for the energy at which the $P_{\frac{1}{2}}$ phase shift passes through 90°. The $Li^6(\gamma,n)Li^5$ reaction[4,30] gives a somewhat lower value of the $Li^5-(p+He^4)$ difference (1.6 ± 0.2 Mev), but because of the difficulty of interpreting these measurements, they should perhaps be given less weight than the aforementioned. A preliminary report on the $Li^6(d,t)Li^5(p)He^4$ reaction[31] gives a $Li^5-(p+He^4)$ energy difference of 1.6 ± 0.1 Mev. It seems reasonable to adopt a value of 1.9 ± 0.2 Mev for the $Li^5-(p+He^4)$ energy difference. This corresponds to $M(Li^5)=5.0140\pm0.0002$ amu or a mass defect of 13.1 ± 0.2 Mev.

It should be mentioned that both the $He^3(d,\gamma)$ and the $He^3(He^3,p)$ reaction should tend to give somewhat too *low* an energy for the Li^5 ground state because of the large width of this state. In the case of the (d,γ) reaction, the E_γ^3 dependence of the $E1$ transition probability favors leaving the Li^5 system at an energy less than the resonance energy for this state as found from the $p+He^4$ scattering data. A detailed discussion of this effect must await a theoretical treatment of radiative transitions between virtual states with large reduced widths.[25]

It would be interesting, but experimentally more difficult, to look for γ rays from the mirror reaction $T(d,\gamma)He^5$. The large yield of energetic neutrons from the (d,n) reaction would complicate the detection procedures, however. Finally, on the basis of the Li^5 level parameters found here the $He^4(p,\gamma)Li^5$ reaction should have a cross section of $\sim10^{-30}$ cm² at $E_p=23$ Mev, the lab energy required to form the 16.7-Mev state of Li^5.

The authors wish to acknowledge the assistance of Dr. K. F. Famularo in several phases of the experiment. Professor John H. Williams provided encouragement and many helpful suggestions.

[28] D. H. Wilkinson, Phil. Mag. **44**, 450 (1953).
[29] Li, Whaling, Fowler, and Lauritsen, Phys. Rev. **83**, 512 (1951).
[30] Sher, Halpern, and Mann, Phys. Rev. **84**, 387 (1951). See comment on p. 392 on $Li^6(\gamma,n)$ reaction.
[31] R. T. Frost and S. S. Hanna, Phys. Rev. **91**, 462(A) (1953).

Beta Spectrum of C^{14}

H. H. Forster and A. Oswald
Department of Physics, University of Southern California, Los Angeles, California
(Received July 6, 1954)

The beta spectrum from thin sources of C^{14} was measured in a double thin-lens β-ray spectrometer; the momentum spectrum and the Fermi plot are presented. The Fermi plot for a source of approximately 15 $\mu g/cm^2$ is a straight line down to about 30 kev; the experiment therefore indicates an allowed shape for the beta spectrum of C^{14}. Existing experimental evidence to the contrary, that is, for a forbidden spectrum, is discussed and compared with the results of the present experiment.

IN recent years the puzzling fact of the extremely long half-life of C^{14} ($\log_{10} ft \sim 9$) led to several theoretical attempts to interpret the problem in terms of nuclear structure[1,2] rather than from the standpoint of beta-decay theory. On the basis of the long half-life the $C^{14} \rightarrow N^{14}$ transition should be forbidden; on the basis of beta-decay theory the well established change in spin from $0 \rightarrow 1$, taken in conjunction with the recent experimental proof by Bromley and Goldman[3] of no change in parity, leads one to expect an allowed transition in accordance with Gamow-Teller selection rules.

Today the interpretations mentioned above[1,2] are no longer tenable; the experiment by Bromley refutes Gerjuoy's hypothesis of a parity change, that of Van de Graaff *et al.*[4] makes the assumption of pure ^1S (C^{14}) and ^3D (N^{14}) states implausible. Experimentally, on the other hand, the answer to the question of forbidden *versus* allowed transition is not clear-cut either, with some investigators claiming an allowed[5] and some a forbidden[6] shape for the C^{14} beta spectrum.

Under these circumstances, and inasmuch as the question is one of considerable theoretical interest, a re-examination of the shape of the C^{14} spectrum seemed indicated, with special attention to those factors which might affect the curvature of the Fermi plot, e.g., instrumental distortion, uniformity and thickness of the source, window thickness, etc. In the present experiment a double thin-lens spectrometer was used with a resolution of 1.5 percent. The detector in the spectrometer was a GM type counter provided with a Nylon window of ~ 30 $\mu g/cm^2$. The source material was $NaHCO_3$, converted chemically from $BaCO_3$ of high specific activity, obtained from the Isotope Division at Oak Ridge. Thin uniform sources were formed on Tygon films of about 10-$\mu g/cm^2$ thickness. To insure proper position, size, and uniformity of the source, the part of the backing foil on which the source was to be placed was wetted with an aqueous solution of insulin prior to the addition of the radioactive material. Thin narrow strips of aluminum (0.17 mg/cm^2) were placed near the end of the deposit to minimize electrostatic effects caused by charging up of the source. For drying, the sources were placed in a desiccator filled with nitrogen in order to avoid any loss of activity due to exchange with CO_2 in the atmosphere. Autoradiographs of sources made in this manner showed a uniform distribution over the whole area covered by the radioactive material. The Tygon backing used in the comparison of sources of different thickness was made from the same film, thus ensuring that any diversity in the results could be relegated to the difference in the sources, but would be independent of the backscattering in the backing foils.

The momentum distribution of the electrons from C^{14} obtained for sources of approximately 15 $\mu g/cm^2$ (A) and 60 $\mu g/cm^2$ (B) are shown in Fig. 1, the Fermi plot of the beta spectra of sources A and B in Fig. 2. Both figures indicate the distortion of the spectrum of the thicker source due to the excess of low-energy electrons. The Fermi plot is a straight line for both sources; the spectrum of the thin source remains straight to ~ 30 kev, where the effect of window

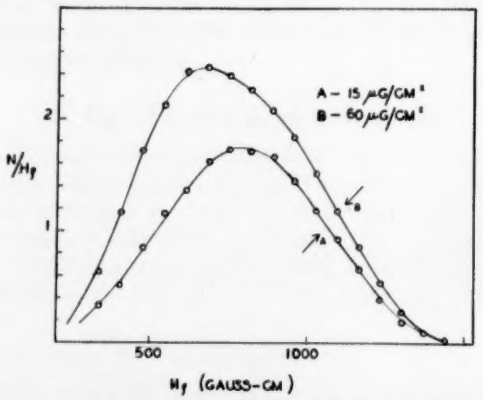

FIG. 1. Momentum distribution of the electrons of C^{14}. The relative number of counts per unit momentum interval is plotted against the momentum in units of gauss-cm.

[1] E. Gerjuoy, Phys. Rev. **81**, 62 (1951).
[2] E. Feenberg and K. C. Hammack, Phys. Rev. **75**, 1877 (1949).
[3] D. A. Bromley and L. M. Goldman, Phys. Rev. **86**, 790 (1051).
[4] Van de Graaff, Sperduto, Buechner, and Enge, Phys. Rev. **86**, 966 (1952).
[5] L. E. Glendenin and A. K. Solomon, Phys. Rev. **74**, 700 (1948); L. Feldman and C. S. Wu, Phys. Rev. **75**, 1286 (1949); C. S. Wu and A. Schwarzschild, Phys. Rev. **91**, 483 (1953).
[6] J. L. Berggren and R. K. Osborne, Phys. Rev. **74**, 1240 (1948); Cook, Langer, and Price, Phys. Rev. **74**, 548 (1949); Angus, Cockraft, and Curran, Phil. Mag. **40**, 522 (1949); S. D. Warshaw, Phys. Rev. **80**, 111 (1950).

absorption in the counter becomes noticeable. The thick source deviates from linearity at ~45 kev, where the experimental points rise above the straight line, indicating thick source distortion. A still thicker source of ~90 μg/cm² (not shown in the diagram) remained straight to ~60 kev, where it also deviated upward. The extrapolated end point for all sources occurred at 155.0±1 kev, in good agreement with the results of other investigators.[5,6]

The results of this experiment, therefore, yield an allowed shape for the beta spectrum of C^{14}. Allowed distributions can be obtained under certain conditions for forbidden transitions; however, whatever the explanation of the long half-life, the other characteristics of the $C^{14} \rightarrow N^{14}$ decay ($\Delta I = 1$, no) put it into the class of allowed transitions in accordance with Gamow-Teller selection rules.

In the light of the present experiment it seems of interest to re-evaluate the experimental evidence for a forbidden spectrum. The spectrum observed by Angus *et al.* gave a straight Kurie plot between 50 and 130 kev. Near the endpoint the authors found a slight excess of particles; below 50 kev the experimental points fell below the straight line, indicating a rapid decrease in intensity toward zero at a few kev. However, it may be argued that the departure from linearity is not too significant inasmuch as the spectrum remains straight over the major part of the energy range; and that near the endpoint the small number of pulses may give rise to an error in the counting rate. The deficiency of low-energy electrons is more difficult to understand since the source material was introduced directly into the counter; yet it also may be traceable to some instrumental distortion. As for the other experiments yielding a forbidden shape of the beta

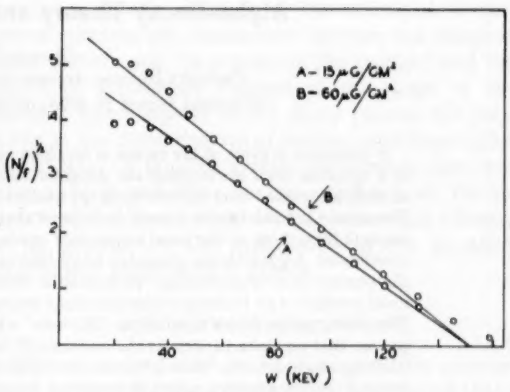

FIG. 2. Fermi plot of C^{14}.

spectrum, Bergeren and Osborne found that for an average source thickness of ~100 μg/cm² the departure from a linear Kurie plot was ~3 percent. According to Cook *et al.*, the slight curvature of the Fermi plot was independent of source thickness for sources ranging from 130–970 μg/cm². On the other hand, Warshaw found that a thick source (180 μg/cm²) gave a straight line plot above 80 kev, while a thin source (60 μg/cm²) was convex to the energy axis within the same energy range; the departure from linearity was of the order of 3 percent. All of the experiments described above had in common the use of thicker sources than were studied in the present experiment. Moreover, "average" source thickness may become meaningless if nonuniform deposits produce local variations in grain density resulting in thick source distortions. A systematic departure from linearity of the order of 3 percent could not have escaped detection in our experiment.

Alpha-Decay Theory and a Surface Well Potential

GEORGE H. WINSLOW
Chemistry Division, Argonne National Laboratory, Lemont, Illinois
(Received August 28, 1953; revised manuscript received July 2, 1954)

A discussion is given of the escape of an alpha particle from a square-well potential which is in the form of a spherical shell surrounding the daughter nucleus. In the present approximation the alpha particle, as such, is excluded from the interior of the nucleus by making the one-body potential infinite in that region. The usual Coulomb barrier is used. It is found that the properties of this model differ in several important respects from those of the usual square-well one-body model, in which the well is located at the origin of coordinates. Arguments are presented which lead to the representation of the many-body decay constant as the product of a dimensionless "preformation factor" and a one-body decay constant, as opposed to the usual product of an intrinsic nonbarrier decay constant and a dimensionless barrier transmission coefficient. The preformation factor involves an "intrinsic" alpha-decay probability and, in addition, the probability per sec that an alpha particle at the nucleus will be absorbed as nucleons. The nuclear physics problem of deriving expressions for these latter two probabilities is not considered, but examples are given which can be used to show expected ranges of numerical values of the preformation factor when the one-body model is either the present one or the usual one.

I. INTRODUCTION

THE potential function traditionally used in the derivation of the alpha-decay constant consists of a square well which is located at the origin of coordinates and which is surrounded by the Coulomb interaction between the daughter nucleus and the alpha particle. The radius of the well is associated with that of the daughter nucleus or with that of the daughter plus an "effective" alpha-particle radius or nucleus-alpha interaction distance. The phrase "one-body decay constant," if not further modified, will be used in this paper in a general sense to mean a decay constant found by treating the motion of an *existing* alpha particle in *any* specified potential which is set up to represent the interaction between the alpha particle and the daughter atom. The treatment is generally of the nature of a straight exercise in quantum mechanics, although the care with which it is done varies. The result is such that if the parameters of the potential function and the relative angular momentum are specified, the corresponding decay energy and decay constant are always, in principle at least, calculable. Such a derivation made with the particular potential described above will be referred to here as the traditional one-body model.

The application of similar ideas and methods to the problem of nuclear cross sections is discussed in the text by Gamow and Critchfield,[1] for instance. It is shown there that the spacing of nuclear levels predicted with the use of the traditional type square-well one-body model for nucleons is much greater than is observed experimentally. Such results led long ago to the realization that these methods were inadequate.

The principal efforts to discuss the many-body problem involved in nuclear processes have been based on the method of Feshbach, Peaslee, and Weisskopf.[2] Briefly, it is considered in this method as presently developed that there is a radius R such that the usual one-body wave functions can be written when $r>R$. An equation is found for the logarithmic derivative of this outside function at $r=R$. Arguments are then made without the use of any particular model of the nuclear interior, i.e., without the use of any particular potential function in $r<R$, as to what should be the properties of the function to which this logarithmic derivative is to be equated. The property of particular interest is the dependence on energy. These arguments lead to a function whose form is the same as would be given by the logarithmic derivative of the traditional one-body inside wave function for zero relative angular momentum but with the argument of its periodic factor replaced by $(\pi/D^*)(E-E_r)$, in the neighborhood of the resonance energy E_r. Here D^* is an energy of the order of the average level spacing between levels of the same angular momentum and parity. The inside wave number at the nuclear surface remains in evidence as a multiplier of the periodic factor. Hence the nucleus is characterized by this wave number, the radius, and the level spacing.

The extension of this (resonance) theory into the higher energy region where the level widths are greater than their spacing and continuum theory should apply has been discussed by Feshbach and Weisskopf.[3] The method has been used in this range by Shapiro,[4] for instance, to calculate cross sections for formation of a compound nucleus by protons, deuterons, and alpha particles. It has been used in the resonance region by Devaney,[5] for instance, to discuss alpha decay. The method and, of particular interest here, Devaney's

[1] G. Gamow and C. L. Critchfield, *Theory of Atomic Nucleus and Nuclear Energy Sources* (Clarendon Press, Oxford, 1949), p. 217.

[2] Feshbach, Peaslee, and Weisskopf, Phys. Rev. **71**, 145 (1947).
[3] H. Feshbach and V. Weisskopf, Phys. Rev. **76**, 1550 (1949).
[4] M. M. Shapiro, Phys. Rev. **90**, 171 (1953).
[5] J. J. Devaney, Phys. Rev. **91**, 587 (1953).

application of it are also discussed in the text by Blatt and Weisskopf.[6]

A picture will be presented here which involves an additional step in the transition between the compound nucleus (or parent) and the separated particle and target (or daughter) nucleus. It is believed to be particularly suitable to the discussion of processes which involve the compound particles, deuterons [where the usual compound nucleus, $C(Z+1, A+2)$ in this case, is formed], and alpha particles, since neither of these are fundamental constituents of nuclei. Wider application is believed to be possible but only the process of alpha decay will be considered here.

A relation will be found between the many-body alpha decay constant, i.e., the experimentally observed decay constant, and a one-body decay constant. It will be shown that, granted the assumptions, the many-body decay constant should be represented as the product of a dimensionless "preformation factor" and a one-body decay constant. The implication is that the solution of the problem of alpha decay would be obtained by finding as independently as possible expressions for *each* of these two factors which most nearly fit the observations on alpha decay or any related observations that could be made. In particular, it is assumed that the traditional model is not necessarily the only, or even the best, representation of the one-body aspects of the problem of alpha decay.

The first part of this paper (Secs. II and III) will be concerned with the details of a possible alternative one-body model. This model will be found to have properties interestingly different from those of the traditional model. It is suggested, but not required, by the picture of the alpha decay process which will be used subsequently (Sec. IV) to discuss the relation between the many-body and a one-body decay constant.

The nature of the quantities which constitute the preformation factor will also appear in this latter discussion. No attempt will be made to solve the problem in nuclear physics which would lead to expressions for them, although some estimates will be made by relating them to quantities now in the literature. Some numerical examples which will be used in the comparisons between the present one-body model and the traditional model can also be used to show the range of values in which the total preformation factor ought to lie, when either of these two models is used as the basis of the accompanying one-body decay constant.

This one-body—many-body problem is certainly one of the more important problems in alpha-decay theory. Nevertheless it should not be forgotten that there are other important problems, none of which will be discussed here. Among these are the effects of nuclear shape associated with the presence of quadrupole moments,[7] a specific example of the effects of a non-central electrostatic interaction between the escaping alpha particle and the protons in the residue,[8] and the effects of appropriate changes in the shape of the barrier.[9] These aspects of the decay process will play a role in the determination of nuclear radii from alpha decay data. Of possibly greater importance, they will have a significant effect on the correlation of, for instance, alpha-decay constants and nuclear spin change, or, in general, on the explanation of the so-called "forbidden" alpha-particle groups.

II. THE SURFACE WELL MODEL

The one-body model to be discussed here can be based on the following arguments. It is presumed that: (a) an alpha particle does not exist *in* a nucleus; (b) in the absence of the external Coulomb field there would be an attractive interaction between the daughter nucleus and the alpha particle which would be very strong at the instant of the appearance of the latter at the nuclear surface, but which would approach zero very strongly as the two separated.

The existence not only of the particular Coulomb potential which applies in alpha decay, but also that of the potential in $r<R$, in other words the existence of a potential for the discussion of the motion of an alpha particle, depends on the existence of the alpha particle. Some different potential even in $r<R$ would be appropriate for neutrons, for instance. Thus, in a one-body interaction potential between the daughter nucleus and the existing alpha particle, a region from which the latter is excluded can be represented by an infinite potential in that region without implying any such peculiarities in the potential appropriate for fundamental particles. The potential near the nucleus indicated by the arguments of the preceding paragraph is a well at the nuclear surface. A potential of this type has been referred to as a Jastrow potential by Greenberg.[10] Jastrow[11] used it, with an exponential form for the nuclear interaction, to discuss nucleon-nucleon scattering. Its use in more general applications is apparently being made by Greenberg. In the present paper the net potential for the one-body alpha decay problem will be approximated by a square well at the nuclear surface surrounded by the usual sharply cut-off Coulomb interaction as illustrated in Fig. 1. In this figure, R is the channel radius as usually defined; that is, it is the location of the center of charge of the alpha particle when

[6] J. M. Blatt and V. F. Weisskopf, *Theoretical Nuclear Physics* (John Wiley and Sons, Inc., New York, 1952). For alpha decay see p. 568.

[7] See, for instance, D. L. Hill and J. A. Wheeler, Phys. Rev. **89**, 1102, 1133 (1953).

[8] See, for instance, M. A. Preston, Phys. Rev. **82**, 515 (1951); S. M. Dancoff, Atomic Energy Commission Unclassified Report AECD-2853 (unpublished).

[9] See, for instance, M. L. Chaudhury, Phys. Rev. **88**, 137 (1952).

[10] J. M. Greenberg, Phys. Rev. **87**, 209 (1952).

[11] R. Jastrow, Phys. Rev. **79**, 389 (1950); **81**, 165 (1951); **91**, 749 (1953). See also M. M. Levy, Phys. Rev. **86**, 806 (1952) and reference 6, pp. 170, 186, 187, and 300.

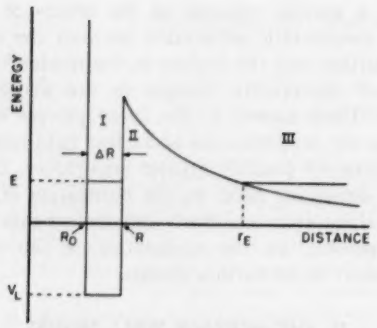

FIG. 1. The potential function for the surface well model. R_0 is taken to be the radius of the alpha daughter, R is the channel radius and $\Delta R = R - R_0$. The exterior classical turning point is at r_e.

the nucleus and the alpha particle just begin to overlap in the sense that nuclear interaction begins.

This "overlap" situation is usually particularized by thinking of the nucleus and the alpha particle as being well defined spheres which, if they approach each other, do not interact until their surfaces are in contact. If it is also supposed that the center of charge of the alpha particle is at the center of the alpha particle, then this highly idealized picture requires that the channel radius be the sum of the radii of the two spheres. Further, it must be considered that the alpha particle is entirely outside the nucleus when the center of charge of the alpha particle is at a vanishingly small distance outside the channel radius R.

The present object is the investigation of a model in which wave functions are written for a well formed alpha particle only in those regions where the alpha particle is entirely outside the nucleus, but to write them everywhere in those regions. One can continue with the idealized picture described above by supposing that the alpha particle is said to be absorbed as nucleons into the nucleus when more than half of the alpha particle sphere has penetrated the nuclear surface. Then in Fig. 1, R_0 and ΔR would be designated as the radius of the daughter nucleus and the alpha particle, respectively. The potential for a well formed alpha particle in $r<R$ is drawn as a well at the nuclear surface to indicate the assumptions that a well formed alpha particle does not exist in $r<R_0$ and that there is a Coulomb barrier for well formed alpha particles, i.e., that the potential energy of a well formed alpha particle close to the nuclear surface is less than $(2Ze^2/R)$.

The description entailing the assignment of such sharply defined radii to the two particles and the specification of the location of the center of charge of the alpha particle is more detailed than is warranted or probably necessary. If the assumptions mentioned in the previous paragraph are granted, it should be sufficient to retain the definitions of R and R_0 and to designate ΔR and the well depth simply as parameters which describe the attractive nuclear interaction in that approximation which consists of a square well at the nuclear surface.

A relation between the observed (many-body) alpha decay constant and one derived with any one-body model will be proposed in Sec. IV. One aspect of the mechanism to be used, the possible reabsorption of a well formed alpha particle into the nucleus as nucleons rather than its emission to the outside region, has been indicated already. The assumption of the possibility of such a process means that the potential function for a well formed alpha particle cannot be conservative. It will be argued later, however, that the mean life of an existing well formed alpha particle prior to emission or reabsorption is sufficiently long to allow one to write alpha particle wave functions in that part of the region $r<R$ which is available to it, but only for those periods during which it is in existence. Thus the potential might be called "quasi-conservative."

An additional question arises with specific regard to the potential function of Fig. 1. One might consider an approach to the problem of deriving the preformation factor, as opposed to the phenomenological arguments used in Sec. IV to show its existence, by setting up equations to represent a smooth outward flow of probability at a rate appropriate to the observed decay constant. The net current of well formed alpha particles out of the region in which they do not exist would be obtained by the use of an imaginary term in the potential in that region. Such a treatment might possibly, but not certainly, indicate that a large imaginary potential rather than a large real potential and a small imaginary potential, would be more appropriate in $r<R_0$. Either would give a small net current; that is, the limiting case of an infinite imaginary potential also leads to a node in the wave function at $r=R_0$, so that the discussion to be given here would not be altered by such a change.

During those periods when the potential of Fig. 1 applies, and if these periods are sufficiently long, one has the conventional picture of a well formed alpha particle attempting to penetrate a potential barrier. The only difference during such periods between this and the traditional one-body model, for instance, is in the size and location of the region available to the alpha particle prior to decay; the barrier is the same.

The principle object of this section, then, is to examine the characteristics of this phase of the process by discussing a one-body model based on the potential function of Fig. 1. Its inclusion in a many-body model of alpha decay will be discussed thereafter. The one-body equations to be derived here have been identically reproduced by the method of complex eigenenergies introduced by Gamow[12] and by Bethe's quasi-stationary state method.[13] The former method is faster (although

[12] See reference 1, p. 156. Also see E. C. Kemble, *The Fundamental Principles of Quantum Mechanics* (McGraw-Hill Book Company, Inc., New York, 1937), p. 192.

[13] H. A. Bethe, Revs. Modern Phys. 9, 69, 161 (1937).

more formal than instructive) and will be used here. It has been used by Devaney[5] and by Preston[14] and, of course, much of the content of the derivation is contained in their work. It is convenient to reproduce it in its entirety, however, for ease of continuity and because it is desired to keep a term which is somewhat more important in this model than it was in their work. It also seems desirable to use, where convenient, the nomenclature of the Coulomb functions[15] which, when multiplied by $(1/r)$, are the solutions of the radial wave equation for this problem in that region where the Coulomb interaction applies.[16]

Devaney[5] has pointed out that previous alpha decay models are included as special cases of his discussion. In general, his procedure will be followed so that this will be true here also. Thus the first results will be in terms of the logarithmic derivative at the place $r=R$.

Let the complex energy be given by

$$W=E-(i\lambda\hbar)/2. \tag{1}$$

The radial wave function must be of the form $(1/r)\phi(r)$. Far out in the region beyond the barrier, Region III (see Fig. 1) $\phi(r)$ must have the form

$$\phi^{\mathrm{III}}(r)\propto A\exp(i\rho), \tag{2}$$

where

$$\rho=kr, \tag{3}$$

$$k=[(2MW)^{\frac{1}{2}}/\hbar], \tag{3a}$$

and M is the reduced mass of the alpha particle. The expression on the right side of Eq. (2) must be that approached at large distances by

$$\phi^{\mathrm{III}}(r)=PG_L+QF_L, \tag{4}$$

where G_L and F_L are the irregular and regular Coulomb functions, respectively, for relative angular momentum quantum number L.

From consideration of the asymptotic expressions for the Coulomb functions,[15] it is seen that

$$Q=iP. \tag{5}$$

Hence, in the barrier, Region II,

$$\phi^{\mathrm{II}}(r)=P(G_L+iF_L). \tag{6}$$

It is shown in the Appendix that in this region, provided that r is not too near the classical turning point, r_E (see Fig. 1), the Coulomb functions can be accurately represented by

$$G_L=|\Phi(\rho)|^{-\frac{1}{2}}\exp[\omega(\rho)], \tag{7}$$

$$F_L=(1/2)|\Phi(\rho)|^{-\frac{1}{2}}\exp[-\omega(\rho)], \tag{8}$$

where

$$|\Phi(\rho)|=2\eta/\rho+(L+\tfrac{1}{2})^2/\rho^2-1, \tag{9}$$

$$\omega(\rho)=\int_{\rho}^{\rho_E}|\Phi(\xi)|^{\frac{1}{2}}d\xi, \tag{9a}$$

$$\eta=(z'Ze^2/\hbar)[M/(2W)]^{\frac{1}{2}}, \tag{9b}$$

and z' and Z are the atomic numbers of the alpha particle and daughter nucleus, respectively.

If by definition

$$f^{\mathrm{II}}/(kR)\equiv[(\phi^{\mathrm{II}})^{-1}(d\phi^{\mathrm{II}}/d\rho)]_{kR}, \tag{10}$$

then

$$f^{\mathrm{II}}=-kR|\Phi|^{\frac{1}{2}}\frac{(1+\gamma)-(i/2)(1-\gamma)\exp(-2\omega)}{1+(i/2)\exp(-2\omega)}, \tag{11}$$

where

$$\omega=\omega(kR), \tag{12}$$

$$|\Phi|=|\Phi(kR)|, \tag{12a}$$

and

$$\gamma=\tfrac{1}{4}|\Phi|^{-1}[d|\Phi(\rho)|/d\rho]_{kR}. \tag{12b}$$

The number γ which arises from the differentiation of $|\Phi(\rho)|^{-\frac{1}{2}}$ in Eqs. (7) and (8) was omitted by Preston[14] and by Bethe.[13] It would be contained in Devaney's[5] v'. Its value will generally be about -0.02.

Equation (1) is now to be used to replace W wherever it occurs in Eq. (11) and separation is then made into real and imaginary parts to the first power of $\exp(-2\omega)$ or of λ. The term which arises from keeping the first power of λ is the one mentioned previously, which was

[14] M. A. Preston, Phys. Rev. **71**, 865 (1947).

[15] For references and discussion see Bloch, Hull, Broyles, Bouricius, Freeman, and Breit, Revs. Modern Phys. **23**, 147 (1951).

[16] Actually the Coulomb functions would apply to the problem of the decay of a bare nucleus. Nevertheless they will be used here, although a correction will be made for the potential produced at the nucleus by the atomic electrons, when calculations are made. G. Ambrosino and H. Piatier, Compt. rend. **232**, 400 (1951), suggested that the potential energy should be corrected as above and that the total energy should be corrected for the difference in total electron binding energy between the parent and the daughter. Rasmussen, Thompson, and Ghiorso, University of California Radiation Laboratory Report UCRL-1473, September, 1951 (unpublished), quoted (as then) unpublished work of Serber and Snyder as showing that if one makes both of these corrections, he is correcting for the same thing twice. In their own subsequent publication, R. Serber and H. S. Snyder, Phys. Rev. **87**, 152 (1952), did not use this particular phraseology but their arguments show that it is so. In the case of alpha decay of a heavy element it is found that even were the alpha-particle velocity very high compared to any orbital electron velocity (which it is not), so that the electrons would undergo no rearrangement during the passage of the alpha particle, the excitation energy of the residue would be only about 500 ev. The principal part of the electron binding energy difference between the parent and daughter atoms is due to the charge change at the nucleus, and only a negligible part of it is due to the rearrangement of the electrons. Since the residue is (essentially) the daughter *atom* in a very nearly unexcited state, the observed alpha-particle kinetic energy plus the recoil energy is the total energy as generally defined. Further it is the proper total energy to use in calculations regarding the (experimentally observed) decay of *atoms*, provided that the potential used is also that in the *atom*, i.e., the *screened* nuclear-alpha Coulomb potential. In *effect*, the screening correction to the potential energy can be made, it turns out, by adding the electron binding energy difference to the observed decay energy in those terms arising from the region $r>R$ and then using the unscreened potential. For references and discussion of this problem as it applies to beta decay, see Freedman, Wagner, and Engelkemeir, Phys. Rev. **88**, 1155 (1952).

omitted by Devaney and Preston but which is of somewhat greater importance in the surface well model. A further remark on the source of this term will be made later, in Sec. III, when more details will be given on exactly what is meant here by the traditional model.

The result of the separation of Eq. (11) into real and imaginary parts is

$$f^{II}=-kR|\Phi|^{\frac{1}{2}}(1+\gamma)+i\{kR|\Phi|^{\frac{1}{2}}\exp(-2\omega)-[MR\lambda(1-\gamma)]/[2\hbar k|\Phi|^{\frac{1}{2}}(1+\gamma)]\}. \quad (13)$$

The nomenclature used in Eq. (11) is repeated in Eq. (13), but it is to be understood that where the energy appears in the latter it is the real part E. A factor $(1-2\gamma)$ in the last term on the right side of Eq. (13) has been replaced by the ratio $(1-\gamma)/(1+\gamma)$ for convenience. Not only is γ small, but the term itself is small.

It is now necessary to discuss the function to which f^{II} is to be equated, i.e., the corresponding function f^{I} in Region I at $r=R$. Following Feshbach *et al.*,[2] this function is written as

$$f^{I}=f^{I}(E)-[(i\lambda\hbar)/2](\partial f^{I}/\partial W)_{E}, \quad (14)$$

since the second term in Eq. (1) is, in absolute value, so small compared to the first. Upon equating f^{I} and f^{II} it is found that

$$f^{I}(E)=-kR|\Phi|^{\frac{1}{2}}(1+\gamma), \quad (15)$$

and

$$\lambda=(2\hbar/M)\frac{k|\Phi|^{\frac{1}{2}}\exp(-2\omega)}{-[\hbar^{2}/(MR)](\partial f^{I}/\partial W)_{E}+(1-\gamma)/[k|\Phi|^{\frac{1}{2}}(1+\gamma)]}. \quad (16)$$

Equation (15) is not to be construed to mean that the right side is an expression for $f^{I}(E)$, i.e., Eq. (15) is not an identity. Rather, once an expression for $f^{I}(W)$ has been chosen, and if other necessary parameters such as R and L were to be assigned, then the decay energy for the corresponding (idealized) one-body model would be found from Eq. (15) and the decay constant would be found from Eq. (16). In practice, with the traditional model, say, and data for an alpha particle group for which L is known, Eqs. (15) and (16) would be solved simultaneously for R and the depth of the well.

For the potential function illustrated in Fig. 1, the logarithmic derivative of the one-body wave function in Region I is determined from

$$\phi^{I}(r)=(\kappa r)^{\frac{1}{2}}[J_{L+\frac{1}{2}}(\kappa r)J_{-(L+\frac{1}{2})}(\kappa R_{0})-J_{-(L+\frac{1}{2})}(\kappa r)J_{L+\frac{1}{2}}(\kappa R_{0})], \quad (17)$$

where κ is the wave number in the well and R_0 is to represent the *nuclear* radius only. The functions J are Bessel functions of the indicated order. From this equation it is found that

$$f^{I}(E)=L+1-\kappa R(v/u) \quad (18)$$

and[17]

$$-[\hbar^{2}/(MR)](\partial f^{I}/\partial W)_{E}=R\{1-[(2L+1)/(\kappa R)](v/u)+(v/u)^{2}-[2/(\pi\kappa Ru)]^{2}\}, \quad (19)$$

where

$$v=J_{L+\frac{1}{2}}(\kappa R)J_{-(L+\frac{1}{2})}(\kappa R_{0})+J_{-(L+\frac{1}{2})}(\kappa R)J_{L+\frac{1}{2}}(\kappa R_{0}), \quad (20)$$

$$u=(\kappa R)^{-\frac{1}{2}}\phi^{I}(R). \quad (20a)$$

[17] The quantity $[J_{L+\frac{1}{2}}(x)J_{-(L+\frac{1}{2})}(x)+J_{-(L+\frac{1}{2})}(x)J_{L+\frac{1}{2}}(x)]$ appears, during the derivation, on the right side of Eq. (19). This quantity can be shown to be the Wronskian $W[J_{L+\frac{1}{2}}(x),J_{-(L+\frac{1}{2})}(x)]$; further, it can be shown that xW is a constant. Evaluation of the constant by letting x be large gives $W=(-1)^{L+1}[2/(\pi x)]$. Also see E. T. Whittaker and G. N. Watson, *A Course of Modern Analysis* (Macmillan Company, New York, 1946), p. 380, example 13.

After a little manipulation, the results of using Eq. (18) in Eq. (15) and Eq. (19) in Eq. (16) can be put in the forms

$$\kappa Rv=(g_{L}+L+1)u \quad (21)$$

and

$$\lambda_{0}{}^{L}=[2\hbar/(MRS_{e})]k|\Phi|^{\frac{1}{2}}\exp(-2\omega), \quad (22)$$

where

$$g_{L}=kR|\Phi|^{\frac{1}{2}}(1+\gamma) \quad (23)$$

and

$$S_{e}=1+(\kappa R)^{-2}\{g_{L}{}^{2}+g_{L}-L(L+1)-[2/(\pi u)]^{2}\}+(1-\gamma)/g_{L}. \quad (23a)$$

The superscript L has been added to λ to show that the result is for other than $L=0$, and the subscript zero is used to emphasize that this is a one-body decay constant.

III. COMPARISON WITH THE TRADITIONAL MODEL

The traditional potential energy function has been used as the basis of derivations of the alpha decay constant which have led to many different results. This situation will be discussed briefly to show what will be meant here by "the traditional model" and why.

In an unpublished investigation of the one-body model of alpha decay[18–20] now being made, it has been shown[19] that the most accurate derivation based on the traditional potential function, which is now in the literature, is that by Preston.[14] Comparison of Preston's result with what is called here, as a consequence of that investigation, the "exact" result showed that the differences are just those terms which Preston pointed out

[18] G. H. Winslow and O. C. Simpson, Argonne National Laboratory Report ANL-4841, June, 1952 (unpublished).
[19] G. H. Winslow and O. C. Simpson, Argonne National Laboratory Report ANL-4901, December, 1952 (unpublished).
[20] G. H. Winslow and O. C. Simpson, Argonne National Laboratory Report ANL-4910, January, 1953 (unpublished).

that he was neglecting. The numerical effect of these terms is small. Indeed, as far as calculated radii are concerned, the numerical effect of the approximations made by Bethe[13] and Rasetti[21] is not large. These latter two results are identical; they yield calculated radii which differ by only about 0.4 percent[22] from those given by the exact result, whereas the radii from some of the other equations can differ by as much as ten percent for the same input data.

This "exact" result was determined by showing that it was identically reproduced by the method of complex eigenenergies used in Sec. II, by Bethe's quasi-stationary state method, and by Rasetti's method of examining the change in time of the nonstationary wave function.[23] These latter two methods give somewhat greater insight into that term in Eq. (13) which is proportional to λ. It arises as a result of recognizing that there is a small part of the wave function which extends into the barrier. This recognition must be made during the normalization process when Bethe's method is used or, equivalently, when, with Rasetti's method, the probability remaining in the source is calculated. Thus this term is, logically, a necessary adjunct of the recognition that the phase of the interior wave function is less than π at $r=R$. The recognition of this latter fact is the principal difference between Preston's or the exact result and the Bethe-Rasetti approximation. Since the phase of the interior wave function at $r=R$ turns out to be smaller for the shell potential than for the traditional potential, that part of the wave function which extends into the barrier plays a more important role in the surface shell model than in the traditional model.

It is the so-called exact result referred to above which is meant here by "the result of the traditional model." Its properties have been discussed by Preston; they will be reviewed here in the process of comparison with the properties of the surface shell model. The equations, in the notation used here, can be quickly obtained from

$$\phi^I(r)=(\kappa r)^{\frac{1}{2}}J_{L+\frac{1}{2}}(\kappa r). \tag{24}$$

After determination of the corresponding f^I and $(\partial f^I/\partial W)_E$ and substitution into Eqs. (15) and (16), the results are that

$$\kappa R J_{L+\frac{1}{2}}(\kappa R)=(g_L+L+1)J_{L+\frac{1}{2}}(\kappa R) \tag{25}$$

and that $\lambda_0{}^L$ has the same form as in Eq. (22), except that S_r is to be replaced by S_T, where

$$S_T=1+(\kappa R)^{-2}[g_L{}^2+g_L-L(L+1)]+(1-\gamma)/g_L. \tag{26}$$

It is now convenient to write

$$\lambda_\alpha{}^L=p_L\lambda_0{}^L, \tag{27}$$

where $\lambda_\alpha{}^L$ is an observed alpha decay constant and, for the moment, p_L is to be considered only as a device by which the traditional model and the surface well model can be compared. It is also convenient to write for both models

$$R=R_0(=r_0A^{\frac{1}{3}})+\Delta R, \tag{28}$$

where R_0 is considered to be the radius of the daughter; hence A is the mass number of the daughter. In the surface well model ΔR is one of the parameters in the square well approximation to the nuclear potential at the nuclear surface. It plays the role of the "effective" alpha particle radius, i.e., it corresponds to the ρ_α used by Blatt and Weisskopf.[6] It is apparent, however, that $\lambda_0{}^L$ calculated with the surface well model will depend separately on R_0 and ΔR but that the value calculated with the traditional model, or with Devaney's[5] model, will depend only on the sum R.

Decay data[24] for Po^{212} have been used as an example to calculate values of $\log p_0$ with the two models. Various values of R and ΔR were used; the results with the traditional model are shown in Fig. 2(a) and those with the surface well model are shown in Fig. 2(b). Apart from the difference in the way the values of $\log p_0$ for the two models depend on R_0 (or r_0) and on ΔR, it can be seen that for a given r_0 and ΔR, the decay constant that would be calculated with the surface well model would be much larger than the one that would be calculated with the traditional model. The explanation for this is seen by examining the depths of the wells as given in Table I. In classical language, the greater kinetic energy in the surface well would mean a higher frequency of impact with the barrier wall.

The next comparison to be made is that of the way in which the two one-body decay constants change with L. The calculations were made with $\eta=20$ and $kR=10$ at each value of L, as an example. Calculated

TABLE I. Comparison of well depths (in Mev) in Po^{212} decay for different radii (in 10^{-13} cm).

R \ ΔR	Surface well model 0.5	1.5	2.5	Traditional Any
7.75	−78.13	−5.23	2.98	8.17
8.25	−76.88	−5.02	3.05	8.26
8.75	−75.69	−4.81	3.12	8.34
9.25	−74.56	−4.61	3.20	8.40

[21] F. Rasetti, *Elements of Nuclear Physics* (Prentice-Hall, Inc., New York, 1936), p. 100.

[22] If the derivation is made with WKB connections throughout, as was done by Kemble (see reference 12, p. 178), the result again yields calculated radii which differ by only about 0.4 percent from those given by the exact result. When following any method in which probability currents are used specifically, as Kemble did, it must be recognized that the amplitude of the outgoing wave in the well, from which wave the current incident on the barrier wall is calculated, is, to the required accuracy, just half of the amplitude of the (nearly stationary) total wave function in the well.

[23] Rasetti's method has been carried out in great detail only for $L=0$. It seems certain, however, that agreement with other methods would be obtained for any L.

[24] The data used in the examples were taken from the new table of isotopes: Hollander, Perlman, and Ghiorso, Revs. Modern Phys. **25**, 469 (1953). The author wishes to emphasize that reference to this very convenient table should not decrease the credit due to the original observers to whom the table refers.

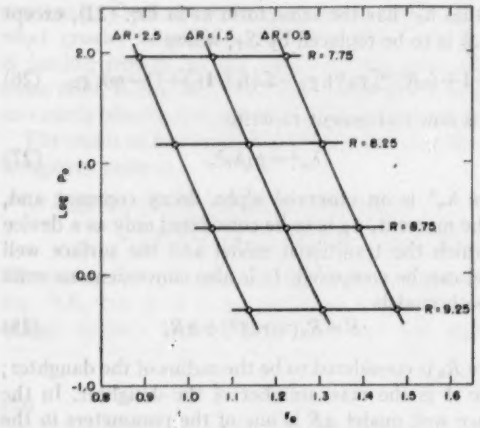

FIG. 2(a). Values of ratios ρ_0 of experimentally observed decay constant of Po^{212} to those calculated with the traditional model for various values of R and ΔR as a function of $r_0[=(R-\Delta R)(208)^{-\frac{1}{3}}]$. All distances are in units of 10^{-13} cm.

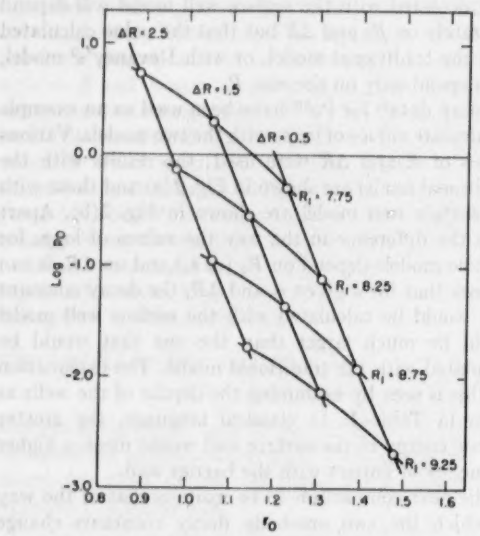

FIG. 2(b). Values of ratios, ρ_0, of experimentally observed decay constant of Po^{212} to those calculated with the surface well model for various values of R and ΔR as a function of $r_0[=(R-\Delta R)(208)^{-\frac{1}{3}}]$. All distances are in units of 10^{-13} cm.

values of $\log(\lambda_0{}^L/\lambda_0{}^0)$ are shown in Fig. 3, where Curve *a* is for the traditional model and Curve *b* is for the surface well model. It is seen that the former goes through a maximum at $L=2$, whereas the latter decreases monotonically. The formal explanation can be made briefly. If the first nonzero root of Eq. (25) is found at successively increasing values of L, it is found that the size of these roots increases rather rapidly. As a result S_T initially decreases more rapidly than does $\exp(-2\omega)$ and it is only after $L=2$ that the decrease in $\log(\lambda_0{}^L/\lambda_0{}^0)$ begins. This is possibly the most startling result of a consistent application of the traditional model and was first pointed out, as already mentioned, by Preston.

These roots of Eq. (21), on the other hand, increase so slowly with L that S_s is essentially constant. Indeed, it has been found with this example that S_s changes only by about three percent between $L=0$ and $L=6$. Thus the Gamow method[25] of treating the effect of changes in L by only including the changes in the exponential term, which represents an arbitrary departure from the traditional model, is the exact result of the surface well model.

It is of interest to examine the dependence of the roots of Eqs. (21) and (25) on L a little more closely. The squares of these roots are proportional to the kinetic energies in the wells; it is these energies which will be considered. With the same example as used to discuss $\log(\lambda_0{}^L/\lambda_0{}^0)$ and with $R=9\times10^{-13}$ cm and (for the surface well model) $\Delta R=1.2\times10^{-13}$ cm, it is found that the kinetic energies in the wells depend on L in the manner shown in Fig. 4. Here, again, Curve *a* is for the traditional model and Curve *b* is for the surface well model. It is seen that this energy increases linearly with $L(L+1)$ for the latter model but not for the former. Further, as indicated previously, these energy changes are a much smaller fraction of the total kinetic energy in the surface well than in the traditional well where the kinetic energy at $L=0$ is of the order of 0.5 Mev.

Since the total energy was held constant for this example, these kinetic energy changes correspond to increases in well depth. The fact that the changes are a small part of the total kinetic energy in the surface well model can be used to find an expression for them with the aid of Eq. (21). Since the result was found to agree with the exact calculation for this case of constant total energy, the same procedure was used to examine

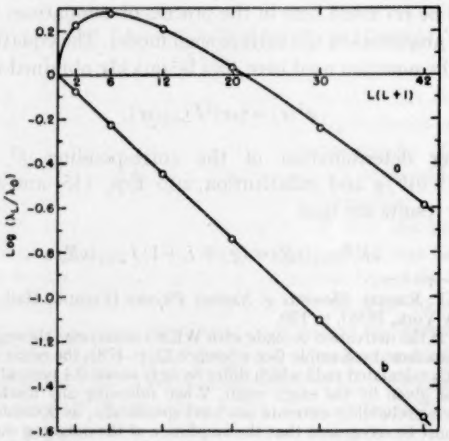

FIG. 3. Comparison of $\log(\lambda_0{}^L/\lambda_0{}^0)$ for constant energy and radii. Curve *a* is for the traditional model and Curve *b* is for the surface well model.

[25] See reference 1, p. 173.

TABLE II. $(\tau_{\text{experimental}}/\tau_{\text{theoretical}})$ for the first weak group.[a]

Parent	a	b	c	d
Cm^{244}	3.32	1.05	1.73	1.8
Cm^{242}	3.22	1.01	1.68	1.7
Pu^{240}	3.14	0.99	1.66	1.7
Pu^{238}	3.41	1.07	1.80	1.9
Pu^{236}	4.33	1.36	2.28	2.2
U^{238}	2.70	0.85	1.45	1.5
U^{236}	2.07	0.65	1.11	1.1
U^{234}	2.48	0.78	1.33	1.3
U^{232}	1.89	0.60	1.01	1.1
U^{230}	2.78	0.88	1.48	1.5
Th^{232}	1.85	0.58	1.00	1.0
Th^{230}	1.80	0.57	0.97	1.0
Th^{228}	1.57	0.50	0.84	0.9
Th^{226}	1.98	0.63	1.06	1.1
Ra^{226}	1.54	0.49	0.84	0.9
Ra^{224}	2.28	0.73	1.24	1.25

[a] Column a: Traditional model, $L=2$.
Column b: Surface well model, $L=2$. These numbers would be essentially those obtained from the traditional model if only the effect of L on the exponential term were included.
Column c: The results if no L terms are included. They were obtained by elimination of such terms from the results in Column b and are to be compared with the results obtained by the use of Kaplan's approximation to Preston's formulation of the traditional model, Column d.
Column d: F. Asaro, reference 27.

the energy changes with a constant well depth. This case is more difficult to solve exactly since the total energy appears in both κ and $(k|\Phi|^{\frac{1}{2}})$. The result[26] is that

$$(\Delta E)_L \doteq [\hbar^2/(2MRR_0)][L(L+1)] \times \frac{[1+R_0/(g_0\Delta R)]}{[1+R/(g_0\Delta R)]}. \quad (29)$$

Finally, some numerical calculations pertaining to the main group and first weak group of alpha particles emitted by even-even isotopes have been made. It was assumed that $L=0$ for the main group and $L=2$ for the weaker group. The values $r_0=\Delta R=1.2\times10^{-13}$ cm were picked arbitrarily, and the ratio (p_0/p_2) was calculated. Some preliminary calculations showed that not only was S_T insensitive to changes in L, but it was also insensitive to the small energy differences involved here and to changes in the values of r_0 and ΔR. This last result has been shown, actually, only for $r_0=\Delta R$. Thus S_T was assumed to be the same for each group from the same isotope, which made it unnecessary to calculate any values of κ for the surface well model.

[26] This result should be compared with the discussion of the relation between the energies and spins of nuclear states given by A. Bohr and B. R. Mottleson in Phys. Rev. 89, 316 (1953). The association of the values of $(\Delta E)_L$ given by Eq. (29) with states of the daughter nucleus has been suggested by O. C. Simpson. It would be argued that there are many possible nucleon configurations corresponding to a given state and that one such configuration should be that of an alpha particle at the surface, i.e., in the surface well. Numerically speaking, the values of $(\Delta E)_L$ calculated from Eq. (29) are too large, particularly for the heavier alpha emitters. Nevertheless the result is attractive and the answer to the numerical difficulty may be an incomplete potential function, i.e., it may not be sufficiently correct to consider the depth of the well as fixed (apart from the angular momentum term) when L is changed.

It was, of course, necessary to find κ in order to calculate (p_0/p_2) for the traditional model, since it is just the large changes in S_T with changes in L which cause that numerical difference between the models which is to be demonstrated here. The same values of r_0 and ΔR were used as with the surface shell model. Insensitivity of the traditional model to values of R was not shown here by direct calculation, but it can be shown by comparison with some numbers calculated by Asaro.[27]

Asaro, with the use of Kaplan's[28] approximation to Preston's[14] result, calculated radii with data for the main groups of several even-even isotopes and then used these radii to find values of a so-called $\tau_{\text{theoretical}}$ (theoretical half-life) for the weaker group emitted by each isotope. This second calculation was again made with Kaplan's equation, i.e., no term which is explicitly dependent on L was included. Asaro then tabulated values of $(\tau_{\text{experimental}}/\tau_{\text{theoretical}})$.

Because of the insensitivity of (p_0/p_2) to the radii (provided, of course, that the same radii are used with each group from a given isotope) it is reasonable, for the moment at least, to refer to these ratios as $(\tau_{\text{experimental}}/\tau_{\text{theoretical}})$ for the weaker group, in the sense used by Asaro. The results are given in Table II. No arguments can be given for the preference of one model over the other on the basis of the values of these ratios themselves. The drop by a factor of two (roughly) as one proceeds down the table can probably not be explained by any model of this type, i.e., a *one-body* model with complete spherical symmetry, with a barrier having a vertical inner face, and in which the distances are given literal meanings, i.e., in which the same radii are used for each group. It is suggested, however, that when the principal interest is alpha-decay theory as opposed to the empirical use of alpha-decay systematics, the effect of L on the exponential term, at least, should be included in such ratios wherever possible. That is, it should be expected that such terms must appear in a

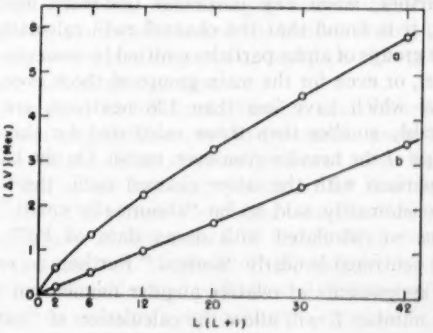

FIG. 4. The increase in kinetic energy in the well as L is increased. Curve a is for the traditional model and Curve b is for the surface well model. Since E was held constant the curves represent the increase in the depths of the wells.

[27] F. Asaro, University of California Radiation Laboratory Report UCRL-2180, June, 1953 (unpublished), Table 19.
[28] I. Kaplan, Phys. Rev. 81, 962 (1951).

complete expression for the alpha-decay constant. Thus, here, the assignment of $L=0$ to the main group and of $L=2$ to the first weak group seems reasonable.

IV. THE MANY-BODY DECAY CONSTANT

Suppose a channel radius is calculated in the traditional way by using, for example, data for the main group of an even-even isotope; that is, the calculation is made by equating the experimental decay constant directly to the expression for the one-body decay constant derived with the traditional potential function. It was shown in the previous section that if this radius, after some reasonable separation into R_0 and ΔR [see Eq. (28)], is now used to calculate a decay constant with the surface well model, then the result will be considerably larger than the experimental decay constant. Nevertheless, the radius used in the latter calculation seems reasonable in the sense that it will be very nearly the same as might be found by summing a radius, taken from some other consideration, for the alpha daughter and a reasonable value for the nuclear interaction distance between the daughter and the alpha particle.

Two remarks immediately suggest themselves. First, the procedure by which this radius was obtained is inconsistent with the idea that alpha decay is *not* a one-body process. Although several of the remarks on this topic[29-31] imply that the traditional model is complete when applied to the main group from an even-even nucleus, nevertheless it should not be expected *a priori* that any one-body model would be complete for any case. Second, if it is desired to continue the use of such values of the channel radii because of their general applicability but if it is also considered that, because of its nature and properties, the surface well model should have some relation to actual alpha decay, then consideration of what might cause an appropriate reduction in decay probability is forced.

Further, when any particular one-body model is used, it is found that the channel radii calculated for most groups of alpha particles emitted by noneven-even nuclei, or even for the main groups of those even-even nuclei which have less than 128 neutrons, are considerably smaller than those calculated for the main groups of the heavier even-even nuclei. On the basis of comparison with the latter channel radii, the former are customarily said to be "abnormally small." The radius so calculated with decay data of Po^{212} itself (128 neutrons) is nearly "normal." Further, no *reasonable* assignments of relative angular momentum quantum number L will allow the calculation of "normal" radii for many of the groups from noneven-even nuclei.[29,30] If these small channel radii are treated directly as nuclear radii, or if a constant interaction distance is used to obtain the nuclear radii from them, then the latter become abnormally small.

This problem is common. In addition to their occurrence with the one-body models, these abnormally small radii are also to be found in a table published by Blatt and Weisskopf,[32] credited to Devaney and calculated with his many-body model in which a constant value of $\rho_\alpha(=\Delta R)=1.2\times10^{-13}$ cm was used. When the parents are, say, Bi^{212}, Po^{210}, and Po^{212}, the values calculated for r_0 are, respectively, 1.14, 1.21, and 1.31, all in units of 10^{-13} cm. These numbers when calculated with Bethe's[13] approximation to the traditional model and $\Delta R=1.2\times10^{-13}$ cm are 1.05, 1.22, and 1.32, respectively. Presumably there should be a relative angular momentum quantum number involved in the case of Bi^{212}. If $L=4$, say,[14] then Devaney's value for r_0 would be raised to about 1.23×10^{-13} cm. Blatt and Weisskopf also consider values of r_0 as low as 1.2×10^{-13} cm to be spurious, as compared to the "normal" values of 1.3×10^{-13} cm to 1.4×10^{-13} cm. They again suggest the reason commonly quoted in discussions of a one-body model, i.e., an inexactitude in the equations such that they do not take into account an expected increased difficulty of assembling an alpha particle when it is necessary to dip into the Pb^{208} core for some of the constituents.

Other estimates of nuclear radii—from total cross sections for fast neutrons, for instance—do not show such a pronounced effect in this region. As an example, the "radii" given by Hildebrand and Leith[33] for 42-Mev neutrons would correspond to r_0 for lead or bismuth, being about three percent less than that for thorium rather than the 10 to 20 percent drop noted in the values deduced from alpha decay data. Further, it has been suggested[30] that the radii of noneven-even nuclei should be larger, if anything, than those of neighboring even-even nuclei.

The arguments which will be made in this section concerning a factor which will reduce the decay probability below that predicted by a one-body model will lead to a result which involves two quantities. One of these will be an "intrinsic alpha-decay constant" which is not, however, directly equal to Devaney's intrinsic alpha-decay constant. The second will be the probability per second that an alpha particle at the nucleus (or at the nuclear surface) will be absorbed into the nucleus as nucleons, i.e., that a compound nucleus will be formed. The appearance of the second of these two quantities might allow the explanation of the abnormally small radii, whereas the first quantity alone might fail in this respect. In conjunction with estimates of these probabilities, to be made in the next section, it will be suggested on the other hand that small *channel* radii might not be abnormal.

[29] Perlman, Ghiorso, and Seaborg, Phys. Rev. **75**, 1096 (1949).
[30] Perlman, Ghiorso, and Seaborg, Phys. Rev. **77**, 26 (1950).
[31] See reference 8, M. A. Preston.
[32] See reference 6, p. 578. The exact source of the values of level spacing which were used does not appear to be given.
[33] R. H. Hildebrand and C. E. Leith, Phys. Rev. **80**, 842 (1950).

Although such estimates will be made, no attempt will be made to derive expressions for these probabilities in terms of such quantities as nuclear spins, relative angular momentum, level widths and spacings, etc. Rather, the way in which they would be expected to appear in an equation for the alpha-decay constant will be shown by a sort of phenomenological argument. The following presumptions are added to those of Sec. II: (c) in the absence of the external Coulomb field there would still be a noninfinite probability per second for the emission of alpha particles; (d) the presence of the barrier, which is the net effect of the Coulomb and nuclear interactions, makes it possible that an alpha particle, once formed, might become unformed and reabsorbed as nucleons rather than be emitted through the barrier. In addition, in order to apply the concept to a model of the traditional type in which the alpha particle is not excluded from the region occupied by the nucleus, it is necessary to amplify somewhat—essentially to modify—the previous presumption (a) that alpha particles do not exist *in* nuclei. To do this use is made of a suggestion by Bethe[33] that "there might be some slight tendency for the preformation of alpha particles in nuclei due to their great stability." This suggestion is applied literally where the corresponding one-body model is of the traditional type. In the case of a surface well model it is considered that there is a tendency for the "preformation" of alpha particles at the nuclear surface. In either case it is assumed here,[34] in order to advance the argument, that there are periods during which one-body wave functions apply in some region behind the Coulomb barrier; that is, some one-body potential (not necessarily, of course, any sort of square well potential) is to be used during these periods, but only during these periods.

Suppose there is only one alpha particle in existence behind the Coulomb barrier at a time, i.e., suppose that there is one species with no alpha particle behind the barrier (hence, actually, no well and no barrier) and a second species with one alpha particle behind the barrier. Let $\lambda_1{}^L$ be the decay probability of the first species to the second, i.e., let it be (or at least very nearly be) the decay constant in the absence of the external Coulomb field. Let $\lambda_2{}^L$ represent the decay constant of the second species to the first, i.e., let it be the probability per second that an alpha particle in the nucleus or at the nuclear surface, as the case may be, will break up and its constituents be reabsorbed. Thus the second species branches by decaying to the first with decay constant $\lambda_2{}^L$ and by emitting alpha particles with decay constant $\lambda_0{}^L$. If the generic relationships between these two species are set up, the effective alpha decay constant can be determined. It turns out that, if $\lambda_0{}^L$ is much smaller than either $\lambda_1{}^L$ or $\lambda_2{}^L$, a reasonable expectation, then there is a net decay by alpha emission with the decay constant

$$\lambda_\alpha{}^L=\lambda_1{}^L\lambda_0{}^L/(\lambda_1{}^L+\lambda_2{}^L). \tag{30}$$

Thus Eq. (27) is now given additional significance beyond that given it at the time it was written in that the many-body alpha decay constant is, according to this picture, to be written as the product of a dimensionless "preformation factor" and a one-body decay constant. The preformation factor is given by

$$p_L=\lambda_1{}^L/(\lambda_1{}^L+\lambda_2{}^L). \tag{31}$$

The reciprocal of p_L is, except for the effects of L in the one-body decay constant, just the "departure factor" (for the traditional model) as used by Perlman, Ghiorso, and Seaborg.[30]

The solution of the problem of deriving expressions for $\lambda_1{}^L$ and $\lambda_2{}^L$ is not to be attempted here, as was stated previously. However, it is considered that the probability $\lambda_1{}^L$ is to be associated with an intrinsic, non-Coulomb barrier, alpha-decay constant and that the probability $\lambda_2{}^L$ is conceptually equivalent to the sticking coefficient ξ as used by Bethe,[35] Peaslee,[36] Weisskopf, and Ewing,[37] for instance, or, more particularly, to the probability P discussed by Feshbach, Porter, and Weisskopf.[38] Thus according to this argument the problem of the probability of formation of a compound nucleus, once the particle involved is at the nucleus, should also appear in the discussion of the theory of alpha decay.

V. DISCUSSION

The many-body model is distinguished in this paper from the one-body model by the requirement that it be recognized in the former that an alpha particle is not always present behind its accompanying Coulomb barrier during the interval between the formation of the alpha active parent and its decay. This requirement is considered to be separate from that of finding the potential which best represents the interaction between an existing alpha particle and the residue during those intervals when there might be an alpha particle present behind its Coulomb barrier.

The method of Feshbach, Peaslee, and Weisskopf,[2] which was used by Devaney[5] to discuss the many-body theory of alpha decay, has been referred to as the use of an "equivalent two-body potential" by Francis and Watson.[39] (The phrase "one-body" used in this paper and generally in discussions of alpha decay has the same meaning as "two-body.") The model has also been used in this way by Blatt and Weisskopf,[40] for instance, to estimate a normalization constant for the interior wave function of an escaping particle. It would

[34] Supporting arguments are given in Sec. V.

[35] See reference 13, Part D of §54, p. 96.
[36] D. C. Peaslee, Phys. Rev. **74**, 1001 (1948).
[37] V. F. Weisskopf and D. H. Ewing, Phys. Rev. **57**, 472 (1940).
[38] Feshbach, Porter, and Weisskopf, Phys. Rev. **87**, 188 (1952).
[39] N. C. Francis and K. M. Watson, Phys. Rev. **92**, 291 (1953).
[40] See reference 6, p. 421.

certainly seem reasonable to adopt this attitude where the "particle" involved is a fundamental particle, although some arguments to be raised later suggest that this attitude should be modified even in such a case.

When one comes to consider the case of a compound particle, such as an alpha particle, reference should be made to the derivation by Weisskopf[41,42] of P (not the P of Feshbach, Porter, and Weisskopf[38]) $=(2\pi\hbar)/D$, where D is an appropriate level spacing, as a nuclear period. It was derived by showing (under the specified assumptions) that P is the repetition rate of a $|\psi(t)|^2$ which corresponds to a particular grouping of nucleons. Such a grouping might correspond to an alpha particle which, however, is "nonexistent" between repetitions of this $|\psi(t)|^2$. Thus the method should meet the principal requirement of a many-body model which was set forth above.

On the other hand, further reference to the derivation of this period P shows that it should be interpreted in this case as the interval between successive appearances of an alpha-particle grouping at, but within, the surface of the parent nucleus. Now, according to Feshbach, Porter, and Weisskopf,[38] there is evidence that the compound nucleus in a nuclear reaction, even when the bombarding particle is a neutron, is formed less rapidly than had been hitherto assumed. This would mean that the formation of a compound nucleus is inhibited by something more—by some other "barrier"—than by the ordinary centripetal barrier, by the partial reflection at a potential jump, or, for charged particles, by the Coulomb barrier. It would be expected that this inhibition would be even more pronounced for an alpha particle and, further, that it would operate in both directions. In Devaney's model it is the Coulomb barrier which permits the existence of the well-defined state whose period is P. It is argued here, however, that this state would still be reasonably well defined in the absence of the Coulomb barrier because of the existence of the further "barrier" discussed above.

The decay constant $\lambda_1{}^L$, then, might be obtained by multiplying $D/(2\pi\hbar)$ by some number less than unity; that is, $\lambda_1{}^L$ is used here to represent the probability per second for the actual division of the compound nucleus (parent) into two entities, the daughter nucleus and a well formed alpha particle. Were there no Coulomb barrier these entities would usually move apart immediately after formation. The decay constant would be $\lambda_1{}^L$ except for the low but not zero reflection at a potential "jump" caused by the rapidly varying attractive nuclear interaction potential. It is this complete separation which is held in check by the Coulomb barrier. Since the latter is so broad and high, the return of the system to its original condition is more likely to occur than is alpha-particle emission.

Expression (30) is to be considered as an approximate expression of these ideas. The goodness of the approximation depends on the life of the divided but unseparated system. Again, however, if the probability of reformation of the compound nucleus (parent) is inhibited as described above, the approximation should be reasonably good, even to the extent of using a strict one-body decay constant for $\lambda_0{}^L$, since many traversals of the region allowed to the alpha particle would occur, on the average, before either reformation of the compound nucleus (parent) or escape of the alpha particle through the barrier. Further, by the very nature of the expression for p_L [Eq. (31)] its value will be less than unity, and so a factor has been found which will reduce the decay probability below that predicted by a one-body model.

It has been stated that Eq. (31), which involves the two quantities $\lambda_1{}^L$ and $\lambda_2{}^L$, might provide a means for explaining the so-called abnormally small radii even if $\lambda_1{}^L$ alone could not do so. If a proper derivation of these two quantities should show that $\lambda_2{}^L$ is relatively much greater in those cases where the small radii occur, then the explanation could be effected even with the same interaction distance for all cases. That is, a decrease of p_L of the proper magnitude, caused by an increase of $\lambda_2{}^L$, could lead to the calculation of normal channel radii.

An attempt to make a rough estimate of $\lambda_1{}^0$ and $\lambda_2{}^0$ has led, on the other hand, to a somewhat different explanation. This suggestion is equally applicable to Devaney's model, to the traditional model, or to expression (30) with the result of the surface well model used for $\lambda_0{}^0$. Suppose in the latter case that $\lambda_2{}^0$ is written as

$$\lambda_2{}^0=[v/(2\Delta R)]\xi, \tag{32}$$

where ξ is the probability of formation of the compound nucleus (parent) per impact of the alpha particle on the surface of the daughter nucleus and v is the velocity in the well. At least for the main groups from even-even nuclei it might be possible to write also that

$$\lambda_1{}^0=[D/(2\pi\hbar)]\xi. \tag{33}$$

If, for Po^{212} as an example, D is taken from Devaney,[22] then one can find the values of r_0 and ΔR which will satisfy Eq. (30) for this model. It is found that the corresponding values of the channel radius R are not exactly constant as they would be in Devaney's or the traditional model, but they are nearly so. The value $r_0=1.31\times10^{-13}$ cm corresponds to $\Delta R=1.2\times10^{-13}$ cm. Generally, for α decay and with distances of this size, $[v/(2\Delta R)]\gg[D/(2\pi\hbar)]$.

If now one proceeds to Po^{210} the same effect is observed here as with the other models, i.e., the channel radius is small. The value of $[v/(2\Delta R)]$ is very nearly the same for every nucleus if ΔR is the same for every nucleus. But the question is now asked, why should one necessarily expect ΔR to be constant and associate the small r_0 which then accompanies a small channel radius,

[41] See reference 6, p. 386.
[42] V. F. Weisskopf, Helv. Phys. Acta **23**, 187 (1950).

with an error in the theory? In the surface well model, at least, ΔR is a parameter in a square-well approximation to the nuclear potential at the nuclear surface. It might very well be the case that such a parameter would be different between the two cases where the daughter nucleus is the closed shell nucleus Pb^{208} and where the daughter lacks two neutrons of being the closed shell nucleus. If this position is taken, then it is found for Po^{210} that $r_0=1.31\times10^{-13}$ cm corresponds to $\Delta R\doteq0.6\times10^{-13}$ cm. If one goes back to Devaney's result[32] for this nucleus, for instance, and uses 0.6×10^{-13} cm for his ρ_a, then his result for r_0 becomes 1.32×10^{-13} cm. This agreement is not surprising, of course. The leading term in Eq. (23a) is, for $L=0$, just $(\Delta R/R)\times[1+g^2/(\kappa R)^2]$. Thus, if only this term is used along with the above expressions for λ_1^0 and $\lambda_2^0(\lambda_2^0\gg\lambda_1^0)$, the expression for λ_a^0 becomes identical with Devaney's Eq. (2.21) with $L=0$.

The above estimates are only based on a suggested possibility. To make them does not exclude the possibility that detailed considerations leading to proper expressions for λ_1^L and λ_2^L would show that p_L changes from alpha emitter to alpha emitter in such a way that $R=r_0A^{\frac{1}{3}}+\Delta R$, with r_0 and ΔR constant, even in those cases where present methods yield abnormally small radii. It must be remembered in other connections also that λ_0^L is only one factor in an expression for λ_a^L. For instance, Fig. 3 shows the way in which λ_0^L depends on L for two possible descriptions of the one-body phase of the alpha decay mechanism; the way in which p_L might be expected to depend on L has not been shown here.

The two solutions of the one-body phase of the problem which have been used here might be considered as extreme cases. Not only variations of each of them but also combinations are possible. For instance, one could use a square well with the potential in $r<R_0$ large but not infinite. As between the two extremes, it is believed that a model of the surface well type is to be preferred. If there is a well-defined *nuclear* surface, as is certainly implied by the subtraction of an "effective" alpha particle radius from the channel radius to obtain the radius of such a nuclear surface,[6] then it is more logical to introduce this surface as a factor to be considered during the derivation of the alpha decay constant. The surface-well model allows one to combine: (a) the well-defined *nuclear* surface; (b) the exclusion of alpha particles, as such, from the interior of a nucleus; (c) the "slow" formation of a compound nucleus[38]; (d) the improbability of a pure Coulomb potential at the *nuclear* surface. Along with this combination of ideas it yields, as an exact result, a linear dependence of $\log\lambda_0^L$ on $L(L+1)$; thus this is the dependence of the *barrier penetrability* term in $\log\lambda_a^L$. The deep surface (square) well is consistent with a large attractive interaction between an alpha particle and a nucleus at close distances. The nature of the dependence of the energy levels in the surface well on $L(L+1)$ is considered to be preferable to the nature of that dependence in the traditional well, in spite of the present difficulty with its magnitude. Finally, it is much easier to use what are presently considered to be normal channel radii, together with an expected $p_L<1$, with the surface well model than with the traditional model. These remarks about the content of the surface well model still apply after one has made those specific assumptions and approximations which lead to Devaney's expression for the alpha-decay constant.

I wish to express my appreciation of many instructive and searching discussions to Dr. O. C. Simpson of this laboratory, who first introduced me to the problem of alpha-decay systematics and theory.

APPENDIX

The question of the accuracy of the WKB wave functions when applied to the solution of the alpha decay problem has been discussed by many others. Among these are Devaney[5] and Preston,[14] to whose work frequent reference has been made here. The present author would like to add some brief remarks to this discussion. They will be developed more fully elsewhere.[43]

The WKB functions for large ρ are trigonometric functions as are the asymptotic expressions for the Coulomb functions. If, in the evaluation of the argument of the WKB functions, reciprocal powers of ρ are neglected compared to ρ, to $\ln\rho$, and to constants, and if $L(L+1)$ is replaced by $(L+\frac{1}{2})^2$, then this argument differs from that which appears in the asymptotic expressions for the Coulomb functions[15] only by

$$\epsilon=1/(24\eta)-[L(L+1)]/(24\eta^2)+\cdots.$$

It is to be remembered that $\eta=20$ is typical for this problem.

In addition, with the typical value $\rho(R)=10$, one can examine the behavior of the WKB functions near the nuclear surface. For L in the range up to $L=4$ it has been found[43] that: (a) The usual WKB functions, i.e., those containing $L(L+1)$ in the "centrifugal" term, obey certain Coulomb function recursion relations to about 10^{-3} percent; (b) The WKB functions with $L(L+1)$ replaced by $(L+\frac{1}{2})^2$, the functions used in this paper, obey these recursion relations to about 0.06 percent; (c) The ratio of the irregular WKB functions modified as in (b) to the usual irregular WKB functions (ratio $\doteq1.01$) is the same as the ratio of the irregular Coulomb functions to the usual irregular WKB functions as given by Bloch *et al.*[44] to about 0.1 percent.

[43] G. H. Winslow and O. C. Simpson, continuation of references 18–20, now in preparation. This report has been issued as Argonne National Laboratory Report ANL-5277, April, 1954 (unpublished).

[44] Bloch, Hull, Broyles, Bouricius, Freeman, and Breit, Phys. Rev. **80**, 553 (1950).

Thus, since one of the recursion relations used contains both the regular and irregular functions, the modified WKB functions are the same as the Coulomb functions to about 0.1 percent *in this range of the variables* ρ and η. In other ranges of these variables the modified functions might or might not be preferred.[45]

The notation which has been used in this paper is a mixture of that used by Bloch *et al.*,[15] Bethe,[13] and Preston.[14] Bethe's C has been replaced by Preston's ω on the grounds that C is generally used to represent a constant of some sort. Bethe wrote the quantity $|\Phi|$ as $|\Phi(\rho)|$ in certain places but did not bring η into evidence. It is believed to be preferable to use the ρ as a notation for kr, and to reserve the symbol x, which was used for kr by Preston[14] and for kR by Devaney,[5] for its older meaning as the ratio of the energy to the height of the barrier.

Examination of Eq. (16) shows that it could be written as

$$\lambda=4E(\hbar kRS')^{-1}[G_L(kR)]^{-2},$$

with

$$S'=-[\hbar^2/(MR^2)](\partial f^1/\partial W)_E+(1-\gamma)g_L^{-1},$$

but, depending on the model used, it might be more convenient in computation to include one factor of $[G_L(kR)]^{-2}$, $|\Phi|^{\frac{1}{2}}$, in the expression of S'. The exponential term will be common, however, to a model to which Eq. (16) applies. To the first power of $(L+\frac{1}{2})^2$,

$$\log_{10}\exp(-2\omega)=(D/E_\alpha^{\frac{1}{2}})f(x)$$
$$+0.75445(D/E_\alpha^{\frac{1}{2}})^{-1}[(1-x)/x]^{\frac{1}{2}}(L+\tfrac{1}{2})^2,$$

where[46]

$$D=1.09449[ZA/(A+4)],$$
$$f(x)=\cos^{-1}x^{\frac{1}{2}}-[x(1-x)]^{\frac{1}{2}},$$

E_α is the alpha-*particle* energy in Mev "corrected" as described in reference 16, and, as before, Z and A are the atomic and mass numbers of the daughter. The first term in the expansion in powers of $(L+\frac{1}{2})^2$ contributes to the third decimal place in $\log_{10}\exp(-2\omega)$ already when $L=0$, where the value of the term is about 0.009. Expansion to higher powers shows that the term in $(L+\frac{1}{2})^4$ does not contribute to the third decimal place until $L=3$, where its value is about 0.002, and the term in $(L+\frac{1}{2})^6$ does not contribute until $L=6$, where its value is about 0.001.

The ratio x is conveniently written as

$$x=E_\alpha R/K,$$

where, with R in units of 10^{-13} cm,

$$K=2.8797_2[ZA/(A+4)].$$

Further convenient formulas related to the g_L of Eq. (23) are

$$k^2R^2|\Phi|=1.32547(D/E_\alpha^{\frac{1}{2}})^2x(1-x)+(L+\tfrac{1}{2})^2$$

and

$$\gamma=-[4kR|\Phi|^{\frac{1}{2}}(1-x)]^{-1}$$
$$\times[1+(k^2R^2|\Phi|)^{-1}(1-2x)(L+\tfrac{1}{2})^2].$$

It was mentioned in the text that γ is generally about -0.02 (and, hence, is frequently omitted); the correction term in the equation for γ is only about 0.05 or so at $L=5$.

[45] Yost, Wheeler, and Breit, Phys. Rev. **49**, 174 (1936).

[46] Values for the necessary atomic constants have been taken from J. W. M. DuMond and E. R. Cohen, Revs. Modern Phys. **25**, 691 (1953) and Li, Whaling, Fowler, and Lauritsen, Phys. Rev. **83**, 512 (1951).

Neutrino Recoil Spectrometer. Investigation of A^{37}

O. KOFOED-HANSEN*
Institute for Theoretical Physics, University of Copenhagen, Copenhagen, Denmark
(Received July 9, 1954)

A neutrino recoil spectrometer has been constructed. The recoil momentum and the charge distribution of the recoil ions from the K capture of A^{37} has been studied. The results are: neutrino energy, (812±8) kev; recoils of charge 1, (26±3) percent; recoils of charge 2, (13±4) percent; recoils of charge 3, (38±4) percent; recoils of charge 4, (18±2) percent; recoils of charge 5, (4±1) percent; and recoils of charge 6, (1±1) percent. Furthermore, the average momentum of the electrons emitted during the ionization of the recoils is 69±1 gauss-cm. The most energetic Auger electrons have a momentum of 162±4 gauss-cm and they occur in (65±5) percent of the decays.

INTRODUCTION

MANY recoil experiments have successfully demonstrated that momentum is missing in β decay and K capture if the neutrino is not postulated.[1] Important information about the angular correlation in β decay has also been obtained.[2] On the other hand, such experiments have so far not given very precise numerical results. The present paper describes a method which at least in principle makes very high precision measurements possible. The instrument permits a study of the motion of recoil ions in crossed electric and magnetic fields. The recoil ions are detected by the current they produce when hitting the detector plates. The main features of the method have been described previously.[3]

THEORY OF THE INSTRUMENT

In principle, the instrument consists of a set of plane parallel condenser plates adjusted so that the magnetic field is parallel to the surface of the plates. The decaying atoms form a gas which decays uniformly inside the volume of the condenser. The current of recoils and electrons going to the plates is measured as a function of the electric field F and the magnetic field H. If H is larger than F, the orbits are always periodic in the direction parallel to F. If $2a$ is the distance between the plates (see Fig. 1), an ion of charge z, mass M, initial velocity u, and starting point x_0 will have the extrema of its orbit $x^{\max}$ and $x^{\min}$, given by

$$\left.\begin{matrix}\omega a\\ -Wa\end{matrix}\right\}=\left.\begin{matrix}x^{\max}\\ x^{\min}\end{matrix}\right\}-x_0=Ba\{1+A\sin\theta\cos\varphi \pm[1+2A\sin\theta\cos\varphi+A^2\sin^2\varphi]^{\frac{1}{2}}\},\quad(1)$$

where θ is the angle between $M\mathbf{u}$ and $\mathbf{H}$ and φ is the azimuth of $M\mathbf{u}$ measured from the y axis. [See reference 3, Eqs. (38) and (40).] We use the abbreviations

$$\mathcal{A}=A\sin\theta=(2aHu/Vc)\sin\theta,\quad(2a)$$

$$B=(2Mc^2V)/[(2aH)^2z],\quad(2b)$$

$$V=2aF.\quad(2c)$$

We also introduce the relative amplitude in the motion

$$L=\omega+W.\quad(2d)$$

The functions ω and W are shown in Fig. 2 as functions of φ in the special case $\mathcal{A}=1$, $B=1$. If $L>2$, no particles can spiral out of the condenser. They will either hit plate 1 or plate 2. When $L<2$, $\frac{1}{2}(2-L)$ particles will spiral out. Let us denote by φ', $0\leqslant\varphi'\leqslant\pi$, the angle where $L=2$, i.e.,

$$\varphi'=\begin{cases}0 & \text{for } B<1/(1+\mathcal{A}),\\ \arccos\left[\dfrac{1}{2\mathcal{A}}\left(\dfrac{1}{B^2}-1-\mathcal{A}^2\right)\right] & \text{for } \dfrac{1}{1+\mathcal{A}}<B<\dfrac{1}{1-\mathcal{A}},\\ \pi & \text{for } B>1/(1-\mathcal{A});\end{cases}\quad(3)$$

when no such angle exists the proper limits 0 or π are given. Furthermore, it is assumed that $V>\frac{1}{2}Mu^2$, which ensures that the function $W<2$.

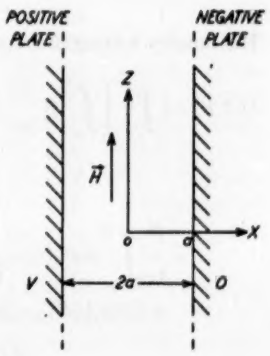

FIG. 1. Principle of the instrument.

*Present address: Columbia University, New York, N Y.
[1] See O. Kofoed-Hansen, Physica 18, 1287 (1952).
[2] B. M. Rustad and S. L. Ruby, Phys. Rev. 89, 880 (1953); J. S. Allen and W. K. Jentschke, Phys. Rev. 89, 902 (1953).
[3] O. Kofoed-Hansen, Kgl. Danske Videnskab. Selskab, Mat.-fys. Medd. 26, No. 8 (1951).

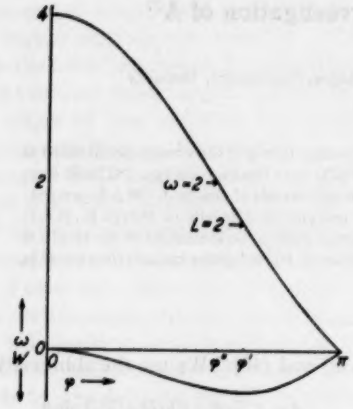

FIG. 2. The functions $\omega(\varphi)$ and $W(\varphi)$ for $\mathcal{A}=1$ and $B=1$.

When $\omega>2$, all particles starting out towards the attracting plate will hit this plate, but when $\omega<2$ some may miss this plate and either hit the repelling plate or spiral out. Let us denote by φ'', $0\leqslant\varphi''\leqslant\pi$, the angle where $\omega=2$, i.e.,

$$\varphi''=\begin{cases}0 & \text{for } B<1/(1+\mathcal{A}),\\ \arccos\left[\dfrac{2}{B\mathcal{A}}-\left[\dfrac{4}{B\mathcal{A}^2}+1\right]^{\frac{1}{2}}\right] & \\ & \text{for } \dfrac{1}{1+\mathcal{A}}<B<\dfrac{1}{1-\mathcal{A}},\\ \pi & \text{for } B>1/(1-\mathcal{A}).\end{cases} \tag{4}$$

For specific values of A and B the relative number of particles spiraling out will, therefore, be given by

$$g(A,B)=\int_0^{\frac{1}{2}\pi}\sin\theta d\theta\int_{\varphi'}^{\pi}(2-L)d\varphi/2\pi$$

$$=\int_0^{\frac{1}{2}\pi}\sin\theta\left\{\frac{\pi-\varphi'}{\pi}-\frac{2B}{\pi}[E(k,\tfrac{1}{2}\pi)-E(k,\tfrac{1}{2}\varphi')](1+\mathcal{A})\right\}d\theta. \tag{5}$$

The number hitting the repelling plate is given by

$$h(A,B)=\tfrac{1}{2}\int_0^{\frac{1}{2}\pi}\left[\int_0^{\pi}W\frac{d\varphi}{2\pi}+\int_{\varphi''}^{\pi}(2-\omega)\frac{d\varphi}{2\pi}-\int_{\varphi'}^{\pi}(2-L)\frac{d\varphi}{2\pi}\right]\sin\theta d\theta$$

$$=\frac{B}{4\pi}\int_0^{\frac{1}{2}\pi}\sin\theta\{(1+\mathcal{A})[4E(k,\tfrac{1}{2}\pi)-4E(k,\tfrac{1}{2}\varphi')+2E(k,\tfrac{1}{2}\varphi'')]-2\pi+\varphi''+(2/B)\times(\varphi'-\varphi'')+\mathcal{A}\sin\varphi''\}d\theta, \tag{6}$$

and the number hitting the attracting plate is given by

$$f(A,B)=1-g(A,B)-h(A,B), \tag{7}$$

where

$$E(k,\varphi)=\int_0^{\varphi}(1-k^2\sin^2t)^{\frac{1}{2}}dt, \tag{8}$$

$$k^2=4\mathcal{A}/(1+\mathcal{A})^2. \tag{9}$$

When the particles have initially a distribution in velocity, the functions f, g, and h have to be integrated over this distribution. Since $A\sim u$, such an integration is essentially an integration over A. If there is a distribution in z, one has to sum over this distribution; since only B contains z, this will be a summation over B. In the case of A^{37} we can primarily confine ourselves to a distribution in z. In such a case the currents going to the two plates and the currents spiraling out are given below. The current will of course also contain a component from the electrons. However, in the present experiments we are mainly dealing with such values of H and F that the approximation in Eq. (49) of reference 3 can be used. Thus we get for the total current to the positive plate (S_z is the charge distribution function and N the total number of disintegrations):

$$i_+\cong\sum_z[S_z\cdot zh(A,B)Ne]-Ne\langle z\rangle\tfrac{1}{4}\pi c\langle p_e\rangle/(2aHe), \tag{10}$$

and to the negative plate:

$$i_-\cong\sum_z[S_z\cdot zf(A,B)Ne]-Ne\langle z\rangle\tfrac{1}{4}\pi c\langle p_e\rangle/(2aHe). \tag{11}$$

LIMITING CASES

The above formulas take especially simple forms in the two cases:

$$B>1/(1-A),\quad A<1; \tag{12}$$

$$B<1/(1+A),\quad A<1. \tag{13}$$

One finds in case (12),

$$h(A,B)\cong\frac{B}{2}\left\{\frac{A^2}{12}+\frac{A^4}{240}+\frac{A^6}{1120}+\frac{5A^8}{16\,128}+\cdots\right\}, \tag{14}$$

$$g(A,B)\equiv 0. \tag{15}$$

Physically, this implies that no particles can spiral out, and one is led to the approximate formulas (50) and (51) of reference 3 for i_+ and i_-. In case (13) one obtains similarly

$$h(A,B)\cong B\left\{\frac{A^2}{12}+\frac{A^4}{240}+\frac{A^6}{1120}+\frac{5A^8}{16\,128}+\cdots\right\}, \tag{16}$$

$$g(A,B)=1-B-2h(A,B). \tag{17}$$

Condition (13) means that $L<2$, i.e., that the largest orbit can lie in the space between the plates. In both these cases the integrations over a possible velocity distribution and the summations over a possible charge distribution can be carried out especially easily. The

final result will depend upon simple average values of z, p, E, etc., for the recoils.

DECAY OF A^{37}

A^{37} is reported to decay into Cl^{37} by 92 percent K capture and 8 percent L capture, with a half-life of 34 days. Primarily electrically neutral Cl^{37} atoms are formed, but successive Auger effects and the charge change of the nucleus from $Z=18$ to $Z=17$ cause a considerable ionization to take place within very short time ($\sim 10^{-10}$ sec) after the decay. The $Cl^{37}(p,n)A^{37}$ threshold shows that 816 ± 4 kev is available for the K capture.

The recoil velocity distribution is primarily a sharp line originating from the practically monoenergetic neutrino emission, but smeared out by ~ 6 percent due to the recoil from the Auger effect and by a similar amount due to the Brownian motion at STP.

This spread will cause a difference of only ~ 2 kev between $c[\langle p^2\rangle]^{\frac{1}{2}}$ and $c\langle p\rangle$, and we can therefore neglect the spread in all our expressions and apply the sharp line formulas (10) and (11), using simply $\langle u\rangle$ in these expressions instead of u. Actually, the velocity distribution could in principle be determined by the experiment, but the present experiments have been carried out at such values of V and H that primarily the charge spectrum has been investigated.

The A^{37} is produced carrier-free by $Ca(n,\alpha)$ in the Harwell pile and sent to Copenhagen enclosed in Ca. It is introduced in the sealed-off vacuum of the instrument by evaporating the Ca inside the vacuum system. Another Ca furnace in the vacuum system keeps the pressure in the instrument at 10^{-5} to 10^{-3} mm Hg for a month, the pressure being initially low and gradually increasing.

THE INSTRUMENT

A diagram of the instrument is shown in Fig. 3. An approximately homogeneous magnetic field is obtained by using a solenoidal coil surrounded by iron. The coils are watercooled and wound with 20 mm by 1 mm flat

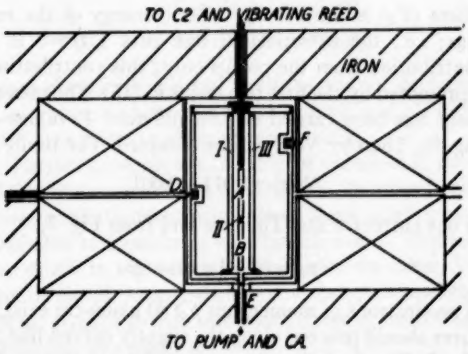

FIG. 3. Diagram of the instrument. The distance between the plates is $2a=0.704$ cm.

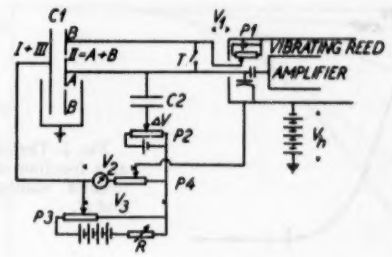

FIG. 4. Circuit diagram.

Cu wire insulated with polystyrene. The inhomogeneities amount to ~ 2 percent close to the pole pieces. The only advantage of this construction is that it is relatively inexpensive. As disadvantages appear the facts that too little space is left for introducing instruments into the field and that thereby some difficulties in handling the equipment occur. Also the field is not as homogeneous as might be desired. Even more troublesome is the fact that the temperature of the vacuum chamber is seriously affected by the heating up of the coils. Therefore an extra watercooled shield is introduced between the coils and the vacuum chamber. Temperature changes of the vacuum chamber influence the concentration of A^{37} between the collector plates.

The vacuum chamber contains a double set of condenser plates. The duplication is used for convenience in the construction only. The central part A of the central condenser plate is electrically insulated from the remainder of the plate, and is connected through a vacuum seal to a vibrating reed electrometer and to an extra condenser $C2$ of the order of 60 cm. $C2$ is placed in vacuum in order to avoid currents from cosmic ray ionization in $C2$. The second plate of $C2$ is connected to a potentiometer so that the vibrating reed electrometer is used as zero indicator only. The current to A is measured by measuring the time t it takes to charge $C2$ to 1 volt.

In order to eliminate temperature drift and changes in concentration due to the decay of A^{37}, measurements have been made by comparing the currents for given values of V and H to the current i_- obtained at $H=2500$ gauss and $V=30$ volts. This latter current is in the following put equal to unity.

The outer part B of the central condenser plate acts as a guard ring and is kept at the same potential as the collector plate A. Nevertheless contact potentials may cause small currents over the many insulators between A and B, and especial care was taken to find insulators which at the same time were sufficiently rigid mechanically and gave sufficiently good insulation even when heavily irradiated with x-rays. Textolite was found to fulfil these conditions.

The outer condenser plates are connected to a group of dry cells in the manner shown in Fig. 4. The potentiometer $P1$ determines the potential V_1 on A and B.

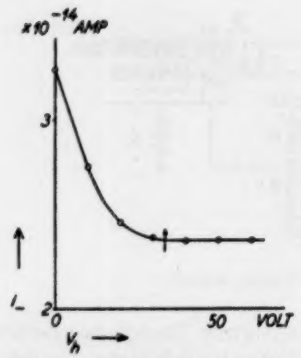

FIG. 5. The current i_- as a function of V_h for definite values of V and H.

V_1 is made equal to the contact potential between the reed and anvil in the vibrating reed electrometer. Thereby the reed indicates zero potential. When the short circuit T is removed, the instrument is ready for a measurement. $P2$ gives a compensating potential on $C2$. This potential can be varied from 0 to 1 volt and is used to keep the reed showing zero and defines the time measurement for a 1-volt raise of $C2$ mentioned above. $P3$ gives the possibility of generating a variable potential V_2 between the outer plate (I+III) and the inner plate (II) of the instrument. V_3 can be adjusted for long-time drift by the variable resistance R. $P4$ divides V_3 so that a certain portion of V_3 is connected to $C2$, and only the remainder V_2 is the main potential between I and III on the one hand and II on the other hand of the collector system $C1$. $P4$ is adjusted so that a variation of V_3 causes no indication on the reed. In this way the influence on the current measurement of short- and long-time variations in V_3 is eliminated, and the measurement can be carried out at an electric potential $V=V_2-V_1$ across $C1$. When V is positive, almost all recoils hit A and electrons move in helical orbits towards the top and the bottom of the vacuum chamber. However, if the electron energy is small and if the electron is created at a positive potential, it cannot move up or down towards the chamber wall but will travel to and fro in the instrument until it ionizes some gas molecule in the residual gas, thus giving a positive ion which adds to the current to A. In order to eliminate this effect the potential V_h is introduced. V_h lifts $C1$ up to such a potential that all electrons can reach the walls of the instrument. This is illustrated by the measurements in Fig. 5. The figure shows the variation of i_- as a function of V_h for definite values of V and H. When $V_h>V$ the pressure effect is reduced to zero. As regards the magnetic field, the most important feature is that the field shall be parallel to the plane of the plates of $C1$. If this is not so, secondary electrons from the walls may spiral up and hit the collector system, reducing the current going to A. The setting of the plane of $C1$ parallel to H is carried out by means of the micrometer screw D, the pivots E, and the phosphorbronze spring F in Fig. 3. Figure 6 shows the results of current measurements as a function of the micrometer reading. It is seen that the best possible setting of the instrument is easily found. Still the field is not strictly homogeneous and the plates are only plane to within 0.02 mm. Therefore some secondary electrons will still hit the plates. This effect is relatively small and, as we shall see later, fairly well represented by the extrapolated current Δi in Fig. 6. Inside the limits of errors, Δi is found to be constant, i.e., independent of H and V, at least in the region used in the present experiment. However, in the present instrument the field inhomogeneities produce the largest systematic error.

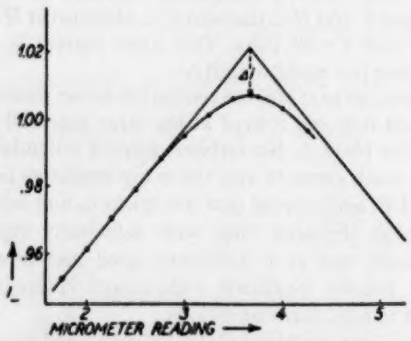

FIG. 6. The current i_- as a function of the micrometer reading. One unit micrometer reading corresponds to a tilting of the instrument of 25′.

MEASUREMENTS

The currents illustrated in the following have been measured at various pressures from 9×10^{-6} mm Hg and upwards, and an extrapolation to zero pressure has been carried out. This correction amounts to at most 1 percent. When i_- is measured as a function of H for $V=60$ volts, the results shown in Fig. 7 are obtained. For 0.4×10^{-3} gauss$^{-1}<1/H<2\times10^{-3}$ gauss^{-1}, the curve follows the expression

$$i_-\cong Ne\langle z\rangle-Ne\langle T_R\rangle/6V \\ -Ne\langle z\rangle[\pi\langle p_e c\rangle/(8aHe)-\langle E_e\rangle Ve/(2aHe)^2], \quad (18)$$

where $\langle T_R\rangle$ is the average kinetic energy of the recoil ions; i.e., the extrapolated line cuts $1/H=0$ in the contribution from the recoils only; this contribution is represented by the first two terms in (18). The measurement has been carried out for different V values (see Fig. 9). Thereby $Ne\langle z\rangle$ can be obtained. The result is

$$Ne\langle z\rangle=1.071\pm0.001, \quad (19)$$

in our current units. Thus we find from Fig. 7,

$$\langle p_e\rangle=69\pm1 \text{ gauss-cm}. \quad (20)$$

If no electrons of momentum $p\gtrsim80$ gauss-cm exist, the curve should proceed along the slightly curved line A in Fig. 7. The deviation shows that electrons exist which get a radius of curvature in their helical orbit which is

larger than a. From the behavior of the curve, one finds that the momentum of these electrons is 162 ± 4 gauss-cm; their relative number also can be estimated. If we take into account the result (22), we find that 65 ± 5 percent of the decays lead to Auger electrons of this momentum, i.e., of energy 2320 ± 120 ev. In this way the contribution to the currents from the electrons is completely accounted for; in the following figure, we correct for this contribution and for the tilting effect Δi mentioned in connection with Fig. 6. The deviation from the extrapolated curve in Fig. 7 for $1/H<0.4\times10^{-3}$ gauss is illustrated in more detail in Fig. 8. This figure has been corrected in the above-mentioned manner so that only the contribution to i_- from the recoils is given.

Within the limits of error this contribution is a constant until H becomes so strong that particles begin to miss the negative plate and either spiral out or hit the positive plate. The curve gives information about the relative numbers of highly charged particles and of the

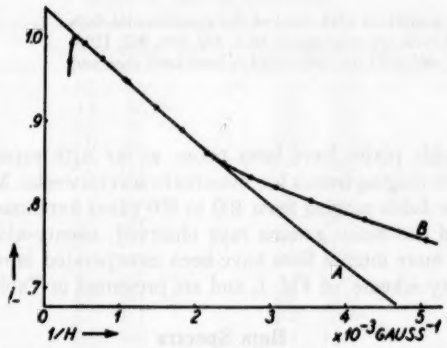

FIG. 7. The current i_- as a function of $1/H$ for $V=60$ volts and $V_k=70$ volts.

momentum of the recoils. The data are fitted to

$$\begin{aligned}\langle Mu_C\rangle &= (812\pm8)\text{ kev},\\ S_6 &= (1\pm1)\text{ percent},\\ S_5 &= (4\pm1)\text{ percent},\\ S_4 &= (18\pm2)\text{ percent},\\ S_3 &= (38\pm4)\text{ percent}.\end{aligned}\qquad(21)$$

Since electrically neutral particles are not detected, S_0 has arbitrarily been put equal to zero, and all which is said here refers to charged recoils only.

Further analysis of i_- for higher values of H leads to rather inaccurate values for S_1 and S_2. In order to obtain more accurate information about these quantities, it is desirable to measure i_+ as a function of V. The results are shown in Fig. 9. From the slope of the curve, $N\langle T_R\rangle$ can be found. As mentioned previously, a knowledge of $\langle Mu_C\rangle$ gives $\langle T_R\rangle$ with sufficient accuracy; thus N can be obtained. The result is

$$Ne=0.405\pm0.008,\qquad(22)$$

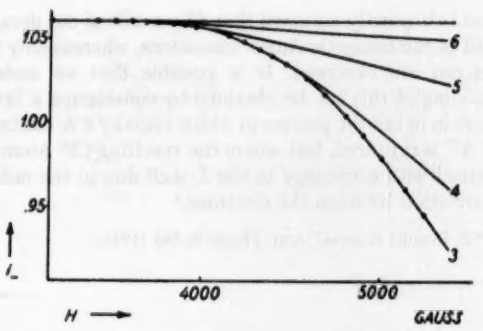

FIG. 8. Recoil contribution to i_- as a function of H.

which together with (19) and (21) gives

$$\begin{aligned}S_1 &= (26\pm3)\text{ percent},\\ S_2 &= (13\pm4)\text{ percent},\\ \langle z\rangle &= 2.64\pm0.08.\end{aligned}$$

If no singly charged recoils of energy greater than 4 ev existed, the curve in Fig. 9 should follow curve A. The deviation gives the independent determination of

$$\begin{aligned}\langle T_R\rangle &= (10\pm1)\text{ ev},\\ S_1 &= (25\pm3)\text{ percent}.\end{aligned}$$

The results thus obtained have been tested by measuring at other V, H values, and all curves so obtained have agreed with the above results. It should also be noted that all currents have been accounted for by performing the correction Δi for the tilting of the instrument; the accuracy is in this way found to be 0.001 of our units of current.

CONCLUSIONS

The experimental results obtained give a slightly lower value for the average charge than that reported by others.[4] This is without doubt connected with the fact

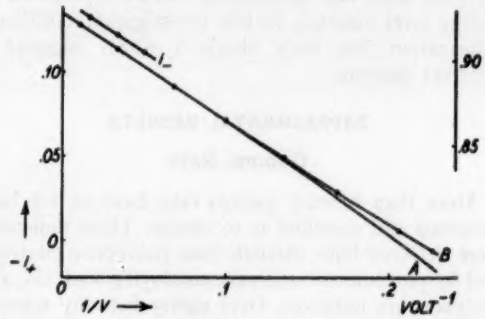

FIG. 9. The currents i_+ and i_- as functions of $1/V$. For i_+ the scale is to the left and for i_- the scale is to the right. The measurements are made at $H=675$ gauss.

[4] M. L. Perlman and J. A. Miskel, Phys. Rev. **91**, 899 (1953); S. Wexler, Phys. Rev. **93**, 182 (1954).

that it is usually assumed that 85 percent of the decays lead to the energetic Auger transitions, whereas only 65 percent are observed. It is possible that an understanding of this can be obtained by considering a little more in detail the process in which initially a K electron in A^{37} is captured, but where the resulting Cl^{37} atom is formed with a vacancy in the L shell due to the radial correlation between the electrons.[5]

[5] P. Benoist-Gueutal, Ann. Physik 8, 593 (1953).

The author wishes to express his thanks to Professor N. Bohr for his interest in this work. I am also grateful to Mr. A. Nielsen for valuable assistance in the experimental work. A detailed description of the instrument and the results obtained with A^{37} will appear in Kgl. Danske Videnskab. Selskab, Mat.-fys. Medd. A discussion of the charge spectrum together with radius of K to L capture and Auger probabilities will be given by A. Winther.

PHYSICAL REVIEW VOLUME 96, NUMBER 4 NOVEMBER 15, 1954

Energy Levels in $_{66}Dy^{160}$†

V. Keshishian, H. W. Kruse, R. J. Klotz, and C. M. Fowler
Kansas State College, Manhattan, Kansas

(Received May 26, 1954)

An energy level diagram for $_{66}Dy^{160}$ is proposed which is consistent with most of the experimental data on this activity, as well as with further data reported here. Levels are proposed at 86.2, 282, 496, 962, 1196, 1259, 1352, and 1532 kev. Beta spectra of 851±10, 557±15, 461±20, and 280±40 kev have been observed and support the diagram.

INTRODUCTION

NEUTRON capture in Tb^{159} leads to Tb^{160} which then decays by beta-minus emission to Dy^{160}. In common with several other even-even nuclear products around this mass number region, a relatively large number of conversion groups were observed by early investigators.[1] Subsequent investigations[2,3] have consistently increased the number of observed transitions, particularly in the higher-energy regions. Reports on the accompanying beta spectra have also varied, not only as to the number and intensities of the spectra, but also in the end-point values. Burson *et al.*[4] recently have summarized in some detail the available information on this activity. In addition, they have reported some new information and have proposed an energy level diagram. In this investigation, additional information has been obtained which suggests a different diagram.

EXPERIMENTAL RESULTS

Gamma Rays

More than seventy gamma rays have so far been observed and classified as to energy. These radiations were detected both through their conversion electrons and by photoelectric analysis, employing lead, tin, and molybdenum radiators. Over eighty beta-ray spectrographic plates have been taken so far with exposure times ranging from a few minutes to several weeks. Magnetic fields ranging from 100 to 800 gauss were used.

Of the many gamma rays observed, twenty-nine of the more intense lines have been incorporated into the decay scheme of Fig. 1, and are presented in Table I.

Beta Spectra

Figure 2 shows a plot of the normalized electron spectrum of Tb^{160} obtained at about 1 percent resolution. The portion of the spectrum below 150 kev is omitted since the density of the source, with backing, was of the order of a few milligrams per square centimeter. Comparison of this source density with those studied by Shull[5] indicates that source scattering effects become noticeable for energies around and below this value.

As remarked earlier, reports on the Tb^{160} beta spectra have shown considerable disagreement among various writers. It is felt here that the major cause of this lack of consistency arises from the presence of a large number of previously unrecognized weak conversion groups superimposed upon the continuous spectrum. Several different runs of the spectrum of Fig. 2, in the 300- to 800-kev region, consistently showed clusters of points several percent too high to allow fitting them with a smooth beta-spectrum type curve. Subsequent observation of spectrographic plates revealed weak conversion groups in the vicinity of all such high point regions. For example, in the region

† Sponsored by the U. S. Atomic Energy Commission.
[1] Cork, Shreffler and Fowler, Phys. Rev. 74, 240 (1948).
[2] Cork, Branyan, Rutledge, Stoddard, and LeBlanc, Phys. Rev. 78, 304 (1950).
[3] Burson, Blair, and Saxon, Phys. Rev. 77, 403 (1950).
[4] Burson, Jordon, and LeBlanc, Phys. Rev. 94, 103 (1954).
[5] F. B. Shull, Phys. Rev. 74, 917 (1948).

2500 to 2750 $B\rho$ of Fig. 2, limited by the letters *b-c*, three weak conversion groups were observed. On the other hand, no groups were observed in the vicinity of the low point *a*. It was therefore assumed that the low points such as *a* should be taken as points on the beta spectrum. The smooth, solid curve of Fig. 2, determined below 2800 $B\rho$ by the low points, is therefore interpreted as the contribution of the continuous spectrum, while the portions of the total spectrum above this curve represent the contributions of conversion groups.

Figure 3 presents the four spectra of allowed shapes obtained by Fermi-Kurie analysis of the smooth curve of Fig. 2. The end points and estimated uncertainties of the spectra are 851±10, 557±15, 461±20, and 280±40 kev. The relative intensities were found to be 30, 32, 19, and 19 percent, respectively. The end-point uncertainty figures were arrived at by making alterations in the smooth curve of Fig. 2, still omitting the high

TABLE I. Transition energies associated with Dy^{160} shown on level diagram of Fig. 1.

Transition energy, kev[a]			Transition energy, kev	
FG	64		*CE*	679
AB	86.2[b,c]		*DG*	762[b]
GH	93	[b,c]	*DH*	856
FH	156		*BE*	876[b,c]
HJ	181		*CF*	915
BC	196	[b,c]	*AE*	962[b,c]
CD	214	[b,c]	*CG*	976
EF	234		*DJ*	1034
GJ	274		*BF*	1110
AC	282	[c]	*BG*	1173[b]
EG	297	[b,c]	*AF*	1196
EH	391	[b,c]	*CJ*	1250
BD	411	[c]	*BH*	1266[b]
DE	466		*BJ*	1447
EJ	569			

[a] Letter notations adjacent to transition energies refer to levels shown on Fig. 1. All transitions listed are supported by both conversion lines and radiator lines. Molybdenum and tin radiators were effective for transitions below 200 kev.
[b] Transitions observed by Burson *et al.* (see reference 4).
[c] Transitions also listed by Cork *et al.* (see reference 2).

regions around conversion groups. Some lower displacement of the continuous spectrum from the low points was necessary, since small line tail contributions of nearby conversion groups usually overlapped the beta spectrum contributions at these points. The end-point uncertainty figures are therefore a reflection of the uncertainty of the line tail contributions at the low points.

Electron-Electron Coincidences

Magnetic-focusing coincidence-spectrometer studies, similar to those described by Fowler and Shreffler,[6] indicated that the *L*-conversion group of the 86.2-kev transition was in coincidence with the *K*-conversion groups of both the 196- and 297-kev transitions. These

[6] C. M. Fowler and R. G. Shreffler, Rev. Sci. Instr. **21**, 740 (1950).

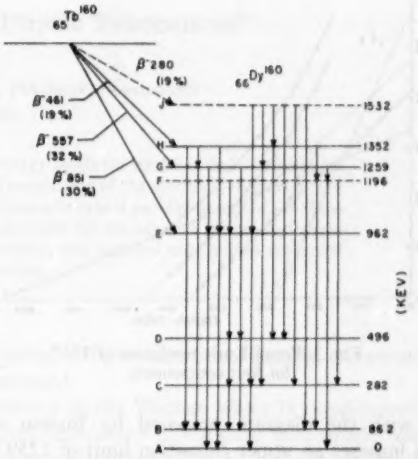

FIG. 1. Proposed energy level diagram for Dy^{160}.

transitions are shown as *AB*, *BC*, and *EG*, respectively, on Fig. 1.

Half-Life Measurements

A single half-life of 72.3±0.5 days has been observed over a time span of nine cycles. The importance of this observation is that it virtually precludes the presence of any activity other than that of Tb^{160}. It is therefore felt that all of the gamma transitions observed here belong to the single activity leading to Dy^{160}.

DISCUSSION

Figure 1 presents features of the energy level diagram of Dy^{160} which are felt to be reasonably well confirmed. The following arguments may be advanced in support of the diagram.

The gamma-ray transition energies are consistent to within experimental accuracy, which is perhaps 1–2 kev for the higher-energy values. Although it is not at present possible to give reliable intensities, the orders of magnitude are consistent. That is, those levels to which intense transitions lead, also have transitions of similar intensity proceeding from them. The transition observed at 1447 kev, shown as (*BJ*) in Fig. 1, con-

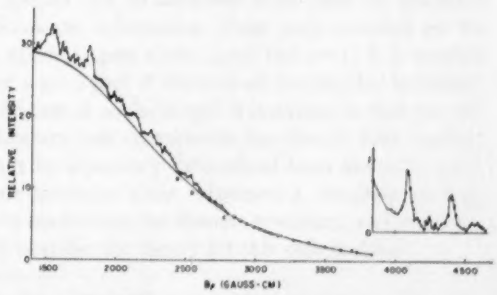

FIG. 2. Normalized electron spectrum of Tb^{160}.

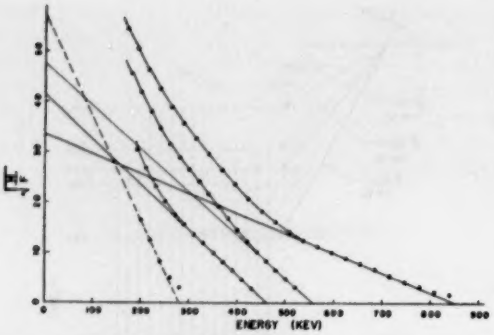

FIG. 3. Fermi-Kurie resolution of Tb^{160} for four components.

flicts with the diagram proposed by Burson *et al.*,[4] which imposes an upper transition limit of 1259 kev.

The beta-spectrum components have energy values which lend themselves to unforced fits with the diagram and again are consistent from the standpoint of intensities.

The scintillation coincidence spectrometer data obtained by Burson *et al.*[4] are interpreted readily by this diagram with one exception. These investigators found that the 214-kev gamma ray (*CD*) was in coincidence with another radiation near the strong 962-kev transition (*AE*). They accordingly postulated a transition of 957 kev which accounted for the coincidence result, and also served to support their diagram. High-energy transitions in this neighborhood, shown in Fig. 1, which should yield coincidences with the 214-kev transition are (*DH*) of 856 kev and (*DJ*) of 1034 kev. Neither transition, however, seems close enough in energy to the 962-kev transition to match the graphical data they present. There is, however, a fairly intense gamma ray of 948 kev, which has not been incorporated into the diagram of Fig. 1. Postulation of a level at 1444 kev would require the 948-kev transition to level *D*. Some other observed transitions, not listed here, also support such a level. The over-all evidence for this additional level however, is not as firm as that for the other levels, and it has therefore not been shown on Fig. 1.

The two levels *F* and *J*, indicated by dashed lines on Fig. 1 are subject to some criticism. Measurements of some of the very weak transitions which support these levels were not too accurate. It was also stated earlier that the uncertainty of the 280-kev beta spectrum end point was quite large.

The energies of levels *B*, *C*, and to a lesser extent *D* are fairly well in line with the Bohr-Mottelson[7] formulation. The spins and parities of these levels would therefore be expected to be 2+, 4+, and 6+. The level *E* at 962 kev also fits approximately into this formulation from an energy standpoint. However, the evidence presented here suggests a 1− assignment for this level, clearly at variance with the 8+ assignment predicted by this theory. The 1− assignment is based upon conversion coefficient data for the two intense transitions *EA* and *EB*. The spectrometer measurements of Fig. 2, together with reasonable branching assumptions, place the *K*-conversion coefficients for those transitions between 0.001 and 0.004. On the other hand, rough measurements of photoelectron intensities along with the *K*-conversion ratios, show that the conversion coefficients are about the same for these transitions. These requirements, coupled with the 0+ and 2+ designations of levels *A* and *B*, lead most plausibly to a 1− assignment for level *E*.

It should finally be remarked that a large number of weak transitions observed have not yet been incorporated into the proposed level diagram. There are, perhaps, a few more higher-energy levels such as those already listed in Fig. 1, which would account for some of these transitions. It is the feeling here, however, that some of the low-energy levels already listed exhibit a fine structure in the sense that there are close-lying levels near them. A number of the weak transitions observed but not shown on Fig. 1 can be explained as transitions to or from such levels, although the evidence is based solely upon transition energy measurements. For example, a number of very weak low-energy transitions have been observed which would support levels near *B* of 80, 84, and 95 kev, and levels of 275 and 285 kev near *C*. Work is still in progress on this phase of the investigation.

[7] A. Bohr and B. R. Mottelson, Phys. Rev. 90, 717 (1953).

Zeeman Splitting of Nuclear Quadrupole Resonances*

C. DEAN†
Radiation Laboratory, University of Pittsburgh, Pittsburgh, Pennsylvania
(Received July 16, 1954)

The theory of the Zeeman splitting of the pure quadrupole energy levels for nuclei of half-integral spin is given in a form that is correct for any electric field gradient. The splitting of the spectra is discussed, and also the simplifications that can be made in the theory when the magnetic field is parallel to any of the three principal axes of the electric field gradient. For spin 3/2 it is shown that the deviation of the gradient from cylindrical symmetry can be determined from the Zeeman spectrum, and detailed calculations are given for this case, along with a discussion of their experimental application.

WHEN there is a strong electric quadrupole coupling between a nuclear species and the gradients of the electric fields at those nuclei due to nearby charges, and when the sample is a crystalline solid so that the average field gradients are constant in time and are the same at equivalent nuclei throughout the sample, we can observe the spectra corresponding to transitions of this species of nucleus between the various energy levels specified by that coupling ("pure quadrupole resonances").[1,2] Since the gradient of the electric field at a given nucleus is produced primarily by the valence electrons belonging to that atom, the details of these resonances provide important information about the way in which the atoms are bound in the solid.[3]

If a homogeneous external magnetic field is applied to such a solid, it will interact with the magnetic dipole moments of the nuclei that we are considering and thereby introduce an additional coupling.[1,4,5] In this paper we shall be concerned with the effect of this additional coupling for small magnetic fields (Zeeman region), in which case each resonance line for a given nucleus is split into either two or four components. The splitting depends on the orientation of the magnetic field with respect to the electric field gradient at that nucleus. In a polycrystalline sample the result is to smear the resonance over a band of frequencies, since there are in effect all possible relative orientations present. However if the sample is a single crystal, we should observe at most as many different Zeeman spectra as there are sites for that species of nucleus in the unit cell. An analysis of such a spectrum for selected magnetic field orientations will determine the orientation of the electric field gradient at each nucleus of the given species, and give additional data on the structure of the sample.[6]

The theory of the Zeeman effect is complicated by the twofold degeneracy of the pure quadrupole energy levels, the complications being most severe for the cases of nuclei of half-integral spin. Calculations for the latter cases have been published for electric field gradients with cylindrical symmetry and for those whose deviation from cylindrical symmetry is small enough to be handled satisfactorily by perturbation theory.[4,5] In the theory given here the magnetic field is again treated only to first order, but the asymmetry of the electric field gradient is treated exactly.

From experimental work[6] it appears that one of the major tasks of the theory is to provide some means of visualizing as a whole all possible cases of Zeeman splitting for a given quadrupole resonance line, since then it is a simple task of recognition to identify approximately the orientation and properties of each electric field gradient from a fairly cursory examination of the splittings due to a sequence of magnetic field orientations. The general form of the Zeeman splitting of the energy levels is given in C, together with a consideration of methods for abbreviating the specific calculations that are required for any one set of electric field gradient parameters. In applying these calculations it is very helpful to plot contours of constant Zeeman splitting of the energy levels, the stereographic net being an excellent chart for this purpose. The contours of constant splitting of the α and β components of the spectra can be obtained from these by graphical addition and subtraction. From such contours for the two extreme cases alone ($\eta=0$ and $\eta=1$) it is possible to get a good part of the over-all picture that is desired.

The case of nuclei of spin $\frac{3}{2}$ is unique in that the two parameters that characterize the electric field gradient cannot be separately determined from the pure quadrupole spectrum alone. However a complete analysis can be made from the Zeeman spectrum, and in section E we consider the theory for this case in detail.

* This research was supported in part by the Air Force under a contract monitored by the Office of Scientific Research of the Air Research and Development Command.
† Portions of this material were included in the thesis submitted by the author in partial fulfillment of the requirements for the Ph.D. degree at Harvard University.
[1] R. V. Pound, Phys. Rev. **79**, 685 (1950).
[2] H. G. Dehmelt and H. Kruger, Z. Physik **129**, 401 (1951).
[3] C. H. Townes and B. P. Dailey, J. Chem. Phys. **17**, 782 (1949); **20**, 35 (1952).
[4] H. Kruger, Z. Physik **130**, 371 (1951).
[5] R. Bersohn, J. Chem. Phys. **20**, 1505 (1952).
[6] C. Dean, Thesis, Harvard, 1952 (unpublished); Phys. Rev **86**, 607 (1952).

A. THE QUADRUPOLE EIGENSTATES

The Hamiltonian for the interaction between the electric quadrupole moment of a nucleus and the charges surrounding the nucleus has been derived elsewhere.[1,5] In this Hamiltonian the effect of the surrounding charges is expressed in terms of the symmetric tensor composed of the second derivatives of the electrostatic potential that they produce at the nucleus, $V_{x_ix_j}=\partial^2V/\partial x_i\partial x_j$. Only that part of the potential that is generated by charges outside of the nucleus is involved; hence Laplace's equation holds and $V_{xx}+V_{yy}=-V_{zz}$. We consider here only those coordinate systems in which the tensor is diagonal. We define the principal coordinate system by requiring that $|V_{zz}|\geq|V_{yy}|\geq|V_{xx}|$, and we introduce the quantities $eq\equiv V_{zz}$ and $\eta\equiv(V_{xx}-V_{yy})/V_{zz}$. In the principal coordinate system we have $0\leq\eta\leq1$, and η is a measure of the deviation of the tensor from cylindrical symmetry around the z axis.

The principal coordinate system is uniquely defined by this convention except in the case $\eta=0$, in which the distinction between the x and the y axes disappears, and in the case $\eta=1$. In the latter case we have $V_{zz}=0$ and $V_{xx}=-V_{yy}$, and it is apparent that by interchanging the z and the y axes and reversing the sign of eq we obtain a new coordinate system which also satisfies our definition of the principal coordinate system; here it is the x axis that is unique.

With the electric field gradient expressed in this manner, the nonzero matrix elements of the Hamiltonian for the quadrupole interaction are

$$(m_z|\mathcal{H}_e|m_z)=A[3m_z^2-I(I+1)],$$
$$(m_z\pm2|\mathcal{H}_e|m_z)=A(\eta/2)f_I(\pm m_z)f_I(1\pm m_z),$$

where

$$f_I(m)=f_I(-m-1)=[(I-m)(I+m+1)]^{\frac{1}{2}},$$
$$A=[e^2qQ/4I(2I-1)], \tag{1}$$

and where I is the spin of the nucleus and m_z is the component of spin along the z axis of the principal coordinate system of the electric field gradient. The quantity eQ is the electric quadrupole moment of the nucleus, defined by $eQ\equiv\langle\rho(3z^2-r^2)\rangle_{Av}$, in which ρ is the charge density of the nucleus and z and r describe the locations of the elements of charge density that are incorporated into the average; the averaging is performed for the nuclear state $m=I$.

This Hamiltonian links only alternate spin states. For the case of half-integral spins with which this paper deals it is readily seen that the two independent submatrices which can be identified are identical except for a reversal of the signs of m involved, and it can be seen that this reversal of sign does not change the matrix elements. It follows that the twofold degenerate energy eigenstates can be divided into two groups which involve identical sets of transformation coefficients and energy levels, $E_{m'}{}^0$:

$$A_{m'}=(1/2|m')\psi_{\frac{1}{2}}+(3/2|m')\psi_{-\frac{1}{2}}+(5/2|m')\psi_{\frac{1}{2}}+\cdots,$$
$$B_{m'}=(1/2|m')\psi_{-\frac{1}{2}}+(3/2|m')\psi_{\frac{1}{2}}+(5/2|m')\psi_{-\frac{1}{2}}+\cdots. \tag{2}$$

The number m' is taken as the value of $|m|$ that applies to the state as $\eta\rightarrow0$.

The above formulation is generally chosen in these problems because of the resulting simplicity of the case $\eta=0$. However the form of the Hamiltonian matrix is unchanged if we use as a basis the states $\psi(I,m_x)$ or $\psi(I,m_y)$ instead of the set $\psi(I,m_z)$. We choose the phase relations between the sets of spin eigenfunctions to correspond to cyclic permutations of the x, y, and z axes, and we introduce the quantities F and G, in which we retain the parameters eq and η to describe the electric field gradient:

$$F_x=-\tfrac{1}{2}A(1-\eta),\quad G_x=-\tfrac{1}{4}A(3+\eta),$$
$$F_y=-\tfrac{1}{2}A(1-\eta),\quad G_y=+\tfrac{1}{4}A(3-\eta), \tag{3}$$
$$F_z=A,\qquad\qquad G_z=\tfrac{1}{2}A\eta.$$

With this notation the Hamiltonian matrix elements for all three cases can be written

$$(m_i|\mathcal{H}_e|m_i)=F_i[3m_i^2-I(I+1)],$$
$$(m_i\pm2|\mathcal{H}_e|m_i)=G_if_I(\pm m_i)f_I(1\pm m_i), \tag{4}$$

in which $i=x$, y, or z denotes the chosen axis of spin quantization. Since the form of the Hamiltonian is the same in each of these formulations, a choice of eigenstates can be made for each with the form given in (2), these alternative sets of states being different linear combinations of the twofold degenerate levels.

The nuclear quadrupole resonances that are observed are all due to magnetic dipole transitions, since it is impossible to produce rf electric fields with gradients at the nuclei that are strong enough to cause appreciable transition probabilities. For $\eta=0$ we observe only the transitions with $\Delta m=\pm1$, which are produced by rf fields in the xy plane. However, because of the mixing of the spin states, we must consider other $\Delta m'$ values and all orientations of the rf field for large values of η. We shall not discuss the pure quadrupole spectra further except for the case $I=\frac{3}{2}$, which is treated in Sec. E. In the remainder of this paper we deal with the splitting of the individual lines of these spectra which is produced by a magnetic field.

We note at this point that the values of the two electric field gradient parameters can be evaluated separately from experimental pure quadrupole spectra for all values of nuclear spin except $\frac{3}{2}$. The coefficients of the secular equation for either submatrix of the Hamiltonian provide $(I+\frac{1}{2})$ equations relating the $(I+\frac{3}{2})$ unknowns, $E_{m'}{}^0$ and η. For $I\geq5/2$ there are two or more pure quadrupole resonance frequencies; the ratios of pairs of these frequencies can be equated to the proper ratios of differences between energy levels, and with these additional relations the unknowns can be evaluated to any desired accuracy. In contrast to

these cases, that of $I=\frac{3}{2}$ provides only a single experimental datum, and the complete analysis is impossible.

B. THE ZEEMAN PERTURBATION

If a magnetic field is applied to the system that we have been discussing, the interaction between it and the magnetic dipole moment of the nucleus must be added to the Hamiltonian.[4,5,7] These additional matrix elements can be written

$$\begin{aligned}(m_z|\,3\mathcal{C}_m\,|m_z)&=2m_z\xi\cos\theta,\\ (m_z+1|\,3\mathcal{C}_m\,|m_z)&=\xi\sin\theta e^{-i\phi}f_I(m_z),\\ \xi&=(\gamma\hbar H/2),\end{aligned}\tag{5}$$

where H is the magnitude of the magnetic field and θ and ϕ are its orientation expressed in polar coordinates that are based on the principal coordinate system, $f_I(m)$ is the function defined in (1), and γ is the gyromagnetic ratio of the nucleus. The magnetic coupling is assumed to be small compared to the quadrupole energies.

We review first the results when the electric field gradient has cylindrical symmetry.[4,5] The states $\psi(I,m_z)$ are correct to first order for $|m|\neq\frac{1}{2}$, but the submatrix $m_z=\frac{1}{2}$, $-\frac{1}{2}$ must be diagonalized for the remaining pair of levels. The energies are

$$\begin{aligned}E_m&=A[3m^2-I(I+1)]\pm 2m\xi\cos\theta,\quad |m|\neq\tfrac{1}{2}\\ E_{\frac{1}{2}\pm}&=A[\tfrac{3}{4}-I(I+1)]\pm\xi[(I+\tfrac{1}{2})^2\sin^2\theta+\cos^2\theta]^{\frac{1}{2}}.\end{aligned}\tag{6}$$

The required mixtures of the $\frac{1}{2}$, $-\frac{1}{2}$ states are given by

$$\begin{aligned}E_{\frac{1}{2}+}:&\quad (\tfrac{1}{2}|+)=\cos\Theta e^{-i\phi/2},\\ &\quad (-\tfrac{1}{2}|+)=\sin\Theta e^{i\phi/2};\\ E_{\frac{1}{2}-}:&\quad (\tfrac{1}{2}|-)=\sin\Theta e^{-i\phi/2},\\ &\quad (-\tfrac{1}{2}|-)=-\cos\Theta e^{i\phi/2};\\ \tan(2\Theta)&=(I+\tfrac{1}{2})\tan\theta.\end{aligned}\tag{7}$$

The specification of Θ in terms of θ comes from the requirement that the matrix element connecting the new states be zero.

For the general case it is necessary to investigate the mixing of each degenerate pair of states $A_{m'}$, $B_{m'}$. We start from the expressions (2) for the exact pure quadrupole states. By definition $3\mathcal{C}_e$ is diagonal in this system, with eigenvalues $E_{m'}{}^0$ which can be calculated when necessary from (1). The transformed matrix elements of the magnetic interaction (5) which we need are

$$\begin{aligned}(A_{m'}|\,3\mathcal{C}_m\,|A_{m'})&=-(B_{m'}|\,3\mathcal{C}_m\,|B_{m'})=\xi a_{m'}\cos\theta,\\ (A_{m'}|\,3\mathcal{C}_m\,|B_{m'})&=\xi\sin\theta(b_{m'}e^{-i\phi}+c_{m'}e^{i\phi}),\end{aligned}\tag{8}$$

in which we use the Zeeman parameters a, b, c defined by

$$\begin{aligned}a_{m'}&=[(1/2|m')^2-3(3/2|m')^2+5(5/2|m')^2-\cdots],\\ b_{m'}&=(I+1/2)(1/2|m')^2+2f_I(3/2)(3/2|m')(5/2|m')\\ &\quad+2f_I(7/2)(7/2|m')(9/2|m')+\cdots,\\ c_{m'}&=2f_I(1/2)(1/2|m')(3/2|m')\\ &\quad+2f_I(5/2)(5/2|m')(7/2|m')+\cdots.\end{aligned}\tag{9}$$

[7] Bloembergen, Purcell, and Pound, Phys. Rev. 73, 679 (1948).
[8] B. Feld and W. E. Lamb, Phys. Rev. 67, 15 (1945).

The quadratic secular equations arising from each such pair of states yield the Zeeman energy levels for the general case:

$$E_{m'\pm}=E_{m'}{}^0\pm\xi[a_{m'}{}^2\cos^2\theta+(b_{m'}{}^2+c_{m'}{}^2+2b_{m'}c_{m'}\cos2\phi)\sin^2\theta]^{\frac{1}{2}}.\tag{10}$$

The Zeeman parameters are defined above in terms of the pure quadrupole transformation coefficients. However they may also be evaluated in part from the terms linear in ξ which occur in expansions of the special solutions for a magnetic field parallel in turn to each of the three major axes. For these orientations (10) becomes

$$E_{m'\pm}=E_{m'}{}^0\pm\begin{cases}\xi|a_{m'}| & H\|z\\ \xi|b_{m'}+c_{m'}| & H\|x.\\ \xi|b_{m'}-c_{m'}| & H\|y\end{cases}\tag{11}$$

The required terms are just the derivatives $(\partial E/\partial\xi)_{\xi=0}$, and exact formulas for them may be found by implicit differentiation of the secular equations for the three special cases. The only limitation on the accuracy of the results in this method is the accuracy of the energy values $E_{m'}{}^0$ that are subsequently inserted in the formulas.

The degeneracy of the quadrupole interaction is easily dealt with in the three special cases needed above, for in each case the complete Hamiltonian can again be split into two independent parts neither of which is itself degenerate. In one method of doing this we choose the axis of spin quantization in (4) to be the one parallel to the magnetic field; adding the proper magnetic elements for these states we obtain

$$\begin{aligned}(m_i|\,3\mathcal{C}_e+3\mathcal{C}_m\,|m_i)&=F_i[3m_i{}^2-I(I+1)]+2\xi m_i,\\ (m_i\pm2|\,3\mathcal{C}_e+3\mathcal{C}_m\,|m_i)&=G_if_I(\pm m_i)f_I(1\pm m_i),\end{aligned}\tag{12}$$

in which $i=x$, y, or z, according to the direction of the magnetic field. Although this method of handling the case $H\|x$ or y is useful in dealing with arbitrary values of η, it is not suitable for perturbation calculations even when η is small, since the off-diagonal quadrupole elements are the same order of magnitude as the diagonal ones.

In an alternate procedure for the case $H\|x$ we use the sum and difference states,

$$\psi_{m\pm}=2^{-\frac{1}{2}}[\psi(I,m_z)\pm\psi(I,-m_z)],\quad m_z=\tfrac{1}{2},\tfrac{3}{2},\cdots I.$$

The Hamiltonian elements for this case then become

$$\begin{aligned}(m_\pm\|m_\pm)&=A[3m^2-I(I+1)]\pm\delta_{m,\frac{1}{2}}\xi f_I(-\tfrac{1}{2}),\\ ((m+1)_\pm\|m_\pm)&=\pm\delta_{m,\frac{1}{2}}A(\eta/2)f_I(-\tfrac{1}{2})f_I(\tfrac{1}{2})+\xi f_I(m),\\ ((m+2)_\pm\|m_\pm)&=A(\eta/2)f_I(m)f_I(m+1).\end{aligned}\tag{13}$$

Since the sum and difference states are correct for $\eta=0$, this formulation is useful for perturbation calculations.

For $H\|y$ apparently we should rotate the sum and difference states 90° about the z axis. However the only distinction between the x and y axes is that $|V_{zz}|$

$\leq |V|_{yy}$ or, equivalently, that $\eta \geq 0$. Therefore the transformation is accomplished in effect by changing the sign of η wherever it occurs. Similar sum and difference states can also be constructed from the bases $\psi(m_x)$ or $\psi(m_y)$ to provide independent nondegenerate submatrices for magnetic fields parallel to the other pairs of the coordinate axes. These states, however, are not useful for perturbation calculations, and they hold no advantage over the simple spin states for the work that we are considering here.

As an illustration we calculate the Zeeman parameters to the first power of η. We take the energies to second order from Eqs. (13) for $H\|x$; we reverse the sign of η in this result to obtain the case $H\|y$; we use the diagonal elements from (12) with $i=z$ for $H\|z$; from these expressions we identify the Zeeman parameters according to the prescription in (11). We find (see Bersohn's results, reference 5)

$$\begin{gathered} a_{m'}=2m', \\ b_{\frac{1}{2}'}=(I+\tfrac{1}{2}), \quad b_{m'}=0 \quad \text{for } m'>\tfrac{1}{2}, \\ c_{\frac{1}{2}'}=-c_{\frac{1}{2}'}=-(I-\tfrac{1}{2})(I+\tfrac{1}{2})(I+\tfrac{3}{2})(\eta/6), \\ c_{m'}=0 \quad \text{for } m'>\tfrac{3}{2}. \end{gathered} \tag{14}$$

C. THE ZEEMAN SPECTRUM

From the general formulation of the energy levels given above, we can see that the dependence of the Zeeman splitting of the spectrum on the orientation of the magnetic field is formally the same for every quadrupole resonance. For the transition $m_1' \leftrightarrow m_2'$, we have

$$\nu=\nu_0 \pm (\xi/h)([m_1']\pm[m_2']), \tag{15}$$

where ν_0 is the appropriate unperturbed frequency and

$$[m]\equiv+[a_m^2\cos^2\theta+(b_m^2+c_m^2+2b_mc_m\cos 2\phi)\sin^2\theta]^{\frac{1}{2}}.$$

We label the pair with the smaller splitting, i.e., with $([m_1']-[m_2'])$, the α components, and the other pair the β components. Additional resonances are possible here, corresponding to the transitions $A_{m'} \leftrightarrow B_{m'}$,[1] but for small magnetic fields they would occur at very low frequencies. They will not be discussed in this paper.

The total intensity of the four components of the Zeeman multiplet is that of the corresponding unsplit pure quadrupole resonance. For the case $\eta=0$, the relative intensities of these four components are easily derived from the approximate states given in (7, 8). Only rf magnetic fields in the xy plane are effective. For transitions between levels with $|m|\neq\frac{1}{2}$ only the α components can be observed, with intensities that are equal and that do not depend on the orientation of the Zeeman field. On the other hand, the mixing of the states $m=\pm\frac{1}{2}$ means that the single pure quadrupole line corresponding to transitions between the states $|m|=\frac{1}{2}, \frac{3}{2}$ splits into four components whose intensities do depend on the orientation of the Zeeman field, according to the rules

$$\begin{aligned} &\alpha\text{:}\quad W(\tfrac{3}{2},\tfrac{1}{2}+)\doteq W(-\tfrac{3}{2},\tfrac{1}{2}-)\sim\cos^2\Theta, \\ &\beta\text{:}\quad W(\tfrac{3}{2},\tfrac{1}{2}-)\doteq W(-\tfrac{3}{2},\tfrac{1}{2}+)\sim\sin^2\Theta. \end{aligned} \tag{16}$$

Because of the general mixing of states by the asymmetry and by the Zeeman field, both the α and the β components may be observable for each pure quadrupole line when η is large. Although we shall not attempt a detailed discussion of relative intensities here, we shall set up the machinery for obtaining certain useful selection rules. We consider the set of nine cases: Zeeman field (H_0) parallel to x, y, or z, together with the rf field (H_1) parallel to x, y, or z. For $H_0\|z$ we imagine the states $\psi(I,m_z)$ arrayed in such a fashion that the submatrix containing the A states of equation (2) is grouped separately from the one with the B states.

In this diagram we consider the locations of the nonzero elements of I_x, I_y, and I_z, whose squares are proportional to the transition probabilities for H_1 parallel in turn to x, y, and z. For selection rules we find that $H_1\|z$ can at most cause transitions between states lying within the same submatrix (transitions which we designate together as $[AA]$), while $H_1\|x$ or y can at most cause transitions for which one state is in A and the other is in B (designated $[AB]$). For $H_0\|x$ or y we use the states $\psi(I,m_x)$ or $\psi(I,m_y)$; the above arguments can be duplicated step by step, and for the selection rules we permute cyclically the names x, y, and z.

These qualitative results are quite general, holding for any relative strength of the dipole and the quadrupole couplings and for any value of the parameter η. For the Zeeman region it is apparent that in these particular cases we shall observe at most either the α components alone or the β components alone.

For a few quadrupole transitions it can be readily determined which of the pairs of components, α or β, is represented by $[AA]$ and by $[AB]$, respectively. In the case $H_0\|z$ with η small, it can be seen from (6) that for transitions between quadrupole states in which $\Delta m'$ is odd, $[AA]$ and $[AB]$ correspond, respectively, to the β and the α Zeeman components, while for the transitions with $\Delta m'$ even the situation is reversed.

Because the levels $m'>\frac{3}{2}$ are unsplit by a Zeeman field parallel to x or y in the second order calculation we cannot so readily investigate the general selection rules for the α and β components except for the transitions $\frac{1}{2}' \leftrightarrow \frac{3}{2}'$. The submatrices of the sum and difference states of (13) are equivalent to the A and B submatrices based on $\psi(I,m_z)$; therefore, we may use second-order energies to show that, for the transitions $\frac{1}{2}' \leftrightarrow \frac{3}{2}'$ with $H_0\|x$, the $[AA]$ pair comprise the α components while the $[AB]$ pair are the β components. For $H_0\|y$ these identifications are reversed.

Although the above identifications were derived on the basis of small η, an intuitive argument leads us to accept them tentatively for all values of η. We have seen by a rigorous argument that only one pair of

Zeeman components can be seen in any of these cases. If we then assume that our various results are continuous functions of the parameter η, we find that a given one of the identifications that we have made for small η can be reversed only for values of η at which either the intensity of the quadrupole resonance becomes zero or the α and the β components coalesce.

It is of interest to note finally that the nuclear induction apparatus of Bloch *et al.*[9] can detect the Zeeman-split quadrupole resonances although it cannot detect the unsplit pure quadrupole lines. In such a spectrometer the transmitter coil bathes the sample in a linearly polarized rf magnetic field. The receiver coil in the apparatus views this field as the sum of two fields with opposite senses of circular polarization, and the essential experimental question which it answers is whether at any given frequency one circular component interacts more strongly with the sample than does the other. In the pure quadrupole resonances both senses of circular polarization are treated alike by the sample, mainly because of the $\pm m$ degeneracy of the system. The Zeeman splitting lifts this degeneracy, and it can be shown that certain of the Zeeman components should be detected by the nuclear induction equipment if the numerous orientations involved in the experiment are favorable.

D. REMARKS ON $\eta=1$

In applying the foregoing theory to obtain an over-all picture of the solutions for a given value of nuclear spin we would desire at least the particular solutions for the end points of the range $0\leq\eta\leq1$. The point $\eta=0$ is easily treated, and nearby values of η can be handled satisfactorily by perturbation theory. We now point out briefly the properties of the problem for $\eta=1$ which simplify the other set of calculations.

(a) The calculation of the energy levels of the quadrupole system involves in general the solution of a secular equation for the $E_{m'}{}^0$ whose order is $(I+\frac{1}{2})$. However for $\eta=1$ it can be shown[6] that the energy levels are symmetric around the value $E=0$, and that the secular equation can be reduced to one involving only powers of $(E_{m'}{}^0)^2$, with an additional single root $E_{m'}{}^0=0$ factored out in those cases where there is an uneven number of values of $|m|$. This situation can be understood on physical grounds by recalling that here we have $V_{zz}=0$ and $V_{yy}=-V_{xx}$. This case can therefore be considered either as the limit of the case where $V_{zz}=eq$ and $-(eq/2)\geq V_{yy}\geq-eq$ (as we do in the principal coordinate system), or as the limit of the case where $V_{yy}=eq'=-eq$ and $-(eq'/2)\geq V_{zz}\geq-eq'$ (as we would in the alternate coordinate system that satisfies our definition of a principal coordinate system in this one case). Because of this the set of energy eigenvalues for $V_{yy}=-V_{zz}$ must be unchanged by a reversal of the sign of the energy unit, e^2qQ.

[9] Bloch, Hansen, and Packard, Phys. Rev. **70**, 474 (1946).

(b) Let us consider the extended range $0\leq\eta\leq3$. An inspection of the defining equation $\eta=(V_{xx}-V_{yy})/V_{zz}$ shows that, whereas $\eta=0$ signifies cylindrical symmetry around the z axis, $\eta=3$ signifies it around the y axis, and the preceding paragraph shows that $\eta=1$ can be considered as the midpoint of the transition from one symmetry case to the other.

From (a) and (b) we can see that the Zeeman splitting of the state $m'=\frac{1}{2}+k$ as a function of the direction of the magnetic field when $\eta=1$ must be the same function as the splitting of the state $m'=I-k$ except for a rotation of 90° around the x axis. Similar relations hold for such functions as the Zeeman splitting of the spectrum and the transition probabilities as functions of the Zeeman and the rf magnetic fields. Also we note that the variations of these functions as η passes through the value 1 must be such as to match the appropriate alternate functions that are based on the rotated coordinate system, providing proper account is taken of the unsymmetrical way in which η describes the two sides of the point $\eta=1$.

E. DETAILS FOR $I=3/2$

Here much of the basic computation can be performed exactly. We begin by listing the principal results for the energy levels in terms of the usual parameter, η. In this case the secular equations from (4) are quadratic, and the exact energy levels are

$$\begin{aligned}&E=-\xi\pm E_0[1+4(\xi^2-\xi F)/E_0{}^2]^{\frac{1}{2}}, \quad \text{(states } A\text{)}\\ &E=+\xi\pm E_0[1+4(\xi^2+\xi F)/E_0{}^2]^{\frac{1}{2}}, \quad \text{(states } B\text{)}\\ &E_0=F^2+(4G/3)=A(1+\tfrac{1}{3}\eta^2)^{\frac{1}{2}}.\end{aligned} \tag{17}$$

Identifying the states by the limiting values of $|m_z|$ as η, $\xi\to0$, we find the approximate energies for small value of ξ to be

$$\begin{aligned}E_{\frac{1}{2}'}&=E_0\pm(1+2F/E_0)\xi,\\ E_{\frac{1}{2}'}&=-E_0\pm(1-2F/E_0)\xi,\end{aligned} \tag{18}$$

Inserting in turn the proper values for F_i, we find the Zeeman parameters from (18) and (11):

$$\begin{aligned}&a_{\frac{1}{2}'}=-1-2/\rho, \quad a_{\frac{1}{2}'}=-1+2/\rho,\\ &b_{\frac{1}{2}'}=1-1/\rho, \quad b_{\frac{1}{2}'}=1+1/\rho,\\ &c_{\frac{1}{2}'}=\eta/\rho, \quad c_{\frac{1}{2}'}=-\eta/\rho,\\ &\rho=(1+\tfrac{1}{3}\eta^2)^{\frac{1}{2}}.\end{aligned} \tag{19}$$

The energy levels for any value of η and correct to first order in the magnetic field are now given by

$$\begin{aligned}&E_{\frac{1}{2}'\pm}=E_0\pm\xi[\tfrac{3}{2}'], \quad E_{\frac{1}{2}'\pm}=-E_0\pm\xi[\tfrac{1}{2}'],\\ &[m]\equiv[a_m{}^2\cos^2\theta+(b_m{}^2+c_m{}^2+2b_mc_m\cos2\phi)\sin^2\theta]^{\frac{1}{2}}.\end{aligned} \tag{20}$$

It can be seen that the radical $[m]$ multiplying ξ does not vanish for any values of (θ,ϕ) except in the singular case $\eta=0$ for which $[3/2]$ is zero along the locus $\theta=90°$.

An alternate formulation of this problem yields simple expressions for the eigenstates and the matrix

elements required for dipole transition probabilities. We write the pure quadrupole states in the automatically orthogonal form:

$$\begin{aligned} A_1&=\cos(\alpha/2)\psi_{\frac{1}{2}}-\sin(\alpha/2)\psi_{-\frac{1}{2}},\\ A_3&=\sin(\alpha/2)\psi_{\frac{1}{2}}+\cos(\alpha/2)\psi_{-\frac{1}{2}},\\ B_1&=\cos(\alpha/2)\psi_{-\frac{1}{2}}-\sin(\alpha/2)\psi_{\frac{1}{2}},\\ B_3&=\sin(\alpha/2)\psi_{-\frac{1}{2}}+\cos(\alpha/2)\psi_{\frac{1}{2}},\\ \tan\alpha&=(2G/\sqrt{3}F). \end{aligned} \tag{21}$$

The subscripts are the value of $|2m|$ for $\alpha=0$. α is specified by the requirement that the off-diagonal quadrupole elements vanish. The diagonal quadrupole elements express the unperturbed energies as

$$\begin{aligned} (A_3\|A_3)=(B_3\|B_3)=-(A_1\|A_1)=-(B_1\|B_1)\\ =E_0=F\sec\alpha=(2G/\sqrt{3})\csc\alpha. \end{aligned} \tag{22}$$

For the moment let us employ the parameters F_z, G_z of (3), but allow η to take all values $-\infty\leq\eta\leq\infty$; this is equivalent to choosing one of the normal coordinates axes at random as the z axis and discussing all possible ratios of V_{xx}, V_{yy}, and V_{zz} in this one coordinate system. We find

$$\tan\alpha=(2G_z/\sqrt{3}F_z)=(\eta/\sqrt{3}). \tag{23}$$

For a small magnetic field always parallel to what we are at present calling the z axis, the perturbation of the energy levels is given by the diagonal elements. Adding these to (22) we find

$$\begin{aligned} (A_1\|A_1)&=-E_0+\xi(2\cos\alpha-1),\\ (B_1\|B_1)&=-E_0-\xi(2\cos\alpha-1),\\ (A_3\|A_3)&=E_0-\xi(2\cos\alpha+1),\\ (B_3\|B_3)&=E_0+\xi(2\cos\alpha+1). \end{aligned} \tag{24}$$

For magnetic dipole transition probabilities we need the matrix elements of I_x, I_y, and I_z; for completeness we include those for the low-frequency transitions:

$$\begin{aligned} &(A_1|2I_x|B_1)=1-2\sin(\alpha-30°),\\ &(A_3|2I_x|B_3)=1+2\sin(\alpha-30°),\\ &(A_1|2I_x|B_3)=(A_3|2I_x|B_1)=2\cos(\alpha-30°),\\ &(A_1|2I_y|B_1)=-i[1+2\sin(\alpha+30°)],\\ &(A_3|2I_y|B_3)=-i[1-2\sin(\alpha+30°)],\\ &(A_1|2I_y|B_3)=(A_3|2I_y|B_1)=i[2\cos(\alpha+30°)],\\ &(A_1|2I_z|A_3)=-(B_1|2I_z|B_3)=2\sin(\alpha). \end{aligned} \tag{25}$$

The foregoing solutions are formally correct for all three of the matrices $i=x$, y, or z, obtained from (4). However, for our working formulas we want these solutions couched in terms appropriate to the principal coordinate system which we have adopted as the standard way to describe a given physical case. Denoting by subscripts the parameters defined by (21) when we use F_z, G_z or F_y, G_y, we can show that

$$\alpha_z=\alpha+60°,\quad \alpha_y=\alpha-60°, \tag{26}$$

where η is given by (23) in terms of the principal coordinate system. To identify the energy levels in terms of the nomenclature appropriate to $\psi(I,m_z)$ we assume e^2qQ to be positive and list the levels for the three cases in order of decreasing energy (the fact that the Zeeman levels do not cross for intermediate orientations of the magnetic field is shown by the nonvanishing of $[m]$ in (20)):

	$H\|z$ $\psi(m_z)$	$H\|x$ $\psi(m_x)$	$H\|y$ $\psi(m_y)$
$E_{\frac{1}{2}+}$	B_3	B_1	A_1
$E_{\frac{1}{2}-}$	A_3	A_1	B_1
$E_{\frac{1}{2}+}$	A_1	B_3	B_3
$E_{\frac{1}{2}-}$	B_1	A_3	A_3

(27)

For the spin matrix elements between these states for $H\|x$ or y the letters x, y, and z are permuted cyclically in (25) and α is modified as shown in (26).

The Zeeman parameters are easily evaluated from (9) and (21):

$$a=-1\pm2\cos\alpha,\quad b=1\pm\cos\alpha,\quad c=\mp\sqrt{3}\sin\alpha. \tag{28}$$

Here the upper and lower signs refer to $m'=\frac{1}{2}$ and $\frac{3}{2}$, respectively.

In the course of experimental work it was found that one of the most useful features of the Zeeman spectrum as a function of magnetic field orientation was the locus along which the α components are unsplit; this relatively strong resonance at the normal pure quadrupole frequency was easy to identify and to interpret. The condition for this locus is $[\frac{3}{2}']=[\frac{1}{2}']$, and by inserting the Zeeman coefficients that were derived above the locus can be explicitly written as the function $\theta_0(\phi)$. Here we shall derive $\theta_0(\phi)$ in a manner to show its importance for all magnitudes of the magnetic field when $I=\frac{3}{2}$. The secular equation for the general case in which any orientation of the magnetic field is allowed is

$$\begin{aligned} 0=E^4&-[2+(2\eta^2/3)+10\xi^2]E^2\\ &-(16\xi^2-24\xi^2\sin^2\theta+8\xi^2\eta\sin^2\theta\cos2\phi)E\\ &+1+2\eta^2/3+\eta^4/9-10\xi^2+12\xi^2\sin^2\theta+9\xi^4\\ &+2\eta^2\xi^2-4\xi^2\eta^2\sin^2\theta+8\xi^2\eta\sin^2\theta\cos2\phi. \end{aligned} \tag{29}$$

The energy unit $A=(e^2qQ)/[4I(2I-1)]$ is used here, so that $\xi=(\gamma\hbar H/2A)$. This equation reduces to a quadratic in E^2 when the coefficient of E is zero, which occurs when

$$\sin^2\theta=2/(3-\eta\cos2\phi). \tag{30}$$

The four solutions have the form

$$E=\pm(A\pm B)^{\frac{1}{2}},$$

and it is easy to verify from this that (30) must define the locus $\theta_0(\phi)$. For magnetic field strengths too large to be treated by first order calculations there will not be in general an unsplit line at the pure quadrupole

frequency, but at least one pair of spectral components will coalesce to a single line along this locus, making it readily identifiable experimentally.

We note finally the methods for determining η from experimental Zeeman data. One set of measurements for this purpose is the location of $\theta_0(\phi)$ of (30). The principal coordinate system for the field gradient under investigation is determined from the symmetry that the Zeeman splittings show as functions of the orientation of the magnetic field and from the fact that $\theta_0(\phi)$ has its maximum and minimum values in the xz and the yz planes, respectively. η is found from the formula:

$$\eta=\frac{3[\sin^2\theta_0(0°)-\sin^2\theta_0(90°)]}{\sin^2\theta_0(0°)+\sin^2\theta_0(90°)}. \tag{31}$$

As we have seen, this method of determining η can be adapted for use with magnetic fields of any magnitude. In this procedure the only precision measurements are those of the direction of the magnetic field; the spectrometer serves only as an indicator.

The other method that our theory provides for determining η requires the measurement of the amounts of splitting when the magnetic field is parallel to one of the principal axes of the field gradient in question. The differences in frequency between the Zeeman components and the unsplit quadrupole resonance, expressed in energy units, are found from (19):

	α	β	
$H\|\|z$	2ξ	$4\rho\xi$	
$H\|\|x$	$2(1-\eta)\rho\xi$	2ξ	(32)
$H\|\|y$	2ξ	$2(1+\eta)\rho\xi$.	

η is therefore found directly from a measurement of the splitting of the proper pair of Zeeman components along one of the principal axes. The magnetic field can be calibrated by measuring the splitting for one of the other pairs.

The author wishes to acknowledge with gratitude the advice and encouragement of Professor R. V. Pound of Harvard University, under whose guidance this work was started.

PHYSICAL REVIEW VOLUME 96, NUMBER 4 NOVEMBER 15, 1954

Particle Derivation of Nuclear Rotation Properties Associated with a Surface Wave

D. R. INGLIS
Argonne National Laboratory, Lemont, Illinois

(Received June 10, 1954; revised manuscript received July 26, 1954)

The dynamical conception of nuclear rotation in terms of a surface wave on a droplet of irrotational fluid has achieved some success in spite of the great differences between nucleons and the particles of a normal classical fluid. As a justification for the simplifying assumption of irrotational fluid flow, the collective rotational energy is here derived from a suitable set of nucleon wave functions in the approximation in which there is a rotating distortion, slow compared with the internal nucleon motions. The wave functions are those of a three-dimensional harmonic oscillator that is made anisotropic by having the force constant along one axis different from those along the other two in a rotating cartesian coordinate system. For the case of steady rotation about a fixed axis, the perturbation problem with first-order wave functions leads to a second-order rotational energy which agrees with the droplet-model result. The observed level spacings appear to lie between this result and that of a rigid rotator, and the discrepancy is probably to be attributed to higher orders. The result is also derived by another method without introducing a steady rotation.

INTRODUCTION

THE spectacular success of the (jj) coupling shell model,[1] in accounting particularly for the magic numbers and the succession of ground-state angular momenta J of the moderately heavy nuclei, leaves little doubt that the extrashellular nucleons have an independence of motion quite different from that of the molecules in a classical fluid. These particular successes were first achieved on the assumptions that the extrashellular nucleons move in a spherically symmetric potential, have large spin-orbit coupling, and interact with one another besides. The equally impressive success of the introduction of a nonsperical core,[2,3] in accounting for the large quadrupole moments and especially the ratios of certain low excitation energies,[4] gives the impression that the degree of freedom permitting distortion of the core is important to the external features of most nuclei without radically modifying the internal coupling of the nucleons as

[1] M. G. Mayer, Phys. Rev. **75**, 1969 (1949); **78**, 16, 22 (1950). Haxel, Jensen, and Suess, Phys. Rev. **75**, 1766 (1949); Naturwiss. **36**, 155 (1949).

[2] J. Rainwater, Phys. Rev. **79**, 432 (1950).

[3] A. Bohr, Phys. Rev. **81**, 134, 331 (1951); Kgl. Danske Videnskab. Selskab, Mat.-fys. Medd. **26**, No. 14 (1952). A. Bohr and B. R. Mottelson, Kgl. Danske Videnskab. Selskab, Mat.-fys. Medd. **27**, No. 16 (1953); D. L. Hill and J. A. Wheeler, Phys. Rev. **89**, 1102 (1953).

[4] F. Asaro and I. Perlman, Phys. Rev. **91**, 763 (1953).

calculated in the original (jj) coupling scheme which neglected this collective degree of freedom. The distortion is assumed to arise from the pressures exerted from within on the surface of a bag of liquid representing the core by the nucleons not belonging to closed shells. It is true that many of the results originally calculated by treating the specific nuclear interactions between the nucleons not belonging to closed shells can be derived by the "strong coupling" assumption[5] that they interact only through their several interactions with a common surface, but it seems likely that their direct interaction is not so unimportant and that both types of interaction contribute to the observed results. In any case, separability into products of nucleon wave functions and strong spin-orbit coupling are needed to justify the individual-nucleon quantum numbers j, and if one chooses to think intuitively of a classical fluid he must consider the mean free path to be long compared with the size of the vessel.

One then has no continuum at all and the classical equations for a continuous fluid with small density fluctuations do not apply. Quantization does introduce a probability density that has one property of a classical fluid in that it obeys the equation of continuity, but it does not follow that it has other properties of usual classical fluids. In particular, one cannot assume low viscosity, for the concept of viscosity loses its meaning with such a long mean free path. There is thus no logical basis for assuming irrotational flow. One may feel that after quantization, in the limit for very slow distortion of the nucleon wave functions, there is no way for the distortion to excite the nucleons, and thus no mechanism for dissipation of energy, which may be intuitively associated with vanishing viscosity, but this conception merely suggests that one should treat quantitatively the departure from the limit of vanishingly slow distortion, as in the following calculation. It is thus unsatisfactory tacitly to assume that the equations of classical fluid and in particular of irrotational flow apply to nuclear matter.

The basic question that is raised by the classical analogy is how much mass motion is to be associated with a given motion of the boundary. A surface wave traveling around a liquid droplet has both angular momentum and kinetic energy, the amount depending classically on the depth of penetration of the wave motion as is calculable by assuming incompressible irrotational flow. The motion of the surface is transmitted to the internal volume elements by the sequence of pressures between the volume elements. A nucleus is perhaps more nearly analogous to a bag of rarified gas with a mean free path somewhat greater than the linear dimensions. The effect of a motion of an element of surface is transmitted mainly by rectilinear flight of the recoiling particles to various remote volume elements, and it has not been shown that the result is the same as with transmission by a sequence of pressures. But this analogy, too, is inadequate because nucleon wavelengths are comparable to nuclear size.

So long as the nucleus or its core is given only a static deformation, the kinematic assumption of irrotational motion is unimportant and the liquid drop model provides a plausible and very useful tool. The energy of surface tension is properly associated with the smaller number of statistically distributed neighbors with which an element of nucleon density near the surface can interact (the interaction being fairly uniformly modified by saturation requirements for various nuclei), and the kinetic energy per unit volume remains constant for the nucleons moving within fixed boundaries, as in an incompressible fluid. This is about all that is used of the droplet model in Weizsäcker's "semiempirical" treatment of nuclear energies, in the Bohr-Wheeler treatment[5] of stability of heavy nuclei against fission, and in Rainwater's discussion[2] of the large quadrupole moments.

The kinematic deformation of the nucleus becomes important in more detailed considerations of the fission process, and the dynamical problem associated with the rate of deformation is recognized by Hill and Wheeler,[3] who, in the discussion of their Figs. 7 and 8, show that in the limit of a large nucleus, wherein a typical nucleon wave function has many nodes, the mass motion may be treated in terms of a quantum analog of a classical velocity potential and that the classical hydrodynamic result for irrotational flow may plausibly be taken over as an approximation. The dynamics of the deformation of the core are likewise important in Bohr's treatment of the circulating surface waves and in Bohr and Mottelson's discussion of the coupling of nucleon motions to these waves,[3] and for simplicity of discussion they assume the equivalence to classical irrotational fluid flow.

The oscillator model provides a somewhat more systematic attempt to approximate the mechanical system than does the droplet model, and is similarly capable of describing a deformation in shape, but with more detailed accounting for the behavior of the nucleons. It introduces a zeroth-order potential V_0 idealized as a three-dimensional harmonic oscillator potential (not necessarily spherically symmetric) for each nucleon, and considers the perturbation to be the difference between the sum of the two-body interactions and this V_0. The oscillator model thus provides an alternative to the droplet treatment and by demonstrating some of the qualitative phenomena accompanying distortion provides an interesting critique of the droplet procedure.

In a very interesting comment on the oscillator model, Gallone and Salvetti[6] show that if one fills a shell (without spin) so that the sum of the three oscillator quantum numbers is less than or equal to k for as many nucleons as possible, the nucleus is stiffer against de-

[5] N. Bohr and J. A. Wheeler, Phys. Rev. **56**, 426 (1939).
[6] S. Gallone and C. Salvetti, Nuovo cimento **10**, 145 (1953).

formation than the droplet model supposes, but that a fairly large static deformation favors transition of some of the nucleons to states $(k+1)$, thus softening the nucleus and making the energy of static deformation vary about as it does in the droplet model. To emphasize the essentially static nature of this excitation of a "higher" shell, let us consider a case in which shell k is almost filled with protons and shell $k+1$ partly filled with neutrons, and that the attractive interaction energy is minimized when both the protons and the neutrons tend to concentrate near the equatorial plane. Then if we consider adding one or two more protons, it may be found to give lower energy to add them in the shell $k+1$ where they may concentrate near the equatorial plane, rather than in the shell k where, in filling the shell, they must concentrate near the poles. This "spilling over" from shell k to $k+1$ thus facilitates the spontaneous distortion of the nucleus, and may contribute to a large quadrupole moment. For an undistorted nucleus consisting of closed shells only, a rather large distortion would have to be imposed to make the spilling over energetically favorable, and it is not apt to happen spontaneously. The energies of the single-nucleon states between which the "spilling over" takes place consist of both potential and kinetic energy, but contribute to the energy as a function of a slow distortion which may be considered a *potential* energy in the same way that the electronic energy of a molecule as a function of internuclear distance is considered to be a potential energy in molecular vibration problems. Collective nuclear rotation, as well as vibration, may be considered to involve a dynamic and temporary transition between single-nucleon states which, being dependent on the rate of change of the shape of the system, contributes to an equivalent *kinetic* energy of the system. For simplicity we confine the treatment to cases where the static "spilling over" does not take place.

ROTATING DISTORTION OF A CLOSED SHELL

The interest in the rotating distortion arises from the physical situation in which outside of closed shells we have, let us say for simplicity, two nucleons of the same fairly large $\mathbf{l}$ (which is approximately equal to $\mathbf{j}$) but oppositely directed so they move almost in a plane with approximately zero resultant angular momentum of their individual orbital motions. They distort the bag of liquid representing the closed shells into an oblate ellipsoid and we consider now the collective degree of freedom corresponding to rotation of this ellipsoid about an axis in the equatorial plane. If we treat nuclear matter as a classical irrotational liquid, this is not a rigid rotation of the nucleus, but rather (aside from the two nucleons not in closed shells) the motion of a surface wave around it, and the rate at which the matter below the surface is swept along is proportional to the amplitude of the wave.

This classical-fluid model gives the result[3] that the nucleus has low rotational states with $J=0, 2, 4, 6 \ldots$ and with rotational energy proportional to $J(J+1)$, the constant of proportionality depending on the nuclear size and deformation. In several nuclei two even excited states are found with excitation energies in the ratio 20/6 (and even a third with ratio to the first 42/6) with remarkable fidelity.[4] The effective moment of inertia is small, making the level spacing large, when the wave has a small amplitude requiring a small mass motion for a given angular speed. The observed spacings of rotational states are in general an order of magnitude larger than would be given by a rigid rotation of the nucleus. This empirical success of the classical-fluid model raises the question why a nucleus which may for many purposes be approximated by a suitable product of single-particle wave functions (or combinations thereof) behaves dynamically so nearly like a simple classical fluid, particularly in its rotational properties.

Once one ignores the coordinates of the individual nucleons within the closed shells and assumes they behave collectively as an incompressible, irrotational fluid, the problem is greatly simplified. There is a definite equation of motion for the fluid from which one can proceed to quantization. This provides a useful tool for treating[3] the more detailed problems of coupling several nucleons to the same nuclear axis. In investigating the validity of the assumption of a simple fluid and the concept of an effective moment of inertia when a wave travels around the nuclear surface, it will suffice to examine the problem not in all its generality but in a special case which retains the essential feature of the circulating wave.

In the special case here treated we find it convenient to introduce a preferred axis, in such a way as to establish the projection M_J of the angular momentum along this axis as a constant of the motion, rather than the total angular momentum J. In this "M representation" the rotational levels associated with a surface wave in the droplet model would be proportional to M_J^2, rather than to $J(J+1)$, and we here derive a similar result from a collective distortion of the nucleon wave functions.

In a hydrodyanmic treatment of this special case we could start with an ellipsoidal container of frictionless and incompressible fluid at rest (rather than the usual free droplet in space), then start it rotating with a constant angular speed Ω and calculate the subsequent motion within the fluid, in which matter is always flowing beneath the surface from recent to future positions of the bulge at the largest diameter. We could then adjust Ω to give a desired value of the angular momentum, such as one allowed by quantization, and could calculate the corresponding kinetic energy of rotation. In this case [apart from the uncertainty of direction associated with the distinction between M_J^2 and $J(J+1)$] the uniformly rotating container becomes rather nonessential because there is no transfer of angular momentum between it and the fluid. In the

oscillator-model treatment, our introduction of a rotating ellipsoidal zero-order potential is analogous to this procedure.

PERTURBATION TREATMENT OF ROTATION

In any treatment of the nuclear rotation problem one must assume in some way that the collective behavior of the nucleons designates a preferred rotating coordinate system, and we assume in particular that the preferred set of axes is that in which the potential energy arising from all of the interactions of the nucleons is best approximated by a sum of single-nucleon energies, so that in it an applied zeroth-order potential best approximates a self-consistent field.

In our first treatment of the problem we avoid introducing an extra coordinate by assuming that the rotating coordinate system rotates about the x axis with a fixed angular velocity Ω, so that $y'=y\cos\varphi+z\sin\varphi$, $z'=-y\sin\varphi+z\cos\varphi$ with $\varphi=\Omega t$. In terms of the primed coordinates x_i' of the rotating system the Lagrangian is

$$\mathfrak{L}(\dot{x}_i',x_i')=(M/2)\sum(\dot{x}_i'+[\Omega\times r]_{i'})^2-V(x_i'), \quad (1)$$

which defines the momenta,

$$p_i'=\partial\mathfrak{L}/\partial\dot{x}_i'=M\dot{x}_i'+[\Omega\times r]_{i'}, \quad (2)$$

whence the Hamiltonian relative to the laboratory but expressed in the primed coordinates is

$$\begin{aligned}\mathfrak{IC}&=\sum p_i'\dot{x}_i'-\mathfrak{L}=(M/2)\sum\{(\dot{x}_i')^2-[\Omega\times r]^2\}+V\\&=\sum(p_i'^2/2M-p_i'[\Omega\times r]_{i'})+V=\mathfrak{IC}^{(0)}+\mathfrak{IC}^{(1)}\end{aligned} \quad (3)$$

with

$$\begin{aligned}\mathfrak{IC}^{(0)}&=-(\hbar^2/2M)\sum\partial^2/\partial x_i'^2+V(x_i'),\\\mathfrak{IC}^{(1)}&=i\hbar\Omega\sum(y_i'\partial/\partial z_i'-z_i'\partial/\partial y_i')=-\hbar\Omega L_x.\end{aligned} \quad (4)$$

Thus the Hamiltonian in the rotating system differs from that which we would have in a stationary system, $\mathfrak{IC}^{(0)}$, only by the term $\mathfrak{IC}^{(1)}$, as is well known. When Ω is small compared to the internal frequencies arising from $\mathfrak{IC}^{(0)}$, the term $\mathfrak{IC}^{(1)}$ may be treated as a perturbation. This is closely related to the adiabatic approximation which one might use if $\mathfrak{IC}^{(1)}$ were to be considered a slowly time-dependent perturbation in the stationary system with an expansion in slowly time-dependent wave functions determined by $\mathfrak{IC}^{(0)}$. Instead it is simpler, and it is customary in moelcular problem,[7] to make use of the circumstance that the time does not appear in $\mathfrak{IC}$ as expressed Eq. (3) in the rotating system, and to assume a stationary solution $\psi(x_i')\exp[(i/\hbar)Et]$ to the Schrödinger equation, $[\mathfrak{IC}-(\hbar/i)\partial/\partial t]\psi(x_i',t)=0$. One thus obtains a time-independent wave equation which may be put in perturbation-theory form:

$$\begin{aligned}&\{\mathfrak{IC}^{(0)}(x_i',\partial/\partial x_i')+\mathfrak{IC}^{(1)}(x_i',\partial/\partial x_i')\\&\quad-E^{(0)}-E^{(1)}-E^{(2)}\}\{U_0(x_i')+\sum{}'a_nU_n(x_i')\}=0.\end{aligned} \quad (5)$$

[7] J. H. Van Vleck, Phys. Rev. **31**, 591 (1928); G. C. Wick, Phys. Rev. **73**, 51 (1947).

ROTATING DISTORTION IN THE OSCILLATOR MODEL

In the "central model" treatment of nucleon interactions it has been found convenient to introduce in zeroth order a spherically symmetric three-dimensional harmonic oscillator potential to define a set of wave functions amenable to analytic integration, and it has been considered a good approximation because this potential possesses a relatively flat bottom corresponding to the presumed roughly constant nuclear density and potential energy. The wave function is separable in the three cartesian coordinates and in each the equation $[-(\hbar^2/2M)\partial^2/\partial x^2+(K/2)x^2]u_n=E_nu_n$ is put in the form $(\partial^2/\partial\xi^2+\lambda_n-\xi^2)u_n(\xi)=0$ by use of the convenient "oscillator coordinate" $\xi=\beta x$, with $\beta=(KM/\hbar^2)^{\frac{1}{4}}=(K/\hbar\omega)^{\frac{1}{4}}=(M\omega/\hbar)^{\frac{1}{2}}$, $\omega=(K/M)^{\frac{1}{2}}$, and $E_n=(n+\frac{1}{2})\hbar\omega$.

We may introduce wave functions to describe a rotating distortion by relinquishing the spherical symmetry and introducing the zeroth-order rotating spherical potential,

$$\begin{aligned}V&=(K/2)[(x^2+y'^2)/b^2+z'^2/a^2]\\&=(\hbar\omega/2)[(\xi^2+\eta'^2)/b+\zeta'^2/a]\\&=(\hbar\omega/2)[(\xi^2+\eta'^2)\alpha^2+\zeta'^2/\alpha^4].\end{aligned} \quad (6)$$

Here the equipotential surfaces are ellipsoids of revolution $(x^2+y'^2)/b^2+z'^2/a^2=R^2$, distorted from the spheres of radius R without change of volume by keeping $ab^2=1$, and the usual "oscillator coordinates" have been introduced appropriate to each dimension by putting $\xi=\beta_1x$, $\eta'=\beta_1y'$, $\zeta'=\beta_3z'$, $\beta_1=\beta/b^{\frac{1}{2}}=\alpha\beta$ and $\beta_3=\alpha^{-2}\beta$, with $\beta=(KM/\hbar^2)^{\frac{1}{4}}=(K/\hbar\omega)^{\frac{1}{4}}=(M\omega/\hbar)^{\frac{1}{2}}$, $\alpha=(a/b)^{1/6}$, where, of course, M is the nucleon mass and $\omega=(K/M)^{\frac{1}{2}}$. The deviation of α from unity measures the distortion of the ellipsoid from a sphere.

In the artificial problem to be compared with the classical fluid in a rotating container, we may simply ignore any further potentials and consider the terms of the Hamiltonian as given in Eq. (4). In a nucleus we may consider it plausible that a similar result is accomplished by introducing into $\mathfrak{IC}^{(1)}$ an additional term $V^{(1)}(x_i')=V(x_i'-x_j')-V(x_i')$, that is, the difference between the potential representing the internucleon interactions and the oscillator potential, and then assuming that the average value of $V^{(1)}$ either vanishes (self-consistent field assumption) or is unaffected by the rotation, so we may neglect it.

The zeroth-order wave function for a single nucleon, though anisotropic, is still separable in the three primed coordinates,

$$\begin{aligned}u_{lmn}(\xi,\eta',\zeta')&=u_l(\xi)u_m(\eta')u_n(\zeta')\\&=H_l(\xi)H_m(\eta')H_n(\zeta')\exp[-(\rho'^2)/2],\end{aligned} \quad (7)$$

where $\rho'^2=\xi^2+\eta'^2+\zeta'^2$, and from these the zero-order wave functions of the system are built up by taking the usual (antisymmetric sum of) products:

$$U=\Pi_iu_{li}(\xi_i)u_{mi}(\eta_i')u_{ni}(\zeta_i'). \quad (8)$$

These are solutions of the zeroth-order term of Eq. (5), $(\mathcal{H}^{(0)}-E_n^{(0)})U_n=0$. The perturbation has no diagonal element for the ground state, so $E^{(1)}=0$, and the rotational energy is given by

$$E^{(2)}=\sum|\mathcal{H}_{0i}^{(1)}|^2/(E_i^{(0)}-E_0^{(0)}).$$

In terms of the oscillator coordinates the angular momentum operator L_x appearing in (4) is

$$L_x=i\sum(\alpha^3\zeta_i'\partial/\partial\eta_i'-\alpha^{-3}\eta_i'\partial/\partial\zeta_i'). \quad (9)$$

The normalized Hermite polynomials appearing in Eq. (7) obey the recursion relations,

$$2^{\frac{1}{2}}\xi H_n(\xi)=(n+1)^{\frac{1}{2}}H_{n+1}+n^{\frac{1}{2}}H_{n-1}, \quad (10)$$
$$\partial H_n(\xi)/\partial\xi=(2n)^{\frac{1}{2}}H_{n-1},$$

and from them we find

$$\partial u_n(\xi)/\partial\xi=(\partial/\partial\xi)H_n\exp(-\xi^2/2)$$
$$=-2^{-\frac{1}{2}}[(n+1)^{\frac{1}{2}}u_{n+1}-n^{\frac{1}{2}}u_{n-1}]. \quad (11)$$

Thus between the ground state and an excited state in which any one of the single-nucleon states appearing in the product Eq. (8), say l, m, n, is replaced by the excited nucleon state l, $m+1$, $n+1$, we have the matrix element,

$$(L_x)_{l,\ m+1,\ n+1,\ lmn}$$
$$=-(i/2)(\alpha^3-\alpha^{-3})(m+1)^{\frac{1}{2}}(n+1)^{\frac{1}{2}}. \quad (12)$$

Each of these states has an excitation energy $E_i^{(0)}-E_0^{(0)}=2\hbar\omega$. Since $\mathcal{H}^{(1)}$ is a sum of single-nucleon terms, there are no exchange terms arising from antisymmetrizing (8), and there are no further matrix elements in this order. The energy of rotation is thus

$$E^{(2)}=(\hbar\Omega^2/2\omega)\sum|(L_x)_{i0}|^2$$
$$=(\hbar\Omega^2/8\omega)(\alpha^3-\alpha^{-3})^2\sum'(m+1)(n+1). \quad (13)$$

The prime on the summation sign is to remind us that it is to be carried out only over those single-nucleon excitations that do not lead to vanishing wave functions because of the antisymmetry, that is, in the closed-shell cases we shall consider, over the proton states or neutron states of the last two filled shells. In the sense that the last filled shells with the highest nucleon energy have density distributions concentrated most predominately toward the outside of the nucleus, we see here that the rotation energy is to some extent a surface phenomenon comparable to the energy of a surface wave.

The angular momentum about the x axis evaluated for the first-order ground-state wave function $\psi_0=U_0+\sum a_iU_i$ with $a_i=\mathcal{H}_{i0}^{(1)}/(E_0^{(0)}-E_i^{(0)})$ is

$$\langle L_x\rangle=\sum[\bar{a}_i(L_x)_{i0}+(L_x)_{0i}a_i]$$
$$=(\Omega/\omega)\sum|(L_x)_{i0}|^2$$
$$=(\Omega/4\omega)(\alpha^3-\alpha^{-3})^2\sum'(m+1)(n+1). \quad (14)$$

By eliminating Ω we may express the rotational energy in terms of this angular momentum:

$$E^{(2)}=2\hbar\omega\langle L_x\rangle^2/[(\alpha^3-\alpha^{-3})^2\sum'(m+1)(n+1)]$$
$$=\hbar^2\langle L_x\rangle^2/2(\vartheta_x)_{\text{calc}}. \quad (15)$$

Here $(\vartheta_x)_{\text{calc}}$ is introduced as an effective moment of inertia calculated from the properties of the nucleons. It is at once apparent that this result has general features anticipated from familiarity with the droplet model, the rotational energy decreasing with increasing distortion as α departs from unity, and the energy decreasing with increasing atomic number A as ω decreases and $\sum'(m+1)(n+1)$ grows larger.

In the droplet model the effective moment of inertia is, in the notation of Bohr,[3]

$$(\vartheta_x)_{\text{droplet model}}=3B\alpha_0^2=(9/8\pi)AMR_0^2\alpha_0^2, \quad (16)$$

where R_0 is the radius of a spherical nucleus, $R_0=A^{\frac{1}{3}}r_0$, and where α_0 is the parameter defining the deviation of the spheroidal surface of the droplet from sphericity,

$$R(\theta)=R_0[1+(\tfrac{5}{16}\pi)^{\frac{1}{2}}(3\cos^2\theta-1)\alpha_0] \quad (17)$$

[Bohr's Eqs. (1), (12), (13) with $\gamma=0$ and with $Y_2=(\frac{5}{16}\pi)^{\frac{1}{2}}(3\cos^2-1)$]. In order to establish the numerical correspondence between (15) and (16) it is necessary to relate α_0 to α in spite of the nebulous nature of the nuclear surface in the more realistic oscillator model. Instead of a definite nuclear surface we have a fairly sudden decay of density induced by the exponential factor from Eq. (7) in competition with the more slowly-varying factors arising from the sum of squares of Hermite polynomials, a sum which is isotropic in ξ, η', ζ' space for closed shells. For closed shells an equi-density surface may be defined by putting $\rho'^2=C$. At this surface the exponential factor in the density is reduced below its maximum value (at the center) by e^{-C} and some arbitrary value of C may be taken to define an equivalent nuclear surface, as is discussed further below. In the coordinate system of the principal axes we have the identity,

$$r^2=x^2+y'^2+z'^2=\rho'^2/\beta^2\alpha^2+(1-\alpha^{-6})z'^2,$$

with $z'=r\cos\theta$, and this equi-density surface is then

$$r=(C^{\frac{1}{2}}/\beta)[1+\tfrac{1}{6}(1-\alpha^{-6})(3\cos^2\theta-1)+\cdots], \quad (18)$$

where higher powers of the small parameter $(1-\alpha^{-6})$ have been omitted. By comparing Eq. (17) and Eq. (18) we have to this order,

$$1-\alpha^{-6}=3(5/4\pi)^{\frac{1}{2}}\alpha_0=2\Delta R/R_0,\ \alpha=1+(5/16\pi)^{\frac{1}{2}}\alpha_0. \quad (19)$$

Here ΔR is the difference between major and minor semiaxes of the equidensity ellipsoid of average radius R_0.

The size of the nucleus is represented in Eq. (15) by the parameter ω and this must be determined in such a way as to facilitate the comparison with the droplet model. In the comparison with experiment the comparison with quardupole moments is important,

and they may be made the same in the two models by selecting ω to make the mean square radius the same in both models. With the wave functions (7) for a closed shell, in which $\sum l=\sum m=\sum n$, we have

$$\sum(r^2)_{av}=(\xi^2+\eta^2+\zeta^2)_{av}/\beta^2=(3\hbar/M\omega)\sum(m+\tfrac{1}{2}), \quad (20)$$

where the sum is to be carried out over the states of all nucleons. In a uniform distribution of A nucleons in a sphere of radius R_0 the corresponding result is

$$\sum(r^2)_{av}=\tfrac{3}{5}AR_0^2, \quad (21)$$

and by equating these we have from Eq. (15) the effective moment of inertia as calculated in the oscillator model expressed in terms of the radius R_0 of a sphere in which a uniform distribution would have the same mean square radius:

$$(\mathcal{I}_x)_{\text{calc}}=\tfrac{1}{5}MAR_0^2(\Delta R/R_0)^2 \times[\sum'(m+1)(n+1)/\sum(m+\tfrac{1}{2})], \quad (22)$$

which differs from the droplet-model result[3] only by half the ratio of the two sums in the square bracket, since $(\mathcal{I}_x)_{\text{droplet model}}=\tfrac{2}{5}MA(\Delta R)^2$.

Superficially these two sums appear quite different, the first being obviously bilinear in the quantum numbers but summed over only the highest two shells of nucleons, and the second apparently linear but acquiring a corresponding quadratic nature through the fact that the summation extends over all filled shells. On evaluating them for the various closed shells one finds in fact the remarkable equality,

$$\sum'(m+1)(n+1)=2\sum(m+\tfrac{1}{2}), \quad (23)$$

which leaves

$$(\mathcal{I}_x)_{\text{calc}}=(\mathcal{I}_x)_{\text{droplet model}}. \quad (24)$$

The closed shells considered here where we neglect spin-orbit coupling are, of course, not closed shells of the "magic numbers," but they provide a valid indication of the trends of these sums through the periodic table. In Table I they are listed both for summation over all nucleons and for summation over protons as is of interest in connection with other data on isotope shifts and on electric quadrupole moments eQ_0, with

$$Q_0=2(\hbar/M\omega)(\alpha^4-\alpha^{-2})\sum_{\text{protons}}(m+\tfrac{1}{2}) \approx\tfrac{4}{5}AR_0^2(\Delta R/R_0)\sum_{\text{protons}}(m+\tfrac{1}{2})/\sum(m+\tfrac{1}{2}). \quad (25)$$

For the cases in which there is a neutron excess, the ratio of sums in Eq. (25) is 7 or 8 percent less than Z/A.

The equality (24) indicates that the assumption of irrotational fluid flow in the droplet model corresponds to the result of calculation of the second-order energy $E^{(2)}$ with nucleon wave functions.

A criterion for the validity of the perturbation approximation may be obtained by requiring that with the perturbation the probability density of ψ is still predominantly associated with U_0, that is, that

$$\sum|a_{i0}|^2=E^{(2)}/2\hbar\omega =(\Omega/4\omega)^2(\alpha^3-\alpha^{-3})^2\sum'(m+1)(n+1) =(\Omega/4\omega)\langle L_x\rangle\ll 1, \quad (26)$$

from Eq. (13) and (14). Since $\langle L_x\rangle$ or J for the states of interest is of order of magnitude 4, we see that this criterion is practically identically identical with the adiabatic condition $\Lambda/\omega\ll 1$. From Eq. (14) the implied contradiction is apparent that Ω/ω is not small and the approximation does not apply in the limit for small values of the deformation parameter $(\alpha^3-\alpha^{-3})$ which has been considered small in our final numerical evaluation [beginning with Eq. (18)]. However, the values of $\sum'(m+1)(n+1)$ listed in Table I [see Eq. (23)] are sufficiently large that Ω/ω is considerably less than unity and the adiabatic approximation is valid for the fairly small J's and substantially finite nuclear deformations of most practical interest.

TABLE I. Sums over the closed shells of the oscillator model. Here k_p is the total quantum number $l+m+n$ for the last proton shell and k_n likewise for neutrons.

k_p	k_n	Z	N	A	$\Sigma(m+\frac{1}{2})$	$\Sigma_{\text{protons}}(m+\frac{1}{2})$
0	0	2	2	4	2	1
1	1	8	8	16	12	6
2	2	20	20	40	210	20
3	3	40	40	80	100	50
3	4	40	70	110	155	50
4	4	70	70	140	210	105
4	5	70	112	182	301	105
5	5	112	112	224	392	196
5	6	112	168	280	532	196

COMPARISON WITH EXPERIMENT

The principal success of such a collective description of nuclear behavior is the agreement with the *ratios* of level spacings in individual nuclei, which depends only on a valid separation of the collective motion from the individual-nucleon motion so as to give an effective moment of inertia, presumably arising from a nuclear distortion, independent of the rotational quantum number. These ratios do not depend on whether the collective motion is more nearly irrotational or rigid and thus do not test the validity of the droplet-model assumptions. The quantitative comparison of the level spacings with experimental values is complicated by the necessity of taking an indication of the deformation from the interpretation of some other experimental data. This has been done for the droplet model by others,[3] especially by Ford[8] who plots against neutron number N the distortions as inferred from rotational levels, from isotope shifts, and from quadrupole moments. There are so many uncertainties involved that it is the study of the trend rather than of individual cases that seems most significant, and the trend is that the moments of inertia effective in the rotation are at least

[8] K. W. Ford, Phys. Rev. **90**, 29 (1953); **95**, 1250 (1954).

about four times as large as calculated on the assumption of irrotational fluid flow, that is, the observed level spacings are about one-fourth as large as calculated by the droplet model. This means that the nucleus seems to rotate more nearly as a rigid body than called for by the first-order wave functions giving rise to the second-order energy $E^{(2)}$. One may plausibly speculate that the configuration interaction of a higher-order calculation would correspond to a transition part way toward a "rigid" alpha model, taking advantage of the inherent stability of a clustering in space into alpha groups.[9]

Configuration interaction results from $V^{(1)}$, that is, from the introduction of two-body forces in place of the oversimplified oscillator potential, and the observed proportionality[4] of rotational energy to $J(J+1)$ seems to indicate that, if this be the significant mechanism, the amount of configuration interaction is not much affected by the "Coriolis term" $\mathcal{H}^{(1)}$ of Eq. (4).

COMPARISON WITH ANOTHER METHOD

In the above treatment we have assumed that a simple approximation to a self-consistent field is best in a certain coordinate system rotating with a constant Ω. Instead one may, before setting up the Hamiltonian, introduce as a coordinate system free to rotate the one defined by the instantaneous principal axes of the system of A nucleons, and treat the orientation angles as coordinates in addition to the position coordinates x_i' of the nucleons in these axes. This means that the system is over-determined, having $3A+3$ coordinates if a general rotation is permitted or $3A+1$ in the special case here discussed with rotation about the x axis only. A similar difficulty is encountered with the center of mass in all shell-model treatments, and especially for large A it may plausibly be hoped that the extra coordinate (s) may cause little trouble, being somehow absorbed in the many coordinates lost in the "core."

We thus consider again only the deviation from cylindrical symmetry about the x axis, and define the orientation angle of the principal axes in the yz plane through the vanishing of the product of inertia,

$$\sum_i y_i' z_i' = \sum_i [(z_i^2 - y_i^2)\cos\varphi \sin\varphi + y_i z_i(\cos^2 - \sin^2\varphi)] = 0. \quad (27)$$

This is equivalent to Eq. (II) of a very recent publication of Bohr,[10] in which he also discusses in somewhat more general terms the approximate equivalence of a particle approach to irrotational flow [Eq. (XIII)]. If we postulate a wave function, $\psi(x_i', \varphi)$, dependent on φ and on the internal coordinates x_i', we may as he suggests write the Hamiltonian in the separated form,

$$\mathcal{H}(x_i, \partial/\partial x_i) = \mathcal{H}_{\text{int}}(x_i', \partial/\partial x_i') + \mathcal{H}_{\text{rot}}(x_i', \partial/\partial\varphi) + \mathcal{H}_{\text{coupl}}(x_i', \partial/\partial x', \partial/\partial\varphi), \quad (28)$$

with

$$\mathcal{H}_{\text{rot}} = -(\hbar^2/2M)\sum_i [(\partial\varphi/\partial y_i)^2 + (\partial\varphi/\partial z_i)^2](\partial^2/\partial\varphi^2). \quad (29)$$

Taking the y_i and z_i derivatives of (27), with $y_i' = y_i'(y_a, z_a, \varphi(y_a, z_a))$ and $\partial y'/\partial\varphi = z'$, $\partial z'/\partial\varphi = -y'$, we have

$$\partial\varphi/\partial y_i = (y_i' \sin\varphi - z_i' \cos\varphi)/\sum[z'^2 - y'^2],$$
$$\partial\varphi/\partial z_i = (y_i' \cos\varphi + z_i' \sin\varphi)/\sum[y'^2 - z'^2]. \quad (30)$$

If in Eq. (28) we put $\mathcal{H}_{\text{int}} = \mathcal{H}^{(0)}$, $\mathcal{H}_{\text{rot}} = \mathcal{H}^{(1)}$ and neglect $\mathcal{H}_{\text{coupl}}$ (which contains several terms and does not contribute to $E^{(1)}$) in a perturbation equation of the form Eq. (5), we have the zeroth-order wave functions,

$$\psi(x_i', \varphi) = U(x_i') R_{Lx}(\varphi), \quad (31)$$

where U is again an antisymmetrized product (8), and obtain

$$E^{(1)} = (0|\mathcal{H}_{\text{rot}}|0) = (\hbar^2/2M)L_x^2 \times \int \bar{U}\{\sum_i (y_i'^2 + z_i'^2)/[\sum_j (y_j'^2 - z_j'^2)]^2\} U d\tau_{3A}', \quad (32)$$

where the integration extends over the $3A$ coordinates of A nucleons. This is closely related to Eq. (IX) of Bohr.[10] Although the summation in the numerator is a sum of single-nucleon functions, the entire curly bracket in the integrand is not, and it is not strictly permissible to neglect exchange terms arising from the antisymmetry nor to carry out any simple evaluation of the integral. The complicating denominator entered Eq. (28) in such a way as to indicate that the greater the gross distortion from spherical symmetry, the smaller the effect of a given small displacement Δy_i of a single particle on the orientation φ of the principal axes. A simple and plausible procedure is then to neglect the fluctuations of this gross distortion about its mean, by evaluating the summations in the numerator and denominator separately with the wave function U which amounts to averaging over the fluctuations in a somewhat indefinite way so the result may be approximately valid even though the zero-point oscillations of shape may in some cases be almost as large as the mean distortion. This gives

$$(0|\mathcal{H}_{\text{rot}}|0) = \hbar^2 L_x^2/2(\mathcal{I}_x)_0 \approx \hbar L_x^2(\alpha^2 + \alpha^{-4})/[2(\alpha^3 - \alpha^{-3})^2 \sum (m + \tfrac{1}{2})], \quad (33)$$

for the case of completely filled shells for which $\sum m_i = \sum n_i$, the summations being carried out over all nucleons. In the approximation in which $\alpha^2 + \alpha^{-4} = 2$ and in the light of Eq. (23), the two expressions Eq. (15) and Eq. (33) for the rotational energy are then identical.

[9] E. Teller and J. A. Wheeler, Phys. Rev. **53**, 778 (1938); D. R. Inglis, Revs. Modern Phys. **25**, 390 (1953); D. M. Dennison, Phys. Rev. **96**, 378 (1954).

[10] A. Bohr, *Rotational States of Atomic Nuclei* (Munksgaards Forlag, Copenhagen, 1954). The unspecified q_a are presumably fewer than our x_i' to keep the right number of coordinates.

Effect of Nuclear Charge on Internally Produced Pairs

G. K. HORTON, *National Research Council of Canada, Ottawa, Canada and Department of Mathematics, University of Alberta, Edmonton, Alberta, Canada*

AND

E. PHIBBS, *Department of Mathematics, University of Alberta, Edmonton, Alberta, Canada*

(Received April 12, 1954)

The effect of nuclear charge on internally converted pairs is investigated using the relativistic Sommerfeld-Maue solutions of the iterated Dirac equation. The orthonormal properties of these wave functions are studied and time-dependent perturbation theory is adapted to allow for their nonorthogonality. The integrals involved are studied using the Fourier transforms of the wave functions. The matrix elements are obtained in terms of one fundamental integral, evaluated by using an integral representation of Butler. The procedure is very simple and promises generalizations. The matrix elements are shown to be complex only through $n=\mp iZ/(137v_\pm)$, where $v_\pm$ is the velocity of the positron or the negatron and Z is the nuclear charge. The following conclusions are drawn. Firstly, the first Born approximation results when multiplied by the well-known Sommerfeld factors of the negatron and positron are accurate to a term proportional to $|n|^2$. For 5-percent resolutions, $Z\lesssim 20$, the kinetic energy must be more than 100 kev. Secondly, this result is valid for all electric and magnetic multipole transitions. Finally, this result is shown to apply to all transitions taking place between unbound states and to hold for higher order perturbation terms.

I. INTRODUCTION

IT is well known that the angular distribution in internal pair production[1] provides a method of distinguishing between different types of nuclear transitions. This method is particularly useful at high transition energies. In this sense, it is alternative to those procedures which are more effective at lower energies, such as the use of the ratios of internal conversion coefficients for the K, L, $\cdots$, etc., atomic shells. The angular distribution in internal pair production has been studied theoretically by Horton[1] and Rose[2] using the first Born approximation. In view of the recent improvements in the experimental techniques, and the subsequent applications of the theory,[3] a re-examination of the region of validity of the first Born approximation is overdue. For external pair production and Bremsstrahlung, the improvement of the first Born approximation, in the relativistic case, has recently been carried out by Bethe, Davies, and Maximon.[4]

Internal and external pair production are, however, essentially different processes. Internal pair production, as a tool in nuclear spectroscopy, is of the greatest value for light nuclei and can take place independently of the nuclear electrostatic field.[5] External pair production, on the other hand, depends inherently on the nuclear electrostatic field and is of considerable interest for heavy nuclei. For this reason, the calculations of Bethe *et al.*[4] have to be valid for a much higher nuclear charge than ours. On the other hand the latter are concerned with much higher energies. External pair formation is produced by an incident plane photon wave of high energy. In internal pair formation the perturbation is caused by a relatively low-energy spherical photon wave. This makes the former problem mathematically much simpler. Furthermore, in internal pair formation, the region of large angular separation of the components of the pair is of particular interest,[6] whereas in the external pair formation problem the small angle approximation is of overriding importance. Considerations of this type again make the mathematical problem in the latter case much less formidable.

It is well known that the first Born approximation is valid as long as

$$|n_\pm|\ll 1, \tag{1}$$

where

$$n_\pm=Zze^2/(i\beta_\pm), \quad k_\pm=\beta_\pm E_\pm; \tag{2}$$

Ze is the nuclear charge, $ze=-e$ for the negatron and $+e$ for the positron, and $n\equiv n_\pm$ throughout. Condition (1) shows that the first Born approximation is valid, $|n_\pm|\leq 0.05$, in the shaded region of Fig. 1. We note

[1] This possibility was first suggested to one of the present authors by R. E. Peierls. See G. K. Horton, Proc. Phys. Soc. (London) **60**, 457 (1948).

[2] M. E. Rose, Phys. Rev. **76**, 678 (1949). For an interesting related paper see G. Goldring, Proc. Phys. Soc. (London) **66**, 341 (1953). See also M. E. Rose and G. E. Uhlenbeck, Phys. Rev. **48**, 211 (1935), and V. B. Beristetskii and I. M. Shmushkevich, J. Exptl. Theoret. Phys. (U.S.S.R.) **9**, 591 (1949).

[3] Internal pair production has been frequently studied experimentally. For the earlier references see G. D. Latyshev, Revs. Modern Phys. **19**, 132 (1947). For transitions studied via the total pair formation coefficient see E. H. S. Burhop, *The Auger Effect* (Cambridge University Press, Cambridge, 1952); S. D. Bloom, Phys. Rev. **88**, 312 (1952); R. G. Thomas and T. Lauritson, Phys. Rev. **88**, 966 (1952); and also G. Harries and W. T. Davies, Proc. Phys. Soc. (London) **65**, 564 (1952). The angular distribution in internal pair creation has been studied by K. Siegbahn, Arkiv Fysik **4**, 233 (1952), G. Harries, Proc. Phys. Soc. (London) **67**, 153 (1954). Paul, River, and Devons, Imperial College, have kindly informed us that they are also studying the angular distribution in internal pair creation experimentally.

[4] H. A. Bethe and L. C. Maximon, Phys. Rev. **93**, 768 (1954); Davies, Bethe, and Maximon, Phys. Rev. **93**, 788 (1954).

[5] It seems, however, that experiments will be carried out for a higher nuclear charge also. ThC″, Mn^{56}, and Co^{60} have already been investigated by Siegbahn, reference 3. For a discussion see Sec. VII of this paper.

[6] See G. Harries and K. Siegbahn, reference 3; in the latter a β-spectrogoniometer is used, which automatically restricts θ to the range $\pi/2\leq\theta\leq\pi$.

that Fig. 1 demonstrates that the first Born approximation is only valid if $Z \leqslant 6$ for E, the total energy, bigger than or equal to $2mc^2$. This conclusion is disturbing because experiments have already been performed with nuclei as heavy as ThC″ with particle kinetic energies well below mc^2. Furthermore, in the experiments it is sometimes necessary[7] to work with rather slow positrons (negatrons). For instance, if the excited state of the nucleus under investigation is formed through β decay, as in the 1.74-Mev excited state of Na^{24}, Siegbahn[7] found it necessary to reject all electron pairs whose negatrons had an energy below the upper energy limit of the accompanying continuous β-ray spectrum. This makes the apparent failure of the first Born approximation (Fig. 1) all the more serious.

In this paper, we make a detailed study of the region of applicability of the first Born approximation. It will, in fact, be shown that the first Born approximation has a much greater range of validity than is suggested by (1). This is discussed in Sec. V by using the solutions of the iterated Dirac equation in the Sommerfeld-Maue approximation given in Sec. II. We use first order perturbation theory. It has been pointed out[8] that it is not necessarily correct to assume that first order perturbation theory, developed in the nonrelativistic approximation, is valid when using the solutions (4) of Eq. (3). In Sec. III we develop a relativistic perturbation theory adapted to overcoming the non-orthogonality difficulty encountered when using the wave function (4). The integrals that arise have been studied by a number of authors[9] in configuration space. In Sec. IV, we use the Coulomb wave function given by one of us[10] in the momentum representation, combined with an idea of Butler (see Bess[9]) to evaluate the relevant integral in a new way. We have given the evaluation in some detail in the hope that it will be possible to adapt the techniques to the evaluation of similar but as yet unsolved problems.[11] In Sec. VI, we discuss the generalization of our results to any transition taking place between unbound states in a nuclear Coulomb field. In Sec. VII, we conclude with a critical examination of the validity of our results.

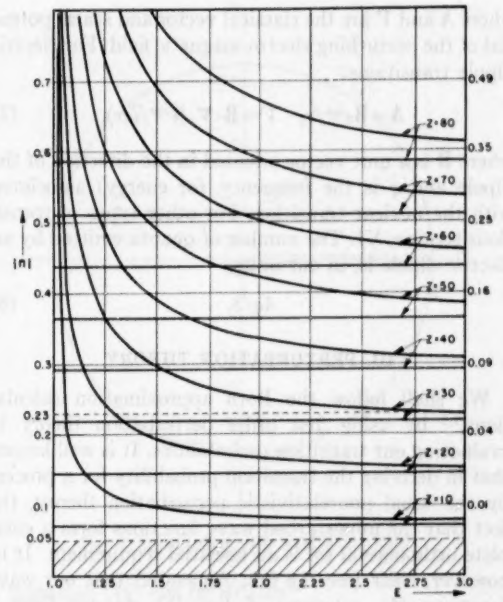

FIG. 1. The vertical scale on the left gives the values of $|n|$ and $|n\beta|$. The scale on the right gives values of $|n|^3$ and $|n^2\beta^2|$. The horizontal scale gives the kinetic energy in units of mc^2.

II. WAVE FUNCTIONS AND PERTURBING POTENTIALS

It has been shown by Sommerfeld and Maue[12] that the normalized solution of the iterated Dirac equation,

$$\nabla^2\psi+\left\{\left(E+\frac{Zze^2}{r}\right)^2-m^2\right\}\psi=\frac{zZe^2}{i}\left(\boldsymbol{\alpha}\cdot\boldsymbol{\nabla}\frac{1}{r}\right)\psi, \quad (3)$$

is

$$\psi(\mathbf{r})=(2\pi)^{-\frac{1}{2}}Ne^{i\mathbf{k}\cdot\mathbf{r}}\{1+(i\beta/r)\boldsymbol{\alpha}\cdot\boldsymbol{\nabla}_k+O(n^2\beta^2)\}\times F(-n,1;\rho)u(\mathbf{k}), \quad (4)$$

where

$$N^2=2\pi|n|/(e^{2\pi|n|}-1),$$

$$F(-n,1;\rho)=\frac{1}{2\pi i}\oint^{(0^+,-1^+)} t^{-n-1}(1+t)^n e^{-\rho t}dt, \quad (5)$$

$$\rho=i(kr-\mathbf{k}\cdot\mathbf{r}).$$

We discuss the orthonormal properties of (4), and, in particular, the derivation of the first relation in (4), in the first appendix.

It is well known that if the effect of an electro-magnetic field on a relativistic charged particle, obeying Dirac's equation, is taken into account by perturbation theory, then the perturbation term in the Hamiltonian is

$$H'=e(\boldsymbol{\alpha}\cdot\mathbf{A}+V), \quad (6)$$

[7] See K. Siegbahn, reference 3.

[8] G. K. Horton and E. Phibbs, Phys. Rev. **94**, 1402 (1954). See also F. J. Dyson, Phys. Rev. **83**, 713 (1948); A. Sommerfeld, *Atombau und Spectrallinien* (F. Vieweg and Son, Braunschweig, 1939), Vol. 2, p. 412.

[9] A. Sommerfeld, reference 8, pp. 502 and 529. See also A. Nordsieck, Phys. Rev. **93**, 785 (1954); L. Bess, Phys. Rev. **77**, 550 (1950).

[10] G. K. Horton and R. T. Sharp, Phys. Rev. **89**, 885 (1953).

[11] We refer, for instance, to the Coulomb excitation of nuclei by low-energy charged particles. See G. K. Horton, Birmingham Dissertation (unpublished), and K. Alder and A. Winther, Phys. Rev. **91**, 1578 (1953); K. A. Ter-Martirosyan, J. Exptl. Theoret. Phys. (U.S.S.R.) **22**, 284 (1952); C. J. Mullin and E. Guth, Phys. Rev. **82**, 141 (1951). Similar integrals arise in the theory of β decay and atomic and nuclear scattering.

[12] See Sommerfeld, reference 8, p. 410; W. H. Furry, Phys. Rev. **46**, 391 (1934). See also H. A. Bethe and L. C. Maximon, Secs. II and III, and G. K. Horton and R. T. Sharp, reference 10. We use natural units $\hbar=c=1$.

where $\mathbf{A}$ and V are the classical vector and scalar potential of the perturbing electro-magnetic field. For electric dipole transitions:

$$\mathbf{A}=\mathbf{B}e^{iqr}/r, \quad V=\mathbf{B}\cdot\nabla_r(e^{iqr}/iqr), \tag{7}$$

where $\mathbf{B}$ is a unit vector oriented in the direction of the dipole and q is the frequency (or energy) associated with the nuclear transition. For other types of transitions see Sec. VI. The number of quanta emitted by an electric dipole is, in our units,

$$4q/3. \tag{8}$$

III. PERTURBATION THEORY

We shall follow the Born approximation calculations,[1,2] by using first order perturbation theory in evaluating our transition probabilities. It is well known that in deriving the transition probability for a process by the usual nonrelativistic perturbation theory, the fact that the unperturbed wave functions form a complete orthonormal set is an essential requirement. It is, however, clear (see the first Appendix) that our wave functions (4), solutions of Eq. (3), do not form a complete orthonormal set of unperturbed wave functions but, as is shown in the first Appendix, satisfy

$$\int_{\Delta_-} d\mathbf{k}_- \int d\tau\psi^*(E_-,\mathbf{r})\left[1+\frac{2zZe^2}{(E_++E_-)r}\right] \times\psi(E_+,\mathbf{r})=1 \text{ or } 0, \tag{9}$$

according as Δ_- includes k_+ or not. This means that the conventional perturbation theory must be amended accordingly. Let

$$\lambda=2zZe^2/i(E_-+E_+)=2zZe^2/iq. \tag{10}$$

We require the solution of the time-dependent Schrödinger equation

$$i\partial\Psi/\partial t=H\Psi, \quad \text{where} \quad H=H_0+H', \tag{11}$$

and

$$H_0\psi(E^{(n)},\mathbf{r})=E^{(n)}\psi(E^{(n)},\mathbf{r}). \tag{12}$$

Let

$$\Psi(\mathbf{r})=\mathfrak{S}_{(n)}a_n(t)\psi(E^{(n)},\mathbf{r})\exp(-iE^{(n)}t), \tag{13}$$

where $\mathfrak{S}_{(n)}$ indicates summation over the discrete and integration over the continuous states, respectively. Substituting (13) into (11) we have

$$\mathfrak{S}_{(n)}i(\partial a_n/\partial t)\psi(E^{(n)},\mathbf{r})\exp(-iE^{(n)}t) =\mathfrak{S}_{(n)}a_n(t)H'\psi(E^{(n)},\mathbf{r})\exp(-iE^{(n)}t). \tag{14}$$

Multiply (14) on the left-hand side by

$$\psi^*(E^{(m)},\mathbf{r})[1+i\lambda/r]\exp(iE^{(m)}t)$$

and integrate over all space. We find

$$\partial a_m(t)/\partial t=-i\mathfrak{S}_{(n)}H_{m,n}'a_n(t)\exp[-i(E^{(n)}-E^{(m)})], \tag{15}$$

where

$$H_{m,n}'=\int d\tau\psi^*(E^{(m)},\mathbf{r})[1+\lambda i/r]H'\psi(E^{(n)},\mathbf{r}). \tag{16}$$

Equation (16) has been given before without proof.[8] From this stage the theory follows the usual nonrelatavistic case. Here we only give the final result. For dipole transitions, the number of pairs per nuclear transition in which E_+ lies between E_+ and E_++dE_+ and hence E_- lies between E_- and E_-+dE_-, the direction of k_+ lies in the element of solid angle $d\Omega_+$, and the direction of k_- lies in the element of solid angle $d\Omega_-$, is

$$P(E_+,E_-,\Omega_+,\Omega_-)dE_+dE_-d\Omega_+d\Omega_-\delta(E_++E_-q) =[3/(32\pi^5q)]\sum|H_{i,f}'|^2k_+k_-E_+E_- \times dE_+dE_-d\Omega_+d\Omega_-\delta(E_-+E_+-q), \tag{17}$$

where

$$H_{i,f}'=\int\psi_{\text{initial}}{}^*H'[1+i\lambda/r]\psi_{\text{final}}d\tau. \tag{18}$$

H' is given by (6) and λ by (10). E is the total energy of the transition. That (17) and (18) are more plausible with $\lambda\neq0$ may also be seen as follows. Consider[13] a constant perturbation H'. For this case (17) will give zero, which is reasonable physically, whereas (17) will not be zero if $\lambda=0$, but proportional to λ.

It could be argued, of course, that it would be desirable to change as little of the exact Dirac theory as possible, and that the requirement of the orthogonality of the initial and final state is not essential. As evidence for this point of view, we note that in many calculations it has simply not been possible to orthogonalize the initial and final wave functions. Similarly, it does not follow that just because a certain form of the transition probability, (17) and (18), seems more plausible than another [(17) and (18) with $\lambda=0$], therefore we will get better agreement with experiment; especially when first order perturbation theory is used. We refer, for instance, to the work of Jackson and Schiff[14] on the electron capture by protons in hydrogen. In a first order perturbation calculation, these authors use initial and final state wave functions which are not orthogonal. In addition, they take into account a term in the interaction Hamiltonian which, for physical reasons, should not contribute to the transition probability and yet gives a large contribution. Their agreement with experiment is excellent.

Another procedure, possibly the most consistent of those outlined in this section, would be to use the iterated Dirac equation, including the electromagnetic potentials representing the nuclear multipole. From this equation one would then have to take the perturbing term H', equivalent to (6) and, after devising a perturbation theory for a second order Schrödinger

[13] We are indebted to Dr. Harry Schiff for this remark.
[14] J. D. Jackson and H. Schiff, Phys. Rev. 89, 359 (1953); see also H. Schiff, Can. J. Phys. 32, 393 (1954).

equation, evaluate the matrix elements with Sommerfeld-Maue wave functions. The equivalence of the two procedures has been discussed by Pauli.[15]

IV. EVALUATION OF AN INTEGRAL

The following integral will be required in Sec. V:

$$I(q)=\lim_{\delta\to 0} N_+N_-^*\int d\tau\,\exp[(iq-\delta)r + i(\mathbf{k}_+-\mathbf{k}_-+\boldsymbol{\sigma})\cdot\mathbf{r}]F^*(-n_-,1;\rho_-) \times F(-n_+,1;\rho_+)/r. \quad (19)$$

Equation (19) was first evaluated by Sommerfeld[16] by contour integral methods. He introduced the integral representation,

$$F(-n,1;\rho)=\frac{1}{2\pi i}\oint^{(0+,-1+)} dt\,t^{-n-1}(t+1)^n e^{-\rho t}. \quad (20)$$

The same integral was subsequently evaluated by Bess[17] who introduced the integral representation

$$F(-n,1;\rho)=\frac{e^\rho}{\Gamma(1+n)}\int_0^\infty e^{-t}t^n J_0[2(\rho t)^{\frac{1}{2}}]dt, \quad (21)$$

with $\mathrm{Re}\,(\rho)>0$.

The integral will be evaluated in this section by means of the Fourier transform of

$$\psi(\mathbf{r},\mathbf{k})=N(2\pi)^{-\frac{1}{2}}e^{i\mathbf{k}\cdot\mathbf{r}}F(-n,1;\rho), \quad (22)$$

$$=(2\pi)^{-\frac{1}{2}}\int d\boldsymbol{\kappa}\,\exp(i\boldsymbol{\kappa}\cdot\mathbf{r})\phi(\boldsymbol{\kappa},\mathbf{k}), \quad (23)$$

where

$$\phi(\boldsymbol{\kappa},\mathbf{k})=-\frac{N}{2\pi^2}\lim_{\epsilon\to 0}\frac{\partial}{\partial\epsilon}\frac{[\kappa^2+(\epsilon-ik)^2]^n}{[\epsilon^2+|\boldsymbol{\kappa}-\mathbf{k}|^2]^{1+n}}. \quad (24)$$

The method[18] is essentially different from that of Sommerfeld or Bess, although it has the powerful contour integral approach in common with the former.

It is well known that integrals similar to (19), occurring in related fields, have so far defied evaluation, and this new technique may suggest ways of reducing them.

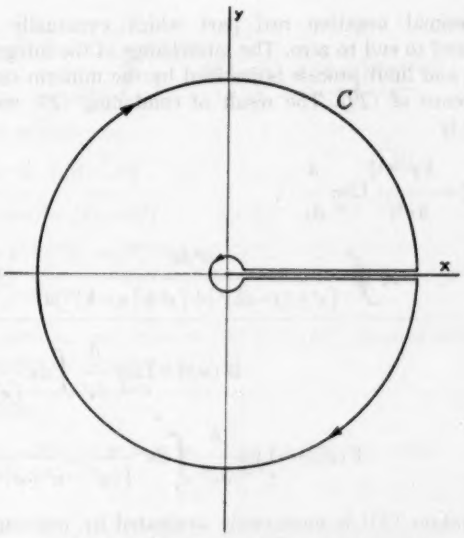

FIG. 2. Integration path used in Eq. (29).

Equation (19) can be written[19]

$$I(q)=\lim_{\delta\to 0}\int\psi^*(\mathbf{r},\mathbf{k}_-)\exp[iq\tau-\delta\tau+i\boldsymbol{\sigma}\cdot\mathbf{r}] \times\psi(\mathbf{r};\mathbf{k}_+)d\tau. \quad (25)$$

By introducing (22) and (23) and carrying out the integration over configuration space,

$$I(q)=\frac{1}{(2\pi)^3}\int d\boldsymbol{\kappa}'\int d\boldsymbol{\kappa}''\phi^*(\boldsymbol{\kappa}')\phi(\boldsymbol{\kappa}'')\frac{4\pi}{|\boldsymbol{\kappa}''-\boldsymbol{\kappa}'+\boldsymbol{\sigma}|^2-q^2}. \quad (26)$$

In order to carry out the integrations in (26) we use[20]

$$a^n/b^{n+1}=-(1/\pi)\sin\pi n\int_0^\infty u^n du/(a+bu), \quad (27)$$

$$a>0,\quad b>0,\quad -1<\mathrm{Re}\,n<0. \quad (28)$$

It is easy to deduce from (27) that

$$a^n/b^{n+1}=-\frac{e^{-in\pi}}{2\pi i}\oint_C u^n du/(a+bu), \quad (29)$$

where C is the contour described in Fig. 2. In order to combine (29) with (24), subject to (28), it is necessary to assume that the n, defined in (2), contains an in-

[15] W. Pauli, *Handbuch der Physik* (Edwards Brothers, Ann Arbor, 1943), Vol. 24, No. 1, p. 239.

[16] See A. Sommerfeld, reference 8. The correct asymptotic behaviour for our wavefunctions demands the substitution $n_\pm\to -n_\pm$ and $k_\pm\to -k_\pm$ in $I(q)$.

[17] See L. Bess, reference 9.

[18] One of us is greatly indebted to Dr. S. T. Butler for pointing out the value of (27) when combined with (24), as well as for a most enlightening discussion on which much of the work in this section is based. We are also grateful to Dr. P. G. Rooney for a discussion on the mathematical aspects of this section.

[19] We have inserted a factor $\exp(i\boldsymbol{\sigma}\cdot\mathbf{r})$ in I, because the trick used by Sommerfeld, Bess, and Bethe *et al.* of keeping $\boldsymbol{\kappa}=\mathbf{k}_--\mathbf{k}_+$ together throughout the integration is not possible here. This approach was previously outlined by E. Guth and C. J. Mullin, Phys. Rev. 83, 667 (1951). Their application of the method to the evaluation of quadrupole transition matrix elements in Coulomb excitation of nuclei was, however, incorrect. This was first noticed by H. McManus (private communication).

[20] W. Gröbner and N. Hofreiter, *Integral Tafel* (Springer Verlag, Wien und Innsbruck, 1950), Vol. II, p. 32, Eq. (9a) with $m=\frac{1}{2}$.

finitesimal negative real part which eventually is allowed to end to zero. The interchange of the integration and limit process is justified by the uniform convergence of (29). The result of combining (29) with (24) is

$$\phi(\kappa)=\frac{N\epsilon^{-in\pi}}{4\pi^3 i}\operatorname*{Lim}_{\epsilon\to 0}\frac{\partial}{\partial\epsilon}\times\oint\frac{u^n du}{[\kappa^2+(\epsilon-ik)^2]+[\epsilon^2+|\kappa-\mathbf{k}|^2]u}. \quad (30)$$

Equation (30) is a far more convenient form than (24) for the Fourier transform of (22), because the branch points in (24) are innocuous in (30). Conditions (28) are obviously satisfied by (30). Inserting (30) into (22), we find

$$I(q)=\frac{N_+N_-^*}{8\pi^6}\exp[-i\pi(n_+-n_-)]=\frac{1}{2\pi i}\oint u^{-n_-}du\frac{1}{2\pi i}\oint v^{n_+}dvW(u,v), \quad (31)$$

where

$$W(u,v)=\operatorname*{Lim}_{\epsilon'\to 0}\frac{\partial}{\partial\epsilon'}\int d\kappa'\frac{V(\kappa',v)}{[\kappa'^2+(\epsilon'+ik_-)^2]+[\epsilon'^2+|\kappa'-\mathbf{k}_-|^2]u}, \quad (32)$$

and

$$V(\kappa',v)=\operatorname*{Lim}_{\epsilon''\to 0}\frac{\partial}{\partial\epsilon''}\int d\kappa''\frac{1}{\{|\kappa''-\kappa'+\sigma|^2-q^2\}\{[\kappa''^2+(\epsilon''-ik_+)^2]+[\epsilon''+|\kappa''-\mathbf{k}_+|^2]v\}}. \quad (33)$$

Equation (33) is most easily evaluated by noticing that the integrand is the product of two factors whose separate Fourier transforms are well known. If we use the convolution theorem of Fourier integrals, Eq. (33) becomes

$$V(\kappa',v)=\operatorname*{Lim}_{\epsilon''\to 0}\frac{\partial}{\partial\epsilon''}\frac{\pi}{2(1+v)}\int\frac{d\tau}{p^2}\exp\left\{i\left[(ip-q)r+\left[\kappa'-\sigma-\left(\frac{v}{1+v}\right)\mathbf{k}_+\right]\cdot\mathbf{r}\right]\right\}, \quad (34)$$

where

$$p^2=[k_+^2v+(\epsilon''-ik_+)^2+\epsilon''^2v]/(1+v)-v^2k_+^2/(1+v)^2. \quad (35)$$

As (34) depends on ϵ'' only through p, we only require

$$\operatorname*{Lim}_{\epsilon''\to 0}p=ik_+/(1+v),\quad \operatorname*{Lim}_{\epsilon''\to 0}\partial p/\partial\epsilon''=-1. \quad (36)$$

Carrying out the differentiation and limit for ϵ'' in (34) and evaluating the integral over $\mathbf{r}$ yields

$$V(\kappa',v)=-2\pi^2(1+v)^{-1}\{|\kappa'-\sigma-\mathbf{k}_+v/(1+v)|^2-[k_+/(1+v)+q]^2\}^{-1}; \quad (37)$$

$W(u,v)$ may be evaluated in an analogous manner. We only give the final result:

$$I(q)=\frac{1}{2\pi^2}e^{-i\pi(n_+-n_-)}N_+N_-^*\frac{1}{2\pi i}\oint u^{-n_-}(1+u)^{-1}du\times\frac{1}{2\pi i}\oint v^{n_+}(1+v)^{-1}\left\{\left|\mathbf{k}_+\left(\frac{v}{1+v}\right)-\mathbf{k}_-\left(\frac{u}{1+u}\right)+\sigma\right|^2-\left[q-\frac{k_-}{1+u}+\frac{k_+}{1+v}\right]^2\right\}^{-1}, \quad (38)$$

$$=\frac{1}{2\pi^2}e^{-i\pi(n_+-n_-)}N_+N_-^*\times\frac{1}{2\pi i}\oint u^{-n_-}\{u[|\mathbf{k}_--\mathbf{k}_+-\sigma|^2-q^2]-[(k_--q)^2-|\mathbf{k}_++\sigma|^2]\}^{-1}du\frac{1}{2\pi i}\oint\frac{v^{n_+}dv}{v-v_0}, \quad (39)$$

where

$$v_0=\frac{u\{(k_++q)^2-|\mathbf{k}_--\sigma|^2\}+\{(k_+-k_-+q)^2-\sigma^2\}}{u\{|\mathbf{k}_--\mathbf{k}_+-\sigma|^2-q^2\}-\{(k_--q)^2-|\mathbf{k}_++\sigma|^2\}}. \quad (40)$$

It can be shown that v_0 does not lie on the positive real axis, provided u does not lie on the negative real axis between

$$u_1=-\{|\mathbf{k}_++\sigma|^2-(k_--q)^2\}/\{|\mathbf{k}_--\mathbf{k}_+-\sigma|^2-q^2\},$$

and (41)

$$u_2=-\{(k_+-k_-+q)^2-\sigma^2\}/\{(k_++q)^2-|\mathbf{k}-\sigma|^2\}.$$

The integration over v can, therefore, be carried out by evaluating the residue of the integrand at v_0.

We remember that the integrand tends to zero along the large circle (see Fig. 2) because of the small real negative part of n_+. Hence,

$$I(q)=(2\pi^2)^{-1}N_+N_-^*\exp\{-i\pi(n_++n_-)\}\frac{1}{2\pi i}\oint\frac{\{u[(k_++q)^2-|\mathbf{k}_--\sigma|^2]+(k_+-k_-+q)^2-\sigma^2\}^{n_+}du}{u^{n_-}\{u[|\mathbf{k}_--\mathbf{k}_+-\sigma|^2-q^2]-[(k_--q)^2-|\mathbf{k}_++\sigma|^2]\}^{n_++1}}. \quad (42)$$

In (42), make the transformation

$$u=u_1(1-t)+u_2t. \quad (43)$$

Hence,

$$I(q)=\frac{N_+N_-^*}{2\pi^2}\frac{[|\mathbf{k}_--\boldsymbol{\sigma}|^2-(k_++q)^2]^{n_+}[|\mathbf{k}_++\boldsymbol{\sigma}|^2-|k_--q|^2]^{-n_-}}{[|\mathbf{k}_--\mathbf{k}_+-\boldsymbol{\sigma}|^2-q^2]^{n_++n_-+1}}\frac{1}{2\pi i}\oint^{(1+,0+)}dt(1-zt)^{-n_-}(1-t)^{n_++n_-+1}. \quad (44)$$

The contour does not include the singularity at $t=1/z$, $z<0$, where

$$z=1-\frac{u_2}{u_1}=1+\frac{\{|\mathbf{k}_--\mathbf{k}_+-\boldsymbol{\sigma}|^2-q^2\}\{(k_+-k_-+q)^2-\sigma^2\}}{\{|\mathbf{k}_--\boldsymbol{\sigma}|^2-(k_++q)^2\}\{|k_++\boldsymbol{\sigma}|^2-(k_--q)^2\}}. \quad (45)$$

$$I(q)=\frac{N_+N_-^*}{2\pi^2}\frac{[|\mathbf{k}_--\boldsymbol{\sigma}|^2-(k_++q)^2]^{n_+}[|\mathbf{k}_++\boldsymbol{\sigma}|^2-(k_--q)^2]^{-n_-}}{[|\mathbf{k}_--\mathbf{k}_+-\boldsymbol{\sigma}|^2-q^2]^{n_++n_-+1}}\,{}_2F_1(n_-,-n_+,1;z). \quad (46)$$

It is understood that the small negative real parts in the n_- and n_+, occurring in (46) and (45), are now allowed to tend to zero. This result agrees with that obtained previously by Sommerfeld.[21]

V. PROBABILITY FOR ELECTRIC DIPOLE TRANSITIONS

In this section we use the evaluation of $I(q)$ presented in Sec. IV in order to evaluate the $H_{i,f'}$ defined in (18). We need the following results:

$$\nabla_r F(-n_\pm,1;\rho_\pm)=-(k_\pm/r)\nabla_\pm F(-n_\pm,1;\rho_\pm), \quad (47)$$

where $\nabla_\pm$ means $\nabla_{k_\pm}$.

$$-i^\mu I_\mu(q)=\int d\tau\,\exp(iq\mathbf{r})\mathfrak{F}(\mathbf{r})/r^{\mu+1}$$
$$=-i^\mu\{\Gamma(\mu)\}^{-1}\int_q^\infty(q-q')^{\mu-1}I(q')dq', \quad (48)$$

where[22]

$$I_0(q)=I(q)=\lim_{\delta\to0}\int d\tau\,\exp(iq\mathbf{r}-\delta r)\mathfrak{F}(\mathbf{r})/r, \quad (49)$$

and

$$\mathfrak{F}(\mathbf{r})=(2\pi)^{-3}N_-^*N_+\exp\{i(\mathbf{k}_+-\mathbf{k}_-+\boldsymbol{\sigma})\cdot\mathbf{r}\}$$
$$\times F^*(-n_-,1;\rho_-)F(-n_+,1;\rho_+),$$

$\mu\gtrless0$, the definition of $\mathfrak{F}(\mathbf{r})$ follows from (19). Relations (48) and (49) are easily established by an interchange in the order of integration and a use of the definition of $\Gamma(\mu)$. Introducing (19), (45), (46), (47), and (48) into (18), we find

$$H_{i,f'}=u^*(\mathbf{k}_-)[\eta+\boldsymbol{\alpha}\cdot(\boldsymbol{\chi}+i\rho\mathbf{v})]eu(\mathbf{k}_+), \quad (50)$$

where

$$\eta=-\mathbf{B}\cdot\{[\beta_+\nabla_+-\beta_-\nabla_--(\beta_++\beta_-)\nabla_\sigma](I_1-\lambda I_2)$$
$$-\nabla_\sigma[I_2/q-I_1-\lambda(I_3/q-I_2)]\}, \quad (51)$$

$$\boldsymbol{\chi}=-\mathbf{B}(I_0+\lambda I_1)-\{\beta_-\nabla_--\beta_+\nabla_++(\beta_++\beta_-)\nabla_\sigma\}\mathbf{B}$$
$$\cdot\nabla_\sigma[I_3/q-I_2-\lambda(I_4/q-I_3)]\}, \quad (52)$$

$$\mathbf{v}=\mathbf{B}\times[-(\beta_+\nabla_+-\beta_-\nabla_-)+(\beta_++\beta_-)\nabla_\sigma](I_1-\lambda I_2); \quad (53)$$

$$\rho=\begin{bmatrix}0&0&0&1\\0&0&1&0\\0&1&0&0\\1&0&0&0\end{bmatrix}.$$

In (51), (52), and (53) it is understood that $\sigma\to0$ as soon as the σ-gradients have been carried out. Terms proportional to $|n|^2\beta^2$ have been omitted as is consistent with the approximate solution (4) of Eq. (3). It was shown in Sec. IV that $I(q)$ is complex only through n_+ and n_-. It follows from the definition (48) that the same conclusion holds for I_1, I_2, etc. Consequently, (51), (52), and (53) are complex only through n_+ and n_-. We must now carry out the summation over the spin directions of the electron and positron using the standard spur and closure theorems. These are applicable because our wave functions have the great advantage that their spinor dependence is that of the plane wave solution of Dirac's Equation. We give only the final result:

$$\sum|H_{i,f'}|^2=(E_+E_-)^{-1}\Big\{(|\boldsymbol{\chi}|^2+|\mathbf{v}|^2-|\eta|^2)(E_+E_-+m^2+\mathbf{k}_+\cdot\mathbf{k}_-)+2\,\mathrm{Re}[(\eta^*E_-+\boldsymbol{\chi}^*\cdot\mathbf{k}_-)(\eta E_+-\boldsymbol{\chi}\cdot\mathbf{k}_+)$$
$$+(\mathbf{v}\cdot\mathbf{k}_-)(\mathbf{v}^*\cdot\mathbf{k}_+)+(\mathbf{v}\cdot\mathbf{k}_-\times\mathbf{k}_+)\eta^*+(\mathbf{v}\times\boldsymbol{\chi}^*\cdot\mathbf{k}_+)E_-+(\mathbf{k}_-\times\boldsymbol{\chi}\cdot\mathbf{v}^*)E_+]\Big\}. \quad (54)$$

Since η, $\boldsymbol{\chi}$, and $\mathbf{v}$ are complex only through n_+ and n_-, it follows that (54) only contains even powers of n_+ and n_-. However, as (50) and consequently (51), (52), and (53) were derived on the assumption that terms proportional to all but the first power of the fine structure constant were negligible, it is consistent with our approximation to neglect similar terms in (54). This yields the final result:

$$\sum_{\text{spin}}|H_{i,f'}|^2=|N_+|^2|N_-|^2\{[\sum_{\text{spin}}|H_{i,f'}|^2]_{\text{first Born approx.}}$$
$$+O[\max(|n|^2,|n|^4,\cdots;|n|^2\beta^2]\}. \quad (55)$$

[21] See A. Sommerfeld, reference 8. We note the difference between the normalization of our wave function and those used by Sommerfeld. Sommerfeld neglected certain terms in his evaluation as he did not require them for his calculations. They have subsequently been given by A. Nordsieck, reference 9, whose results agree with ours also after allowing for a change in notation.

[22] The I_μ defined by (48) and (49) does not converge for $\mu>1$. However, it occurs only in conjunction with σ-gradients when $\mu>1$ and always in such a way that the resultant integrals do converge.

This result has already been assumed, *ad hoc*, by Bloom.[23] The Born approximation calculations now continue as before.

VI. HIGHER ORDER MULTIPOLE TRANSITIONS AND THE EXTENTION TO OTHER UNBOUND TRANSITIONS

In the first part of this section, we shall show that the results obtained in Sec. V for electric dipole transitions hold for all nuclear electromagnetic transitions.

It is well known that nuclear transitions differ in character, and can be classified as electric and (or) magnetic multipole transitions with different selection rules for angular momentum and parity applying to each type. A thorough discussion of this problem has been given by Blatt and Weisskopf.[24] Our result (55) in the electric dipole case depended essentially on the fact that $H_{i,f}'$ was complex only through n_+ and n_-. Consider the case of an electric quadrupole transition; it is easily shown that

$$V=\left(\frac{\mathbf{c}\cdot\nabla_r}{iq}\right)\left(\frac{\mathbf{c}\cdot\nabla_r}{iq}\right)\frac{e^{iqr}}{r},$$

$$\mathbf{A}=3\mathbf{c}\left(\frac{\mathbf{c}\cdot\nabla_r}{iq}\right)\frac{e^{iqr}}{r}.$$

In other words, the electric quadrupole potentials are obtained from the electric dipole potentials, apart from a real multiplying constant, by the application of the operator $\mathbf{c}\cdot\nabla_r/iq$. It can now be shown very easily, by using (48) and (19), that the $H_{i,f}'$ for electric quadrupole transitions is again complex only through n_+ and n_-. This argument is easily extended to cover all electric multipole transitions. The same result holds for all magnetic multipole transitions. The proof follows the electric multipole case closely.

Furthermore, we see that if the Born approximation matrix element is real, i.e., the transition takes place between two unbound states, then our result must hold in general. This result is of interest in the estimation of the errors due to the use of the Born approximation in processes like the pair formation by direct nuclear interaction in the 6.05-Mev $0^+\rightarrow 0^+$ transition in O^{16}. On the basis of our general result the error caused by the neglect of the nuclear Coulomb field should be of the order of $\frac{1}{3}$ of 1 percent. This is rather smaller than the present experimental error.[25] Similar considerations apply to the 7.25-Mev $0^+\rightarrow 0^+$ transition in C^{12}, first observed with certainty by Harris.[24] The error due to the neglect of the nuclear Coulomb field is rather less than $\frac{1}{3}$ of 1 percent.

[23] See S. D. Bloom, reference 3.

[24] J. M. Blatt and V. Weisskopf, *Theoretical Nuclear Physics* (John Wiley and Sons, Inc., New York, 1952); G. Harries, reference 3.

[25] Devons, Goldring, and Lindsey, Proc. Phys. Soc. (London) **67**, 134 (1954).

VII. CONCLUSIONS

Apart from the exact calculations of Jaeger and Hulme[26] on the total pair production probability in lead ($Z=84$), the only theoretical calculations available to compare with the growing experimental evidence are based on the first Born approximation. When the latter calculations are compared with the exact results of Jaeger and Hulme, an error of about 20 percent is found. This is not at all in agreement with (1) which suggests that the error should be of the order of 65 percent. It is, however, shown[27] in this paper that the first Born approximation calculation is much better than might have been expected on the basis of (1). We find that the condition for its validity is

$$|n|^2\ll 1, \quad |n|^2\beta\ll 1, \quad |n|^2\beta^2\ll 1, \tag{56}$$

rather than

$$|n_+|\ll 1, \quad |n_-|\ll 1. \tag{1}$$

The corrections to the first Born approximation are of two types. There are terms proportional to $|n|^2\beta^2$, or $(Z/137)^2$, and there are terms proportional to $|n|^2$ and $|n|^2\beta$ (we ignore terms proportional to $|n|^4$, etc.). As we are concerned primarily with low-energy transitions, we cannot evaluate the former terms in (55) because the wave functions (4), used in (16), are only accurate[28] to the order of this correction term. The latter terms correspond essentially to higher order Born approximation terms and they may, in principle, be calculated to any order. There is at present, little hope that the very complicated integrals involved can be evaluated in general.[29] In Appendix II we outline a procedure for taking the terms proportional to $|n|^2$ and $|n|^2\beta$ into account.

It is clear that for a given nuclear charge and given positron (negatron) energy,

$$|n|^2>|n|^2\beta>|n|^2\beta^2.$$

The condition $|n|^2\beta^2\ll 1$ is independent of the particle energy, in contradistinction to (1), and so $|n\beta|$ plotted against the particle energies gives straight lines. These lines, for various values of Z are shown in Fig. 1. As indicated in (55), our transition probability also contains terms proportional to $|n|^2$. The conditions

[26] J. C. Jaeger and H. R. Hulme, Proc. Roy. Soc. (London) **148**, 708 (1935).

[27] It has been suggested by Rose, see reference 2, that in the Born approximation the integral features of the pair production process will yield even better agreement with the exact calculations as the effect of the Coulomb field is to suppress the number of slow positrons and increase the number of fast ones. Upon integration over the energy spectrum the two effects largely cancel out. This might account for the surprising excellence of the first Born approximation. A similar effect was found by Bethe *et al.*, reference 4, for external pair production. In both processes the negatron-positron interaction has so far been ignored. That this is reasonable has been shown by R. H. Dalitz, Proc. Roy. Soc. (London) **A206**, 521 (1951).

[28] In the case of external pair creation, Bethe *et al.* were able to concentrate on the case of large primary energy, and so calculate terms we must neglect.

[29] Far less complicated integrals have so far defied evaluation; see reference 11.

$|n_+|^2 \ll 1$, $|n_-|^2 \ll 1$, give curves which depend on the energy of the particle and the nuclear charge. They are also given in Fig. 1. (right hand ordinate scale) We note that because electrons have a small rest mass the curves and the straight lines in Fig. 1 diverge only at small energies. For particle kinetic energies above one Mev and the nuclear charge less than or of the order of 30, the corrections to the first Born approximation are of the order of 5 percent ($|n|^2 \lesssim 0.05$, i.e., $|n| \lesssim 0.23$). In view of the status of the experimental techniques, this is probably satisfactory at present. If the particle kinetic energy is above 100 kv, a five-percent error requires the nuclear charge to be less than or of the order of twenty.

Clearly this situation is again improved if ratios of transition probabilities, say, at various angle are considered. The error term may then be expected to be of order $\mathrm{Max}(|n|^4, |n^2\beta^2|)$.

In the first Born approximation, the transition probabilities are symmetrical between the positron and negatron. As soon as the nuclear electrostatic field is no longer neglected, by the inclusion of the "Sommerfeld factors," this symmetry is absent. It is only through the presence of these factors that our results differ from those obtained in the first Born approximation calculation. It is known that they occur in many other similar processes such as the external pair production.[30] These factors are known to affect the transition probabilities considerably for low negatron or positron energies. In Sec. VI, we proved that condition (56) gives the region of validity for all first Born approximation calculations, in which the initial and final states concerned belong to the continuous spectrum. This is clearly not the case for the internal conversion process for which, therefore, condition (1) and not (56) is applicable.[31] This fact explains clearly why the first Born approximation gives results with a very much more restricted range of validity in the internal conversion than in the internal pair production process.[32]

Our work uses a transition matrix element that differs from that usually used by a term that arises from the non-orthonormal properties of the Sommerfeld-Mauer wave functions. We emphasize that our conclusions in this paper are independent of whether λ in (18) is different from zero or not. The question of what is the correct matrix element clearly requires further study.

APPENDIX I

Let ψ_+ and ψ_- be two solutions of (3) for $E=E_+$ and E_-, respectively. Then[33]

$$\psi_+^*\nabla^2\psi_- - \psi_-\nabla^2\psi_+^* + (E_-^2 - E_+^2)(1+i\lambda/r)\psi_+^*\psi_- = 0. \quad \text{(A1)}$$

[30] See. W. Heitler, *Quantum Theory of Radiation* (Oxford University Press, London, 1947).
[31] S. M. Dancoff and P. Morrison, Phys. Rev. **55**, 122 (1939).
[32] Rose, Goertzel, Spinrad, Harr, and Strong, Phys. Rev. **76**, 1882 (1949).
[33] A similar procedure is sketched by Sommerfeld, reference 8, p. 412, for the case of the discrete spectrum.

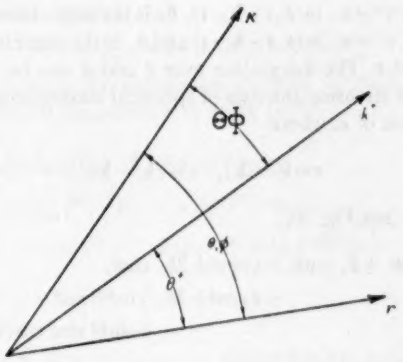

FIG. 3. Definition of angular variables in Appendix I.

Integrating over coordinate space and applying Green's Theorem, we obtain

$$\int_{\Delta_-} d\mathbf{k}_- \int \psi_+^*(1+i\lambda/r)\psi_- d\tau = f(E_+,E_-), \quad \text{(A2)}$$

where

$$f(E_+,E_-) = \mathrm{Limit}_{r_\sigma\to\infty} \int_{\Delta} \frac{d\mathbf{k}}{E_-^2 - E_+^2} \times \int \left(\psi_+^* \frac{\partial}{\partial r}\psi_- - \psi_+ \frac{\partial}{\partial r}\psi_-^*\right) d\sigma. \quad \text{(A3)}$$

Since we are concerned with wave functions in the continuous spectrum, an integration over a spherical shell of thickness Δ_- in $\mathbf{k}_-$ space has been introduced. σ represents a sphere of radius r_σ. Our task is to evaluate $f(E_+,E_-)$. The asymptotic form of the wave function (4) may be shown to be

$$\psi = \frac{Ne^{\frac{1}{2}i\pi\gamma}}{(2\pi)^{\frac{3}{2}}\Gamma(1+n)} \exp\{i\mathbf{k}\cdot\mathbf{r} + n\ln(kr - \mathbf{k}\cdot\mathbf{r})\} \times [1+O(1/r)]. \quad \text{(A4)}$$

We have omitted the spinor $u(\mathbf{k})$, since its effect on the orthonormalization integral would simply be to introduce an additional Kronecker delta. Inserting (A4) into (A3) and neglecting terms of order $1/r_\sigma$ gives

$$f(E_+,E_-) = \mathrm{Lim}_{r_\sigma\to\infty} \int_{\Delta_-} d\mathbf{k}_- N_+^* N_- \exp\{\tfrac{1}{2}i\pi(n^+ + n^-)\} \times [(2\pi)^3\Gamma(1-n_+)\Gamma(1+n_-)]^{-1} r_\sigma^2 \times \int_\sigma d\varphi d\cos\theta i(k_+\cos\theta_+ + k_-\cos\theta_-) \times \exp[i(\mathbf{k}_- - \mathbf{k}_+)\cdot\mathbf{r} + (\gamma^- - \gamma^+)], \quad \text{(A5)}$$

where $\gamma^+=n_+\ln(k_+r-\mathbf{k}_+\cdot\mathbf{r})$, θ_+ is the angle between $\mathbf{k}_+$ and $\mathbf{r}$, $\gamma^-=n_-\ln(k_-r-\mathbf{k}_-\cdot\mathbf{r})$ and θ_- is the angle between $\mathbf{k}_-$ and $\mathbf{r}$. The integration over θ and ϕ can be carried out by choosing the axis of spherical coordinates in the reaction of κ, where

$$\kappa=\mathbf{k}_--\mathbf{k}_+,\quad \kappa=|\mathbf{k}_--\mathbf{k}_+|.$$

Then (see Fig. 3),

$$\begin{aligned}k_-\cos\theta_-+k_+\cos\theta_+&=\kappa\cos\theta+2k_+\cos\theta_+\\&=\kappa\cos\theta+2k_+[\cos\Theta\cos\theta\\&\qquad+\sin\Theta\sin\theta\cos(\Phi-\phi)].\end{aligned}$$

Hence,

$$\begin{aligned}&f(E_+,E_-)\\&=\frac{i}{(2\pi)^2}\int_{\Delta_-}\frac{d\mathbf{k}_-}{E_+^2-E_-^2}\cdot N_+^*N_-\exp\{\tfrac{1}{2}i\pi(n_++n_-)\}\\&\times\operatorname{Lim}_{r_\theta\to\infty}r_\theta^2\int_{-1}^{1}d\cos\theta e^{i\kappa r_\theta\cos\theta}(\kappa+2k_+\cos\Theta)\cos\theta,\quad\text{(A6)}\end{aligned}$$

where we have dropped the terms involving γ and will ignore the k_- dependence of n_-. This is easily justified in the limit $r_\theta\to\infty$. The integration over θ can now be carried out. The result is

$$\begin{aligned}f(E_+,E_-)&=\frac{N_+^*N_-\exp\{\tfrac{1}{2}i\pi(n_++n_-)\}}{2\pi^2\Gamma(1-n_+)\Gamma(1+n_-)}\\&\times\operatorname{Lim}_{r_\theta\to\infty}\int_{\Delta_-}\frac{d\mathbf{k}_-}{E_+^2-E_-^2}(\kappa+2k_+\cos\Theta)\\&\times\left(\frac{r_\theta}{\kappa}\cos\kappa r_\theta-\frac{1}{\kappa^2}\sin\kappa r_\theta\right).\quad\text{(A7)}\end{aligned}$$

We now introduce spherical polar coordinates in the $\mathbf{k}_-$ integration. Carrying out the integration over the azimuthal angle yields

$$\begin{aligned}&f(E_+,E_-)\\&=N_+^*N_-\{\pi\Gamma(1+n_-)\Gamma(1-n_+)\}^{-1}\exp\{\tfrac{1}{2}i\pi(n_++n_-)\}\\&\times\operatorname{Lim}_{r_\theta\to\infty}\int_{k-\Delta/2}^{k-+\Delta/2}\{E_+^2-E_-^2\}^{-1}k_-^2dk_-\\&\times\int_{-1}^{1}d\cos\beta\left[\frac{r_\theta}{\kappa}\cos\kappa r_\theta-\frac{1}{\kappa^2}\sin\kappa r_\theta\right]\\&\times\left\{\kappa+2\frac{k_+}{\kappa}(k_-\cos\beta-k_+)\right\},\quad\text{(A8)}\end{aligned}$$

where β is the angle between $\mathbf{k}_-$ and $\mathbf{k}_+$. If the variable κ is used instead of β for the angular integration,

$$\begin{aligned}f(E_+,E_-)&=\frac{N_+^*N_-\exp\{\tfrac{1}{2}i\pi(n_++n_-)\}}{\pi\Gamma(1+n_-)\Gamma(1-n_+)}\\&\times\operatorname{Lim}_{r_\theta\to\infty}\int_{k-\Delta/2}^{k-+\Delta/2}\frac{k_-}{k_+}\frac{dk_-}{E_+^2-E_-^2}\\&\times\begin{Bmatrix}(k_++k_-)\sin r_\theta(k_--k_+)\\-(k_--k_+)\sin r_\theta(k_++k_-)\end{Bmatrix},\quad\text{(A9)}\\&=\operatorname{Lim}_{r_\theta\to\infty}\left[\int_{u_-}^{u+}f(u)\frac{\sin ur_\theta}{u}du\right.\\&\qquad\left.-\int_{v_-}^{v+}f(v)\frac{\sin vr_\theta}{v}dv\right],\end{aligned}$$

where

$$\begin{aligned}&u=k_--k_+,\quad u_\pm=k_--k_+\pm\Delta/2,\\&v=k_-+k_+,\quad v_\pm=k_-+k_+\pm\Delta/2,\\&f(0)=\{N_+^*N_-k_-\exp[\tfrac{1}{2}\pi i(n_-+n_+)]\}\\&\qquad\times\{\pi k_+\Gamma(1+n_-)\Gamma(1-n_+)\}^{-1}.\end{aligned}$$

Using

$$\int_{-\infty}^{\infty}(\sin u/u)du=\pi,$$

we find that

$$f(E_+,E_-)=|N_+|^2e^{i\pi n_+}/|\Gamma(1+n_+)|^2,\text{ or }0,\quad\text{(A10)}$$

according as Δ_- includes $\mathbf{k}_+$ or not. Hence the normalizing condition,

$$f(E_+,E_+)=1,\quad\text{(A11)}$$

yields

$$|N_+|^2=2\pi|n_+|/(e^{2\pi|n+|}-1).\quad\text{(A12)}$$

Equations (A2), (A10), (A11), and (A12) may be compared with the nonrelativistic normalization condition,

$$\int_{\Delta_-}d\mathbf{k}_-\int\psi_+^*\psi_-d\tau=1\text{ or }0,\quad\text{(A13)}$$

according as Δ_- contains $\mathbf{k}_+$ or not. For the ψ in (A13) the solution of the nonrelativistic Schrödinger equation with a Coulomb potential, the normalizing constant may be shown to be the same as (A12). This has probably obscured the essential difference between (A2), (A10), (A11), and (A12) on the one hand, and (A13) combined with (A12) on the other. It is clear that if we carry out the transition to the nonrelativistic limit, $c\to\infty$ or $\lambda\to0$, (9) goes directly over into (A13).

APPENDIX II

In this appendix we show how I_μ can be evaluated in detail to order $|n|^2$ even if $\mu>0$. Consider, for example, I_1.

$$I_1=(2\pi)^{-3}N^{-4}N_+\int d\tau\,\exp\{i(\mathbf{k}_+-\mathbf{k}_-+\boldsymbol{\sigma})\cdot\mathbf{r}+iq\mathbf{r}\}$$
$$\times F^*(-n_-,1;\rho_-)F(-n_+,1;\rho_+)r^{-2}.$$

We now use the fact that

$$F(-n,1;\rho)=1-n\,\mathrm{Ei}(\rho)+O(|n|^2),$$

where $\mathrm{Ei}(\rho)$ is the exponential integral function. It is easily shown that correct to order $|n|^2$,

$$I_1=\int d\tau\,\exp\{i(\mathbf{k}_+-\mathbf{k}_-+\boldsymbol{\sigma})\cdot\mathbf{r}+iq\mathbf{r}\}$$
$$\times[F^*(-n_-,1;\rho_-)+F(-n_+,1;\rho_+)$$
$$+|n_+n_-|\,\mathrm{Ei}(\rho_+)\,\mathrm{Ei}^*(\rho_-)-1]r^{-2}.$$

PHYSICAL REVIEW VOLUME 96, NUMBER 4 NOVEMBER 15, 1954

Decay of UX_1, UX_2, and UZ†

SVEN A. E. JOHANSSON*
Department of Physics and Institute for Atomic Research, Iowa State College, Ames, Iowa
(Received March 31, 1954; revised manuscript received August 20, 1954)

The decay of Th^{234}(UX_1) and Pa^{234}(UX_2 and UZ) has been investigated by means of a coincidence scintillation spectrometer. Three gamma rays at 29, 63, and 92 kev were found in UX_1. Four gamma rays at 250, 750, 1000, and 1810 kev were found in UX_2, and four gamma rays at 250, 760, 910, and 1680 kev were observed in UZ. The coincidence relations between the gamma rays, and also between the gamma rays and the beta radiation, have been investigated. A decay scheme is proposed and spin and parity assignments have been made for some of the levels of Pa^{234} and U^{234}.

THE beta-emitting substance in natural uranium was isolated by Crookes[1] as early as 1900 and called UX. Later on Fajans and Göhring[2] showed that this substance is a radioactive equilibrium of two isotopes, UX_1 and UX_2, in modern nomenclature Th^{234} and Pa^{234}, respectively. Hahn[3] showed that Pa^{234} decays with two different half-lives and that both activities emit beta and gamma rays. The long-lived activity was given the symbol UZ. Actually, UX_2 and UZ were the first example of an isomeric pair.

The radiation from UX_1, UX_2, and UZ has been studied extensively for a long time. At first absorption technique was used, but more recently the beta radiation has been investigated by means of magnetic spectrometers, and is therefore fairly well known. Almost nothing is known about the gamma radiation, however, and it has been difficult to set up a consistent decay scheme. It seemed therefore worthwhile to make a complete reinvestigation of the radiation from UX_1, UX_2 and UZ, using a coincidence scintillation spectrometer.

The apparatus used in this work has been described elsewhere.[4] It consists of two scintillation spectrometers. Each one can be used as a beta- or gamma-ray spectrometer, depending on the crystal material. The pulses from the first spectrometer are led to a single channel analyzer, which selects pulses corresponding to a certain energy-range. The pulses from the second spectrometer are displayed on an oscilloscope screen and are recorded by photographic methods. The oscilloscope sweep is triggered by coincidences between the selected pulses from the first spectrometer and pulses from the second spectrometer. Hence, a recorded pulse distribution shows the spectrum of the radiation which is in coincidence with the radiation component selected by the analyzer. One can, for example, select beta rays within a certain energy range and study the corresponding coincidence gamma-ray spectrum. It is also possible to select a certain gamma ray and record the corresponding beta component. One can finally study gamma-gamma coincidences by selecting a certain gamma ray and recording the corresponding coincidence gamma spectrum. Hence, this apparatus makes possible a complete investigation of the coincidence relations in a radioactive decay.

The radioactive material used for making sources was isolated from natural uranium by an ether-water extraction method. It was precipitated as the fluoride with lanthanum as the carrier. After a short while it contains UX_1, UX_2, and UZ in equilibrium. The work on UX_1 and UX_2 has been done with sources made up of this material. The activity of UZ is so low that it does not interfere with the measurements on UX_1 and UX_2. The radiation of UX_1 is of low energy, that of

† Contribution from the Institute for Atomic Research and Department of Physics, Iowa State College, Ames, Iowa. Work was performed in the Ames Laboratory of the U. S. Atomic Energy Commission.
* On leave from the University of Lund, Lund, Sweden.
[1] W. Crookes, Proc. Roy. Soc. (London) **A66**, 409 (1900).
[2] K. Fajans and O. Göhring, Naturwiss. **1**, 399 (1913).
[3] O. Hahn, Naturwiss. **9**, 84 (1921).
[4] S. A. E. Johansson, Ames Laboratory Report ISC-431 (unpublished).

UX_2 of high energy. It is therefore possible to investigate their radiation without being bothered by overlapping spectra.

UZ was isolated from the equilibrium material by a separation of protactinium from thorium. The protactinium fraction contains both UX_2 and UZ, but UX_2 decays very fast (half-life 1.18 min) giving a pure UZ source. The separation was made in the following way using tantalum as the carrier: The radioactive material, containing the equilibrium amount of UZ, was dissolved in dilute sulfuric acid. A solution of potassium tantalate was added and the solution was heated. The tantalum oxide precipitate was filtered, washed, and dried.

UX_1

UX_1 (Th^{234}) has a half-life of 24.1 days. It emits low-energy beta rays and a strong low-energy gamma radiation. The continuous beta rays have been investigated several times by absorption technique and cloud chambers. More recently Bradt and Sherrer,[5] using a 180° magnetic spectrometer, determined the end point as 205 kev. Jnanananda,[6] with a lens spectrometer, found the end point to be at 190 kev. Quite recently Stoker, Heerschap, and Hok[7] reported a careful investigation of the UX_1 beta spectrum, using a double focusing spectrometer. They were able to resolve the continuous beta spectrum into two components with end points at 193 and 103 kev.

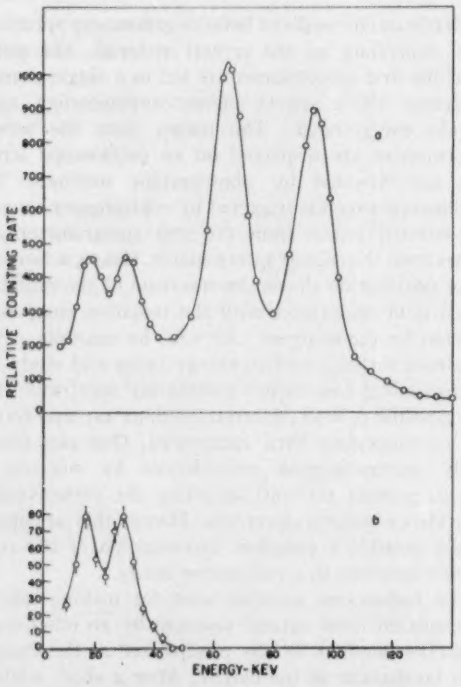

FIG. 1. (a) Gamma-ray spectrum of UX_1. (b) Spectrum of the gamma radiation in coincidence with the 63-kev gamma ray.

Superimposed upon the continuous beta spectrum are several internal conversion lines. Very early, Meitner[8] reported some lines due to the conversion of a 92 kev gamma-ray. Bradt and Sherrer[5] arrived at the same results. Stoker, Heerschap, and Hok[7] in more recent work have found very many internal conversion and Auger lines. Besides strong lines due to a 91.5-kev gamma ray, there are also weaker lines assigned to gamma rays at 63, 47, 43, and 29 kev.

A sodium iodide scintillation spectrometer was used to find the gamma spectrum of UX_1, shown in Fig. 1(a). It consists of two main peaks at 94 and 64 kev, and two weaker ones at 30 and 17 kev. The 94-kev peak is presumably made up of two components. Part of it is due to K x-rays emitted in internal conversion of the UX_2 gamma rays. The mean energy of the uranium K x-rays is 96 kev. The 94-kev peak is so strong, however, that it cannot be solely due to the x-rays. The greater part of it must be due to a gamma ray. In order to determine its energy one must know how much of the peak is due to x-rays and then subtract this part of the peak. The x-ray intensity is not known accurately, however, and therefore it is only possible to say that the energy is a little less than 94 kev, probably 92–93 kev. This value is close to the value 91.5 kev found from the energy of the conversion lines in the beta spectrum.[7]

The 64-kev peak must be due to a gamma ray. The energy is close to the value 63 kev found from the internal conversion lines. The 30-kev peak is probably made up of two components. Part of it is an "escape peak" from the 63-kev gamma ray, having an energy of about 34 kev. The intensity of this escape peak should be about 10 percent of the 64-kev peak. The greater part of the 30-kev peak must therefore be due to a gamma ray with an energy of about 29 kev. This value coincides with one of the gamma-ray energies found in the internal conversion spectrum. The 17-kev peak finally is attributed to L x-rays of protactinium, emitted in the internal conversion of the UX_1 gamma rays. The L_α and L_β x-rays have the energy values 13 and 17 kev, respectively.

In order to establish a decay scheme some coincidence measurements have been performed. The relation between the beta and gamma radiation was investigated in the following way: One of the gamma rays was picked out from the spectrum by means of a sodium iodide scintillation spectrometer and the single-channel analyzer. Those pulses from an anthracene spectrometer, which were in coincidence with the selected gamma ray, were recorded. The results are rather qualitative because of the low counting rate and the poor resolution of the anthracene scintillation

[5] H. Bradt and P. Sherrer, Helv. Phys. Acta **19**, 307 (1946).
[6] S. Jnanananda, Phys. Rev. **69**, 570 (1946).
[7] Stoker, Heerschap, and Hok, Physica **19**, 433 (1953).
[8] L. Meitner, Z. Physik **17**, 54 (1923).

spectrometer at low energies. They definitely show, however, that the gamma rays at 92, 63, and 29 kev are all in coincidence with a beta group having an end point at about 100 kev.

To get a further check on the decay scheme some gamma-gamma coincidence measurements were performed. With the channel set to pick out the 92-kev gamma ray, no coincidences were obtained except for a few accidental ones. With the channel selecting the 63-kev gamma ray, the coincidence spectrum shown in Fig. 1(b) was obtained. It consists of a peak from the 29-kev gamma ray and a peak from the L x-rays emitted in the internal conversion of the gamma ray.

These coincidence measurements show that all three gamma rays are in coincidence with the same beta-ray group. The 63-kev and 29-kev gamma rays form a cascade with the 92-kev ray as a cross-over transition.

UX

The isotope $UX_2(Pa^{234})$ has a half-life of 1.18 min. It emits high-energy beta rays and a very weak gamma radiation. Except for absorption and cloud-chamber measurements the first investigation of the continuous beta spectrum was made by Marshall[9] using a 180° magnetic spectrometer. He found the end point to be at 2320 kev and some evidence for a low-energy beta group with an end point at 1500 kev. Recently the continuous beta spectrum was measured by Stoker *et al.*[7] They report three beta groups with end points at 2305, 1500, and 580 kev and relative intensities of 90 percent, 9 percent, and 1 percent, respectively.

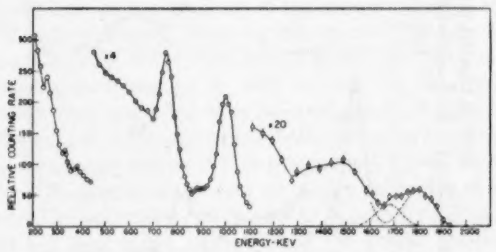

FIG. 2. Gamma-ray spectrum of UX_2 and UZ.

The most striking feature of the UX_2 beta spectrum is the presence of some strong internal conversion lines at about 800 kev. They were first found in 1933 by Meitner[10] and have been remeasured several times since then. The agreement between the various measurements is very poor, however. Most probably there is just one transition with an energy of 810 kev. If there are some more lines, they are very weak. The conversion lines of the 810-kev transition are surprisingly strong.

[9] J. S. Marshall, Proc. Roy. Soc. (London) **173**, 391 (1939).
[10] L. Meitner, *Handbuch der Physik* (Springer, Berlin, 1933), Vol. 22.

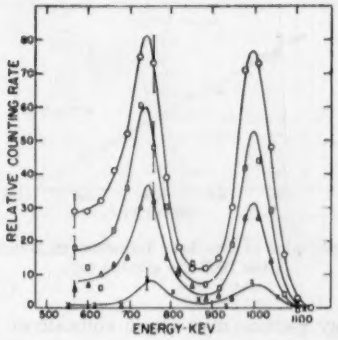

FIG. 3. Spectra of the gamma radiation in coincidence with beta radiation of different energies. The energies are (from the top) 690, 930, 1170, and 1410 kev, respectively.

The intensity of the K line is 0.52 percent of the UX_2 beta rays.[7]

The gamma-ray spectrum of UX_2 from a sodium iodide scintillation spectrometer is shown in Fig. 2. There are well-defined photopeaks at 250, 750, and 1000 kev, indicating gamma rays of these energies. There are also two small bumps at 330 and 380 kev. The corresponding gamma rays must be very weak and it is uncertain whether they belong to UX_2 or to some impurity. They will not be dealt with any further in this work. At 900 kev there is another small peak. It belongs to UZ and will be discussed later in connection with the decay of UZ. There is also some high-energy gamma radiation. The pulse distribution is most easily interpreted as due to two gamma rays of 1680 and 1810 kev. The two components are shown with dotted lines in Fig. 2.

A series of coincidence measurements was performed in order to find out the coincidence relations in the decay of UX_2. The first type is beta-gamma coincidences. A thin source was mounted between two scintillation spectrometers with anthracene and sodium iodide crystals, respectively. Figure 3 shows a series of gamma spectra obtained with the channel set to select beta particles at 1410, 1170, 930, and 690 kev. The channel width was 240 kev. The spectra are all of the same shape. This fact shows that the two gamma rays at 750 and 1000 kev are in coincidence with the same beta-ray group.

Next, some gamma-beta coincidence measurements were performed. With the channel set on the 1000-kev peak, a spectrum was obtained which is shown in Fig. 4 as a Fermi plot. The end point is around 1350 kev. Adding the gamma-ray energy one gets a disintegration energy of 2350 kev, which is approximately the same as the end point of the high-energy beta group.

An attempt was also made to select the gamma rays at 1800 kev and record the corresponding coincidence beta spectrum. The result was rather qualitative due to the low counting rate. It shows, however, that these

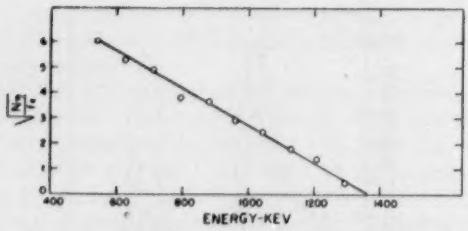

FIG. 4. Fermi plot of the beta radiation in coincidence with the 1000-kev gamma ray.

high-energy gamma rays are in coincidence with beta rays of about 600-kev maximum energy.

Finally, the coincidence spectrometer was used to make some gamma-gamma coincidence measurements. The source was mounted between two sodium iodide spectrometers. A lead shield was placed between the two crystals in order to prevent back-scattered radiation from one crystal from reaching the other crystal. Figure 5 shows the coincidence spectrum obtained with the channel of the analyzer set on the 250-kev peak. Apparently the 750-kev gamma ray is in coincidence with the 250-kev ray. There is also a weak peak at 900 kev, indicating that the gamma ray of this energy, which belongs to UZ, also is in coincidence with the 250-kev gamma ray.

From these coincidence measurements one can conclude that the 1000-kev gamma ray is a cross-over transition to a cascade of the 750- and 250-kev gamma rays. The gamma rays are in coincidence with a beta-ray group having an end point at about 1350 kev.

UZ

An isomeric state of Pa^{234} with a half-life of 6.7 hours is UZ. The decay has been investigated by Feather, Bretscher, and Dunworth[11,12] using absorption and coincidence technique. They found a complex beta spectrum with the end point at 1200 kev. The gamma radiation, with a mean energy of about 700 kev, showed

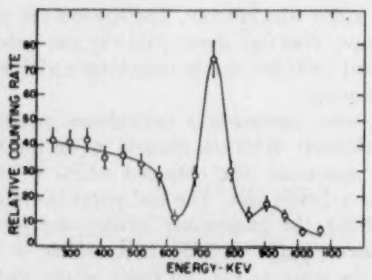

FIG. 5. Spectrum of the gamma radiation in coincidence with the 250-kev gamma ray.

[11] N. Feather and E. Bretscher, Proc. Roy. Soc. (London) **A165**, 530 (1938).

[12] N. Feather and J. V. Dunworth, Proc. Roy. Soc. (London) **A168**, 566 (1939).

a high coincidence rate. Bradt and Sherrer[13] made further experiments using the same technique. In addition they investigated the beta radiation using a 180° magnetic spectrometer. They were able to resolve the spectrum into two groups. For the low-energy group they report an end point at 450±30 kev. The analysis of the spectrum is rather unreliable, however, because of the low counting rate.

Figure 6(a) shows the gamma-ray spectrum of UZ. It has been resolved into two components belonging to gamma rays at 760 and 910 kev. They are shown with dotted lines in the figure. The intensity ratio of the two rays is 0.8. The UZ source was very weak. Therefore, it was difficult to get a reliable pulse distribution at lower energies because of the background of the crystal.

The coincidence relations between the gamma rays were investigated using the coincidence spectrometer. The channel was set on the 910-kev peak and the

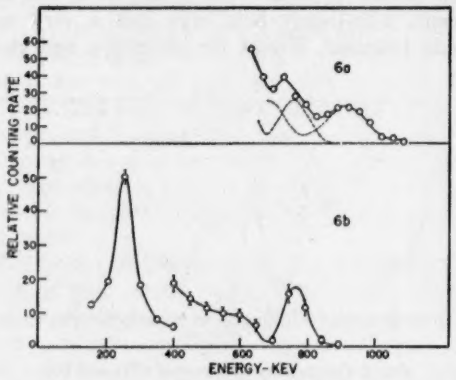

FIG. 6. (a) Gamma-ray spectrum of UZ. (b) Spectrum of the gamma radiation in coincidence with the 910-kev gamma ray.

corresponding coincidence gamma spectrum was recorded. It is shown in Fig. 6(b). The 760-kev gamma ray shows up much better in this coincidence spectrum because there is no interference from the 910-kev ray. The spectrum also contains a 250-kev gamma ray, which was completely hidden in the background of the spectrum shown in Fig. 6(a). The intensity is roughly the same as that of the 760-kev gamma ray.

Hence UZ decays by emission of three gamma rays in cascade. It is interesting to compare the present results with the absorption and coincidence measurements of Feather *et al.*[11,12] They found the mean energy of the gamma rays to be 700 kev. This value is definitely lower than the mean energy of the two gamma rays at 760 and 910 kev. It shows that there must be some low-energy gamma ray present. The coincidence measurements gave a coincidence rate which was higher than could be expected from a decay with only

[13] H. Bradt and P. Sherrer, Helv. Phys. Acta **18**, 405 (1945).

two gamma rays in coincidence. This, too, can be explained by the presence of a third gamma ray in coincidence with the other two.

DECAY SCHEME

The results obtained in the present work make it possible to set up a consistent decay scheme, which is shown in Fig. 7.

The gamma ray at 1810 kev is assumed to belong to UX_2 because the spectrum of UZ does not contain a high-energy gamma ray of this intensity. It is in coincidence with a 600-kev beta group and must therefore go directly to the ground state. The 1680-kev gamma ray is assumed to be a cross-over transition in UZ. Its energy is close to the sum of 760 and 910 kev. Furthermore, the spectrum of UZ contains some high-energy gamma radiation although it is too weak to permit accurate energy measurements. If there is any high-energy gamma radiation present in UZ one would actually expect it to go to the 250-kev level, from spin considerations.

The uncertain point in this decay scheme is the position of the UZ level with respect to the UX_2 level. It depends on the accuracy of the energy values of the UZ beta radiation. Adopting the value[11] 1200 kev for the end point of the high-energy group, one obtains a disintegration energy of 2360 kev for UZ. The low-energy beta group will then have an energy of 440 kev, which is in good agreement with the value reported by Bradt and Sherrer.[13] This places the UZ level above the UX_2 ground state with an energy difference of 40 kev. The uncertainty in this value is considerable, and the UZ level might quite well be the ground state of Pa^{234}. The two levels must be fairly close together, however.

It is known from the decay of Pu^{238} [14] that there is a level in U^{234} at 45 kev. It is therefore possible that the gamma rays at 250, 1000, and 1810 kev do not go to the ground state but to this excited state. In this case there would be a gamma ray at 45 kev almost completely converted. It should show up as a conversion line in the beta spectrum of Stoker *et al.*[7] There is, however, no line corresponding to a gamma ray at about 45 kev with the intensity required in this case. It therefore seems probable that the gamma rays at 250, 1000, and 1810 kev go directly to the ground state.

As mentioned above, the UX_2 beta spectrum is characterized by the presence of some strong internal conversion lines arising from a gamma transition at 810 kev. No trace of a gamma ray of this energy can be found in the gamma spectrum of Fig. 2. Hence the gamma ray must be completely converted. The only way to account for this is to assume a 0–0 transition going from an excited state at 810 kev to the ground state of U^{234}.

[14] Hollander, Perlman, and Seaborg, Revs. Modern Phys. **25**, 469 (1953).

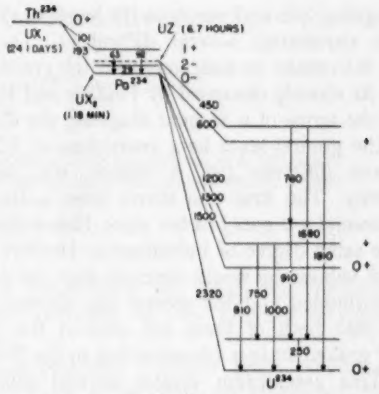

FIG. 7. Proposed decay scheme for Th^{234} and Pa^{234}.

The intensities of the various gamma rays were measured in the following way. By using an anthracene spectrometer and a thin source in a known geometry, the number of beta particles from UX_2 was measured. The number of gamma-quanta from the same source was measured by a sodium iodide spectrometer. The intensities were calculated from these measured values, the shape of the spectrum, the crystal size and shape, and the absorption coefficients of sodium iodide. Secondary absorption processes in the crystal were taken into account. The intensities of the internal conversion lines[7] were added in order to get the total intensities. The intensity values of the gamma-ray peaks and the conversion lines have been used to calculate approximate values on the *L*-conversion coefficients of the UX_1 gamma rays. Table I gives the energy values, the intensities in percent of the total number of disintegrations, and the *L*-conversion coefficients for the UX_1 gamma rays.

The branching ratios of the various beta groups have been obtained from the gamma intensities. The corresponding log *ft* values have been calculated using the graphs and nomograms of Moszkowski.[15] The branching ratios and log *ft* values are tabulated in Table II.

TABLE I. Gamma-ray intensities and *L*-conversion coefficients.

Decay	Energy kev	Intensity in percent of total disintegrations	*L*-conversion coefficient
UX_1	29	6.5	10
UX_1	63	6.5	0.25
UX_1	92	14.8	2.5
UX_2, UZ	250	0.19	
UX_2	750	0.12	
UZ	760	0.06	
UZ	910	0.07	
UX_2	1000	0.37	
UZ	1680	0.02	
UX_2	1810	0.04	

[15] S. A. Moszkowski, Phys. Rev. **82**, 35 (1950).

In assigning spin and parity to the levels of Pa^{234} and U^{234} one encounters several difficulties. The main problem is to make an assignment for the ground state of Pa^{234}. As already discussed by Feather and Richardson[16] in the terms of a Sargent diagram, the difficulty is that the ground state beta transitions of UX_1 and UX_2 have different log *ft* values, 6.4 and 5.5, respectively. The first one starts from a 0+ state and the second one goes to a 0+ state. Hence they must have the same degree of forbiddeness. However, from the log *ft* values one would conclude that the first one is first forbidden and the second one allowed. If we assume that both of them are allowed the spin of the Pa^{234} ground state is 1+ according to the Nordheim rule.[17] This assumption creates several difficulties, however. The 1500-kev transition to the 0+ state of U^{234} must then also be allowed but its log *ft* value is 7.1. The first excited state of an even-even nucleus is known to be a 2+ state almost without exception. A transition to a 2+ state must be allowed if the spin of the Pa^{234} ground state is 1+. There is however no transition with an allowed log *ft* value except the ground state transition.

Therefore it seems more natural to assume that the ground state of Pa^{234} has the spin 0− and to regard the 2320-kev beta group as an unusual fast first forbidden transition. The 1300- and 600-kev beta transitions have log *ft* values which characterize them as first forbidden. We therefore assume even parity for these levels.

TABLE II. Branching ratios and log *ft* values for the beta groups.

Decay	Energy	Branching ratio %	Log *ft*
UX_1	101	28	5.9
UX_1	193	72	6.4
UX_2	600	0.04	6.8
UX_2	1300	0.49	7.0
UX_2	1500	0.63	7.1
UX_2	2320	98.8	5.5
UZ	450	90	5.6
UZ	1200	10	8.1

The 193-kev beta transition is according to its log *ft* value first forbidden, $\Delta I=0$, in agreement with the spin assignment 0− for the Pa^{234} ground state. The 103-kev beta transition is probably allowed and the spin of the 92 kev level 1+. The 29-kev level is assumed to have spin 2−. The corresponding beta transition is then first forbidden, $\Delta I=2$, and must be very weak compared to the other two transitions. This assignment makes the 63-kev gamma ray an electric dipole and the 29-kev gamma ray an electric quadrupole transition, giving good agreement between the theoretical[18] and experimental values of the internal conversion coefficients. However, the 92-kev gamma ray is an electric dipole transition according to the spin assignments but an electric quadrupole transition according to its conversion coefficient. There seems to be no way of removing this discrepancy without creating new ones.

Very little can be said about the spin of the UZ level of Pa^{234} without knowing its exact position. A value of 3 or 4 seems rather likely.

The spin values proposed here are only tentative. The main difficulty is, as pointed out above, to make an assignment for the ground state of Pa^{234}. No spin value seems to give complete agreement with the experimental results. This state might be an example of the mixed configurations recently discussed by de-Shalit and Goldhaber.[19]

ACKNOWLEDGMENTS

The author is greatly indebted to Dr. D. J. Zaffarano for his interest and assistance in this work. The technical assistance of Mr. G. Eakins and Mr. J. Powers is gratefully acknowledged.

[16] N. Feather and H. O. W. Richardson, Proc. Phys. Soc. (London) **61**, 452 (1948).
[17] L. W. Nordheim, Revs. Modern Phys. **23**, 3321 (1951).
[18] Gellman, Griffith, and Stanley, Phys. Rev. **50**, 866 (1950).
[19] A. de-Shalit and M. Goldhaber, Phys. Rev. **92**, 1211 (1953).

Polarization of Protons by Scattering from Beryllium*

H. G. DE CARVALHO,† J. MARSHALL, AND L. MARSHALL
Institute for Nuclear Studies, The University of Chicago, Chicago, Illinois

(Received June 16, 1954)

The polarization of high-energy protons scattered from beryllium has been investigated as a function of energy and angle of the scattered protons. It was found that the elastically scattered protons are much more strongly polarized than the quasi-free nucleon-scattered protons.

INTRODUCTION

THE possibility of spin polarization of high-energy nucleons was adumbrated in 1951 by an experiment of Wouters[1] who looked for such an effect to occur in n-p interactions. A couple of years later, large polarizations of high-energy proton beams were discovered by Oxley and co-workers[2] in the scattering of 220-Mev protons. In their experiments the fractional polarization of protons first scattered from a given element was estimated from the measured asymmetry of second scattering from an effective hydrogen target. Using first and second scattering angles of about 20° and 25° respectively, they measured polarizations of 20 percent for H, 45 percent for D, about 45 percent for Li, Be, B, and Cu, and about 25 percent for Al, Si, and Ag. The energy and angle of first scattering were such that for all these elements it was believed that the scattered protons were produced mainly by nucleon-nucleon scattering in the nucleus (hereafter called "quasi-free nucleon scattering") and to a negligible extent by diffraction scattering. Preliminary reports of the large polarizations found by Oxley *et al.* led us to look for a similar effect at 340 and 430 Mev. We made double-scattering experiments[3] with beryllium, both scatterings being made at about 30°. This investigation required energies and angles for scattered protons consistent with quasi-free nucleon scattering and showed zero asymmetry of double scattering within about four percent statistical error. Since the polarization varies as the square root of one-half the asymmetry, it follows that around 30° the polarization in beryllium due to quasi-free nucleon scattering is not larger than $(0.02)^{\frac{1}{2}}=15$ percent at these energies.

An important discovery in the field of high-energy proton polarization was made at Berkeley, and was reported at the October 1953 Physical Society meeting by Professor Emilio Segrè. He described preliminary results of his group indicating production of a high-energy polarized proton beam by small angle scattering from carbon. Following this event, the polarization of hydrogen for protons was measured,[4–6] with the aid of beams polarized by the method of small angle scattering.

Using a polarized 310-Mev beam, we investigated the polarization of beryllium by measuring the asymmetry of second scattering from an external beryllium target as a function of angle and energy. At each angle investigated, the marked increase in asymmetry with increasing energy of the scattered protons led to the conclusion[5] that the elastic scattering from the beryllium nucleus was the main polarized component and showed large polarization (up to 80 percent). Polarization by quasi-free nucleon scattering was apparently much less important, but no reliable decision could be made on the basis of those data[5] as to whether or not it was polarized at small angles.

Recently, measurements similar to those on beryllium have provided evidence that also for elements other than beryllium and over a range of energies, polarization by elastic scattering is much larger than polarization by quasi-free nucleon scattering. Evidence for large polarizations by elastic scattering of 133-Mev protons from carbon and uranium has been reported by Dickson and Salter.[6] A similar measurement on carbon for 310-Mev protons indicating strong polarization by elastic scattering has been made by Segrè and co-workers.[7]

An explanation of proton polarization by elastic scattering has been proposed[8] in terms of a spin-orbit interaction of proton and nucleus of the same magnitude as that assumed for the nuclear shell model. According to this explanation, one effect of the spin-orbit interaction is to cause the elastic scattering pattern to be shifted to somewhat smaller angles when the orbital angular momentum vector L is parallel to the proton spin and to somewhat larger angles when L is anti-

* Research supported by a joint program of the U. S. Office of Naval Research and the U. S. Atomic Energy Commission.

† Now at the Conselho Nacional de Pesquisas, Rio de Janeiro, Brazil.

[1] L. F. Wouters, Phys. Rev. **84**, 1069 (1951).

[2] Oxley, Cartwright, and Rouvina, Phys. Rev. **93**, 806 (1954).

[3] Marshall, Nedzel, and Marshall, Phys. Rev. **93**, 927 (1953).

[4] Chamberlain, Segrè, Tripp, Wiegand, and Ypsilantis, Phys. Rev. **93**, 1430 (1954).

[5] Marshall, Marshall, and De Carvalho, Phys. Rev. **93**, 1431 (1953); De Carvalho, Heiberg, Marshall, and Marshall, Phys. Rev. **94**, 1796 (1954).

[6] J. M. Dickson and D. C. Salter, Nature (to be published).

[7] Chamberlain, Segrè, Tripp, Wiegand, and Ypsilantis, reported by Clyde Wiegand, invited paper at the Washington Meeting of the American Physical Society, May 1954 [Phys. Rev. **95**, 644 (1954)].

[8] E. Fermi, Nuovo cimento, April 1954, exact calculation privately communicated; W. Heckrotte and J. V. Lepore, Phys. Rev. **95**, 1109 (1954); B. J. Malenka, Phys. Rev. **95**, 522 (1954); Snow, Sternheimer, and Yang, Phys.Rev. **94**, 1073 (1954).

parallel. At angles near the elastic diffraction minima, these shifts in the elastic scattering pattern move the diffraction minima for the two cases apart in such a way that the polarization changes violently from positive to negative to positive with increasing scattering angle in the region of a diffraction minimum.

At least this is true if one assumes a potential well with a sharp edge. For an actual nucleus, one supposes that the edge is not well defined, and consequently, that the polarization will show dips instead of changes in sign near the diffraction minima. In agreement with the predictions of the spin-orbit coupling hypothesis, a strongly marked dip has been reported in the polarization by elastic scattering of 310-Mev polarized protons from aluminum.[7]

In the case of the lightest nuclei, the concept of a sharp-edged potential well is even less realistic and one might expect the dips in the polarization curve to be less evident. In the case of carbon[7] and beryllium[9] for elastic scattering of 310-Mev protons, the dips have been looked for and are not as yet in evidence.

As for quasi-free nucleon scattering, investigations made on carbon show that both p-p and p-n non-exchange collisions[10] at 310 Mev produce about 25 percent maximum polarization. The p-n exchange collision produces about 25 percent maximum polarization at 310 Mev[10] and about 20 percent maximum polarization at 120 Mev.[11] These data give additional confirmation to the conclusion that polarization by quasi-free nucleon scattering is in fact small compared with polarization by elastic scattering.

In part, the present paper is a more complete report on the earlier work at 310 Mev,[5] containing as well more data which have accumulated in the meantime. Furthermore, it is a report of a similar set of measurements on polarization by elastic scattering of 435-Mev protons polarized from beryllium.

EXPERIMENTAL

Two mechanisms are known by which fast protons scattered from nuclei can be polarized, namely by scattering of the incoming proton from the whole nucleus, a phenomenon in which all the component nucleons cooperate, and secondly by quasi-free nucleon collision, an event which to some extent resembles a free nucleon-nucleon collision. A complicating feature of the second mechanism is that the target nucleons have a momentum distribution characteristic of the nucleus which contains them.

The cooperative scattering apparently is complicated[12] in that the nucleus can be left in any of several excited states differing very little in energy. Groups of protons scattered in such a way as to leave the nucleus in different excited states have small energy differences compared with their kinetic energy of 300 or 400 Mev. Consequently, the cooperative scattering has a fine structure beyond the sensitivity of the measurements to be described here. In the present paper we call the entire cooperative phenomenon "elastic" for want of a detailed understanding of the process. The work to be reported here mainly gives information on polarization by the so-called elastic scattering.

An unpolarized beam, such as the circulating beam of the cyclotron, is one for which the expectation value of the spin in any direction is zero. Such a beam may be polarized by undergoing a spin dependent scattering. In this event there is no asymmetry of total number of scattered protons but there is an asymmetry of number of scattered protons of given spin direction, that is, for a given direction of scattering the scattered protons have a net polarization. The polarization at a given angle, $P(\theta)$, is defined as the difference between the fraction of the protons scattered with spin up and the fraction with spin down.

In general, if a polarized beam undergoes a spin-dependent scattering the probabilities for protons to be scattered on opposite sides of the beam will be different. For a scattering in the horizontal plane, the asymmetry, A, is defined as twice the difference between the numbers scattered to the right and to the left, divided by their sum. It is well known that the asymmetry resulting after the second scattering is maximal in the plane defined by the first scattering. There is no resultant asymmetry in a plane normal to the plane of the first scattering, and this fact is used to test that the detecting apparatus is properly aligned.

If the first and second scattering are equivalent, the asymmetry after the second scattering may be used to evaluate the polarization due to the first scattering of a previously unpolarized beam. The relationship is $P=(\frac{1}{2}\,\text{asym})^{\frac{1}{2}}$. If a first scattering produces the polarization $P_1(\theta)$ and a second scattering would produce

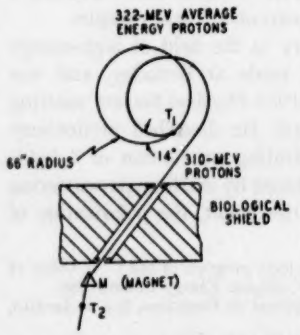

FIG. 1. Plan view of 450-Mev synchrocyclotron showing trajectory of proton beam.

[9] De Carvalho, Heiberg, Marshall, and Marshall, reported by J. Marshall, invited paper at the Washington Meeting of the American Physical Society, May 1954, [Phys. Rev. 95, 644 (1954)].

[10] H. Bradner and R. Donaldson, Phys. Rev. 95, 1701 (1954).

[11] A. Roberts and J. Tinlot, reported by John Tinlot, invited paper, Washington meeting of the American Physical Society, May 1954 [Phys. Rev. 95, 644 (1954)].

[12] Karl Strauch, Rochester Conference on High Energy Physics, January, 1954 (University of Rochester, Rochester, 1954).

$P_2(\theta)$ in an unpolarized beam, the effect of the two in succession is to produce an asymmetry given by asym$=2P_1(\theta_1)P_2(\theta)_2$.

The plane of the first scattering was the plane of the rotating (unpolarized) cyclotron beam. Only protons scattered to the right at a well defined angle and energy could reach the experimental area, owing to the combined selective action of the collimating system (Fig. 1) and analytical action on the long proton trajectory by the magnetic field of the cyclotron and its fringing field. For the first scattering, the angle and energy loss corresponded to an elastic scattering.

For the lower energy experiments, an internal beryllium target (specified as T_1 in Fig. 1) was placed at 66 inches radius corresponding to 322-Mev average energy protons in the cyclotron. For the higher energy experiments, the internal beryllium target was placed at 76 inches corresponding to 440-Mev average energy protons. A beam of protons scattered from the beryllium target T_1 at angle θ_1 to the right was analyzed in the fringing field of the cyclotron and emerged through the shield into the experimental area.

After the collimated beam was further analyzed by a magnet M in the experimental area, it was incident on the second beryllium scatterer. The asymmetry of second scattering was measured with counters mounted on a framework which held them and swung them symmetrically about the beam as an axis. The description and method of alignment of this framework has been extensively discussed in a previous paper,[13] as has also the method of location of the deflected beam. Also included is a description of the method of adjustment of the scintillation counters in multiple coincidence. We omit further details here.

The spectrum of protons scattered from beryllium at a small angle θ may be roughly described as shown in Fig. 2. The elastically scattered protons are represented as a line, of slightly less than the incident energy E_1, whose width is determined by straggling in the

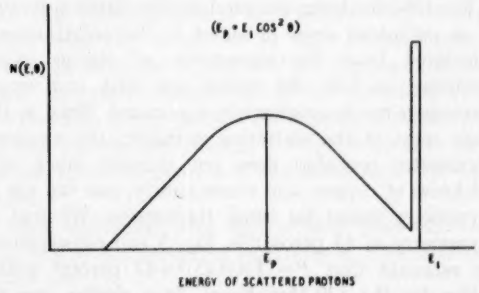

FIG. 2. Schematic diagram showing energy spectrum of protons scattered at angle θ when incident proton beam of energy E_1 strikes a nucleus. The line spectrum represents elastically scattered protons. The continuous spectrum at lower energies represents quasi-free nucleon scattered protons.

[13] Marshall, Marshall, Nagle, and Skolnik, Phys. Rev. **95**, 1020 (1954).

FIG. 3. Absorption curve (see reference 5) for doubly scattered protons (337-Mev protons scattered at 14°R from Be emerge with 331-Mev energy and are scattered a second time at $\theta_2=23°$ from 2-in. thick Be), showing counting rate left and right *versus* thickness of copper absorber. The elastic scattering cross section is not well measured by these data because the scattered protons are enormously attenuated in a complicated way by the copper absorber. However, since the attenuation is the same to left and right owing to the fact that counters and absorbers are rotated about the beam, the asymmetry of scattering is measured in a precise way.

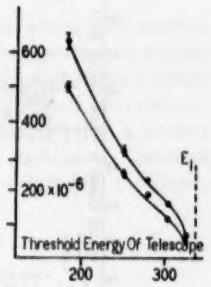

scatterer. The quasi-free nucleon scattering is a broad band whose center of gravity is the energy of a free p-p scattering, $E_p=E_0\cos^2\theta$, whose shape is determined by the momentum distribution of the target nucleons in the nucleus.[14] At the highest energies, the quasi-free nucleon scattering becomes indistinguishable from elastic scattering. As the scattering angle decreases, the center of gravity of the quasi-free nucleon scattering, E_p, approaches the elastic scattering energy, so that more protons are scattered with energies in the elastic region. The situation would become quite ambiguous except for the fact that as the scattering angle decreases, elastic scattering becomes the major phenomenon, i.e., the area of the elastically scattered "line" becomes large compared with the area of the broad band. So for example at 310 Mev and at 10°, it is estimated that about 70 percent of the protons scattered from beryllium are elastically scattered.

To examine the asymmetry of the elastically scattered protons, as compared with the asymmetry of all scattered protons, varying thicknesses of copper are placed in front of the counters which detect scattered protons. When the copper absorber is very thin, almost all protons scattered by the two mechanisms are counted. As the absorber is made thicker, more and more of the quasi-free nucleon-scattered protons fail to reach the counters, so that one measures protons of which an increasingly larger fraction is elastically scattered. For the greatest thicknesses of absorber, the protons detected are almost entirely elastically scattered. At small enough angles, the elastic scattering dominates, and even for small amounts of absorber, or no absorber at all, the measured asymmetry is due mostly to elastically scattered protons. Figure 3 shows the behavior of the counting rates to the right and the left as the thickness of copper absorber is increased.

The dependence of asymmetry on scattering from Be as found by this procedure is shown for 310-Mev protons in Fig. 4 and for 430-Mev protons in Fig. 5. At all angles for which sufficient measurements were made, the asymmetry appears to rise to high values

[14] Cladis, Hess, and Moyer, Phys. Rev. **87**, 425 (1952).

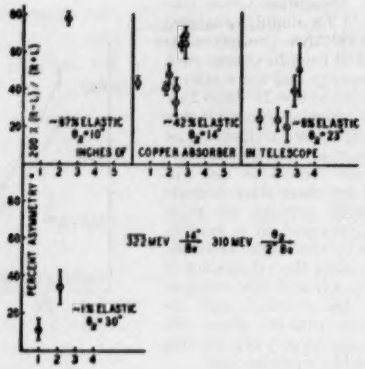

FIG. 4. Asymmetries measured for second scattering of protons from beryllium, as a function of thickness of copper in the detecting telescope, and as a function of laboratory angle, for 310-Mev, 55 percent polarized protons.

with increasing thickness of copper, from which the conclusion is drawn that the elastic scattering component is strongly polarized, and in fact, considerably more polarized than the nucleon-scattered protons.

The asymmetry as measured for small thicknesses of copper is large at small angles and small at large angles, varying roughly as the fraction of elastically scattered protons. This observation also supports the conclusion that the elastic scattering is considerably more strongly polarized than the quasi-free nucleon scattering.

The fraction of elastic scattering has been estimated using the elastic cross sections of beryllium measured by Richardson *et al.*[18] together with the differential cross sections for total scattering from beryllium as measured in the present experiment. The latter were measured directly by the triple or quadruple coincidence rate (two counters in incident beam plus one or two counters in scattered flux) divided by double coincidence rate (two counters in incident beam). The cross sections so measured were of 3 percent or 4 percent statistical accuracy but had a somewhat poorer over-all accuracy owing to the necessity to correct for loss of protons by nuclear scattering in the beryllium and copper. These estimated corrections ranged from 8 percent to 35 percent. Estimates of the percentage of elastic scattering so obtained are given in Fig. 4.

The polarization was estimated from the relationship $2P_1(\theta_1)P_2(\theta)=\text{asym}$. For example, the polarization of the 310-Mev proton beam may be calculated from the largest asymmetry observed for the case of $\theta_2=14°$. In this case, both first and second scatterings are elastic and at the same angle so that, except for a small difference in energy between the first and second scattering, $P_1(\theta_1)=P_2(\theta_2)$. One finds about 65 percent asymmetry in Fig. 4 from which $P=(\frac{1}{2}\times 0.65)^{\frac{1}{2}}=55$ percent polarization for the 310-Mev beam.

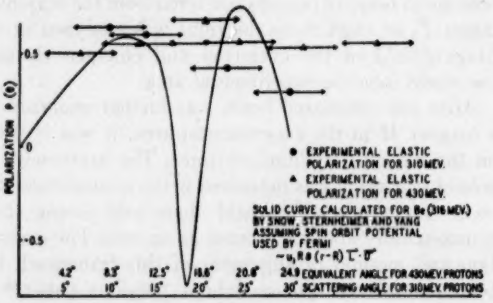
POLARIZATION P(θ)
EXPERIMENTAL ELASTIC POLARIZATION FOR 310 MEV.
EXPERIMENTAL ELASTIC POLARIZATION FOR 430 MEV.
SOLID CURVE CALCULATED FOR 0e (310 MEV.) BY SNOW, STERNHEIMER AND YANG ASSUMING SPIN ORBIT POTENTIAL USED BY FERMI
24.9 EQUIVALENT ANGLE FOR 430 MEV. PROTONS
30° SCATTERING ANGLE FOR 310 MEV. PROTONS

FIG. 6. Polarization of 310- and 430-Mev protons by elastic scattering from beryllium shown plotted *versus* laboratory angle, and compared with theoretical predictions of the spin-orbit coupling hypothesis. To facilitate comparison of the 430-Mev data with the 310-Mev data, the 430-Mev data are plotted at angles increased by the ratio of the De Broglie wavelengths (i.e., $\theta_{340\ \text{Mev}}\times\lambda_{340\ \text{Mev}}/\lambda_{430\ \text{Mev}}$) for the reason that the elastic diffraction pattern shrinks proportionally as the wavelength decreases.

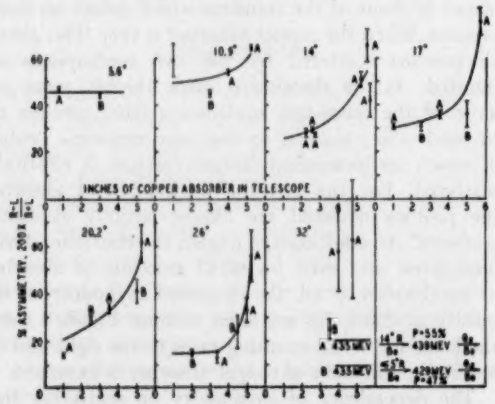

FIG. 5. Asymmetries measured for second scattering of protons from beryllium, as a function of thickness of copper in the detecting telescope, and as a function of laboratory angle, for 429-Mev, 47 percent polarized protons and for 439-Mev, 55 percent polarized protons.

The 429-Mev beam was produced by elastic scattering at an estimated angle of about 5°. Its polarization is calculated from the asymmetry of elastic second scattering at 5.6°, for which case first and second scatterings are approximately equivalent. Since at this angle most of the scattering is elastic, the measured asymmetry probably does not increase much with thickness of copper, and consequently, one can use an asymmetry found for small thicknesses. We find an asymmetry of 45 percent in Fig. 5 and consequently, we estimate that $P=(\frac{1}{2}\times 0.45)^{\frac{1}{2}}=47$ percent polarization for the 429-Mev beam. In a similar way the polarization of the 439-Mev beam is found to be 55 percent from the data at 14° second scattering angle.

With the known beam polarizations and the maximum measured asymmetries at each angle, one readily evaluates the polarization of the elastically scattered component as a function of angle. These are shown

[18] Richardson, Ball, Leith, and Moyer, Phys. Rev. 86, 29 (1952).

plotted in Fig. 6. The polarizations for the higher-energy beams are plotted there, also, and in fact are plotted at an angle increased by the ratio of the De Broglie wavelengths for 310 and for 430 Mev, accordingly as the elastic diffraction pattern shrinks with increasing energy. For comparison with the predictions of the spin-orbit coupling hypothesis,[8] the polarization of beryllium calculated for the lower energy is plotted. Although it would be preferable to recalculate this curve for the higher energy, yet one expects that probably it will be very much the same in its major features.

One sees that large dips in the elastic polarization curve are not in evidence. Higher proton intensities and, correspondingly, measurements with better angular resolution are needed to prove or disprove the existence of small dips. The present data suggest that a nuclear potential with smooth features such as a Gaussian would give a somewhat better description of the elastic polarization in light nuclei.

PHYSICAL REVIEW VOLUME 96, NUMBER 4 NOVEMBER 15, 1954

Changes in Amplitude of the Cosmic-Ray 27-Day Intensity Variation with Solar Activity*

PETER MEYER AND J. A. SIMPSON
Institute for Nuclear Studies, University of Chicago, Chicago, Illinois
(Received July 29, 1954)

Both cosmic-ray neutron and ionization-chamber intensity observations reveal that the amplitude of the 27-day recurring intensity variation has been changing over an interval of several years. A method for studying this phenomenon using ionization chamber data for the period 1936–1946 and neutron intensity data for 1951–1953 is described which not only selects preferentially the 27-day variations but also selects the variations which are world wide.

The amplitude of the 27-day intensity variation over these years displays minima and a maximum closely related in time to the minima and maxima of the approximately 11-year cycle in general solar activity. Thus, these results provide additional, and independent, evidence that solar active regions are responsible for producing the mechanism which controls the 27-day cosmic-ray primary intensity variations.

I.

IN continuing the study of the 27-day recurring intensity variations[1,2] we have observed that the amplitude of this variation displays a remarkable decrease over the years 1951 to 1954. A network of widely distributed neutron intensity monitors was completed in 1951 to detect this world-wide variation in the low-energy portion of the primary cosmic radiation spectrum. It was clear from the measurements in 1951 that the amplitude of the variation was 4–5 times larger than the amplitude at high primary particle energy as measured by shielded ion chambers. In later years the relative amplitudes of the variations in the low and high energy parts of the primary spectrum have become increasingly difficult to measure because of the decline in the amplitude of the variations over these years.

Since individual solar regions have been associated with the 27-day recurring variations in 1951, and since the synodic rotation period for equatorial regions of the sun is ~27 days, we have searched for an association between the decline of amplitude in the intensity variations and the changing level of solar activity over the ~11-year solar "cycle." In this paper we propose to investigate this change of amplitude and demonstrate that a close association exists between this phenomenon and the general level of solar activity.

II.

The decline in amplitude of the mean daily 27-day neutron intensity is most readily demonstrated by using a method devised by Chree[3] for the analysis of recurrences of geomagnetic character figures. The method requires adding together the intensity of all days that display a maximum (or minimum) intensity. These days are called day zero. The summation is carried over the preceding and following days out to day n, where n extends beyond the period of the variation being investigated. This superposition of data will display any recurrence tendency among the maxima of mean daily intensities and give the average period of the recurrence. The Chree-type curves shown in Fig. 1 have been obtained for 10 neutron intensity maxima from eight months of data in 1951, 22 neutron maxima in

* Assisted by the Office of Scientific Research, Air Research and Development Command, U. S. Air Force.

[1] For example, A. T. Monk and A. H. Compton, Revs. Modern Phys. 11, 173 (1939). A complete list of publications through 1951 is found in the review article by H. Elliot, *Progress in Cosmic Ray Physics* (North-Holland Publishing Company, Amsterdam, 1952), Chapt. VIII.

[2] J. A. Simpson, Phys. Rev. 94, 426 (1954) and references therein.

[3] C. Chree, Trans. Roy. Soc. (London) A212, 75 (1913).

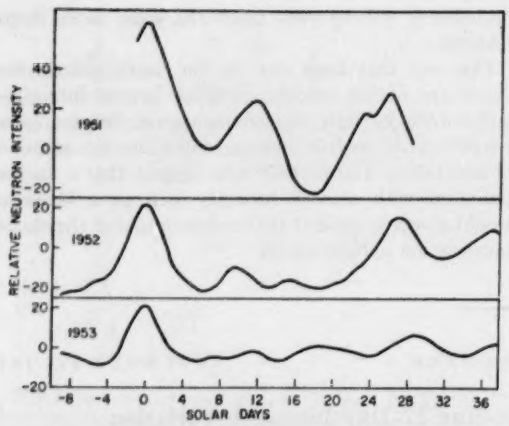

FIG. 1. Superposition of neutron intensity maxima for data obtained using a neutron monitor at Climax, Colorado. These curves represent the 3-day running average of the mean daily intensity and show the decline of amplitude for 27-day recurrence in successive years.

1952, and 28 maxima in 1953. The approximately 27-day recurrence is quite apparent in all of these curves. The amplitudes of the recurring maxima, however, are decreasing with each successive year.

In order to explore this phenomenon over an entire solar cycle prior to 1951 it is necessary to study the ionization chamber measurements which have been obtained and published by Lange and Forbush[4] over the years 1936 to 1946 at three independent stations. To these results we shall add the neutron data for the period 1951 through 1953. Since it has already been shown that 27-day intensity variations observed in ion chambers are closely related in time and relative amplitude to the same type of variations detected by low-energy neutron detectors, we shall use both kinds of detectors in our analysis.

We first explain the method adopted to measure the amplitude of the 27-day recurring variation in different years. There are two conditions which must be fulfilled:

(1) The method must select preferentially those variations of intensity which have a "quasi periodicity" of 27 days.

(2) Only world-wide intensity variations should be measured. Hence, we are to consider only the variations which appear simultaneously at widely separated observing positions.

In order to satisfy the first condition, we study the differences of increments in average daily intensity at Station A for *pairs* of days separated by τ days from each other:

$$\delta_A = [I_A(t) - I_A(t+\tau)]/\langle I_A \rangle,$$

where $I_A(t)$ is the cosmic-ray intensity at day t and $\langle I_A \rangle$ is the average intensity; hence, $\sigma_A = \langle \delta^2 \rangle^{\frac{1}{2}}$ is the standard deviation of a set of δ's. Fonger[5] has shown for the neutron and ion chamber data of 1951 that σ_A has a maximum value for $\tau = 14$ days, which is a consequence of the existence of 27–28 day recurring intensity variations. We shall use our definition of σ_A as a quantitative measure of the 27-day amplitude at station A. To preferentially select the 27-day variations we also choose $\tau = 14$ days.

The second condition is fulfilled by applying the above procedure to a second station detector, called station B, widely separated from station A; thus, we determine σ_B. We then obtain the correlation coefficient between the δ's for the two stations A and B; namely,

$$r_{AB} = \langle \delta_A \times \delta_B \rangle / (\sigma_A \times \sigma_B),$$

where r_{AB} has an absolute value between zero and unity depending on how perfectly the increments δ from the two stations agree in time and relative amplitude, i.e., how well the station data track each other. Finally, the parameter which we define as the measure of the amplitude of the world-wide 27-day intensity variation is

$$\sigma_A(\text{tracking}) = |r_{AB}| \times \sigma_A,$$

which is the standard deviation of that portion of the increments of intensity, δ, which tracks perfectly. We call station B the reference station.[5]

For variations of neutron intensity the data were analyzed for the period 1951 through 1953 by using the Climax neutron detector as station A and the Chicago neutron detector as station B, or reference station. Half-year intervals were used with the numerical results given in Table I. The Forbush ion chamber data for the period 1936–1946 at Huancayo (Peru), Cheltenham, Maryland (U.S.A.), and Christchurch (New Zeland) were divided into 6-month intervals for computing σ(tracking). We arbitrarily selected Huancayo as station A and used successively Cheltenham and Christchurch as two independent reference stations for computing the correlation coefficients with the numerical results shown in Table II. In Fig. 2, σ(tracking) is plotted as a function of time between 1936 and 1953. The ordinate

TABLE I. Analysis of neutron pile intensity data.

Period	σ Climax %	σ Chicago %	r correlation coefficient Climax-Chicago	σ(tracking) Climax correlated to Chicago %
1951 July–Dec.	3.3	3.9	0.60	2.0
1952 Jan.–June	2.3	1.8	0.58	1.3
1952 July–Dec.	1.2	0.9	0.54	0.7
1953 Jan.–June	1.5	1.2	0.68	1.1
1953 July–Dec.	0.9	0.8	0.05	0.0

[4] I. Lange and S. E. Forbush, "Cosmic ray results from Huancayo Observatory, Peru, June 1936–December 1946", Researches of the Department of Terrestrial Magnetism, Washington, D. C. (1948), Vol. 14, Pub. 175.

[5] W. H. Fonger, Phys. Rev. **91**, 351 (1953); see this reference for a more detailed description of the procedure for determining σ(tracking).

on the left refers to Huancayo values of σ(tracking) with respect to both Cheltenham and Christchurch. The scale on the right refers to the larger values of σ(tracking) for the Climax neutron detector with reference to the Chicago neutron detector. No continuous data were available for the period 1947 through 1950 for either ion chamber or neutron detectors.

There are two kinds of nonperiodic intensity changes which disturb the results of the analysis we have reported here. The first of these is the solar flare effect which is a sudden but temporary increase in cosmic-ray intensity; the second is the sharp decrease of cosmic-ray intensity followed by a slow recovery to normal intensity, discovered by Forbush. It is principally this latter type of intensity variation which leads to spurious and large values for σ(tracking) since these sudden decreases of intensity are world wide.[6-12] Accordingly, a list of these large and nonrecurring type variations was prepared and the cosmic-ray data for these periods were deleted from the study. These special events with their deleted periods are shown in Table III. There were, in addition, events of a similar character but of much smaller magnitude which we did not remove from the reported results since they do not shift the points in Fig. 3 by as much as the probable error of the individual points. The points in 1946 may be an exception. Even though the large changes of intensity reported in Table III were removed, there still remain some moderately large variations which may be nonperiodic in character; hence, these terminal points on the curve should be viewed with caution.

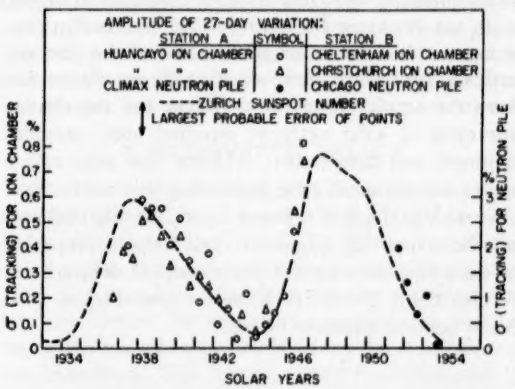

FIG. 2. Amplitude of the 27-day recurring intensity variations as a function of time. Data for the period 1947 through 1950 are not available. The left-hand scale refers to Carnegie Institution ion chamber data; the right-hand scale refers to neutron detector intensity.

TABLE II. Analysis of ionization chamber data.

Period	σ Huancayo %	σ Cheltenham %	r correlation coefficient Huancayo-Cheltenham	σ(tracking) Huancayo correlated to Cheltenham %
1937 May–Oct.	0.67	0.86	0.61	0.41
1938 Jan.–June	0.82	1.16	0.72	0.59
July–Dec.	0.81	0.80	0.68	0.55
1939 Jan.–June	0.78	1.08	0.71	0.55
July–Dec.	0.65	0.90	0.62	0.41
1940 Jan.–June	0.75	1.09	0.69	0.51
July–Dec.	0.55	0.83	0.63	0.34
1941 Jan.–June	0.63	0.91	0.29	0.18
July–Dec.	0.58	0.73	0.64	0.37
1942 Jan.–June	0.43	0.83	0.25	0.11
July–Dec.	0.40	0.77	0.38	0.15
1943 Jan.–June	0.37	0.85	0.10	0.04
July–Dec.	0.43	0.84	0.50	0.21
1944 Jan.–June	0.36	0.75	0.13	0.05
July–Dec.	0.41	0.77	0.23	0.09
1945 Jan.–June	0.43	0.72	0.32	0.14
July–Dec.	0.51	0.83	0.40	0.20
1946 Jan.–June	0.88	0.98	0.53	0.46
July–Dec.	1.04	1.08	0.78	0.82

Period	σ Huancayo %	σ Christchurch %	r correlation coefficient Huancayo-Christchurch	σ(tracking) Huancayo correlated to Christchurch %
1936 July–Dec.	0.58	0.69	0.34	0.20
1937 Jan.–June	0.73	0.81	0.52	0.38
July–Dec.	0.56	0.83	0.63	0.35
1938 Jan.–June	0.82	0.87	0.61	0.50
July–Dec.	0.81	0.85	0.64	0.52
1939 Jan.–June	0.80	0.80	0.55	0.44
July–Dec.	0.63	0.93	0.52	0.33
1940 Jan.–June	0.76	1.01	0.58	0.44
July–Dec.	0.55	0.68	0.44	0.24
1941 Jan.–June	0.57	0.87	0.50	0.29
July–Dec.	0.58	0.80	0.42	0.24
1942 Jan.–June	0.41	0.83	0.48	0.20
1943 April–Sept.	0.40	0.77	0.34	0.14
1944 Jan.–June	0.37	0.73	0.14	0.05
July–Dec.	0.43	0.92	0.35	0.15
1946 Jan.–June	0.86	0.93	0.62	0.54
July–Dec.	1.07	1.10	0.69	0.74

III.

In 1951, when σ(tracking) for the neutron monitor stations was relatively large, we were able to associate special regions of solar activity with individual 27-day variations.[13] These solar regions were recognized by enhanced coronal emission (in the green and red spectral lines), radio noise, H_α flares, local magnetic fields, calcium plage areas, and, many times, by nearby sun spots. If we now wish to select a quantitative measure of the frequency of occurrence and magnitude of these solar active regions, as early as 1936 we encounter the problem that only sunspot measurements cover the entire period in question. Quantitative measurements of coronal activity, flare observations, and radio noise on a routine basis were developed much later. Consequently, we compare the changing ampli-

[6] S. E. Forbush, Terrestrial Magnetism and Atm. Elec. **43**, 203 (1938).
[7] S. Chapman and J. Bartels, *Geomagnetism* (Clarendon Press, Oxford, 1951), Vol. 1, p. 328.
[8] Terrestrial Magnetism and Atm. Elec. **46**, 473 (1941).
[9] Terrestrial Magnetism and Atm. Elec. **47**, 85 (1942).
[10] S. E. Forbush and I. Lange, Terrestrial Magnetism and Atm. Elec. **47**, 331 (1942).
[11] Terrestrial Magnetism and Atm. Elec. **51**, 287 (1946).
[12] S. E. Forbush, Phys. Rev. **70**, 771 (1946).
[13] Simpson, Fonger, and Wilcox, Phys. Rev. **85**, 366 (1952).

TABLE III. List of extraordinary events which are associated with very large cosmic-ray intensity changes. The periods in which these changes occurred were deleted from the correlation data.

Date of special event	Type of event	Deleted period	Reference
1938 Jan. 16	cosmic-ray decrease associated with magnetic storm	Jan. 3–Jan. 23	6
1938 April 16	cosmic-ray decrease associated with magnetic storm	March 29–April 20	7
1941 Sept. 18–21	cosmic-ray decrease associated with magnetic storm	Sept. 5–Sept. 24	8
1941 Dec. 1–2	cosmic-ray decrease associated with magnetic storm	Nov. 17–Dec. 6	9
1942 Feb. 28 and March 7	cosmic-ray increase and decrease associated with solar flare and magnetic storm	Feb. 14–March 11	10
1946 Feb. 7-8	cosmic-ray decrease associated with magnetic storm	Jan. 22–Feb. 14	11
1946 July 26	cosmic-ray increase and decrease associated with solar flare and magnetic storm	July 11–July 31	12

tude of the 27-day intensity variations with sunspot number as shown by the dashed line in Fig. 2. Although we assume that sunspot numbers are closely related to the solar active regions, we do *not* wish to imply that the sunspots are the underlying cause of these cosmic-ray intensity changes. The minima in the solar cycle are quite clearly associated with σ(tracking) minima. The corresponding maxima and slopes of the two curves also appear to be in agreement.

It is now quite clear why attempts to measure a 27-day intensity variation with ion chambers and counter telescopes were more successful for some observers than for others. For example, Monk and Compton[1] detected the variation in 1937–1938 when σ(tracking) was near maximum.

One of the important consequences of using the nucleonic-component neutrons to measure intensity variations is the possibility of determining the amplitude of the variation as a function of primary-particle energy. Initial measurements were made in 1951,[2,5] but during 1952 and 1953 it became increasingly difficult to repeat the observations not only because σ(tracking) decreased sharply but also because the nontracking fluctuations among all stations remained large. Therefore, attempts to measure the ratio of the amplitude variations, (neutron intensity)/(ion chamber intensity) or the ratio (neutron intensity)/(counter telescope intensity) encounter serious difficulties near the minimum of solar activity, i.e., when the 27-day intensity variation is no longer the predominant variation and the number of active solar regions on the sun is considerably reduced.

Although an investigation of the origin of the nontracking intensity fluctuations detected by ion chambers and neutron piles has not been undertaken, we believe at the present time that these fluctuations may be caused by non-world-wide variations of primary intensity.

In view of the fact that σ(tracking) for both neutron detectors and ion chambers in Fig. 2 appear to fit a common curve provided the scale ratio σ(neutron tracking)/σ(ion chamber tracking) is approximately 5, we find no indication that this ratio has appreciably changed with time.

IV.

Although there is strong evidence that the cosmic-ray 27-day intensity variation is extra terrestrial in origin, we do not yet know the nature of the mechanism producing the modulation or acceleration of the primary particles. We believe, however, that the association between the amplitude of the variation and the eleven-year cycle of solar activity, reported here, provides additional and independent evidence that solar active regions are responsible for generating this mechanism.

We wish to thank Mr. James Ayers, Dr. Ely Gelbard, and the computing group for their help in preparing the data and carrying out the numerical calculations. We also thank Dr. R. P. Kane for providing us with special neutron intensity tables.

Cloud-Chamber Evidence for a Charged Counterpart of the θ^0 Particle*

A. L. Hodson, J. Ballam, W. H. Arnold, D. R. Harris, R. Ronald Rau, George T. Reynolds, and S. B. Treiman
Palmer Physical Laboratory, Princeton University, Princeton, New Jersey

(Received August 11, 1954)

A photograph obtained in a Wilson cloud chamber, operated in a magnetic field, shows the following unusual event: A positive particle, produced in an interaction above the cloud chamber, decays in flight into a positive particle less massive than a K meson. Four other lightly ionizing particles also originate from the decay point; these appear in the form of two small-angle pairs, each pair consisting of one positive and one negative particle. The observed momenta and ionizations are consistent with three of these four particles being either electrons or mesons; the fourth must be an electron.

The event may be interpreted as the decay:

$$K^+ \rightarrow \binom{\pi^+}{\mu^+} + \pi^0 + Q \text{ Mev},$$

followed by the decay of the π^0 meson into four electrons (a possible but hitherto unobserved mode of decay):

$$\pi^0 \rightarrow e^+ + e^- + e^+ + e^-.$$

This interpretation leads to a remarkable internal consistency of the data and is supported by the following experimental facts:

(i) There is good overall transverse-momentum balance in two mutually perpendicular planes.

(ii) If we assume that all the particles in the above group of four are electrons resulting from the decay of a neutral particle the mass of the latter, determined from energy-momentum balance, is $(255_{-10}^{+18})m_e$, in good agreement with the known mass of the π^0 meson.

(iii) A transformation to the rest system of the π^0 meson shows that in this frame the four electrons come off as two small-angle pairs traveling in opposite directions. This is the most probable configuration in the four-electron decay of a π^0 meson.

The Q values calculated for the K^+ decay are: $Q(\pi^+,\pi^0) = (213_{-10}^{+18})$ Mev and $Q(\mu^+,\pi^0) = (207_{-10}^{+18})$ Mev. Comparison of the first Q values with that for the θ^0 particle $Q(\pi^+,\pi^-) = 214 \pm 5$ Mev, suggests that the unstable meson observed in this event and designated phenomenologically above as a K^+ meson may be a charged counterpart of the θ^0 particle.

This interpretation may explain at least some of the cases, observed by other workers, in which γ rays appear to be associated with S particles.

Other possible interpretations of the event are considered.

1. INTRODUCTION

DURING the course of an investigation of the unstable particles produced in cosmic-ray nuclear interactions, the unusual cloud-chamber photograph shown in Fig. 1 was obtained.[1] A particle (No. 1) enters the cloud chamber and is believed to decay; five ionizing tracks (Nos. 2, 3, 4, 5, 6) diverge from the decay point. An enlargement of the region around this point is shown in Fig. 2. The details of this event are presented in this paper and possible interpretations are considered.

2. EXPERIMENTAL DETAILS

The event was photographed in a Wilson cloud chamber operated in a magnetic field of 5500 gauss at Echo Lake, Colorado (altitude 10 700 ft). The illuminated region of the chamber has average dimensions, 16 in.×16 in.×5 in. The cloud chamber was expanded by coincidences between two proportional counter trays, one placed immediately above the chamber and one beneath it. The counter system was designed to detect penetrating showers produced in a layer of lead 6½ in. thick placed above the chamber. Two photographs were taken at a stereo angle of 17° on Kodak Linagraph Panchromatic 70-mm film, using two matched 3½ in. Goertz Dagor lenses at an aperture of $f/19$. The cloud chamber was filled with argon and saturated with the vapor of a 70 percent–30 percent mixture of ethyl alcohol and water; the total pressure in the compressed position was 82.8 cm of mercury.

The photograph shown in Fig. 1 is one of 30 000 photographs so far taken with this cloud chamber, using various proportional-counter trigger schemes to detect penetrating showers. In this set of photographs 270 V^0 particle decays and 60 $V^\pm$ decays were observed.

3. ANALYSIS PROCEDURE

The two stereo photographs of the event shown in Fig. 1 were reprojected through a glass plate onto a screen perpendicular to the axes of the two camera lenses. The thickness of this glass plate was equal to the total thickness of a double window arrangement through which the photographs were taken. The two negatives were first aligned in the stereo projector so that the images of a series of horizontal and vertical fiducial lines ruled on the inside of the front window of the cloud chamber (see Fig. 1) appeared stationary on the screen when the two views were projected alternately. For this alignment the screen-film distance was set equal to the correct fiducial plane-film distance. The apparent spacing of the fiducial lines was checked against the known spacing to make sure that the negatives were being reprojected at the correct magnification.

The projector was mounted on the table of a small milling machine so that it could be moved in a direction parallel to the axes of the camera lenses (the Z direction) until a particular point on a track appeared stationary when the two views were projected alternately. By

* This work was supported by the Office of Naval Research and the U. S. Atomic Energy Commission.

[1] This event was the subject of a post-deadline paper presented at the Washington Meeting of the American Physical Society, May, 1954. Further details were presented at the Seattle Meeting of the American Physical Society, July, 1954. [D. R. Harris and A. L. Hadson, Phys. Rev. 95, 661(A) (1954)].

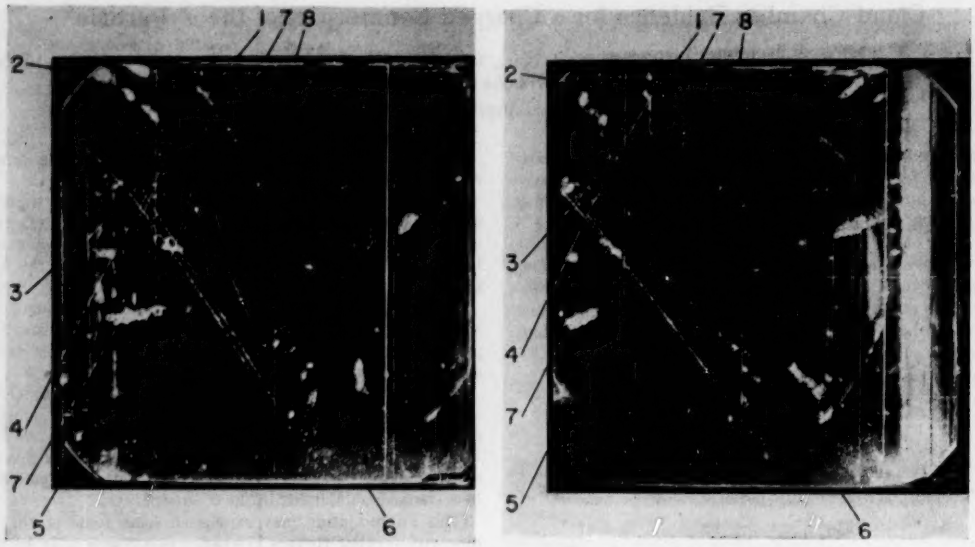

FIG. 1. Stereoscopic views of a cloud-chamber photograph believed to show the decays: $\theta^+ \rightarrow \pi^+ + \pi^0$; $\pi^0 \rightarrow e^+ + e^- + e^+ + e^-$.

carefully marking the position of this point on a large sheet of paper attached to the screen and repeating the procedure for many points along each track, an orthogonal projection of the event in the plane of the screen (called here the XY plane) was obtained. The apparent Z reading of each point was noted alongside the point as it was plotted. These readings were then converted into true Z readings, taking the fiducial plane as $Z=0$ and correcting each reading for the displacement of the tracks in the Z direction which occurred when the cloud chamber was expanded. Finally, on a drawing board, a YZ and an XZ projection were constructed point by point from the points on the XY projection and their corrected Z values (Fig. 3).

From Fig. 3 it is clear that tracks Nos. 1–6 all meet at one point (M) in the middle of the illuminated region of the cloud chamber. During the reprojection a careful search was made around this point for a possible ionizing recoil fragment. No indication of any such recoil fragment was found. It might be mentioned that

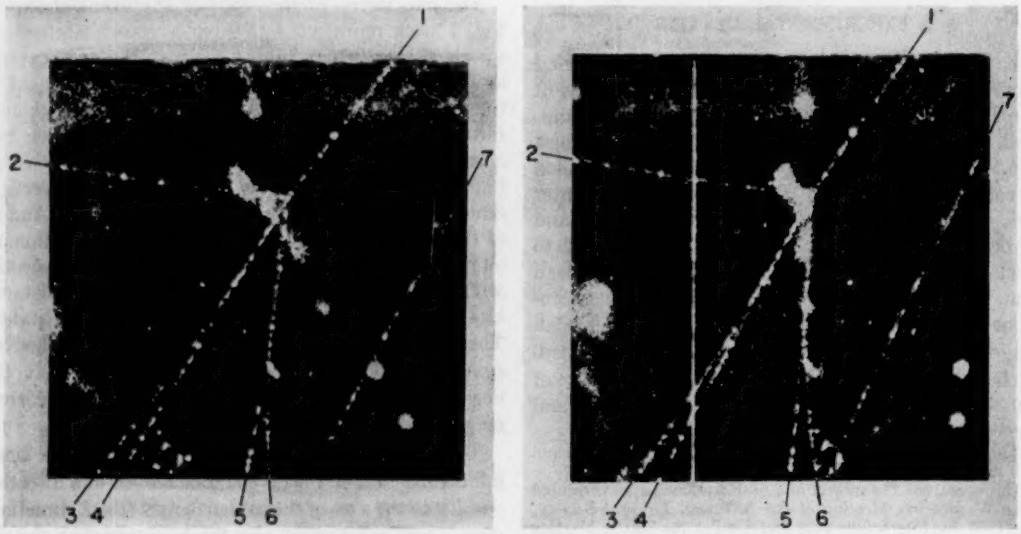

FIG. 2. Enlargement of part of the cloud-chamber photograph shown in Fig. 1.

although a cluster of old ionization partly obscures this region in the right view it is not space-related and the point M is quite clear on reprojection.

For a study of the dynamics of the event shown in Fig. 1 we need to know the directions of the momentum vectors (P) of particles 1–6 at the point M. The directions of these vectors may be defined by the two angles γ and ψ shown in Fig. 4. Thus γ is the angle between the Y axis and the tangent (at the point M) to the projection of the track in the XY plane; ψ is the angle between the Y axis and the tangent to the projection of the track in the YZ plane. The tangents to the tracks in the XY projection were determined in the following manner: For the most highly curved tracks a long compass was set to the correct radius in the XY plane (calculated from the curvature on the film) and the center of curvature was found by graphical construction. The direction of the tangent at M was then found by drawing a radius from the center of curvature to the point M. When the required radius was too large for this method to be practical, a chord was drawn from M and the angle between the tangent and the chord was calculated. The latter method was also used

TABLE I. Basic angle data for event shown in Fig. 1.

Track number	γ (degrees)	ψ (degrees)
1	−33.6±0.3	−19.0±0.7
2	−92.2±0.5	−96.4±1.5
3	−29.5±0.2	−13.3±0.3
4	−29.1±0.2	−13.6±0.3
5	− 2.7±0.2	−15.2±0.5
6	− 4.4±0.4	−15.4±0.5

for finding the tangents to the curved projections in the YZ plane. [It may be noted that since the path of a charged particle in a uniform magnetic field is a helix whose axis is the field direction, the projections in the YZ and XZ planes are parts of sine curves, modified here by the transverse field (i.e., the component in the XY plane) and variations of the longitudinal field (i.e., the component in the Z direction) along a track.]

For one track (No. 2), it is impossible to find ψ from the YZ projection. Since this track is nearly horizontal and curving upwards, the projection in the YZ plane is mainly the projection of the upwards curvature. The direction of this track at M was therefore determined by measuring angles with respect to the X axis in the XY and XZ projections. The true value of ψ in the YZ plane was then calculated.

A second observer also measured the angles γ and ψ by an independent method. The space coordinates of three points on each track near the point M were found from direct comparator measurements on the film; the angles γ and ψ were then calculated from these coordinates. For example, γ was found by fitting a circle to the projection of these points in the XY plane and

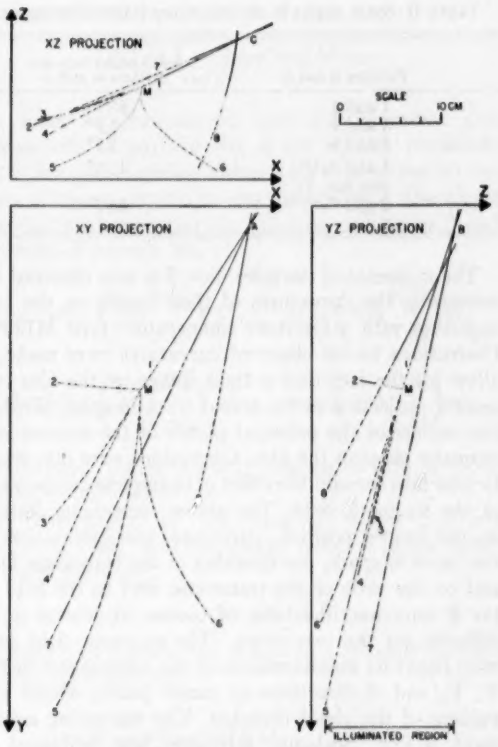

FIG. 3. Orthogonal projections of the tracks in three mutually perpendicular planes.

finding the slope of its tangent at the point M. The two methods gave values for these angles which were in good agreement; the final values of γ and ψ (given in Table I) were therefore obtained by combining the results of both methods. The space angles between various pairs of tracks are given in Table II.

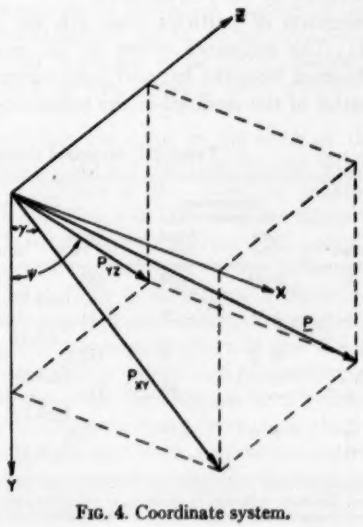

FIG. 4. Coordinate system.

TABLE II. Space angles in the laboratory frame of reference.

Particles m and n	Space angles between particles m and n
1 and 2	55.7°
3 and 4	0.5°
5 and 6	1.7°
1 and "π^0," (see Sec. 5)	11.0°
2 and "π^0"	66.7°

The momenta of particles Nos. 2–6 were obtained by measuring the curvatures of their tracks on the two negatives with a Gaertner comparator (type M1229). Corrections to the observed curvatures were made to allow for the fact that a track image on the film is a conical projection of the actual track in space through the centers of the principal planes of the camera lens onto the plane of the film. Corrections were also made to take into account the effect of transverse components of the magnetic field. The above corrections depend on the length, position, curvature, and orientation of the track in space, the direction of the transverse field and on the ratio of the transverse field to the field in the Z direction; they are, of course, in general quite different for the two views. (The magnetic field data were based on measurements of the components in the X, Y, and Z directions at many points within the volume of the cloud chamber. The measuring equipment, a Pye "Scalamp" fluxmeter, was calibrated at several field values using the proton resonance method.) The magnetic field values used in the calculation of the above corrections and in the calculation of the final momenta were obtained by taking the values of the longitudinal field and the transverse field at three points along each track, then suitably weighting and averaging these three values. (We are indebted to R. W. Williams and G. Ascoli for details of an averaging method which they have developed.)

The momenta of particles Nos. 2–6 are given in Table III. The estimated errors in the momentum values obtained from the left and right views because of the scatter of the readings in the comparator measurements of the curvatures are given in parentheses. It will be seen that, considering these errors, the momentum values obtained from the left and right views after making the above corrections are in satisfactory agreement. The actual percentage corrections that had to be applied to the film curvatures are also given in Table III. The components of the momenta in the XY and YZ planes, denoted by P_{XY} and P_{YZ}, respectively, are given in the last two columns of this table.

4. DISCUSSION OF THE INDIVIDUAL TRACKS

Particle No. 1.—This particle came from an interaction in the lead above the cloud chamber. In the XY projection, track No. 1 and two other tracks (No. 7 and No. 8) of apparently the same age may be extrapolated back to a fairly well-defined origin, A (Fig. 3). In the YZ projection, the extrapolation of tracks No. 1 and No. 7 intersect at a point B whose Y value is consistent with the Y value found for the origin (A) in the XY projection (Fig. 3). Although the extrapolation of track No. 8 in the YZ projection misses point B (probably caused by scattering of particle No. 8 before entering the chamber), it can reasonably be concluded that a nuclear interaction occurred in the lead at or near to the point (A,B) and that particle No. 1 was produced in this interaction.

Unfortunately, since particle No. 1 had a high momentum and its track is very short, it is not possible to determine directly the sign of its charge.

Particles Nos. 2–6.—Upper limits for the masses of these particles can be obtained from their momenta and visual estimates of their ionizations—these limits are given in column 9 of Table III. We see that particle No. 4 was considerably less massive than a proton, that particles Nos. 2, 3, and 5 were light particles (mesons or electrons), and that particle No. 6 must have been an electron. (A μ^- meson with the momentum of particle No. 6 would be ionizing at a rate 3.2 times the minimum value.) Note the very small angles at the point M between (positive) particle No. 3 and (negative) particle No. 4 and between (positive) particle

TABLE III. Measured momenta of particles involved in event shown in Fig. 1.

Particle No.	Sign	Momentum correction (%) Left view	Right view	Corrected total momenta P (Mev/c) From left view	From right view	Mean value	Ionization (×minimum ionization)	Mass from momentum and ionization (m_e)	Probable identity (see Sec. 5)	P_{XY} (Mev/c)	P_{YZ} (Mev/c)
2	+	−10	−24	156 (±6.7)[a]	150	153 ±10[b]	<2	< 440	$\pi^+(\mu^+)$	144	50
3	+	+ 1	− 8	131 (±2.6)[a]	133.5	132 ± 5[b]	<2	< 370	e^+	130	116
4	−	+ 2	− 6	372.5 (±8.6)[a]	363	368 ±35[b]	<2	<1090	e^-	360	324
5	+	− 3	−10	121 (±0.7)[a]	121	121 ± 4[b]	<2	< 340	e^+	117	121
6	−	+ 6	+11	52.6 (±0.4)[a]	53.5	53.1± 2[b]	<2	< 150	e^-	51	53

[a] Estimated standard deviation in momentum value for each view caused *only* by scatter of readings in comparator measurement of curvature.
[b] Combined errors caused by all sources of uncertainty (see Sec. 5).

No. 5 and the (negative) electron No. 6 (Fig. 1 and Table II).

From the values of P_{XY} and P_{YZ} given in Table III and the values of γ and ψ in Table I, we may obtain the transverse momenta of particles Nos. 2–6 (relative to the direction of particle No. 1) in the XY and YZ planes. The transverse momentum of particle No. 2 in the XY plane is -123.3 Mev/c; the total transverse momentum of particles Nos. 3–6 is $+122.6$ Mev/c. The unbalanced transverse momentum in the XY plane is thus -0.7 ± 10 Mev/c. The corresponding momenta in the YZ plane are -48.8 Mev/c and $+53.3$ Mev/c; the imbalance here is thus $+4.5\pm10$ Mev/c. From the excellent balance of transverse momenta in both the XY and YZ planes it seems very unlikely that the event shown in Fig. 1 also gave rise to any neutral particles or γ rays which have escaped detection.

5. POSSIBLE INTERPRETATION

There is no evidence to suggest that the event was a nuclear interaction in the gas of the cloud chamber. We therefore consider an interpretation based on the decay of a positively charged particle. Although we cannot exclude the direct decay of particle No. 1 into five particles, we will show that the following interpretation is remarkably consistent with the experimental data: Particle No. 1 decayed into a light particle (No. 2) and a π^0 meson, which subsequently decayed into four electrons (Nos. 3, 4, 5, 6).

With the above interpretation, the apparent origin of the five secondary tracks (No. 2–6) at one point is readily explained. Because of the extremely short mean life[2] ($\sim5\times10^{-15}$ sec) of π^0 mesons, the decay points of the positive unstable particle (No. 1) and of the π^0 meson were separated in space by a distance ($\sim8\times10^{-4}$ cm), too small to be resolved in the cloud-chamber photograph.

If we assume that particles Nos. 3–6 were all electrons resulting directly or indirectly (via processes in which energy and momentum losses were negligible) from the decay of a neutral particle, the momentum and mass of this hypothetical neutral particle can be calculated. We find that the four "electrons" were kinematically equivalent to a particle of mass $(255_{-10}^{+15})m_e$ and momentum 662 Mev/c, traveling in the direction specified by $\gamma_0=-22.65°$ and $\psi_0=-14.0°$. This mass value is in such good agreement with the accepted mass of the π^0 meson $(263.7\pm0.7m_e)$[3,4] that, barring an unlikely coincidence, a π^0 meson must indeed have been involved in this event. (The possible processes whereby two negatron-positron "pairs" may result from the decay of a π^0 meson will be discussed later.)

Let us therefore assume that particle No. 1 decayed via the scheme:

$$K^+\rightarrow\begin{pmatrix}\pi^+\\ \mu^+\end{pmatrix}+\pi^0+Q \text{ Mev.}$$

(It must be remembered that the ionization and momentum of particle No. 2 are equally consistent with this particle being either a π^+ or a μ^+ meson; its mass is known only to be less than $440m_e$.) The above two decay schemes give the following values for Q and the mass of particle No. 1:

$$Q(\pi^+,\pi^0)=\begin{pmatrix}213^{+15}_{-10}\end{pmatrix}\text{ Mev},\quad m_1=\begin{pmatrix}954^{+30}_{-20}\end{pmatrix}m_e,$$

and

$$Q(\mu^+,\pi^0)=\begin{pmatrix}207^{+15}_{-10}\end{pmatrix}\text{ Mev},\quad m_1=\begin{pmatrix}876^{+30}_{-20}\end{pmatrix}m_e,$$

respectively (taking $m_{\pi^+}=273.4m_e$, $m_{\pi^0}=(876_{-20}^{+30})m_e$, and $m_{\mu^+}=207.0m_e$).[3,4]

A comparison of the first Q value, $Q(\pi^+,\pi^0)=(213_{-10}^{+15})m_e$, with the energy released in the decay of the θ^0 particle:[5]

$$\theta^0\rightarrow\pi^++\pi^-+214\pm5 \text{ Mev},$$

suggests that particle No. 1 may be a charged counterpart of the θ^0 particle:

$$\theta^+\rightarrow\pi^++\pi^0+\begin{pmatrix}213^{+15}_{-10}\end{pmatrix}\text{ Mev}.$$

Discussion of Errors

The quoted errors in the mass of the hypothetical neutral particle and in the Q values (approximately a standard deviation in each case) were estimated by considering the errors possible in the angle measurements and the standard deviations in the momenta caused by the scatter of the readings in the comparator measurements of the curvature, to possible distortions in the cloud-chamber tracks, to multiple scattering of the electrons in the gas of the cloud chamber, and to uncertainties in the magnetic field effective on the particles.

In computing the error in the mass of the hypothetical neutral particle, the contribution which is most difficult to estimate is that caused by possible distortions in tracks Nos. 3–6. However, the calculated mass is rather insensitive to such distortions, providing they were reasonably uniform over the region between tracks Nos. 3 and 6. This is so because a distortion which reduces the apparent momentum of a positive particle increases that of a negative particle and *vice versa*, the two changes being partly self-compensating in the analysis of this event. For example, even if the distortion in this particular expansion were such that it would have given a straight track a curvature corresponding

[2] B. M. Amand, Proc. Roy. Soc. (London) **A220**, 183 (1953).
[3] W. Chinowsky and J. Steinberger, Phys. Rev. **93**, 586 (1954)—for $\pi^--\pi^0$ mass difference.
[4] Smith, Birnbaum, and Barkas, Phys. Rev. **91**, 765 (1953)—for π^- mass.
[5] Thompson, Burwell, Cohn, Huggett, and Karzmark, Phys. Rev. **95**, 661 (1954).

to a positive 2-Bev/c particle ("positive distortion") or corresponding to a negative 2-Bev/c particle ("negative distortion"), the correction to the above value of $255m_e$ that this would necessitate would only be $-8m_e$ or $+13m_e$, respectively. From previous experience we know that the distortion is generally negative in this region and that the "distortion momentum" is certainly not less than 2 Bev/c.

The distortions near the top of the cloud chamber are known to be lateral distortions; therefore these are not likely to have much effect on track No. 2 which is nearly horizontal.

The Decay of the π^0 Meson

We must now consider three possible explanations to account for the observation of the two electron "pairs":

(a) The π^0 meson decayed via the scheme

$$\pi^0 \rightarrow \gamma + \gamma, \qquad \text{(i)}$$

and then the γ rays materialized into negatron-positron pairs in the electromagnetic fields of two nuclei of the gas of the cloud chamber, after traversing distances so short that the apexes of the two pairs cannot be resolved in the photograph from the decay point of the positive unstable particle, No. 1.

The probability of both γ rays materializing within 2 mm, a distance appreciably greater than the track width in the chamber (0.7 mm), is 4×10^{-10}.

(b) The π^0 meson decayed via the scheme

$$\pi^0 \rightarrow e^+ + e^- + \gamma, \qquad \text{(ii)}$$

and then the γ ray materialized within a distance of 2 mm.

This mode of decay was first suggested theoretically by Dalitz.[6] The occurrence of high-energy pairs of electrons within a few microns' distance from nuclear interactions has been observed in photographic emulsions by Daniel *et al.*,[7] Lord *et al.*,[8] Amand,[2] and Schein *et al.*[9] The frequency of these pairs is about twenty times higher than would be expected if they were caused by the materialization of γ rays produced in decay scheme (i).[2] Under the assumption that all the close pairs are produced by the decay of π^0 mesons via decay scheme (ii), the following values were obtained for the branching ratio

$$\frac{\pi^0 \rightarrow e^+ + e^- + \gamma}{\pi^0 \rightarrow \gamma + \gamma}:$$

0.020 ± 0.006,[7] 0.013 ± 0.004.[2] Lindenfeld *et al.*,[10] using counter techniques, obtained the value $0.0145^{+0.008}_{-0.0045}$. The experimental values are in excellent agreement with the theoretical value, $1/80=0.012$, calculated by Dalitz.[6]

Taking Dalitz' calculated value for the branching ratio, we find the probability that the π^0 meson decayed via scheme (ii) and that the γ ray then materialized within 2 mm is 2.2×10^{-7}.

(c) The π^0 meson decayed into four electrons:

$$\pi^0 \rightarrow e^+ + e^- + e^+ + e^-. \qquad \text{(iii)}$$

This decay scheme has not previously been observed experimentally. However, the probability for this mode of decay is expected to be about $1/(160)^2=4\times10^{-5}$ times that for a decay into γ rays.[11]

From a comparison of the relative probabilities, $<4\times10^{-10}$, $<2.2\times10^{-7}$, and 4×10^{-5}, given above, we conclude that the most probable explanation of the origin of the two electron pairs is the direct decay of the π^0 meson into four electrons. This conclusion is supported by a comparison of the angular relationship of the four electrons in the rest system of the π^0 meson with that expected theoretically. The most likely decay configuration in the rest system of a π^0 meson is one in which the four electrons form two small-angle pairs which travel in opposite directions and which have essentially equal total energies. The angles between the pairs, observed in this event, in the rest system of the π^0 meson and the total energies of the electrons in this system are given in Table IV.

A determination of the angle between the two planes defined by the pairs at the decay point would be of interest, but unfortunately it has not been found possible. A worthwhile determination would necessitate a much more accurate knowledge of the original directions of the electrons at the decay point since the opening angles of the pairs are so small; this is difficult to achieve since the magnetic field causes the electrons to lose rapidly their original directions.

6. OTHER ATTEMPTS AT INTERPRETING THIS EVENT

It is necessary to inquire whether there is some other interpretation of the event shown in Fig. 1 which is as consistent with the experimental data as the interpretation given above.

TABLE IV. Energies and angles in the rest system of the π^0 meson.

Particle	Energy (Mev)	Space angle
3	17.9	$\theta_{3,4}=3.8\pm2.2°$
4	48.3	
5	46.3	$\theta_{5,6}=4.6\pm1.4°$
6	17.9	

[6] R. H. Dalitz, Proc. Phys. Soc. (London) **A64**, 667 (1951).
[7] Daniel, Davies, Mulvey, and Perkins, Phil. Mag. **43**, 753 (1952).
[8] Lord, Fainberg, Haskin, and Schein, Phys. Rev. **87**, 538 (1952).
[9] Schein, Fainberg, Haskin, and Glasser, Phys. Rev. **91**, 973 (1953).
[10] Lindenfeld, Sachs, and Steinberger, Phys. Rev. **89**, 531 (1953).
[11] R. H. Dalitz (private communication). This estimate neglects exchange terms; however, these are expected to be fairly small.

Let us examine the possibility of the initial decay being that of a τ^+ meson, via the decay mode recently observed by Crussard *et al.*:[12]

$$\tau^+ \rightarrow \pi^+ + \pi^0 + \pi^0.{}^{13}$$

Since there is good evidence that all four electrons came from only one π^0 meson, the τ^+ decay would have had to satisfy the requirement of transverse momentum balance between the π^+ meson and only one π^0 meson. (The measured transverse momenta of particle No. 2 and the π^0 meson are 126.2 Mev/c and 126.6 Mev/c, respectively.) This, of course, could obtain if the other π^0 meson happened to travel in a direction close to the line of flight of the τ^+ meson before decay. However, the maximum apparent Q value for such a decay, if analyzed as a two-body decay, is $Q(\pi^+,\pi^0)=84$ Mev, whereas the observed value is $Q(\pi^+,\pi^0)=(213_{-10}^{+15})$ Mev. Thus the event shown in Fig. 1 cannot be caused by the decay:

$$\tau^+ \rightarrow \pi^+ + \pi^0 + \pi^0 + 84 \text{ Mev}.$$

Any explanation of this event on the basis of a purely electromagnetic interaction, such as direct production of two electron pairs in the field of an argon nucleus, is extremely improbable because the electron pairs would have to appear kinematically equivalent to a π^0 meson.

7. SUMMARY AND CONCLUDING REMARKS

The cloud-chamber photograph shown in Fig. 1 can be interpreted in the following way: A heavy meson (designated phenomenologically as a K^+ meson) decayed into a light meson and a π^0 meson. The π^0 meson then decayed, most probably "directly," into four electrons. A comparison of the energy released in the decay of this K^+ meson, $Q(\pi^+,\pi^0)=(213_{-10}^{+15})$ Mev, with that released in the decay of a θ^0 particle, $Q(\pi^+,\pi^-)=(214\pm5)$ Mev, suggests that this K^+ meson may be a charged counterpart of the θ^0 particle:

$$\theta^+ \rightarrow \pi^+ + \pi^0 + \left(213\begin{matrix}+15\\-10\end{matrix}\right) \text{ Mev}.$$

The mass value corresponding to this decay scheme is $(954_{-20}^{+30})m_e$; the momentum of the π^+ meson and the π^0 meson in the rest system of the θ^+ particle is

$$p^*(\pi^+,\pi^0)=(201_{-6}^{+9}) \text{ Mev}/c.$$

If the above interpretation is correct and θ^+ particles do indeed exist, they must be responsible for some of the V^+ decay events which have been observed. Charged π mesons have already been identified among the decay products of charged V particles and S particles.[14–17] θ^+ particles may also be responsible for at least some of the events, observed by other workers,[18] in which γ rays appear to be associated with S particles.

The π^0 meson emitted in the decay of a θ^+ particle will usually disintegrate into two γ rays and so escape detection, unless the event occurs in a multiplate cloud chamber or a thick stack of photographic emulsions. However, on the average about 1 in 80 decays of θ^+ particles should show two electrons coming from the decay point, because of the decay mode: $\pi^0 \rightarrow e^+ + e^- + \gamma$. The fact that this type of event has not been observed before the much rarer decay into four electrons must be attributed to an unusual statistical fluctuation.

If our interpretation is correct we can calculate an upper limit to the *average* rate at which events similar to that shown in Fig. 1 should be observed in the future. With the present experimental arrangement, we observe about one charged V particle decay in 500 cloud-chamber photographs. Since all these events cannot be attributed to θ^+ particles and since, on the average, only one π^0 meson in 2.6×10^4 will decay into four electrons, an upper limit to the above rate is one event in $500\times2.6\times10^4=13\times10^6$ cloud-chamber photographs! It may eventually be possible to increase the present detection efficiency for decay events but, in any case, photographs similar to that shown in Fig. 1 are likely to remain extremely rare.

---

[12] Crussard, Kaplon, Klarmann, and Noon, Phys. Rev. **93**, 253 (1954).

[13] The Q value expected for this mode of decay is 84 Mev, if one assumes the mass of the τ^+ meson to be $965m_e$.

[14] H. S. Bridge and M. Annis, Phys. Rev. **82**, 445 (1951).

[15] C. C. Butler, Report of the Bagnères de Bigorre Conference 1953 (unpublished), p. 90.

[16] Gregory, Lagarrigue, Leprince-Ringuet, Muller, and Peyrou, Nuovo cimento **11**, 292 (1954).

[17] Kim, Burwell, Cohn, Karzmark, and Thompson, Phys. Rev. **95**, 661 (1954).

[18] Bridge, Courant, DeStaebler, and Rossi, Phys. Rev. **91**, 1024 (1953).

Low-Energy Differential Range Spectrum of Cosmic-Ray μ Mesons*†

A. Fafarman and M. H. Shamos
Department of Physics, Washington Square College, New York University, New York, New York

(Received July 1, 1954)

The differential range spectrum of cosmic-ray μ mesons was investigated in the region from 0 to 410 g/cm² Pb for evidence of minima. Delayed coincidences in a tank of liquid scintillator were used to identify stopping mesons. The spectrum decreases monotonically with decreasing energy and shows no irregularity. Although only relative readings were taken, the method is adaptable to a precision determination of the *absolute* range spectrum. The delay data yield for the natural mixture of sea level cosmic-ray μ mesons a mean life in carbon of 2.13±0.07 μsec.

I. INTRODUCTION

SEVERAL investigators have reported a minimum in the low-energy spectrum of cosmic-ray μ mesons. Rogozinski and Lesage[1] found a pronounced minimum under approximately 25 cm of lead (corresponding to a meson momentum of about 450 Mev/c). On the other hand, Kellermann and Westerman[2] found a marked minimum under 10 cm of lead. Since these investigators used anticoincidence methods, they attributed the anomalous rise at low momenta principally to cosmic-ray protons (and to a small residual electronic component arising from the inefficiency of their methods for eliminating electrons). Some experiments done in this laboratory[3] by means of a GM counter delayed-coincidence technique had indicated that there might be some irregularity in the meson spectrum itself in this energy region. Inasmuch as there was available an experimental arrangement which included a liquid scintillator tank of appreciable volume (3 liters), we were presented with the opportunity for a quick independent check of the spectrum of cosmic-ray μ mesons.

II. APPARATUS

The geometry of the experiment is shown in Fig. 1. The apparatus consists of two particle detectors, a GM counter tray "A" (30 cm×50 cm) and a 3-liter tank of liquid scintillator "B" (15 cm diameter×20 cm deep containing 5 g/liter terphenyl in toluene), with variable thickness of absorber between the two. Delayed coincidences $AB+B$ (delayed 0.5 to 8.0 μsec), i.e., events in which a coincidence AB is followed by a second pulse in the tank B with a delay of 0.5 μsec to 8.0 μsec, are used to identify μ mesons stopping in the tank. For each such event the delay between B and B (delayed) was recorded by a 4-channel delay discriminator.

III. METHOD

The following counting rates were recorded:

(a) B, the counting rate of the tank.

(b) AB, the twofold coincidence rate. This is essentially the integral cosmic-ray flux through the tank within the solid angle defined by the GM counters.

(c) $AB+B$ (delayed):

1. $AB+B$ (delayed 0.5 to 2.5 μsec),
2. $AB+B$ (delayed 2.5 to 4.4 μsec),
3. $AB+B$ (delayed 4.4 to 6.3 μsec),
4. $AB+B$ (delayed 6.3 to 8.0 μsec).

The B rate served as a continuous check on the operation of the tank and varied from ~7.7 to 6.7 counts/second depending on the absorber in the telescope.

The AB rate served as a monitor of the meson flux and to some extent as an indicator of the tank sensitivity. The AB rate varied from ~1250 to 800 counts/hr, depending on the absorber thickness. The calculated meson flux through the tank is approximately 1000/hr. For small thicknesses of absorber, a portion of the soft component will contribute to the AB rate and this accounts for the significant difference between the highest AB rate and the meson flux. The accidental rate, both as computed and as measured, is insignificant. Since the measurements required a period of several weeks, the AB data were used to normalize the stopped meson rate. This served to eliminate the effects of variations of cosmic-ray intensity and to some extent variations in detector efficiencies.[4]

IV. CORRECTIONS

There is a small correction for random or accidental AB events (about 20/hr) and for accidental $AB+B$ (delayed) events [of the order of 0.01 (counts/hour) per channel]. The correction applied is a computed one; however, the accuracy of this procedure has been checked by two methods:

* Assisted by the U. S. Atomic Energy Commission and the U. S. Office of Naval Research.

† A previous report has been given: A. Fafarman and M. H. Shamos, Phys. Rev. 95, 648(A) (1954).

[1] A. Rogozinski and M. Lesage, *Cosmic Radiation* (Interscience Publishers, Inc., New York, 1949), p. 63

[2] E. W. Kellermann and K. Westerman, Proc. Phys. Soc. (London) 62, 356 (1949).

[3] C. L. Eisen, Master of Science thesis, New York University, September, 1952 (unpublished).

[4] The AB data were used to normalize the stopped meson rate in two ways: (a) by comparison with the average AB rate for all runs under a given absorber thickness; (b) by comparison with the AB rate under a given absorber thickness as determined from a separate plot of the AB rate *vs* absorber thickness taken over a short period (i.e., within an 8-hour interval).

(a) Use of artificial pulses in the A or B channels,
(b) Use of a radium source to increase the counting rate in the B channel.

Periodic checks were made of counting rates, waveforms, and critical voltages of the equipment. However, it is probable that there were some small changes in the sensitivity for $AB+B$ (delayed) events over the course of the experiment, since with the poor light collection of a single 5819 in the large tank of scintillator we were working with pulse heights where the efficiency for detecting some of the beta particles from μ-meson decay showed considerable variation with the bias. Unfortunately, the twofold coincidence AB rate shows considerably less dependence on this change of sensitivity (because of the much greater energy loss of a meson passing essentially vertically through the tank) and cannot be used to give an indication of these changes of sensitivity; also the independent variations of the AB rate caused by ordinary barometric fluctuations in cosmic-ray intensity make it difficult to apply this correction to the tank sensitivity. One might expect that the B counting rate (tank rate) could be used as an independent check on tank sensitivity. However, this would have required a knowledge of the relation between the beta sensitivity and the counting rate of the tank—a relation for which only a very rough approximation could be obtained. Hence no further correction beyond the normalization of the $AB+B$ (delayed) to the AB was applied. The essential constancy of the B rate, together with the substantial agreement within the statistical errors of the results obtained at various times for a particular absorber thickness, indicate the adequacy of this correction.

A serious source of error in this type of experiment exists in the possible contribution to the delayed counting rate by afterpulsing of the photomultiplier. It was found with several 5819 photomultipliers that a contribution to the delayed coincidence rate (particularly in the first channel of the delay discriminator) occurred in going to sufficiently small pulse heights. A convenient method for checking the presence of afterpulsing in our apparatus was to increase the accidental rate of $B+B$ (delayed) events by using a 1-mC radium source to cause a considerable increase in the counting rate (and hence the accidental rate) of the tank. The presence of afterpulsing was evidenced by a significant departure from equality of the rates in the four channels of the delay discriminator, in particular a high count in the first channel.

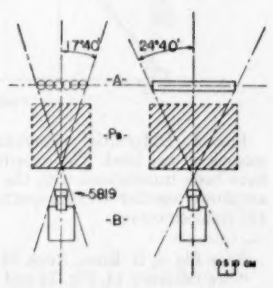

FIG. 1. Experimental arrangement for μ-meson range spectrum. A is a tray of GM counters 30 cm×50 cm, and B is a tank of liquid scintillator 15 cm in diameter and 20 cm deep.

TABLE I. Observed stopped-meson data and delay distribution.

Absorber	Hours	AB	$AB+B$(delayed) 1	2	3	4
0	86.6	10.98×10^4	89	30	19	8
55 g/cm² Fe	99.6	10.73×10^4	127	57	26	8
55 g/cm² Fe+115 g/cm² Pb	317.1	33.40×10^4	483	197	97	26
55 g/cm² Fe+230 g/cm² Pb	419.9	40.98×10^4	590	271	116	37
55 g/cm² Fe+345 g/cm² Pb	348.0	29.88×10^4	532	192	78	38

TABLE II. Calculated stopped-meson rates.

Range g/cm² (air equiv.)	Momentum Mev/c	$AB+B$ (delayed) rate minus random rate (counts/hr) (a) Observed	(b) Corrected by concurrent AB rate	(c) Corrected by short dur. AB rate	(d) Column (c) plus est. Scattering correction
11.1±8.7	112^{+28}_{-42}	1.64±0.14	1.63±0.14	1.78±0.16	1.78±0.16
48±9	212±20	2.14±0.15	2.12±0.15	2.28±0.17	2.28±0.17
127±9	368±17	2.48±0.09	2.48±0.09	2.37±0.10	2.39±0.10
204±9	525±17	2.37±0.07	2.37±0.07	2.36±0.09	2.41±0.09
277±9	670±17	2.36±0.08	2.37±0.08	2.53±0.10	2.55±0.10

For the 5819 with voltage and bias settings used in obtaining the results given in Sec. V, no evidence of afterpulsing was observed either visually on the oscilloscope or by the above mentioned method—nor was any observed at bias settings giving considerably higher B rates. However, even for this tube, it was possible, by increasing sufficiently the voltage across the tube to obtain a contribution from afterpulsing.[5]

An additional indication that there was no significant contribution from afterpulsing is the mean life obtained for the μ mesons (2.13±0.07 μsec) from the delay discriminator data.

The 4-channel delay discriminator was essentially the unit described by Morewitz and Shamos[6] and was calibrated by means of artificial pulses from a delay line-controlled double-pulse generator. The delay between the pulses was continuously variable by the insertion of a small variable delay line[7] between the fixed delay line steps.

V. RESULTS

The observed data for AB and $AB+B$ (delayed) events are collected and shown in Table I.

In Table II are listed the computed stopped-meson

[5] It should be noted that the noise pulses from the tube are considerably fewer when the tank is at the potential of the photocathode of the 5819. We have observed this effect in almost all photomultipliers. It seems reasonable that these additional noise pulses arise from positive ion bombardment of the photocathode. Whenever light collection is a problem and pulse measurements must be carried down into the noise region, it is advisable to use a shield at the potential of the photocathode. Despite the presence of a metallic coating at cathode potential inside the glass envelope of the 5819, the shield effect was present in our tank.

[6] H. A. Morewitz and M. H. Shamos, Phys. Rev. **92**, 135 (1953).

[7] Advance Electronics Company, Model 302.

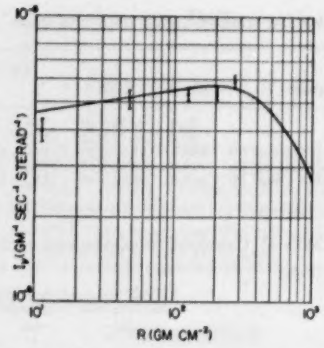

FIG. 2. Differential range spectrum of cosmic-ray μ mesons at sea level. The abscissa is the range in g cm^{-2} (air equivalent). The experimental points have been normalized to the spectrum given by Rossi (see reference 13) (smooth curve).

rates. The conversion from absorber thickness (of Table I) to equivalent range in air[8] was made with the aid of the following information:

(a) 2.4 g/cm^2 (air equivalent) minimum absorbing material (roof, framework, etc. above tank).

(b) Because of scattering, the range in Pb is 11 percent greater than the thickness traversed.[9]

(c) The thickness of the liquid scintillator was 17.4 g/cm^2 air equivalent.

The conversion from range to meson momenta was made by using the Gross range-momentum curves[10] for air with momenta increased by 5 percent to correct for the meson mass ($210m_e$ instead of $200m_e$).

The remaining columns of Table II give the stopped-meson rate, corrected for a small random rate of 0.05/hr, and further corrected as follows:[4]

(*a*) Observed $AB+B$ (delayed) rate events/hr,

(*b*) $AB+B$ (delayed) rate corrected by the concurrent AB rates,

(*c*) $AB+B$ (delayed) rate corrected by using an AB rate curve taken over a comparatively short time interval $\sim$8 hr. The standard error has been increased to take account of the statistics of the short duration AB curve,

(*d*) Results in Column (*c*) plus an estimated scattering correction.

Inasmuch as the scattering correction for this arrangement is small, the correction was estimated from the "second correction" of Germain,[11] multiplied by a factor $(2\pi)^{\frac{1}{2}}$ as suggested by York.[12] As a rough check on Germain's calculations, an approximate calculation was made to determine an upper limit of the scattering loss for our apparatus. The result was 8 percent for the maximum absorber thickness as compared to 5 percent from Germain's calculation; the latter were used in obtaining the last column (*d*) of the $AB+B$ (delayed) rates.

It is seen that the difference is insignificant between columns (*a*) and (*b*) and substantially within the error limits for columns (*a*) and (*b*), (*c*), or (*d*). The insignificant difference between columns (*a*) and (*b*) indicates that the ratio $AB+B$ (delayed)/AB was a constant for a given absorber thickness. Since, as indicated in the foregoing, the tank detects essentially all μ mesons, whereas only a fraction of the decay betas are detected, the constancy of this ratio is at least a first order check of the tank stability. In addition, this constancy points to the absence of afterpulsing.

The differential range spectrum obtained from the column (*d*) $AB+B$ (delayed) rates of Table II has been fitted to the curve given by Rossi[13] and is plotted in Fig. 2. The values used for Fig. 2 have also been used to obtain a plot of the differential momentum spectrum.[14] The corresponding ordinates are plotted in Fig. 3, together with the momentum spectrum given by Rossi. The agreement in Fig. 2 is fairly good with the possible exception of the lowest point. Because of the excessive ratio of the thickness of the tank to the mean range (i.e., range corresponding to the center of the tank) for this lowest point, one might expect some disagreement. Furthermore it must be noted that the normalization procedure compares ordinates at the higher values of absorber where the spectrum is flat with values at little or no absorber where the spectrum is decreasing rapidly. Despite these considerations, a graphical analysis shows that the lowest point (11.1 g/cm^2) is plotted correctly, provided that the range spectrum is linear throughout the region 11.1$\pm$8.7 g/cm^2: a reasonable estimate of the nonlinearity correction for the mean range of the lowest point is

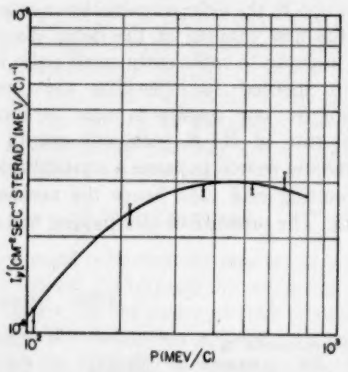

FIG. 3. Differential momentum spectrum of cosmic-ray μ mesons at sea level. The experimental points plotted in Fig. 2 have been transformed with the range-momentum relations and are shown together with the spectrum given by Rossi (see reference 14) (smooth curve).

[8] The conversion was made by using the Gross range-energy tables for Pb and air. [E. P. Gross, *Range, Energy, Ionization Curves* (Princeton University Press, Princeton, New Jersey, 1947)].

[9] H. P. Koenig, Phys. Rev. **69**, 590 (1946).

[10] See E. P. Gross, reference 8.

[11] L. Germain, Phys. Rev. **80**, 618 (1950).

[12] C. M. York, Phys. Rev. **85**, 1002 (1952).

[13] See Fig. 6, B. Rossi, Revs. Modern Phys. **20**, 543 (1948).

[14] See reference 13, Fig. 24 and Fig. 4.

-3 percent. Hence, it does not appear possible to bring this point into good agreement with the curve.

The possibility that there might be a distortion of the counting rates because of afterpulsing or because of high random background is rendered unlikely by the fact that the delay rates in channels 2 to 4 show the same variation.

The lifetime data for the cosmic-ray μ mesons are shown in Fig. 4, in which are plotted the counting rates in each channel (corrected for random counts) as a function of the delay of the channel. One of these curves represents the delay distribution of a separate run of $B+B$ (delayed) events; the other is compiled from the delay distribution of $AB+B$ (delayed) events obtained in the range spectrum runs. The lifetimes, computed by the method of Peierls[15] are 2.13 ± 0.07 μsec and 2.18 ± 0.07 μsec. The errors are standard errors and do not include an estimate of systematic errors. Somewhat more reliance is placed on the first (lower) value since GM counters were not used in this measurement. The former value is also in good agreement with that of Bell and Hincks[16] 2.12 ± 0.02 and with the value 2.10 ± 0.02 obtained by Harrison, Cowan, and Reines[17] in a 12-hour run with their 300-liter scintillation tank.

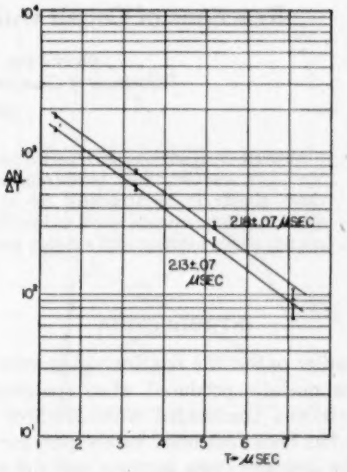

FIG. 4. Delay distribution of $B+B$ (delayed) events (lower curve) and $AB+B$ (delayed) events (upper curve) in the 4-channel delay discriminator.

VI. DISCUSSION

The results of this experiment are essentially similar to those of Sands,[18] who used a delayed coincidence technique. In general it appears that all the differential range methods in which fairly good identification of mesons is possible give results somewhat higher than those obtained by magnetic measurements in cloud chambers.

The earlier delayed-coincidence technique suffered from the disadvantage that only relative results were obtainable. However, the present method should permit a determination of the absolute intensity of mesons, particularly in the region below 300 Mev/c where the scattering correction can be kept quite small. It should be noted that this conclusion has been arrived at independently by at least one cloud-chamber investigator,[19] who has studied this portion of the cosmic-ray spectrum. Aside from its phenomenological importance, the *absolute* low-energy meson spectrum is significant in analyzing cloud chamber and differential absorption data for protons in the cosmic radiation. Although in this experiment only relative readings were taken, the method is readily adaptable to a precision determination of the absolute differential range spectrum of low-energy mesons, a region of the spectrum where some uncertainty[12,19] exists. In performing such an experiment, one can use a large plastic or liquid scintillator with (or without) a direction-defining telescope.[20]

VII. ACKNOWLEDGMENT

We wish to thank Dr. H. A. Morewitz for his assistance in the initial stages of the experiment.

[15] R. Peierls, Proc. Roy. Soc. (London) **A149**, 473 (1935).
[16] W. E. Bell and E. P. Hincks, Phys. Rev. **88**, 1424 (1952).
[17] Harrison, Cowan, and Reines, Nucleonics **12**, 44 (1954).
[18] M. Sands, unpublished data cited by Rossi.
[19] P. G. Lichtenstein, Phys. Rev. **93**, 858 (1954).
[20] Shortly before submission of this paper, a report of essentially this experiment has come to our attention. N. T. Seaton Bull. Am. Phys. Soc. **29**, No. 6, 18 (1954).

Reactions of Cobalt with Protons at 60, 100, 170, and 240 Mev*

GENEVIEVE D. WAGNER† AND EDWIN O. WIIG
Department of Chemistry, University of Rochester, Rochester, New York

(Received August 13, 1954)

Absolute cross sections are reported for the production of the nuclides Co^{58}, Co^{56}, Co^{55}, Fe^{52}, Mn^{54}, Mn^{52}, Mn^{51}, Cl^{39}, and $Cl^{38,34}$ from bombardment of Co^{59} with protons of energies 60, 100, 170, and 240 Mev. The yields appear to be accounted for at the lower energies by a combination of compound nucleus model, knock-on cascade model and for the production of chlorine isotopes a fission mechanism. A knock-on cascade model together with a fission mechanism may be used to explain the yields at the higher energies.

INTRODUCTION

IN an earlier paper[1] the relative yields were reported for the nuclides produced when spectroscopically pure cobalt was bombarded with 240-Mev protons. The work has been continued for the purpose of determining the absolute cross sections and the excitation functions from 60 to 240 Mev of nine of the product nuclides. Data of the latter type are of interest in connection with current theories[2] of high-energy nucleon-nucleus interactions and there is a paucity of such data. Similar studies of the spallation product yields from 60- to 240-Mev protons on vanadium, yttrium, and cesium have been completed in this laboratory.

Rudstam[3] has reported the yields relative to Cr^{49} of a number of nuclides produced by the reaction of 187-Mev protons on cobalt but none of the nuclides reported here was investigated. Where some of the nuclides were studied earlier by us at 240 Mev, Rudstam's yields compare favorably with ours. Belmont[4] has determined the absolute cross sections at 370 Mev of the nuclides for which we report data to 240 Mev. His values, which have been included in our graphs for the sake of completeness, are in every case consistent with ours.

EXPERIMENTAL

Cobalt sponge powder (spectroscopically pure) wrapped in 1-mil aluminum foil shaped in the form of an envelope $\frac{1}{16}$-in. square in cross section and $1\frac{1}{4}$ in. long was bombarded in the internal beam of the Rochester 130-inch synchrocyclotron at radii corresponding to energies of 60, 100, 170, and 240 Mev. The targets could be considered thin since the expected energy loss was less than 2 Mev. Chemical separations and identification of nuclides have already been described.[1] Samples were counted with end-window, helium-filled, alcohol-quenched Geiger-Müller tubes with thin mica windows (1.5–1.9 mg/cm^2).

The production of Na^{24} by the reaction $Al^{27}(p,3pn)Na^{24}$, the cross section of which has been determined at high energies,[5,6] was selected as the monitor for the proton beam striking the cobalt target. For this purpose four sheets of 1-mil aluminum foil were used, two each placed on the front and back of the target envelope. In the determination of the yield of Na^{24}, only the two inner foils were used in order to insure compensation for recoils[7] out of the foils. In each experiment the yield of the product nuclide Co^{55} was used as an internal standard. It was counted in the same geometry as all other samples, including the monitor foils.

In the calculation of the yields to infinite bombardment time, the following corrections to the observed counting rates were considered: (1) background, (2) coincidence loss, (3) decay of the nuclide after bombardment, (4) percent chemical yield, (5) mode of decay, (6) absorption by air and the counter window, (7) back scattering, (8) scattering from the walls of the counter housing and the air between the sample and the counter window, (9) self-scattering and self-absorption, and (10) counter efficiency for electromagnetic radiation.

The first four of these corrections are easily made. The decay schemes of the nuclides included in this study are well-known with the exception of Co^{56}, where there is an uncertainty of 25 percent in the branching ratio for orbital-electron capture. Correction for air and window absorption was made by the method of Gleason, Taylor, and Tabern.[8]

Since many conditions affect the back scattering of beta-emitters, empirical correction factors were determined for the specific types of mounting and counting used in these experiments. To obtain these factors, standard samples of Na^{22} (positron emitter) and of an equilibrium mixture of Sr^{90}-Y^{90} (negatron emitters) were mounted on thin Zapon films and on disks identical

* The investigation was supported by the U. S. Atomic Energy Commission. This report is based on a thesis submitted by Genevieve D. Wagner in partial fulfillment of the requirements for the Ph.D. degree at the University of Rochester, 1952.

† Present address: Lewis Flight Propulsion Laboratory, National Advisory Committee for Aeronautics, Cleveland, Ohio.

[1] G. D. Wagner and E. O. Wiig, J. Am. Chem. Soc. 74, 1101 (1952).

[2] See E. Segrè, editor, *Experimental Nuclear Physics* (John Wiley and Sons, Inc. New York, 1953), Vol. II, p. 141.

[3] S. G. Rudstam, Phil. Mag. 44, 1131 (1953).

[4] E. Belmont, U. S. Atomic Energy Commission Report NYO 3198, 1952 (unpublished).

[5] L. Marquez and I. Perlman, Phys. Rev. 81, 953 (1951); L. Marquez, Phys. Rev. 86, 405 (1952).

[6] N. M. Hintz and N. F. Ramsey, Phys. Rev. 88, 19 (1952).

[7] S-C. Fung and I. Perlman, Phys. Rev. 87, 623 (1952).

[8] Gleason, Taylor, and Tabern, Nucleonics 8, No. 5, 12 (1951).

with those used in other experiments. All counting of samples was done with a half-inch stainless steel block backing under the disks, i.e., under conditions of saturation back scattering. The observed counting ratios checked favorably with the literature values except that the difference for positron and negatron sources was of the order of 3 percent, rather than 10 percent as reported by Seliger.[9]

No correction for wall scattering of β rays was used, since the change in the counting rate with and without housing was within that expected for the error in the corresponding sample to window distances. Burtt[10] observed a change in counting rate of the order of 1 percent for a similar counter housing. Interpolation of the data of Nervik and Stevenson[11] was used to obtain the correction for self-scattering and self-absorption for the beta emitters studied.

For γ rays the usual counter efficiency of 1 percent was used. In the case of capture processes with little or no electron conversion and accompanied by γ emission, as for Co^{55}, an efficiency of 5 percent was taken for the type of counter used. This value was compatible with the ratio of counting rates due to beta emission to the total counting rate of the sample as observed in aluminum absorption curves for nuclides of known branching ratio.

For each nuclide the error in the counting rate at infinite bombardment was obtained from the square root of the sums of the squares of the estimated errors in each of the correction factors just discussed and that caused by irreproducibility of area of the sample used for counting. The probable errors in the values of the absolute cross sections given in Table I were then obtained from the square root of the sum of the squares of the error just calculated for a given nuclide and for Co^{55} (the internal monitor) and the error in the cross section for Co^{55} (which takes account of the errors in the counting rate of Na^{24}).

TABLE I. Experimental values of the cross sections in millibarns.

Nuclide	240 Mev	170 Mev	Energy 100 Mev	60 Mev
Co^{58}	140±70	180±90	310±155	960±480
	110±55	190±95	450±225	770±385
	110±55		330±165	
Co^{56}	26±13	29±15	75±38	130±65
	20±10	31±16	110±55	110±55
	20±10		81±41	
Co^{55}	6.6±1.3	9.4±1.9	21±4	5.7±1.1
		9.3±1.9		
Fe^{52}	0.67±0.20	0.65±0.19	0.47±0.14	0.0006±0.0003
	0.59±0.18	0.65±0.19	0.62±0.19	0.0012±0.0006
			0.58±0.18	
Mn^{56}	16±4	11±3	14±3	15±3.8
	16±4	12±3	14±3	8.6±2.3
	9.0±2.3		14±3	
Mn^{52}	42±10	31±8	36±9	1.2±0.3
	39±10	31±8	40±10	1.5±0.4
	23±6		31±8	
Mn^{51}	18±6	4.9±1.7	6±3	...
	14±5	6.7±2.3		
Cl^{39}	0.07±0.05	0.011±0.008		
	0.23±0.16	0.003±0.002	...	...
$Cl^{38,34}$	0.15±0.08	0.018±0.009	0.11±0.06	0.006±0.003
	0.22±0.11	0.018±0.009	0.03±0.02	0.004±0.002
Na^{24}	11.7[a]	13.2[a]	15.2[b]	14.0[b]

[a] Interpolated values.
[b] Values given by Hintz and Ramsey. (See reference 6)

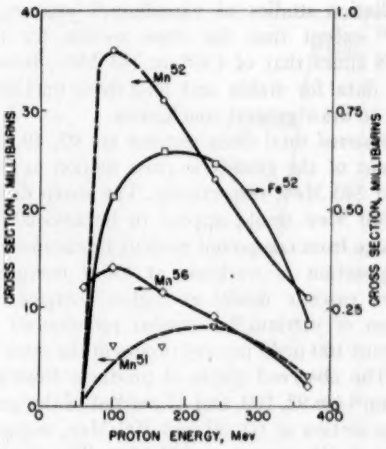

FIG. 1. Yields of Mn isotopes and Fe^{52} from Co^{59} as a function of proton energy. The arrows on each curve point to the appropriate ordinate scale.

RESULTS AND DISCUSSION

The experimental cross sections obtained for nine nuclides at energies of 60, 100, 170, and 240 Mev are presented in Table I. The first two values for Mn^{52} and Mn^{56} in the table appear to be about twice the actual value. The third values given agree closely with the relative yields obtained in the first studies[1] at 240 Mev. There appears to be some experimental error associated with the manganese fractions for these two runs. The source of this difficulty is not completely understood but appears to be associated with the chemical yield for these fractions. The lower values for these isotopes are shown in Fig. 1. In addition, the values for Mn^{51}, both obtained from the same chemical fractions which gave the larger values for the other two isotopes, were reduced by the same factor before plotting the data in Fig. 1. These values are all consistent with Belmont's values[4] at 370 Mev.

From the table it is seen that the yield of Co^{58} is largest at all energies, while that of Co^{56}, which is second largest at 60 and 100 Mev, is surpassed at the higher energies by the $(Z\text{-}2)$ nuclide Mn^{52}. The yields of the latter are minimum values since the isomer, Mn^{52m}, has not been included. Similar relative yields as a function of energy are in general observed in

[9] H. N. Seliger, Phys. Rev. **78**, 491 (1950).
[10] B. P. Burtt, Nucleonics **5**, No. 2, 28 (1949).
[11] W. E. Nervik and P. C. Stevenson, Nucleonics **10**, No. 3, 18 (1952).

the spallation studies of vanadium,[12] yttrium,[13] and cesium,[14] except that the cross section for Cs^{131} is almost 8 times that of Cs^{122} at 240 Mev. Because of lack of data for stable and long-lived nuclides it is difficult to draw general conclusions.

The *observed* total cross sections are 92, 49, 25, and 20 percent of the geometric cross section at 60, 100, 170, and 240 Mev, respectively. The sharp drop from 60 to 100 Mev would appear to be associated with the change from compound nucleus formation followed by evaporation of nucleons at lower energies to a knock-on cascade model at higher energies. In the spallation of yttrium,[13] a similar pronounced change from about 100 to 43 percent occurs in the same energy range. The observed yields of products from protons on cesium[14] are 92, 100, and 87 percent of the geometrical cross section at 60, 80 and 100 Mev, respectively, dropping to 53 percent at 150 Mev. The results with cesium may reflect the influence of the larger size of the nucleus.

Cobalt Yields

The cross sections for Co^{58}, Co^{56}, and Co^{55} as a function of proton energy are shown in Fig. 2. The yields of Co^{58} and Co^{56} decrease continuously with proton energy while that of Co^{55} exhibits a maximum value in the region of 100 Mev. The threshold for the reaction $Co^{59}(p,p4n)Co^{55}$ is less than the lowest energy, 60 Mev, available in this study. The yields of Co^{55} are always smaller than those for Co^{56}, as might be expected.

The excitation function for Co^{58} beyond 60 Mev is in general the same as that for C^{11} from C^{12}, which has

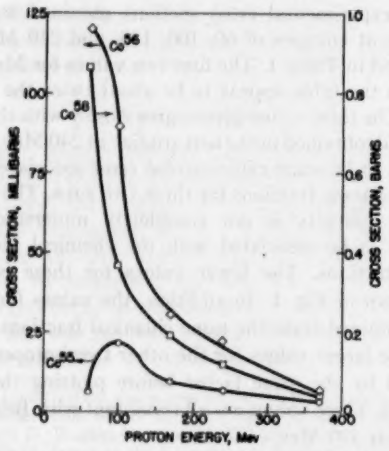

FIG. 2. Yields of Co isotopes from Co^{59} as a function of proton energy. The arrows on each curve point to the appropriate ordinate scale.

[12] C. G. Heininger, Jr., Ph.D. thesis, University of Rochester, 1954 (unpublished).
[13] A. A. Caretto, Jr., Ph.D. thesis, University of Rochester, 1953 (unpublished).
[14] R. W. Fink and E. O. Wiig, Phys. Rev. **96**, 185 (1954).

been studied[15] up to 340 Mev, except that the cross section for Co^{58} is of the order of ten times as great as that for C^{11}. Qualitatively, the high yield of Co^{58} in the lower-energy range is understandable in view of the possible contributions from (1) the charge exchange process to form Ni^{59} followed by evaporation of a proton, (2) the contribution of the pickup process[2] with the emission of a deuteron, and (3) the favorable competition of the (p,pn) process over the $(p,2n)$ owing to the greater level density of the odd-odd product nucleus of the former process as compared to the even-even product nucleus of the latter. Ghoshal[16] has shown this for reaction of low-energy protons on Cu^{63} to produce Cu^{62} and Zn^{62}.

In the energy range beyond 100 Mev, where the knock-on cascade model would be expected to apply, the yields of Co^{58} relative to other nuclides produced appear high but are consistent with the yields of the analogous $(A\text{-}1)$ nuclides produced at high energies from C^{12}, Y^{89},[13] Cs^{133},[14] and Cu^{63}.[17] These Co^{58} cross sections are also consistent with that of Belmont[4] at 340 Mev.

Iron and Manganese Yields

The cross sections for the formation of Mn isotopes and Fe^{52} are shown in Fig. 1. The relatively high yield of Mn^{56} at 60 Mev would seem to indicate compound nucleus formation and the reaction $Co^{59}(p,pHe^3)Mn^{56}$ or a similar reaction. This process together with contribution from the knock-on model may account for roughly the same yields at 100 to 170 Mev.

The yields of Co^{56}, Co^{55}, and Mn^{52} at 100 Mev are roughly of the same order of magnitude (21–89 mb) and again at 170 Mev (9–31 mb). This would seem to suggest that an excited Co^{55} or Co^{57}, rather than an excited iron nucleus, remains as a result of the initial nuclear collision and cascade process. Subsequent evaporation of neutrons to form Co isotopes or an alpha-particle and neutrons to form Mn^{52} readily accounts for these nuclides. Evaporation of neutrons from an excited Fe^{58} or Fe^{57} would favor formation of stable iron isotopes or Fe^{55}. Facilities for detection of the latter were not available at the time this work was performed. This shielding of Fe^{52} by stable Fe^{54}, Fe^{56}, Fe^{57} and long-lived Fe^{55}, and the favored emission of alpha particles from an excited Co nucleus may serve to account for the high yield of Mn^{52} relative to Fe^{52}. Also, evaporation of neutrons from excited iron nuclei to form Fe^{52} would necessarily involve Fe^{53} as one step. Since the latter is neutron-deficient the "governor" factor[2,18] which reduces departure from the region of stable nuclei in the cooling process, would be operative. Loss of a proton would be energetically less

[15] Aamodt, Peterson, and Phillips, Phys. Rev. **88**, 739 (1952).
[16] S. N. Ghoshal, Phys. Rev. **80**, 939 (1950).
[17] Batzel, Miller, and Seaborg, Phys. Rev. **84**, 671 (1951).
[18] K. S. LeCouteur, Proc. Phys. Soc. (London) **A63**, 259 (1950).

difficult than loss of an additional neutron and Mn^{52} would result, rather than Fe^{52}.

LeCouteur[18] has calculated the probability of alpha-particle emission from an excited nucleus by using the evaporation model. By basing the calculations on a nucleus of mass 98, the ratio of the probability of alpha emission to that for proton emission was found to vary from 0.3 to 0.5 for excitation energies from 30 to 400 Mev. Hodgson[19] in a study of stars produced in photographic emulsions by 50–125 Mev protons on silver and bromine found strong evidence that alpha particles take part. The proportion of alpha particles among all the particles emitted showed no significant variation with energy. About 25 percent of the cascade particles were found to be alpha particles and there was no significant difference in yield between evaporation and cascade alpha particles. If the excited nucleus were iron, then neither Mn^{52} nor Fe^{52} could be formed by an alpha process. In the event where charge exchange occurred between the incident proton and a neutron in the nucleus, leaving an excited Ni nucleus, Fe^{52} could be formed by evaporation of an alpha particle whereas Mn^{52} would require an alpha particle and a proton. Since the yield of Mn^{52} is so very much greater than that of Fe^{52}, either this process is unimportant or Fe^{52} formation is blocked by the formation of stable iron isotopes.

Chlorine Yields

Some activity was observed in all chlorine fractions, even those from targets bombarded at 60 Mev. At the lower energies all this activity appeared to have a half-life consistent with the presence of Cl^{38} and/or Cl^{34}. Because of the difficulty in resolving the decay curve, it was not possible to rule out the presence of Cl^{39} at these energies and the cutoff for the formation of this nuclide, shown in Fig. 3 to be at some energy greater than 100 Mev, may be merely the reflection of experimental difficulties.

The formation of chlorine isotopes requires a large loss of nucleons from the target nucleus. Bernardini *et al.*[20] have found that the cutoff for charged particle emission, as observed in photographic plates, appears to be at eight particles for incident proton energies of 350–400 Mev. From an examination of the angular distribution of the particles, they found that about

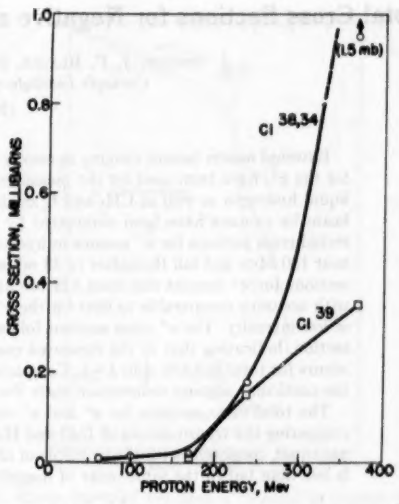

FIG. 3. Yields of Cl isotopes from Co^{59} as a function of proton energy.

40 percent were the result of a knock-on process, i.e., associated with the nucleonic cascade, and about 60 percent were evaporation nucleons. Assuming the maximum energy for such evaporation particles, about 30 Mev, such an eight particle event corresponds to a transfer of about 150 Mev of excitation energy to be dissipated by evaporation. Since such an event would be expected to be accompanied by evaporation of a large number of neutrons not observable in an emulsion, this energy estimate is conservative. Thus, it is not difficult to imagine how chlorine could be formed from a cobalt target nucleus with protons of high energy, particularly if aggregates of nucleons, such as alpha particles, are taken into consideration.

For protons in the 60- to 100-Mev range, it is difficult to imagine such formation on the basis of loss of individual nucleons. At these energies an event in which the nucleus undergoes a type of fission is a more reasonable picture, since the energy requirements for such a process are less than for the former.[21] It is probable that both processes contribute to the yield of chlorine isotopes in the higher energy range.

We wish to thank Professor S. W. Barnes and the crew of the Rochester 130-in. cyclotron for their cooperation in making this study possible.

[19] P. E. Hodgson, Phil. Mag. **45**, 190 (1954).
[20] Bernardini, Booth, and Lindenbaum, Phys. Rev. **85**, 826 (1952).
[21] R. E. Batzel and G. T. Seaborg, Phys. Rev. **79**, 528 (1950).

Total Cross Sections for Negative and Positive Pions in Hydrogen and Deuterium*

J. ASHKIN, J. P. BLASER, F. FEINER, J. G. GORMAN,† AND M. O. STERN
Carnegie Institute of Technology, Pittsburgh, Pennsylvania

(Received July 2, 1954)

External meson beams, ranging in energy from 135 Mev to 260 Mev for the π^-, and 135 Mev to 198 Mev for the π^+, have been used for the measurement of total cross sections by an attenuation experiment using liquid hydrogen as well as CH_2 and C as absorbers. Possible errors introduced by contamination of the π^+ beam by protons have been eliminated by use of time-of-flight and pulse-height discrimination. The corrected cross sections for π^- mesons in hydrogen rise from 47 mb at 133 Mev to a maximum of about 66 mb near 180 Mev and fall thereafter to 38 mb at 258 Mev, with typical uncertainties of ±5 percent. The cross sections for π^+ mesons rise from 122 mb at 128 Mev to around 200 mb between 170 Mev and 196 Mev, with accuracy comparable to that for the π^- mesons except for the very high energies where the beams are of low intensity. The π^+ cross sections follow very well the curve representing three times the total π^- cross section, indicating that in the measured energy range the dominant interaction between pion and nucleon occurs for total isobaric spin $I=\frac{3}{2}$. Comparison of the π^- cross section with $(8/3)\pi\lambda^2$ supports the idea that the particular angular momentum state $J=\frac{3}{2}$, $L=1$ (for $I=\frac{3}{2}$) is especially prominent in the scattering.

The total cross sections for π^+ and π^- mesons interacting with deuterium have also been measured by comparing the transmissions of D_2O and H_2O cells. Within the accuracy, the π^+ and π^- total cross sections are equal, consistent with the principle of charge symmetry. The total scattering cross section of deuterium is less than but of the same order of magnitude as the sum of the hydrogen cross sections for π^+ and π^-.

ATTENUATION measurements, made at this laboratory, of the total interaction cross section of negative pions in hydrogen have been reported previously.[1] They give results in good agreement with the extensive work at Chicago,[2-4] reaching up to 217 Mev for the pion energy, and extend the measurements to 260 Mev, well beyond the maximum in the total cross section.

Since then we have found it possible to obtain energetic positive pion beams from the synchrocyclotron which are weak in intensity but strong enough to allow a comparison of the positive pion cross section with that for negative pions up to an energy of 200 Mev. Such a comparison is essential in any attempt to discover the states of isobaric spin and angular momentum which are prominent in the scattering. The range of the present measurements is from 128 to 196 Mev for positive pions and 133 to 258 Mev for negative pions. We have also measured the total cross sections of deuterium by finding the difference in transmission of heavy water and ordinary water.

Following is a more detailed presentation of the results obtained and the methods used. The major part of the discussion is concerned with the hydrogen experiments. At the end there is a brief report of the heavy water—ordinary water differences and their possible significance.

I. EXPERIMENTAL METHOD

A. General Arrangement

Figure 1 shows a plan view of the Carnegie Tech Cyclotron taken in the plane of the beam. The pions produced when the 440-Mev protons strike an internal copper or beryllium target are analyzed and focused by the fringing field of the cyclotron and enter the experimental area through channels in the lead and concrete shield wall, 8 feet thick. A 45°-sector deflecting magnet of aperture 4 in.×4 in. serves to purify the beam and provides double focusing of an incident parallel beam at a distance of two meters from the magnet exit. At a given channel set for the detection of negative pions, one can obtain a positive pion beam of the same energy, traversing the same trajectory but unfortunately greatly reduced in intensity, by reversing the direction of the circulating proton beam, thereby taking the pions produced in a backward direction with respect to the proton beam.

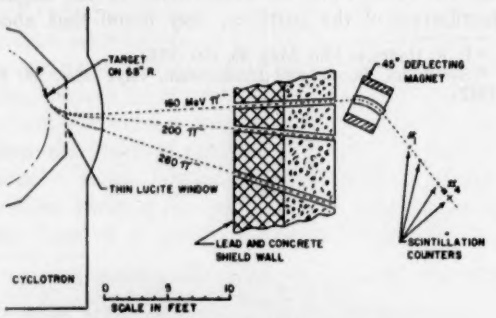

FIG. 1. General experimental arrangement.

* Research partially supported by the U. S. Atomic Energy Commission.

† A thesis based on this work has been submitted by J. G. Gorman in partial fulfillment of the requirements for the degree of Doctor of Philosophy at Carnegie Institute of Technology.

[1] Ashkin, Blaser, Feiner, Gorman, and Stern, Phys. Rev. **93**, 1129 (1954).

[2] Anderson, Fermi, Long, Martin, and Nagle, Phys. Rev. **85**, 934 (1952).

[3] Fermi, Glicksman, Martin, and Nagle, Phys. Rev. **92**, 161 (1953).

[4] M. Glicksman, Phys. Rev. **94**, 1335 (1954); the scattering of 187-Mev π^- mesons has also been measured (private communication).

For a measurement of total cross section, the pions are made to pass through a monitoring telescope of three scintillation counters in coincidence recording the number of particles incident, and then through an absorber (liquid hydrogen) to a fourth detecting counter, in coincidence with the monitor. The typical transmission geometry for the negative pion measurements is shown in Fig. 2. Ideally, the cross section is obtained by comparing the transmissions (ratio of quadruple coincidences, hereafter called Q, to triple coincidences, hereafter called T) with and without the absorber. Thus, if σ is the total cross section per atom of the absorber and N is the surface density of the absorber in atoms/cm^2,

$$\exp(-N\sigma)=\frac{(Q/T)_{\text{absorber}}}{(Q/T)_{\text{no absorber}}}. \quad (1)$$

In practice, the final cross section is obtained only after suitable corrections have been made for contamination of the pion beam, chance coincidences, scattering through small angles, etc., as we shall see in the following.

As far as possible, we have aimed at an over-all accuracy of three to five percent in the measurements.

B. Production and Composition of the Pion Beams

For producing the negative pions we used a beryllium target of dimensions 2 inches in the direction of the proton beam, $\frac{1}{2}$ inch high, and $\frac{1}{4}$ inch thick. The three-fold coincidence rate in the standard geometry, Fig. 2, ranged, in counts/min, from 100 000 for the 135-Mev negative pions to 2000 for the 260-Mev negative pions. For producing the positive pions a $\frac{3}{4}$-inch by $\frac{1}{2}$-inch by $\frac{1}{4}$-inch copper element was used. The three-fold coincidence rate in the time-of-flight geometry, Fig. 6, ranged, in counts/min, from 5300 for the 135-Mev positive pions to 150 for the 198-Mev positive pions.

The choice of target was not based on a detailed study. But in comparing the above two, we found that the beryllium gave about five times the intensity of 260-Mev negative pions while the intensity at 135 Mev

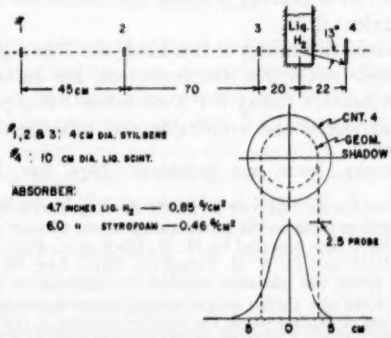

FIG. 2. Transmission geometry for the negative pion measurements. The curve represents the beam profile taken along the horizontal diameter of counter No. 4 (160-Mev π^- beam).

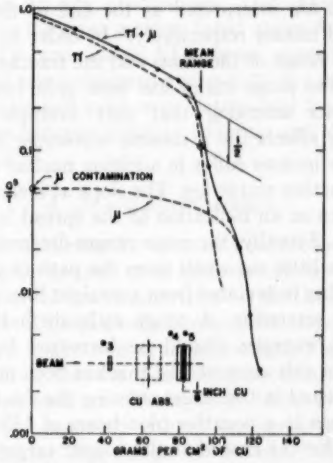

FIG. 3. Range curve of 194-Mev π^- mesons in copper, showing decomposition into pions and muons and construction of the mean range.

was the same. The copper gave about four times the intensity of positive pions at 160 Mev and usable intensities at higher energies where positive pions from the beryllium target escaped detection.

It is of course important to have a more precise indication of the energy of the pion beams than is provided by the nominal values associated with each channel. In addition the extent of the beam contamination has to be measured. For the negative pion beams, the principal contamination consists of muons of the same momentum following the pion trajectory, and a small fraction of electrons. For the positive pion beams, the major contamination consists of a very large number of low energy protons having the same momentum as the pions.

In order to determine the energy of the beams and the extent of the contaminations, we took integral range curves with copper absorber. For this purpose we used, besides the monitor, two detecting counters separated by a $\frac{1}{8}$-inch copper absorber in the configuration indicated in the inset of Fig. 3. The effect of the additional counter and thin absorber was to discriminate against neutron and proton star fragments that might otherwise give a false indication especially near the end of the pion range. (Clean range curves were nevertheless taken with only one detecting counter in the case of the positive pion beams.)

Figure 3 represents a typical range curve and shows how the beam energy[5] and the μ contamination are obtained graphically. The copper absorber was built up symmetrically about a fixed point (center of the total absorber required). This gives range curves with more constant initial slope. The two sharp drops in

[5] We used the range-energy relation of W. A. Aron, University of California Radiation Laboratory Report UCRL-1325, 1951 (unpublished).

the curve are interpreted as the end of the range of pions and muons respectively.[6] In order to determine the mean range of the pions and the fraction of muons present, the range curve has been split into π and μ components assuming that only multiple Coulomb scattering affects the μ mesons traversing the copper, whereas π mesons suffer in addition nuclear absorption and diffraction scattering. The slope at mean range has been taken as an indication of the spread in energy of the beam. Actually, the mean ranges determined in this way are a little too small since the path of the pion in the absorber is deviated from a straight line by multiple Coulomb scattering. A rough estimate indicates that the mean energies should be increased by about 1 percent on this account and this has been done for the energies listed in the tables showing the final results.

Electrons in a negative pion beam of 135 Mev were detected for the case that the copper target was used. The range curve, when compared with one for a beam of the same energy produced with the usual beryllium target, showed a pronounced penetrating tail, not previously encountered, and interpretable as a residue of electrons. The contaminated beam was estimated to have between 5 and 10 percent of electrons by comparing cross sections measured in the two beams. The absence of such tails in all range curves for the actual beams used justifies neglect of the electron contamination. This is consistent with the experience of Martin[7] with the 450-Mev Chicago cyclotron.

As already mentioned, we discovered early in our investigation of the positive pion beams that especially those of high energy were very badly flooded with low-energy protons coming from the meson target and elsewhere in the cyclotron. Elimination of these protons was the major problem in the positive pion measurements and will be discussed in detail later in Sec. IV. The beams remaining after removal of the protons were analyzed by measuring integral range curves in the manner previously described to give the energies and muon contaminations listed in Table VII. We found no evidence for any appreciable positron contamination of the beams in spite of the fact that the copper meson target was used. This is in agreement with measurements of Bodansky *et al.* at Columbia[8] and shows that at the same energy the positive pion beams have much smaller electron contaminations than do the negative pion beams.[9]

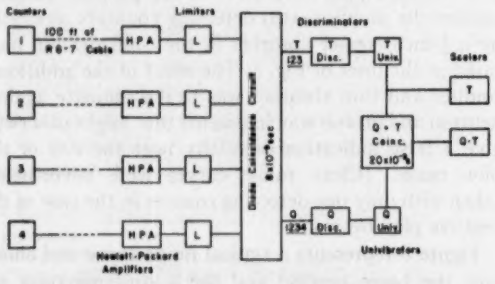

FIG. 4. Block diagram of the electronics.

C. Detection Equipment

For various practical reasons (see Sec. I D), the absorbers used in the measurements have been chosen of such a size that they produce relatively small changes in transmission, in some cases as small as two percent. To achieve an accuracy of something like three percent in the cross section, therefore, requires that the transmissions be reliably measured to better than one part in 1000. This puts rather stringent requirements on the detection apparatus. Small drifts in the electronic equipment, deadtime in the detection, background counts, etc., must be seriously considered for their effect on the final accuracy.

1. Stability

As shown in the block diagram of Fig. 4, the pulses from the scintillation counters are amplified in wide-band distributed amplifiers, then limited to about 1.5 volts and clipped by shorted stubs to a length of 8 mμsec. They are fed into a multiple coincidence circuit using crystal diodes,[10] providing fast outputs for the monitor triples $T(123)$ and transmitted quadruples $Q(1234)$. In general these output pulses vary around a certain average height, the fluctuations being mainly due to time-jitter and statistical variations in ionization and photoelectron emission. In addition some mesons may traverse the edge of a counter and thereby produce smaller output pulses. Because of this inherent ambiguity in pulse size, the transmission Q/T, as obtained from direct counting of Q and T, depends on the settings of the T and Q output discriminators and will vary by as much as a percent if these discriminators undergo independent drift.

To avoid difficulties of this kind, the T and Q pulses, after their respective discriminators, are transformed by univibrators (using E F P-60 tubes[11]) into pulses of constant shape and amplitude and subsequently put

[6] Only μ mesons having traversed the focusing magnet have a defined range and can be detected by this method. μ mesons originating from π decays occurring after the focusing magnet could be hidden under the curve as they do not have a unique energy. As their number cannot exceed about 2 percent, their possible effect has been incorporated in the error attributed to the determination of the μ contamination.

[7] R. L. Martin, Phys. Rev. **87**, 1052 (1952).

[8] Bodansky, Sachs, and Steinberger, Phys. Rev. **93**, 1367 (1954).

[9] The reason for this may be partly the large excess of positive over negative pions in the production process. π^+ to π^- ratios of 7 to 10 have been reported by M. M. Block *et al.*, Phys. Rev. **88**, 1239 (1952), and by A. H. Rosenfeld, Phys. Rev. **95**, 638 (A) (1954). Since the absolute number of electrons or positrons coming from the meson target should be proportional to the production of neutral pions, the relative number in the π^+ beam should be a factor 7 to 10 smaller than for the π^-.

[10] S. DeBenedetti and H. J. Richings, Rev. Sci. Instr. **23**, 37 (1952).

[11] J. Fischer, University of Chicago (private communication).

into coincidence. The Q discriminator is adjusted so as to accept even very small Q pulses, whereas the T discriminator is set to reject the smaller pulses. By counting in this manner only those Q's which have undergone the secondary Q-T coincidence, and by having T pulses of absolutely constant height, it is guaranteed that only those T's are registered which also act as a possible coincidence partner for a Q and *vice versa*. The resulting ratio Q/T is found in practice to be quite insensitive to drift in either discriminator. Plateaus were obtained with a slope of 0.1 percent over a range of a factor 2 in the T pulse height whereas the T's and Q's alone had a slope of some 10 percent over the same range.

2. Deadtime Effects

The minimum interval in time for two pulses to be counted separately was of the order 0.2–0.3 μsec, this being the deadtime of the univibrators. With the more intense negative pion beams, at intensities desirable for good statistics, the probability for one pion to be followed by another in this time span is several percent. The resulting counting losses would be inadmissibly large were it not for the effect of the secondary Q-T coincidence circuit.

If one makes the deadtime of the T univibrator the longer one, it is easy to see that the second of two mesons separated by an interval less than this deadtime is eliminated from further consideration by the failure of the T univibrator to send a pulse to the Q-T circuit. The ratio Q/T obtained this way is still correct up to the point where the spacing gets smaller than the resolving time of the secondary coincidence circuit. In the experiment, this time was 0.02 μsec, thereby reducing the error to the cases where two mesons arrive within the same rf cycle (one revolution of the protons circulating with 20 Mc/sec inside the cyclotron). The resulting error was in all cases well below one percent. There is no effect of the 0.1-μsec deadtime of the Hewlett-Packard scalers since all pulses reaching the scalers are spaced 0.3 μsec or more apart.

3. Background

Background events in the monitor telescope will give T's not originating from a complete meson traversal. As long as this rate does not vary, it will not affect the cross-section measurement. But if a few percent of the T's are background events, any variation in machine operation producing a change of 0.1 percent in the contribution of the accidentals is harmful. By the use of three monitor counters it was possible to keep the accidental T's well below one percent, thus avoiding any correction when the cyclotron was normally stable.

Background events in the Q's result mainly from a meson traversing the monitor only and combining with a random count in counter No. 4. Since this happens only when the meson is not transmitted, the effect is proportional to the attenuation. The corresponding correction to the cross section, listed under Accidentals in Table IV and Table VII, never exceeded three percent and was considered accurate to ± 1 percent.

The background rates were determined by inserting delay cables between different counters and the coincidence circuit.[12]

4. Scintillation Counters

The three small monitor counters used for the defining telescope each consist of a stilbene crystal 4 cm in diameter and 0.5 cm thick, viewed from the side by a single RCA 1P21 photomultiplier. The large monitor counter used in the time of flight method, Fig. 6, to be discussed later for the positive pion measurements, consists of a plastic scintillating disk[13] 15 cm in diameter and 1 cm thick mounted with silicone grease in a Lucite holder following the design of Garwin.[14] The pulse height variation over the face of the counter is less than 10 percent.

In all the negative pion measurements, the transmitted particles were detected with a liquid[15] scintillation counter 10 cm in diameter and 2.5 cm thick, enclosed in a Lucite cell, Lucite serving as the light pipe to an RCA 5819. The response of the counter was uniform to within 10 percent. For the π-range curves, two such counters were used. In the positive pion measurements, which required pulse height selection and a better transmission geometry (see Fig. 6), we resorted to a single larger counter. This counter consisted of a plastic scintillating disk 20 cm in diameter, in optical contact at one face with a short Lucite light pipe leading to a DuMont 6292 photomultiplier. The scintillant was thus viewed end-on, the axis of the whole assembly coinciding with the beam. We used a DuMont tube because of its good pulse-height characteristics. In addition, the other face of the disk was machined to a spherically concave surface of such curvature as to give uniform pulses over the entire area of the counter.

D. Absorbers

In deciding on the thickness of absorber to use, it is necessary to make a balance between conflicting requirements. With a thick absorber the attenuation is large and therefore easier to measure accurately. On

[12] It should be noted however that it is not in general possible to find a configuration of delays which enables one to measure the background actually significant for the measurement. This is due to the presence in each counter of random counts, "bunched" counts (those having the periodicity of the circulating proton beam), as well as counts due to simultaneous traversals of several counters.

[13] The plastic scintillator was made by the compression molding technique: G. G. Eichholz and J. L. Horwood, Rev. Sci. Instr. **23**, 305 (1952). We are especially indebted to F. Chen of the Brookhaven National Laboratory for detailed notes on this technique (unpublished).

[14] R. L. Garwin, Rev. Sci. Instr. **23**, 755 (1952).

[15] H. Kallman and M. Furst, Phys. Rev. **81**, 853 (1951).

TABLE I. Absorber data.

Absorber	Density, d g/cm³	Atomic wt.	Thickness, l (cm)	Surface density g/cm²	N (10^{23} molecules/cm³)
C	1.670	12.010	3.173	5.299	2.656
C′	1.670	12.010	4.357	7.276	3.647
CH_2	0.913±0.2%	14.026	6.779±0.2%	6.189±0.35%	2.656±0.009
Liquid hyd.	0.0709	1.008	12.0±0.2	0.85 ±0.02	5.10 ±0.1 (atoms/cm²)
Styrofoam	0.03	...	15.2	0.46	...
D_2O	1.111	20.03	6.447	7.163	2.155
H_2O	0.997	18.02	6.454	6.435	2.151

the other hand, the cross sections in hydrogen show a rather strong energy dependence so that it is advisable to minimize the energy loss of the primary pions in the target. In addition, the forward scattering corrections, discussed in Sec. III, would be even more uncertain for a target that is too long. As a reasonable compromise, we have chosen roughly five inches as the thickness of liquid hydrogen in the beam direction, giving a total energy loss of about 4 Mev for the pions in the hydrogen.

The liquid hydrogen is contained in the inner box (2.5-liter capacity) of a double-walled Styrofoam chamber[16] with the hydrogen exhaust at the bottom of the outer box. With a useful volume of one liter in the region of the beam and an evaporation rate of about 1.3 liters per hour, the desired statistical accuracy in the transmission could usually be obtained with one or two fillings at a given energy. The inner box is lined with a one-mil copper form to prevent the hydrogen from touching the plastic and to define the path length better, although actually the walls shrink by a few percent when cooled to liquid hydrogen temperature. This shrinkage as well as bubbling in the liquid was checked by observing the inside of a similar chamber with clear Lucite covers during a filling and also by measuring the weight of the chamber against depth as the liquid evaporated. To within an uncertainty of ±2 percent, the surface density was measured as 0.85 g/cm² of hydrogen. This uncertainty is taken into account in the final error quoted on the cross sections but should not affect the relative values at different energies. Table I contains the data for the hydrogen chamber.

For some of the transmission measurements we used a set of carbon and polyethylene (CH_2) absorbers. The absorber labeled C in Table I has the same surface density of carbon atoms as does the CH_2, while the one labeled C′ has approximately the same stopping power as the CH_2.

The deuterium measurements, described in Sec. VI, were made with two nearly identical glass cells containing heavy water and water, respectively, as indicated in Table I.

TABLE II. Different transmission geometries. R is the radius of the last counter. θ is the half-angle subtended by the last counter at the center of the liquid hydrogen. r is the radius of the circular intersection of the last counter with the "shadow" cone, defined by rays traversing the extreme edges of the monitor counters. δ is the angular displacement from the edge of the shadow circle to the edge of the last counter, measured at the center of the hydrogen. P.H. = pulse-height method; T.F. = time-of-flight method.

Geometry	R cm	θ deg	r cm	δ deg
π^-	5	13°	3.5	4.0°
P.H. or T.F.	10	13°	4.3	7.5°
T.F.	10	6.4°	4.8	3.4°

II. CHOICE OF GEOMETRY

Because of unavoidable effects due to Coulomb scattering at small angles, it is never possible, with charged particles, to make transmission measurements in very good geometry. Although the multiple small-angle Coulomb scattering in hydrogen can generally be neglected,[17] there remains the effect of single Coulomb scattering insofar as the Coulomb scattering amplitude interferes with the nuclear amplitude for the scattering of the pion. It is therefore essential to make the acceptance angle of the fourth transmission counter large enough so that pions scattered out are practically not affected by the Coulomb interference. To obtain the total nuclear cross section one must then supplement the experimental attenuation with some estimate, based on an assumed angular distribution, of the nuclear cross section for scattering into the acceptance cone of the last counter. It should be noted that with protons as the target nuclei, free to recoil, it is also necessary to estimate the cross section for protons to be projected forward so as to hit the last counter.

With these considerations in mind, the geometry used in the experiments was as follows. For all experiments with the negative pions, the relevant dimensions are indicated in Fig. 2 and Table II. We shall call this the π^- geometry. The half-angle θ subtended by the last counter (radius $R=5$ cm) at the center of the liquid hydrogen is 13° and the "shadow" cone, defined by rays traversing the extreme edges of the monitor counters, intersects the last counter in a circle of radius $r=3.5$ cm. The angular displacement δ from the edge of the shadow circle to the edge of the counter

[16] We wish to thank L. Marshall for information about the Styrofoam target for liquid hydrogen which was used in connection with the proton-proton scattering experiments at Chicago.

[17] The Gaussian distribution for the multiple scattering is characterized by a root-mean-square angle of 0.4 degrees or less.

corresponds to 4° measured at the center of the hydrogen. A pion passing along the axis of the counter system must therefore be scattered through more than 13° to contribute an attenuation, while a pion skimming the extreme edges of the monitor counters need be scattered only slightly more than 4°, but in a limited azimuthal range, to miss the detecting counter.

Because of the Coulomb force, the scattering cross section at 4° becomes quite large, about 60 mb/sterad in the present energy range, compared to 5 or 10 mb/sterad for the purely nuclear elastic scattering of π^-. However, only a small fraction of this scattering near 4° gives an attenuation since most of the 2π azimuth remains within the detecting counter. In addition only a very small fraction of the incident pions traverse the monitor counters near the edge of the shadow cone. This was observed directly by exploring one of the beams (160 Mev) with a 2.5 cm diameter probe counter in the plane of the last detecting counter. The intensity is concentrated in a region of about 2.5 cm vertical extent, with a horizontal variation as shown in Fig. 2. The beam is evidently well concentrated near the central axis. In the neighborhood of 13° it is possible to show from the known angular distributions and estimated phase shifts of the negative pion scattering[3,4] that the Coulomb interference effect is minor. The forward-scattering correction was therefore made by extrapolating the measured elastic scattering cross section[3,4] to zero degrees, without Coulomb forces, and taking for the average forward solid angle that subtended by the last counter at the center of the hydrogen. The size of the correction, taking account of the forward-scattered recoil protons as well as mesons, is indicated in column 6 of Table IV and amounts roughly to 3 mb out of a total cross section ranging from 40 to 65 mb.

For the sake of comparison, most of the experiments with the positive pions were made with essentially the same geometry as just described for the negative pions. The geometry, labeled P.H. (for pulse height), differs from the π^- in having a more favorable angle δ, 7.5° instead of 4°. This was made possible by the introduction of the large 20-cm diameter plastic scintillation counter described earlier. Unfortunately, the correction for the forward scattering of π^+ is much less certain than the corresponding correction for the π^- since the available data[18] on the angular distribution of the positive pion scattering are not as precise. In addition, the correction is relatively more serious since the elastic scattering of the π^+ accounts for all the interaction, while for the π^- the elastic scattering contributes roughly only one third of the total cross section, the charge exchange scattering being more important.[3,4] The extent of the uncertainty is indicated in Table VII, where the forward scattering correction is listed for two widely different assumed angular distributions: (1) isotropic in the center-of-mass system, and (2) $1+3\cos^2\theta$. In the geometry characterized by the 13° half-angle, the difference in the forwarding scattering correction according to the distribution (1) and (2) is more than the estimated uncertainty in the cross section due to all other causes.

For this reason it was decided to make some experiments in the last geometry listed in Table II with half-angle 6.4°, less conservative in regard to the Coulomb interference effect, but safer insofar as the forward scattering correction itself is smaller. Estimates using the π^+ scattering phase shifts of Homa *et al.*[18] and Glicksman[4] show that even at 6.4° the Coulomb interference effect is not very serious. At 170 Mev, for example, the true cross section for nuclear scattering through an angle greater than 6.4° probably differs from the corresponding cross section including the Coulomb effect by not more than 2 or 3 millibarns. The total forward scattering correction for the 6.4° geometry is shown in Table VII at 171 Mev and 196 Mev. The difference between the isotropic and $1+3\cos^2\theta$ distributions is of course greatly reduced. By comparing with the results at 171 Mev using the 13° geometry it is evident that the correction based on $1+3\cos^2\theta$ is nearer to the truth.

III. TOTAL CROSS SECTIONS OF NEGATIVE PIONS IN HYDROGEN

In Table III we have listed the primary transmission data from which the total cross sections are eventually

TABLE III. Transmission data for negative pions in hydrogen.

Energy Mev	Absorber	Triples counts	Quadruples counts	Q/T	σ (uncorrected) 10^{-27} cm^2
133±7	Dummy	351 067	334 629	0.95317±0.00037	38.7±1.1
	Hydrogen	350 405	327 447	0.93448±0.00043	
152±13	C	551 103	466 805	0.84703±0.00053	52.0±1.6
	CH_2	450 782	371 429	0.82396±0.00063	
157±8	Dummy	956 691	912 420	0.95372±0.00022	53.0±0.8
	Hydrogen	1 000 147	928 391	0.92825±0.00027	
179±8	Dummy	471 553	450 944	0.95629±0.00031	58.7±1.0
	Hydrogen	405 844	376 639	0.92803±0.00042	
194±7	Dummy	400 308	382 801	0.95626±0.00033	56.0±1.0
	Hydrogen	500 024	464 653	0.92926±0.00038	
195±7	Dummy	500 176	468 153	0.93597±0.00036	55.2±1.0
	Hydrogen	500 236	455 200	0.90997±0.00043	
215±8	Dummy	451 376	435 282	0.96434±0.00028	49.1±0.8
	Hydrogen	553 174	520 248	0.94047±0.00032	
236±7	Dummy	150 098	144 797	0.96468±0.00049	40.5±1.5
	Hydrogen	160 377	151 547	0.94494±0.00059	
240±7	Dummy	200 069	191 798	0.95865±0.00045	38.4±1.4
	Hydrogen	199 935	187 954	0.94007±0.00055	
258±9	Dummy	60 141	57 439	0.95507±0.0009	33.3±2.7
	Hydrogen	50 133	47 073	0.93896±0.0011	

[18] Homa, Goldhaber, and Lederman, Phys. Rev. **93**, 554 (1954); R. A. Grandey and A. F. Clark, Phys. Rev. **94**, 766(A) (1954); Orear, Tsao, Lord, and Weaver, Phys. Rev. **95**, 624(A) (1954); Fowler, Lea, Shephard, Shutt, Thorndike, and Whittemore, Phys. Rev. **92**, 832 (1953). [The mean energy of the pions has been revised downward from 260 Mev to about 230 Mev (private communication).]

obtained. For each energy investigated[19] we give the transmission Q/T measured with hydrogen absorber and with an empty styrofoam box (dummy), or, as in the case of the 152-Mev point, with CH_2 and C absorbers. The quoted uncertainty in the transmissions is based entirely on counting statistics.[20] The last column of Table III contains the *apparent* or uncorrected cross section given by Eq. (1).

The *experimental* cross section for the geometry used, that is, the proper cross section for removing charged particles from the acceptance cone of the last counter, is obtained only after appropriate corrections are made. Most of these corrections have been mentioned already. Following are the effects to be considered.

(1) Muon contamination. The 5 to 10 percent dilution of the incident beam caused by the presence of muons results in a decrease of the apparent cross section assuming that the muons have no nuclear interaction with hydrogen. For small contaminations we may correct for this by dividing the apparent cross section by the fraction of pions in the beam. The muon contaminations listed in column 3 of Table IV we regard as uncertain to 2 or 3 percent due to inherent difficulties in interpreting the range curve. The electron contamination is considered negligible.

(2) Accidental coincidences. These have been discussed under Background in Sec. I C. On account of background events in the quadruples, the apparent cross section must be increased by the fraction indicated in column 4 of Table IV.

(3) There are a number of other small effects that could be listed. For example, there is a small contribution to the attenuation due to those pion decays, occurring after the monitor, which give rise to muons falling outside the last counter. Since the decay probability depends on the pion energy, this contribution is changed slightly by the additional 4-Mev energy loss when the hydrogen absorber is present. However, with the geometry used and the measured beam divergence shown in Fig. 2 only a negligible fraction of the muons miss the last counter, and the effect is quite unimportant. Similarly all other effects due to the divergence of the beam are unimportant. We are also justified in neglecting any corrections for γ rays converted in the hydrogen chamber or the last counter, or for neutrons which may give recoil protons in the hydrogen or be counted in the last counter.

TABLE IV. Cross sections for negative pions in hydrogen.

Energy Mev	σ (uncorrected) 10^{-27} cm²	μ contamination percent	Accidentals percent	σ (exp) 10^{-27} cm²	Forward scattering 10^{-27} cm²	σ (corrected) 10^{-27} cm²
133±7	38.7±1.1	11.0	0.8	43.8±2.2	3.1	46.9±2.4
152±13	52.0±1.6	8.6	1.0	57.5±2.8	3.2	60.7±3.0
157±8	53.0±0.8	8.6	3.0	59.7±2.2	3.2	62.9±2.4
179±8	58.7±1.0	5.5	0.8	62.6±2.3	3.3	65.9±2.5
194±7	56.0±1.0	5.4	3.4	61.2±2.3	3.4	64.6±2.5
195±7	55.2±1.0	4.3	3.5	59.7±2.3	3.4	63.1±2.5
215±8	49.1±0.8	4.5	1.6	52.2±2.0	3.3	55.5±2.2
236±7	40.5±1.5	4.3	1.5	43.0±2.2	3.1	46.1±2.4
240±7	38.4±1.4	4.0	1.0	40.4±2.1	3.1	43.5±2.3
258±9	33.3±2.7	4.6	1.0	35.2±3.1	3.0	38.2±3.4

[19] The energy quoted is the mean energy of the pion in the center of the absorber, and the energy spread is compounded from the spread in the incident beam, as estimated from the range curve, and the energy loss in the absorber.

[20] If T is the given number of triples, Q the number of quadruples, and p the probability that a meson is transmitted, the root-mean-square fluctuation in Q is $\Delta Q=[T(1-p)p]^{\frac{1}{2}}$. Very nearly, $\Delta Q=[T(1-p)]^{\frac{1}{2}}=[T-Q]^{\frac{1}{2}}$ for p close to unity.

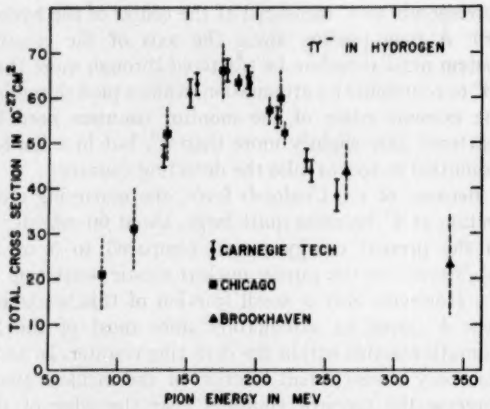

FIG. 5. Total cross sections for negative pions in hydrogen. The Chicago points at 89, 112, 135, 176, and 217 Mev represent the transmission measurements of Anderson *et al.* (reference 2). The Chicago points at 187, 209, and 220 Mev represent transmission measurements of Glicksman (reference 4). The Brookhaven points at 265 Mev and 340 Mev give the results of transmission measurements of Yuan and Lindenbaum (reference 22); these points have energy spreads of ±30 Mev and ±40 Mev, respectively.

The resulting experimental cross section is given in column 5 of Table IV with the error compounded out of the statistical error in the uncorrected cross section and the estimated errors in the corrections. There is left finally the correction for the forward scattering as discussed in detail in Sec. II. The best estimate, based on the available angular distributions,[3,4] is given in column 6.

The final cross sections, $\sigma_H(\pi^-)$, after all corrections have been made, are listed in the last column of Table IV, with an estimate of the total error.[21] Figure 5 shows the comparison of the present measurements with those of other laboratories. In general there is good agreement with the original transmission measurements of Anderson, Fermi, *et al.*[2] and also with the more recent results of Glicksman.[4] The Brookhaven measurement[22] at 265 Mev appears to be somewhat above the curve extrapolated from the present lower energy data. The maximum in the cross section, clearly exhibited by the data, occurs near 180 Mev.

[21] If we assume that there is unlikely to be a systematic error varying strongly with meson energy, we may get an idea of the relative accuracy of the results from the statistical errors quoted in column 2, Table IV.

[22] L. Yuan and S. J. Lindenbaum, Phys. Rev. **93**, 917 (A) (1954) and *Proceedings of Fourth Annual Conference on High Energy Physics* (University of Rochester Press, Rochester, 1954).

IV. TOTAL CROSS SECTIONS FOR POSITIVE PIONS IN HYDROGEN

The essential new feature of the π^+ measurements, apart from the low intensity of the beams relative to the π^-, was the very large contamination of protons which it was necessary to eliminate. Although it was possible to reduce the contamination very much by appropriate shielding[23] near the cyclotron, the protons remained 5 or 10 times more numerous than the pions in the energetic beams of energy 170 Mev and above.

There would be no real difficulty if *all* of these protons were of nearly the same momentum as the pions. They would then have energies from 40 to 50 Mev and could be removed with a suitable absorber. However, even a few protons of higher energy could be very serious inasmuch as some might penetrate the monitor and reach the detector with the hydrogen target empty, but fail to do so with the target full.[24] It was therefore necessary to eliminate the protons completely. We used principally two methods to accomplish this: (A) time-of-flight discrimination against protons in the monitor and (B) pulse-height discrimination in the detecting counter.

A. Time-of-Flight Method

With 220-cm distance between first and last monitor counters, as shown in Fig. 6, the time of flight difference between protons and pions of the same momentum is between 20 and 25 mμsec, depending on the pion energy and the proton energy loss in the first two counters. There is a difference of about 12 mμsec for protons of 65 Mev, which are just stopped by ionization loss in the monitor and the liquid hydrogen. Pulses separated

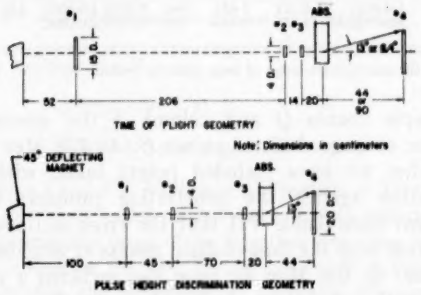

FIG. 6. Geometries for the π^+ measurements.

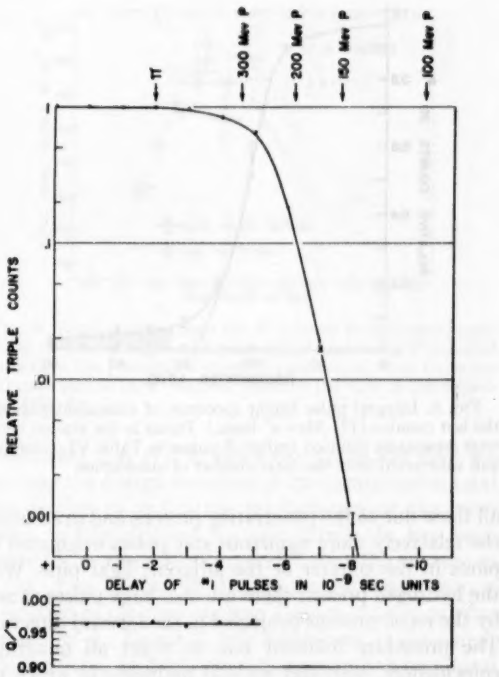

FIG. 7. Response of the monitor coincidence circuit to pulses in delayed coincidence and the transmission Q/T as a function of delay. The arrow labeled π indicates the operating point for pions; the displacements of the arrows labeled P, relative to the π, give the time-of-flight differences between the pions and protons of various energies.

in time by this much are easily rejected by the monitor coincidence circuit. This is clear from Fig. 7, which shows the response of the circuit to monitor pulses in delayed coincidence and also the transmission Q/T for each delay. It is evidently possible to find an operating point for which mesons are counted with 100 percent efficiency while pulses in delayed coincidence by 6 mμsec or more (corresponding to protons of 140 Mev or less) are for practical purposes completely rejected.

B. Pulse-Height Method

It may be expected that the penetrating protons,[25] because they are slower than the pions, will give appreciably larger pulses in the last counter. We therefore attempted pulse height discrimination using the special 20-cm diameter counter described earlier and the Tektronix 517 oscilloscope as an improvised integral pulse height analyzer.[26]

Figure 8 shows the pulse-height spectrum for the 171-Mev π^+ experiment, with no hydrogen in the target. The small residue of large pulses should contain

[23] Since the protons lose more momentum than the pions by ionization loss in the air, those coming from the meson target, with the proper momentum to eventually follow the pions through the external deflecting magnet, must have somewhat different trajectories than the pions near the cyclotron. This makes it possible with shielding to cut out a very large fraction of the protons without materially affecting the pion intensity. Thus, for the 170-Mev beam, the protons were more numerous than the pions by a factor of 100. Insertion of lead shielding reduced this factor to 4.

[24] Suppose, for example, that for each 100 pions traversing the monitor, there are 500 protons incident of which, on the average, one has the above-mentioned disagreeable property. Since on the average only 8 of the pions are removed by the hydrogen, we would find too large a cross section by over 10 percent.

[25] The protons with the same momentum as the pions were stopped by ionization loss in an absorber before the monitor.

[26] The quadruples coincidence output was used to trigger the sweep and all pulses above a certain height were counted with a photomultiplier viewing the oscilloscope screen.

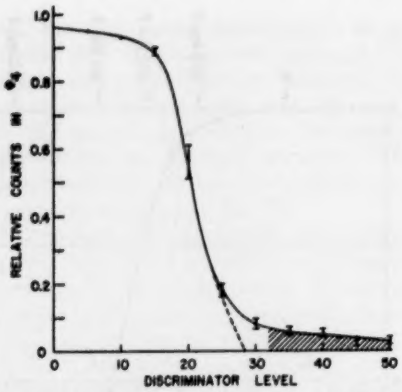

FIG. 8. Integral pulse height spectrum of coincident pulses in the last counter (171-Mev π^+ beam). Pulses in the shaded region were separately counted (called B pulses in Table VI, column 5) and subtracted from the total number of quadruples.

all those due to the penetrating protons and in addition, the relatively more numerous star pulses originated by pions in the counter or the adjacent light pipe. With the hydrogen present there are also large pulses caused by the recoil protons projected in the forward direction. The procedure followed was to reject all quadruple coincidences, with and without hydrogen in which the pulses in the detecting counter were larger than a certain limit set rather arbitrarily by examining the pulse height spectrum. Rejection of the star-producing pions does not alter the cross section since the fraction rejected is the same with and without the hydrogen. Rejection of the recoil protons makes it unnecessary to correct the experimental cross section on that account.

This method is open to the criticism that there is no unique division in the pulse-height spectrum between the meson pulses and the "large" pulses. One could attempt to show that the resulting cross section is essentially independent of the dividing line chosen, but this becomes too difficult with the very weak π^+ beams at high energy. For this reason we prefer to rely more on the time of flight method, about which there can be little question, using the observed agreement between the results (see below) as an indication that there are no serious systematic errors in either procedure.

TABLE V. Transmission data for positive pions in hydrogen by time-of-flight method.

Energy Mev	Absorber	Triples counts	Quadruples counts	Q/T	σ (uncorrected) 10^{-27} cm²
135±6	Dummy	190 016	181 609	0.9557±0.0005	103.5±2
	Hydrogen	100 010	90 656	0.9065±0.0010	
152±12	C	64 007	53 940	0.8427±0.0017	145 ±5
	CH_2	80 008	62 431	0.7803±0.0019	
156±6	Dummy	60 004	57 374	0.9562±0.0008	142 ±3.5
	Hydrogen	60 010	53 379	0.8895±0.0014	
166±12	C	64 010	54 489	0.8511±0.0017	150 ±5.5
	CH_2	54 002	42 433	0.7858±0.0023	
171±6	Dummy	36 005	34 515	0.9586±0.0011	157 ±4
	Hydrogen	40 004	35 385	0.8845±0.0017	
171±6	Dummy (6.4°)	37 002	34 431	0.9305±0.0014	184 ±5
	Hydrogen (6.4°)	40 002	33 885	0.8471±0.0020	
185±8	Dummy	15 506	14 899	0.9609±0.0016	151 ±6
	Hydrogen	18 000	16 016	0.8898±0.0024	
196±8	Dummy (6.4°)	12 830	12 013	0.9363±0.0023	183 ±9
	Hydrogen (6.4°)	9 508	8 107	0.8527±0.0042	

C. Results

Table V gives the transmission data and the uncorrected cross sections obtained with the time-of-flight method. Table VII contains the final corrected cross sections including the correction for forward scattering as discussed in Sec. II. The energy range from 135 Mev to 196 Mev has been covered in more or less uniform steps using mostly liquid hydrogen as absorber, with checks using the polyethylene-carbon difference at 152 Mev and 166 Mev.

Table VI contains the transmission data obtained by the pulse-height method, with column 4 giving all the quadruple counts Q and column 5 the associated number of large detector pulses B. At 128 Mev and 142 Mev we have included points taken with no precaution against the penetrating protons; it is apparent from Table VII that the cross sections are consistent with the time-of-flight results at neighboring energies. At 166 Mev we have also included a point taken with polyethylene and carbon absorbers of the same stopping power, since in this case the cross section should in first approximation be independent of the penetrating proton contamination.

TABLE VI. Transmission data for positive pions in hydrogen by pulse-height method.

Energy Mev	Absorber	Triples counts T	Quadruples counts Q	B counts[a]	$\frac{Q-B}{T}$	σ (uncorrected) 10^{-27} cm²
128±6	Dummy	40 070	37 975	···	0.9477±0.0012	98.5±4
	Hydrogen	35 600	32 083	···	0.9012±0.0017	
142±6	Dummy	45 558	43 013	···	0.9441±0.0011	122 ±4
	Hydrogen	45 340	40 211	···	0.8869±0.0016	
166±13	C	61 005	51 419	4492	0.7692±0.0020	172 ±6
	CH_2	61 000	47 301	4475	0.7020±0.0024	
	C′	56 006	44 626	···	0.7968±0.0024	151 ±9
	(none)	6 001	5 813	···	0.9686±0.0023	
171±8	Dummy	45 002	42 726	2842	0.8862±0.0016	187 ±5
	Hydrogen	46 007	40 080	3021	0.8055±0.0020	
182±9	Dummy	8 277	7 681	646	0.8499±0.0042	148 ±12
	Hydrogen	11 836	10 072	746	0.7879±0.0042	

[a] B is the associated number of large detector pulses.

All of the results, with an indication of the method and the geometry (either 13° or 6.4° half-angle), are assembled in Table VII and plotted in Fig. 9. The graph shows only the values corrected according to the $1+3\cos^2\theta$ distribution in the center-of-mass system, since the comparison of the two geometries at 171 Mev seems to indicate that this is more realistic. There is evidently no systematic difference between the results obtained with the two methods.

Figure 10 shows the relation of the present measurements to those of other laboratories. There is satisfactory agreement with the original transmission measurements of Anderson *et al.*[27] at Chicago and with photographic plate measurements of Grandey and Clark[18] at Carnegie Tech and Orear *et al.*[18] at Chicago. The photographic measurements of Homa *et al.*[18] at Columbia and the transmission measurements of Yuan and Lindenbaum[22] at Brookhaven give values somewhat lower than ours.

V. DISCUSSION OF THE HYDROGEN CROSS SECTIONS

Under the assumption that the total isobaric spin of the pion-nucleon system is conserved by the pion-nucleon interaction, it is possible to analyze the present data for the relative importance of the different isobaric spin states which are involved. If $\sigma(\frac{3}{2})$ and $\sigma(\frac{1}{2})$ denote, respectively, the total cross sections for pion-nucleon interaction in the isobaric spin states $\frac{3}{2}$ and $\frac{1}{2}$, it is

TABLE VII. Cross sections for positive pions in hydrogen.

Energy Mev	σ (uncorr.) 10^{-27} cm²	μ contam. per cent	Acid. per cent	σ (exp) 10^{-27} cm²	σ(corrected) 10^{-27} cm² (isotropic)	$(1+3\cos^2\theta)$	Method[a]
128±6	98.5	8	0.7	108±5	115±7	122±8	(as for π^-)
135±6	103.5	7	0.5	112±4	119±4	126±4	T. of F.
142±6	122	7	0.7	132±5	143±7	150±8	(as for π^-)
152±12	145	5	0.3	153±6	165±6	175±6	T. of F.
156±6	142	5	0.5	150±5	160±5	170±5	T. of F.
166±13	172	7.5	0.6	187±9	191±10	194±12	P.H.
	151	7.5	0.6	164±11	176±11	188±11	thick carbon
166±12	150	7.5	0.3	163±7	175±7	187±7	T. of F.
171±8	187	7.5	0.3	203±8	207±10	210±12	P.H.
171±6	157	7	0.5	170±6	184±6	196±6	T. of F.
171±6	184	7	0.5	199±6	202±6	205±6	T. of F.(6.4°)
182±9	148	7	0.3	160±14	164±18	166±20	P.H.
185±8	151	6	0.5	161±8	176±8	188±8	T. of F.
196±8	183	7	0	197±14	200±14	202±14	T. of F.(6.4°)

[a] T. of F. = time-of-flight method; P.H. = pulse-height method.

easily verified that[28]

$$\sigma(\tfrac{3}{2})=\sigma(\pi^+ + p), \tag{2}$$

$$\sigma(\tfrac{1}{2})=\tfrac{1}{2}[3\sigma(\pi^- + p)-\sigma(\pi^+ + p)]. \tag{3}$$

Figure 9 and Fig. 10 show a comparison of $3\sigma(\pi^- + p)$ with $\sigma(\pi^+ + p)$ based on the data of this experiment. The permissible range of the negative pion cross section is indicated by the two dotted curves. It is apparent that within the experimental accuracy, the positive pion cross sections lie between the dotted curves, with deviations that show no systematic trend. The measurements therefore indicate that in the energy range from 130 Mev to 200 Mev the cross section $\sigma(\frac{1}{2})$ is very small.

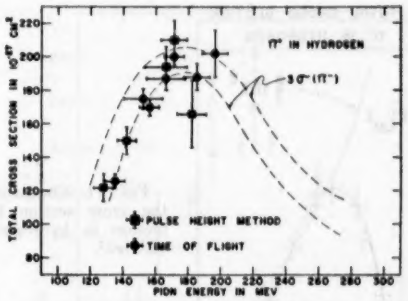

FIG. 9. Total cross sections for π^+ mesons in hydrogen; comparison of time-of-flight and pulse-height methods. The dotted curves show the permissible range of variation of three times the total cross section for π^- mesons, based on the data of this experiment (Fig. 5).

Assuming that $\sigma(\frac{1}{2})$ is small also up to 260 Mev, we may take the energy variation of the negative pion total cross section as indicating the behavior of the cross section $\sigma(\frac{3}{2})$ (multiplied by one third). It has been suggested on theoretical grounds[29] that the maximum in the cross section is due to an especially strong interaction in the pion-nucleon P-state of total angular momentum $\frac{3}{2}$. To see if this hypothesis is consistent with the data, we may compare the negative pion total cross section with the maximum possible contribution of the state $I=\frac{3}{2}$, $J=\frac{3}{2}$, $L=1$. For a phase shift of 90° in this state, the partial cross section which it contributes is $(8/3)\pi\lambda^2$, where λ is the de Broglie wavelength of the pion in the c.m. system. The dotted curve in Fig. 11 shows $(8/3)\pi\lambda^2$ over the energy range of the

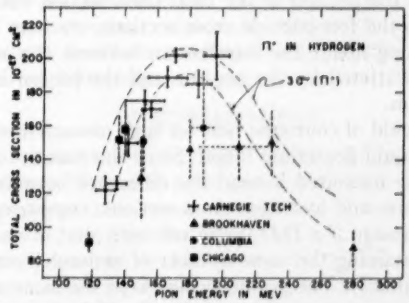

FIG. 10. Comparison of total cross sections for π^+ mesons in hydrogen with results from other laboratories. The Chicago points at 118 Mev and 136 Mev represent the transmission measurements of Anderson *et al.* (reference 27). The Chicago point at 140 Mev represents the photographic measurement of Orear *et al.* (reference 18). The point at 151 Mev gives the combination of photographic measurements of Grandey and Clark at Carnegie Tech with Homa *et al.* (reference 18) of Columbia. The Columbia point at 188 Mev is also due to Homa *et al.* (reference 18). The Brookhaven points at 150 Mev, 180 Mev, 210 Mev, and 280 Mev give the preliminary results of transmission measurements of Yuan and Lindenbaum (reference 22); the point at the revised energy of 230 Mev (with a rather large energy spread) is a result of the cloud chamber measurements of Fowler *et al.* (reference 18). Typical energy spreads are shown on one point each for Columbia and Brookhaven measurements.

[27] Anderson, Fermi, Long, and Nagle, Phys. Rev. **85**, 936 (1952).

[28] In these relations the $\pi^- + p$ total cross section should not include the cross section for radiative capture: $\pi^- + p \to n + \gamma$. For the energy range of the present measurements, the radiative cross section is 0.5 mb or less, as estimated from the photopion production data of J. Steinberger and A. S. Bishop, Phys. Rev. **86**, 171 (1952), and White, Jacobson, and Schulz, Phys. Rev. **88**, 836 (1952). In view of the other errors, this correction has not been made.

[29] K. A. Brueckner, Phys. Rev. **86**, 106 (1952).

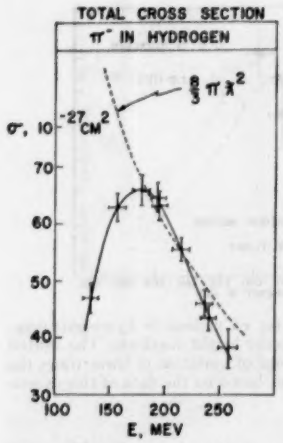

FIG. 11. Comparison of the cross section for π^- mesons in hydrogen with $(8/3)\pi\lambda^2$.

measurements. In the energy interval 185 Mev to 215 Mev, the curve drawn through the experimental points lies above the curve of $(8/3)\pi\lambda^2$. It is therefore possible that somewhere near 200 Mev the phase shift for the $P_{\frac{3}{2}}$, $I=\frac{3}{2}$ state passes through 90°, with the other states contributing little to the total cross section. From the total cross section measurements alone it is not possible to decide this question.[30]

VI. DEUTERIUM CROSS SECTIONS

The total cross sections for pions interacting with deuterium are of interest for two reasons. (1) According to the principle of charge symmetry, positive and negative pions should have equal total cross sections. (2) By comparison of the total cross section with the sum of the free-particle cross sections, we may learn something about the interference between the amplitudes scattered by the neutron and the proton in the deuteron.

It would of course be best for such measurements to use a liquid deuterium target. Since this was not available, we measured instead the difference between the deuterium and hydrogen cross sections, comparing the transmission of a D_2O liquid cell with that of an H_2O cell containing the same number of molecules per cm² (see Table I). The geometry was kept the same as for most of the measurements with liquid hydrogen; the last counter subtended a cone of half-angle 13° at the center of the absorber.

The experimental difference cross sections σ_{D-H}, corrected for everything except the forward scattering of charged particles into the 13° cone, are given in the second columns of Table VIII and Table IX for positive and negative pions, respectively. In the measurements with the positive pions, the accompanying protons having the same momentum as the pions were in most cases eliminated by placing a suitable thickness of Lucite before the monitor. Since the H_2O and D_2O cells have the same stopping power, the possible small remnant of more energetic protons is of no importance. At the highest energy, 181 Mev, the time-of-flight method was used. The poor statistical accuracy of the positive pion results is due to the small measured difference in the transmissions of D_2O and H_2O. By adding the experimental cross section in hydrogen, for the 13° geometry, to the experimental difference cross section σ_{D-H} we obtain the experimental total cross section for deuterium as indicated in the fourth columns of Table VIII and Table IX.

Before examining the data from the standpoint of charge symmetry, it is essential to make some guess about the forward scattering. The existing experimental information[31,32] does not cover the range of small angles of interest to us. We have therefore used a theoretical estimate of Brueckner,[33] based on the impulse approximation and taking account of the rescattering of the outgoing meson waves from one nucleon by the other nucleon in the deuteron. According to this estimate there is a rather pronounced forward peak of pions which are scattered elastically by the deuteron. It seems reasonable to assume a forward peak of comparable magnitude for the inelastically scattered pions as well. The fifth columns of Table VIII and Table IX give the cross sections for nuclear scattering of the pions into the 13° forward cone, obtained on this basis. The scattering cross sections of positive and negative pions have been taken equal in accordance with the principle of charge symmetry. Deuterons scattered in the forward direction seem to be relatively unimportant[31,33] and have been neglected.

TABLE VIII. Deuterium cross sections for positive pions.

Energy Mev	σ_{D-H} (exp) 10^{-27} cm²	σ_H (exp) 10^{-27} cm²	σ_D (exp) 10^{-27} cm²	π^+ forward 10^{-27} cm²	p forward 10^{-27} cm²	$\sigma_D(\pi^+)$ 10^{-27} cm²
123±12	26±4	96±8	122±9	13	5	140±9
137±12	31±5	120±8	151±9	17	6	174±9
162±12	25±11	162±8	187±14	20	10	217±14
181±13	32±14	170±8	202±16	24	11	237±16

For protons scattered forward, we can expect a difference between the positive and negative pion experiments, since the neutron and proton are expected to exchange roles in the interaction. A possible estimate

[30] Extensive analysis by de Hoffmann, Metropolis, Alei, and Bethe, by R. L. Martin (private communication), and by Glicksman[4] of the angular distribution of the negative pion scattering as a function of energy, taken in conjunction with the present measurements of positive pion total cross sections, has shown that there exists a consistent set of scattering phase shifts which includes a passage through 90° for the $P_{\frac{3}{2}}$, $I=\frac{3}{2}$ phase shift, near 195 Mev. Nevertheless, this solution is not unique, mainly because of the scarcity of experimental information on the differential positive-pion cross section in this energy range.

[31] Arase, Goldhaber, and Goldhaber, Phys. Rev. **90**, 160 (1953).
[32] D. E. Nagle, Phys. Rev. **93**, 918 (A) (1954).
[33] K. A. Brueckner, Phys. Rev. **89**, 834 (1953); **90**, 715 (1953). We wish to thank Dr. Brueckner for discussion of the deuterium scattering.

might be based on the free pion-proton (or pion-neutron) differential cross sections for the case that the pion is scattered backward (or, for positive pions incident, that a neutral pion emerges backward). However, the theoretical indication[33] is that the cross section is reduced from the free particle approximation by the multiple scattering of the pion between the nucleons in the deuteron, as well as other effects neglected in the impulse approximation. We might also expect the angular distribution of backward, inelastically scattered pions to be less peaked than it may be for the scattering by a free nucleon. For these reasons we have corrected for protons scattered forward by taking, rather arbitrarily, one-half of the estimate based on the free pion-proton, or pion-neutron differential cross sections. The corresponding cross sections are listed in the sixth columns of Table VIII and Table IX.

The last columns of Table VIII and Table IX contain our estimates of the total cross section for positive or negative pions interacting with deuterium. The errors indicated are due only to statistics and uncertainties

TABLE IX. Deuterium cross sections for negative pions.

Energy Mev	σ_{D-H} (exp) 10^{-27} cm²	σ_H (exp) 10^{-27} cm²	σ_D (exp) 10^{-27} cm²	π^- forward 10^{-27} cm²	p forward 10^{-27} cm²	$\sigma_D(\pi^-)$ 10^{-27} cm²
128±12	95±5	40±3	135±6	14	0.5	150±6
152±13	117±5	58±3	175±6	19	1	195±6
175±13	133±4	63±3	196±5	23	1	220±5
189±12	132±4	62±3	194±5	26	1	221±5
210±13	125±5	55±3	180±6	25	1	206±6
231±12	107±4	46±3	153±5	23	1	177±5

in the μ contamination and background. The uncertainties in the corrections for forward scattering are no doubt larger but difficult to assign.

As may be seen in Fig. 12, the results are consistent with the requirement of charge symmetry, but, in view of the large uncertainties in the corrections, cannot provide a completely convincing demonstration. From the comparison with the sum of the free-particle cross sections also shown in Fig. 12, it is clear that the deuteron scatters less than would be indicated on the assumption of incoherent scattering from the neutron and proton. This difference becomes somewhat more pronounced if the absorption cross section for the reaction, pion+deuteron→nucleon+nucleon,[34] is subtracted from the measured total cross section to give a total scattering cross section of the deuteron 10 or 15

[34] Durbin, Loar, and Steinberger, Phys. Rev. 84, 581 (1951).

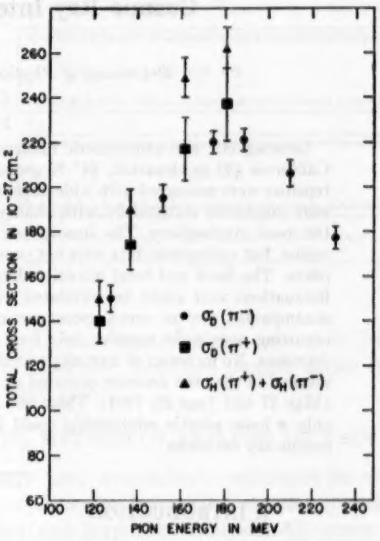

FIG. 12. Deuterium total cross sections for positive and negative pions.

mb lower, depending on how one extrapolates the lower energy data.[34] Brueckner[33] has shown, by using a model for the multiple scattering of the meson within the deuteron, that such a depression of the deuteron scattering cross section may be expected even though the waves scattered singly by the neutron or proton may interfere constructively.

The earlier measurements of the deuterium cross sections, made at Chicago,[35] and the results reported here are consistent with each other, although the corrections for the forward scattering have been made somewhat differently.

ACKNOWLEDGMENT

It is a pleasure to thank Dr. Simeon Friedberg and Dr. James Zimmerman of the Carnegie Tech Low-Temperature Laboratory for expert advice on the production and handling of liquid hydrogen. We are especially grateful to Mr. James Thompson and Mr. Homer Collins for their efforts to keep the cyclotron in good running order and for excellent technical advice on many problems. The active cooperation of Dr. Lloyd Smith in the initial experiments with the meson beams was an important factor in getting these experiments under way.

[35] Anderson, Fermi, Nagle, and Yodh, Phys. Rev. 86, 413 (1952).

Cosmic-Ray Intensity Fluctuations at Sea Level*

ROBERT L. CHASSON†
Department of Physics, University of California, Berkeley, California

(Received August 9, 1954)

Geomagnetic and atmospheric influences on sea-level cosmic radiation have been studied at Berkeley, California (95-m elevation, 44° N geomagnetic latitude). The hard (20-cm lead absorber) and total intensities were measured with wide-angle triple-coincidence counter telescopes, and fluctuations of intensity were compared statistically with changes of barometric pressure, pressure-altitude, and temperature of the lower stratosphere. The atmospheric coefficients found by Duperier were verified for the 100-millibar region, but radiosonde data were not complete enough to permit calculations for higher strata of the atmosphere. The hard and total intensity data, corrected to constant barometric pressure, were examined for fluctuations that could be correlated with geomagnetic disturbances. No apparent cosmic-ray changes accompanied any of seven geomagnetic sudden commencements. Of eighteen magnetic storm periods occurring over eight months, only four appeared definitely to be accompanied by cosmic-ray intensity decreases. No increases of intensity occurred during these periods. Of the four decreases observed, two were unusual in that the decrease occurred an appreciable time before the measurable geomagnetic disturbance (May 27 and June 25, 1951). These two events occurred during times of very great sunspot activity, but only a loose genetic relationship could be established between the sunspot behavior and the prestorm cosmic-ray decreases.

I. INTRODUCTION

FLUCTUATIONS of cosmic-ray intensity observed at sea level may arise partly from changes of the primary flux of charged particles resulting from alterations of the geomagnetic field.[1,2] Other fluctuations may be caused by changes in the distribution of atmospheric mass. By means of multiple correlation and regression analysis of intensity data, Duperier[3,4] has shown that it is possible to separate three main atmospheric effects. They are the barometric effect (mass absorption of muons), the pressure-altitude effect (decay of muons), and the upper-air temperature effect (attributed by Duperier to competition between the decay and nuclear interaction processes for charged pions).

The purpose of the work reported here was to obtain further statistics regarding the time and magnitude of cosmic-ray changes associated with magnetic storms.[5–17] It was also desired to investigate further the atmospheric effects described by Duperier.

II. EXPERIMENTAL PROCEDURE

The apparatus used to monitor the hard and total sea-level cosmic radiation was of simple conventional design. It consisted of two separate Geiger counter triple-coincidence telescopes having wide acceptance angle. The geometrical features of these two counter arrays were made as close to identical as possible. One of them (the "soft" telescope) had no absorber other than the counter walls and the thin pressed-wood material used to make the counter trays. The other (the "hard" telescope) contained 20 cm of lead and 1.25 cm of iron absorber. Figure 1 gives the dimensions of the telescopes and the disposition of the absorber in the hard telescope. The lower limits of momentum for the hard telescope were approximately 370 Mev/c for muons and 1 Bev/c for protons.[18]

Each tray contained 7 external-cathode Geiger counters[19] of 1½-inch diameter and 24-inch length, yielding an effective tray area of about 1600 cm². Triple coincidences were selected by Rossi-type circuits, followed by scales-of-eight, which actuated mechanical registers. Photographic records were made of the scaled hard and total counts every 14.4 minutes (1/100 day). The approximate triple-coincidence rates were

$$\text{hard: } 2.4\times10^4/\text{hr}$$

and

$$\text{total: } 3.5\times10^4/\text{hr}.$$

These rates were such that the statistical probable error was less than 1 percent over the 14.4-minute recording interval. It is believed that such precision makes it

* Assisted by the Joint Program of the U. S. Office of Naval Research and the U. S. Atomic Energy Commission.

† Now at the Department of Physics, University of Nebraska, Lincoln, Nebraska.

[1] G. Lemaitre and M. S. Vallarta, Phys. Rev. **43**, 87 (1933).
[2] G. Lemaitre and M. S. Vallarta, Phys. Rev. **50**, 493 (1936).
[3] A. Duperier, Proc. Phys. Soc. (London) **A62**, 684 (1949).
[4] A. Duperier, J. Atm. Terrest. Phys. **1**, 296 (1951).
[5] Altman, Walker, and Hess, Phys. Rev. **58**, 1011 (1940).
[6] T. H. Johnson, Revs. Modern Phys. **10**, 193 (1938). Contains an extensive list of references to earlier work.
[7] D. H. Loughridge and P. Gast, Phys. Rev. **57**, 938 (1940).
[8] K. Sittkus, Z. Naturforsch. **1**, 204 (1946).
[9] V. F. Hess and E. B. Berry, Phys. Rev. **60**, 746 (1941).
[10] S. Korff, Terrestrial Magnetism and Atm. Elec. **48**, 217 (1943).
[11] I. Lange and S. E. Forbush, Terrestrial Magnetism and Atm. Elec. **47**, 185 (1942).
[12] I. Lange and S. E. Forbush, Terrestrial Magnetism and Atm. Elec. **47**, 331 (1942).
[13] E. B. Berry and V. F. Hess, Terrestrial Magnetism and Atm. Elec. **47**, 251 (1942).
[14] A. Duperier, Nature **149**, 579 (1942).
[15] D. W. N. Dolbear and H. Elliot, Nature **159**, 58 (1947).
[16] H. Elliot and D. W. N. Dolbear, J. Atm. and Terrest. Phys. **1**, 205 (1951).
[17] B. Trumpy, Univ. Bergen Skrifter No. 3, 3 (1949).
[18] D. J. X. Montgomery, *Cosmic Ray Physics* (Princeton University Press, Princeton, 1949), Appendix E.
[19] M. L. MacKnight and R. L. Chasson, Rev. Sci. Instr. **9**, 700 (1951).

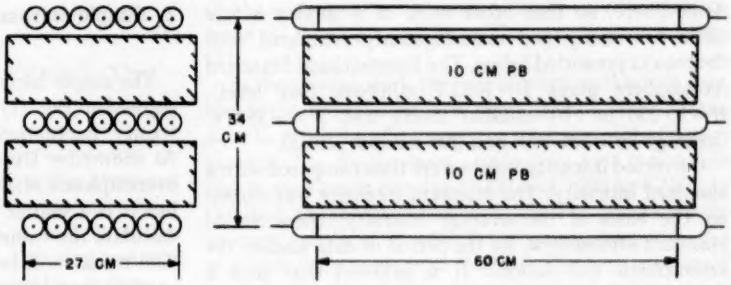

FIG. 1. Counter telescope geometry, showing disposition of 20 cm of lead in the hard telescope. Telescope opening angle is 75°×120°. Effective absorber is approximately 240 g/cm² for hard telescope and approximately 3 g/cm² for total telescope.

possible to study sudden intensity variations and their time relationship with other geophysical phenomena with considerable confidence in the statistics.

The resolving time of the coincidence input circuits (measured with a pulse-pair generator having a provision for varying the time interval between pulses) was 3.5 microseconds; thus the accidental coincidence rate was completely negligible.

Meteorological data for Oakland, California, were obtained from the United States Department of Commerce Weather Bureau and the United States Navy. Reports of geomagnetic activity were received regularly from the Instituto Geofísico de Huancayo, Peru (1° S geomagnetic latitude). The choice of an equatorial magnetic observatory as a reference for geomagnetic activity was made upon the recommendation of Forbush.[20] In considering the world-wide nature of cosmic-ray changes accompanying geomagnetic field variations, Forbush concluded that the principal changes of intensity follow the time changes in the dipole component of the magnetic storm field. Variations in the dipole component affect the magnetic records over the whole world, but such changes are superimposed upon the diurnal variation; also, such storms result in what Chapman calls the disturbance daily variation.[21] The latter is especially troublesome at high latitudes since it means that one cannot obtain a very sensible picture for the dipole component by subtracting the ordinary diurnal variation, which itself varies considerably in magnitude from day to day. Thus Forbush recommended that the records from low-latitude magnetic observatories would be of greatest significance in the consideration of cosmic-ray magnetic-storm effects.

One complete intensity unit, consisting of a pair of counter telescopes and associated electronic and recording equipment, went into operation on November 22, 1950. Its location was the Cosmic Ray Deck, Le Conte Hall, University of California, Berkeley, California (95-m elevation, 44° N geomagnetic latitude). The apparatus lay under a thin aluminum roof (0.3 g/cm²).

A similar complete unit went into operation on March 31, 1951. It was located about one mile from the Le Conte Hall site, and was housed under a ⅛-inch pressed wood roof.

[20] S. E. Forbush (private communication).

[21] S. Chapman and J. Bartels, *Geomagnetism* (Clarendon Press, Oxford, 1940), Vol. 2.

III. METHOD OF ANALYSIS OF DATA

Intensity and atmospheric relationships were examined statistically by use of standard methods of correlation and regression analysis. All errors quoted are statistical probable errors, based upon least-squares. The qualitative estimates of levels of significance of correlation were determined by a method developed by Fisher.[22]

The atmospheric dependence of intensity was assumed to fit linear regression relationships used in similar work;[3,23] that is,

$$\delta I = \beta(\delta B) \tag{1}$$

for the simple barometric correlation, and

$$\delta I = \mu(\delta B) + \mu'(\delta H) + \alpha(\delta T) \tag{2}$$

for the complete atmospheric correlation. δ represents the deviation of a variable from its mean value, and the symbols used are I=intensity, B=barometric pressure, H=pressure altitude (100-millibar level), T=average temperature between 100- and 200-millibar levels, β=simple barometric coefficient, μ=mass absorption (barometric) coefficient, μ'=decay (pressure altitude) coefficient, and α=temperature coefficient (referred to T defined above). Subscripts: t refers to total intensity, h refers to hard intensity, and s refers to soft intensity.

Data taken during periods of appreciable geomagnetic disturbance were not used in the calculation of atmospheric coefficients. This precaution insures the exclusion of significant intensity fluctuations not resulting primarily from atmospheric effects, although it seems that most magnetic storms are not accompanied by appreciable cosmic-ray disturbances.

The atmospheric coefficients obtained were used to correct the raw intensity data to a standard atmosphere, chosen to correspond with the International Standard

[22] R. A. Fisher, *Statistical Methods for Research Workers* (Oliver and Boyd, Edinburgh, 1946).

[23] D. W. N. Dolbear and H. Elliot, J. Atm. Terrest. Phys. 1, 215 (1951).

Atmosphere, so that other work of a similar nature could be readily and unambiguously compared with the results presented below. The International Standard Atmosphere gives $B=1013.2$ millibars (sea level), $H=16\,250$ m (100-millibar level), and $T=-55.0°C$ (average between 100- and 200-millibar levels).

Corrected intensity values were then compared with a standard intensity. The standard intensity was chosen on the basis of the average intensity, corrected to standard atmosphere, for the period of data used in the atmospheric calculations. It is believed that such a standard reference intensity is more useful in the study of trends of intensity changes. Although magnetic-storm effects may appear to be more dramatic when the intensities are plotted with respect to some arbitrary prestorm average intensity, as has been usual, such a technique might easily separate the magnetic-storm period from the true context of surrounding periods. It is believed that the examination of the whole period of data gives a much more reliable picture and leads to more fruitful results. This procedure is followed in Figs. 3, 4, and 5.

IV. RESULTS AND DISCUSSION

1. Inter-unit Correlation

It was immediately apparent that the records of the two separate intensity units were almost completely parallel. A statistical comparison was made between the two separate records of both hard and total intensity for a three-month period of joint operation. The daily average hard intensity for the Le Conte Hall unit was about 0.7 percent lower than that for the second unit, whereas the average total intensity was about 0.8 percent higher for the Le Conte Hall unit. These small discrepancies are undoubtedly due to slightly different sensitivities of the coincidence input units and to small differences of effective telescope geometry.

Most important, however, is the generally excellent parallelism existing between the records. The inter-unit correlation coefficients bear this out, having been found to be

$$r_h=0.94 \quad \text{(hard)},$$

and

$$r_t=0.96 \quad \text{(total)}.$$

Both values are highly significant, according to the criterion of Fisher,[22] indicating that, for the period of observation and the distance involved, there were no sensible major spatial differences in the magnitude of cosmic-ray fluctuations. As a whole, the results indicate a striking degree of homogeneity of sea-level radiation, taken over a small but significant horizontal distance. This is in agreement with the more general observations (between New York and Maryland) of Altman, Walker, and Hess.[5]

2. Simple Barometric Effect for Hard, Total, and Soft Intensities

The simple barometric coefficient β is calculated from regression Eq. (1) under the assumption that all intensity fluctuations are due to barometric changes. As shown by Duperier,[3] such an assumption leads to overemphasis of the contribution of pressure changes, but it is a matter of considerable practical interest to calculate the value of the simple barometric coefficient. The results will be applied later to the intensity data as what may be considered a first order correction.

Daily mean values of pressure and of hard and total intensity were calculated. The data covered a six-month period of operation, with the exclusion of days of marked geomagnetic activity or when the intensity data were not reliable because of equipment failure. The following values were found for the simple barometric regression and correlation coefficients:

$$\beta_h=-(2.07\pm0.14) \text{ percent/cm Hg},$$

$$(r_{IB})_h=-0.63 \text{ (highly significant)} \quad \text{(108 days)},$$

$$\beta_t=-(2.87\pm0.21) \text{ percent/cm Hg},$$

$$(r_{IB})_t=-0.68 \text{ (highly significant)} \quad \text{(100 days)}.$$

The regression coefficients are expressed in percent of the mean value of the daily mean intensity.

The value for β_h is in close agreement with that found for long periods of observation by other workers.[3,23,24] The value of β_t agrees substantially with other determinations.[25,26]

Clearly β_t is numerically larger than β_h. The difference could be accounted for by the excess of electronic component at sea level arising from cascade processes generated by the decay of neutral pions. Greisen[27] has pointed out that radiation thus born could make it appear that there is not muon-electron equilibrium at sea level. The electronic component would be especially sensitive to barometric pressure changes since the absorption coefficient for low energy electrons is approximately 0.025 cm²/g, whereas the absorption coefficient for muons is of the order of 10^{-3} cm²/g. Thus the electronic component could well account for the large barometric dependence of the total intensity. In partial support of this contention is the barometric coefficient of approximately -10 percent/cm Hg found by Daudin and Daudin[28] for extensive air showers.

From the values of the simple barometric coefficients for hard and total intensity, it is possible to derive the coefficient for the soft. Returning to the definition of β given by Eq. (1), one may write for the total intensity

[24] D. C. Rose, Can. J. Phys. **29**, 97 (1951).
[25] F. Lindholm, Arkiv. Mat. Astron. Fysik. **A30**, No. 3 (1944).
[26] Caro, Law, and Rathgeber, Australian J. Sci. Research **A1**, 261 (1948).
[27] K. Greisen, Phys. Rev. **73**, 521 (1948).
[28] A. Daudin and J. Daudin, J. phys. et radium **10**, 394 (1949); **14**, 169 (1953).

(hard plus soft)

$$\delta I_t = (\beta_h + \beta_s)\delta B, \tag{3}$$

where β is in terms of counts/(pressure×time). Thus

$$\beta_t = \beta_h + \beta_s. \tag{4}$$

If the β's are to be expressed in terms of percent intensity change per unit pressure change, it is necessary to weight each term of Eq. (4) by the respective fraction of the total intensity included in each intensity component. Equation (4) becomes, by using average values of intensity to construct the weighting factors,

$$\beta_t = \frac{\langle I_t\rangle_{Nt} - \langle I_h\rangle_{Nt}}{\langle I_t\rangle_{Nt}}\beta_s + \frac{\langle I_h\rangle_{Nt}}{\langle I_t\rangle_{Nt}}\beta_h. \tag{5}$$

In Eq. (5) each β is in units of percent/pressure.

From the data used to calculate β_h and β_t, it was found that $\langle I_h\rangle_{Nt}/\langle I_t\rangle_{Nt}=0.6918$. Thus the simple barometric coefficient for the soft intensity is

$$\beta_s = -(4.67\pm0.65) \text{ percent/cm Hg.}$$

The value of β_s compared with the value of β_h shows very clearly how much more barometrically sensitive the soft component is when compared with the hard. Only a few percent of the soft sea-level radiation is composed of slow mesons;[29] hence most of the contribution to the soft barometric effect is due to electron absorption. Since, however, most electrons at sea level result from muon decay and knock-on processes,[30] the apparent barometric dependence of these electrons will rest considerably on that of the muons. Thus β_s will be numerically smaller than might be expected if one considered simply the absorption of electrons in air.[31]

3. Complete Atmospheric Correlation

It is now assumed that the intensity fluctuations caused by atmospheric changes are expressed by the multiple linear regression equation (2). Duperier[3,4] has shown that this relationship assumes greater validity as higher levels in the atmosphere are considered for the temperature term. His analysis shows that the height of the 100-millibar level gives the best correlation for the pressure altitude (decay) effect. He found better correlation for the temperature effect if the mean temperature between 50 and 200 millibars (T_{52}) is used rather than that between 100 and 200 millibars (T_{12}). The result was that the temperature coefficient α_{52} is twice as large as α_{12}, indicating that a large fraction of primary interactions take place in the first 50 g/cm² of the atmosphere. The high-altitude balloon observations of Winckler and Stroud[32] more directly confirm this.

In the present work the lack of much radiosonde data above the 100-millibar level made it impossible to consider in detail the effect upon the intensity of the fluctuations of T_{52}. Furthermore, since only two radiosonde flights were made per day (0300 and 1500 hr GMT) at Oakland, California, it was not possible to calculate daily average values of H and T for comparison with the available daily average of B and I. The best that could be done was to use the average intensity and sea-level barometric pressure for the 3-hour period of the day bracketing each radiosonde flight period. To avoid complications possibly arising from the diurnal variation and random fluctuations of H and T, the calculations of atmospheric coefficients were made using either morning or afternoon flight periods, but not mixing them in a single calculation. Missing atmospheric data could not be interpolated, as judged from unsuccessful attempts to interpolate and reproduce known values of H and T.

For six months of operation, during which there were 78 afternoon radiosonde flights that reached 100 millibars, the calculation of the atmospheric coefficients gave

$$\mu = -(1.56\pm0.23) \text{ percent/cm Hg,}$$

$$\mu' = -(3.22\pm0.49) \text{ percent/km,}$$

and

$$\alpha_{12} = (0.068\pm0.018) \text{ percent/°C.}$$

The multiple correlation coefficient was

$$R_{I\cdot BHT} = 0.61 \quad \text{(highly significant).}$$

The acceptance angle and general geometry of the telescopes used in the present work were essentially the same as those used by Duperier in his more recent determinations of the atmospheric coefficients.[4] The over-all agreement with Duperier is excellent.[33]

4. Correction of Intensity Data for Atmospheric Effects

Before comparing intensity fluctuations with geomagnetic data, it is necessary to eliminate, as far as possible, the effects of atmospheric changes. In the present experiment only about one-fourth of the intensity data for one day could be reliably corrected for the three atmospheric effects, assuming that both daily radiosondes reached 100 mb. Actually, only about two-thirds of the flights reached the requisite altitude. It would be a very undesirable procedure with regard to the study of geomagnetic effects if one were forced to

[29] B. Rossi, Revs. Modern Phys. **20**, 537 (1948).

[30] Bernardini, Cacciapuoti, and Querzoli, Phys. Rev. **73**, 335 (1948).

[31] D. I. Dawton and H. Elliot, J. Atm. Terrest. Phys. **3**, 295 (1953), have directly calculated the absorption coefficient for the soft intensity using regression Eq. (2). They obtained a value of $-(4.70\pm0.23)$ percent/cm Hg. This agreement with the simple β_s in the present work indicates that the soft intensity fluctuations most strongly reflect barometric pressure changes alone.

[32] J. Winckler and J. R. Stroud, Phys. Rev. **76**, 1012 (1949).

[33] Duperier (to be published) finds a value of the barometric coefficient, using 40 cm of lead absorber, of $-(1.21\pm0.06)$ percent/cm Hg, which is in perfect agreement with the presently determined value and the value from the absorption curve in water.

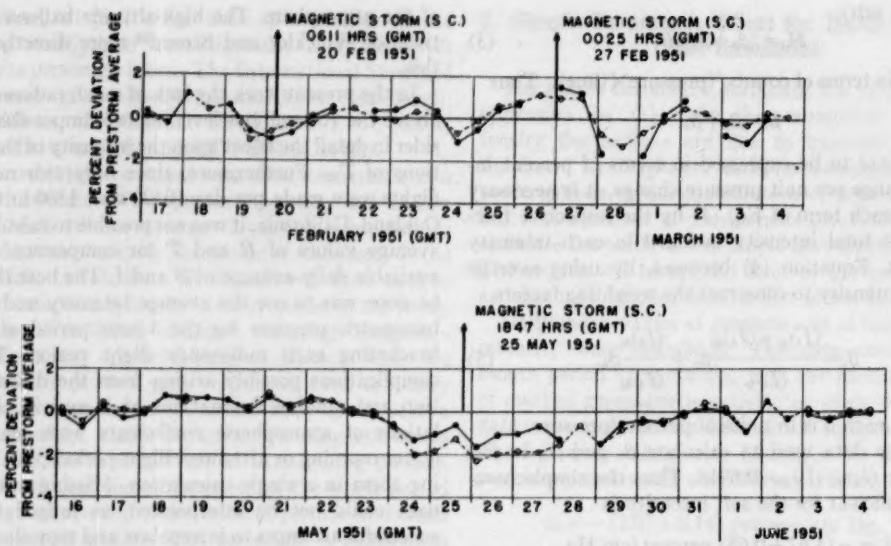

FIG. 2. Variations of hard cosmic-ray intensity when corrected for both barometric pressure and altitude of 100-millibar isobar (solid curve) and for barometric pressure alone (dashed curve). Radiosonde ascents made at 0300 and 1500 hr GMT. Points on curves represent intensity means for approximately ½ day, centered about the time of radiosonde ascent. Missing points on solid curves indicate absence of 100-millibar radiosonde data. (S.C. = sudden commencement.)

rely upon intensity data corrected only for such restricted periods. Thus it was necessary to test whether or not a simple barometric correction, which could be done for a whole day of data, would give a set of corrected intensity values reliable enough to be used in examining the geomagnetic effects. The following procedure was carried out: two different periods of intensity data (16 and 20 consecutive days) were chosen, and the portions of data corresponding to the times of the morning and afternoon radiosonde flight periods were corrected according to the three atmospheric regression coefficients. (The net positive temperature effect was much smaller than that of barometric pressure and pressure-altitude.) The same raw data were also corrected using only the simple barometric coefficient. The data adjusted in the two different ways are plotted together in Fig. 2. It is seen that it is adequate to correct the intensity data by means of the simple barometric coefficient without seriously altering the sense of the results. Although this was certainly the less desirable alternative, it was the only way, under the circumstances, that the whole day of intensity data could be effectively used. The magnitude of the simple barometric correction seems, fortuitously, almost equivalent to the combined barometric and pressure-altitude corrections. Thus all intensity data shown graphically, with the exception of solid portions of Fig. 2, were corrected only for the simple barometric effect.

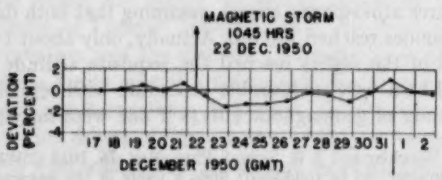

FIG. 3. Variations of hard cosmic-ray intensity during geomagnetic storm of December 22, 1950. Ordinate is daily mean percent deviation from standard intensity. For convenience, points are centered upon 2200 hr GMT.

5. Analysis of Sudden Commencements

The intensity trend for several 14.4-minute intervals, surrounding each of seven different geomagnetic sudden commencement periods, was examined for significant fluctuations that could be considered coherent with the sudden commencement. The amplitudes of the sudden commencements ranged from +14 to +101 gamma, but no significant cosmic-ray intensity changes were found that could be associated with any of the seven events.

It is evident, under the statistical limitations of the counting experiment, that any alteration of the allowed cone of radiation or change of incident primary flux occurring during sudden commencements would not produce large enough effects to be resolved.

6. Intensity Variations during Geomagnetic Storm Periods

Counting data for the hard component were corrected (simple barometric) for 18 of 19 magnetic storms that occurred between November 22, 1950, and July 9, 1951. No intensity data were available for the magnetic storm of December 12, 1950. Examination of the in-

tensity trends over the storm and surrounding periods indicates the following general distribution of results: (The amplitudes of maximum horizontal field disturbance at Huancayo are given. Greenwich dates are used throughout.)

(a) No clear magnetic-storm effect (14 storms):
November 24, 1950 (−250 gamma),
January 22 and 29, 1951 (−322 and −364 gamma),
February 4, 21, and 27, 1951 (−319, −320, and −284 gamma),
March 6 and 13, 1951 (−268 and −234 gamma),
April 2 and 18, 1951 (−249 and −436 gamma),
May 1 and 9, 1951 (−402 and −307 gamma),
June 25, 1951 (−167 gamma),
July 1, 1951 (−292 gamma).

(b) Probable magnetic-storm effects (4 storms):
December 22, 1950 (−282 gamma),
January 26, 1951 (−405 gamma),
May 25, 1951 (−375 gamma; prestorm cosmic-ray decrease),
June 17, 1951 (−393 gamma; prestorm cosmic-ray decrease).

The daily mean percent deviation from standard hard intensity is plotted for these latter four periods in Figs. 3, 4, and 5. Missing points are for days when the cosmic-ray data were not reliable because of equipment failure. For convenience, means are centered on 2000 hr GMT. The fluctuations of total intensity closely paralleled those of the hard.

Altman, Walker, and Hess[5] examined 20 magnetic storms over an interval of eleven months and reported that 16 lowered the cosmic-ray intensity and 4 raised it. They remarked that the positive effects were for small storms (250 gamma or less), while the negative effects were for storms ranging to 850 gamma. Their technique of looking at the data consisted of a comparison of the corrected intensities for the day of maximal magnetic disturbance with the intensities for the preceding undisturbed or little-disturbed day. There are serious objections to such a technique since application of simple atmospheric corrections to short intervals of data is not very reliable, and the separation from the context of surrounding periods of data can be quite misleading. For example, if one considers only the data for February 26, 27, and 28, 1951, in Fig. 2, he may conclude that the magnetic storm of February 27 definitely caused an intensity decrease. But examination of the general intensity record for the periods immediately preceding and following indicates that the negative fluctuation starting on February 27 may well have been only a part of the normal fluctuation pattern that applies to the whole period. One cannot say that the decrease of February 27 is uniquely associated with the magnetic storm. In view of this interpretation of the records, it is doubtful that the storm-effect statistics of Altman, Walker, and Hess can be considered as reliable.

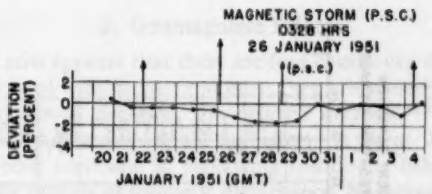

FIG. 4. Variations of hard cosmic-ray intensity during geomagnetic storm of January 26, 1951. Unlabelled arrows are for commencements of magnetic storms not accompanied by apparent cosmic-ray changes. (P.S.C. = pulsating sudden commencement.)

7. Prestorm Effect

Two events of unusual interest were noted; namely, the marked intensity decreases that preceded the advent of the geomagnetic storms of May 25 and June 17, 1951.[34] Records from both independent intensity units were the same throughout. Records of hard and total intensity for these periods at Manchester, England, are in excellent agreement with the Berkeley results.[35] Also, the high altitude neutron records show even larger negative fluctuations during these periods.[36] A considerable decrease of intensity started on May 23, followed by the moderate magnetic storm of May 25, which lasted for about 1½ days. The intensity slowly returned to its "prestorm" value after the end of the magnetic disturbance, as is characteristic when cosmic-

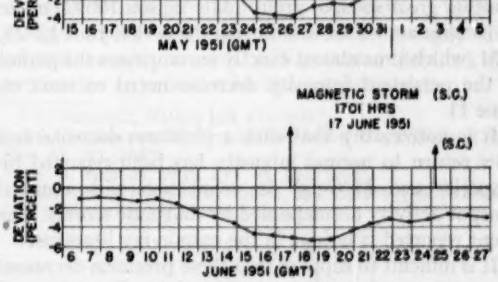

FIG. 5. Variations of hard cosmic-ray intensity for geomagnetic storms of May 25 and June 17, 1951, showing prestorm cosmic-ray decreases. Sunspot group Mt. Wilson 10662 disappeared around the west limb of the sun on May 23, 1951, and sunspot group Mt. Wilson 10692 passed across the solar disk during June 12–25, 1951.

[34] Reported to the American Physical Society at Chicago, Illinois, October 24–27, 1951. See R. L. Chasson, Phys. Rev. 85, 719(A) (1952).
[35] H. Elliot (private communication).
[36] Reported to the American Physical Society at Chicago, Illinois, October 24–27, 1951. See Simpson, Fonger, and Wilcox, Phys. Rev. 85, 720(A) (1952).

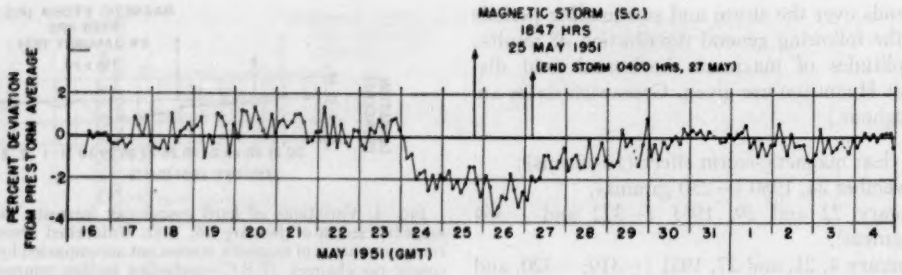
MAGNETIC STORM (S.C.)
1847 HRS
25 MAY 1951
(END STORM 0400 HRS, 27 MAY)
PERCENT DEVIATION FROM PRESTORM AVERAGE
2
0
-2
-4
16 17 18 19 20 21 22 23 24 25 26 27 28 29 30 31 1 2 3 4
MAY 1951 (GMT)

FIG. 6. Variations ($\frac{1}{10}$-day means) of hard cosmic-ray intensity for geomagnetic storm of May 25, 1951, showing details of prestorm cosmic-ray decrease. Sunspot group Mt. Wilson 10662 disappeared around west limb of sun on May 23, 1951.

ray decreases accompany magnetic storms. The fine structure of the hard intensity variations ($\frac{1}{10}$ day intervals) for this period may be seen in Fig. 6. There is remarkable agreement between the amplitudes for hard and total intensity.

The second prestorm decrease was of considerably larger amplitude, but it displayed entirely different characteristics at the beginning. The intensity drop started on about June 11, 1951, and the intensity kept dropping slowly for several days. A moderate magnetic storm started on June 17 and lasted about one day. The intensity remained very low for several days and then slowly began to increase. The intensity had not quite reattained its normal value by the beginning of August, 1951.

These prestorm decreases were somewhat associated in time with unusual sunspot activity. A great sunspot group (Mt. Wilson 10662), one of the largest ever recorded, completed its passage across the disk of the sun and disappeared around the West Limb on May 23, 1951, the date of onset of the sharp cosmic-ray decrease. Another great sunspot group (Mt. Wilson 10692) made its passage across the disk during the period June 12–25, 1951, which time almost exactly encompasses the period of the persistent intensity decrease noted to start on June 11.

It is noteworthy that such a prestorm decrease and slow return to normal intensity has been reported by Duperier and McCaig[37] in connection with unusual sunspot activity accompanied by magnetic storms. The event reported is unique in the cosmic-ray literature.

It is difficult to suppose that these prestorm decreases of cosmic-ray intensity, considered by Duperier and McCaig to be the logical counterpart of storms accompanied by no intensity decrease at all, are not in some way associated with the large-scale sunspot activity. It seems impossible, however, to establish any other than a loose genetic relationship. Hogg[38] has made a five-year study of the relation between cosmic rays and various solar phenomena. Correlation with formation and central meridian passage of sunspots and with solar flare activity failed to show any significant effect with respect to cosmic rays unless geomagnetic disturbances were also observed. Hogg gave no information with regard to any particular event, however.

Solar flare activity was normal during the period of the unusual events discussed above, and it cannot be said that there is any unique relationship between the sunspot passages and the time of the cosmic-ray decreases. The occurrence of geomagnetic disturbances at the time fits in with the general conclusions of Hogg.

Also, there were no unusual fluctuation trends in the pressure-altitude or upper-air temperature during these periods. Therefore it is believed that the unusual decreases cannot be explained in terms of measurable atmospheric influences. Figure 2 also contains the storm period of May 25, 1951. It is seen that the intensity trends are well preserved when the complete atmospheric correction is applied to a restricted amount of data.

V. CONCLUSIONS

1. Atmospheric Effects

The atmospheric regression coefficients of Duperier have been confirmed up to the 100-millibar level of the atmosphere. Duperier has originally interpreted the positive temperature effect as a strict consequence of the competition between decay and nuclear interaction processes, depending upon upper air density, as the ultimate fate of pions. According to the theoretical calculations made by Olbert[39] for the vertical intensity, however, all of the atmospheric effects could be explained satisfactorily in terms of the barometric pressure, pressure-altitude, and a mean temperature of part of the troposphere. According to this theory the temperature coefficient is negative, and it arises as a result of considering ionization losses by muons during their traversal of the atmosphere. It is apparent that the Duperier positive temperature coefficient is much too large to be consistent with the known mean life and nuclear collision cross section for muons.

[37] A. Duperier and M. McCaig, Nature **157**, 477 (1946).
[38] A. R. Hogg, J. Atm. Terrest. Phys. **1**, 56 (1950).
[39] S. Olbert, Phys. Rev. **92**, 454 (1953). The author is deeply indebted to Dr. Olbert for supplying a prepublication copy of his paper and for several very enlightening discussions regarding the problem.

There seems to be no doubt that the positive temperature effect is statistically real, but the degree of its physical reality is an open question. It may be only a reflection, as Olbert has suggested, of the strong negative correlation that exists between temperature changes of the troposphere and the lower stratosphere.

A possible indicator of the significance of the positive temperature effect is the observation that the regression coefficient decreases as the opening angle of the cosmic-ray telescope is increased.[4] Duperier explained this effect in terms of the fact that only the most energetic muons would penetrate the very great amount of atmosphere presented to them at large zenith angles. Such muons would have come from the decay of pions of such extremely high energy that they would not show any dependence upon density changes of the lower stratosphere. Duperier correctly predicted the ratio of the two positive temperature coefficients that he found in his experiments, but he failed to predict the magnitude of the individual coefficients. He ascribed this failure to the possible existence of intermediate particles of extremely short lifetime. The trouble may lie, in part, in the Duperier interpretation of the positive temperature coefficient. The observed zenith-angle dependence may be largely consistent with the sign reversal of temperature changes discussed above, coupled with the change of average muon survival probability as the telescope opening angle is altered and longer paths through the atmosphere are included.

If, however, one could determine the degree of physical reality of the positive temperature effect, he could, by using the zenith-angle dependence of the temperature coefficient, calculate the relative-number spectrum for high energy pions at creation. Direct upper-air cosmic-ray data are difficult to interpret in this respect because of the extremely short duration of balloon flights, the great number of complex multiplicative events taking place in the region, and the limitations on the amounts of absorber that can be balloon-borne to great altitudes.[40]

[40] A counting experiment is presently in progress at the University of Nebraska, from which a precise test of the Olbert theory will be made. Two more points on the opening-angle *vs* temperature coefficient curve will also be obtained from this work.

2. Geomagnetic Effects

It now appears that there are four cosmic-ray effects associated with magnetic storms; they are, namely, the simultaneous decrease, the delayed decrease,[15,16] the prestorm decrease, and the null effect. As yet no theory has been successful in explaining cosmic-ray behavior during periods of magnetic disturbance. No exhaustive calculations have been made on the basis of the ring-current hypothesis of Chapman,[41,42] and special calculations based upon the ring-current theory gave results which were opposite to those expected from qualitative argument.[43,44]

No precise test of any theory of the relationship of cosmic-ray intensity to geomagnetic field disturbances will be possible until more reliable magnetic storm statistics are available. It is evident that such statistics will not be available until the problem of atmospheric influences has been rather completely solved.

ACKNOWLEDGMENTS

The author is indebted to Professor R. B. Brode, who first suggested the broad outlines of this investigation and made many valuable suggestions during its progress. He is also grateful to the following people for their generous aid: H. R. Snodgrass (meteorological aspects), B. J. Harris and M. L. MacKnight (electronics), and J. Lipson (photography). The staffs of the Oakland, California, Airport Station and the Climatology Division of the United States Weather Bureau were unreservedly cooperative in supplying radiosonde and surface pressure information. Monthly reports of geomagnetic activity were very kindly supplied by Dr. A. A. Giesecke, Director of the Instituto Geofísico de Huancayo, Peru. Dr. S. B. Nicholson and staff of the Mt. Wilson and Palomar Observatories (Carnegie Institution of Washington and California Institute of Technology) kindly permitted the author to study their original sunspot records and provided detailed prepublication reports of solar flare activity.

[41] S. Chapman, Nature **140**, 423 (1937).
[42] S. Chapman and V. Ferraro, Terrestrial Magnetism and Atm. Elec. **45**, 245 (1940).
[43] S. B. Treiman, Phys. Rev. **89**, 130 (1953).
[44] Hayakawa, Nishimura, Nagata, and Sugiura, J. Sci. Research Inst. (Tokyo) **44**, 121 (1950).

Properties of Bethe-Salpeter Wave Functions

G. C. Wick
Carnegie Institute of Technology, Pittsburgh, Pennsylvania
(Received June 30, 1954)

A boundary condition at $t=\pm\infty$ (t being the "relative" time variable) is obtained for the four-dimensional wave function of a two-body system in a bound state. It is shown that this condition implies that the wave function can be continued analytically to complex values of the "relative time" variable; similarly the wave function in momentum space can be continued analytically to complex values of the "relative energy" variable p_0. In particular one is allowed to consider the wave function for purely imaginary values of t, or respectively p_0, i.e., for real values of $x_4=ict$ and $p_4=ip_0$. A wave equation satisfied by this function is obtained by rotation of the integration path in the complex plane of the variable p_0, and it is further shown that the formulation of the eigenvalue problem in terms of this equation presents several advantages in that many of the ordinary mathematical methods become available.

In an especially simple case ("ladder approximation" equation for two spinless particles bound by a scalar field of zero rest mass) an integral representation method is presented which allows one to reduce the problem exactly (and for arbitrary values of the total energy of the bound state) to an eigenvalue problem of the Sturm-Liouville type. A complete set of solutions for this problem is obtained in the subsequent paper by Cutkosky.

1. INTRODUCTION

THE formulation of a completely relativistic wave equation for two-body systems[1] has, in a certain sense, solved a long-standing problem of quantum mechanics. The natural and simple way in which relativistic invariance is achieved is, of course, very real progress, which may lead one to hope that the main features of the equation are more permanent than the solidity of its present field theoretic foundation might suggest. Furthermore, it is hardly necessary to recall that the usefulness of the equation has been amply demonstrated in several high-precision calculations of energy levels.[2]

Nevertheless, it is generally recognized that several serious and valid doubts remain about the significance and the self-consistency of the equation. Some of these doubts, of course, stem from the remaining unresolved convergence questions of renormalized quantum electrodynamics (and other similar theories). It goes without saying, however, that these deeper questions lie entirely beyond the scope of the present investigation[3] The questions and doubts we shall be concerned with[4] arise at a less formidable level; they have to do with the several unfamiliar features of the equation itself.

These are (and the list is probably incomplete):

(a) The appearance of a relative time (or respectively a relative energy) variable, the physical role of which is not entirely clear; in particular, it is admitted that the boundary conditions on the wave function for infinite values of the relative time have not been adequately formulated.

(b) The presence of strong singularities in the interaction kernel, to be avoided by special prescriptions. Standard mathematics has practically nothing to say about integral equations of this type. In particular, the prescriptions referred to imply properties of analyticity, about which one would like to know a lot more.

(c) The absence of a positive-definite norm for the wave function and of any orthogonality theorem.

(d) The fact that when the coupling constant λ is set equal to zero, the equation admits obviously improper solutions. Notwithstanding all that can be said about it, this feature is a little disturbing. It is connected to the other feature that the "order" of the differential operator in the equation is higher than that of the corresponding one-body equation. This leads to the expectation that the equation may have "too many" solutions. On the other hand, circumstance (b) has led some authors to suspect that there are no solutions at all!

(e) Finally, as explained by Goldstein,[4] we are faced with the paradoxical circumstance that, owing to the nonrelativistic perturbation approach employed, the highly successful numerical results obtained do not really offer any direct clue as to the actual properties of the relativistic equation.

The investigation described in the following pages was aimed at throwing some light on these questions. It really consists of two quite different lines of attack. The first of these starts from the remark (Sec. 2) that an additional condition for the Bethe-Salpeter (B-S) wave function follows from its definition[5] supplemented by simple stability requirements. From this, then, some unexpected consequences can be derived about

[1] E. E. Salpeter and H. A. Bethe, Phys. Rev. **84**, 1232 (1951); J. Schwinger, Proc. Natl. Acad. Sci. **37**, 455 (1951). Other closely related but more general relativistic schemes recently developed by various authors will not be discussed here.

[2] E. E. Salpeter, Phys. Rev. **87**, 328 (1952); R. Karplus and A. Klein, Phys. Rev. **87**, 848 (1952).

[3] In particular, expressions such as "the general structure" of the equation, "the analytic properties" of the interaction kernel, etc., will be used on the assumption that such properties may be inferred correctly from truncated expressions of finite order in the coupling constant, for example, from the lowest-order ("ladder") approximation.

[4] See, especially, J. S. Goldstein, Phys. Rev. **91**, 1516 (1953).

[5] M. Gell-Mann and F. Low, Phys. Rev. **84**, 350 (1951).

the analytic continuation of the wave function to complex values of the relative time (or relative energy) variable. As far as we can tell these properties cannot be obtained from the B-S equation itself. Vice versa, they can be used (Sec. 3) to transform the equation, by rotation of the integration path in the complex plane, to an equation in which $x_4=ix_0$ (respectively $p_4=ip_0$) is real. While the concept of an imaginary relative time variable does not help physical intuition, it has mathematically several advantages. A discussion of the eigenvalue problem in terms of the transformed equation will be given (Sec. 4), and the existence of solutions will be shown to follow, under fairly general assumptions, from considerations similar to those commonly employed in the nonrelativistic case. No claim of completeness or rigor is made for this "proof." Finally in Sec. 5 we shall merely itemize various approximation methods that have been studied, but will be reserved for another publication.

The second line of attack (Sec. 6), which is the subject of a more extensive investigation in the subsequent paper by Cutkosky,[6] is rather different in nature. It is an attempt to make much more specific statements about the exact solutions of the equation, by restricting the character of the equation to an especially simple type. It has not been possible so far to extend this approach to any case of real practical interest. But the fact that in one case, which is not entirely artificial, one can get a complete picture of all the solution (as is shown more completely in the following paper[6]) is not perhaps devoid of general interest. In particular the presence of "abnormal" solutions, which do not possess a nonrelativistic limit, and the circumstances under which they occur may well give a qualitative indication as to properties that will occur also in the cases of real physical interest.

2. THE STABILITY CONDITIONS

The relativistic wave function $\chi(x)$ for a system of two particles, a and b, bound together in a state $|\alpha\rangle$ is defined[5] as the matrix element, between α and the "true" vacuum state $|0\rangle$, of the time ordered product of the Heisenberg field operators ψ_a and ψ_b describing the two kinds of particles. If, for example, the relative time $t=t_a=t_b$ is positive,

$$\chi(x)=e^{-iP\cdot X}\langle 0|\Psi_a(x_a)\Psi_b(x_b)|\alpha\rangle, \tag{1}$$

where $x=x_a-x_b$, $X=(m_ax_a+m_bx_b)/(m_a+m_b)$, and $P\cdot X$ is the four-dimensional scalar product of X with the total momentum P of the system in state α. If for simplicity we assume that the compound system is at rest, then $P=(\mathbf{0}, iE)$, E being the total energy. For a bound state,

$$E=m_a+m_b-B<m_a+m_b. \tag{2}$$

Now the matrix element in (1) can be written

$$\sum_n\langle 0|\Psi_a(x_a)|n\rangle\langle n|\Psi_b(x_b)|\alpha\rangle. \tag{3}$$

The sum extends in principle over all states, but in fact the states n giving a nonzero contribution will belong to a rather special class. Consider for example the case where a and b are an electron and proton, respectively. If Ψ_a and Ψ_b were noninteracting fields, it is obvious that only one-electron states would have to be considered in the sum (3). In the presence of interaction, the states n may also contain photons, electron-positron pairs and proton-antiproton pairs. But at any rate the fundamental integrals of the motion N_a (number of electrons − number of positrons) and N_b (number of protons − number of antiprotons) must have the same values,

$$N_a=1, \quad N_b=0, \tag{4}$$

as the one-electron states. This may be rigorously shown from the commutation properties of N_a and N_b with the field operators, $(N_a+1)\Psi_a=\Psi_aN_a$, etc.

In a similar manner, one can show that the total angular momentum quantum number J for a state n, when measured in a system of reference in which the total momentum $\mathbf{p}$ is zero, must be equal to $\frac{1}{2}$.

Now all states known to us in nature, and satisfying condition (4), also satisfy the inequality,

$$E_n^2-\mathbf{p}^2\geqslant m_a, \tag{5}$$

E_n and $\mathbf{p}$ being the total energy and momentum in the state n. Furthermore, the equality sign holds true only for one-electron states.

The inequality (5) means that among all the states having the same values of the fundamental constants of the motion $\mathbf{p}$, N_a, N_b, etc., as a one-electron state, the latter is the state of lowest energy. We shall refer to (5), therefore, as the stability condition for an electron.

In a similar way, when the relative time t is negative, the wave function χ may be shown to depend on the sum

$$\sum_{n'}\langle 0|\Psi_b(x_b)|n'\rangle\langle n'|\Psi_a(x_a)|\alpha\rangle, \tag{3'}$$

in which the contributing states n' must satisfy the condition,

$$N_a=0; \quad N_b=1, \tag{4'}$$

and hence the inequality,

$$E_{n'^2}-\mathbf{p}^2\geqslant m_b, \tag{5'}$$

which shall be called the stability condition for a proton.

Summing up, we have three inequalities (2), (5), and (5'), which will form the basis of the following discussion. It should be pointed out that the above considerations can be extended to other systems. If a and b were a neutron and proton, bound together in the ground state α of the deuteron by a meson field, with the customary assumptions, one would then have, as integrals of the motion, the number of nucleons minus antinucleons N and the total electric charge Q. The states n could be shown to have values $N=1$, $Q=0$ and the states n' the values $N=1$, $Q=1$. In a theory

[6] R. Cutkosky, following paper [Phys. Rev. 96, 1135 (1954)].

which neglects the β-decay interaction, one has the right to regard both neutron and proton as essentially stable particles. If there were states $n(n')$ not satisfying conditions (5) (5′) the neutron (proton) could decay into those states by emission of photons, without violating any of the known conservation theorems. Thus it is extremely reasonable to postulate that these conditions must again be satisfied.

Now going back to (1) and using (3) with the conditions (2) and (5), we see that for $t>0$, and assuming $P=(0,iE)$, $\chi(x)$ is of the form

$$\chi(x)=\int d\mathbf{p}\int_{\omega_{\min}}^{+\infty} d\omega f(\mathbf{p},\omega)\exp(i\mathbf{p}\cdot\mathbf{x}-i\omega t), \quad (6)$$

where

$$\omega_{\min}=B\mu_a+(m_a^2+\mathbf{p}^2)^{\frac{1}{2}}-m_a>B\mu_a>0, \quad (7)$$

with $\mu_a=m_a/(m_a+m_b)$. Thus, when $t>0$, $\chi(x)$ is a superposition of positive frequency terms only.

Similarly, from (2) and (5′) it follows that, when $t<0$, $\chi(x)$ contains negative frequencies only. Thus we find that $\chi(x)$ has properties with which we are familiar in the case of Feynman propagation kernels. There is, of course, an analogy between the definition of these kernels and Eq. (1).

Let us now consider t as a complex variable. Equation (6) shows that $\chi(x)$ can be continued analytically in the lower half-plane, in the region $0\geqslant\arg t>-\pi$. Similarly starting from the negative real axis, $\chi(x)$ can be continued in the upper half-plane, in the region $\pi\geqslant\arg t>0$. There is, of course, no analytic continuation from one half-plane to the other; the two regions touch one another at one point only, $t=0$.

It should be pointed out that the statements just made are not dependent on the assumption that the state α is bound; they follow from well-known properties of the Laplace transform from the mere fact that ω is finite. If, however, $B>0$ and hence $\omega_{\min}>0$, we can further assert that $\chi(x)\to 0$ when t tends to ∞ in any direction in the lower or upper half-plane different from the real axis. This suggests that the eigenvalue problem may take a more familiar and a simpler form if the wave function and the wave equation are considered on the imaginary t axis (i.e., for $x_4=it$ real).

In order to examine this possibility carefully, it is desirable to go over to momentum space. We write $\chi(x)=\chi_1+\chi_2$, where $\chi_1=0$ for $t<0$ and $\chi_2=0$ for $t>0$. Let us calculate the Fourier transform of χ_1.

$$\phi_1(\mathbf{p},p_0)=(2\pi)^{-4}\int d_3x e^{-i\mathbf{p}\cdot\mathbf{x}}\int_0^{+\infty} dt e^{ip_0t}\chi(x). \quad (8)$$

From (6) one easily finds

$$\phi_1(\mathbf{p},p_0)=\frac{1}{2\pi i}\int_{\omega_{\min}}^{+\infty} f(\mathbf{p},\omega)(\omega-p_0-i\epsilon)^{-1}d\omega, \quad (9)$$

where ϵ is an infinitesimal positive constant. We must assume, of course, that the wave function exists for real values of p_0 [i.e., that the integral (9) converges]. From the theory of Stieltjes transforms, we then infer that (9) defines an analytic function of p_0 in the whole complex plane, in the region

$$2\pi>\arg(p_0-\omega_{\min})\geqslant 0. \quad (10)$$

Similarly ϕ_2 is defined in the region

$$-\pi<\arg(p_0-\omega_{\max})<\pi, \quad (11)$$

where

$$-\omega_{\max}=B\mu_b+(m_b^2+\mathbf{p})^{\frac{1}{2}}-m_b>B\mu_b>0.$$

Thus $\phi(p)=\phi(\mathbf{p},p_0)=\phi_1+\phi_2$ is defined in the complex p_0 plane with two cuts from $\omega_{\min}$ to $+\infty$ and from $-\infty$ to $\omega_{\max}$ (Fig. 1). In this case analytic continuation from the lower to the upper half-plane is ensured through the gap between the two cuts. ($B>0$ is essential for the existence of the gap.) Notice also that the sense of rotation implied by (10) and (11) is the opposite of that in the t plane. From the real p_0 axis one goes continuously into the upper half-plane if $p_0>\omega_{\min}>0$, into the lower half-plane if $p_0<\omega_{\max}<0$.

3. TRANSFORMATION OF THE B-S EQUATION

We shall now use the analytic properties of the wave function to transform the B-S equation by a rotation of the axis of integration in the complex p_0 (respectively x_0) plane.

The equation[1] may be written

$$F_aF_b\phi=I_{ab}\phi, \quad (12)$$

where ϕ is the wave function in momentum space, i.e., the Fourier transform of $\chi(x)$; it is a function of the relative momentum p defined by

$$p_a=\mu_aP+p,\quad p_b=\mu_bP-p, \quad (13)$$

P, μ_a and μ_b being the total momentum and the mass ratios previously defined. F_a and F_b are one-particle propagators, which, if one neglects radiative corrections

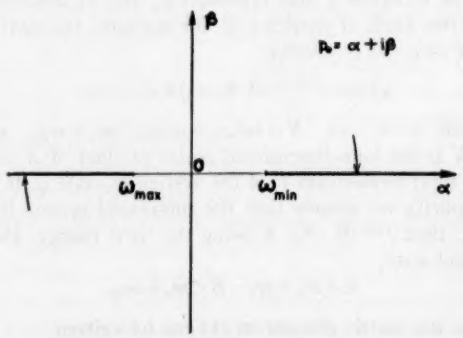

FIG. 1. The complex plane of the variable p_0. The wave function is analytic everywhere, excluding the cuts (heavy lines) on real axis.

reduce to

$$F_a=\gamma_a p_a-im_a, \quad F_b=\gamma_b p_b-im_b, \quad \text{(Dirac particles)} \tag{14}$$
$$F_a=p_a^2+m_a^2, \quad F_b=p_b^2+m_b^2. \quad \text{(Klein-Gordon)}$$

Finally, I_{ab} is the interaction operator, which has different forms, depending on the kind of theory. The following form[4] covers several cases, for the lowest order ("ladder") approximation:

$$I_{ab}\phi(p)=(\lambda/\pi^3)\int \frac{[dk]}{(p-k)^2+\kappa^2}\rho_a\rho_b\phi(k), \tag{15}$$

where $[dk]=idk_0d\mathbf{k}$. The various cases are obtained from the various possible assumptions about the "photon mass" κ, and the factors $\rho_a\rho_b(\rho_a\rho_b=1$, scalar interaction, etc.).

For simplicity we shall carry out the transformation under the assumptions (14), (15), but the proof can be easily generalized to include radiative corrections to any desired order.[7]

Let us consider the right-hand side of Eq. (12), as given by (15). The poles of the interaction kernel are at

$$k_0=p_0\pm[(\mathbf{p}-\mathbf{k})^2+\kappa^2]^{\frac{1}{2}}. \tag{16}$$

Let us carry out the integration over k_0 first. The integration is along the real axis in the plane of the complex k_0 variable, passing just under the cut on the negative axis and above the cut on the positive axis. It is also important to remember that κ in (16) is assumed to have an infinitesimal negative imaginary part, so that the pole with the larger real part lies under the integration path and the pole with the smaller real part above the path. Suppose for instance $p_0>0$, then depending on the relative magnitude of the two terms in (16) the poles will lie as in Fig. 2(a) or 2(b). For simplicity, the cuts of Fig. 1 are not indicated in Fig. 2, but they do not interfere with the following operations. First the integral path may be deformed along the dashed line [there is an *assumption* here, that $\phi(k)$ tends to zero at least like k_0^{-2} when $k_0\to\infty$ in any direction]. Now we move p_0 upwards along a circle so as to end on the positive imaginary axis. In Fig. 2(b) the path need not be changed. In Fig. 2(a) the left pole, around which the path is bent, moves to the left of the imaginary axis, and the path can be straightened. In both cases we end up with p_0 on the positive imaginary axis, and the integral over k_0 along the imaginary axis, from $-i\infty$ to $+i\infty$.

A similar consideration applies when p_0 is on the negative real axis; it then moves to the negative imaginary axis. The net result is a counter-clockwise rotation of the axis on which the wave function is used, on both sides of the equation.

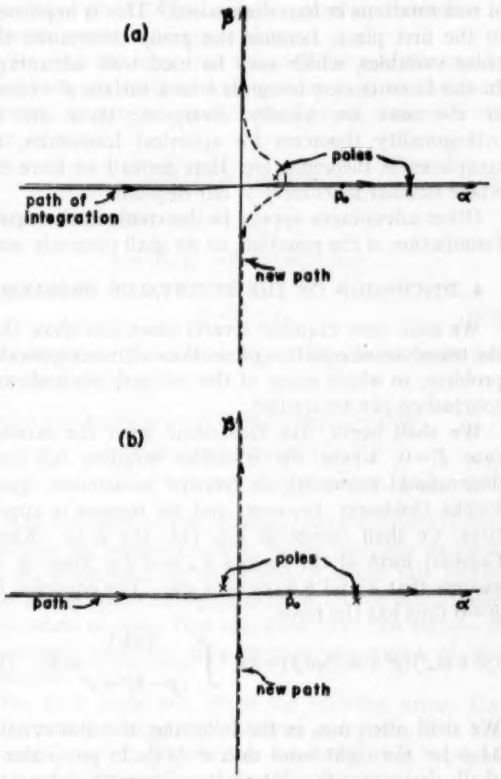

FIG. 2. Integration paths for the variable k_0 in Eq. (15).

Equation (12) is thus reduced to an integral equation in a Euclidean vector space, with the metric

$$p^2=p_1^2+p_2^2+p_3^2+p_4^2. \tag{17}$$

One does not really have to change anything to the equation, except for the understanding that a real vector now has a real component p_4 and that, in Eq. (15)

$$[dk]=dk_1dk_2dk_3dk_4 \tag{18}$$

the integral over k_4 being from $-\infty$ to $+\infty$. The fixed vector $P=(\mathbf{0}, iE)$ is now, of course, regarded as pure imaginary.

One sees at once several advantages of this transformation. The singularities of the interaction kernel [and with them the difficulties mentioned under (b) in the Introduction] are eliminated, and what is equally important, the zeros of the Klein-Gordon factors (14), i.e., the singularities of the inverses F_a^{-1}, F_b^{-1}, have similarly disappeared from the space of real p vectors. Furthermore the symmetry group of the equation is no longer the Lorentz group, but the group

[7] A higher-order term includes, in general, a number of integrations over fourth components k_0, k_0', k_0'', . . . The proof is most easily carried out if all these are regarded as complex variables and their integration paths are rotated simultaneously. An examination of higher-order corrections also requires a closer look at the factors F_a, F_b. The analytical nature of the propagators F_a^{-1}, F_b^{-1} (i.e., of the S_F', Δ_F' functions) is well understood (see reference 14), and it is easy to show that they have no singularities that stand in the way of our transformation.

of real rotations in four dimensions.[8] This is important in the first place, because the group determines the polar variables, which may be used with advantage. In the Lorentz case integrals over a surface $p^2=$const, or $x^2=$const are usually divergent; there are no orthogonality theorems for spherical harmonics, no completeness theorems, etc. Here instead we have the whole familiar machinery at our disposal.

Other advantages appear in the configuration space formulation of the equation, as we shall presently see.

4. DISCUSSION OF THE EIGENVALUE PROBLEM

We shall now examine several cases and show that the transformed equation presents us with an eigenvalue problem, to which many of the ordinary methods and conclusions can be applied.

We shall begin, like Goldstein,[9] with the extreme case $E=0$, where the equation acquires full four-dimensional symmetry in relative momentum space. Unlike Goldstein, however, and for reasons to appear later, we shall choose in Eq. (14) the K.G. (Klein-Gordon) form of the factors F_a and F_b. That is, we assume that a and b have zero spin. The equation for $E=0$ thus has the form

$$(p^2+m_a^2)(p^2+m_b^2)\phi(p)=\lambda\pi^{-2}\int\frac{[dk]}{(p-k)^2+\kappa^2}\phi(k). \quad (19)$$

We shall often use, in the following, the abbreviation $\lambda I_\kappa\phi$ for the right-hand side of (19). In particular I_0 shall designate the interaction operator when the "photon" mass κ is zero.

We can now, of course, separate ϕ, using polar variables, and reduce the problem to a one-dimensional integral equation. If for example ϕ is a function of p^2 only, the integration over angular variables on the right-hand side of (19) is quite elementary. For simplicity we shall write the one-dimensional integral equation for this case only. Let $p^2=s$, $\phi(p)=u(s)$; then

$$(s+m_a^2)(s+m_b^2)u(s)=2\lambda\int_0^\infty tu(t)dt/\{s+t+\kappa^2+[(s+t+\kappa^2)^2-4st]^{\frac{1}{2}}\}. \quad (20)$$

With the further change of variables

$$x=f(s), \quad y=f(t),$$

$$f(s)=\int_0^s ds'/(s'+m_a^2)(s'+m_b^2), \quad (21)$$

$$s^{\frac{1}{2}}(s+m_a^2)(s+m_b^2)u(s)=v(x),$$

Eq. (20) becomes a symmetric integral equation,

$$v(x)=\lambda\int_0^a K(x,y)v(y)dy, \quad (22)$$

with the finite kernel,

$$K(x,y)=2(st)^{\frac{1}{2}}/\{s+t+\kappa^2+[(s+t+\kappa^2)^2-4st]^{\frac{1}{2}}\}, \quad (23)$$

and the finite interval $a=f(\infty)$. Fredholm's theory can then be applied, to conclude that (22) has a discrete eigenvalue spectrum. The case where ϕ is proportional to a four-dimensional spherical harmonic can be similarly handled.

It may be pointed out that if $\kappa=0$, Eq. (20) can be reduced to a second order differential equation either by differentiating twice, or by a parametric representation of the solution. Both methods will be used later, and especially in the subsequent paper by Cutkosky,[6] to obtain more precise information about this case.

Let us now consider briefly Goldstein's Eq. (10), which applies to the case of two Dirac particles. When written in our notation, the equation is quite similar to (19) except that it contains only one quadratic factor in p on the left. Goldstein manages to reduce the equation to the one dimensional form, his Eq. (14), in exact analogy to our Eq. (20); the transformation in the usual frame, however, is far from trivial.[10] Unlike Eq. (20), however, Goldstein's (14) is not reducible to the Fredholm type. The difference in behavior is not an effect of our transformation, but is really due to the different power of p^2 on the left-hand side. The difficulties which Goldstein encounters in defining the eigenvalue spectrum, and which he surmounts by a special cut-off procedure, are thus not a general property of the B-S equation, but rather of the special case considered by him.

For the purpose of obtaining a more general viewpoint, let us now examine the problem in configuration space, i.e., in terms of the function $\chi(x)$. Consider first again the case $E=0$. The Fourier transform of Eq. (19) is

$$[(-\Box+m_a^2)(-\Box+m_b^2)-\lambda V(R)]\chi(x)=0, \quad (24)$$

where the "potential" $V(R)$ is

$$V(R)=4\kappa R^{-1}K_1(\kappa R), \quad R=(x_\mu x_\mu)^{\frac{1}{2}}, \quad (25)$$

K_1 being a modified Hankel function. The expression for $V(R)$ in the case $\kappa=0$,

$$V(R)=4R^{-2}, \quad (25a)$$

also gives the singularity of V at the origin in the general case.

Goldstein's Eq. (10) becomes similarly

$$[\Box-m^2+\lambda V(R)]\chi(x)=0, \quad (26)$$

[8] Four-dimensional rotations must be applied simultaneously, of course, to the relative momentum p and to the total P. If one uses the c.m. system to begin with, so that P is pure imaginary, it will stay pure imaginary after a real rotation. For Dirac particles, a linear transformation of the χ or ϕ function must accompany the rotation; this can be established in the usual way. Contrary to the Lorentz case, however, the transformation here is always *unitary*.

[9] See reference 4. Like Goldstein, we find it convenient, in general, to regard E as given, λ as the eigenvalue to be found.

[10] The author is indebted to Dr. Goldstein for various interesting conversations, and in particular for pointing out to him the peculiar "Euclidean" nature of his Eq. (14). This remark was one of the early motivations for the present study.

which presents a striking analogy to the ordinary three-dimensional Schrödinger equation. With x_4 real, (26) is, of course, an elliptic differential equation. This, together with the boundary condition $\chi(x)\to 0$ at infinity, allows a discussion of the eigenvalue problem along familiar lines.

A special difficulty, also encountered by Goldstein, is presented by the boundary condition at the origin $R=0$, about which we have unfortunately no definite indication from general field-theoretic considerations. The difficulty arises because of the Fuchsian singularity (25a); if the potential were regular everywhere, there would be little doubt that $\chi(x)$ must be regular too.

One can see at once, however, that the singularity of the potential affects (24) and (26) in a very different manner. Consider, for example, spherically symmetric solutions. The radial equation corresponding to (26), or

$$[d^2/dR^2+(3/R)(d/dR)-m^2+\lambda V(R)]\chi=0, \quad (26a)$$

has two solutions near the origin, of the type $\chi=R^\alpha \times(1+c_1R+\cdots)$ with

$$\alpha=-1\pm(1-4\lambda)^{\frac{1}{2}}. \quad (27)$$

Thus, if $\lambda<\frac{1}{4}$, it is possible to make a distinction between the "regular" (less singular) and the "irregular" solution. If $\lambda>\frac{1}{4}$, it seems highly unlikely that a plausible condition to determine the right solution can be found. In the case $\kappa=0$, moreover, the equation can be solved explicitly,[4] the "regular" solution being $R^{-1}J_n(iR)$, where $n=+(1-4\lambda)^{\frac{1}{2}}$. This solution, however, never satisfies the condition at infinity. We thus reach the conclusion that no value $\lambda<\frac{1}{4}$ is an eigenvalue. In our opinion, for $\lambda>\frac{1}{4}$ the eigenvalue problem becomes ill-defined. We shall not try to discuss further here[11] whether the limiting case $\lambda=\frac{1}{4}$ can actually be regarded as an eigenvalue.[4]

In Eq. (24), on the other hand, the singularity (25a) does not affect the indicial equation. The radial equation for a spherically symmetric solution, for example, has four independent solutions near origin, say $\chi_1, \chi_2, \chi_3, \chi_4$, behaving respectively like R^2, R^0, $\ln R$, and R^{-2}. If there were no potential, we would clearly say that the acceptable solution is a linear combination $c_1\chi_1+c_2\chi_2$ of the two "regular" solutions. We shall make the same assumption when there is a potential.[12] Likewise we can define, for large R values, four solutions behaving respectively like $R^{-\frac{1}{2}}\exp(\pm\mu_a R)$ and $R^{-3}\exp(\pm\mu_b R)$. The solution $c_1\chi_1+c_2\chi_2$ will be a linear combination of these four. In order to satisfy the condition $\chi\to 0$ at infinity, two coefficients must be zero; that is, we have two conditions. One of these may be satisfied by a suitable choice of c_1/c_2; the remaining one gives a condition on λ. This will, in general, determine a discrete spectrum of eigenvalues.

We shall see later that for $\kappa=0$ the analysis can be carried much further. Let us now turn to the more interesting general case $E\neq 0$. Let us write (in the c.m. system)

$$P=(0,iE)=i(m_a+m_b)\eta, \quad (28)$$

where η is the four vector

$$\eta=(0,\epsilon), \quad \epsilon=E/(m_a+m_b).$$

Notice that

$$\eta^2=\epsilon^2<1. \quad (29)$$

The factor on the left of Eq. (19) now becomes, remembering (13):

$$(m_a^2+p_a^2)(m_b^2+p_b^2)=p^4+(m_a^2+m_b^2)(1-\eta^2)p^2 +4m_am_b(p\eta)^2+m_a^2m_b^2(1-\eta^2)^2 +2i(m_a-m_b)(p^2-m_am_b)(p\eta). \quad (30)$$

It is at first sight rather puzzling that the equation now contains an imaginary term whose presence depends on m_a being $\neq m_b$. In configuration space this means that the operator corresponding to (30) is self-adjoint only when $m_a=m_b$. One can show that this feature is connected with the time-reversal properties of the equation.

We shall point out, when the occasion arises, the differences produced by the term in m_a-m_b. For the moment, we shall consider only the case $m_a=m_b$ ($=m$, say). The analog of Eq. (24) then is

$$\{[-\Box+m^2(1-\eta^2)]^2-4m^2\eta^2\partial^2/\partial x_4^2\}\chi(x) =\lambda V(R)\chi(x). \quad (31)$$

Since complete separation of variables is impossible, a solution must now be a superposition $\chi=\sum_n f_n(R)Y_n$ of four-dimensional spherical harmonics Y_n of different orders. The radial functions f_n satisfy a system of coupled fourth-order differential equations, and it is no longer possible to discuss the eigenvalue problem in terms of a single radial function. This is a considerable complication, but one may notice, nevertheless, that the term in (31) which produces the coupling is of second order only, so that the indicial equation for each radial function f_n is the same as in Eq. (24). If one writes $f_n(R)=R^\alpha(1+c_1R+\ldots)$ the possible values for α are $\pm n$, $\pm(n+2)$; we may assume that only the positive values are allowed in a "regular" solution, just as in Eq. (24). Thus there is no qualitative difference between the two equations, with regard to the behavior of solutions near $R=0$.

The asymptotic behavior of $\chi(x)$ at infinity, on the other hand, is more interesting. It will be shown below that when x tends to infinity, χ behaves asymptotically like $\exp[-R\varphi(\theta_4)]$, i.e., it tends to zero exponentially but with a coefficient depending on the direction, more specifically on the angle θ_4 with the "4" axis. For our present purpose, however, it is only interest-

[11] It may be remarked that in reference 6 Goldstein's eigenvalue is also obtained from Eq. (19) in the limit $m_b/m_a\to 0$ (and $\kappa=0$).

[12] One can argue that $\chi\sim\ln R$ is not really a solution of (24) since it gives an additional term $\sim\delta_4(x)$. $\chi\sim R^{-2}$ gives a term $\Box\delta_4(x)$.

ing to notice that $\varphi(\theta_4)$ has a positive lower limit $\varphi \geqq 1-\epsilon$ so that, in a certain sense, there is again no fundamental difference in behavior between the solutions of (31) and those of (24), and we may expect that in both cases the boundary conditions at $R=0$ and $R=\infty$ will determine a discrete λ spectrum.

The elementary considerations developed previously seemed of interest, because of the analogy with considerations often made with regard to the ordinary Schrödinger equation. In this sense we may say that (31) presents an analogy to the Schrödinger equation for a particle in an asymmetric field, where again the reduction of the eigenvalue problem to a simple one-dimensional Sturm-Liouville problem is not feasible.

In either case, a rigorous discussion of the eigenvalue problem can only be achieved by less elementary means, such as the reduction of the problem to an integral equation. We do not wish to carry out such a study here, but we may point out along what lines it could be carried out.

We already have, of course, in Eq. (19) and its generalization for $E \neq 0$, an integral formulation of the problem. In the case $m_a = m_b$ corresponding to Eq. (31), the equation can be reduced to the real symmetric form

$$\Phi(p) = \lambda \int H(p,k)\Phi(k)[dk], \tag{32}$$

where

$$\begin{aligned} \Phi(p) &= f^{\frac{1}{2}}(p)\phi(p) \\ f(p) &= [p^2 + m^2(1-\eta)]^2 + 4m^2\eta^2 p_4^2 \\ H(p,k) &= \pi^{-2}[f(p)]^{-\frac{1}{4}}[(p-k)^2+\kappa^2]^{-1}[f(k)]^{-\frac{1}{4}}. \end{aligned} \tag{33}$$

Now by counting powers of p and k it is easy to see that

$$\int H^2(p,k)[dp][dk] < \infty, \tag{34}$$

which together with other similar inequalities, which the mathematically inclined reader can readily discover, may be used to show that (32) is "nonsingular" and thus possesses a discrete λ spectrum. Furthermore all eigenvalues are real. Finally, one can see that the kernel is positive-definite[13] so that $\lambda > 0$.

An alternative integral formulation can be obtained as usual in configuration space. In fact, Eq. (31) together with the regularity condition at the origin and the boundary condition $\chi(x) \to 0$ at infinity, can be replaced by an integral equation,

$$\chi(x) = \lambda \int G(x-x')V(R')\chi(x')[dx'], \tag{35}$$

or $\chi = \lambda GV\chi$, where G is the inverse of the differential operator on the left-hand side of (31). When $m_a = m_b$, the function $G(x)$ is even: $G(x) = G(-x)$, so that (35) can be easily symmetrized. The function $G(x)$ is constructed in the Appendix, and it may be seen from Eqs. (A7) and (A8) there that $G(x)$ has a very weak singularity at the origin (it is in fact finite at $x=0$) and tends to zero at infinity like

$$G(x) \sim g e^{-R\varphi(\theta_4)}, \tag{36}$$

where g is a factor which varies slowly compared to the exponential and

$$\begin{aligned} \varphi(\theta_4) &= m(1-\epsilon\cos\theta_4) \quad |\cos\theta_4| > \epsilon \\ &= m(1-\epsilon^2)^{\frac{1}{2}}\sin\theta_4 \quad |\cos\theta_4| < \epsilon. \end{aligned} \tag{37}$$

If $V(R) \to 0$ sufficiently rapidly when $R \to \infty$, the asymptotic behavior of $\chi(x)$ as given by the integral in Eq. (35) will reflect that of $G(x)$, from which the conclusions previously mentioned may be obtained. Incidentally it may be noticed that in the nonrelativistic limit, $\epsilon \approx 1$, the lower form in Eq. (37) covers almost the whole solid angle, and furthermore $\varphi \approx (mB)^{\frac{1}{2}}\sin\theta_4$, $R\varphi(\theta_4) = (mB)^{\frac{1}{2}}r$, where $r^2 = x_1^2 + x_2^2 + x_3^2$. We thus find the typical exponential of the three-dimensional Schrödinger function. It is indeed rather remarkable that in this region, i.e., with the exception of a narrow cone around the x_4 axis, the asymptotic form of $\chi(x)$ is not time-dependent.

In the foregoing discussion we have, perhaps, laid too much stress on the special case of two spinless particles with the special interaction I_s of Eq. (19). It is clear that none of the conclusions we have reached as to discreteness of the λ-spectrum, etc., must necessarily remain true if we change the propagators F_a, F_b or the interaction kernel.

If, for example, we write the analog of (32) with Dirac propagators, the conclusion that the equation is nonsingular no longer holds true. As pointed out above, Goldstein[4] already met this situation for the special case $E=0$. It is, of course, also possible to formulate the problem in a form similar to (35), namely,

$$\chi(x) = \lambda \int G_D(x-x')V(R')\chi(x')[dx'], \tag{38}$$

where

$$\begin{aligned} G_D(x) = &[\gamma_a(\partial/\partial x) - m_a(1+\gamma_a\eta)] \\ &\times [\gamma_b(\partial/\partial x) + m_b(1+\gamma\eta)]G(x). \end{aligned} \tag{39}$$

In this case the singular character of the equation comes about because $G_D(x)$ has a much stronger singularity than $G(x)$, near $x=0$. When this is combined with the $1/R^2$ singularity of $V(R)$ [Eqs. (25) and (25a)], Eq. (38) becomes singular. This does not mean that discrete eigenvalues of λ will not exist, but only that a much more detailed study of the equation will be necessary. One could, of course, also consider the possibility of less singular potentials $V(R)$, in which case the general theory of integral equations might again be applicable.

It seems pointless at present to investigate in detail such possibilities. One will bear in mind, however, that within the framework of our transformed system of

[13] G. C. Wick, Nuovo cimento (to be published).

coordinates, such questions can be attacked by ordinary mathematical methods.

5. APPROXIMATION METHODS

It is also possible to show that our transformed equation has several advantages if one wants to employ approximate methods of solution. We have in mind, in particular: (a) a perturbation expansion in the neighborhood of $E=0$ (see also reference 4), (b) variational principles, (c) nonrelativistic approximations, without special restrictions as to the form of $V(R)$. These questions will be discussed in a paper which the author hopes to present shortly in another periodical.[13]

6. EXACT SOLUTIONS FOR $\kappa=0$

A comparison of Eqs. (25) and (25a) suggests that the problem of solving the B-S equation exactly may be far more elementary in the latter ($\kappa=0$) case. This is borne out by Goldstein's solution[4] for Eq. (26), and we shall see in a moment that also Eq. (24) has quite simple solutions if $\kappa=0$ and $m_a=m_b$. And, of course, one will remember that the ordinary nonrelativistic Schrödinger problem is far more elementary with a Coulomb than with a Yukawa potential.

At first, however, one would regard this analogy as encouraging only for the special case $E=0$, when the B-S equation is separable. We were, therefore, quite surprised when we first realized that for $\kappa=0$ even the nonseparable Eq. (31) can be reduced to a one-dimentional integral equation, or alternatively to a one-dimensional eigenvalue problem of the Sturm-Liouville type. We shall explain the basic idea for the simplest type of solution and for $m_a=m_b$ only. The extension to other cases was carried out by Cutkosky and is described in the accompanying paper.

Choosing $m_a=m_b$ ($=m$, say), let us first examine the separable case, Eq. (24). In momentum space, the equation has the form

$$(p^2+m^2)^2\phi(p)=\lambda I_\phi\phi(p), \tag{40}$$

which is very similar to the nonrelativistic hydrogen equation in momentum space. The latter, of course, is a three-dimensional equation and does not have the square power on the left, but it will appear that the analogy is closest when the two changes are made simultaneously.

In particular, the ground-state wave function of hydrogen: $\phi(p)=(p^2+p_0^2)^{-2}$, is duplicated here by the solution

$$\phi(p)=(p^2+m^2)^{-3} \tag{41}$$

corresponding to the eigenvalue $\lambda=2m^2$. That (41) satisfies Eq. (40) can be verified most easily if one first writes, à la Feynman:

$$(k^2-2k\cdot p+p^2)^{-1}(k^2+m^2)^{-3}=\int_0^1 3(1-x)^2dx \times[(k-xp)^2+(1-x)(m^2+xp^2)]^{-4}. \tag{42}$$

One then finds easily that

$$I_\phi\phi=(1/2m^2)(p^2+m^2)^{-1}, \tag{43}$$

showing that Eq. (40) is satisfied.

More generally, one can see that I_0 applied to $(p^2+2p\cdot q+M^2)^{-3}$, where M^2 and the vector q are constants, gives $(p^2+2p\cdot q+M^2)^{-1}$, apart from a proportionality factor. This peculiar self-reproducing property of a quadratic form in p, under the operation I, is characteristic of the case $\kappa=0$.

Consider now the equation for $E\neq 0$. For simplicity let $m=1$ from now on. The equation is

$$[p^2+2ip\cdot\eta+1-\eta^2][p^2-2ip\cdot\eta+1-\eta^2]\phi=I_\phi\phi. \tag{44}$$

Clearly ϕ cannot be a function of p^2 alone; it must be at least a function of p^2 and $p\cdot\eta$ (for an S state). The above considerations suggest that we may be able to generalize solution (41) by writing ϕ as a superposition of terms[14] of the type $(p^2+2p\cdot q+M^2)^{-3}$ where q is parallel to η, say, $q=iz\eta$. That is

$$\phi(p)=\int dzdM^2g(z,M^2)[p^2+2izp\cdot\eta+M^2]^{-3}. \tag{45}$$

One then sees immediately that

$$I_\phi\phi=\tfrac{1}{2}\int dzdM^2g_1(z,M^2)[p^2+2izp\cdot\eta+M^2]^{-1}, \qquad g_1(z,M^2)=g(z,M^2)/(M^2+z^2\eta^2). \tag{46}$$

Inserting on the right of (44) and dividing by the two quadratic factors on the left, one then tries to reduce the result again to the form (45) by reassembling the three quadratic denominators into a cube [in a similar way as in Eqs. (42) and (A3) in the Appendix]. One sees at once that if $M^2=1-\eta^2$ the "mass term" reproduces itself. Thus we set

$$g(z,M^2)=g(z)\delta(M^2-1+\eta^2). \tag{47}$$

Carrying out the transformations indicated above and writing

$$Q(z)=1-\eta^2+z^2\eta^2, \tag{48}$$

we find

$$\phi(p)=\tfrac{1}{2}\lambda\int Q^{-1}(z)g(z)dz\int_{-1}^{+1}dy\int_0^1 \times xdx[p^2+2i\zeta p\cdot\eta+1-\eta^2]^{-3}, \qquad \zeta=xy+(1-x)z. \tag{49}$$

[14] An expression of this type has a certain resemblance to the parametric representations for S_F' and Δ_F' developed by M. Gell-Mann and F. E. Low, Phys. Rev. **95**, 1300 (1954). G. Källén [Helv. Phys. Acta **25**, 417 (1952)] has previously used similar representations for other quantities that are a little less closely related to the B-S wave function, Eq. (1). In the case of these quantities, and of the functions $S_F'\Delta_F'$, it is possible as the above-mentioned authors have shown, to derive the general form of the parametric representation from the definition of the quantities, and from considerations of relativistic invariance. The author has not been able to do the same for Eq. (1). Nevertheless the analogy with S_F' and Δ_F' was used to "guess" the form of Eq. (45).

Eliminating y in favor of ζ, and carrying out the integrations over x and z first, (49) acquires indeed the general form required by (45) and (47). Writing that the two expressions are identical gives an integral equation for $g(z)$.

To this end notice that if z in (45) is allowed to vary between -1 and $+1$, ζ will also vary between the same limits. Writing $d\zeta=xdy$ and noting that for given z and ζ,

$$\int dx=R(\zeta,z)=\begin{cases}(1+\zeta)/(1+z) & \text{if } z>\zeta\\ (1-\zeta)/(1-z) & \text{if } z<\zeta,\end{cases} \tag{50}$$

one finds

$$\phi(p)=\int_{-1}^{+1}\gamma(\zeta)[p^2+2i\zeta p\cdot\eta+1-\eta^2]^{-1}d\zeta, \tag{51}$$

where $\gamma(\zeta)$ is given by the right-hand side of Eq. (52) below. The condition $g=\gamma$ thus gives the integral equation

$$g(\zeta)=\tfrac{1}{2}\lambda\int_{-1}^{+1}R(\zeta,z)Q^{-1}(z)g(z)dz. \tag{52}$$

This is, of course, an integral equation of Fredholm's type, and has a discrete λ spectrum. We thus have achieved the surprising result that the B-S equation (44), although nonseparable (as far as we can tell), can be reduced to a one-dimensional problem.

Further Reduction of the Problem

Equations (45), (47), and (52), of course, do not give all the solutions; they do not even give all the S states. The necessary generalizations, however, are natural and will be described in the accompanying paper. Let us instead study (52) a little further. From (50) and (52) one can see that

$$g(+1)=g(-1)=0. \tag{53}$$

Furthermore, differentiating (52) twice, we get

$$g''(z)+\lambda(1-z^2)^{-1}Q^{-1}(z)g(z)=0. \tag{54}$$

These equations formulate the problem as a Sturm-Liouville eigenvalue problem. Thus it is easy to predict qualitatively the dependence of λ on η^2.

Thus consider first $\eta^2=0$; then $g(z)=(1-z^2)$ is a solution, and clearly it corresponds to the lowest eigenvalue since it has no nodes. The higher solutions are also polynomials.[15] The lowest eigenvalue is $\lambda=2$, as we know already. The "potential" $Q^{-1}(z)$ is an increasing function of the parameter η^2. Hence every eigenvalue λ must decrease as η^2 increases.

When $\eta^2\to 1$, $Q^{-1}(z)$ develops a singularity at $z=0$, in fact,

$$Q^{-1}(z)\approx(1-\eta^2+z^2)^{-1}\approx\pi(1-\eta^2)^{-\frac{1}{2}}\delta(z). \tag{55}$$

[15] See the general discussion in reference 6.

The lowest eigenfunction simply develops a kink at $z=0$, while the behavior of the higher states is more complicated; if one inserts the approximation (55) into (52), one finds

$$g(\zeta)=\tfrac{1}{2}\pi(1-\eta^2)^{-\frac{1}{2}}g(0)\lambda(1-|\zeta|), \tag{56}$$

which requires

$$\lambda=(2/\pi)(1-\eta^2)^{\frac{1}{2}}. \tag{57}$$

This is, of course, just what one expects from the nonrelativistic Balmer formula for the lowest eigenvalue.

Clearly the limit $\eta^2\to 1$ requires a more careful treatment for the higher eigenvalues. The reason is that all the nodes of the eigenfunction tend to concentrate near $z=0$ so that the approximation (55) is not adequate.

It is easy to see that λ does not tend to zero for the higher eigenvalues. Thus, none of the higher eigenvalues of Eq. (54) has anything to do with the states known from the nonrelativistic case. It will be shown by Cutkosky[6] that the other known states are contained in other families of solutions of the B-S Equation; each of these families, however, contains in addition "abnormal" solutions that have no nonrelativistic limit.

We shall now examine the behavior of the "abnormal" eigenvalues of Eq. (54) when $\eta\to 1$ and show that all these eigenvalues converge to a common limit $\lambda\to\frac{1}{4}$. First we can see that $\lambda<\frac{1}{4}$ cannot be an eigenvalue other than (57). Consider in fact the second eigenvalue; the corresponding eigenfunction must be odd and have a node at $z=0$. Hence we need only examine a solution of (54) with the boundary conditions $g(0)=g(1)=0$. Assuming

$$1-\eta^2\ll 1, \tag{58}$$

we divide the interval $0-1$ into two parts,

$$0<z<z_0 \quad\text{and}\quad z_0<z<1, \tag{59}$$

choosing z_0 to satisfy

$$(1-\eta^2)^{\frac{1}{2}}\ll z_0\ll 1. \tag{60}$$

In the first interval we write the equation with a slight change of variables,

$$\begin{aligned}&x=\eta(1-\eta^2)^{-\frac{1}{2}}z,\\ &d^2g/dx^2+\lambda(1+x^2)^{-1}g=0,\end{aligned} \tag{61}$$

neglecting terms of order $\leq(1-\eta^2)^{\frac{1}{2}}$. (One can see *a posteriori* that this approximation is justified for our purposes.) Equation (61) is of Riemann's type, and the solution we want is

$$\begin{aligned}&g=g^+-g^-,\\ &g^\pm=(1+x^2)^{\frac{1}{2}}F_1(\tfrac{3}{2}+\rho,\tfrac{3}{2}-\rho;2;\tfrac{1}{2}(1\pm ix)),\\ &\rho=(\tfrac{1}{4}-\lambda)^{\frac{1}{2}}.\end{aligned} \tag{62}$$

In the second interval we write $Q(z)=z^2$, again neglecting terms of order $(I-\eta^2)^{\frac{1}{2}}$ at most, and write

$$s=z^2, \quad d^2g/ds^2+\tfrac{1}{2}s^{-1}dg/ds+\tfrac{1}{4}\lambda g/(1-s)s^2=0, \quad (63)$$

which again is of Riemann's type. The solution satisfying $g=0$ at $z=1$ is

$$g=(1-z^2)z^{\frac{1}{2}+\rho}{}_2F_1(1\tfrac{1}{4}+\tfrac{1}{2}\rho, \tfrac{3}{4}+\tfrac{1}{2}\rho; 2; 1-z^2). \quad (64)$$

We will first show that if $\lambda<\frac{1}{4}$, the "internal" and "external" solutions (62) and (64) cannot join smoothly at $z=z_0$, i.e., $x=x_0=\eta z_0(1-\eta^2)^{-\frac{1}{2}}$. In fact, since $x_0\gg 1$, we may evaluate (62) by means of the asymptotic formula for the hypergeometric function. One finds, omitting a proportionality factor,

$$g_{\text{int}}\sim x^{\rho+\frac{1}{2}}(1+\cdots)+A(\rho)x^{-\rho+\frac{1}{2}}(1+\cdots). \quad (62')$$

The dots indicate expansions in powers of x^{-1}, and since $\rho<\frac{1}{2}$ it is consistent to keep the first term of the second expansion, while neglecting the higher terms of the first expansion. Furthermore,

$$A(\rho)=2^{2\rho}\tan(\tfrac{1}{4}\pi-\tfrac{1}{2}\pi\rho)\Gamma(2\rho)/\Gamma(-2\rho) \quad (65)$$

is a negative quantity which varies from 0 to -1 as λ varies from 0 to $\frac{1}{4}$.

Similarly, (64) may be evaluated for small values of z by means of the known transformation of $F(a, b, c, 1-s)$ to hypergeometric functions of the variable s. One finds

$$g_{\text{ext}}\sim z^{\rho+\frac{1}{2}}(1+\cdots)+B(\rho)z^{\rho+\frac{1}{2}}(1+\cdots), \quad (64')$$

where the dots now indicate expansions in powers of z^2, and

$$B(\rho)=2^{2\rho}\Gamma(\rho)\Gamma(\tfrac{3}{2}-\rho)/\Gamma(-\rho)\Gamma(\tfrac{3}{2}+\rho) \quad (66)$$

is a quantity which on the whole interval $0<\lambda<\frac{1}{4}$ $(0<\rho<\frac{1}{2})$ stays quite close to -1 (and is in fact <-1).

Rewriting (62′) in terms of the variable z and omitting again a proportionality factor, we find

$$g_{\text{int}}\sim z^{\rho+\frac{1}{2}}+A(\rho)(1-\eta^2)^{\rho}z^{-\rho+\frac{1}{2}}, \quad (67)$$

which is of the same form as (64′), but with a coefficient for the second term which is smaller than $B(\rho)$ in absolute value, for all values of ρ in the stated interval. Hence (64′) and (67) can never join smoothly. In addition it is easy to verify that the slope g'/g is larger for (67) than for (64′), as one expects if λ is *too low* to be an eigenvalue.

Let us now turn to the case $\lambda>\frac{1}{4}$. One can see that essentially the same formulae will hold, except that ρ will be a pure imaginary, say $\rho=i\sigma$, $\sigma=(\lambda-\frac{1}{4})^{\frac{1}{2}}$. One sees, then, that (64′) and (67) take the respective forms

$$g_{\text{ext}}\sim z^{\frac{1}{2}}\sin(\sigma\ln z+\beta) \quad (64'')$$

and

$$g_{\text{int}}\sim z^{\frac{1}{2}}\sin(\sigma\ln z-\tfrac{1}{2}\sigma\ln(1-\eta^2)+\alpha), \quad (67')$$

where α and β are phases depending on σ, which for small values of σ are of the form

$$\alpha=a\sigma, \quad \beta=b\sigma, \quad (68)$$

a and b being constants, whose precise value we shall not determine.

Obviously (64″) and (67′) can be joined smoothly if $\alpha-\beta-\frac{1}{2}\sigma\ln(1-\eta^2)=n\pi$, where n is an integer. If $1-\eta^2$ is so small that $-\ln(1-\eta^2)\gg 1$, the above equation will have small roots σ so that by using (68),

$$\sigma\equiv(\lambda-\tfrac{1}{4})^{\frac{1}{2}}=n\pi/[a-b-\tfrac{1}{2}\ln(1-\eta^2)]. \quad (69)$$

To an even cruder approximation, one has

$$\sigma\sim-2\pi n/\ln(1-\eta^2); \quad \lambda=\tfrac{1}{4}+[2\pi n/\ln(1-\eta^2)]^2. \quad (70)$$

Equation (70), for $n=0, 1, 2,\cdots$ gives an infinity of eigenvalues all tending to $\lambda=\frac{1}{4}$ when $\eta^2\to 1$. It should be pointed out that these correspond to odd eigenfunctions. In a similar way one can show, however, that the same formula, with $2n$ replaced by $2n+1$, gives the eigenvalues for the even eigenfunctions.

About the possible significance of these "abnormal" solutions we shall not try to speculate here. Since they occur only for finite values of λ $(\lambda\gtrsim\frac{1}{4})$, it would be unwise to assume that they are a property of the complete B-S Equation. Certainly the ladder approximation cannot be trusted to that extent. If the theory is used only for small values of the coupling constant, the abnormal solutions do not exist, in the case we have studied, and no contradiction with known facts can be established. Nevertheless it would seem that these solutions deserve further study.

ACKNOWLEDGMENTS

The present work was begun while the author was a guest of the Institute for Advanced Study, Princeton, New Jersey. The author is happy to acknowledge his indebtedness to the Director of the Institute, Professor J. R. Oppenheimer, for the stimulation and encouragement he derived from a year's stay at the Institute. Various members of the Institute, in particular, Professor F. Dyson, Professor G. Källén, Professor A. Pais, Professor W. Pauli, and Professor R. Jost gave kind encouragement and invaluable criticism. Special thanks are due to Dr. Murray Gell-Mann for suggesting that the analogy discussed in reference 14 might be of help.

APPENDIX

We shall construct here the Green's function $G(x)$, which is a solution of $(p_a^2+m_a^2)(p_b^2+m_b^2)G(x)=\delta(x)$, p_a and p_b being defined by Eqs. (13) and (28), with $p=-i$ Grad. We shall calculate G for the general case $m_a\neq m_b$, since this involves no additional difficulty. Using Fourier transforms, one sees at once that

$$G(x)=(2\pi)^{-4}\int[(p_a^2+m_a^2)(p_b^2+m_b^2)]^{-1}e^{ipx}[dp]. \quad (A1)$$

In the following we use $\frac{1}{2}(m_a+m_b)$ as the unit of mass, setting

$$m_a=1+\Delta, \quad m_b=1-\Delta. \tag{A2}$$

Furthermore we transform, *à la* Feynman,

$$[(p_a^2+m_a^2)(p_b^2+m_b^2)]^{-1}=\tfrac{1}{2}\int_{-1}^{+1}[p,y,\Delta]^{-2}dy, \tag{A3}$$

where

$$[p,y,\Delta]\equiv p^2+2i(y+\Delta)(p\cdot\eta) +(1-\eta^2)(1+2y\Delta+\Delta^2). \tag{A4}$$

Furthermore, applying to $Q\equiv[p,y,\Delta]$ the formula

$$Q^{-2}=\int_0^\infty e^{-\alpha Q}\alpha d\alpha$$

and inserting into (A1), the integration over p may be performed, with the result

$$G(x)=(32\pi^2)^{-1}\int_{-1}^{+1}dy\int_0^\infty \alpha^{-1}d\alpha \times\exp[-\alpha U-\tfrac{1}{4}R^2\alpha^{-1}+(y+\Delta)(x\eta)], \tag{A5}$$

with

$$U=(1+2y\Delta+\Delta^2)(1-\eta^2)+\eta^2(y+\Delta)^2. \tag{A6}$$

Owing to (29), U is positive for $|y|\leq 1$; hence the integral over α in (A5) is always meaningful.

We then find that

$$G(x)=(4\pi)^{-2}e^{i\Delta x_4}\int_{-1}^{+1}dy \times e^{iyx_4}K_0(R(1-\eta^2+\Delta^2+2y\Delta+y^2\eta^2)^{\frac{1}{2}}), \tag{A7}$$

where $K_0(z)$ is the modified Hankel function, $i(\pi/2)\times H_0^1(iz)$. The asymptotic behavior of (A7) when $R\to\infty$ in a specified direction (i.e., keeping x_4/R constant) is found noting that $K_0(z)\sim(\pi/2z)^{\frac{1}{2}}e^{-z}$. The exponential part of (A7) is then

$$G(x)\sim\cdots\int dy\exp[-Rf(y)],$$

where

$$f(y)=[(1-\eta^2)(1-y^2)+(y+\Delta)^2]^{\frac{1}{2}}-\epsilon(y+\Delta)x_4R^{-1}.$$

It is easy to see that $f(y)>0$ in the whole interval $-1\leq y\leq+1$. Hence $G(x)$ satisfies the boundary condition $G\to 0$ as $R\to\infty$ in any direction. If y_m is the point in the interval where $f(y)$ is a minimum, then the strongest factor in the asymptotic dependence of $G(x)$ is

$$G(x)\sim\exp[-Rf(y_m)]. \tag{A8}$$

Notice that y_m depends on the direction. Consider, for example, the simplest case $\Delta=0$. Then if $|x_4|<\epsilon R$, y_m is defined by the minimum condition

$$y_m\epsilon R=x_4(1-\epsilon^2+y^2\epsilon^2)^{\frac{1}{2}}; \tag{A9}$$

that is, writing $x_4/R=\cos\theta_4$, $y_m\epsilon=(1-\epsilon^2)^{\frac{1}{2}}\cot\theta_4$. If $|\cos\theta_4|>\epsilon$ the root (A9) is not inside the interval, so the minimum of $f(y)$ occurs at $y=\pm 1$, according as $\cos\theta_4\gtrless 0$; summarizing, one has

$$\begin{aligned} &|\cos\theta_4|>\epsilon \quad f(y_m)=1-\epsilon|\cos\theta_4| \\ &|\cos\theta_4|<\epsilon \quad f(y_m)=(1-\epsilon^2)^{\frac{1}{2}}\sin\theta_4. \end{aligned} \tag{A10}$$

Notice that in the latter case,

$$G(x)\sim\exp[-(1-\epsilon^2)^{\frac{1}{2}}r\sin\theta_4]=\exp[-(1-\epsilon^2)^{\frac{1}{2}}r],$$

if r is the length of the space component of x. In the former case, instead, $G(x)\sim e^{-R+\epsilon|x_4|}$; in particular, in the time direction $G(x)$ tends to zero like $\exp[-(1-\epsilon)\times|x_4|]$.

Solutions of a Bethe-Salpeter Equation

R. E. CUTKOSKY
Carnegie Institute of Technology, Pittsburgh, Pennsylvania
(Received June 30, 1954)

The discussion in the preceding paper of a simplified Bethe-Salpeter equation is continued. Two methods are used to find a complete set of solutions, an integral transform method, and an adaption of Fock's treatment of the hydrogen atom. The degeneracy is found to be the same as that of the nonrelativistic hydrogen. In addition to the solutions which have the expected nonrelativistic limit, a large number of anomalous solutions are obtained. The behavior in the limit in which the mass of one particle becomes infinite is considered, and it is found that in this limit the ladder approximation gives an equation which does not correspond to the motion of a particle in the field of a fixed center of force.

I. INTRODUCTION

THE Bethe-Salpeter equation for two scalar particles has an especially simple form when these particles are assumed to interact through a massless scalar field. In the preceding paper,[1] Wick has given a general discussion of the Bethe-Salpeter equation and has concluded by examining some of the solutions of this particular equation. The study of this equation is continued in this paper, using the methods introduced by Wick, which enable one to obtain a complete set of bound-state solutions. Since this relativistic equation for two bosons can be solved easily, it not only provides an excellent illustration of the general results of Wick, but also gives one an insight into the techniques that one might apply to other equations, which would be more complicated, but also more realistic.

If we use the notation of Wick, the equation we wish to solve is written in momentum space as

$$[(p+i\eta\mu_a)^2+m_a^2][(p-i\eta\mu_b)^2+m_b^2]\phi(p) = \frac{\lambda}{\pi^2}\int\frac{d^4k\phi(k)}{(p-k)^2}. \quad (1)$$

The relative energy has been continued to the imaginary axis, in accordance with Wick's theorem. The energy of a bound state, which is proportional to ϵ, is considered to be given, so that the corresponding interaction constant λ, which is to be determined, is then an eigenvalue of the above equation. We begin by supposing that the two interacting particles have equal masses. The general case can be treated by exactly the same methods, but for simplicity is deferred to the last part of this paper.

Two methods, which supplement each other but are essentially independent, are used in the discussion of Eq. (1), the stereographic projection method of Fock,[2] and the integral transform method already introduced by Wick. When η is set equal to zero, in addition to the masses being equated, Eq. (1) is formally very much like the three-dimensional equation for the nonrelativistic hydrogen atom, as has already been pointed out by Wick. This remark led to the conjecture that the method Fock used to study the hydrogen atom could be applied here as well.[3] Fock's transformation does indeed lead to a great simplification in the form of Eq. (1), and is particularly useful for exhibiting the completeness as well as the degeneracy of its solutions. In the third section of this paper, Wick's integral transformation method, the essence of which is that one writes the solution as a superposition of one-particle propagation functions, is extended so that a complete set of solutions is also obtained by that method, which appears to be more readily applicable to other problems.

II. FOCK'S TRANSFORMATION

If the mass of each particle is set equal to unity, Eq. (1) becomes

$$[(p+i\eta)^2+1][(p-i\eta)^2+1]\phi(p) = \frac{\lambda}{\pi^2}\int\frac{d^4k\phi(k)}{(p-k)^2}. \quad (2)$$

By following the method of Fock and Lévy, the four-dimensional momentum space is mapped upon the surface of a five-dimensional sphere by a stereographic projection. A polar coordinate system is first chosen in momentum space, with polar angles β, θ, ϕ; β being the angle between the four vector p and the (imaginary) relative time axis. These angles are then used for three of the polar angles in five-dimensional space, the fourth angle ζ being defined by $p_0\tan\frac{1}{2}\zeta = |p|$, where $|p|$ is the magnitude of the momentum four vector and $p_0=(1-\eta^2)^{\frac{1}{2}}$ is the diameter of the five-dimensional sphere. Before continuing, it should be remarked that Wick's analytic continuation theorem plays an essential although somewhat hidden role in this transformation. In fact, it is possible to map the momentum space upon a closed manifold in an invariant manner, only because the momentum space of Eq. (2) has a positive definite metric. Upon making the stereographic mapping, it is found that on the left-hand side of (2),

$$[(p+i\eta)^2+1][(p-i\eta)^2+1] = p_0^2\sec^4\tfrac{1}{2}\zeta[1-\eta^2+\eta^2\sin^2\zeta\cos^2\beta]. \quad (3)$$

[1] G. C. Wick, preceding paper [Phys. Rev. **96**, 1124 (1954)].
[2] V. Fock, Z. Physik **98**, 145 (1935); M. Lévy, Proc. Roy. Soc. (London) **A204**, 145 (1950).
[3] I am indebted to Professor Wick for discussions of various aspects of Fock's method.

In the integral on the right-hand side,

$$[d^4k]=\tfrac{1}{16}p_0^4\sec^5\tfrac{1}{2}\zeta' d\Omega_5', \tag{4}$$

where $d\Omega_5'$ is an element of solid angle in five dimensions, and

$$(p-k)^2=\tfrac{1}{2}p_0^2\sec^2(\tfrac{1}{2}\zeta)\sec^2(\tfrac{1}{2}\zeta')(1-\cos\alpha), \tag{5}$$

where α is the angle between the images of p and k on the sphere. Thus with the definition $H(\zeta,\beta,\theta,\phi)=\sec^6(\tfrac{1}{2}\zeta)\phi(p)$, Eq. (2) becomes:

$$(1-\eta^2+\eta^2\sin^2\zeta\cos^2\beta)H(\zeta,\beta,\theta,\phi)=\frac{\lambda}{8\pi^2}\int\frac{d\Omega_5' H(\zeta',\beta',\theta',\phi')}{1-\cos\alpha}. \tag{6}$$

If $\eta=0$, Eq. (6) is clearly invariant under all rotations of the five-dimensional sphere. It follows that a complete set of solutions is given by the spherical harmonics in five-dimensions, which can be constructed from the Gegenbauer polynomials.[4] In Appendix A it is shown that when $\eta=0$, the eigenvalues of (6) are $\lambda_N=N(N+1)$, where N is a positive integer. It likewise follows immediately that the degeneracy is that associated with the rotation group in five dimensions, so the Nth eigenvalue is $\frac{1}{6}N(N+1)(2N+1)$-fold degenerate.

When ϵ is positive, Eq. (6) is no longer invariant in all rotations of five-dimensional space. However, there is still an axis of symmetry, which can be seen if a set of Cartesian coordinates ξ_a is introduced in the five-dimensional space. For points on the sphere of diameter p_0,

$$\begin{aligned}\xi_5&=\tfrac{1}{2}p_0\cos\zeta,\\ \xi_4&=\tfrac{1}{2}p_0\sin\zeta\cos\beta,\\ \xi_3&=\tfrac{1}{2}p_0\sin\zeta\sin\beta\cos\theta,\end{aligned} \tag{7}$$

and so forth. Since in Eq. (6) the coordinates are contained explicitly only in the combination $\sin\zeta\cos\beta=\cos\gamma$, where γ is the angle with the ξ_4 coordinate axis, all rotations which leave this axis unchanged also leave unchanged the form of Eq. (6). For positive values of ϵ the degeneracy is therefore that associated with the four-dimensional rotation group, which is known to be the degeneracy of the nonrelativistic hydrogen atom.[2] Thus no fine-structure splitting is exhibited by Eq. (2), for any value of the interaction constant.

An interesting equation is obtained if the points on the sphere are mapped onto another flat four-dimensional space, by using a stereographic projection of which ξ_4 is the polar axis, instead of ξ_5. With $q=\tan(\frac{1}{2}\gamma)$ and $Q(q)=\cos^6(\frac{1}{2}\gamma)H$, Eq. (6) is transformed into

$$[q^4+2(1-2\eta^2)q^2+1]Q(q)=\frac{\lambda}{\pi^2}\int\frac{d^4q'Q(q')}{(q-q')^2}. \tag{8}$$

This equation is of the same form as Eq. (1) at zero energy, except that the difference of the masses is imaginary. From the form of either Eq. (6) or Eq. (8), it is evident that any solution can be written as a product of a four-dimensional spherical harmonic and a function of q^2, this function being the solution of a one-dimensional integral equation. There is therefore evidently a connection between the degeneracy of Eq. (2) and the fact that by using Wick's transform method it is possible to find solutions in terms of a simple one-parameter integral. It will be shown that the method of Wick is indeed exactly equivalent to solving (8) directly, so it is not necessary to pursue further the solution of this equation at this point.

III. THE INTEGRAL TRANSFORMATION METHOD

Wick was able to find a set of solutions to (2) in terms of an integral over an unknown function $g(z)$, which is the solution of a simple integral equation. In order to find a complete set of solutions, a somewhat more complicated ansatz must be used, and a clue as to the appropriate generalization is given by the structure of the spherical harmonics, which are solutions at zero energy. One is thus led to try to find solutions which are linear combinations of functions of the form

$$\phi_n{}^{lm}(p,z)=\mathcal{Y}_l{}^m(\mathbf{p})/[p^2+2izp\eta+1-\eta^2]^{n+2}, \tag{9}$$

where $\mathcal{Y}_l{}^m(\mathbf{p})$ is a solid harmonic function of the three space components of p. In order to determine what linear combinations to take, it is necessary to find out what happens when $\phi_n{}^{lm}(p,z)$ is inserted into the right-hand side of the integral equation (2).

The integration over the momentum k is done in the usual way, by using Feynman's formula

$$\begin{aligned}\frac{1}{\pi^2}\int\frac{d^4k}{(p-k)^2}\phi_n{}^{lm}(k,z)&=\frac{n+2}{\pi^2}\int_0^1 u^{n+1}du\int\frac{d^4k\,\mathcal{Y}_l{}^m(\mathbf{k}+(1-u)\mathbf{p})}{[k^2+u(1-u)p^2+u(1-\eta^2)+z^2u^2\eta^2+2izu(1-u)p\eta]^{n+3}}\\ &=\frac{1}{n+1}\int_0^1(1-u)^l du\,\mathcal{Y}_l{}^m(\mathbf{p})[(1-u)p^2+1-\eta^2+z^2u\eta^2+2iz(1-u)p\eta]^{-n-1}\\ &=\sum_{k=0}^{n-l-1}\frac{(n-l-1)!(n-k-1)!}{(n+1)!(n-l-k-1)!}\frac{\phi_{n-k-2}{}^{lm}(p,z)}{(1-\eta^2+\eta^2z^2)^{k+1}}.\end{aligned} \tag{10}$$

[4] E. T. Whittaker and G. N. Watson, *Modern Analysis* (Cambridge University Press, London, 1950), p. 329.

In performing the above computations, it has been supposed that $n>l$. Now, following Wick, this is divided by $[(p+i\eta)^2+1][(p-i\eta)^2+1]$ and the result expressed by another use of Feynman's integral formula

$$\pi^{-2}[(p+i\eta)^2+1]^{-1}[(p-i\eta)^2+1]^{-1}\int\frac{d^4k}{(p-k)^2}\phi_n{}^{lm}(p,z)$$
$$=-\frac{1}{2}\sum_{k=0}^{n-l-1}\frac{(n-l-1)!(n-k+1)!}{(n+1)!(n-k-l-1)!}\int_{-1}^{1}dt$$
$$\times\int_0^1\frac{x(1-x)^{n-k-l}dx}{(1-\eta^2+\eta^2z^2)^{k+1}}\phi_{n-k}{}^{lm}(p,\,xt+(1-x)z). \quad (11)$$

It is thus evident that a function of the form

$$\phi_n{}^{lm}(p)=\sum_{k=0}^{n-l-1}\int_{-1}^{1}g_{nl}{}^k(z)\phi_{n-k}{}^{lm}(p,z)dz \quad (12)$$

will be a solution.

The functions $g_{nl}{}^k(z)$ are determined by inserting this into the integral equation (2). Making use of (11), one finds that

$$\sum_{k=0}^{n-l-1}\int_{-1}^{1}g_{nl}{}^k(z)\phi_{n-k}{}^{lm}(p,z)dz$$
$$=\tfrac{1}{2}\lambda\sum_{k=0}^{n-l-1}\sum_{k'=0}^{k}\left\{\frac{(n-k+1)!(n-k'-l-1)!}{(n-k'+1)!(n-k-l-1)!}\right.$$
$$\times\int_{-1}^{1}g_{nl}{}^k(z)dz\int_{-1}^{1}dt\int_0^1\frac{x(1-x)^{n-k-l}dx}{(1-\eta^2+\eta^2z^2)^{k-k'+1}}$$
$$\left.\times\phi_{n-k}{}^{lm}(p,\,xt+(1-x)z)\right\}. \quad (13)$$

Since the $\phi_n{}^{lm}(p,z)$ are a linearily independent set of functions in momentum space, Eq. (13) requires that the $g_{nl}{}^k(z)$ be solutions of the following set of integral equations:

$$g_{nl}{}^k(z)=\tfrac{1}{2}\lambda\sum_{k'=0}^{k}\left\{\frac{(n-k+1)!(n-k'-l-1)!}{(n-k'+1)!(n-k-l-1)!}\right.$$
$$\times\int_0^1dt\int_0^1x(1-x)^{n-k-l}dx$$
$$\left.\times\int_{-1}^{1}\frac{\delta(z-[xt+(1-x)\zeta])}{(1-\eta^2+\eta^2\zeta^2)^{k-k'+1}}g_{nl}{}^{k'}(\zeta)d\zeta\right\}. \quad (14)$$

Upon examining this set of integral equations, it is seen that $g_{nl}{}^0(z)$ is the solution of a single homogeneous equation, from which equation λ is determined. For $n>l+1$, the additional functions $g_{nl}{}^k(z)$ are the solutions of inhomogeneous integral equations which involve the eigenfunction $g_{nl}{}^0(z)$. The homogeneous equation does not depend upon the orbital angular momentum l, so that neither $g_{nl}{}^0(z)$ nor λ depends on l. This degeneracy, which the discussion of the previous section has already shown to exist, is again seen to be exactly the same as that of the nonrelativistic hydrogen atom.

The integral equation for $g_{nl}{}^0(z)$, which is the only function of practical importance, is found, after integrating over x and t and also dropping the indices 0 and l, to be

$$g_n(z)=\frac{\lambda}{2n}\int_{-1}^{1}[R(z,\zeta)]^n\frac{g_n(\zeta)d\zeta}{1-\eta^2+\eta^2\zeta^2}, \quad (15)$$

where $R(z,\zeta)$ is the same function introduced by Wick

$$R(z,\zeta)=(1\pm z)/(1\pm\zeta), \quad \text{for} \quad \zeta\gtrless z. \quad (16)$$

Differentiating Eq. (15), one finds that[5]

$$g_n''(z)+2(n-1)z(1-z^2)^{-1}g_n'(z)-n(n-1)(1-z^2)^{-1}g_n(z)$$
$$+\lambda(1-z^2)^{-1}(1-\eta^2+\eta^2z^2)^{-1}g_n(z)=0. \quad (17)$$

The boundary conditions are $g_n(\pm1)=0$.

This equation has an infinite number of solutions, with discrete eigenvalues λ_κ, the index κ denoting the number of zeros of $g_n(z)$ within the interval $(-1, 1)$. For odd values of κ, the g_n are odd functions of z; therefore the corresponding solutions of the Bethe-Salpeter equation are odd functions of the relative time. In Appendices A and B, the solutions of Eq. (17) are discussed in the two limits $\epsilon=0$ and $\epsilon=1$. At zero energy, where $\lambda_\kappa=(n+\kappa)(n+\kappa+1)$, a one-one correspondance can easily be made between the spherical harmonics of five dimensions and the solutions obtained by the method of this section, thus showing that the set of functions of the form (12) provides a complete set of solutions. As $\eta^2\to1$, only those eigenvalues λ_κ for which $\kappa=0$ approach the values obtained from the Schrödinger equation for the hydrogen atom, as $\lambda_\kappa\to\frac{1}{4}$ if κ is not zero.[6] In Fig. 1, curves for λ *versus* η^2 are shown for some of the lowest-lying states. The exact solutions for $\epsilon=0$ and $\epsilon=1$ have been supplemented by some numerical calculations for intermediate points.

The method outlined above was satisfactory as a way of obtaining the eigenvalues λ, but when $n>l+1$ the construction of the Bethe-Salpeter amplitude is rather cumbersome, as first a set of inhomogeneous equations must be solved successively. However, this can be circumvented if use is also made of the method of Sec. II. When $l=n-1$, the sum in Eq. (12) reduces to a single term. This integral formula for the amplitude function is transformed into

$$Q_n{}^{n-1,m}(q)=p_0{}^{-n+1}\int_{-1}^{1}\frac{\mathcal{Y}_{n-1}{}^m(\mathbf{q})g_n(z)dz}{[1+q^2+iz\epsilon p_0{}^{-1}(1-q^2)]^{n+2}}, \quad (18)$$

[5] The inhomogeneous integral equations can be replaced by second order differential equations similar to (17).

[6] In the previous paper (see reference 1), Wick has treated in detail the case $n=1$. I am grateful to Professor Wick for discussing this limit with me.

when the momentum space is mapped onto the queer space introduced at the end of Sec. II. This amplitude is degenerate with all the amplitudes obtained by rotations in the q space, which can be constructed with the four-dimensional spherical harmonics:

$$Q_n^{lm}(q) = p_0^{1-n}\int_{-1}^{1}\frac{\mathcal{Y}_l^m(\mathbf{q})q^{n-l-1}C_{n-l-1}^{l+1}(q_4/q)g_n(z)dz}{[1+q^2+iz\epsilon p_0^{-1}(1-q^2)]^{n+2}}. \quad (19)$$

Transforming back to ordinary momentum space, one finds

$$\phi_n^{lm}(p)=\int_{-1}^{1}\frac{g_n(z)dz\mathcal{Y}_l^m(\mathbf{p})R^{n-l-1}C_{n-l-1}^{l+1}(X/R)}{[p^2+2izp\eta+1-\eta^2]^{n+2}}, \quad (20)$$

where

$$X=1-\eta^2-p^2, \quad R^2=(p^2+1-\eta^2)^2-4p_4^2(1-\eta^2). \quad (21)$$

Returning to (19), with the substitution $z=(p_0\zeta+i\epsilon)/(p_0+i\epsilon\zeta)$, and the dropping of irrelevant factors, this becomes

$$Q_n^{lm}(q) = \int_{-1}^{1}\frac{(p_0+i\epsilon\zeta)^n g_n(z(\zeta))d\zeta\mathcal{Y}_l^m(\mathbf{q})q^{n-l-1}C_{n-l-1}^{l+1}(q_4/q)}{[q^2+1-2\eta^2+2ip_0\epsilon\zeta]^{n+2}}. \quad (22)$$

By using the results of the next section it can be shown directly that this is a solution of Eq. (8), which, as has been remarked already, is of the same type as (1) but with complex masses, thus demonstrating the equivalence of the two methods we have used to discuss the Bethe-Salpeter equation (2).

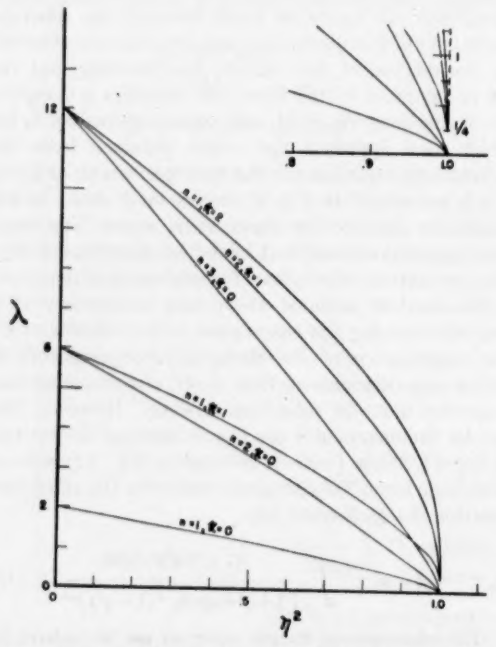

FIG. 1. λ *versus* η^2 for equal masses. The curves with $n=1$ are nondegenerate, while the curves with $n=2$ are 4-fold degenerate, and the curve with $n=3$ is 9-fold degenerate. The inset shows the region near $\eta^2=1$ in greater detail.

IV. UNEQUAL MASSES

The methods of Secs. II and III can both be used to study the more general Eq. (1), which is rewritten with the notation $m_a=1+\Delta$, $m_b=1-\Delta$:

$$F_+F_-\phi=\frac{\lambda}{\pi^2}\int\frac{\phi(k)d^4k}{(p-k)^2}, \quad (23\text{-a})$$

$$F_\pm=p^2\pm 2i(1\pm\Delta)p\eta+(1-\eta^2)(1\pm\Delta)^2. \quad (23\text{-b})$$

First consider the stereographic projection method of Fock and Lévy, in which $p=p_0\tan\frac{1}{2}\zeta$, with $p_0^2=(1-\eta^2)(1-\Delta^2)$. The right-hand side of (23-a) is transformed in the same way as before, but on the left-hand side,

$$F_\pm=\sec^2(\tfrac{1}{2}\zeta)[p_0^2\pm i\eta p_0(1\pm\Delta)\sin\zeta\cos\beta \pm\Delta(1\pm\Delta)(1-\eta^2)(1+\cos\zeta)]. \quad (24)$$

Now let $\cos\gamma=\cos\alpha\cos\zeta+\sin\alpha\sin\zeta\cos\beta$, where α is chosen such that

$$\tan\alpha=i\eta\Delta^{-1}(1-\Delta^2)^{\frac{1}{2}}(1-\eta^2)^{-\frac{1}{2}}. \quad (25)$$

Then,

$$F_+F_-=p_0^2\sec^4\tfrac{1}{2}\zeta[(1-\eta^2)+(\eta^2-\Delta^2)\cos^2\gamma]. \quad (26)$$

The equation which results is formally very much like (6). There is now an imaginary symmetry axis, rotated from the ξ_5 axis through the angle α in the $\xi_5-\xi_4$ plane. The degeneracy is thus not destroyed by taking the masses to be different.

A four-dimensional equation with complete rotational invariance can again be obtained by making a stereographic mapping of which the symmetry axis is the pole. With the definition, as in Sec. II, $q=\tan(\frac{1}{2}\gamma)$ and $(q^2+1)^3Q(q)=(p^2+p_0^2)^3\phi$, an equation very similar to (8) is obtained

$$(1-\Delta^2)\left[q^4+2\left(1-2\frac{\eta^2-\Delta^2}{1-\Delta^2}\right)q^2+1\right]Q(q) = \frac{\lambda}{\pi^2}\int\frac{d^4q'Q(q')}{(q-q')^2}. \quad (27)$$

The q_μ are at first supposed to vary over complicated contours in their respective complex planes; however, as these contours can be deformed back to the real axes without any difficulty, use of Eq. (27) is quite rigorous. The form of the left-hand side indicates that $\lambda/(1-\Delta^2)$ is a function only of $(\eta^2-\Delta^2)/(1-\Delta^2)$, a relation which was of considerable use in constructing Fig. 2. Furthermore, the solutions of (27), as functions of q, depend only on $(\eta^2-\Delta^2)/(1-\Delta^2)$, which implies a

corresponding, but more complicated, relationship between the solutions of (23) for different values of Δ.

The foregoing discussion makes it clear that the integral transform method used in the previous section can be applied to Eq. (23) with very little change. The observation that

$$F_+^{-1}F_-^{-1}=\tfrac{1}{2}\int_{-1}^{1}dz[p^2+2i(z+\Delta)p\eta +(1-\eta^2)(1+\Delta^2+2z\Delta)]^{-2} \quad (28)$$

gives the hint that the definition (9) should be generalized to

$$\phi_n^{lm}(p,z,\Delta)=\frac{\mathcal{Y}_l^m(\mathbf{p})}{[p^2+2i(z+\Delta)p\eta+(1-\eta^2)(1+\Delta^2+2z\Delta)]^{n+2}}. \quad (29)$$

The calculation leading to Eqs. (14), (15), and (17) can be carried out, the appropriate changes being made, exactly as before. One ends with integral and differential equations for the new function $g_n(z,\Delta)$ which differ only little from (15) and (17)

$$g_n(z,\Delta)=\frac{\lambda}{2n}\int_{-1}^{1}\frac{[R(z,\zeta)]^n g_n(\zeta,\Delta)d\zeta}{[(1-\eta^2)(1+\Delta^2+2\Delta\zeta)+\eta^2(\Delta+\zeta)^2]}, \quad (30)$$

$$g_n''(z,\Delta)+2(n-1)z(1-z^2)^{-1}g_n'(z,\Delta) -n(n-1)(1-z^2)^{-1}g_n(z,\Delta) +\lambda(1-z^2)^{-1}[(1+\Delta^2+2z\Delta)(1-\eta^2) +\eta^2(z+\Delta)^2]^{-1}g_n(z,\Delta)=0. \quad (31)$$

The relationship between the solutions of Eqs. (23) and (2), which was proved above by using the Fock projection, can be demonstrated more directly in the integral transform method.[7] We let $\tilde{z}=(z-\Delta)/(1-\Delta z)$ and $g_n(z,\Delta)=(1-\Delta\tilde{z})^{-n}g_n(\tilde{z})$. After noting that $R(z,\zeta)=(1-\Delta\tilde{\zeta})(1-\Delta\tilde{z})^{-1}R(\tilde{z},\tilde{\zeta})$ and that

$$(1-\eta^2)(1+\Delta^2+2z\Delta)+\eta^2(z+\Delta)^2 =(1-\Delta z)^2\frac{1-\eta^2}{1-\Delta^2}+(z-\Delta)^2\frac{\eta^2-\Delta^2}{1-\Delta^2}, \quad (32)$$

we can transform Eq. (30) into

$$g_n(\tilde{z})=\frac{\lambda}{2n(1-\Delta^2)}\int_{-1}^{1}[R(\tilde{z},\tilde{\zeta})]^n g_n(\tilde{\zeta})d\tilde{\zeta} \times\left[1-\frac{\eta^2-\Delta^2}{1-\Delta^2}(1-\tilde{\zeta}^2)\right]^{-1}. \quad (33)$$

This is identical with Eq. (15), which again shows that $\lambda/(1-\Delta^2)$ depends only upon $(\eta^2-\Delta^2)/(1-\Delta^2)$.

In Fig. 2, λ is plotted against η^2 for $\Delta^2=0.36$, or $m_a=4m_b$. These curves were obtained from the curves

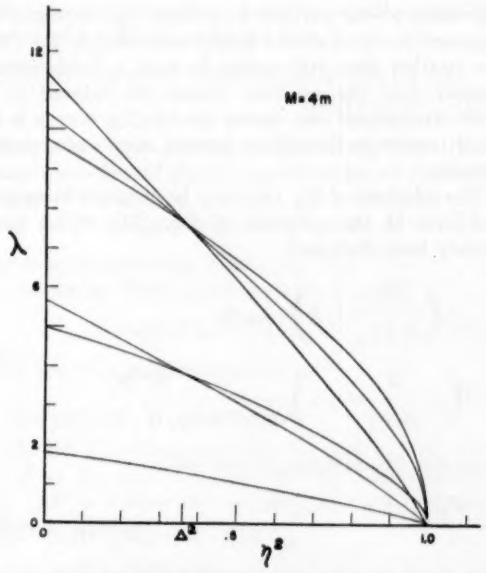

FIG. 2. An example with unequal masses. The quantum numbers are the same as for the corresponding curves of Fig. 1.

of Fig. 1 by using the similarity transformation. Note, in particular, that the curves cross at $\eta^2=\Delta^2$. This corresponds to a critical energy $E_c=m_a-m_b$ for the bound state; if there existed a state of two particles with an energy smaller than E_c, the heavier of the two original particles would be unstable, as it could decay into the bound system and the antiparticle of b. Nevertheless, solutions of Eq. (33) exist and are perfectly well behaved analytically when $\eta^2<\Delta^2$, although it seems that the various solutions can no longer be distinguished in a clear way on the basis of their dependence upon the relative time.[8]

A question of some interest is the behavior of Eq. (23) and of its solutions in the limit $\Delta\to 1$. One may either think of one of the particles becoming infinitely massive, with the binding energy being a fixed multiple of the mass of the lighter particle, or one may suppose that the mass of one particle vanishes, with the binding energy remaining finite. In the first case, the similarity transformation gives the eigenvalues unambiguously, but it is nevertheless worth while to examine the limit directly. We define

$$\Delta=(M-1)/(M+1), \quad \epsilon=(M+1-B)/(M+1), \quad \Lambda=\lambda(1-\Delta^2)^{-1}, \quad p'=(1-\Delta)^{-1}p. \quad (34)$$

Now let $M\to\infty$, with the binding energy B remaining fixed. The limit of Eq. (23) is

$$(p'^2-2ip_4')(2ip_4'+2B)\phi(p')=\frac{\Lambda}{4\pi^2}\int\frac{d^4k'\phi(k')}{(p'-k')^2}. \quad (35)$$

[7] The transformation which follows is due to G. C. Wick.

[8] The ladder approximation is of course complete nonsense when the interaction is this strong.

The mass of one particle is so large that it might be supposed no recoil effects should occur, but in Eq. (35) the relative time still enters in such a fundamental manner that the equation cannot be reduced to a three-dimensional one, unless the binding energy is so small that even the lighter particle moves nonrelativistically.

The solutions of Eq. (35) may be obtained by taking the limit of the solutions of Eq. (23), which have already been discussed

$$g_n\left(\frac{2t}{M+1}-1,\Delta\right)\to G_n(t),$$
$$\phi_n{}^{lm}\left(p,\frac{2t}{M+1}-1,\Delta\right)\to\frac{\mathcal{Y}_l{}^m(\mathbf{p}')}{[p'^2+2ip_4'(t-1)+2Bt]^{n+2}}. \tag{36}$$

Equation (31) becomes, in the limit

$$0=tG_n''(t)-(n-1)G_n'(t)+\Lambda[(t-1)^2+2Bt]^{-1}G_n(t). \tag{37}$$

The eigenvalue Λ is the same function of $(\frac{1}{2}B)$ that λ is of $(1-\eta^2)$ when $\Delta=0$. In contrast to the three-dimensional theory, from the form of the above equation we see that there is no upper limit on B. The limit of Eq. (37) and of Λ as $B\to\infty$ is discussed in Appendix C.

When $\eta^2=0$, Eq. (23) has a particularly interesting limiting form. With $p=(1-\Delta)p'$, as before, Eq. (19) becomes

$$\left[1+\left(\frac{1-\Delta}{1+\Delta}\right)^2p'^2\right](1+p'^2)\phi(p')=\frac{\lambda}{\pi^2(1+\Delta)^2}\int\frac{d^4k'\phi(k')}{(p'-k')^2}. \tag{38}$$

If one takes the limit $\Delta\to1$, the ensuing equation is the same as the Bethe-Salpeter equation for two Dirac particles in a singlet state at zero energy, which has been found by Goldstein[9] to have a rather singular behavior. However, if $\Delta\neq1$, there is another factor of p'^2 on the left-hand side of (38), which provides a kind of "cutoff," at large momenta. The solutions are then given by the methods already discussed; we must solve the equation

$$(1-z^2)g_n''(z,\Delta)+2(n-1)zg_n'(z,\Delta)-n(n-1)g_n(z,\Delta)+\lambda(1+\Delta^2+2\Delta z)^{-1}g_n(z,\Delta)=0, \tag{39}$$

which is just a special case of (31). As has been remarked before, this equation has a set of eigenfunctions with discrete eigenvalues, the κth eigenfunction having κ zeros within the interval $(-1,1)$. The corresponding Bethe-Salpeter amplitude has κ nodal hyperspheres in configuration space. In Appendix C it is shown that as $\Delta\to1$, all the eigenvalues for a given n tend to exactly the same limit: $\lambda_\kappa\to\lambda_0=n^2$. For $n=1$, this is the same as the value Goldstein found for the symmetric solutions of the limit of Eq. (38). In configuration space, the nodal hyperspheres of the amplitudes all shrink into the origin, and at finite distances the amplitudes for given n, l, and m all approach the same limiting function.

In summary, we have found a complete set of bound-state solutions for a simplified Bethe-Salpeter equation. These solutions have been discussed for all values of the bound state energy and for various values of the masses. The simple form of the solutions of this equation, as well as the degeneracy of the eigenvalues, which is the same as the degeneracy in the nonrelativistic hydrogen atom, are shown to be due to the complete separability of the equation in a transformed coordinate system. Although this unexpected symmetry is not a general feature of the Bethe-Salpeter equation, one is nevertheless able to learn a great deal from this example. It was found that for large values of the interaction constant, the equation studied has abnormal solutions, which do not correspond to any familiar physical situation. The limiting form of the solutions when one of the masses becomes infinite does not correspond to the motion of a particle in the field of a fixed center of force, and at zero energy sheds some light upon the pathological character of the two-fermion equation.

I am very grateful to Professor G. C. Wick for many helpful discussions and much useful advice while this work was being carried out.

APPENDIX A

In the text following Eq. (6), it was pointed out that at zero energy the solutions of this equation were spherical harmonics. It suffices to consider the Gegenbauer polynomials $C_{N-1}{}^1(\cos\zeta)$ as the spherical harmonics constructed from one of these with the use of the addition theorem are of course degenerate with it. When $\zeta=0$, Eq. (6) becomes

$$C_{N-1}{}^1(1)=\frac{\lambda_N}{8\pi^2}\int\frac{C_{N-1}{}^1(\cos\zeta')\sin^2\zeta'd\zeta'd\Omega_4'}{1-\cos\zeta'}. \tag{A-1}$$

This integral can be evaluated with the aid of the generating function for the Gegenbauer polynomials

$$\sum_0^\infty r^nC_n{}^\nu(x)=(1-2rx+r^2)^{-\nu}. \tag{A-2}$$

Therefore

$$\sum_1^\infty\lambda_N{}^{-1}r^{N-1}C_{N-1}{}^1(1)=\tfrac{1}{4}\int_0^\pi\frac{\sin^2\zeta'd\zeta'}{(1-\cos\zeta')(1-2r\cos\zeta'+r^2)^1}$$
$$=\tfrac{1}{2}(1-r)^{-1}. \tag{A-3}$$

From (A-2) it is found that $C_{N-1}{}^1(1)=\frac{1}{2}N(N+1)$; thus $\lambda_N=N(N+1)$.

[9] J. S. Goldstein, Phys. Rev. **91**, 1516 (1953).

The eigenvalues at zero energy can also be obtained from Eq. (16) of the text.[10] Let $g_n(z)=(1-z^2)^n f_n(z)$. The equation satisfied by $f_n(z)$ is

$$(1-z^2)f_n''(z)-2(n+1)f_n'(z)+[\lambda-n(n+1)]f(z)=0, \quad \text{(A-4)}$$

which is the differential equation of the Gegenbauer polynomials. It is thus found that

$$g_n(z)=(1-z^2)^n C_\kappa^{n+1}(z),$$

with $\lambda=(n+\kappa)(n+\kappa+1)=N(N+1)$.

APPENDIX B

We shall now consider the differential Eq. (17) in the limit $\eta^2\to 1$,

$$(1-z^2)g_n''+2(n-1)zg_n'-n(n-1)g_n+\lambda(1-\eta^2+\eta^2z^2)^{-1}g_n=0. \quad \text{(17)}$$

If, as $\eta^2\to 1$, $g_n(z)$ approaches a limit uniformly, we may replace $(1-\eta^2+\eta^2z^2)^{-1}$ by $\pi(1-\eta^2)^{-\frac{1}{2}}\delta(z)$ in the original integral equation (15), from which we find $g_n(z)\sim(1-|z|)^n$ and $2-2\epsilon=B\sim(\lambda\pi)^2/8n^2$, where B is the binding energy. This is the solution for $\kappa=0$. By inserting the asymptotic form of $g_n(z)$ into (20), we find the asymptotic form of the amplitude:

$$\phi(p)\sim(p^2+1-\eta^2)^{-n}[(p+i\eta)^2+1]^{-l}[(p-i\eta)^2+1]^{-l}\times R^{n-l-1}C_{n-l-1}^{l+1}(X/R)\mathcal{Y}_l^m(\mathbf{p}). \quad \text{(B-1)}$$

In (B-1), we see that the important values of p_4 are of the order $1-\eta^2$, while $|\mathbf{p}|\sim(1-\eta^2)^{\frac{1}{2}}$. Thus,

$$\phi(p)\sim\pi\delta(p_4)(\mathbf{p}^2+1-\eta^2)^{-l-2}C_{n-l-1}^{l+1}\times\left(\frac{1-\mathbf{p}^2}{1+\mathbf{p}^2}\right)\mathcal{Y}_l^m(\mathbf{p}). \quad \text{(B-2)}$$

This will be recognized as the general form of the solutions of Schrödinger's equation for the hydrogen atom, so that in the limit $\lambda\to 0$, not only the right energy but also the correct nonrelativistic wave function is obtained. Equation (B-1) actually gives a rather good approximation to $\phi(p)$ for all values of η^2.

To obtain the limit for $\kappa\geq 1$, we set $\eta^2=1$ in (17),

$$(1-z^2)g_n''+2(n-1)zg_n'-n(n-1)g_n+\lambda z^{-2}g_n=0. \quad \text{(B-3)}$$

[10] This was first done by G. C. Wick, for the case $n=1$.

The solution of the above equation which satisfies the boundary conditions at $z=\pm 1$ is

$$g_n(z)=(1-z^2)^n z^{\frac{1}{2}+\rho}F[\tfrac{1}{4}(2n+3+2\rho),\tfrac{1}{4}(2n+1+2\rho);n+1;1-z^2], \quad \text{(B-4)}$$

where ρ has been defined by Wick's Eq. (62). To examine the behavior of $g_n(z)$ at $z=0$, we let $x=z(1-\eta^2)^{-\frac{1}{2}}$, whence

$$d^2g_n/dx^2+\lambda(1+x^2)^{-1}g_n=0, \quad \text{(B-5)}$$

which is identical with Wick's Eq. (61).

Continuing Wick's analysis, we find again,

$$\lambda_\kappa\sim\tfrac{1}{4}+\pi^2(\kappa-1)^2[\ln(1-\eta^2)]^{-2}. \quad \text{(B-6)}$$

Note that this is independent of n.

APPENDIX C

The limit $\Delta\to 1$ is found from Eq. (39) if $\eta^2=0$, while for $\eta^2\sim 1$ Eq. (37) must be used. By letting $\Delta\to 1$ in Eq. (23) a connection between these two extreme values is provided

$$(1-\eta^2)q^2Q(q)=\frac{\lambda}{4\pi^2}\int\frac{d^4q'Q(q')}{(q-q')^2}; \quad \text{(C-1)}$$

therefore, $\lambda=\lambda_0(1-\eta^2)$. From the definitions (30), it follows that when B is very large, $\Lambda\sim\frac{1}{2}B\lambda_0$.

From Eq. (35) it is found that

$$(1-z^2)g_n''(z,1)+2(n-1)zg_n'(z,1)-n(n-1)g_n(z,1)+\tfrac{1}{2}\lambda_0(1+z)^{-1}g_n(z,1)=0. \quad \text{(C-2)}$$

The indices at $z=-1$ are $\frac{1}{2}n\pm\frac{1}{2}(n^2-\lambda_0)^{\frac{1}{2}}$. In order to examine the boundary condition at $z=-1$, we take the limit of (35) with $z+1=\frac{1}{2}(1-\Delta)^2u$, which gives

$$ud^2g_n/du^2-(n-1)dg_n/du+\lambda_0g_n/4(1+u)=0. \quad \text{(C-3)}$$

The indices of this at $u=\infty$ are also $\frac{1}{2}n\pm\frac{1}{2}(n^2-\lambda_0)^{\frac{1}{2}}$. Equations (C-2) and (C-3) can be solved in terms of hypergeometric functions; using the same method that was used to study the limit $\eta^2\to 1$, we find that $\lambda_0\to n^2$ for all values of κ.

Now consider Eq. (37) with $2Bt=u$ when B is large,

$$ud^2G_n/du^2-(n-1)dG/du+\Lambda G_n/2B(1+u)=0. \quad \text{(C-4)}$$

If $\Lambda=\frac{1}{2}B\lambda_0$, Eqs. (C-3) and (C-4) are identical.

If we take the limit with $t=2Bz$, we find

$$d^2G_n/dz^2-(n-1)z^{-1}dG_n/dz+\Lambda G_n/2Bz^2(1+z)=0. \quad \text{(C-5)}$$

Matching the solutions of (C-4) and (C-5) we find $\Lambda\sim\frac{1}{2}Bn^2$, which is consistent with the result inferred from Eq. (C-1).

Limiting Processes in the Formal Theory of Scattering

F. COESTER,* MORTON HAMERMESH, AND KATSUMI TANAKA
Argonne National Laboratory, Lemont, Illinois
(Received August 13, 1954)

The equivalence of different formal limiting processes employed in the theory of scattering is discussed by comparing the integral equations which hold for finite values of the parameter.

IN the theory of scattering, one always introduces or implies formal limiting processes such as the adiabatic switching on of the interaction. Recent work[1-4] has emphasized the importance of these limiting processes. The relations between alternative limiting processes, however, are not as clear as one might desire. It is the purpose of this note to clarify these relations by comparing the integral equations which hold for finite values of the parameter.

Let $H=K+V$ be the Hamiltonian of the system. V is the interaction and $V(t)$ is the Hamiltonian in the interaction representation,

$$V(t)=e^{iKt}Ve^{-iKt}.$$

We consider the unitary[5] matrix $U(t,t_0)$ which satisfies the Schrödinger equation,

$$i\partial U(t,t_0)/\partial t=V(t)U(t,t_0) \tag{1}$$

($\hbar=1$), and the initial condition $U(t,t_0)=1$. It satisfies the integral equation[6]

$$U(t,t_0)=1-i\int_{t_0}^{t}dt'V(t')U(t',t_0), \tag{2}$$

and

$$U(t_0,t)=1+i\int_{t_0}^{t}dt'U(t_0,t')V(t'). \tag{3}$$

An explicit solution is given by[7]

$$U(t,t_0)=e^{iKt}e^{-i(K+V)(t-t_0)}e^{-iKt_0}. \tag{4}$$

Our concern is with the definitions of $U(t,-\infty)$ and $U(\infty,t)$. These operators may be defined either by adiabatic switching on of the interaction or by a certain average over initial or final times proposed by Gell-Mann and Goldberger.[1] In either case, we obtain an operator family $U_\epsilon(t,-\infty)$ and $U_\epsilon(\infty,t)$ depending on a parameter ϵ ($\epsilon>0$) and we define the operators $U(t,-\infty)$ and $U(\infty,t)$ by

$$U(t,-\infty)=\lim_{\epsilon\to 0}U_\epsilon(t,-\infty), \tag{5}$$

and

$$U(\infty,t)=\lim_{\epsilon\to 0}U_\epsilon(\infty,t). \tag{6}$$

Such a procedure is necessary since the limit $\lim_{t_0\to-\infty}U(t,t_0)$ does not exist in general. Our operator family should be defined, however, in such a way that

$$\lim_{\epsilon\to 0}U_\epsilon(t,-\infty)=\lim_{t_0\to-\infty}U(t,t_0),$$

if the latter limit exists. It is easy to verify that this is true for the definition (8) below.[8]

The operator $U_\epsilon(t,-\infty)$ may, for instance, be defined as the solution of the integral equation,

$$U_\epsilon(t,-\infty)=1-i\int_{-\infty}^{t}dt'e^{\epsilon(t'-t)}V(t')U_\epsilon(t',-\infty), \tag{7}$$

which is obtained from (2) by switching on the interaction adiabatically and letting t_0 go to $-\infty$. The qualitative idea of switching on the interaction does not determine the factor $e^{\epsilon(t'-t)}$ uniquely. If one starts from the differential Schrödinger equation, one is led to substitute for instance, $V(t)\to e^{-\epsilon|t|}V(t)$.[2,3] It is easy to see that for finite t a factor $e^{\epsilon|t'|}$ in (7) instead of $e^{\epsilon(t'-t)}$ would give the same $U(t,-\infty)$ in the limit $\epsilon\to 0$, if this limit exists. Our choice (7) will prove to be particularly useful.

An alternative definition has been proposed by Gell-Mann and Goldberger:[9]

$$U_\epsilon(t,-\infty)=\epsilon\int_{-\infty}^{t}dt_0e^{\epsilon(t_0-t)}U(t,t_0). \tag{8}$$

* Permanent address: Department of Physics, State University of Iowa, Iowa City, Iowa.

[1] M. Gell-Mann and M. L. Goldberger, Phys. Rev. **91**, 398 (1953).

[2] F. J. Belinfante and C. Møller, Kgl. Danske Videnskab. Selskab, Mat.-fys. Medd. **28**, No. 6 (1954).

[3] S. Fubini, Atti accad. naz. Lincei **12**, 298 (1952).

[4] The formal theory of scattering is also discussed in detail in a forthcoming book by J. M. Jauch and F. Rohrlich, on *Quantum Electrodynamics* (Addison-Wesley Press, Cambridge, 1955), Chap. 7.

[5] For a proof of the unitarity of U see, for instance, reference 2, p. 28.

[6] J. Schwinger, Phys. Rev. **74**, 1439 (1948).

[7] S. T. Ma, Phys. Rev. **87**, 652 (1952), Eq. (42).

[8] It is important to realize that

$$\lim_{\epsilon\to 0}\epsilon\int_{t_1}^{t_2}dte^{\epsilon t}f(t)=0$$

for any function f for which the integral exists provided $\epsilon t_1\to 0$ and $\epsilon t_2\to 0$.

[9] Reference 1, Eq. (3:19). This equation gives

$$U_\epsilon(t,-\infty)=\epsilon\int_{-\infty}^{0}dt_0e^{\epsilon t_0}U(t,t_0)$$

which is different from (8). However, the limit $\epsilon\to 0$ is the same if it exists. See reference 8.

We may substitute the right-hand side of (4) for $U(t,t_0)$ in (8) and obtain a closed expression for $U_\epsilon(t,-\infty)$:

$$U_\epsilon(t,-\infty)=e^{iKt}U_\epsilon(0,-\infty)e^{-iKt}, \tag{9}$$

where

$$U_\epsilon(0,-\infty)=\epsilon\int_{-\infty}^{0}d\tau e^{\epsilon\tau}e^{i(K+V)\tau}e^{-iK\tau}. \tag{10}$$

We shall now show that the two definitions of the operator $U_\epsilon(t,-\infty)$, [Eqs. (7) and (8)] are in fact identical. This can be shown by proving that the operator defined by (8) satisfies the integral equation (7): Multiply (2) by $\epsilon e^{\epsilon(t_0-t)}$ and integrate over t_0 from $-\infty$ to t. The first term on the right-hand side is then equal to 1, the second term is identical with the second term in (7) after the order of the two integrations has been interchanged. Similarly we can show that the two definitions of the operator $U_\epsilon(\infty,t)$,

$$U_\epsilon(\infty,t)=1-i\int_t^\infty dt'U_\epsilon(\infty,t')V(t')e^{-\epsilon(t'-t)} \tag{11}$$

and

$$U_\epsilon(\infty,t)=\epsilon\int_t^\infty dt_0e^{-\epsilon(t_0-t)}U(t_0-t), \tag{12}$$

are identical. We have thus shown that the averaging process (8) or (12) is equivalent to an adiabatic switching on or switching off of the interaction.

The connection with the time-independent scattering theory is easily established as follows: Inserting (9) in (7), we find,

$$U_\epsilon(0,-\infty)=1-i\int_{-\infty}^{0}dte^{\epsilon t}e^{iKt}VU_\epsilon(0,-\infty)e^{-iKt}, \tag{13}$$

which proves that $U(0,-\infty)$ is identical with Møller's[10] wave matrix $\Omega^{(+)}$. Indeed $\Omega^{(+)}$ is *defined* by the integral equation

$$(q|\Omega_\epsilon^{(+)}|q')=(q|1|q')+(E_{q'}-E_q+i\epsilon)^{-1}\times(q|U\Omega_\epsilon^{(+)}|q'), \tag{14}$$

and $\Omega^{(+)}=\lim_{\epsilon\to 0}\Omega_\epsilon^{(+)}$. Equation (14) is written in a representation in which K is diagonal. If we evaluate the integration in (13) in this representation we see that $U_\epsilon(0,-\infty)=\Omega_\epsilon^{(+)}$.

In analogy to (9), we have from (4) and (12)

$$U_\epsilon(\infty,t)=e^{iKt}U_\epsilon(\infty,0)e^{-iKt}, \tag{15}$$

and one verifies easily that $U(\infty,0)^*=\Omega^{(-)}$, where $\Omega^{(-)}$ is defined by

$$(q|\Omega_\epsilon^{(-)}|q')=(q|1|q')+(E_{q'}-E_q-i\epsilon)^{-1}\times(q|V\Omega_\epsilon^{(-)}|q'), \tag{16}$$

and $\Omega^{(-)}=\lim_{\epsilon\to 0}\Omega_\epsilon^{(-)}$. We have thus shown that the insertion of a small imaginary part in the energy denominator of the time-independent scattering theory is equivalent to an adiabatic switching of the interaction.

The S matrix in the time-dependent scattering theory is usually defined by[11]

$$S=U(\infty,-\infty). \tag{17}$$

It appears that the definition (17) may be ambiguous without detailed prescriptions about the limits involved. We shall show that there is no ambiguity if the limits are taken in any one of the several ways discussed below. We may define $U(\infty,-\infty)$, for instance, by

$$U(\infty,-\infty)=\lim(\epsilon\to 0,\epsilon'\to 0)U_{\epsilon'}(\infty,t)U_\epsilon(t,-\infty)$$
$$=\lim(\epsilon\to 0,\epsilon'\to 0)\epsilon\epsilon'\int_t^\infty dt_0'\int_{-\infty}^{t}dt_0\times e^{\epsilon t_0-\epsilon' t_0'+t(\epsilon'-\epsilon)}U(t_0',t_0). \tag{18}$$

We see that the right-hand side of (18) is independent of t and the ratio ϵ'/ϵ for finite t in the limit $\epsilon\to 0$, $\epsilon'\to 0$. We see, also, that it is equal to

$$\lim(t_0'\to+\infty,t_0\to-\infty)U(t_0',t_0),$$

if these limits exist.[8]

We can further show that

$$U(\infty,-\infty)=\lim(t\to\infty,\epsilon t\to 0)U_\epsilon(t,-\infty)$$
$$=\lim(t\to-\infty,\epsilon t\to 0)U_\epsilon(\infty,t). \tag{19}$$

Inserting (9) and (15) in (7) and (11), respectively, we see that the double limit $t\to\pm\infty$, $\epsilon t\to 0$ exists provided the energy dependence of $VU_\epsilon(0,-\infty)$ and $U_\epsilon(\infty,0)V$ is sufficiently regular. Since these limits exist, (19) follows from (18).[8]

The equivalence of the S matrix defined by (17) and the S matrix of the time-independent scattering theory follows from the relations $U(0,-\infty)=\Omega^{(+)}$ and $U(\infty,0)=\Omega^{*(-)}$.[12]

We are indebted to Dr. J. M. Jauch for stimulating discussions and critical comments.

[10] C. Møller, Kgl. Danske Videnskab. Selskab, Mat-fys. Medd. **23**, No. 1 (1945). Møller denotes the wave matrix by Ψ; we follow the notation of reference 1.

[11] This definition was first given by E. C. G. Stueckelberg, Helv. Phys. Acta **17**, 3 (1944). See also J. Schwinger, reference 5, and F. J. Dyson, Phys. Rev. **75**, 486, 1736 (1949).

[12] This equivalence was first demonstrated by E. C. G. Stueckelberg, Helv. Phys. Acta **18**, 195 (1945). See also S. Fubini, reference 3.

Solution of Many-Body Scattering Problems by Fredholm's Equation

P. SWAN
Physics Department, University of Melbourne, Melbourne, Australia
(Received July 20, 1954)

A reduction is made of the second-order linear integro-differential equation describing many-body elastic collisions to a Fredholm equation, for which an analytic solution can be constructed. The Fredholm equation is easier to solve numerically, an example being solved by iteration as an illustration of its use.

AN important type of equation which occurs in the treatment of many-body collisions is the second order linear integro-differential equation,

$$\left[\frac{d^2}{dr^2}+k^2-\frac{l(l+1)}{r^2}-U(r)\right]f_l(r)=\lambda\int_0^\infty K_l(r,r')f_l(r')dr', \quad (1)$$

where $K_l(r,r')$ is a symmetric kernel such that $\int_0^\infty K_l(r,r')dr'$ is finite for all r and approaches 0 asymptotically for $r\to\infty$, and λ is an arbitrary parameter. $U(r)$ is a short range potential function such that $|U(r)|<A/r$ for $r\to\infty$, and $U(r)$ is less singular than $1/r^2$ at $r=0$.

Equations of the form (1) appear in the treatment of the scattering of electrons by atoms[1] and in the collisions of neutrons and protons with deuterons,[2] tritons,[3,4] and other nuclei.

A function $G(R,r)=(R-r)$ exists which satisfies the usual Green's function conditions except that

$$\frac{d^2}{dr^2}G(R,r)=0.$$

Its use on (1) leads to

$$f_l(R)=f_l(0)+f_l'(0)R+\int_0^\infty\left[M_l(R,r)+\lambda N_l(R,r)\right]f_l(r)dr, \quad (2)$$

where

$$M_l(R,r)=(R-r)[U(r)+l(l+1)/r^2-k^2], \quad (r<R)$$
$$=0, \quad (r>R) \quad (3)$$
$$N_l(R,r)=\int_0^R(R-r')K_l(r,r')dr'.$$

As $f_l(0)=0$ and $f_l'(0)$ can be regarded as a fixed parameter for S-wave interactions ($l=0$), Eq. (2) has the form of a Fredholm equation or integral equation of the second kind, the solution of which is well-known.[5] If $l>0$, then $f_l'(0)=0$ and this solution breaks down; but Whittaker and Watson[5] have constructed one valid for this case. However, these solutions are impractical for actual numerical calculations so that iterative or difference-equation methods must be used.

The iterative process used on (3) has advantages as compared to (1) provided the kernel $N_l(R,r)$ can be evaluated analytically. This may be done for elementary cases of electron-atom collisions in terms of exponential and $[\mathrm{Ei}(x)]$ functions, and for nuclear collisions such as n-H^3 scattering in terms of Gaussian and error functions, provided appropriate ground state functions of Gaussian form are used.[3,4]

Whereas iteration of (1) involves the repetition of the two steps of integrating with a trial function over the kernel product and solving a second order differential equation, (3) does not require the latter step. This simplifies calculation if the number of steps needed to solve the differential equation is large.

It has been shown[6] that neutron-deuteron scattering is very approximately described by the equation

$$\left(\frac{d^2}{dr^2}+k^2\right)f(r)=\lambda\int_0^\infty rr'e^{-\alpha(r+r')}f(r')dr'. \quad (4)$$

The scattering phase-shift η involved in the asymptotic solution for large r, $\sin(kr+\eta)$, is given by

$$\cot\eta=-(\alpha^2-k^2)\{8\alpha^4\lambda+(\alpha^2+k^2)^2[4\alpha^3(\alpha^2+k^2)^2-(3\alpha^2+k^2)\lambda]\}/16\alpha^5\lambda k. \quad (5)$$

For $\lambda=-1$, $\alpha=1$, $k=0.1$, one obtains $\eta=2.912$. Eq. (4) reduces to the Fredholm Eq. (2) with

$$M(R,r)=-k^2(R-r), \quad (r<R),$$
$$N(R,r)=r(r-2)e^{-\alpha r}[1-(1+R)e^{-R}]+re^{-\alpha r}R^2e^{-R}. \quad (6)$$

During the iterative process, one may either maintain a fixed initial gradient $f'(0)$, or adjust $f'(0)$ at each iteration so as to obtain unit asymptotic amplitude. Adopting the former method and using an initial trial function $f_0(r)=\sin kr$ in (2), one obtains successively $\eta=0$, 3.11, 2.88, 2.92, so that the convergence of the iteration is reasonable and comparable to its use on (1).

[1] N. F. Mott and H. S. W. Massey, *Theory of Atomic Collisions* (Clarendon Press, Oxford, 1949).
[2] Buckingham, Hubbard, and Massey, Proc. Roy. Soc. **A211**, 183 (1952).
[3] P. Swan, Proc. Phys. Soc. (London) **A66**, 238 (1953).
[4] P. Swan, Proc. Phys. Soc. (London) **A66**, 740 (1953).
[5] E. T. Whittaker and G. N. Watson, *A Course of Modern Analysis* (Cambridge University Press, London, 1950), fourth edition, p. 213.
[6] R. A. Buckingham and H. S. W. Massey, Proc. Roy. Soc. (London) **A179**, 123 (1941–2).

Vacuum Polarization in Mesonic Atoms

A. B. MICKELWAIT* AND H. C. CORBEN†
Carnegie Institute of Technology, Pittsburgh, Pennsylvania
(Received August 11, 1954)

The effects of vacuum polarization on the energy levels of π and μ mesonic atoms are computed to the lowest order for states $1s(Z\leqslant 12)$, $2p(Z\leqslant 30)$, $3d(Z\leqslant 82)$, $4f(Z\leqslant 82)$. If one ignores the finite size of the nucleus, these results may be written explicitly in a closed form. The effect of the finite size of the nucleus is estimated and shown to be <8 percent for all states considered. Since the virtual pairs are described here by plane waves, the fractional error in these results is of order $(Z\alpha)^2$.

THE radiative corrections to an energy level of an ordinary atom are composed of two separate effects, of which by far the more important is the raising of an s level due to the modification of the electron self-energy in that state. In addition, however, there is a small negative contribution arising from the polarization of the vacuum by the field of the nucleus. The first of these is, in first approximation, inversely proportional to the square of the electron mass, and in a mesonic atom it would therefore contain the square of the meson mass in the denominator. On the other hand, the electrostatic potential is modified by vacuum polarization in a manner quite independent of the mass of the orbital particle. It has therefore been pointed out[1] that for a mesonic atom the correction due to vacuum polarization is of order 10^3 of that due to self-energy effects. Indeed, this fact causes vacuum polarization to be the dominant feature of the electrodynamic radiative corrections to any process, such as p-p scattering, meson-nucleon scattering, involving the interaction of two-systems, neither of which is an electron. It also follows that all mesonic atom levels are lowered by this effect and that, because of the much smaller size of these atoms, states of orbital angular momentum $\neq 0$ are also appreciably affected. The magnitude of the correction is, of course, greatly enhanced by the closeness of nucleus and meson in the mesonic atom, and, owing to the rapidly increasing accuracy with which it is becoming possible to measure mesonic atom energy levels,[2] it becomes important to compute the correction as accurately as possible.

To terms of first order in α, an external current density j_μ which is of the form $\exp(iqx)$ but which does not have enough energy to produce real pairs ($q^2>-4\mu^2$, $\mu=mc/\hbar$) induces a vacuum current, the physically significant part of which is

$$\delta j_\mu=\frac{\alpha}{4\pi}\int_0^1 z(1-z)^{-\frac{1}{2}}\ln\left(1+\frac{zq^2}{4\mu^2}\right)dz\,j_\mu. \qquad (1)$$

For a point nucleus, the corresponding fractional change in potential then becomes

$$\frac{\delta\varphi}{\varphi}=\frac{\alpha}{2\pi}\int_0^1 z(1-z)^{-\frac{1}{2}}dz\int_{2\mu r z^{\frac{1}{2}}}^\infty\frac{e^{-x}}{x}dx$$

$$=\frac{\alpha}{3\pi}\int_1^\infty e^{-2\mu r z}(x^2-1)^{\frac{1}{2}}(2x^2+1)x^{-4}dx. \qquad (2)$$

This ratio is graphed in Fig. 1. For $\mu r\gg 1$ it becomes

$$\frac{\delta\varphi}{\varphi}\sim\frac{\alpha}{4\sqrt{\pi}}\frac{e^{-2\mu r}}{(\mu r)^{\frac{1}{2}}},$$

while for $\mu r\ll 1$ it tends to

$$\delta\varphi/\varphi\sim-(2\alpha/3\pi)\ln(4.08\mu r).$$

In the latter limit the corresponding induced charge density is

$$\delta\rho\sim(-2\alpha/3\pi)(Ze/4\pi r^3).$$

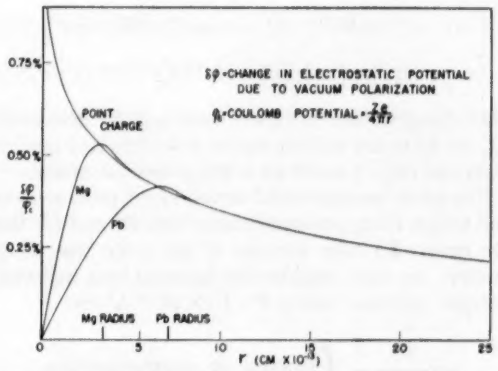

FIG. 1. The radial dependence of the change $\delta\varphi$ in electrostatic potential due to vacuum polarization for (a) a point charge, (b) Pb nucleus, (c) Mg nucleus, assuming a uniform charge distribution for cases (b) and (c). φ_c = Coulomb potential $=Ze/4\pi r$.

* Submitted in partial fulfillment of the requirements for the degree of Doctor of Philosophy at Carnegie Institute of Technology.

† At present on leave to the Ramo-Wooldridge Corporation, 8820 Bellanca Ave., Los Angeles 45, California.

[1] A. D. Galanin and I. Ya. Pomeranchuk, Doklady Akad. Nauk. (S.S.S.R.) **86**, 251–3 (1952); L. N. Cooper and E. M. Henley, Phys. Rev. **92**, 801 (1953); H. C. Corben, Phys. Rev. **94**, 787 (1954); H. C. Corben, "The Lamb Shift in Mesic Atoms," Carnegie Institute of Technology Technical Report (unpublished); Koslov, Fitch, and Rainwater, Phys. Rev. **95**, 291 (1954); L. L. Foldy and E. Eriksen, Phys. Rev. **95**, 1048 (1954).

[2] V. L. Fitch and J. Rainwater, Phys. Rev. **92**, 789 (1953); DeBenedetti, Stearns, Stearns, Richings, and Leipuner, Phys. Rev. **94**, 766 (1954); Stearns, Stearns, DeBenedetti, and Leipuner, Phys. Rev. **95**, 1353 (1954).

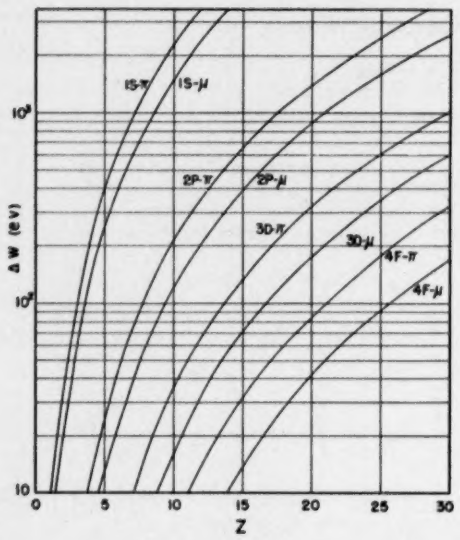

FIG. 2. The Z dependence of level shifts in π and μ mesonic atoms due to vacuum polarization for $1s$, $2p$, $3d$, and $4f$ levels, $Z \leqslant 30$.

The energy shift of a particular mesonic atom level is then given by

$$\Delta W = -e\int \psi^* \psi \delta\varphi d^3r, \tag{3}$$

which becomes, for a state for which $l=n-1$ (Coulomb wave functions),

$$\frac{\Delta W}{Mc^2} = \frac{-\alpha^3}{3\pi}\left(\frac{Z}{n}\right)^2 \int_\epsilon^{1+\epsilon} dx \frac{(x-\epsilon)^{2n-1}}{x^{2n}} \times (2+\epsilon^2-2\epsilon x+x^2)(1-\epsilon^2+2\epsilon x-x^2)^{\frac{1}{2}}, \tag{4}$$

where $\epsilon = nm/ZM\alpha$. (M = meson mass, m = electron mass). For $1s$ states this yields

$$\Delta W = (-\alpha^3/3\pi)MZ^2\{-11/3+3\pi\epsilon/2-4\epsilon^2+2\pi\epsilon^3 + (2-\epsilon^2-4\epsilon^4)(1-\epsilon^2)^{-\frac{1}{2}} \ln[\epsilon^{-1}(1+(1-\epsilon^2)^{\frac{1}{2}})]\}.$$

Similar expressions in closed form may be derived for $2p$, $3d$, $4f$ states and the values to which they lead are shown in Figs. 2 and 3 for π and μ mesonic atoms.

The above results would be valid for a point nucleus, and within the approximations of Eqs. (1) and (3) they are exact. To take account of the finite size of the nucleus, we may consider the latter to be a uniformly charged sphere of radius $R = 1.2\times10^{-13}$ A$^{\frac{1}{3}}$ cm:

$$\rho = \frac{Ze}{(2\pi)^3}\frac{3}{R^3}\int (\sin qR - qR\cos qR) q^{-3} e^{i\mathbf{q}\cdot\mathbf{r}} d^3q.$$

The energy shift is then modified by the consequent changes in both $\delta\varphi$ and ψ. Comparing $\delta\varphi$ to the potential φ_c of a point nucleus of charge Ze, we have, instead of (2), for $r \leqslant R$:

$$\frac{\delta\varphi}{\varphi_c} = \frac{\alpha}{\pi\eta^3}\int_1^\infty dx e^{-\eta x}(x^2-1)^{\frac{1}{2}}(2x^2+1)x^{-7} \times [\sigma\eta x e^{\eta x} - (1+\eta x)\sinh(\sigma\eta x)] \tag{2'}$$

$$= \frac{\alpha\sigma}{3\pi}\int_1^\infty dx e^{-\eta x}(x^2-1)^{\frac{1}{2}}(2x^2+1)x^{-4}[\tfrac{1}{2}(3-\sigma^2) + \tfrac{1}{2}(1-\sigma^2)\eta x + \tfrac{1}{8}(1-\tfrac{1}{3}\sigma^4)\eta^2x^2 + \cdots], \tag{2''}$$

where $\eta = 2\mu R$, $\sigma = r/R$. For $r > 2R$, the corresponding expression is represented by (2) to within 1 percent for $Z=12$. For $r=R$, a direct comparison between (2) and (2″) is possible, (2″) being approximately 2 percent greater than (2) at this point. A simple approximation to (2″), valid to within 1 percent, may be obtained by expansion and the function is graphed in Fig. 1 for Mg and Pb. From such an expansion it may be shown that the error in ΔW due to the deviation of (2′) from (2) is, for example, <5 percent for $Z=12$, $1s$ state (π), $Z=30$, $2p$ state (π), and $Z=82$, $3d$ state (π), and <2 percent for a $Z=82$, $4f$ state (π). Since this error in ΔW for a μ state is smaller than for a π state with the same n and Z, this error will be <5 percent for all n and Z values of Figs. 2 and 3.

The effect on ΔW of the deviation of the wave functions ψ from the hydrogen wave functions used in deriving (4) may be estimated from elementary per-

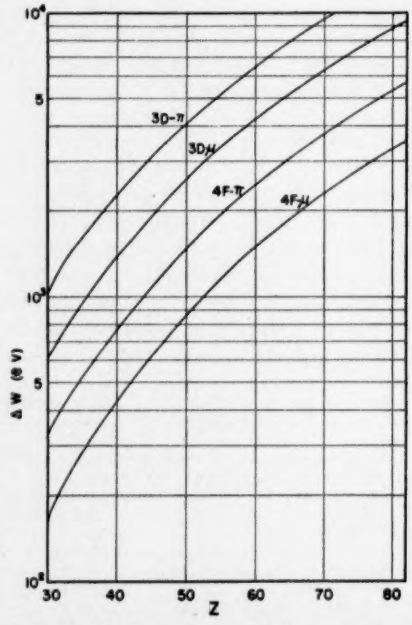

FIG. 3. The Z dependence of level shifts in π and μ mesonic atoms due to vacuum polarization for $3d$ and $4f$ levels, and $30 \leqslant Z \leqslant 82$.

turbation theory. Here again the states most greatly affected are the $1s$ states and for these the error is less than 3 percent for $Z=12(\pi)$, and less than 2 percent for $Z=12(\mu)$.

It should be noted that our results for the μ states, $2p$ and $2s$ in carbon, are in agreement with the values published by Pomeranchuk.[1] However, since no account is taken of the effect of the Coulomb field on the motion of the virtual electron-positron pairs, the values given here includes a fractional error of order $(Z\alpha)^2$.

PHYSICAL REVIEW VOLUME 96, NUMBER 4 NOVEMBER 15, 1954

Quantization of Multiple Frequency Linear Systems

J. K. PERCUS
Department of Electrical Engineering, Columbia University, New York
(Received June 29, 1954)

The commutation relations and constants of motion for a wave equation whose frequencies have a common degeneracy are discussed. Although the quantum relations separate into those of simple subsystems, the corresponding decomposition holds only for a restricted class of constants of motion, excluding the energy.

A DETAILED investigation of the quantum mechanics of linear systems[1] has brought to light some points of interest relating to the multiple frequency systems first considered by Pais and Uhlenbeck.[2]

The quantization formalism employed by the writer[3] for E.B. systems is briefly as follows: Suppose the linear system to be given by $\Sigma M_{\alpha\beta}\psi_\beta(x)=0$, or $M\psi=0$, where $M=(M_{\alpha\beta})$ is a self-adjoint matric differential operator; x stands for all n independent variables one of which, x_0, is timelike in the sense that there is a complete set of solutions ψ which vanish strongly at ∞ of any surface $x_0=$constant, and M is of finite degree d in $\partial_0=\partial/\partial x_0$. If we now introduce the expression

$$\mathcal{T}(\omega,\psi)=i/h\int\omega^T[M,Z(x_0-x_0')]\psi dx^n, \tag{1}$$

where $Z(y)$ is the step function $[1+\mathrm{sgn}(y)]/2$ and ω^T is the transpose of ω, the commutation relations may be written in the form,

$$\mathcal{T}(\omega,\psi)\cdot F\psi(x')=F\omega(x'), \tag{2}$$

for any vector $\omega=(\omega_\alpha(x))$ and any linear operator F of degree $<d$ in ∂_0; here $A\cdot B$ stands for $[A,B]$. (Actually, it suffices to consider only ω for which $M\omega=0$; in such a case, $\mathcal{T}(\omega,\psi)$ is independent of x_0 and F may be taken as arbitrary.) Furthermore, if the system is invariant under the operator T ($T\psi$ is a solution whenever ψ is), then if $\mathcal{T}(\psi,T\psi)+\mathcal{T}(T\psi,\psi)=0$ as well, the constant of motion corresponding to T is given by

$$Q_T=\tfrac{1}{2}ih\mathcal{T}(\psi,T\psi), \tag{3}$$

which transforms correctly and also satisfies

$$[F\psi,Q_T]=ihFT\psi. \tag{4}$$

Now consider the multiple frequency linear system $N^r\psi=0$, where N is self-adjoint, of degree s in ∂_0; since an operator F of degree $<d=rs$ in ∂_0 can generally be written as $F=\sum_{b=0}^{r}H_bN^b$, where H_b is of ∂_0-degree $<s$, (1) and (2) are equivalent to

$$(i/\hbar)\int\omega^T[N^r,Z(x_0-x_0')]\psi dx^n\cdot HN^b\psi(x')=HN^b\omega(x'),$$

or to

$$(i/\hbar)\sum_{k=0}^{r-1}\int(N^k\omega)^T[N,Z(x_0-x_0')]N^{r-k-1}\psi dx^n \cdot HN^b\psi(x')=HN^b\omega(x'), \tag{5}$$

where H is of ∂_0-degree $<s$. The kth integral in (5) depends only on $N^k\omega$, $\partial_0N^k\omega$, $\cdots$, $\partial_0^{r-1}N^k\omega$, evaluated at $x_0=x_0'$; since these functions may be chosen independently, (5) decomposes into

$$(i/\hbar)\int(N^a\omega)^T[N,Z(x_0-x_0')]N^{r-a-1}\psi dx^n \cdot HN^b\psi(x')=\delta_{a,b}HN^b\omega(x'). \tag{6}$$

According to (6), only $KN^a\psi\cdot HN^{r-1-a}\psi\neq0$ for K, H of degree $<s$ in ∂_0; thus the commutation relations decompose in a pairwise manner, with an additional single set if r is odd. Moreover, we obtain from (6), on redefining ω, the relations,

$$(/\hbar)\int\omega^T[N,Z(x_0-x_0')]N^{r-1-a}\psi dx^n \cdot HN^a\psi(x')=H\omega(x'), \tag{7}$$

$$(i/\hbar)\int(N\omega)^T[N,Z(x_0-x_0')]N^a\psi dx^n \cdot HN^{r-1-a}\psi(x')=HN\omega(x'),$$

[1] J. K. Percus, Columbia University Dissertation, 1954 (unpublished).
[2] A. Pais and G. E. Uhlenbeck, Phys. Rev. **79**, 145 (1950).
[3] The formalism used here may be shown to be equivalent to those of other authors when they are applicable to a given linear system; a more detailed discussion of this point will appear in a subsequent paper.

between $KN^a\psi$ and $HN^{r-1-a}\psi$, precisely those which would result between $K\varphi$ and $HN\varphi$ for $N^2\varphi=0$ (unless $a=r-1/2$, in which case the first of (7) corresponds to the relations between $K\varphi$ and $H\varphi$ for $N\varphi=0$).

The Eqs. (6) may also be written in the form

$$\mathcal{T}^{(a)}(\omega,\psi)\cdot H\begin{vmatrix} N^b \\ N^{r-1-b}\end{vmatrix}\psi(x')=\delta_{a,b}H\begin{vmatrix} N^b \\ N^{r-1-b}\end{vmatrix}\omega(x'),$$

where

$$\mathcal{T}^{(a)}(\omega,\psi)$$

$$=(i/\hbar)\int\{(N^a\omega)T[N,Z(x_0-x_0')]N^{r-1-a}$$

$$+(N^{r-1-a}\omega)T[N,Z(x_0-x_0')]N^a\}\psi dx^n, \quad (8)$$

$$\mathcal{T}^{(r-1/2)}(\omega,\psi)$$

$$=(i/\hbar)\int(N^{(r-1)/2}\omega)T[N,Z(x_0-x_0')]N^{(r-1)/2}\psi dx^n$$

respectively for $a<r-1/2$ and for $a=r-1/2$ if r is odd. Now let us write $Q_T=\Sigma Q_T^{(a)}$, where $Q_T^{(a)}=\frac{1}{2}ih\mathcal{T}^{(a)}(\psi,T\psi)$, no longer a constant; it readily follows from (8) that if the ∂_0-degree of T is 0, then $[Q_T^{(a)},Q_T^{(b)}]=0$, and the commutation relations between $Q_T^{(a)}$ and the $KN^a\psi$, $HN^{r-1-a}\psi$ are identical with those between Q_T, $K\varphi$, $HN\varphi$ for $N^2\varphi=0$, so that e.g. eigenvalues are also the same. Such a decomposition may not however obtain if T is of ∂_0-degree>0: Thus, if Q_{∂_0} (=energy) is a constant of the motion, we would require, for $a,b\leq r-1/2$, $[Q_{\partial_0}^{(a)},Q_{\partial_0}^{(b)}]=0$ as well as $[HN^b\psi,Q_{\partial_0}^{(a)}]=ihHN^b\partial_0\psi\delta_{a,b}$; now there certainly exists an H of ∂_0-degree$<s$ such that $H\partial_0=N+f$, where f is of ∂_0-degree 0. We then have $[H\psi,Q_{\partial_0}^{(0)}]=ihH\partial_0\psi=ihN\psi+ihf\psi$, whence $[[H\psi,Q_{\partial_0}^{(0)}],Q_{\partial_0}^{(1)}]=-\hbar^2N\partial_0\psi$; on the other hand, since $[Q_{\partial_0}^{(0)},Q_{\partial_0}^{(1)}]=0$, this should equal $[[H\psi,Q_{\partial_0}^{(1)}],Q_{\partial_0}^{(0)}]=[0,Q_{\partial_0}^{(0)}]=0$, which of course cannot be.

This last result contradicts one of Pais and Uhlenbeck ([2]Appendix) for the case $r=3$; the discrepancy is due to the fact that in their "contact transformation," $[P_0,P_2]\neq 0$. While a pairwise decomposition of the Hamiltonian, equivalent to expressing a solution of $N^r\psi=0$ as a sum of solutions of $N^2\psi=0$, is in principle impossible, we have at least verified their conjecture, insofar as commutation relations and ∂_0-independent constants of motion are concerned, as to the decomposition of the system into twofold subsystems.

Letters to the Editor

PUBLICATION of brief reports of important discoveries in physics may be secured by addressing them to this department. The closing date for this department is five weeks prior to the date of issue. No proof will be sent to the authors. The Board of Editors does not hold itself responsible for the opinions expressed by the correspondents. Communications should not exceed 600 words in length and should be submitted in duplicate.

Superconductivity of a Charged Boson Gas

M. R. SCHAFROTH
F. B. S. Falkiner Nuclear Research Laboratory, School of Physics, The University of Sydney, Sydney, Australia*
(Received September 7, 1954)

IT is the purpose of this note to point out that there exists a relatively simple physical system which exhibits the essential equilibrium features of a superconductor,[1] namely a phase transition of the second kind at a critical temperature T_c and the occurrence of a Meissner-Ochsenfeldt effect below it. This system is the ideal gas of charged bosons. The existence of a transition point is well known.[2]

If one establishes the relation between the Fourier components of the current density, $\mathbf{i}(\mathbf{q})$ and of the vector potential, $\mathbf{A}(\mathbf{q})$, of an applied weak inhomogeneous magnetic field in the form

$$\mathbf{i}(\mathbf{q})=K(q^2)\mathbf{q}\times(\mathbf{q}\times\mathbf{A}(\mathbf{q})), \tag{1}$$

then, as was shown elsewhere,[3] a pole in $K(q^2)$ for $q=0$ means the occurrence of the Meissner-Ochsenfeldt effect. The particular case,

$$K(q^2)=1/c\lambda q^2, \tag{2}$$

is equivalent to the London[1] equation,

$$\operatorname{curl}(\lambda\mathbf{i}(x))=-(1/c)\mathbf{H}(x). \tag{3}$$

The thermal average current density for our model is easily evaluated by perturbation theory on the distribution function in a manner described before[3] and yields below the transition point:

$$K(q^2)=n_s\frac{e^2}{mc}\frac{1}{q^2}+K_0(q^2), \tag{4}$$

where n_s is the density of condensed bosons and $K_0(q^2)$ has a singularity of order $1/q^1$ only. This proves our assertion.

The fact that $K_0(q^2)$ still has a singularity shows that (3) is not valid but has to be replaced by an integral relationship. (This was already proposed by Pippard[4] for real superconductors.) In particular the penetration depth is not determined by n_s alone.

The very uniqueness of the phenomenon of Bose-Einstein condensation might be taken as a clue that this model is essentially the only one which exhibits the phenomenon of superconductivity. One would then have to show that in a metal at low temperatures charge-carrying bosons occur, e.g., because of the interaction of electrons with lattice vibrations.[5] In this connection it might be worthwhile investigating the possibility of existence of bound two-electron states. A more detailed discussion of this work will appear in a forthcoming paper.

I am greatly indebted to Dr. J. M. Blatt and Dr. S. T. Butler for stimulating discussion.

* Also supported by the Nuclear Research Foundation within the University of Sydney.

[1] F. London, *Superfluids* I (John Wiley and Sons, Inc., New York, 1950).
[2] A. Einstein, Preuss. Akad. Wiss. Berlin Ber. **22**, 261 (1924); **23**, 3 (1925); F. London, Phys. Rev. **54**, 947 (1938).
[3] M. R. Schafroth, Helv. Phys. Acta **24**, 645 (1951).
[4] A. B. Pippard, Proc. Roy. Soc. (London) **216**, 547 (1953).
[5] H. Fröhlich, Phys. Rev. **79**, 845 (1950).

Superfluidity of a Boson Gas

J. M. BLATT AND S. T. BUTLER
F. B. S. Falkiner Nuclear Research and Adolph Basser Computing Laboratories, School of Physics, University of Sydney, Sydney, Australia*
(Received September 7, 1954)

WE have made a theoretical analysis of an idealized version of Andronikashvili's[1] experiment establishing the superfluid character of liquid helium below the λ point. A vessel is filled with liquid helium and set into rotation. The apparent moment of inertia is less than the classical value $I_0=\frac{1}{2}NMR^2$ (N = number of atoms, M = mass of atom, R = radius of vessel). The ratio between the observed moment of inertia and I_0 is by definition the "concentration of normal fluid."

We now make a calculation of the equilibrium value of the angular momentum L of an ideal Bose-Einstein gas as a function of the angular velocity ω. The result is shown in Fig. 1. Above the λ point, L is given by the dashed straight line, with slope equal to I_0. Below the λ point, L is a discontinuous function of ω, as shown by the full lines. The discontinuities occur whenever the angular velocity increases by an amount $\Delta\omega=\hbar^2/MR^2$, for then a new value of the angular momentum quantum number m gives rise to the lowest state of an atom in the vessel. Hence at this point a macroscopic number of atoms shifts from the lowest state with quantum number $m-1$ to the lowest state with quantum number m, and this accounts for the sudden jump in the equilibrium angular momentum L.

If equilibrium is reached, the observed moment of inertia is the mean slope of the solid curve, averaged over these quantum mechanical fluctuations; that is,

the equilibrium value of the angular momentum is $L=I_0\omega$, the classical value. Hence the equilibrium state of an ideal Bose-Einstein gas is not superfluid.

A superfluid state is reached if, for some reason, the "condensed" particles fail to shift over to the new ground state. Then the angular momentum falls along the dotted line in Fig. 1, and the observed moment of inertia is less than I_0. Order-of-magnitude estimates of the lifetime of this state are difficult to make, but do not disagree with a macroscopic relaxation time.

We suggest, therefore, that the actual liquid helium superfluid state is also metastable rather than an equilibrium state. A crucial experiment to decide whether the superfluid state is metastable or thermodynamically stable is the following: the vessel is set into rotation above the λ point, and then cooled down

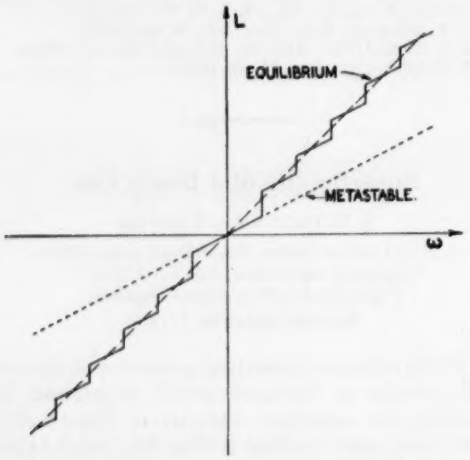

FIG. 1. The angular momentum L of an ideal Bose-Einstein gas below the condensation temperature, as a function of the angular velocity ω of the container.

without application of torques. If the superfluid state is stable, the vessel's rate of rotation must speed up as it cools down. If our theory is right, the vessel will maintain its speed. The experiment has not been done so far.

In this connection, another experiment of Andronikashvili[2] might be thought to raise a difficulty; Andronikashvili showed, in essence, that as liquid helium is cooled down and more and more of the fluid becomes superfluid, this newly created superfluid does not take part in the rotation of the normal fluid. This looks at first sight as if the superfluid state were thermodynamically stable. However, Andronikashvili started rotating and cooling at a temperature below the λ point, so that there were already macroscopically many particles in the state with quantum number $m=0$ at the time the experiment started. Now it is characteristic of Bose-Einstein statistics that the transition probability to a state i is proportional to N_i+1, where N_i is the number of particles already occupying state i. In other words, Bose-Einstein statistics work according to the principle: "To him that hath shall be given." As the temperature drops, and more and more particles get pushed out of the high-energy states, the already highly populated state with $m=0$ provides the center of condensation, rather than the true ground state. Of course, eventually equilibrium must be reached, but this presumably did not occur in the time interval Andronikashvili used for cooling down. This provides a lower limit for the relaxation time, of the order of minutes.

The only other experiment relevant to this discussion[3] employed angular velocities so high that the circumferential velocity near the wall of the vessel was higher than the critical velocity for superfluid flow. Hence it is not surprising that Osborne found all the fluid taking part in the rotation.

Once this explanation of the superfluid properties of liquid helium is accepted, the concentration of normal fluid can be computed by standard methods of equilibrium statistical mechanics. This is possible because, for angular velocities less than $\hbar^2/MR^2$, the metastable state is the same as the equilibrium state. This calculation has been done for the ideal Bose-Einstein gas, where it gives the expected result $I=(T/T_\lambda)^{\frac{5}{2}}I_0$, and it has been set up for the interacting gas, using methods developed for a study of the thermodynamic properties of liquid helium.[4] The approximation of a hard-sphere gas gives corrections in the right direction, but of insufficient magnitude. This is the same situation as occurs for the calculation of the specific heat.

A detailed paper on this subject is in preparation.

We would like to thank Dr. M. R. Schafroth for many stimulating discussions.

* Also supported by the Nuclear Research Foundation within the University of Sydney.

[1] E. L. Andronikashvili, J. Phys. (U. S. S. R.) **10**, 201 (1946).
[2] E. L. Andronikashvili, J. Exptl. Theoret. Phys. (U. S. S. R.) **22**, 62 (1952).
[3] D. V. Osborne, Proc. Phys. Soc. (London) **A63**, 909 (1950).
[4] M. H. Friedman and S. T. Butler, Phys. Rev. **91**, 465 (A) (1953), and papers in preparation.

Color-Center Magnetic Resonance in LiF*

C. K. JEN AND N. W. LORD
Applied Physics Laboratory, The Johns Hopkins University, Silver Spring, Maryland
(Received September 21, 1954)

PARAMAGNETIC resonance phenomena at microwave frequencies in LiF crystals, colored by irradiation, have been studied by Hutchison[1] and by Schneider.[2] Hutchison observed a g value of 2.00 in neutron-bombarded crystals of LiF which he assumed was due to F centers. Schneider, on the other hand, reported observations on LiF crystals subjected to

180-kv x-rays and interpreted a broad intense peak ($g=2.020$) as due to V centers, while ascribing a subsidiary resolved set of lines to the hyperfine structure of F centers.

We have studied the magnetic resonance in LiF single crystals, with some samples irradiated by x-rays at 50 kv and others bombarded by a cyclotron proton beam at approximately 360 Mev. The sample, usually less than 0.4 cc in volume, is placed on one end plate of rectangular cavity, oscillating in the TE_{011} mode and resonating at the frequency of a stabilized klystron around 9130 Mc/sec. The signal showing the magnetic resonance is derived from a modulation of the static field at 400 cps. The resonance is exhibited either in the form of the derivative of the absorption curve or in the form of the dispersion effect shown by the shift in the resonance frequency of the cavity. The steady magnetic field, measured by a proton resonance probe, is varied slowly through the resonance value while the signal is being recorded automatically. All our experiments have been carried out at room temperature.

In each of our samples a single, broad, approximately Gaussian, resonance peak has been observed. The signal-to-noise ratios ranged from about 30 for an x-rayed sample to 500 for a proton-bombarded sample. No resolved hyperfine structure lines have been detected in any of our recordings. The g factor calculated from a large number of recorded curves is $g=1.999\pm0.001$ for the x-rayed samples, and $g=2.002\pm0.001$ for the proton-bombarded ones. As a simple measure of the absorption line width, we use the field separation between two points of maximum slope, designated here as ΔH_m. The value of ΔH_m for a given resonance curve is obtained by extrapolating to zero field modulation. The observed values of ΔH_m are 65 oersteds for the x-rayed samples and 110 oersteds for the proton-bombarded samples. Both the g factor and the line width have been shown experimentally to be independent of the concentration of the color centers for samples subjected to the same kind of radiation. Consequently, the effects of dipolar interaction appear to be negligible.

Using the approximate theory of Kahn and Kittel,[3] one can show that the g factor for an F-center resonance in LiF should be smaller than the free electron g by not more than about 10^{-5}. This prediction agrees with the g value obtained for the proton-bombarded sample, but not with the g value of the x-rayed sample.

Kip *et al.*[4] assumed the line width to be caused by hyperfine interactions and predicted a nearly Gaussian shape for the envelope of the hyperfine components. They showed that the width of the envelope at half-maximum ($\Delta H_{\frac{1}{2}}$) was $1.12\xi A$ cm^{-1} for a nuclear spin of 3/2. Here ξ is the fractional effective s character of the valence electron and A is the hyperfine interaction constant. For Li^7 (95 percent abundant), we have $I=3/2$ and $A=0.0134$ cm^{-1}.[5] This gives $\Delta H_{\frac{1}{2}}=161\xi$ oersteds. Our experimental values of ΔH_m give $\Delta H_{\frac{1}{2}}=76.5$ oersteds for the x-rayed sample and 130 oersteds for the bombarded sample if Gaussian line shape is assumed. This would require $\xi\approx0.5$ for the x-rayed sample if the resonance is to be attributed to F centers. Such a value for ξ seems to be reasonable for Li^7. The value $\xi\approx0.8$ required to account for the line width of the proton-bombarded sample appears to be somewhat high. It is to be noted, however, that Hutchison has also observed a line width of approximately 160 oersteds for his neutron-bombarded sample.

The results on the x-rayed LiF strongly favor the F center interpretation. The g factor is less than the free electron value and the line width agrees well with the theory of Kip *et al.*[4] for F centers. While this evidence does not exclude the presence of other one-electron color centers, it does eliminate any sizable contribution from V centers. The case of the proton-bombarded LiF is far less clear cut. It may be that the resonance is still due to F centers with their environment drastically changed by heavy particle bombardment. It is also conceivable that the contributions of M centers, R_1 centers, and possibly other one-electron centers are large enough to affect the line shape.

We wish to thank Miss M. C. Williams, Jr., for preparing the x-rayed samples and Dr. W. J. Leivo of the Carnegie Institute of Technology for the proton-bombarded samples. We are also indebted to B. S. Gourary and S. N. Foner for some stimulating discussions.

* Supported by the Bureau of Ordnance, Department of the Navy.

[1] C. A. Hutchison, Jr., Phys. Rev. **75**, 1769 (1949).
[2] E. E. Schneider, Phys. Rev. **93**, 919 (1954).
[3] A. H. Kahn and C. Kittel, Phys. Rev. **89**, 315 (1953).
[4] Kip, Kittel, Levy, and Portis, Phys. Rev. **91**, 1066 (1953).
[5] J. B. M. Kellogg and S. Millman, Revs. Modern Phys. **18**, 323 (1946).

Measurement of the Complex Tensor Permeability of Ferrites

J. H. Rowen and W. von Aulock
Bell Telephone Laboratories, Murray Hill, New Jersey
(Received August 9, 1954)

Artman and Tannenwald[1] have described a method for determining the components of the permeability tensor of a ferrite by measuring the frequency shift and change in Q produced by the insertion of a small spherical sample in a degenerate-mode cavity. The cylindrical TE_{111} mode cavity permits splitting of the cavity resonance into two frequencies corresponding to the resonance of the cavity for each of the counter-rotating circular components of the incident linear polarization. We have found that there are several advantages to be gained by using a very thin disk in a similar cavity. Not only is it possible to pro-

duce larger effects without violating the basic assumptions of the perturbation theory but the results obtained can more readily be interpreted in terms of the intrinsic properties of the material.

In a sphere placed in a uniform field, H^0, the internal field, H^i, is determined from the boundary conditions to be:

$$H^i = H^0 - 4\pi M/3.$$

If we write the perturbation equations in terms of this internal field and assume a tensor permeability, we find that the frequency shift in a degenerate cavity is given by

$$\frac{2\delta\omega}{\omega_0} = \frac{[(\mu-1)(\mu+2)-K^2]C_1}{(\mu+2)^2-K^2} \pm \frac{KC_2}{(\mu+2)^2-K^2}, \quad (1)$$

where the $\pm$ sign refers to the two senses of circular polarization, where C_1 and C_2 are constants of the geometry, and where μ and K are the components of the *intrinsic* permeability tensor. An alternate procedure sometimes suggested refers to Kittel's[2] equation of motion for magnetization to show that all the demagnetization factors cancel out for a spherical sample. Then, one can write

$$2\omega/\omega_0 = (\mu_1-1)C_1 \pm K_1C_2 \quad (2)$$

and expect μ_1 and K_1 to be the same functions of H^0 as μ and K are of H^i. Where Polder's[3] relations hold, it is sufficient to measure the quantities μ_1 and K_1 as functions of H^0 and state that the curves so obtained also represent the behavior of the intrinsic parameters, μ and K, as functions of H^i.

In a polycrystalline ferrite, however, it is hardly reasonable to expect Polder's equations to hold exactly, and one must use Eq. (1) to determine the intrinsic parameters precisely.

It will be observed that Eq. (1) is not a sensitive way to determine μ and K when $(\mu+2)^2-K^2$ is small. This is a region of great interest where $H^0 \approx \omega/\gamma$, $H^i \ll H^0$, where γ is the gyromagnetic ratio. Furthermore it is difficult to separate the imaginary parts of μ and K so that they may be related to the measured changes in the Q of the cavity. Thirdly, one must use spheres no more than 0.020 inch in diameter in order to obtain a uniform internal field. Such spheres produce very small effects at fields far from resonance.

Through the use of a disk all of these difficulties are avoided. At the end wall of a TE_{111} mode cylindrical cavity there are only transverse components of H, namely H_θ and H_r. If a very thin disk is placed against the end wall, we may state with good accuracy that $H_\theta^i = H_\theta^0$ and $H_r^i = H_r^0$ while $H_z^i = H_z^0 - 4\pi M$. Then the frequency shift is given by

$$2\delta\omega/\omega = (4t/\lambda_g^3)\lambda^2(\mu-1)R_1 \pm KR_2, \quad (3)$$

where R_1 and R_2 are constants of the geometry and t is the thickness of the disk. The free-space wavelength is λ and λ_g is the guide wavelength. Here μ and K are intrinsic properties of the medium which relate the true *internal* **H** to *internal* **B** and which are measured as functions of a known *internal* dc field: $H_z^0 - 4\pi M$.

In this relationship it is easy to treat $\delta\omega$ as complex and determine real and imaginary parts of μ and K.

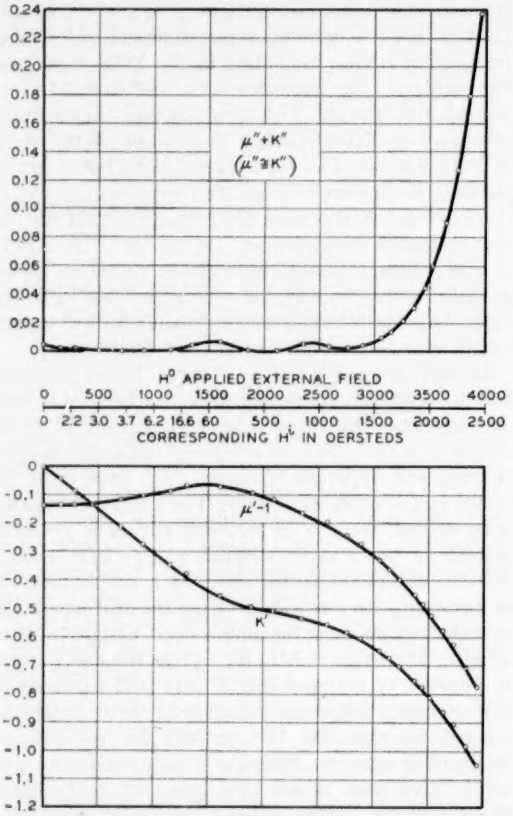

FIG. 1. Complex μ and K as functions of external and internal static fields. $\mu = \mu' - j\mu''$; $K = K' - jK''$. B.T.L. Ferrite No. 2089. $\epsilon = 8.7 - j(2\times10^{-4} \pm 2\times10^{-4})$.

Because of the relatively large volume of material it is possible to measure values of $(\mu''+K'')$ as small as 0.0004 if one can measure Q to within 2 percent. Since the thickness (order of 0.010 in.) is the only dimension over which the field is assumed constant there is no loss of validity if the disk diameter approaches the cavity diameter. To verify this several measurements were made in which diameter and thickness were varied, and good agreement was obtained as long as the ratio of diameter to thickness was very large. The only limitation thus far encountered is a difficulty in obtaining disks thin enough to permit measurements at ferromagnetic resonance where a thick disk absorbs so much power that the cavity resonance disappears.

In Fig. 1 we show a sample of data obtained in the low-field region. Both real and imaginary parts are

shown. These are plotted against the applied field and the corresponding values of internal field as determined from an experimental $B-H$ curve are shown on the auxiliary scale. The extra absorption peaks are repeatable and are being investigated in detail.

By placing the disk at the center of the cavity at the electric field maximum we obtain the real and imaginary dielectric constant of the same sample.

We should like to thank Dr. A. M. Clogston for his assistance in this investigation.

[1] J. O. Artman and P. E. Tannenwald, Phys. Rev. **91**, 1014 (1953).
[2] C. Kittell, Phys. Rev. **73**, 155 (1948).
[3] D. Polder, Phil. Mag. **40**, 99 (1949).

Hollow Dislocations and Etch Pits

N. Cabrera, M. M. Levine and J. S. Plaskett
Department of Physics, University of Virginia, Charlottesville, Virginia
(Received September 20, 1954)

SOME time ago Frank[1] showed that dislocations having large Burgers vectors should be hollow. The present letter considers the conditions necessary to open up any dislocation (forming an etch pit) by placing the crystal in an undersaturated medium. The idea is simply to generalize Frank's analysis (limited to equilibrium conditions) to the general case of growth or evaporation. Let us consider a crystal containing a hollow dislocation of radius r and Burgers vector b. The crystal is *not* in equilibrium with the surrounding medium, and the decrease in free energy of the system by the formation of a unit volume of crystal (supposed perfect) is ΔG_v. If $\Delta G_v>0$, the crystal is growing; if $\Delta G_v<0$, the crystal is evaporating.

Then an increase by dr of the radius of the hollow will produce a change dG in the free energy of the system, per unit length of dislocation, equal to

$$dG=\Delta G_v 2\pi r dr+\gamma 2\pi dr-(\mu b^2/8\pi^2 r^2)2\pi r dr,$$

where γ is the crystal-medium surface energy, and μ the shear modulus. The value of r satisfying the condition $dG/dr=0$ will correspond to a steady state situation where the radius of the hollow remains constant, while the crystal grows or evaporates. This value of r is given by

$$r=\tfrac{1}{2}\rho_c\{[1+4(r_0/\rho_c)]^{\frac{1}{2}}-1\},$$

where $\rho_c=\gamma/\Delta G_v$ is the critical radius for two-dimensional nucleation on the surface of the crystal and $r_0=\mu b^2/8\pi^2\gamma$ is the radius of the hollow when the crystal is in equilibrium with the surroundings.

If $\rho_c>0$ ($\Delta G_v>0$), the hollow tends to close up as ρ_c decreases (ΔG_v increases). If $\rho_c<0$ ($\Delta G_v<0$), the hollow tends to open up giving a steady-state solution as long as $|\rho_c|$ is larger than the critical value $|\rho_c'|$ given by

$$\rho_c'=-4r_0.$$

For larger undersaturations the surface energy is not large enough to keep a constant radius for the hollow, and the etch pit is formed. If the surrounding medium is either vapor or dilute solution, $\Delta G_v=(kT/\Omega)\ln(p/p_0)$, where Ω is the molecular volume and p_0 the saturated pressure or concentration; the critical undersaturation ratio p_0/p_c is then given by

$$\ln(p_0/p_c)=2\pi^2\gamma^2\Omega/kT\mu b^2. \quad (1)$$

There is qualitative evidence for the critical opening up of a dislocation in the dissolution of CdI_2 crystals where the Burgers vectors are quite large (for instance, in the General Electric motion picture film). More quantitative experiments to test formula (1) would be worthwhile. Concerning the formation of etch pits in dislocations of small Burgers vectors, it is clear that this is only possible in a medium in which γ is considerably below the value corresponding to the free surface of a crystal.

[1] F. C. Frank, Acta Cryst. **4**, 497 (1951).

Ferromagnetic Resonance in Iron-Nickel Alloys*

Raymond Hoskins, *Department of Physics, University of California, Berkeley, California*
and
George Wiener, *Westinghouse Research Laboratories, East Pittsburgh, Pennsylvania*
(Received September 27, 1954)

AN anomalous sharp dip in the g value of iron-nickel alloys in the range of 30 to 50 percent nickel in colloidal suspensions has been reported by Bagguley,[1] the g value for 40 percent nickel falling to 2.01. Ferromagnetic resonance experiments have been made on disk-shaped bulk samples in an effort to verify this variation in g value with changing nickel concentration. Wavelengths of 6 mm, 1.2 cm, and 3 cm were used. Little or no variation in g value was observed in the four samples of varying nickel concentration investigated.

Disks 0.450 in. in diameter and about 0.010 in. thick, prepared from cold-rolled strip recrystallized at 1080°C for four hours, were polished with jewelers rouge, annealed in vacuum for two hours at 800°C, cooled slowly, and electropolished in a hot phosphoric acid-chromic acid solution. A small hole was drilled in the wall of a rectangular microwave cavity and the samples were clamped firmly to this wall. The 3-cm and 1.2-cm experiments were made using a reflection-type cavity forming one arm of a magic-T bridge. In the 6-mm experiments a crystal harmonic generator driven by a 2K33, K-band klystron was used as a

source of power, and a transmission-type cavity was used. The microwave absorption was measured in all cases by the magnetic field modulation method.

Two orientations of the plane of the sample with respect to the external field were used in the 1.2-cm measurements, one parallel to the field in fields of about 3000 oersteds and the other normal to the field in fields of about 22 000 oersteds. The two resonance conditions are given by:[2]

$$\omega=\gamma[H_0(H_0+B_s)]^{\frac{1}{2}},$$

and

$$\omega=\gamma(H_0-B_s),$$

where H_0 is the external field for maximum absorption corrected for finite sample thickness, B_s the saturation induction, and $\gamma=ge/2mc$. From these two equations B_s and g can be calculated. The 6-mm and 3-cm measurements were made with the plane of the sample parallel to the external field in fields of about 10 000 and 800 oersteds respectively and the g-value calculated using the value of B_s given by the 1.2-cm measurements. The results are given in Table I. Values of B_s measured by a force method on samples of the same composition are given for comparison. The fields were measured by a rotating coil fluxmeter calibrated with a free radical compound to an accuracy of 1 percent. The demagnetization factor correction of several hundred oersteds applied to H_0 in the 3-cm measurements limits the accuracy of these measurements to about 5 percent.

TABLE I. Summary of results. B_s is the saturation induction in kilogauss. ΔH is the full width between points of maximum slope in oersteds. $\perp$ and $\parallel$ refer to the orientation of the plane of the sample with respect to the external field.

		Percent nickel			
		36	40	44	48
1.2 cm	g	2.12	2.14	2.14	2.13
	B_s	15.0	15.7	15.7	16.3
	$\Delta H_\perp$	225	200	200	175
	$\Delta H_\parallel$	125	125	125	125
6 mm	g	2.10	2.08	2.11	2.08
	$\Delta H_\parallel$	250	250	250	250
3 cm	g	2.2	2.2	2.3	2.3
	$\Delta H_\parallel$	120	120	90	90
Force method	B_s	15.2	15.7	16.2	16.0

The width of the resonance lines is surprisingly narrow in contrast to the widths reported for spheres in colloidal suspension.[1] The width of the 3-cm lines corresponds to a half-width at half-power points of from 100 to 80 oersteds for a Lorentzian curve, compared to 1000 to 250 oersteds reported for the colloidal spheres.[1] These are believed to be the sharpest ferromagnetic resonance lines to be reported for metals. The anisotropy fields are quite low in these alloys, $2K_1/M_s$ varying from 35 to 16 oersteds, thus their contribution to the line width is negligible.

It is seen that the bulk measurements here reported give no sign of the variation in g value with changing nickel concentration as seen in the colloidal spheres. The discrepancy might lie in the fact that it is difficult to determine g values accurately from very broad lines such as Bagguley reports.[1]

We should like to express our thanks to Professor C. Kittel for suggesting this experiment and for several helpful discussions; to Professor A. F. Kip for many helpful suggestions regarding the measurements; to Mr. Tom Hazelett for annealing the samples; and to Mr. Glen Wagoner for his assistance with the 3-cm measurements. The metallurgical work and magnetic measurements were made at the Westinghouse Research Laboratories and the ferromagnetic resonance experiments were carried out at the University of California.

* This research was supported in part by the U. S. Office of Naval Research and the U. S. Signal Corps.

[1] D. M. S. Bagguley, Proc. Phys. Soc. (London) **A66**, 765 (1953).
[2] C. Kittel, Phys. Rev. **73**, 155 (1948).

Resonances in the Proton Bombardment of C^{14}

G. A. BARTHOLOMEW, F. BROWN, H. E. GOVE, A. E. LITHERLAND, AND E. B. PAUL

Physics Division, Atomic Energy of Canada Limited, Chalk River Laboratories, Chalk River, Canada

(Received September 20, 1954)

THE $C^{14}(p,\gamma)N^{15}$ reaction has been studied from 0.25 to 1.8 Mev by means of the Chalk River electrostatic accelerator. We wish to report a broad resonance observed in this reaction at a proton energy of 1.50 Mev which has not been reported in studies of the $N^{14}(n,n)$, $N^{14}(n,p)$, or $C^{14}(p,n)$ reactions.[1] Targets of elemental carbon, containing 25 percent C^{14} on tantalum backings, were prepared by heating the backings by induction to a bright red heat in the presence of CO gas containing radioactive carbon.

The yield curve of the ground state γ ray between proton energies of 0.9 and 1.7 Mev is shown in Fig. 1. These results were obtained in two experiments using two NaI(Tl) crystals 2 inches long by 2 inches in diameter mounted at angles of 0° and 90° to the direction of the proton beam in the first experiment and at angles of 143° and 90° in the second experiment. The neutrons from the $C^{14}(p,n)N^{14}$ reaction were also observed at 90° in each experiment. They were detected in a BF_3 counter surrounded with paraffin. The γ-ray yield curve has also been observed at 90° by Spearman, Hudspeth, and Morgan,[2] and the neutron yield curve by Roseborough, McCue, Preston, and Goodman.[3] The γ-ray yield exhibits a broad resonance with a maximum near a proton energy of 1.5 Mev. This resonance is only just discernible in the yield curves of the $C^{14}(p,n)N^{14}$ and the $N^{14}(n,p)C^{14}$ reactions where presumably it is

responsible for the background between the resonances at 1.31 and 1.67 Mev. The γ-ray yield curves clearly show evidence of interference between the broad resonance and those at 1.17 Mev and 1.31 Mev. The interference pattern is a function of angle at the 1.17-Mev resonance but is independent of angle at 1.31 Mev.

The angular distributions of the neutrons at all three resonances and of the ground state γ ray at the 1.31- and 1.50-Mev resonances were all isotropic while that of the ground state γ ray at 1.17 Mev showed a term proportional to $\cos\theta$. The isotropy of the neutron angular distribution at 1.17 and 1.31 Mev has also been observed elsewhere.[4] Since the 1.31-Mev resonance is known from the neutron scattering measurements[5] to be formed by s-wave neutrons, it may be deduced from the present results that the 1.31- and 1.50-Mev resonances are both $\frac{1}{2}+$ and that the 1.17-Mev resonance is probably $\frac{1}{2}-$ ($\frac{3}{2}-$ is also possible but less likely).

Estimates of total width, Γ, neutron width, Γ_n, proton width, Γ_p, and the partial width for the emission of the ground-state γ ray, $\Gamma_\gamma(\gamma_0)$, obtained from the yield curves are given in Table I. In estimating $\Gamma=475\pm25$ kev and $E_r=1.50\pm0.05$ Mev for the broad resonance, the γ-ray data were fitted with a single-level Breit-Wigner curve including the effect of the Coulomb barrier and ignoring the interference effects near the narrow resonances. With Γ and E_r fixed in this way, the (p,n) yield curve was analyzed to give the neutron yield of the broad resonance. The neutron counter

TABLE I. Resonance properties of N^{15}. The proton energy at resonance is given in the first column; the spin and parity in the second; and the total width, neutron width, proton width, and partial width for the emission of the ground state gamma ray are given in the third, fourth, fifth, and sixth columns respectively.

E_r Mev	J	Γ kev	Γ_n kev	Γ_p kev	$\Gamma_\gamma(\gamma_0)$ ev
1.17	$\frac{1}{2}-$	12	1.6	10.4	0.25
1.31	$\frac{1}{2}+$	41	33.	8.	2.3
1.50	$\frac{1}{2}+$	475	5.	470.	28.

efficiency at 1.31 Mev was obtained by assuming that the neutron yield obtained at this resonance is that computed by detailed balance from the known absolute yield of the $N^{14}(n,p)C^{14}$ reaction.[6] This absolute efficiency, when used to compute Γ_n and Γ_p for the other neutron resonances, leads to results in fair agreement with those obtained from neutron scattering.[5]

The properties of the broad state strongly suggest a nearly single-particle motion for the odd proton. The proton width is approximately equal to the single-particle width for s states defined by Lane,[7] while the value of $\Gamma_\gamma(\gamma_0)$ is about $\frac{1}{10}$ of the value given by the Weisskopf and Moszkowski single-particle formula.[8] It has been pointed out[9] that the proton bombardment of C^{14} produces excited states in N^{15} with isotopic spin quantum numbers $T=\frac{1}{2}$ and $\frac{3}{2}$ and therefore, since decay of $T=\frac{3}{2}$ states by neutron emission is forbidden at low bombarding energies while radiation is allowed, it may be possible to distinguish such states by com-

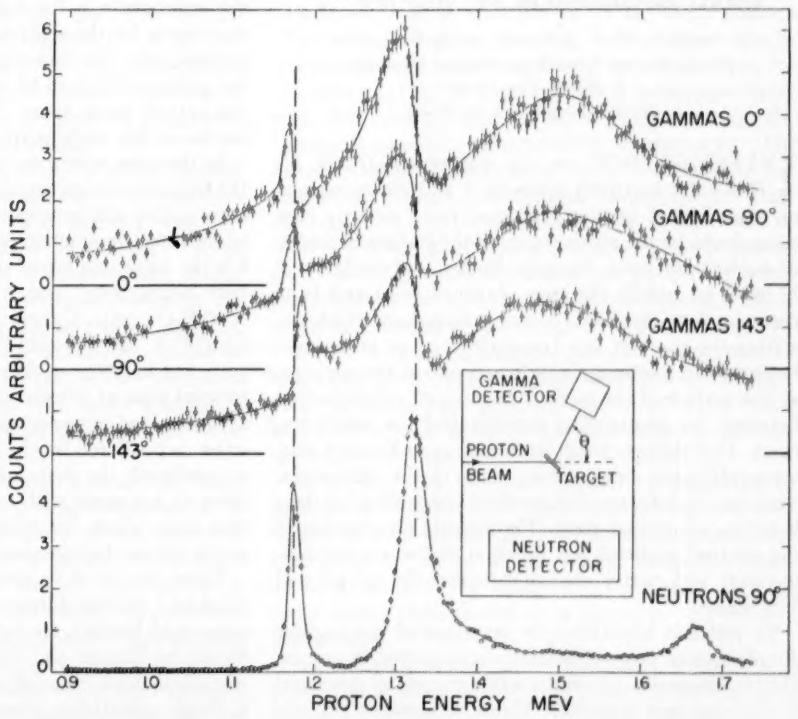

FIG. 1. Yield curves for the reaction $C^{14}(p,\gamma_0)N^{15}$ at three angles 0°, 90°, and 143° and for the reaction $C^{14}(p,n)N^{14}$ at 90° to the proton beam. The ordinate scales are shifted for comparison. The target arrangement is shown schematically in the inset.

paring the neutron and γ-ray yields. The calculated[10] energy of the first $T=\frac{3}{2}$ state in N^{15} (corresponding to the ground state of C^{15}) is 10.9 Mev. For the 1.50-Mev resonance at an excitation energy of 11.54 Mev the ratio of Γ_n to the single-particle width is exceptionally small, and it may be that this state has $T=\frac{3}{2}$ and is therefore the analog of a low-energy state in C^{15}.

The interference between the 1.31- and 1.50-Mev resonances is unusual in that it appears in the total cross section. This can only occur between states of the same spin and parity. Between two such interfering states of $J=0$ or $\frac{1}{2}$, terms higher than P_0 do not occur. A more detailed report of this work is being submitted to the *Canadian Journal of Physics*.

[1] These reactions have been studied by a large number of authors. See F. Ajzenberg and T. Lauritsen, Revs. Modern Phys. **34**, 321 (1952).
[2] Spearman, Hudspeth, and Morgan, Phys. Rev. **94**, 806 (1954) and I. L. Morgan (private communication).
[3] Roseborough, McCue, Preston, and Goodman, Phys. Rev. **83**, 1133 (1951).
[4] Kay, Mark, and Goodman, Phys. Rev. **91**, 472 (1953).
[5] Hinchey, Stelson, and Preston, Phys. Rev. **86**, 483 (1952).
[6] C. H. Johnson and H. H. Barschall, Phys. Rev. **80**, 818 (1950).
[7] A. M. Lane, Atomic Energy Research Establishment, Harwell Report T/R 1289, 1954 (unpublished).
[8] V. F. Weisskopf, Phys. Rev. **83**, 1073 (1951); S. A. Moszkowski, Phys. Rev. **83**, 1071 (1951).
[9] This has been pointed out by V. L. Telegdi and by W. E. Burcham (private communications).
[10] D. C. Peaslee, Phys. Rev. **95**, 717 (1954).

Direct Interaction in $Fe^{56}(p,p')Fe^{56*}$†

G. Schrank, P. C. Gugelot, and I. E. Dayton
Palmer Physical Laboratory, Princeton University, Princeton, New Jersey
(Received September 28, 1954)

INVESTIGATIONS on the energy spectra of inelastically scattered nucleons[1-3] and measurements on the yield of nuclear reactions[4] have recently case some doubt on the applicability of the statistical theory of nuclear reactions. Austern, Butler, and McManus,[5] in order to explain the large observed (n,p) and (n,α) cross sections, proposed a new mechanism which describes the reaction as a consequence of an interaction between the incoming particle and one of the nucleons at the surface of the nucleus in place of an interaction between the bombarding particle and the whole nucleus. This theory, which is analogous to Butler's deuteron stripping calculations, predicts the differential cross section for a reaction in which the residual nucleus is left in an excited state. The angular distribution of the emitted particles is a function of the angular momentum and parity change between the initial and final states.

To test this hypothesis we investigated the angular distribution of protons inelastically scattered from iron. The experimental apparatus was the same as described by Dayton and Schrank.[6] Figure 1 presents the observed absolute differential cross sections for the inelastic scattering of 17-Mev protons (c.m. energy) to the 0.822-Mev level[7] of Fe^{56}. Some care had to be taken at small scattering angles in the separation of the inelastic and elastic scattering. The errors include the uncertainty in the correction which was necessary to account for the spilling over of elastically scattered protons into the inelastic channels. For this reason the point at 25° is to be regarded as an upper limit to the actual value there. The elastic scattering cross section at this angle is 767 mb/sterad.

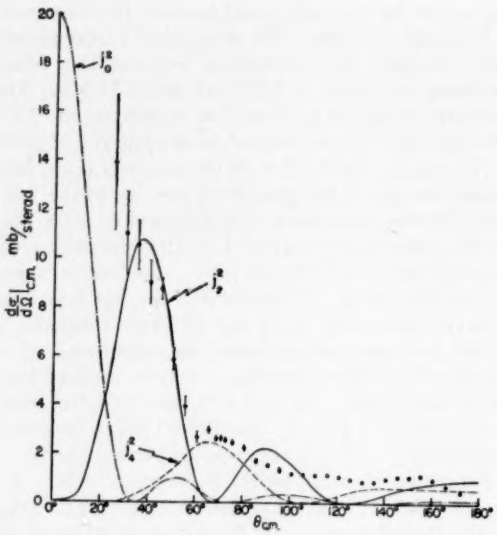

FIG. 1. Scattering of 17-Mev protons to the 822-kev level of Fe^{56}. The curves shown are the squares of the spherical Bessel functions of zeroth, second, and fourth order obtained from the work of Austern, Butler, and McManus.

In this case, where the initial state has zero spin and the final state is presumably a 2^+ level, the differential cross section will be proportional to $[j_2(QR)]^2$ according to the direct interaction picture, where $Q=|\mathbf{k}_{in}-\mathbf{k}_{out}|$, k is the wave number of the incoming or outgoing particle respectively, and R is the nuclear radius ($1.5\times10^{-13}A^{\frac{1}{3}}$ cm). Curves are shown for $[j_0(QR)]^2$, $[j_2(QR)]^2$, and $[j_4(QR)]^2$. The normalization is arbitrary for each curve. The figure shows that the main forward peak of the experimental cross section may be approximated by the spherical Bessel function of second order as predicted by the theory of Austern *et al.* Also, as predicted, the first-order and the third-order functions do not agree with the observed angular distribution since these functions of odd order prescribe a parity change between initial and final states.

These results show that this low-lying state is excited by a process different than that of the decay of a compound nucleus, since the angular distribution predicted by Hauser and Feshbach[8] on the basis of the statistical theory should be symmetric around 90°, and a rough calculation showed that the distribution is

expected to be almost isotropic. Besides, any reasonable level density function[9] will predict a cross section for this scattering process which is several orders of magnitude smaller than the observed value of about 40 mb. Further work will be carried out to improve the separation of the elastic and inelastic scattering at small angles in order to test the theory of Austern, Butler, and McManus.

† This work was supported by the U. S. Atomic Energy Commission and the Higgins Scientific Trust Fund.

[1] B. L. Cohen, Phys. Rev. **92**, 1245 (1953).
[2] R. M. Eisberg, Phys. Rev. **94**, 139 (1954).
[3] P. C. Gugelot, Phys. Rev. **93**, 425 (1954).
[4] E. B. Paul and R. L. Clarke, Can. J. Phys. **31**, 267 (1953).
[5] Austern, Butler, and McManus, Phys. Rev. **92**, 350 (1953).
[6] I. E. Dayton and G. Schrank (to be published).
[7] Hollander, Perlman, and Seaborg, Revs. Modern Phys. **25**, 469 (1953).
[8] W. Hauser and H. Feshbach, Phys. Rev. **87**, 336 (1952).
[9] J. M. Blatt and V. F. Weisskopf, *Theoretical Nuclear Physics* (John Wiley and Sons, Inc., New York, 1952).

Conservation of the Number of Nucleons*

F. Reines and C. L. Cowan, Jr., *University of California, Los Alamos Scientific Laboratory, Los Alamos, New Mexico*

and

M. Goldhaber, *Brookhaven National Laboratory, Upton, New York*

(Received September 27, 1954)

It has often been surmised that there exists a conservation law of nucleons, i.e., that they neither decay spontaneously nor are destroyed or created singly in nuclear collisions.[1] In view of the fundamental nature of such an assumption, it seemed of interest to investigate the extent to which the stability of nucleons could be experimentally demonstrated.[2]

To investigate the possible decay of a free proton, the large scintillation detector developed for the neutrino search[3] was employed. The detector was partially shielded from cosmic rays by placing it in an underground room with about 100 feet of rock above. The counting rate and pulse spectrum as seen by the detector may be used in arriving at a lower limit for the proton lifetime for certain postulated modes of decay. For fast particles the output of the detector is proportional to the energy deposited in the scintillator and hence for minimum ionizing particles to the track length in the scintillator.

The spectrum expected from any hypothetical proton decay depends then on the geometrical disposition of the protons as well as on the decay scheme assumed. As to the decay, we are free to assume any scheme which is consistent with the laws of conservation of charge, energy, momentum, and angular momentum. In view of the proton rest energy of 0.9 Bev and the known lighter particles into which it might conceivably decay, it seems reasonable to expect that these charged products would have a kinetic energy of the order of 100 Mev. If this decay occurred within the scintillator, the spectrum would essentially reflect the detector geometry because the decay-particle ranges would probably exceed the maximum detector dimension ($\sim$100 cm, equivalent for minimum ionizing particles to $\approx$140 Mev). There are 1.5×10^{28} protons in the scintillator (approximate chemical formula C_7H_8). The scintillator was surrounded by paraffin walls 2 ft thick. This effectively doubled the source of protons, giving $\sim3\times10^{28}$ protons. The pulse-height distribution observed is shown in Fig. 1. The integrated counting rate

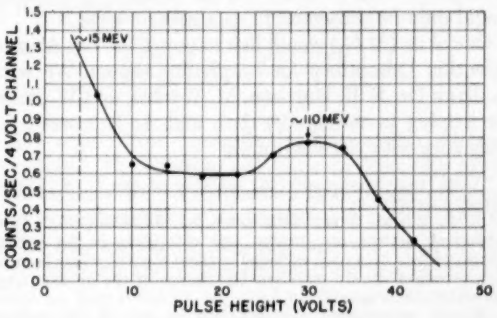

Fig. 1. Pulse-height spectrum in 300-liter liquid scintillator located underground. Time of run = 1000 sec per point. The integrated area for pulses larger than the cut-off bias, which corresponds to $\sim$15 Mev, is 6.6 counts/sec.

for pulses >15 Mev is 6.6 counts/sec. This corresponds to a lower limit of 1.5×10^{20} yr for the mean lifetime of an unbound proton. However, most of the counts in our experiment can be attributed to cosmic rays for two reasons: (1) The counting rate is in fair agreement with that expected from cosmic-ray μ mesons; (2) the spectral shape with its characteristic maximum at $\sim$110 Mev is consistent with what would be expected for cosmic-ray mesons underground traversing our scintillator. It seems, therefore, safe to conclude that at most $\sim\frac{1}{3}$ of the observed counts could be due to proton decay, and hence the lifetime of free protons is $>10^{21}$ yr. Lifetimes for some specific decay schemes which might be assumed can be shown to be even greater.

In our scintillator bound nucleons are an order of magnitude more numerous than hydrogen atoms. This yields a lifetime for bound nucleons $>10^{22}$ yr, a result which can also be interpreted as indicating the absence of "nucleon-destroying" collisions within nuclei.

It is clear that the technique here employed is capable of considerably higher sensitivity, but we believe that the values already obtained are of sufficient interest to be put on record. Higher sensitivity could be obtained both by using larger counters and by going deeper underground or in the ocean to eliminate cosmic rays.

We cannot conceive of an experiment which would prove the absolute stability of nucleons, but judging from the demonstrated "practical" stability of nucleons

we conclude that the law of conservation of nucleons can be used with considerable confidence in discussions of "practically observable" nuclear reactions. It proves very useful, for example, for hyperon reactions where it permits the conclusion that particles observed to decay into nucleons must be made from pre-existing nucleons or be produced in pairs (particles plus antiparticles). It also follows that nucleons must be found among the ultimate decay products of such hyperons; otherwise the decay of nucleons via virtual hyperon states would be observable. If nucleon pair production processes should be observed, the number of nucleons would only be conserved in an algebraic sense.

One of us (M.G.) would like to thank the Los Alamos Scientific Laboratory for hospitality shown. We wish to thank Dr. F. B. Harrison, M. Warren, and W. Baird for helping in taking the data and A. Brousseau for assistance with the electronics.

* Work performed under the auspices of the U. S. Atomic Energy Commission.

[1] E. P. Wigner, Proc. Natl. Acad. Sci. **38**, 449 (1952). Conversion of neutron into proton and vice versa in the normal process of beta decay are excluded in these considerations because such processes merely represent the change of the nucleon from one state to another.

[2] Earlier unpublished considerations by one of the authors (M.G.) based on the observed spontaneous fission rate of Th^{232} [partial half-life $\sim 1.4\times 10^{18}$ yr; see E. Segrè, Phys. Rev. **86**, 211 (1952); Hollander, Perlman, and Seaborg, Revs. Modern Phys. **25**, 469 (1953)] leads to a nucleon lifetime for bound nucleons in excess of 10^{20} yr. This follows if one makes the plausible assumption that the decay of a nucleon leaves sufficient energy for fission to take place with high probability.

[3] Reines, Cowan, Harrison, and Carter, Rev. Sci. Instr. (to be published).

Variational Principle in Quantum Mechanics

N. M. HUGENHOLTZ

CERN, Theoretical Study Group, Institute for Theoretical Physics, University of Copenhagen, Copenhagen, Denmark

(Received September 15, 1954)

ALTHOUGH, strictly speaking, a Lagrangian formalism in quantum theory is not known, it has nevertheless very often been used as a starting point for quantized field theories. The usual procedure is to apply the Lagrangian formalism before the quantization in order to derive the field equations and the Poisson brackets for the field variables. The quantization is performed afterwards by replacing the Poisson brackets by commutators. In order to overcome the apparent disadvantages of this way of proceeding, Schwinger[1] has recently developed a quantum mechanical variational principle. It is the purpose of the present note to investigate how far this attempt has succeeded.

For simplicity, we shall not consider a field theory, but a mechanical problem with n degrees of freedom. Classically, this system is described by n second order differential equations in the variables $q_k(t)$ $(k=1,\cdots,n)$ or, if one introduces n extra variables, the conjugate momenta $p_k(t)$, by a set of $N=2n$ first order equations. These canonical equations of motion can be derived from the variational principle:

$$\delta\int_{t_1}^{t_2} L\,dt=0, \tag{1}$$

where

$$L=\sum_{k=1}^{n} p_k\dot{q}_k-H(p_k,q_k,t). \tag{2}$$

If one goes over to other variables $y_l(p_k,q_k)$, where $l=1,\cdots,N$, the equations of motion are again described by (1), where now L is expressed in the new variables. If the transformation is such that L expressed in the new variables has again the form (2), apart from an irrelevant time derivative, then one speaks of a canonical transformation.

Let us now compare this with Schwinger's variational formalism in quantum mechanics. Here, one starts with a Lagrangian of the form

$$L=\tfrac{1}{2}\sum_{k,\ l=1}^{N} a_{kl}(x_k\dot{x}_l-\dot{x}_kx_l)-H(x_k,t),$$

where the matrix a_{kl} is antisymmetric and has determinant $\neq 0$. The variables $x_k(t)$ are now operators in Hilbert space. The variations have to be restricted to c-number variations. Using Schwinger's prescription, one finds the equations of motion $2\sum_l a_{kl}\dot{x}_l=\partial H/\partial x_k$ and the commutation relations $(i/\hbar)[x_k,2\sum_m a_{lm}x_m]=\delta_{kl}$. With these commutation rules, one can write the equations of motion as $\dot{x}_k=(i/\hbar)[H,x_k]$. It appears that the commutation relations are determined by the matrix a_{kl}, and the equations of motion by the Hamiltonian operator H.

We shall now see what happens if we go over to new variables $y_k=Ux_kU^{-1}$ by means of a unitary transformation which does not depend explicitly on the time. For these variables, the commutation rules are the same and the equations of motion have again the form $\dot{y}_k=(i/\hbar)[H,y_k]$. The Lagrangian function must therefore, apart from a time derivative, have the form $L'=\frac{1}{2}\sum_{k,l}a_{kl}(y_k\dot{y}_l-\dot{y}_ky_l)-H$. The fundamental point is whether this expression L' differs from L only by a time derivative. We shall show with an example that this is not the case. We take a system with one degree of freedom, where a_{kl} has the simple form $a_{11}=a_{22}=0$ and $a_{12}=-a_{21}=1$. The Lagrangian is $L=\frac{1}{4}(p\dot{q}+\dot{q}p-\dot{p}q-q\dot{p})-H$; or, if we add $\frac{1}{4}(d/dt)(qp+pq)$, we have $L=\frac{1}{2}(p\dot{q}+\dot{q}p)-H$. We apply the unitary transformation $U(p,q)=\exp(\frac{1}{3}iq^3/\hbar)$, which gives $p'=p-q^2$ and $q'=q$. The new Lagrangian is $L'=\frac{1}{2}(p'\dot{q}'+\dot{q}'p')-H$. We can easily see that $L'-L=-\frac{1}{2}(q^2\dot{q}+\dot{q}q^2)$. This difference is not the time derivative of a function of p and q and thus the two Lagrangian functions are essentially

different. It appears therefore that one needs a different Lagrangian function for each set of canonical variables, which means that this method is actually not a physical principle as in classical physics, but rather a set of rules prescribing how to find the equations of motion and the commutation rules for a given set of variables. The Lagrangian function is known when the matrix a_{kl} and the Hamiltonian operator are given; in other words, one has to know the commutation rules and the Hamiltonian beforehand. The variational method seems then to be completely superfluous.

Instead of taking a new Lagrangian function after a change of variables, it is also possible to keep the same Lagrangian expressed in the new variables. It is clear that the allowed variations for these new variables will now not be c numbers. Therefore, this procedure is just as unsatisfactory as the first.

[1] J. Schwinger, Phys. Rev. **91**, 713 (1953).

Electron Spectrum from μ-Meson Decay*

F. B. Harrison, C. L. Cowan, Jr., and F. Reines
University of California, Los Alamos Scientific Laboratory, Los Alamos, New Mexico
(Received September 24, 1954)

In a recent Letter to the Editor,[1] Sagane *et al.* state that our measurements[2] of the μ-meson decay electron spectrum give a value $\rho \sim 0$, corresponding to a zero intercept at the upper-energy end. Unfortunately, the distortions due to end effects and bremsstrahlung are severe in the detector described, and we concluded that it was not possible for us to say anything about the value of ρ. The measured spectrum was shown in our article to illustrate a method of energy calibration using the end point, which we believe is not significantly affected by the above-mentioned effects.

* Work performed under the auspices of the U. S. Atomic Energy Commission.
[1] Sagane, Dudziak, and Vedder, Phys. Rev. **95**, 863 (1954).
[2] Harrison, Cowan, and Reines, Nucleonics **12**, No. 3, 44 (1954)

Nonuniform Charge Distributions and μ-Meson Capture

F. Ferrari and C. Villi
Istituti di Fisica dell 'Universita' di Padova e Trieste, Padova and Trieste, Italy and Istituto Nazionale di Fisica Nucleare-Sezione di Padova, Padova, Italy
(Received September 28, 1954)

Extensive calculations have been carried out to evaluate the transition probability for μ-meson capture in terms of several electric charge distributions, suggested by theoretical analyses of observations on μ-mesonic x-rays and high-energy electron-nucleus scattering.

By means of the density law $\rho(x)=\rho_0 f(x)(x=r/a)$ we have derived the maximum momentum $p(x)=P_0 f^{\frac{1}{2}}(x)$ of a proton at a distance x from the nucleus center: $P_0=[3Z\pi/4I(\infty)]^{\frac{1}{2}}(\hbar/a)$ is the maximum momentum at $x=0$ and $I(\infty)$ is the second order moment of the shape function $f(x)$.

According to a nuclear model based on this relationship between the density of particles $\rho(x)$ and the maximum momentum $p(x)$, the capture probability of the meson is:

$$\Lambda=g^2\frac{M^2c}{2\pi\hbar^4}\int\psi^*\psi\left\{\frac{\nu_{\max}{}^2-\nu_{\min}{}^2}{q}\right\}_{\hbar c}dZ,$$

where $\psi(x)$ is the normalized meson wave function, $q=|\mathbf{N}+\boldsymbol{\nu}|$ ($\mathbf{N},\boldsymbol{\nu}$ neutron and neutrino momenta measured in units Mc). The quantity in brackets, averaged over the neutron-neutrino angle, is a sensitive function of the neutron excess: $\nu_{\max}$ and $\nu_{\min}$ are, respectively, the maximum and minimum neutrino momentum derived as functions of the proton momentum p in accordance with the exclusion principle and the conservation of energy and momentum.

It follows that the capture of the meson is forbidden for all protons having momentum $p<p_0(x)$; therefore, the summation over protons must be carried out in momentum space from p_0 to P_0, where

$$p_0(x)=[1+2N_0f^{\frac{1}{2}}(x)+P_0{}^2f^{\frac{1}{2}}(x)+2(\mu^2/3N_0)f^{-\frac{1}{2}}(x)-2(M_\mu/M)+2\epsilon_0]^{\frac{1}{2}}-1,$$

N_0 being the maximum neutron momentum at $x=0$, μ the meson momentum and ϵ_0 the meson binding energy on the K orbit. Consequently, the conservation of momentum requires that the integration in the ordinary space be extended from 0 to x_0, defined by the equation $p_0(x_0)=0$.

For simplicity's sake it is still possible to determine the *average* behavior of the capture probability according to the formula[1] $\Lambda=(1/\tau_0)(Z_{\text{eff}}/Z_0)^4$ ($\tau_0=2.22$ μsec) provided the effective atomic number is defined through the relation $Z_{\text{eff}}=\{(\hbar^2/M_\mu e^2)^3\pi\rho_0\phi(Z)\}^{\frac{1}{2}}$, where

$$\phi(Z)=\int_0^{x_0}\{f(x)-[p_0(x)/P_0]^3\}(x\psi)^2dx\Big/\int_0^\infty(x\psi)^2dx.$$

The Schrödinger equation, with Coulomb potentials derived from the assumed charge distributions, has been solved by usual nonlinear variational methods.

Numerical inspection of the equation defining Z_{eff} shows that while the exclusion principle and the energy-momentum conservation tend to reduce the effective atomic number, an opposite effect arises from nonuniform charge distributions allowing larger central concentrations. For this reason the values of Z_{eff} for

TABLE I. Results for the exponential charge distribution: $\rho(x)=\rho_0 e^{-x}$. ($\bar{Z}_0=11.3$). $x=r/a$.

Nucleus	$a(10^{-13}$ cm)	Z_{eff}	$\Lambda(\mu$ sec$^{-1})$
Be[a]	0.74	3.52	0.004
	0.90	3.49	0.004
C[b]	1.00	5.19	0.020
Pb[a]	1.6	27.9	16.6
	2.2	26.1	12.8
	2.9	23.9	9.0

[a] See reference 2.
[b] See reference 3.

lighter elements are not very different from those calculated by Wheeler on the basis of his simplified nuclear model.

Tables I and II give results for two limiting cases: exponential charge distribution and smoothed uniform charge distribution.

The size parameter of the exponential distribution giving the best fit in the atomic number interval including Hg, Bi, and Pb is $1.56\leq a\leq 2.3$. Values of a, smaller than those determined by Schiff[2] using the Born approximation, are consistent with the phase shift analysis of data on fast electron scattering. By fitting the transition rates measured in Fe and Sb, the size parameter of the same distribution is found to be:

Fe: $a=(1.29\pm0.20)\times10^{-13}$ cm;

Sb: $a=(1.58\pm0.25)\times10^{-13}$ cm.

The calculations with the distribution of Table II have been performed under the assumption that the thickness of the surface layer is independent of the mass number A. The calculated capture probability for C, Al, and S appear to be in good agreement with recent measurements of Alberigi-Quaranta and Pancini.[5]

According to Wheeler's theory and to shell model calculations,[6] the ratio $\Lambda_{Pb}/\Lambda_{Ca}$ is 14.3 and 6.1, respectively, whereas, on the basis of the assumed smoothed uniform distribution, one finds 6.91. This figure, however, cannot be considered as conclusive, either because increasing the rms radius by 5 to 10 percent would not be in conflict with the phase shift analysis of high-energy electron scattering data or because only the *average* behavior of the capture probability has been so far considered.

A detailed discussion on these topics will be published soon in the *Nuovo Cimento*.

TABLE II. Results for the smoothed uniform charge distribution:[a] $\rho(x)=\rho_0[1+e^{(x-1)/b}]^{-1}$. ($\bar{Z}_0=11$). $b=(0.2869\times10^{-13}/r_0)A^{-\frac{1}{3}}$; $r_0=1.05\times10^{-13}$ cm. $x=r/a$.

Nucleus	Z	Z_{eff}	$\Lambda(\mu$ sec$^{-1})$
Be	4	3.59	0.005
C	6	5.28	0.024
O	8	7.29	0.087
Al	13	11.25	0.493
S	16	13.55	1.037
Ca	20	16.25	2.145
Fe	26	18.80	3.842
Zn	30	19.94	4.863
Ag	47	22.95	8.534
Sb	51	23.48	9.350
Ba	56	24.05	10.292
Hg	80	26.20	14.497
Pb	82	26.35	14.830
U	92	27.10	16.594

[a] See reference 4.

[1] J. A. Wheeler, Revs. Modern Phys. **21**, 133 (1949).
[2] L. I. Schiff, Phys. Rev. **92**, 988 (1953).
[3] Shah, Patel, and Gatha, Proc. Phys. Soc. (London) **A67**, 92 (1954).
[4] Yennie, Ravenhall, and Wilson, Phys. Rev. **95**, 500 (1954).
[5] A. Alberigi-Quaranta and E. Pancini, Nuovo cimento **11**, 607 (1954).
[6] J. M. Kennedy, Phys. Rev. **87**, 953 (1952).

Evidence for Two-Body Spin-Orbit Forces in Nuclei

J. P. ELLIOTT AND A. M. LANE*
Atomic Energy Research Establishment, Harwell, Berkshire, England
(Received September 27, 1954)

IT is well known that the spins, level spectra, and other properties of many nuclei can be explained on the basis of a shell model in which one-body spin-orbit forces of the type $\xi(\mathbf{l}\cdot\mathbf{s})$ are assumed in addition to two-body central forces. A significant feature of this explanation is that different nuclei appear to be best fitted by different values of ξ. Apart from a possible general tendency for ξ to increase with mass number (as evidenced by the apparent improvement in the $j-j$ coupling approximation towards heavy nuclei), there is also a tendency for ξ to increase as particular shells are filled. Inglis[1] has shown that the value of ξ appears to double as the $1p$ shell is filled (the $1p_{\frac{1}{2}}-1p_{\frac{3}{2}}$ splitting is ~3 Mev at He^5, ~6.3 Mev at N^{15}). There is also some evidence of a trend towards $j-j$ coupling as the $2s$ and $1d$ shells are filled.[2] These facts suggest that a force of the simple type $\xi(\mathbf{l}\cdot\mathbf{s})$ may not be a real force in the nucleus, but rather that it is a "caricature" of a more complicated force. It has been suggested that this may be a tensor force[3] or a two-body spin-orbit force.[4]

We have investigated the second type of force:

$$T(12)\{(\boldsymbol{\sigma}_1+\boldsymbol{\sigma}_2)\cdot[(\mathbf{r}_1-\mathbf{r}_2)\times(\mathbf{p}_1-\mathbf{p}_2)]\}V(r_{12}), \quad (1)$$

where $T(12)$ may be 1 (neutral) or $(\boldsymbol{\tau}_1\cdot\boldsymbol{\tau}_2)$ (symmetric), and where $V(r_{12})$ is some potential which we have taken to be:

$$V(r_{12})=V_0\frac{e^{-r_{12}/a}}{r_{12}/a}. \quad (2)$$

It has been shown before[5] that an interaction such as (1), acting between closed shells and a loose nucleon

outside, produces on the latter an effective force of the type $\xi(\mathbf{l}\cdot\mathbf{s})$. (The fact that ξ cannot be written as a Thomas-type constant because of exchange integrals[6] is of no consequence for our purposes). In a nucleus consisting of an unfilled shell outside closed shells, the loose nucleons experience their mutual spin-orbit forces in addition to this effective one-body force. It is the presence of the mutual forces that can cause the effective ξ to change as a shell is filled. In particular, the value of ξ for one hole in a shell may be considerably different from that for one particle.

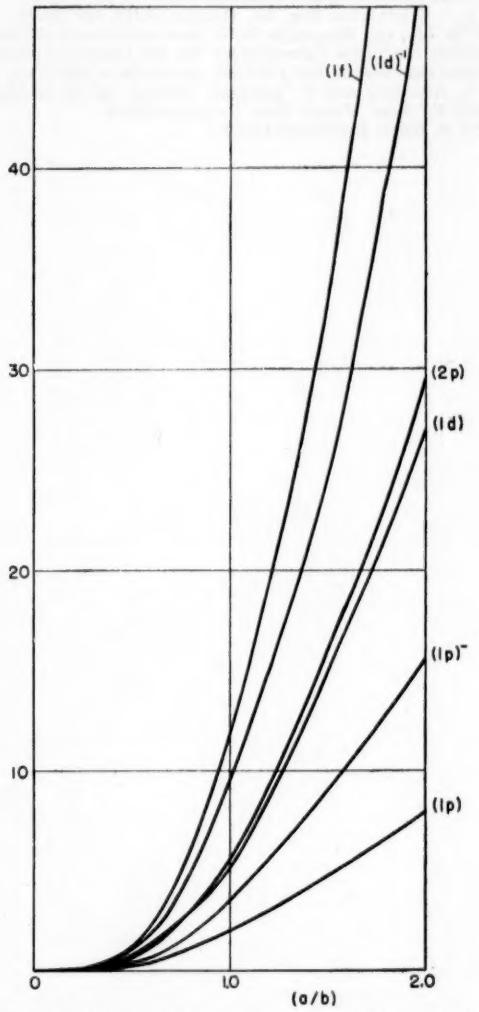

FIG. 1. Doublet splitting in units of V_0 (neutral interaction).

Using previously described methods,[7] we have evaluated the single-particle and single-hole splittings $\epsilon(nl)$ for various orbits (nl) (taking oscillator wave functions, e.g., $u_{1s}(r)=2\pi^{-\frac{1}{4}}\exp(-\frac{1}{2}\rho^2)$ where $\rho=r/b$). The results are given in Figs. 1 and 2 for neutral and symmetric forces. Rough values of the observed splittings are: $\epsilon(1p)\sim 3$ Mev,[6] $\epsilon(1p^{-1})\sim 6.3$ Mev, and $\epsilon(1d)\sim 5.1$ Mev[8] (from He^5, N^{15}, O^{17} respectively).[9]

It can be seen that, for all values of a/b, the neutral case gives qualitatively the correct ratios of the splittings, whereas the symmetric case is completely wrong.

When comparing the observed $(1p^{-1})$ and $(1d)$ splittings (ratio 6:5) with the curves (ratio 2:3), it must be remembered that we are taking the same value of a/b for both orbits, whereas consideration of Coulomb energies[10] suggests that b increases across the O^{16} closed-shell by $\sim$15 percent. Allowing for this increase brings the two ratios close together.

An interesting feature of Fig. 1 is the tendency, at any given value of a/b, for $\epsilon(nl)$ to increase rapidly on going to higher orbits. In particular, the $2p$ and $4f$ orbits are split about three and six times more than the $1p$. This suggests that the $j-j$ coupling approximation improves for nuclei above Ca^{40}. The splitting of $1d^{-1}$ (K^{39}) is predicted to be $\sim 5/3$ of the $1d$ (O^{17}) splitting, i.e., about 9 Mev. (This increase arises partly from the presence of four extra $2s$ nucleons). It should be noted, however, that if b increases with A,[10] these effects will be diminished.

For nuclei with two or more particles in an unfilled shell, detailed studies show that the usual effect of mutual neutral forces acting between the loose particles is approximately to reinforce the effective one-body splitting arising from the interaction with closed shells. In the $1p$ shell, in particular, the two-body forces give rise to an effective force $\xi(\mathbf{l}\cdot\mathbf{s})$, where ξ increases

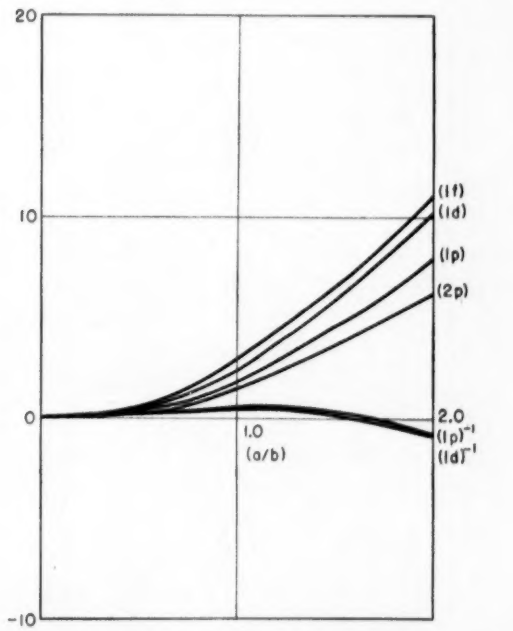

FIG. 2. Doublet splitting in units of V_0 (symmetric interaction).

steadily between He^5 and N^{15}. Consequently we conclude that a constant two-body neutral force can explain all data explicable with a one-body force of varying ξ.

Finally, we should mention that calculations similar to ours[4] made with wave functions $u_l(r)=r^l e^{-r/b}$ do not show nearly such a strong dependence of $\epsilon(nl)$ on (nl) as we have found. For $a/b=1$, their $1p$, $1d$, and $1f$ splittings are 0.75, 1.09, and 1.17 in units of V_0.

* On leave at the Massachusetts Institute of Technology, Cambridge, Massachusetts.

[1] D. R. Inglis, Revs. Modern Phys. **25**, 390 (1953).
[2] J. P. Elliott (unpublished work).
[3] E. P. Wigner, Rio de Janeiro Conference on Nuclear Physics, 1952 (unpublished).
[4] C. H. Blanchard and R. Avery, Phys. Rev. **81**, 35 (1951).
[5] J. Hughes and K. T. LeCouteur, Proc. Phys. Soc. (London) **A63**, 1219 (1950).
[6] Sack, Biedenharn, and Breit, Phys. Rev. **93**, 321 (1954).
[7] J. P. Elliott, Proc. Roy. Soc. (London) **A218**, 345 (1953).
[8] The $1d_{5/2}$ and $1d_{3/2}$ states in O^{17} have considerably different boundary conditions. Correcting for this (see reference 6 for the $1p$ case) increases the observed $\epsilon(1d)$, perhaps by a Mev or so.
[9] F. Ajzenberg and T. Lauritsen, "Energy Levels of Light Nuclei V," Revs. Modern Phys. (to be published).
[10] J. P. Elliott (unpublished work).